University of Plymouth

PEARL **https://pearl.plymouth.ac.uk**

04 University of Plymouth Research Theses 01 Research Theses Main Collection

2017

Numerical modelling of turbulence and sediment concentrations under breaking waves using OpenFOAM

Brown, Scott Andrew

http://hdl.handle.net/10026.1/8665

http://dx.doi.org/10.24382/699
University of Plymouth

All content in PEARL is protected by copyright law. Author manuscripts are made available in accordance with publisher policies. Please cite only the published version using the details provided on the item record or document. In the absence of an open licence (e.g. Creative Commons), permissions for further reuse of content should be sought from the publisher or author.

This copy of the thesis has been supplied on condition that anyone who consults it is understood to recognize that its copyright rests with its author and that no quotation from the thesis and no information derived from it may be published without the author's prior consent.

Numerical modelling of turbulence and sediment concentrations under breaking waves using OpenFOAM®

Scott Andrew Brown

A thesis submitted to the University of Plymouth in partial fulfillment of the requirements for the degree of:

DOCTOR OF PHILOSOPHY

School of Marine Science and Engineering

University of Plymouth

February 2017

Abstract

Numerical modelling of turbulence and sediment concentrations under breaking waves using OpenFOAM®

Scott Andrew Brown

This thesis presents the development of a novel numerical model capable of evaluating suspended sediment dynamics under breaking waves, and is based in the open source Computational Fluid Dynamics software, OpenFOAM®. The hydrodynamics were determined by solving the incompressible, Reynolds-Averaged Navier-Stokes equations for a two-phase fluid using the Finite Volume method, along with a Volume of Fluid scheme that modelled the interface between the air and water phases.

A new library of five turbulence models was developed to include weakly compressible effects through the introduction of density variations in the conservation equations. This library was thoroughly evaluated against existing physical data for surf zone dynamics. A skill score was applied, based on the MSE, to rank the models, with the nonlinear $k-\varepsilon$ performing best overall, and the $k-\omega$ predicting turbulent kinetic energy most accurately. Furthermore, the numerical model was shown to predict the near-bed hydrodynamics well, through comparison with new in-house physical data obtained in the COAST laboratory.

Suspended sediment concentrations were determined using an advection-diffusion methodology, with near-bed processes modelled using a flux based approach that balances entrainment and deposition. The model was validated against existing experimental data for steady state flow conditions, as well as for regular and breaking waves. The agreement was generally good, with the results indicating that the model is capable of capturing complicated processes such as sediment plumes under plunging breakers.

The validated model was applied to investigate the properties of the sediment diffusivity, ν_s, which is a vital parameter in suspended sediment dynamics. In physical experiments, ν_s is commonly estimated implicitly, based on the vertical concentration profile. In this work, this approach was applied to the numerical concentration predictions, and compared with the value directly determined within the model. The estimated value was generally acceptable providing that large horizontal concentration gradients were not present, and diffusion dominated flow advection. However, near the breaking point of waves, large errors were observed at mid-depth of the water column, which strongly correlates with a region of large flow advection relative to diffusion. Therefore, when using this estimation, caution is recommended since this approach can potentially lead to substantial discrepancies.

Acknowledgements

This thesis would not have been possible without the support of a number of people. Firstly, I would like to thank my supervisors Professor Deborah Greaves, Dr Vanesa Magar and Dr Daniel Conley for their constant support and advice over the past four years. Your guidance has been greatly appreciated.

I would also like to express my thanks to my colleagues: Dr Edward Ransley and Thomas Vyzikas for numerous productive discussions relating to OpenFOAM®, Dr Colin Whittaker for his guidance regarding physical experiments, and Robert Jane for many entertaining conversations.

I would also like to gratefully acknowledge Peter Mills for his support with the HPC facilities at Plymouth University, as well as the technical staff at the COAST laboratory for help throughout the experiments conducted there.

Finally, I would like to thank my family and friends for their love and support: in particular, I express my gratitude to my parents for their emotional and financial assistance, even if they did continually ask me whether I had finished yet. A special mention goes to my partner, Avril Daykin, for her patience, and for living through the highs and the lows of the past four years with me.

This work has been funded by the School of Marine Science and Engineering at Plymouth University; this financial support is gratefully acknowledged.

Scott Andrew Brown

February 2017

Author's Declaration

At no time during the registration for the degree of Doctor of Philosophy has the author been registered for any other University award.

Work submitted for this research degree has not formed part of any other degree either at the University of Plymouth or at any other establishment.

Relevant scientific seminars and conferences were attended at which work was often presented. As lead author, one paper has been accepted for publication in a refereed journal.

Signed: _____

Date: _____

Publications as lead author :

Brown, S.A., Greaves, D.M., Magar, V. and Conley D.C. (2016), 'Evaluation of turbulence closure models under spilling and plunging breakers in the surf zone', *in Coastal Engineering*, Volume 114, 177-193, doi:10.1016/j.coastaleng.2016.04.002

Conference proceedings :

Brown, S.A., Magar, V., Greaves, D.M., and Conley D.C. (2014), 'An evaluation of RANS turbulence closure models for spilling breakers', *in Coastal Engineering Proceedings*, 34, waves.5, 15-20 June 2014, Seoul, Korea, doi:10.9753/icce.v34.waves.5

Word count for the main body of this thesis: 67000

Contents

List of Figures

List of Tables

Abbreviations

ABS acoustic backscatter system.

ACVP acoustic concentration and velocity profiler.

AR aspect ratio.

CCM conductivity concentration meter.

CFD Computational Fluid Dynamics.

CI confidence interval.

COAST Coastal, Ocean and Sediment Transport.

DCIV digital correlation image velocimetry.

DEM discrete element method.

DES detached eddy simulation.

DNS direct numerical simulation.

FOV field of view.

FPS frames per second.

HRN high Reynolds number.

LDV laser doppler velocimetry.

LES large eddy simulation.

LRN low Reynolds number.

MMC maximum matching cost.

MSE mean square error.

MWL mean water line.

NL nonlinear.

NRMSE normalised root mean square error.

OBS optical backscatter system.

OWT oscillating water tunnel.

PID particle identification.

PISO Pressure Implicit with Splitting of Operators.

PIV particle image velocimetry.

PTV particle tracking velocimetry.

RANS Reynolds-Averaged Navier-Stokes.

RAS Reynolds-averaged simulation.

RMSE root mean square error.

RNG renormalised group.

RSM Reynolds stress model.

SIMPLE Semi-Implicit Method for Pressure-Linked Equations.

SPH Smoothed Particle Hydrodynamics.

SSD suspended sediment dynamics.

SST shear stress transport.

SWL still water level.

TKE turbulent kinetic energy.

TSS transverse suction system.

VOF volume of fluid.

Nomenclature

Relevant Parameters

α	Angle of the beach to the horizontal.
α_1	Colour function for the VOF scheme.
α_R	Relaxation zone weight.
β	Inverse Schmidt number.
χ_R	Relaxation zone coordinate.
Δz_w	Cell size adjacent to the bottom boundary.
δ	Height of boundary layer.
δ_v	Height of viscous sublayer.
δ_w	Height of wave boundary layer.
ε	Turbulent kinetic energy dissipation rate.
η	The surface elevation of the wave.
η_k	Kolmogorov microscale.
γ	Angle between tangential flow and direction of steepest slope.
κ	The von Kármán constant.
λ	Length of the relaxation zone.
μ	Dynamic viscosity.
μ_s	Static friction.
μ_t	Dynamic eddy viscosity.
ν	Kinematic viscosity.
$\nu_{s,est}$	Estimated sediment diffusivity.

$\nu_{s,num}$ Numerically applied sediment diffusivity.

ν_s Sediment diffusivity.

ν_t Kinematic eddy viscosity.

ω 1) Characteristic frequency of turbulence; 2) Angular frequency.

ϕ Velocity flux.

ϕ_i Angle of repose.

ϕ_r Final angle of repose.

ψ Stream function.

ρ Density of the fluid.

ρ_s Density of the sediment.

σ Standard deviation.

σ_c Schmidt number.

τ 1) Stress Tensor; 2) Reynolds stress tensor.

$\tau_{\alpha,cr}$ Critical shear stress on bed of angle α.

τ_{cr} Critical bed shear stress.

τ_w Wall shear stress.

θ Shields parameter.

θ_{cr} Critical Shields parameter.

ξ Iribarren number.

ζ Ratio of eddy and molecular viscosities.

a Wave amplitude.

b Rouse parameter.

C Suspended sediment concentration.

C_a Concentration at the height $z = a$.

c_a Absolute phase speed (including currents).

c_D Drag coefficient.

C_o Courant number.

c_p Wave phase speed.

c_r Current speed.

C_s Roughness constant.

D Deposition.

d Sediment grain size.

d_{50} Median sediment grain size.

D_f Diffusion.

E 1) Entrainment; 2) Error.

f Face centre.

g Acceleration due to gravity (magnitude).

H Wave height.

h Water depth.

I Turbulent intensity.

K Mean kinetic energy.

k 1) Turbulent kinetic energy; 2) Wavenumber.

k_N Nikuradse roughness.

k_N^+ Non-dimensionalised form of the Nikuradse Roughness.

L Wavelength.

m Elliptic integral parameter.

N Centre of neighbouring control volume.

P Centre of present control volume.

p Pressure.

p_0 Reference pressure.

P_k Turbulent kinetic energy rate of production.

p_{rgh} Non-hydrostatic pressure.

q Fluid speed in the reference frame moving with the wave.

Re Turbulent Reynolds number.

Re_g Grain Reynolds number.

s Ratio of fluid and sediment densities.

SS Skill score.

T Wave period.

t Time.

u Horizontal component of velocity (cross-shore).

u^+ The dimensionless mean velocity tangential to the wall.

u_* The friction velocity.

U_r Ursell parameter.

V Volume of the control volume.

v Horizontal component of velocity (long-shore).

w Vertical component of velocity.

$w_{s,hind}$ Hindered settling magnitude.

w_s Settling velocity magnitude.

x Horizontal coordinate.

x_b x coordinate at which wave breaking occurs.

y Horizontal coordinate.

z Vertical coordinate.

z^+ The dimensionless distance from the wall.

z_0 Roughness height.

z_a Reference height, $z = a$.

$\mathbf{d}$ Vector joining two cell centres.

$\mathbf{S}$ Rate of strain tensor.

$\mathbf{s}$ Surface normal vector.

$\mathbf{w_s}$ Settling velocity vector.

$\mathbf{\Omega}$ Mean rate of rotation tensor.

$\mathbf{u}$ Velocity vector.

cn Jacobian elliptical functions.

$\mathbf{I}$ Identity Matrix.

Conventions

Δf Change in variable f.

$\overline{f}$ Time-average of variable f.

$\widetilde{f}$ The phase-average of variable f.

f The instantaneous value of variable f.

f' Fluctuations in variable f.

$\mathbf{F}$ Rank 2 Tensor.

$\mathbf{f}$ Vector.

f/F Scalar.

Subscripts

f_0 Value of variable f in deep water.

f_τ Tangential component of variable f.

f_{bed} Value of variable f at the sediment bed.

f_b Value of variable f at the breaking point.

f_{log} Value of variable f in the logarithmic sublayer.

f_{max} Maximum value of variable f.

f_{nb} Value of variable f in the cell above the sediment boundary.

f_P Property f of the particle.

f_{vis} Value of variable f in the viscous sublayer.

f_w Wall value of variable f.

Operators

$\cdot$ Dot product.

$\nabla \times \mathbf{f}$ Curl of vector variable $\mathbf{f}$.

$\nabla \cdot \mathbf{f}$ Divergence of vector variable $\mathbf{f}$.

: Double inner product.

∇f Gradient of scalar variable f.

$\nabla^2 f$ Laplacian of scalar variable f.

$\times$ Cross product.

$\mathbf{f}^T$ Transpose of variable $\mathbf{f}$.

Chapter 1

Introduction

Coastal sediment transport is a vital consideration for coastal engineering applications since beaches help to protect coastal regions by dissipating energy through the process of wave breaking. The effectiveness of a particular beach at doing this depends largely on its topography, which is influenced by the wave climate and the sediment types available in the region. The types of sediment also impact marine life which can depend on certain sediment sizes for breeding and feeding, and, hence, coastal sediment transport is also of considerable interest to marine biologists. Both the morphology of a beach, and the sediment types available, at a particular location are controlled by the balance of accretion, which tends to occur during calm sea state conditions, and large erosion events caused by sea storms. With climate change experts predicting an increase in the frequency and strength of these sea storms (IPCC 2013), it is possible that coastal regions could dramatically change in the future. This will potentially have major implications for coastlines and marine life and, therefore, it is vital that the processes behind coastal sediment transport are well understood.

Sediment transport is traditionally split into two classifications: bed load and suspended load. Suspended sediment transport is most influential in environments where large quantities of fine sands are found. As well as having a large influence on coastal erosion, suspended sediment concentrations can also impact upon biological processes, such as light penetration for ecosystems, making it essential to be able to predict levels of sediment suspension and transport accurately. As a consequence, substantial research effort has been put into understanding the processes behind suspended sediment dynamics (Puleo et al. 2003; van Rijn 2007).

In the near-shore region, waves represent a major driver of suspended sediment concentrations. Breaking waves in the surf zone generate turbulence, which, together with bottom stresses, undertow, and other near-shore currents, are capable of suspending and transporting large quantities of sediment. The characteristics of this wave-induced turbulence are influenced by many parameters such as the energy of the wave and the gradient of the beach. Turbulence generated by breaking waves on a sloping beach has been investigated both experimentally (Ting and Kirby 1994, 1995, 1996) and numerically (Lin and Liu 1998*a*; Bradford 2000; Christensen 2006) by a number of authors. However, the results of the research vary, with numerical simulations generally over-estimating levels of turbulent kinetic energy (TKE).

In numerical models that describe suspended sediment dynamics, substantial consideration must be given to the incorporation of turbulent effects. Suspended sediment concentrations in the surf zone are controlled by the balance between downward settling of the particles, due to gravity, and upward mixing of sediment arising from turbulent motions and wave orbital motion. It is commonly assumed that the turbulent contributions can be described in terms of sediment concentration gradients (Ogston and Sternberg 2002). This leads to many numerical models being based on advection-diffusion theory (Nielsen 1992; Hsu and Liu 2004; van Rijn 2007; Roelvink et al. 2009; Ma et al. 2014), which for a steady flow, without horizontal gradients, can be expressed as

$$wC - w_s C = \nu_s \frac{\partial C}{\partial z}. \tag{1.1}$$

Here C is the suspended sediment concentration, w is the vertical component of the flow velocity, w_s is the sediment settling velocity, and ν_s is the sediment diffusivity coefficient. In general, the settling velocity is well understood, with numerous parameterisations available (Rubey 1933; Soulsby 1997), and the distribution of suspended sediment concentrations can be measured with reasonable accuracy, both in the laboratory and the field. However, greater uncertainties still remain regarding the sediment diffusion process, and hence this has been the focus of many studies (Ogston and Sternberg 2002; Aagaard and Jensen

2013; Malarkey et al. 2015).

When using a numerical model, it is common to assume that ν_s is proportional to the eddy viscosity, $\nu_s = \beta\nu_t$, and is usually obtained through a turbulence closure model. The constant of proportionality, β, is the inverse of the turbulent Schmidt number, σ_c, which relates the turbulent and sediment mixing. A value of $\beta = 1$ implies that sediment mixes at the same efficiency as turbulent motion, whereas $\beta > 1$ or $\beta < 1$ implies greater or less efficiency, respectively. The value of β has also been the focus of a number of experimental studies (van Rijn 1984*b*; Cellino 1998; Ogston and Sternberg 2002), with values varying substantially between studies ($0.1 < \beta < 10$). Many numerical models reproduce laboratory concentration profiles more accurately when using values of β greater than one (Hsu and Liu 2004; Ma et al. 2014; Malarkey et al. 2015). The inconsistency between studies could imply that both the sediment diffusivity and the eddy viscosity are difficult to measure accurately.

The experimental method used to estimate ν_s in steady horizontal flows is relatively simple, and is based on perfectly acceptable assumptions. Rearranging equation (1.1), and neglecting the vertical velocity term, yields a formulation for ν_s, which only depends on the vertical distribution of the suspended sediment concentration,

$$\nu_s = \frac{-w_s C}{\partial C/\partial z}. \tag{1.2}$$

This is clearly a very attractive method for estimation of the sediment diffusivity, since the formulation is simple and the suspended sediment concentration can be obtained with reasonable accuracy. Hence, many researchers extend the use of this methodology to wave-driven environments. However, in these conditions, the suspended sediment concentrations are continuously changing due to the time-dependent nature of waves. A commonly used work-around for this problem, is to time-average over a series of waves, allowing a steady state to be obtained. Although this permits equation (1.2) to be extended to wave-driven conditions, significant uncertainty is introduced since the assumption that the phase-resolved components are negligible has largely been untested.

In this study, it is hypothesised that substantial error may be introduced to sediment diffu-

sivity predictions in the surf zone due to the process of time-averaging, which ignores the fluctuations of ν_s. It is also proposed that neglected factors, such as horizontal suspended sediment concentration gradients and wave orbital motion, could negatively influence the estimations. Any error introduced through the methodology may contaminate comparisons between ν_s and ν_t, making it difficult to determine the correct value for the Schmidt number. Since this value is a common consideration in numerical models, understanding and eliminating any sources of error in β is a vital process for improvement of these models and, hence, gaining additional confidence in predicted values.

1.1 Description of the Project

The overall aim of the present study is to improve the understanding of the role played by turbulent motion in suspended sediment dynamics. The project focuses on the sediment diffusivity, and in particular the methodology used to calculate the profile. Further understanding and confidence in the calculation of this parameter is key to determining the relationship between turbulent motion and sediment diffusion, and hence improving numerical predictions of suspended sediment transport. In order to assess this problem, it is crucial that the numerical model accurately captures time variant flows, resolves the free surface and accounts for both horizontal (cross-shore) and vertical sediment transport. This will allow evaluation of the neglected contributions such as fluctuations in the eddy viscosity, wave orbital motion, and horizontal sediment transport.

To achieve this, the project utilises the open source Computational Fluid Dynamics (CFD) code, OpenFOAM®, to model the generation of turbulence by breaking waves. Waves are generated using `waves2Foam`, a wave generation toolbox which solves the Reynolds-Averaged Navier-Stokes (RANS) equations and uses a two-phase volume of fluid (VOF) advection scheme to track the free surface. A suspended sediment module will then be integrated into the existing functionality of OpenFOAM®.

This project is split into three main objectives, which are as follows:

- The first objective of this work is to validate that `waves2Foam` is capable of predicting

surf zone turbulence to at least the same degree of accuracy as previous work with Reynolds-averaged simulations (RASs). In order to determine this, comparisons are made, both with previous experimental (Ting and Kirby 1994) and numerical results (Lin and Liu 1998*a*; Bradford 2000; Jacobsen et al. 2012). Considering the importance of accurate predictions of wave breaking characteristics and turbulence generation in the surf and swash zone, the validation process includes a detailed evaluation of available turbulence models in order to assess which best represents laboratory data. A number of turbulence models have previously been considered by different researchers (Bradford 2000; Lin and Liu 1998*a*; Jacobsen et al. 2012). However, to the best of the present author's knowledge, there does not exist a direct comparison of popular two-equation turbulence closure models for the application of breaking wave simulations in a two-phase VOF model.

- The second objective of this work is to develop and implement a sediment transport module for OpenFOAM®, capable of predicting suspended sediment concentrations under a range of different flow conditions. Previous sediment transport and morphological numerical models have been developed in the OpenFOAM® framework (Liu 2008; Jacobsen 2011) using advection-diffusion theory for the suspended load, but they have not been made publicly available. Building upon the published records of these studies, a solver based on advection-diffusion theory is designed and implemented along with a novel boundary condition capable of assessing the exchange of sediment at the bed. The ability of the numerical model to give both qualitative and quantitative predictions of vertical suspended sediment profiles is then thoroughly validated against existing experimental (Sumer et al. 1996; Cellino 1998; Dohmen-Janssen and Hanes 2002; Otsuka and Watanabe 2012; Sato et al. 1990) and numerical data (Hsu and Liu 2004; Ma et al. 2014).

- The third objective of this study is to analyse the accuracy of a common experimental calculation for the sediment diffusivity, under a range of fluid flows. In the numerical model, the sediment diffusivity is a known input, which is based on the numerical pre-

diction for the eddy viscosity, obtained through a turbulence closure model at each time step. Therefore, the time-averaged sediment diffusivity can be directly determined from the eddy viscosity, which is fundamental to the approach adopted in this study.

The experimental methodology (equation 1.2) is applied to obtain estimations for the sediment diffusivity profiles using the predicted vertical suspended sediment concentration distributions obtained in the validation of the numerical model. These predictions are then compared with the value directly determined from the eddy viscosity, allowing quantification of the error associated with using the methodology in conditions of varying complexity. This is clearly the key advantage of using a numerical model to assess this problem, since experimental studies do not have the option of validating the values obtained with this methodology. Furthermore, a large amount of additional data can be retrieved from a numerical model, which cannot be measured experimentally. This can potentially be used to explain any discrepancies between the directly determined and estimated profiles, through the analysis of contributions neglected in the derivation of the methodology.

It is hypothesised that the estimated and directly determined values agree under certain simplified conditions, such as steady state flows, but can be a substantial source of error in more complex time variant cases. An estimated error is presented for each of the flow types considered in this study. This provides a valuable indication of confidence regarding the application of this methodology to any future research.

1.2 Outline of Thesis Chapters

The objectives set out for this project have been achieved and published in the nine chapters composing this thesis. In Chapter 2 previous studies, which both relate to and provide motivation for this work, are briefly reviewed. These studies focus on the processes involved in breaking waves, and in particular the generation of turbulence under different breaker types. Sediment transport is also covered with particular attention on the profiles of suspended loads, and investigations into the sediment diffusivity. Laboratory and numer-

ical studies are discussed separately, with the main emphasis of the numerical component being on previous CFD studies.

Chapter 3 summarises established theory, which is relevant to this study. Three main areas are covered: turbulence, waves, and sediment transport. This chapter is intended to fill in any knowledge gaps for the reader, making the concepts and discussion in the later analysis easier to follow.

Chapter 4 outlines methodologies used in CFD, with special attention given to the implementation in OpenFOAM®. These processes include discretisation, pressure-velocity coupling techniques and wave generation. The turbulence models, and near-wall treatment, available within OpenFOAM® are then examined, along with how they have been implemented. The development of the suspended sediment concentration model is then described along with the new boundary condition for use at sediment beds.

Chapter 5 presents the validation of hydrodynamic predictions under spilling and plunging breakers on a beach of constant gradient, using OpenFOAM® and `waves2Foam`. Mesh generation techniques are discussed along with boundary and initial conditions. Sensitivity analysis is presented to both justify these choices as well as to create high quality simulations. A large component of this chapter is dedicated to an evaluation of five turbulence closure models for surf zone dynamics. Turbulence closure modelling is considered to be a vital component of the numerical model since it simplifies very complicated procedures and is far more computationally efficient than attempting direct numerical simulations to resolve turbulent structures. Furthermore, the eddy viscosity obtained from the turbulence closure model feeds directly into the suspended sediment concentration model, and hence is one of the fundamental requirements to achieving physically correct results. In order to assess the turbulence models, a skill score technique is employed to rank them, based on comparison with experimental data for free surface elevation, time-averaged velocity and TKE (Ting and Kirby 1994). Qualitative comparison with observations from further laboratory experiments is then performed before comparison with other numerical predictions, using the highest ranking turbulence model.

In Chapter 6, the hydrodynamic conditions near the bed are explored in more detail. Time series obtained 1 cm above the sediment bed, at various sampling locations within the surf zone, are compared with experimental data for velocity and TKE (Otsuka and Watanabe 2012). Discrepancies between the numerical predictions and experimental data are then addressed through a series of particle tracking velocimetry (PTV) experiments conducted in a wave flume located in the Coastal, Ocean and Sediment Transport (COAST) laboratory at Plymouth University. The setup of these experiments, along with comparison of results with both the numerical model and previous experimental data of Otsuka and Watanabe (2012), are then presented.

In Chapter 7, a number of validation cases for the suspended sediment concentration model are presented. The cases progressively increase in complexity, starting from a case which has an analytical solution, and building up to chaotic and turbulent conditions observed under breaking waves. All cases are compared with existing experimental data and previous numerical studies, where possible. Sensitivity analysis is performed to assess mesh resolution, in particular the near-wall cell size, and the effect of the Schmidt number.

Chapter 8 is dedicated to the analysis of sediment diffusivity predictions. Following a methodology commonly used in the manipulation of physical data, estimates of the sediment diffusivity profiles are obtained, and compared to the profiles directly determined from the eddy viscosity. The process utilises vertical suspended sediment concentration profiles, obtained from each of the cases considered in the validation of the numerical model. The error associated with use of this methodology is quantified for each case and, where large errors are observed, further analysis is presented to assess the origin of such errors.

In Chapter 9 a summary of this project is given with emphasis on the novel contributions made and the conclusions drawn. Suggestions for future research directions, building on this project, are also provided.

Chapter 2

Review of Literature

This chapter focuses on the discussion of previous research effort that is relevant to the present project, incorporating both physical and numerical studies. The chapter is loosely split up so that the three objectives stated in Chapter 1 are considered separately: breaking waves and turbulence generation are addressed in Section 2.1, suspended sediment concentrations in Section 2.2, and sediment diffusivity in Section 2.3.

2.1 Breaking Waves

2.1.1 Laboratory Experiments

Investigations into turbulent kinetic energy (TKE) production and dissipation in the surf zone have been conducted by a number of authors. Nadaoka et al. (1989) examined the structure of turbulent flow fields under breaking waves in the surf zone using fibre-optic laser doppler velocimetry (LDV). The results implied that the large eddies are mainly responsible for generation of Reynolds stress in the upper water layer and have varying characteristics depending on their position in the wave. Near the wave crest, horizontal eddies dominate, which are almost 2-D with axes parallel to the crest, whereas behind the wave crest the eddy structure becomes more 3-D with obliquely descending eddies. Furthermore, by decomposing the velocity field into two components, an irrotational motion corresponding to the waves, and a rotational motion describing the turbulent eddies, Nadaoka et al. (1989) studied the breaking wave dynamics of mean vorticity associated with the large scale eddies. The eddying motion component was shown to cause substantial increase in mass and momentum transport, and that the vorticity effects have a large influence on the water surface elevation of breaking waves.

Ting and Kirby (1994, 1995, 1996), conducted a thorough set of laboratory experiments into both spilling and plunging breakers on a beach with $1/35$ slope. Cnoidal waves were generated at the wave flume inlet, and measurements along the beach were performed. The measurements were phase-averaged over a period of twenty minutes. Ting and Kirby (1994) analysed the evolution of the surface elevation, as well as the variation of mean horizontal velocity and TKE with depth under breaking waves. The fluid velocities were obtained using a fibre-optic laser-Doppler anemometer and the TKE values were then calculated through application of the formula

$$k = \frac{2}{3}(\widetilde{u'^2} + \widetilde{w'^2}), \tag{2.1}$$

where $\sim$ represents phase-averaging. The turbulent fluctuations, u' and w', were obtained from separate experiments, since only one velocity component could be measured at a time. Despite similarities in the wave profiles in the turbulent bore region of both breaker types, TKE characteristics differ substantially between the two cases. TKE is transported seaward under the spilling breakers and the dissipation rate is slow, whereas under the plunging breaker TKE is transported landward and is dissipated within one wave cycle. Furthermore, the TKE varies with depth in the spilling case, which is not evident under the plunging breakers. Based upon the correlation between TKE and undertow, as well as the peak of turbulent velocity measurements, Ting and Kirby (1994) also suggest that plunging breakers can transport sediment landward and hence correspond to accretional wave conditions, whereas the spilling breakers are associated with erosion.

Ting and Kirby (1995, 1996) extended this work further by examining the turbulence structure and transport processes under plunging and spilling breakers, respectively. They concluded that the turbulent structures, such as the length and velocity scale of the large eddies, under breaking waves are determined by the wave characteristics. They suggested that under plunging breakers, the most important characteristics are the ratios of wave height to water depth, H/h, and the water depth to wavelength, h/L. Furthermore, they observed that under the crest of plunging breakers the turbulence intensity is at its largest,

before rapidly dissipating after the wave passes, causing the turbulence to die out between breakers. On the other hand, turbulence generated by spilling breakers is generally well developed in the surf zone, which is indicated by the presence of a $-5/3$ gradient in the energy spectrum (see Section 3.1.2.12 for further details). Differences between the two cases were also observed when considering the rates of mixing. They found that for plunging breakers the rate of vertical mixing is large since turbulence is spread downwards by the large eddies, leading to saturation of the entire water depth in the inner surf zone. Ting and Kirby (1996) showed, moreover, that the mixing length of the spilling case is much smaller, being within a factor of $10-20\%$ of the water depth. Furthermore, the surface generated turbulence in spilling breakers is spread slowly downwards, mainly through diffusion, whereas in the plunging case both advective and diffusive transport are important since the large eddies generated in the surface roller are advected behind the wave front. Therefore, turbulence production below the trough of a spilling breaker only amounts to a small portion of the total wave energy loss.

Another study into velocity, turbulence and mean water levels under plunging and spilling breakers was performed by Govender et al. (2002), who obtained velocities throughout the whole water column using digital correlation image velocimetry (DCIV). The results were consistent with previous experiments where the highest velocities and turbulence generation occurs in the front part of the wave crest near the roller region. Furthermore, TKE levels were found to compare well with the LDV experiments conducted by Ting and Kirby (1994).

More recently, Kimmoun and Branger (2007) used particle image velocimetry (PIV) to investigate the flow structure under a spilling-plunging breaker in the surf and swash zones on a beach with $1/15$ slope. By using PIV instead of LDV, they could examine a small space-time field rather than a single point in space over time. The results were found to be consistent with the data from Ting and Kirby (1994) and Govender et al. (2002). As was found by Nadaoka et al. (1989), Kimmoun and Branger (2007) also present evidence to imply that horizontal eddies are generated at the front of the breaking crest before being advected obliquely towards the bottom of the tank, moving at a slower speed than the wave

crest. Furthermore, only a small portion of the wave energy loss was found to be dissipated below the trough level.

2.1.2 Numerical Studies

The mean characteristics of surf zone turbulence have also been investigated using Reynolds-averaged simulation (RAS) solvers and have been validated against the laboratory data of Ting and Kirby (1994, 1995, 1996). Lin and Liu (1998*a*) developed a model which used a volume of fluid (VOF) scheme to track the free surface and a nonlinear Reynolds stress model, based on the work of Shih et al. (1996), to investigate the Reynolds stresses and the strain rate of the mean flow below spilling breakers.

The advantage of the turbulence model of Shih et al. (1996) is that it attempts to introduce anisotropic effects through an additional nonlinear stress term, based on a weighting of the fluctuating components. As well as comparing the phase-averaged wave periods of various mean quantities with the data of Ting and Kirby (1994), Lin and Liu (1998*a*) also produced results for mean velocity, turbulence transport mechanisms, and the spatial distribution of turbulence and vorticity fields. Their results suggested that turbulence in spilling breakers is a local process, since the mean vorticity and turbulence intensity are very weak in all regions outside of the breaking wave front, and large within this region. Furthermore, they identified three distinct regions within the water column: the surface roller region where turbulence is generated, a transitional region about three times the size of the roller region where mean vorticity is generated, and a bottom region of nearly uniform mean horizontal velocity. The different mechanisms for turbulence transport also vary between the three regions. The processes are very weak in the bottom region, and in the transition region the dominant mechanisms are turbulence production, vertical diffusion and vertical convection. The production component is correlated with the passage of the breaking wave, and gives an initial increase in TKE, with the convection and vertical diffusion creating a second, larger increase at around $0.1T$ after the passage of the wave front. Dissipation gradually increases until it overpowers all of the other turbulent contributions, reducing the rate of change of TKE throughout the water column. Lin and Liu (1998*a*) also conducted a sensitivity analysis on

the coefficients in the turbulence model, concluding that the model was only sensitive to the production rate of turbulence dissipation.

Lin and Liu (1998*b*) also investigated turbulence and solute mixing under plunging breakers using the same model as presented by Lin and Liu (1998*a*), with the addition of a solute transport model. They found that although turbulence was generated as the plunging jet hit the trough, the effects are only felt locally, and the jet has little impact on turbulence transport mechanisms further downstream. Instead, the most active region of turbulence and vorticity generation occurs in the roller region, which is moving with the front of the wave. Furthermore, the plunging breaker's roller spreads downward as the breaking wave front propagates, with penetration up to half the water depth. This differs from the spilling breaker where the roller is generally confined to the top of the wave, implying that turbulence transport is much larger in plunging breakers.

Bradford (2000) also used a RAS solver, along with a VOF scheme, to simulate spilling and plunging breakers over a sloping bed, and compared the results with the laboratory data from Ting and Kirby (1994). A comparison between three turbulence models was presented: a one-equation turbulence model, where the transport equation for TKE, k, is solved and the dissipation rate, ε, is approximated by

$$\varepsilon = c_\mu \sqrt{\frac{3}{2}} \frac{k^{3/2}}{l_m}, \tag{2.2}$$

where c_μ is an empirical constant and l_m is a representative length scale of the turbulent eddies; and two-equation turbulence models, the $k-\varepsilon$ model from Launder and Sharma (1974) and the RNG $k-\varepsilon$ developed by Yakhot et al. (1992). Furthermore, the calculation for the eddy viscosity included a damping function, which Bradford (2000) suggested was necessary due to regions of low turbulence. Therefore, the eddy viscosity was calculated using

$$\nu_t = c_\mu f_\mu \frac{k^2}{\varepsilon}, \qquad f_\mu = \exp\left(\frac{-3.4}{(1+\frac{Re}{50})^2}\right), \tag{2.3}$$

where $Re = \frac{k^2}{\nu\varepsilon}$ is the turbulent Reynolds number. However, the simulations had a couple of

limitations. Firstly, the generation of waves caused a constant increase of mean water volume in the domain, limiting the number of wavelengths that could be simulated. Secondly, the curling wave crest in the plunging breakers could not be resolved, with explanations given as a lack of surface resolution or poor representation of the wave dynamics in the crest region.

The results of Bradford (2000) implied that the use of the one-equation turbulence model with a mixing length proportional to the water depth was inadequate since the model was overly dissipative prior to wave breaking. Although undertow predictions were similar to the two equation model, the additional dissipation led to under-prediction of wave heights and over-prediction of mean water line (MWL) throughout most of the surf zone. The two-equation models produced more accurate results, with the RNG $k-\varepsilon$ turbulence closure model predicting higher initial breaking wave heights and smaller heights after breaking. This was due to smaller predictions of turbulence magnitudes in the outer surf zone, compared to the $k-\varepsilon$ model. This reduction in turbulence led to larger wave heights before breaking, therefore causing more energy dissipation after breaking and, consequently, smaller wave heights. Therefore, they concluded that the RNG $k-\varepsilon$ model could predict the outer surf zone dynamics more accurately than the $k-\varepsilon$ or one-equation models, and also generally predicted TKE levels more accurately in the inner surf zone.

Christensen et al. (2000) modelled TKE levels and sediment transport in the surf zone using a RAS type solver along with a $k-\omega$ turbulence model developed by Wilcox (1988) and a sediment transport model. Similar to the other RASs, the results are compared with Ting and Kirby (1994). Like Lin and Liu (1998*a*,*b*) and Bradford (2000), Christensen et al. (2000) found that the levels of TKE in the surf zone were generally over-predicted, by a factor that could be $2-3$ times larger. Furthermore, in the sediment transport model, the suspended sediment distribution was found using an advection-diffusion equation, which relies on the eddy viscosity. Since the values of TKE were too large, the eddy viscosity, and hence the sediment transport rates, were also over-estimated. However, despite these large discrepancies, and over-estimated undertow, the model still predicted the correct qualitative

behaviour under the two breaker types: offshore transport under spilling breakers and onshore under plunging breakers.

Jacobsen et al. (2012) created a RAS solver in the open source Computational Fluid Dynamics (CFD) software OpenFOAM®, which also included a modified $k-\omega$ turbulence model. The $k-\omega$ turbulence model was developed by Wilcox (2006) but in Jacobsen et al. (2012) the production term for TKE is modified according to Mayer and Madsen (2000), who suggested that it should be related to the vorticity rather than the mean strain rate of the flow. Jacobsen et al. (2012) validated the model by comparing surface elevation and undertow under spilling breakers with the data from Ting and Kirby (1994). The results implied that the model could predict surface elevation in the surf zone to a reasonable accuracy as long as the aspect ratio (AR) was approximately 1, i.e. $\Delta x \approx \Delta z$. Undertow results were also reasonable, with more accurate performance before and just after breaking, and larger discrepancies in the turbulent bore.

The aim of this study is to simulate the turbulent characteristics of plunging and spilling breakers with a CFD method, before exploring their effects on sediment dynamics. Comparisons will be made with both the previous experimental and numerical data considered within this section, with particular focus on the work of Ting and Kirby (1994), as it has been used as a benchmark test for many numerical models. This should ensure that the turbulent characteristics under breaking waves are represented as well as possible in the present model.

2.2 Suspended Sediment Dynamics

2.2.1 Laboratory Studies

Suspended sediment concentrations have been studied in great detail for a range of fluid flows including steady channel flows (Coleman 1970; Sumer et al. 1996; Cellino 1998), oscillatory flows (Ribberink and Al-Salem 1995; Thorne et al. 2002; Dohmen-Janssen and Hanes 2002) and breaking wave conditions (Sato et al. 1990; Kobayashi and Lawrence 2004; Otsuka and Watanabe 2012). This section is dedicated to

describing the outcomes of these studies, and discussion of the common findings between them.

2.2.1.1 Steady Flow

Substantial research effort has focused on the study of the suspended sediment transport processes under horizontal channel flow conditions (Coleman 1970, 1986; Lyn 1988; Wang and Qian 1989; Sumer et al. 1996; Cellino 1998). These studies were conducted in recirculating flumes, with the concentration profiles generally following a modified Rouse equation (Cellino 1998). The modification occurs in the Rouse parameter, b, which is divided by a fitted parameter, β, representing the mixing efficiency of the sediment (this will be discussed in further detail in Section 2.3). For additional information on the Rouse profile see Section 3.3.4.1.

It is well established that suspended sediment distributions in steady horizontal channel flow follow a Rouse profile away from the near-bed region. Hence, the emphasis of the experimental studies performed in tilting flumes is often not on the distribution of the concentration but instead focus on the processes driving sediment transport. This includes sediment diffusivity (Coleman 1970; Cellino 1998) as well as concentration effects on the velocity profiles (Vanoni 1946; Einstein and Chien 1955; Coleman 1986; Lyn 1988; Sumer et al. 1996) and turbulence (Wang and Qian 1989). The velocity and turbulence studies are briefly analysed here but the sediment diffusivity is discussed in detail in Section 2.3.

Coleman (1986) varied the suspended sediment concentration while keeping the flow depth and slope of the flume constant. This allowed the mean velocity profile, measured using a Pitot-tube, to be assessed as a function of sediment concentration. It was found that the logarithmic velocity region reduced in size for larger concentrations. This logarithmic region was also shifted compared to clear water flows, with the bottom edge occurring at lower values in terms of wall units (see Section 3.1.3.2).

Lyn (1988) used an asymptotic similarity approach, based on power laws with varying exponent, along with laboratory measurements, obtained using the laser Doppler technique, to examine the effect of concentration on velocity profiles. The results implied that the con-

centration needed to be described by two length scales, representing the inner and outer flow regions, whereas the velocity could be described by a single parameter. Furthermore, the effect of suspended sediment on the mean velocity profile was found to be confined to a reasonably thin layer near the bed.

Sumer et al. (1996) focused on the velocity and concentration profiles in the sheet flow layer, which is adjacent to the bed, and contains much higher concentrations and gradients. The concentrations were obtained using a conductivity concentration meter (CCM), with velocities obtained using a Pitot-tube. The velocity profile near the bed was shown to follow a logarithmic profile provided the bed level is taken from the centre of the sheet flow layer, contrary to the findings of Coleman (1986). The velocity in the main region of the sheet flow layer followed a power law and the width of this layer was shown to increase with the Shields parameter (Shields 1936). The concentration profile was found to linearly decrease with depth from the bed to the centre of the sheet flow law, and follows the Rouse profile above this point, which agrees with the findings of Lyn (1988).

Wang and Qian (1989) conducted experiments aimed at assessing the effect of concentration on the turbulent structure in open channel flows. Velocity has been measured in a variety of conditions using a fluctuating velocimeter, with the fluctuations used to obtain the turbulent results. The turbulence intensity was shown to decrease with increasing sediment concentration, implying that turbulence is damped by the presence of sediment. However, if the particles are non-cohesive the fundamental turbulent structure does not change, allowing mixing length theory to still be applicable in sediment-laden flows.

2.2.1.2 Oscillatory Flows

A number of authors have focused on suspended sediment dynamics under oscillatory flow conditions, by conducting laboratory experiments using oscillating water tunnels (OWTs) (Horikawa et al. 1982; Ribberink and Al-Salem 1995; van der Werf et al. 2006, 2007; van der A et al. 2010). An OWT can be used to mimic the near-bed flow under regular wave conditions, allowing greater focus to be placed on the near-bed sediment dynamics.

Ribberink and Al-Salem (1995) used this approach, measuring the concentration profiles

using a combination of an optical technique, a CCM and a transverse suction system (TSS). The flows that were considered represented two asymmetric and one sinusoidal wave. The results implied that a thin sheet flow layer existed very near the bed, which contained very large concentrations $(100 - 1600\,\text{g/l})$. Above the sheet flow region, a suspension layer was present, with much lower concentrations observed. The concentration profiles responded to the oscillatory flow with two entrainment and two deposition phases for each wave cycle. In the sheet flow layer the concentration profile was shown to be in phase with the flow velocity. The lower region of the suspension layer exhibited peaks at maximum flow velocity, with smaller secondary peaks occurring around flow reversal. Progressing further up the water column, the suspended concentrations reduced in magnitude and an increasingly large phase lag with respect to the flow velocity, was observed. These phase lags led to an offshore suspended flux in the suspension layer, whereas the transport direction is onshore in the sheet flow layer.

A number of studies have utilised the OWT facilities in Aberdeen and at WL|Delft Hydraulics (O'Donoghue et al. 2006; van der Werf et al. 2006, 2007; van der A et al. 2010). These large scale facilities are capable of producing near-bed hydraulic flows equivalent in period and amplitude to those produced by full scale waves. van der Werf et al. (2006, 2007) presented experimental results, obtained at both laboratories, for the time-averaged sediment concentrations and transport rates under regular and irregular oscillatory flow conditions, over rippled beds. The concentrations were obtained using a TSS, and implied that in the near-bed region (less than twice the height of the ripples) the time-averaged concentration profile is best represented by an exponential profile with height-independent sediment diffusivity. The distribution and characteristics of the sediment concentration were found to be strongly dependent on the formation and ejection of vortices on the lee slope of the ripples. These vortices caused three peaks in the concentration profiles. The first occurred at the on-offshore flow reversal, whereas the other two peaks occur due to sediment advection from neighbouring ripples. Similar to Ribberink and Al-Salem (1995) the flux in the suspension layer was found to be offshore, whereas the near-bed flux was onshore.

van der A et al. (2010) also used the Aberdeen OWT to study the effect of acceleration skewness on the transport of sediment in the sheet flow layer, capturing the net transport using mass conservation principles and a laser bed profiler. The net transport was shown to be always in the direction with highest acceleration, defined as positive, and increased with increasing acceleration skewness. This is in contrast to velocity skewed flows, where the phase lag effects cause negative transport of fine sand. This is attributed to the phases of peak positive and negative flow velocity, which occur relatively early and late in the wave cycle, respectively, in acceleration skewed flows.

Experimental studies focusing on the dynamics of suspended sediment concentrations have also been conducted in large scale wave flumes by a number of researchers (Dohmen-Janssen and Hanes 2002; Thorne et al. 2002, 2009; Hurther and Thorne 2011). Dohmen-Janssen and Hanes (2002) conducted experiments in a large wave flume, primarily focusing on the sheet flow layer under monochromatic waves. The study used several instruments: two CCMs, two acoustic backscatter systems (ABSs) and a TSS were all installed and used to measure the suspended sediment concentrations. The results implied that the behaviour of the sheet flow layer under waves is similar to that in an OWT. The sheet flow layer is several millimetres thick, with a much larger concentration gradient than observed in the suspension layer. Asymmetry in the near-bed velocity is reflected in the sheet flow layer, with very little phase lag observed in the region, indicating quick sediment response to hydrodynamic conditions. The phase lags observed in the suspension layer by Ribberink and Al-Salem (1995) are also exhibited in these experiments. However, the time-averaged suspended sediment concentrations under waves were shown to be much higher than from similar hydrodynamic conditions in an OWT. Dohmen-Janssen and Hanes (2002) suggested that this may be caused by the rigid lid suppressing the vertical velocity component.

Thorne et al. (2002) presented another experimental study that used a large wave flume to investigate suspended sediment concentrations. It focused on regular and irregular non-breaking waves over a rippled bed, with the concentrations measured using ABS and

pumped suction. It was found that in the near-bed region, pure diffusion, with a constant, height-independent eddy viscosity, provides a reasonable representation of time-averaged suspended concentrations, which agrees with results from OWTs (van der Werf et al. 2006). Above this layer, an advection-diffusion approach, or alternatively the use of pure diffusion with a "two layer" eddy viscosity, gave good agreement. This eddy viscosity was defined such that it was constant near the bed, and linearly increasing with height above the near-bed region.

Another laboratory study conducted in a large scale wave flume is presented by Hurther and Thorne (2011), and focuses on skewed waves in the shoaling region. ABS and acoustic concentration and velocity profiler (ACVP) were deployed to provide high-resolution velocity and sediment concentration profiles in both the suspension and sheet flow layers, over a sloping, rippled bed. Similar to the studies on horizontal beds, the suspended flux was found to be offshore in the suspension layer and onshore near the bed. The suspended sediment concentration was found to be asymmetric due to the skewed nature of shoaling waves, with a near-bed phase lag of 20%, in reasonable agreement with values obtained in an OWT (van der Werf et al. 2007). This phase lag over a rippled bed is much larger than that observed in the wave boundary layer over a smooth bed (Ribberink and Al-Salem 1995; Dohmen-Janssen and Hanes 2002), and is due to ripple vortex entrainment (Hurther and Thorne 2011).

2.2.1.3 Breaking Waves

The violent, turbulent nature of breaking waves make suspended sediment dynamics much less predictable in these flow conditions, with concentrations often larger than observed under non-breaking waves, and sediment suspended to larger heights above the bed (Ribberink et al. 2014*a*). The strong flows associated with breaking waves can also lead to large horizontal sediment fluxes, making it essential to understand sediment transport processes in coastal regions where substantial erosion or accretion can occur. Hence, considerable effort has been put into the understanding of the processes behind suspended sediment dynamics in the surf zone (Sato et al. 1990; Kobayashi and Lawrence

2004; Sumer et al. 2013; Otsuka and Watanabe 2012, 2014).

A number of laboratory scale studies have been conducted using large scale wave flumes (Shimizu and Ikeno 1996; Cáceres and Alsina 2012; Ribberink et al. 2014*a*,*b*). Shimizu and Ikeno (1996) investigated suspended sediment transport in the surf and swash zones using this approach, with beaches of $1/10$, $1/20$ or $1/50$ initial slope. The concentration was measured using a pumping tube and an optical turbidity meter. A series of experiments were conducted using regular and irregular waves, and were run for long periods (up to 24 hours) allowing the beach profile to change. The results implied that morphological changes occur faster under swell conditions than under wind wave conditions. Furthermore, around the breaking point, a low frequency component of suspended sediment transport due to the presence of long waves causes offshore transport, whereas a high frequency one produces onshore transport.

Cáceres and Alsina (2012) also considered suspended sediment concentrations in the swash and inner surf zones using data obtained in the CIEM wave flume in Barcelona. They set up a stepped beach configuration, with an initial $1/13$ beach followed by a horizontal region and then a final $1/15$ beach. Irregular waves, following a JONSWAP spectrum, were produced and the suspended sediment concentrations were measured at a number of locations using optical backscatter systems (OBSs). The results implied that different mechanisms drive the suspended sediment concentrations in the different regions. In the surf zone, incident wave/bore events dominate, whereas in the swash zone, the wave-swash interactions control the concentrations. The interaction between waves and the backwash is the most likely forcing to create high levels of suspended sediment concentration.

Ribberink et al. (2014*a*,*b*) also presented a series of experiments conducted in the CIEM wave flume. These studies considered regular waves on $1/10$ or $1/20$ sloping beaches, which produced plunging or intermediate breakers, respectively. Suspended sediment concentrations were obtained using a variety of techniques including CCMs, OBSs, ABSs and TSSs. A combination of onshore net transport in the shoaling zone and offshore net transport in the surf zone created a breaker bar in the flume. The sediment flux in the sheet flow

layer was found to be much larger than in the suspension layer. In the surf zone, the net transport in the suspension layer was offshore-directed and dominated by a large undertow. Furthermore, sediment mixing due to the breaking process was large and, hence, relatively high concentrations were obtained further up the water column.

Experimental studies have also been performed in smaller scale wave flumes (Sato et al. 1990; Okayasu et al. 2004; Kobayashi and Lawrence 2004; Otsuka and Watanabe 2012), with varying beach gradients and breaker types. Sato et al. (1990) conducted experiments in a wave flume with a beach of gradient $1/20$, with suspended sediment concentrations measured using a light absorption device. Results for both spilling and plunging breakers were presented, along with a new methodology to remove the influence of the entrained air bubbles from the concentration distribution. The results showed that a large quantity of sand was suspended by the plunging breaker at the plunging point due to the production of a large scale vortex. The concentration profiles also indicated that sand suspension is intermittent under all breaker types, particularly for spilling breakers, and consequently caused little sand to be suspended.

Kobayashi and Lawrence (2004) studied the cross-shore sediment transport under a series of eight breaking solitary waves in a wave flume with a beach of gradient $1/12$. Both positive and negative solitary waves were presented and the bed profile change was measured, along with the suspended load using a fibre optic sediment monitor. The positive solitary waves caused plunging breakers, leading to suspension of a large quantity of sand. Following the run-up, a strong down-rush was also observed, causing sediment resuspension and seaward sediment transport, with deposition occurring seaward of the wave run-down. For the negative solitary wave, a collapsing breaker was formed which did not suspend as much sediment as observed in the positive case. In this case the run-up was much smaller, leading to smaller backwash. This caused deposition at the foreshore and erosion near the collapsing point of the wave. This study highlights one of the complexities of modelling suspended concentrations in the surf zone: the concentrations depend largely on the incident wave profile as well as the interaction with other waves, and the phases at which these

interactions occur.

Otsuka and Watanabe (2012, 2014) investigated the concentrations under spilling, plunging and intermediate breakers on a sloping beach of constant gradient $1/20$, using optical concentration sensors and PIV. Like many of the other studies, it was shown that suspended sediment concentrations were higher under plunging breakers, which is attributed to large-scale vortices that entrain a large quantity of sediment. Furthermore, despite the TKE dissipating in deeper regions of the surf zone, the concentration increases with time, which is due to the transport of sediment by the undertow. In shallower water, the concentration linearly increased with TKE. Smaller-scale vortices dominate under spilling breakers, with the bore entraining little sediment in both breaker types since the vortices develop into weak turbulent bores.

Further studies have also considered the generation of sediment clouds (Okayasu et al. 2004), or sediment plumes (Sumer et al. 2013), generated in the surf zone through laboratory experiments. Okayasu et al. (2004) studied spilling breakers with a gradient of $1/20$, using a computed tomography technique to obtain 2-D (horizontal) measurements of the sediment concentration. Intermittent clouds of high concentration were shown to cause the horizontal distribution of suspended sediment to be quite inhomogeneous. The primary cause of these clouds was suggested to be due to pickup of sediment by intermittent eddies from the breaking process that interact with the bed.

Sumer et al. (2013) investigated a similar process under plunging breakers on a slope of $1/14$. The distribution of suspended sediment in the horizontal-vertical plane was recorded using a digital video recorder. The footage implies that the plunging breaker generates a series of large vertical vortices through the over-turning of the wave and interaction with the backwash of the previous wave. These vortices entrain a large amount of sediment into the main body of the water through a suction type process caused by an upward-directed pressure gradient, leading to "sediment plumes".

2.2.2 Numerical Studies

There have been a large number of numerical models developed to assess suspended sediment transport, with many based on continuity (Christensen et al. 2000; Kobayashi and Johnson 2001; Hsu and Liu 2004; Suzuki et al. 2007; Bakhtyar et al. 2009; Ma et al. 2014). One relatively simple approach is to use a classic advection-diffusion equation to describe the transport of suspended sediment, which can be implemented in 1-D (Kobayashi and Johnson 2001; Conley et al. 2008) or 2-D horizontal-vertical (Hsu and Liu 2004; Bakhtyar et al. 2009), as well as fully 3-D (Suzuki et al. 2007; Liu 2008; Ma et al. 2014; Jacobsen et al. 2014) models. Using this methodology, most of the uncertainty lies with the boundary condition describing the exchange of sediment at the bed. Common methods for assessing this problem are to set a reference concentration based on empirical formulae (Christensen et al. 2000; Conley et al. 2008), or consider the balance of deposition and entrainment using a pickup model (Hsu and Liu 2004; Suzuki et al. 2007; Ma et al. 2014).

Conley et al. (2008) implemented the advection-diffusion approach into the General Ocean Turbulence Model (GOTM), which is a 1-D water column model. A reference concentration technique related to the bed shear stress (Smith and McLean 1977), was used for the sediment bed boundary condition. The numerical model was applied to examine the effect of sediment stratification, on cross shore sediment transport, and the results were compared to field observations. The concentrations were shown to increase near the bed and reduce further up the water column for medium sands. However, finer sands led to suppression of turbulence and suspension of sediment outside the wave boundary layer. It was also shown that the numerical predictions agreed better with field data when stratification was included.

Hsu and Liu (2004) extended the Cornell Breaking Wave and Structure (COBRAS) hydrodynamic model to include a sediment transport model based on the advection-diffusion approach. The sediment transport model was implemented in two different ways for comparison. The first method treated the sediment as dilute and passive, with only one-way coupling from the fluid to the suspended concentration. The second method involved treat-

ing the fluid and sediment as a two-phase system with two-way coupling, obtained through Favre-averaging (Hsu et al. 2003). The sediment bed boundary condition used a pickup model (van Rijn 1984*a*; Nielsen 1992). The hydrodynamic model solved the 2-D Reynolds-Averaged Navier-Stokes (RANS), and used a $k-\varepsilon$ turbulence closure model, modified to include effects from the sediment concentration. The model was validated against channel flow (Sumer et al. 1996), oscillating flow (Ribberink and Al-Salem 1995), regular wave (Dohmen-Janssen and Hanes 2002) and breaking wave data (Sato et al. 1990). The results were generally encouraging, particularly near the bed, although additional calibration was required, through variation in the Schmidt number and an additional source of turbulence under breaking waves, to obtain agreeable results in some of the cases. It was also found that the two-phase approach was more robust since the Schmidt number required adjustment according to flow type in the single-phase model.

Bakhtyar et al. (2009) also developed a 2-D model where the sediment concentration and fluid are treated as a two-phase, two-way coupled system using Favre averaging. In this model the bottom boundary was set to the maximum attainable concentration (see Section 3.3.3.4 for more details) and the $k-\varepsilon$ model was used for turbulence closure. This model was initially designed for study of the sheet flow layer under oscillatory flow conditions and was validated against experimental data (Horikawa et al. 1982), confirming that the shape of the vertical concentration profile was well represented. The model was later applied to study suspended sediment dynamics under breaking waves in the surf and swash zones (Bakhtyar et al. 2010).

Ma et al. (2014) used a different approach to obtain a two-way coupled system. The concentration was used to change the density of the fluid, hence influencing the results from the hydrodynamic model. The sediment module was implemented into NHWAVE (Ma et al. 2012), which solves the incompressible RANS equations, and uses a nonlinear $k-\varepsilon$ model for turbulence closure. Experimental data for non-breaking (Dohmen-Janssen and Hanes 2002), and breaking waves (Sato et al. 1990) was used for validation, with slightly more accurate results than presented by Hsu and Liu (2004). This seems to be partly attributed

to more accurate modelling of phase lags and suspension time.

One-way coupled systems have also been commonly utilised in previous studies (Christensen et al. 2000; Suzuki et al. 2007; Liu 2008; Jacobsen et al. 2014). Suzuki et al. (2007) coupled a 3-D large eddy simulation (LES) with a sediment transport module. At the sediment bed boundary, a pickup function for unsteady flow (van Rijn 1984*a*; Nielsen 1992) was utilised. The numerical model was validated under breaking wave conditions against time-averaged spatial experimental data Sato et al. (1990). The results showed some qualitative resemblance to the experimental data but predicted substantially larger values.

The single-phase approach has also been used in numerical models describing the full morphological processes under a range of conditions (Liu 2008; Jacobsen et al. 2014). Liu (2008) developed a numerical model in OpenFOAM®, for application to scour. The model calculated the bed and suspended load and adjusted the sediment bed accordingly. The suspended concentration was modelled using an advection-diffusion approach along with a pickup function (van Rijn 1984*a*; Nielsen 1992) at the bed. Jacobsen et al. (2014) developed a similar model in OpenFOAM® to examine beach morphodynamics. The suspended component of the model differed from Liu (2008) in that a reference concentration (Engelund and Fredsøe 1976) technique was employed, leading to the suspended load being solved on a second mesh that did not include the near-bed region. Furthermore, the governing equation for the suspended sediment was modified to stop sediment entering the air phase. The predictions of the suspended load were validated against experimental data under breaking waves (Shimizu and Ikeno 1996), starting at the equilibrium beach profile from the experiments. The model has been further applied to scour around both submarine pipelines (Fuhrman et al. 2014), and vertical monopiles (Baykal et al. 2015), exhibiting reasonable agreement with experimental observations.

An alternative to the advection-diffusion methodology is to use a particle tracking algorithm (Magar and Davies 2005; Calantoni et al. 2006; van der Werf et al. 2008). This method considers single particles, rather than a concentration, and their path is tracked by considering the advection, settling and diffusion, with the latter modelled using a random walk

technique. Magar and Davies (2005) used this approach, coupling it with a discrete-vortex model for the hydrodynamics (Malarkey and Davies 2002). This model solves the vorticity transport equation directly through representation of the vorticity field as a sum of a large number of point vortices (van der Werf et al. 2008). The model was applied to investigate oscillatory conditions, representative of regular waves, over a single ripple. Sediment particles were continuously released from the crest of the ripple, and any particles which hit the bed were removed from the simulation. It was shown that a vortex developed downstream of the ripple, which carried with it a cloud of sediment. A comparison of the numerical predictions against experimental data (van der Werf et al. 2007) was later presented by van der Werf et al. (2008). The results implied that the model was capable of accurately capturing the growth of the sediment clouds, but the concentrations were over-predicted within the vortices, and under-estimated outside. The model was later used to study the mixing efficiency of sediment with respect to turbulent diffusion (Malarkey et al. 2015).

Calantoni et al. (2006) also used a particle tracking technique, which was coupled with the Navier-Stokes solver, RIPPLE (Kothe et al. 1991; Liu and P. 1997). The model was applied to cases on a sloping beach of constant gradient $1/10$, with emphasis on events in the swash zone. Although the model demonstrates that it can capture sediment suspension events, validation against experimental data was not presented.

Further studies aimed at predicting suspended sediment dynamics have been conducted using OpenFOAM®. Brennan (2001) developed a solver based upon the Drift Flux model where the governing equations for mass and momentum are solved for a mixture of sediment and water, together with an advection-diffusion equation for modelling the distribution of the dispersed phase. The numerical model was validated against data for both model (Dahl 1995) and full scale (Ueberl 1995) settling tank experiments. Bohórquez (2008) created a three phase solver for water, air and sediment which used the mixture equations for non-cohesive sediment transport derived from the ensemble-averaged Navier-Stokes equations. When applied to dam break and shallow water flows, Bohórquez (2008) showed that the results were encouraging. Furthermore, a particle tracking style approach has

also been implemented in the OpenFOAM® environment. An open source library (CFDEM 2014) has been developed and released, where OpenFOAM® is coupled with LIGGGHTS, an open source discrete element method (DEM) software. This library can be coupled with existing OpenFOAM® solvers and has been used in a variety of applications including local scour downstream of a weir (Gruber 2012).

2.3 Sediment Diffusivity

Vertical sediment diffusivity profiles have been investigated under a variety of flow conditions including horizontal channel flows (Coleman 1970; Cellino 1998), non-breaking (van Rijn 1993; Ogston and Sternberg 2002; Thorne et al. 2009), and breaking waves (Sheng and Hay 1995; Ogston and Sternberg 2002; Aagaard and Jensen 2013). A widely used technique for estimation of the time-averaged sediment diffusivity under oscillatory flow conditions (Sheng and Hay 1995; Ogston and Sternberg 2002; Thorne et al. 2009; Aagaard and Jensen 2013) is to use the formulation

$$\overline{\nu_s} = \frac{-w_s \overline{C}}{\partial \overline{C}/\partial z}, \tag{2.4}$$

which is derived from the advection-diffusion equation (see Chapter 8 for more details). This approach is popular since it only requires knowledge of the mean vertical concentration profile and the settling velocity of the sediment.

Under regular waves a number of expressions for the vertical sediment diffusivity have been suggested (Nielsen 1992; van Rijn 1993; Ogston and Sternberg 2002). van Rijn (1993) empirically derived a three-layer expression to describe the sediment diffusivity over the whole water column,

$$\nu_s = \begin{cases} \nu_m & \text{for} \quad z \geq 0.5h \\ \nu_b + (\nu_m - \nu_b)\left[\frac{z-\zeta_s}{0.5h-\zeta_s}\right] & \text{for} \quad \zeta_s < z < 0.5h \\ \nu_b & \text{for} \quad z \leq \zeta_s, \end{cases} \tag{2.5}$$

where ν_b and ν_m are constants, ζ_s is the thickness of the near-bed mixing layer, and h is the water depth. Therefore the whole profile consists of two regions of constant sediment diffusivity in the top half of the water column and near the bed, and linearly increasing with height above the bed between these two regions.

There is some disagreement about the near-bed sediment diffusivity with some studies suggesting that it is constant with depth (Nielsen 1992; van Rijn 1993) whilst others state that it increases linearly with height above the bed (Grant and Madsen 1979; Lee et al. 2002; Ogston and Sternberg 2002). There is some evidence to suggest that the constant profile is valid for rippled beds whereas the linear increase occurs for plane beds (Thorne et al. 2009). Thorne et al. (2009) applied equation (2.4) to obtain estimated time-averaged sediment diffusivity profiles, using large wave flume data of regular waves propagating over a rippled bed (Thorne et al. 2002). Fine and medium sands were considered separately. It was shown that the near-bed sediment diffusivity was constant for the medium sand, whereas a linear increase with height was observed for the fine sand case. Thorne et al. (2009) suggested that the lower steepness ripples in this case led to behaviour dynamically similar to a plane bed, where the turbulent eddies increase in size with height above the bed.

Thorne et al. (2009) also compared the results obtained using equation (2.4) with the expression (equation 2.5) suggested by van Rijn (1993). The results implied that the linearly increasing region ($\zeta_s < z < 0.5h$) fitted the experimental data with reasonable accuracy assuming the bed roughness to be $k_N = 2.5d$ and the sediment and turbulent mixing to be equivalent. This reinforces the application of a multi-layer sediment diffusivity profile, which has been suggested by a number of authors (van Rijn 1993; Thorne et al. 2002; Ogston and Sternberg 2002). Further evidence of this concept has been provided by Ogston and Sternberg (2002) who, using field and wave flume data, also obtained a three layer expression for the sediment diffusivity using equation (2.4). In this case the near-bed region (less than twice the width of the wave boundary layer, δ_w) was found to linearly increase with height above the bed. The profile was constant with height from $3\delta_w$ upwards,

with a linear fit in between the near-bed and constant regions.

In the surf zone, the sediment diffusivity varies according to the region that is being measured, as well as a function of depth, due to injection of turbulence from breaking waves (Ogston and Sternberg 2002; Aagaard and Jensen 2013). Aagaard and Jensen (2013) investigated time-averaged sediment diffusivity profiles in the breaker and inner surf zones using field data collected at three beaches (Aagaard et al. 2005; Aagaard and Hughes 2006). The former corresponds to the region where plunging breaking occurs, whereas the latter represents the region where a spilling bore has formed. The results implied that plunging breakers enhance near-bed mixing processes in the breaker zone, leading to larger mean sediment diffusivities than seen in the inner surf zone. Further up the water column, the time-averaged sediment diffusivities are similar in both the inner surf and breaker zones. In the inner surf zone the sediment diffusivity was shown to linearly increase with height above the bed. This increase in mean sediment diffusivity is consistent with Ogston and Sternberg (2002), who used a combination of wave flume and field data to obtain an estimation for the $\overline{\nu_s}$ profile. However, Ogston and Sternberg (2002) found that the time-averaged sediment diffusivity increased exponentially with height above the bed, as opposed to the linear increase observed by Aagaard and Jensen (2013). The disagreement could be due to the large scatter in the data used by Aagaard and Jensen (2013), which they suggest was caused by the different breaking points of the waves.

The penetration depth of mixing generated by the breaking process is also of interest when assessing sediment diffusivity. Sheng and Hay (1995) considered a range of different wave energies and found that the vertical mixing length was substantially less than the total water depth. On the other hand, Aagaard and Jensen (2013) found it to be between 50% and 100% at the beaches considered in their study. Uncertainty in the vertical mixing length generates error in the sediment diffusivity profiles. Furthermore, the penetration depth of the mixing generally varies wave to wave and hence it seems unlikely that there exists an expression for the sediment diffusivity that will perfectly fit all beach types and conditions. Therefore, it would be beneficial to obtain a relationship between the sediment diffusiv-

ity and other quantities, such as the eddy viscosity. This would allow sediment diffusivity profiles to be predicted using numerical models, which are capable of resolving flow characteristics both in time and in space. This relationship is the focus of the rest of this chapter.

2.3.1 Relationship Between Turbulent and Sediment Mixing

Substantial research effort has been spent investigating the relationship between turbulent diffusion and sediment mixing, both through experimental (Cellino 1998; Thorne et al. 2009; Buscombe and Conley 2012) and numerical studies (Amoudry et al. 2005; Absi 2010; Malarkey et al. 2015). The approach that is often adopted is to assume that the sediment diffusivity, ν_s, is proportional to the eddy viscosity, ν_t,

$$\nu_s = \beta \nu_t. \tag{2.6}$$

The constant of proportionality, β, has been investigated in a number of different studies, with substantial variation in the reported values, ranging from 0.1 to 10 (Ogston and Sternberg 2002; Buscombe and Conley 2012), depending on flow conditions, bed forms, and sediment grain diameter. A value less than unity indicates a reduction in sediment diffusion relative to the turbulent mixing, and vice versa. Authors who find that $\beta < 1$ often argue that sediment particles are unable to fully respond to the turbulent fluctuations (van Rijn 1984*b*). On the other hand, some investigators who conclude that $\beta > 1$ reason that, due to the higher density of the sediment particles, the centrifugal forces would be greater than on the fluid particles, leading to increased mixing lengths and diffusion (van Rijn 1984*b*). Another theory for increased mixing is that it is caused by 2-D or 3-D temporal-spatial correlations between the concentration and velocity (Magar and Davies 2005; Thorne et al. 2009). Davies and Thorne (2005) suggested that, on average, regions of high suspended concentration correlate with high vertical velocity above rippled beds, which is used to determine the sediment diffusivity. On the other hand the eddy viscosity is determined through the correlation between horizontal and vertical components of the velocity (Thorne et al. 2009). This dependence on correlations of flow parameters highlights the complexity of the sediment diffusion process and the difficulties in determining its

relationship with turbulent diffusion.

Cellino (1998) evaluated the β coefficient for horizontal channel flow conditions, through experimental data fitting. Experimental data from new laboratory tests were assessed along with concentration profiles from previous studies (Einstein and Chien 1955; Coleman 1986; Lyn 1988; Wang and Qian 1989; Sumer et al. 1996). The experimental data presented by Cellino (1998) implied that $\beta < 1$ for flat beds. However, there is evidence to support a dependence on grain size. For a sediment grain size of 0.135 mm, β ranged from 0.35 to 0.65, whereas for larger sediment ($d = 0.23$ mm) the value of β was generally larger ($0.6 - 0.7$). This increase in β is consistent with van Rijn (1984*b*) who evaluated laboratory and field data (Coleman 1970) to obtain a relationship based on the settling and friction velocities. When considering other studies, Cellino (1998) also observed some dependence on grain diameter (Einstein and Chien 1955; Coleman 1986; Sumer et al. 1996), with values for β ranging from 0.5 to 2.5.

Buscombe and Conley (2012) conducted experiments using an oscillatory grid over a bed of fine or coarse sediment. A simple differencing scheme (Thorne et al. 2009) was deployed to obtain the sediment diffusivity profiles. The results implied that the sediment diffusivity is almost constant with depth and that the magnitude depended on Reynolds number and grain size. The value of β was always less than 1 and it was smaller for the finer sand ($70 - 110\,\mu$m) than the coarser sand ($145 - 205\,\mu$m), for both Reynolds number presented. In the higher Reynolds number case, β was approximately 0.14 and 0.4 for the finer and coarser sand, respectively. In the smaller Reynolds number case, these values were higher at around 0.25 and 0.5, respectively. One of the suggested explanations for the dependence on grain diameter was that finer grains settle faster through turbulence than through still water.

Cellino (1998) also considered the effect of having bed forms present in the finer sediment case. In this case the value of β was shown to be substantially larger ($1.1 < \beta < 1.4$) than observed for the plane bed. Therefore Cellino (1998) concluded that $\beta < 1$ for plane beds and $\beta > 1$ for rippled beds, which is consistent with studies of regular

waves over rippled beds (Thorne et al. 2002; Malarkey et al. 2015). Nielsen (1992) suggested that $\beta \approx 4$ above rippled beds and setting β to this value has also provided promising results in the near-bed region in a number of numerical models (Davies and Thorne 2005; Magar and Davies 2005). Furthermore, a recent numerical study (Malarkey et al. 2015) based on a 2-D discrete-vortex, particle tracking model, performed harmonic analysis to evaluate β for flows over a rippled bed, obtained values in the range $1.3 < \beta < 1.8$. Malarkey et al. (2015) also presented fitted values to experimental data which yielded a value of $\beta \approx 3$.

Further up the water column, channel flow experimental evidence exists (Graf and Cellino 2002) to suggest that β increases as a function of height above the bed. For coarse sediments, Absi (2010) introduced a depth dependent value,

$$\beta = 1 + c_\beta z^2, \tag{2.7}$$

where c_β is a constant, into their 1-DV gradient diffusion model while still keeping $\beta = 1$ for fine sands. This allowed upward convex or upward concave profiles from experimental data to be reproduced for fine and coarse sediment, respectively.

Over plane beds, other numerical models have also found that different values of β were required to obtain similar results as experiments at various heights above the bed. Hsu and Liu (2004) found that near the bed, $\beta \approx 1.43$ gave good predictions, whereas further up the water column $\beta = 2.5$ gave a more accurate fit. Based on this information, Amoudry et al. (2005) introduced a concentration dependent Schmidt number to the numerical model developed by Hsu and Liu (2004) which took the form

$$\sigma_c = \sigma_{c0}\left(1 - \frac{C}{C_0}\right) + \left(\frac{C}{C_0}\right)^q. \tag{2.8}$$

However, introduction of such a parameter relies on empirical fitting to experimental data and hence the practicality of such an expression is likely to be limited.

It is worth noting that numerical models often find $\beta > 1$ even in flows over plane beds

(Hsu and Liu 2004; Ma et al. 2014). Conversely, experimental studies regarding flows over plane beds often suggest that $\beta < 1$. This trend continues in numerical simulations of the surf zone dynamics. Both Hsu and Liu (2004) and Ma et al. (2014) find that β must be less than unity in order to predict similar concentration profiles as observed in laboratory experiments. On the other hand, Ogston and Sternberg (2002) used field data (DUCK94) to show that $0.23 < \beta < 0.5$ in the wave boundary layer under broken waves, whereas Sheng and Hay (1995) showed $\beta \approx 1$. Hsu and Liu (2004) justified the choice of β based on a term described as the "advective drift" not being implemented in their model. This additional term arises from the gradient of the mean square particle velocity fluctuations and can enhance transport of suspended sediment (Hsu and Liu 2004). Therefore, β is required to be less than unity so that the "apparent" sediment diffusivity increases to match experimental data. Further work is clearly required to explain the inconsistencies between experimental and numerical studies in more detail.

In general numerical models choose a single value for β, which is either 1 (Christensen et al. 2000; Liu 2008; Jacobsen et al. 2014) or is determined through an initial study (Hsu and Liu 2004; Ma et al. 2014). In the present numerical study, the simple approach of assuming that $\beta = 1$ is adopted unless otherwise stated. However, model sensitivity to the value of β will be evaluated and discussed in Chapters 7 and 8.

Chapter 3

Background Theory

The aim of this chapter is to briefly describe a number of key concepts that are fundamental to the work conducted in this study. The intention is to fill in any knowledge gaps of the reader making the analysis in later chapters easier to follow. The chapter is split into three main categories: turbulent flows, wave generation and breaking, and sediment transport.

3.1 Turbulent Flows

Turbulence is the state of a fluid flow which contains apparently random fluctuations arising from chaotic 3-D vortices, and is responsible for high energy dissipation, mixing and heat transfer. Turbulence originates from small disturbances in the fluid streamlines of a laminar flow, which can develop or dissipate depending on the ratio of the inertial and viscous forces (Tu et al. 2008). This leads to the introduction of the Reynolds number, Re, a non-dimensional number, defined as the ratio of inertial and viscous forces,

$$Re = \frac{\text{Inertia Force}}{\text{Viscous Force}} = \frac{uL}{\nu}, \tag{3.1}$$

where u and L are a characteristic velocity and length scale, respectively (Tu et al. 2008). At a low Reynolds number, the viscous forces dominate, leading to the dissipation of the disturbances and the flow remains laminar. At a higher Reynolds number the inertial forces dominate, which can amplify the disturbances leading to the onset of turbulence (Tu et al. 2008).

This section is dedicated to the introduction of the concept of turbulence and how it is structured, both in the free stream, and in the boundary layer. A discussion on the common

techniques used in the examination of turbulence is included, starting from the governing equations for fluid flows.

3.1.1 Governing Equations for Incompressible Flows

The Navier-Stokes equations, along with the instantaneous continuity equation, are the governing equations for Newtonian fluids, i.e. a fluid in which the viscous stresses are proportional to the rate of change of deformation. The Navier-Stokes and continuity equations represent the conservation of momentum and mass, respectively (Versteeg and Malalasekera 1995). In an incompressible fluid, the density does not vary and hence the instantaneous continuity equation can be shown to be equivalent to

$$\nabla \cdot \mathbf{u} = 0, \tag{3.2}$$

and the momentum equations are

$$\frac{\partial u}{\partial t} + \nabla \cdot (u\mathbf{u}) = -\frac{1}{\rho}\frac{\partial p}{\partial x} + \nu \nabla^2(u), \tag{3.3}$$

$$\frac{\partial v}{\partial t} + \nabla \cdot (v\mathbf{u}) = -\frac{1}{\rho}\frac{\partial p}{\partial y} + \nu \nabla^2(v), \tag{3.4}$$

$$\frac{\partial w}{\partial t} + \nabla \cdot (w\mathbf{u}) = -\frac{1}{\rho}\frac{\partial p}{\partial z} + \nu \nabla^2(w). \tag{3.5}$$

The Navier-Stokes equations represent the exact properties of the flow, including all the turbulent fluctuations and therefore are nonlinear and difficult to solve. In order to obtain a solution, the Navier-Stokes equations must be discretised and integrated over infinitesimal distances and time, making it necessary to use a computer. Therefore, it is common to make assumptions about the flow in order to manipulate the equations into a form which is easier to work with.

3.1.2 Mean Equations

In this section turbulence is considered as a statistical average and therefore the instantaneous fluctuations are discarded. Although this method discards a lot of information, it is

commonly used since it is often interesting to study the mean properties of the flow, and not the details of the turbulence specifically.

3.1.2.1 Reynolds Decomposition

In order to study the mean properties of the flow, a method to isolate these properties from the instantaneous fluctuations is required. A common method for this is "Reynolds Decomposition", which splits the instantaneous flow property, ϕ, into mean, $\overline{\phi}$, and fluctuating, ϕ', components

$$\phi = \overline{\phi} + \phi'(t). \tag{3.6}$$

In terms of this work, the mean component corresponds to the ensemble-averaged solution, i.e. under laboratory conditions, the solution that would be obtained by averaging a large number of results from an identical experimental setup.

3.1.2.2 Rules of Reynolds Decomposition

Suppose that there are two flow properties, $\phi = \overline{\phi} + \phi'$ and $\psi = \overline{\psi} + \psi'$, then the rules which govern time-averaged flows are:

$$\begin{gathered}\overline{\phi'} = \overline{\psi'} = 0, \quad \overline{\overline{\phi}} = \overline{\phi}, \quad \overline{\frac{\partial \phi}{\partial f}} = \frac{\partial \overline{\phi}}{\partial f}, \quad \overline{\int \phi \mathrm{d}f} = \int \overline{\phi} \mathrm{d}f, \\ \overline{\phi + \psi} = \overline{\phi} + \overline{\psi}, \quad \overline{\phi\psi} = \overline{\phi}\ \overline{\psi} + \overline{\phi'\psi'}, \quad \overline{\phi}\overline{\psi} = \overline{\phi}\ \overline{\psi}, \quad \overline{\phi'} = 0,\end{gathered} \tag{3.7}$$

where f is any scalar variable.

3.1.2.3 Reynolds-Averaged Navier Stokes Equations

Applying Reynolds decomposition (equation 3.6) to the velocity components and pressure of a flow gives,

$$\mathbf{u} = \overline{\mathbf{u}} + \mathbf{u}' \qquad u_i = \overline{u_i} + u_i' \qquad p = \overline{p} + p'. \tag{3.8}$$

By substituting equation (3.8) into the Navier-Stokes equations (equations eqs. (3.2)

to (3.5)), taking the time-average and applying the rules for Reynolds Decomposition (equation 3.7) the Reynolds-Averaged Navier-Stokes (RANS) equations are obtained

$$\nabla \cdot \overline{\mathbf{u}} = 0 \tag{3.9}$$

$$\frac{\partial u}{\partial t} + \nabla \cdot (\overline{u}\overline{\mathbf{u}}) = -\frac{1}{\rho}\frac{\partial \overline{p}}{\partial x} + \nu\nabla^2(\overline{u}) - \frac{1}{\rho}\left[\frac{\partial(\rho\overline{u'^2})}{\partial x} + \frac{\partial(\rho\overline{u'v'})}{\partial y} + \frac{\partial(\rho\overline{u'w'})}{\partial z}\right] \tag{3.10}$$

$$\frac{\partial \overline{v}}{\partial t} + \nabla \cdot (\overline{v}\overline{\mathbf{u}}) = -\frac{1}{\rho}\frac{\partial \overline{p}}{\partial y} + \nu\nabla^2(\overline{v}) - \frac{1}{\rho}\left[\frac{\partial(\rho\overline{u'v'})}{\partial x} + \frac{\partial(\rho\overline{v'^2})}{\partial y} + \frac{\partial(\rho\overline{v'w'})}{\partial z}\right] \tag{3.11}$$

$$\frac{\partial \overline{w}}{\partial t} + \nabla \cdot (\overline{w}\overline{\mathbf{u}}) = -\frac{1}{\rho}\frac{\partial \overline{p}}{\partial z} + \nu\nabla^2(\overline{w}) - \frac{1}{\rho}\left[\frac{\partial(\rho\overline{u'w'})}{\partial x} + \frac{\partial(-\rho\overline{v'w'})}{\partial y} + \frac{\partial(\rho\overline{w'^2})}{\partial z}\right] \tag{3.12}$$

3.1.2.4 Reynolds Stresses

As can be seen in equations (3.10)-(3.12), the process of Reynolds-averaging yields a new set of terms in the governing equations. The new terms are the turbulent momentum fluxes and, since momentum flux can be thought of as a stress, they are called the Reynolds stresses. Note that they have been written in component form above but are more commonly expressed in the form $\tau_{ij} = -\rho\overline{u_i'u_j'}$, where τ_{ij} is symmetric and represents the six unknown quantities created by Reynolds-averaging.

For a general three-dimensional flow, there are now ten unknowns in the governing equations, namely, the six Reynolds stress components, along with the three velocity components and pressure of the mean flow. Since there are only four equations the system can not be closed, and hence more equations must be developed in order to compute turbulent flows using the RANS equations.

3.1.2.5 Turbulence Closure Problem

By taking the time-average of the product of the Navier-Stokes equations and various fluctuating components, additional equations can be obtained. By doing this and considering

each term in turn it can be shown (Wilcox 2006) that the Reynolds stress equation is

$$\frac{\partial \tau_{ij}}{\partial t} + \overline{u}_k \frac{\partial \tau_{ij}}{\partial x_k} = -\tau_{ik}\frac{\partial \overline{u}_j}{\partial x_k} - \tau_{jk}\frac{\partial \overline{u}_i}{\partial x_k} + \varepsilon_{ij} - \Pi_{ij} + \frac{\partial}{\partial x_k}\left[\nu \frac{\partial \tau_{ij}}{\partial x_k} + C_{ijk}\right], \tag{3.13}$$

where

$$\Pi_{ij} = \overline{\frac{p'}{\rho}\left(\frac{\partial u_i'}{\partial x_j} + \frac{\partial u_j'}{\partial x_i}\right)}, \tag{3.14}$$

$$\varepsilon_{ij} = 2\nu \overline{\frac{\partial u_i'}{\partial x_k}\frac{\partial u_j'}{\partial x_k}}, \tag{3.15}$$

$$\rho C_{ijk} = \rho \overline{u_i' u_j' u_k'} + \overline{p' u_i'}\delta_{jk} + \overline{p' u_j'}\delta_{ik}. \tag{3.16}$$

Unfortunately, by considering additional equations, 22 new unknowns have been created. This is the turbulence closure problem: as higher moments of the Navier-Stokes equations are taken, more unknowns will be created than will be found. At some point the system must be closed using approximations for the unknowns based on the known flow properties. These are known as turbulence closure models.

This illustrates the problem with using Reynolds-averaging: much of the information contained within the Navier-Stokes equations is lost through the averaging process.

3.1.2.6 Eddy Viscosity

Before continuing it is important to note that the overbars on the mean quantities have been dropped so the notation is now $\phi = \overline{\phi}$.

A common group of turbulence closure models are the eddy viscosity models. In this type of model an analogy between the action of viscous and Reynolds stresses on the mean flow is assumed. For incompressible (Newtonian) fluids, Newton's law of viscosity states that the viscous stresses are proportional to the rate of deformation (Versteeg and Malalasekera 1995)

$$\tau_{ij} = \mu \mathbf{S} = \mu \frac{1}{2}\left(\frac{\partial u_i}{\partial x_j} + \frac{\partial u_j}{\partial x_i}\right). \tag{3.17}$$

In analogy to this, it is common to assume that the Reynolds stresses are proportional to

the mean rates of deformation,

$$\tau_{ij} = -\rho\overline{u_i'u_j'} = \mu_t\left(\frac{\partial u_i}{\partial x_j} + \frac{\partial u_j}{\partial x_i}\right) - \frac{2}{3}\rho k\delta_{ij}, \tag{3.18}$$

where, k is the turbulent kinetic energy (TKE), and μ_t is the dynamic eddy viscosity. Note that the kinematic eddy viscosity is defined as $\nu_t = \mu_t/\rho$. The extra term on the right hand side ensures that the normal Reynolds stresses ($i = j$) give the correct form, i.e. the sum of the normal Reynolds stresses should give the turbulent kinetic energy per unit volume, $\frac{1}{2}(\overline{u'^2} + \overline{v'^2} + \overline{w'^2})$.

Through this approximation the problem has been reduced to modelling the eddy viscosity. However, this method has a major drawback in that it implies that the normal Reynolds stresses are isotropic which is often inaccurate. Eddy viscosity turbulence models will be discussed in more detail in Section 4.4.

3.1.2.7 Mean Kinetic Energy Equation

It is possible to derive an expression for the mean flow kinetic energy, K. By multiplying the x, y and z-component of the RANS equations (equations 3.10-3.12) by the mean flow components u, v and w, respectively. Manipulating the summation of these three equations can eventually give the time-averaged governing equation for the mean kinetic energy (Tennekes and Lumley 1972)

$$\frac{\partial(\rho K)}{\partial t} + \nabla\cdot(\rho K\mathbf{u}) = \nabla\cdot(-p\mathbf{u} + 2\mu\mathbf{u}\mathbf{S} - \rho\overline{u_i'u_j'}\mathbf{u}) - 2\mu\mathbf{S}\mathbf{:}\mathbf{S} + \rho\overline{u_i'u_j'}\cdot\mathbf{S}. \tag{3.19}$$

The divergence terms represent (from left to right) transport of mean kinetic energy by convection, pressure, viscous stresses and Reynolds stresses, respectively. The final two terms on the right hand side represent the dissipation of mean kinetic energy due to viscous stresses and the loss of K to turbulent production. Note that the sign of the last term is positive but actually represents a loss of mean kinetic energy since the Reynolds stress is defined as $-\rho\overline{u_i'u_j'}$, producing a double negative.

3.1.2.8 Turbulent Kinetic Energy Equations

Applying a similar method as for the mean kinetic energy equation, the three components of both the instantaneous Navier-Stokes equations and the RANS equations are multiplied by the corresponding turbulent velocity component. By summing the three equations for both sets of governing equations, and subtracting one from the other an equation for the TKE is derived (Tennekes and Lumley 1972)

$$\frac{\partial(\rho k)}{\partial t} + \nabla \cdot (\rho k \mathbf{u}) = \nabla \cdot (-\overline{p'\mathbf{u}'} + 2\mu\overline{\mathbf{u}'\mathbf{S}'} - \frac{\rho}{2}\overline{u_i' \cdot u_i' u_j'}) - 2\mu\overline{\mathbf{S}':\mathbf{S}'} - \rho\overline{u_i' u_j'} \cdot \mathbf{S}. \tag{3.20}$$

This equation takes a very similar form as the mean kinetic energy equation. There are transport terms for convection, pressure, viscous stresses, Reynolds stress and a dissipation term due to viscosity. The final term is interesting, it is, in fact, exactly the same as the final term in equation (3.19) except that it has the opposite sign. This is because this term represents the kinetic energy being lost from the mean flow to produce the TKE. Hence in equation (3.20) there is a production, rather than destruction, term.

3.1.2.9 Vortex Stretching

At this point the concept of vortex stretching is introduced since it is fundamental to how energy is passed between the different scales of turbulence. The basic idea of vortex stretching is that if an element is stretched in any particular direction, then, in order to conserve angular momentum, the component of vorticity in the direction of stretching must change.

In short, this means that if the rate of strain is positive then there is a vorticity increase in the direction of the strain rate, and if it is negative there is a decrease.

3.1.2.10 Energy Cascade

Turbulence consists of eddies of varying sizes. Therefore, a turbulent flow can conceptually be considered to be divided into all eddies smaller than a given size, and all eddies larger than that size. The large eddies interact with the mean flow and receive energy from

it. Therefore, the largest eddies in turbulence contain the most energy. Furthermore, the large eddies can pass the energy down to the smaller eddies through the process of vortex stretching. This occurs since the smaller eddy is exposed to the rate of strain of the larger eddies and therefore has an increase in vorticity. This results in an increase in energy in the small eddy at the expense of the large eddy and hence there is a flux of energy from larger to smaller eddies.

It turns out that most of the energy that is exchanged at a given eddy size is taken from the next largest eddy and is passed on to the next smallest eddy. This is known as the energy cascade, described by Tennekes and Lumley (1972) as being "like a series of waterfalls, each one filling a pool that overflows into the next one".

3.1.2.11 Kolmogorov Microscale

At the other end of the scale, as the eddies become small, viscous stresses become larger until eventually they completely dominate, and all the energy passed into this size eddy is dissipated as heat. This smallest scale is known as the Kolmogorov microscale, η_k, which is still much larger than the molecular level.

3.1.2.12 Turbulent Energy Spectrum

As has been previously discussed, the structure of turbulence can be split up into three regions such that the large eddies contain most of the energy, the small eddies dissipate the energy and the eddy sizes in between both receive and pass on energy. The names given to each of these ranges are the energy production range, dissipation range and inertial range, respectively. For the latter range, Kolmogorov (Tennekes and Lumley 1972) used dimensional analysis to deduce how the energy contained within an eddy changes with size. Kolmogorov found that the energy scaled proportional to $k^{-5/3}$ where k is the wavenumber. Although only valid in the inertial subrange, the form of the spectrum is:

$$E(k) = \alpha \varepsilon^{2/3} k^{-5/3} \tag{3.21}$$

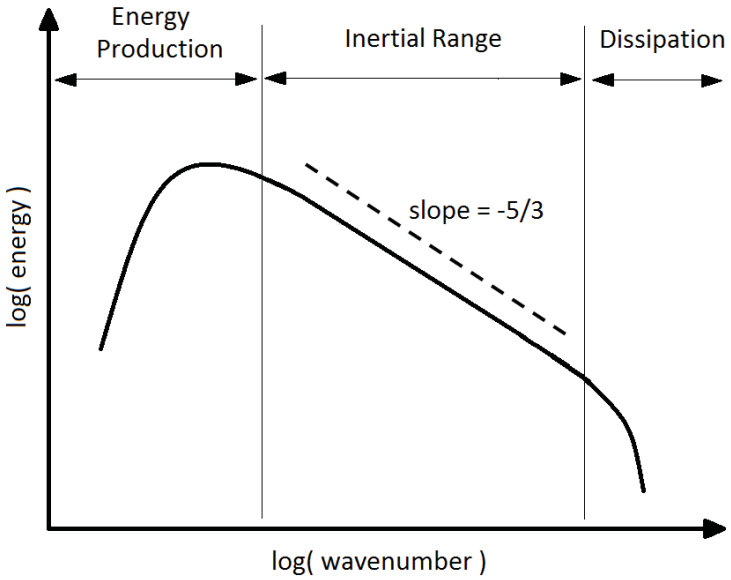

Figure 3.1: An illustration of the shape of the turbulent energy spectrum.

Therefore, the turbulent energy spectrum must take a form similar to Figure 3.1, where the small wavenumbers (large eddies) contain most of the energy, and the inertial subrange scales proportional to $k^{-5/3}$, with the energy reducing further in the dissipation range. However, if there is not a large scale separation, i.e. the small eddies are not much smaller than the large, then the inertial subrange may not be evident in the turbulent energy spectrum.

3.1.3 Turbulent Flows with Boundaries

Near a solid boundary a turbulent boundary layer exists. The wall boundary layer consists of two main layers, the inner and the outer layer, with the inner layer further split into three sublayers: the viscous sublayer, the buffer sublayer, and the inertial sublayer. Before describing the properties of each of these sublayers, a number of useful parameters are presented.

3.1.3.1 Wall Shear Stress and Friction Velocity

Another key concept is the wall shear stress. The shear stress consists of two components, the viscous component and the Reynolds stress:

$$\tau(z) = \mu \frac{\partial u}{\partial z} - \overline{u'w'}. \tag{3.22}$$

At the wall, the Reynolds stress is zero since a no slip condition must apply, i.e. the velocity of the fluid at a solid surface must be equal to the velocity of the surface itself. Furthermore, near the wall the velocities will remain small, and it is valid to assume that in the wall boundary layer the shear stress is approximately constant and equal to the wall shear stress, τ_w. This layer is known as the constant-shear layer and obeys

$$\tau(z) \approx \mu \frac{\partial u}{\partial z} = \tau_w. \tag{3.23}$$

Using dimensional analysis, it is clear that the wall shear stress has units of [density]$\times$[velocity]^2 and therefore

$$\tau_w = \rho u_*^2 \Longleftrightarrow u_* = \sqrt{\frac{\tau_w}{\rho}}. \tag{3.24}$$

This yields a characteristic velocity scale for flow near the wall, u_*, known as the friction velocity.

3.1.3.2 Wall Units

For convenience, it is common to define dimensionless velocity, u^+ and dimensionless distance from the wall, z^+ as

$$u^+ = \frac{u}{u_*}, \qquad z^+ = \frac{z u_*}{\nu}, \tag{3.25}$$

where u_* is the friction velocity, ν is the kinematic viscosity, and u is the mean flow.

3.1.3.3 Outer Layer - Velocity Defect Law

Far away from the wall, the velocity is influenced by the wall shear stress but not by the viscosity itself. Using dimensional analysis the mean velocity can be shown to scale as a function of z/δ where z is the distance from the wall, and δ is the height of the boundary layer. However, it is more convenient to assume that the wall shear stress is the cause of

any velocity deficit and hence to write the equation in the form

$$\frac{u_0 - u}{u_*} = g\left(\frac{z}{\delta}\right), \tag{3.26}$$

where u_0 is the free stream flow. This is known as the velocity-defect law. By writing the equation in the above form it must be true that as the boundary layer's edge is approached, the velocity deficit decreases. The region where this property holds is known as the Defect or Outer layer (Wilcox 2006).

3.1.3.4 Inner Layer - The Law of the Wall

Using dimensional analysis, (Tennekes and Lumley 1972), it is possible to show that near the wall, the mean velocity scales as a function of distance from the wall

$$u^+ = f(z^+). \tag{3.27}$$

Equation (3.27) is known as the Law of the Wall and takes a different value in each sublayer of the inner layer.

3.1.3.5 Viscous Sublayer

The viscous sublayer is the layer closest to the wall. At the wall, the velocity must be zero, and therefore any turbulent eddy motions must also stop very close to the wall. Hence, the region closest to the wall the flow is dominated by viscous effects and equation (3.23) can be applied. Integrating and applying the boundary condition $u = 0$ at $z = 0$ yields

$$u^+ = z^+. \tag{3.28}$$

This suggests that in the viscous sublayer the velocity scales at a linear rate with respect to the distance from the wall. For this reason the layer is sometimes called the linear sublayer. It is also worth noting that the viscous sublayer is very thin (Versteeg and Malalasekera (1995) suggest that $z^+ < 5$). The length scale of the viscous sublayer has been determined

experimentally to be (Fredsøe and Deigaard 1992)

$$\delta_v = 11.6\frac{\nu}{u_*}. \tag{3.29}$$

This gives an expression which could be considered a type of Reynolds number,

$$Re_* = \frac{1}{11.6}\cdot\frac{\delta_v u_*}{\nu}, \tag{3.30}$$

which implies that the viscous and turbulent stresses are of comparable magnitude when $Re_* \approx 1$.

3.1.3.6 Inertial Sublayer

There are now two different length scales, an inner length scale, δ_v and an outer length scale δ. It would be unphysical for the velocity to instantaneously jump from one scaling to another and therefore there must exist a region of overlap (Versteeg and Malalasekera (1995) suggests $30 < z^+ < 500$). By assuming that the scale separation is large, i.e. the inner scaling is much smaller than the outer, and that the shear stress is constant throughout the layer and equal to the wall shear stress, it is possible to obtain a form for this overlap region. To proceed in this case, two further assumptions must be made. Firstly, the shear stress is constant throughout the layer and equal to the wall shear stress and secondly, that the mixing length of the turbulence is $z\kappa$. Using asymptotic matching (Tennekes and Lumley 1972), and searching for an area of overlap between the velocity defect law and the law of the wall (equations 3.26 and 3.27, respectively) the result

$$u^+ = \frac{1}{\kappa}\ln(z^+) + a, \tag{3.31}$$

is derived, which is known as the log-layer law. The region where this equation holds is known as the inertial or logarithmic sublayer. The constant, a, in equation (3.31) must be determined experimentally (or by numerical solution of the full Navier-Stokes equation).

3.1.3.7 Buffer Layer

Between the inertial and viscous sublayers, (Versteeg and Malalasekera (1995) suggests $5 < z^+ < 30$) neither the log-layer nor the linear law hold and hence neither viscous nor turbulent effects can be neglected. Tennekes and Lumley (1972) notes that the turbulence dynamics in the buffer layer are vigorous since the turbulent energy production rate reaches a maximum at the value of $z^+ \approx 12$, which is where the Reynolds shear stress equals the viscous stress.

3.1.3.8 Rough Surfaces

As discussed previously, for a perfectly smooth wall, a boundary layer exists of size δ_v. However, if the wall is rough then it is important to take this into consideration. By studying the flow over a bed of uniform grain size, d, (secured with a thin lacquer), Nikuradse (1933) found the constant a in equation (3.31) to be (Fredsøe and Deigaard 1992)

$$\begin{aligned} a &= 8.5 - \frac{1}{\kappa}\ln(k_N) && \text{for hydraulically rough flows,} \\ a &= 5.7 - \frac{1}{\kappa}\ln\left(\frac{\nu}{u_*}\right) && \text{for hydraulically smooth flows.} \end{aligned} \tag{3.32}$$

Substituting each of these into equation (3.31) and assuming a solution of the form

$$u = \frac{u_*}{\kappa}\ln\left(\frac{z}{z_0}\right), \tag{3.33}$$

yields values for the roughness height, z_0, based on the Reynolds number, Re_*, namely

$$z_0 = \frac{\nu}{9u_*} \qquad \text{for} \quad Re_* < 5 \tag{3.34}$$

$$z_0 = \frac{k_N}{30} \qquad \text{for} \quad 70 < Re_* \tag{3.35}$$

$$z_0 = \frac{\nu}{9u_*} + \frac{k_N}{30} \qquad \text{for} \quad 5 < Re_* < 70. \tag{3.36}$$

Based on this observation, the equivalent Nikuradse roughness, k_N, is defined as (Nielsen 1992)

$$k_N = 30 z_0. \tag{3.37}$$

If the Nikuradse roughness (or the roughness height) is larger than the viscous sublayer, the flow is considered to be rough (Nielsen 1992). Therefore, the Nikuradse roughness, along with the viscous sublayer determine the type of flow as is shown in Table 3.1.

Condition	Flow type
$\delta_\nu > k_N$	hydraulically smooth flow
$\delta_\nu \approx k_N$	transitional flow
$\delta_\nu < k_N$	hydraulically rough flow

Table 3.1: Conditions for assessment of the flow roughness.

3.2 Waves

A wave on a surface of water is generated by a disturbing force such as the wind, which transfers energy to the water, that is then transported across the water surface. As the water is disturbed in the vertical direction, the force of gravity acts to return the surface to its equilibrium position. Since the returning surface has inertia, it passes the equilibrium position leading to an oscillation, which disturbs the adjacent water causing the wave to propagate across the surface. As it propagates, the oscillatory motion is maintained through the interaction of inertia and gravity (Sorensen 2006). At the coast, the waves become steeper, through shoaling, and eventually break leading to large energy dissipation and turbulence generation.

This section focuses on the modelling of surface gravity waves through analytical theories. Propagation of the waves near the coast is then examined, leading to discussion of the shoaling process and the different types of breaker.

3.2.1 Wave Theories

There exist many analytical descriptions for wave shapes and velocities. Commonly used theories, such as linear (Airy 1845) or Stokes (Stokes 1847) waves, make many assump-

tions including the depth of water in which the wave is propagating. This generally limits wave theories to very specific conditions, depending on the water depth, as well as the wave height. In this work, the water depth is generally considered to be shallow and hence this work focuses on Cnoidal and Stream Function wave theories.

3.2.1.1 Cnoidal Wave Theory

As was previously discussed, the application of Stokes wave theory is not valid in shallow water, and therefore a finite amplitude theory based upon the water depth must be used (Sorensen 2006). A commonly used method is cnoidal wave theory or, if the depth is very shallow, solitary wave theory. Cnoidal wave theory is based upon an equation originally developed by Korteweg and de Vries (1895):

$$\frac{\partial \eta}{\partial t} + c_p \frac{\partial \eta}{\partial x} + \frac{3c_p}{2h}\eta \frac{\partial \eta}{\partial x} + \frac{c_p h^2}{6}\frac{\partial^3 \eta}{\partial x^3} = 0, \tag{3.38}$$

and Jacobian elliptical functions, commonly designated by cn, must be used in order to obtain a solution. This function is defined such that

$$\mathrm{cn}^2(F(\phi, m)) = \cos^2 \phi, \tag{3.39}$$

where $F(\phi, m)$ is the incomplete elliptic integral of the first kind, with amplitude ϕ and parameter m (Svendsen 2006). The elliptic integral parameter, m, is a function of water depth, wavelength, and the vertical distance between the bottom and the crest, and the trough of the wave (Sorensen 2006). The parameter m lies in the range 0 and 1, with a small value representing a nearly sinusoidal wave (linear wave theory) and 1 being the solitary wave limit. The function cn also depends upon another parameter, U_r, known as the Ursell number, which is a dimensionless parameter that is often used to define a range for the application of wave theories.

The derivation of the equations is long and therefore has been omitted from this work (see Svendsen (2006), Chapter 9 for full details). Therefore, the equations for surface elevation, as well as the horizontal and vertical components of velocity, used to generate cnoidal

waves in the present model are:

$$\eta = H\left[\frac{1}{m}\left(1-\frac{E}{K}\right)-1+\mathrm{cn}^2\left(2K\left(\frac{t}{T}-\frac{x}{L}\right),m\right)\right], \tag{3.40}$$

$$u = c_p\left[\frac{\eta}{h}-\frac{\eta^2}{h^2}+\frac{h}{2}\left(\frac{1}{3}-\frac{(z+h)^2}{h^2}\right)\frac{\partial^2\eta}{\partial x^2}\right], \tag{3.41}$$

$$v = -c_p(z+h)\left[\frac{1}{h}\left(1-2\frac{\eta}{h}\right)\frac{\partial\eta}{\partial x}+\frac{h}{6}\left(1-\frac{(z+h)^2}{h^2}\right)\frac{\partial^3\eta}{\partial x^3}\right]. \tag{3.42}$$

Here K and E are complete elliptic integrals of the first and second kind (Svendsen 2006) and depend on the parameter m. The phase speed, c_p, of the wave must also be known in order to complete the procedure. This can be obtained using the expression

$$c_p^2 = gh+\frac{gH}{m}\left(2-m-3\frac{E}{K}\right). \tag{3.43}$$

3.2.1.2 Stream Function Wave Theory

The Stream Function wave theory is a numerical solution to the exact governing equations (Svendsen 2006), originally developed by Dean (1965). The methodology expands the unknown stream function and surface elevation into Fourier series. The given solution is for a constant wave shape in a constant water depth, and is horizontally symmetrical around the wave trough and crest (Svendsen 2006). The original method did not apply to the highest waves so a later version, developed by Rienecker and Fenton (1981), is described here, although a numerical implementation described by Fenton (1988) is applied in the present numerical model.

Stream Function wave theory makes two fundamental assumptions: the wave motion is irrotational, and the water is incompressible. To make the derivation easier, it is common to change the coordinate system from being a fixed system (x,z) with particle velocities (u,w) to a system moving with the wave. Since the waves are of a constant form the flow will be considered to be steady. Therefore, the new coordinate system is (x_1,z) moving with speed

c_a, the absolute phase velocity including currents, yielding

$$x_1 = x - c_a t, \qquad u_1 = u - c_a, \qquad w = w. \tag{3.44}$$

The stream function, ψ, is now introduced and is defined by the equations

$$\frac{\partial \psi}{\partial z} = u_1, \qquad \frac{\partial \psi}{\partial x_1} = -w, \tag{3.45}$$

which always satisfy the Laplace equation,

$$\frac{\partial^2 \psi}{\partial x_1^2} + \frac{\partial^2 \psi}{\partial z^2} = 0, \tag{3.46}$$

ensuring that the assumption regarding irrotational flow always holds. The boundary conditions are now chosen so that, in the moving coordinate system, the free surface and bottom are streamlines of constant ψ,

$$\psi(x_1, -h) = 0, \tag{3.47}$$

$$\psi(x_1, \eta(x_1)) = -Q, \tag{3.48}$$

where Q is the total flow between bottom and surface (Svendsen 2006). Furthermore, the solution must satisfy the dynamic surface condition at the free surface, hence at $z = \eta(x_1)$,

$$\frac{1}{2}\left[\left(\frac{\partial \psi}{\partial x_1}\right)^2 + \left(\frac{\partial \psi}{\partial z}\right)^2\right] + \eta(x_1) = C, \tag{3.49}$$

must hold, where C is the Bernoulli constant for the steady flow. Using Fourier expansion, the stream function can be expressed as the series

$$\psi(x_1, z) = B_0(z+h) + \sum_{j=1}^{N} B_j \frac{\sinh(jk(z+h))}{\cosh(jkh)} \cos(jkx_1), \tag{3.50}$$

where each of the terms in the sum unconditionally satisfies the bottom boundary condition (equation 3.47) and the Laplace equation (equation 3.46). Therefore, the coefficients $B_0, ..., B_N$ must be determined so that the surface boundary conditions (equations 3.48 and

3.49) are satisfied and also determine the unknown values η, k, C and Q (Svendsen 2006). By substituting equation (3.50) into the surface boundary conditions (equations 3.48 and 3.49), two equations containing a number of unknowns (η's, B_j's, k, Q and C),

$$B_0(\eta+h)+\sum_{j=1}^{N} B_j \frac{\sinh(jk(\eta+h))}{\cosh(jkh)}\cos(jkx_1) = -Q \tag{3.51}$$

$$\frac{1}{2}\left[\left(B_0+k\sum_{j=1}^{N} jB_j\frac{\cosh(jk(\eta+h))}{\cosh(jkh)}\cos(jkx_1)\right)^2-\left(k\sum_{j=1}^{N} jB_j\frac{\sinh(jk(\eta+h))}{\cosh(jkh)}\sin(jkx_1)\right)^2\right] +(\eta+h)=C. \tag{3.52}$$

The solution is then obtained by requiring that these two equations are exactly satisfied at $N+1$ points in x_1, where points 0 and N are at the wave crest and trough, respectively. This creates $2N+2$ equations to solve with a total of $2N+5$ unknowns ($N+1$ B_j's, $N+1$ η's, k, Q and C) (Svendsen 2006). Hence three more equations are required in order to solve the problem. The first equation defines the wave height as the difference between the maximum and minimum surface elevation, i.e.

$$\eta_0-\eta_N=0. \tag{3.53}$$

The second requirement is that the wavelength must be related to the speed of the wave relative to the water speed (the current) c_r, such that $L=c_rT$. Furthermore, it can be shown that the coefficient B_0 is equal to the relative wave speed, c_r. Finally the mean surface elevation must be zero:

$$\overline{\eta}=\frac{2}{L}\int_0^{L/2}\eta\,dx_1=0. \tag{3.54}$$

If the wave height, H, and period, T, are known, then the system of equations can be solved to obtain the wave motion in a given water depth, h. Once the stream function is known, the velocity components can be calculated through differentiation. To obtain the values of the B_j coefficients, a generalised iterative solution scheme, such as the Newton-Raphson method, is required as is illustrated in Rienecker and Fenton (1981).

As was previously mentioned, the method of Fenton (1988) is used in the present numerical model. Hence for a wave propagating in water with zero current, the expressions for η, u and w are:

$$\eta = \sum_{j=1}^{N} A_j \cos\left((j+1)(k\cdot\mathbf{x}-\omega t)\right), \tag{3.55}$$

$$u = \frac{\omega}{k} + \sum_{j=1}^{N} B_j \frac{\cosh(k(j+1)(z+h))}{\cosh(jkh)} \cos\left((j+1)(k\cdot\mathbf{x}-\omega t)\right), \tag{3.56}$$

$$w = \sum_{j=1}^{N} B_j \frac{\sinh(k(j+1)(z+h))}{\cosh(jkh)} \sin\left((j+1)(k\cdot\mathbf{x}-\omega t)\right), \tag{3.57}$$

where the A_j and B_j coefficients are obtained using an iterative method.

3.2.2 Depth Limited Breaking Waves

3.2.2.1 Shoaling

As a wave propagates into shallower water, it begins to transform in shape. To understand how this occurs consider the propagation of a linear wave, which must satisfy the dispersion relation (Holthuijsen 2007)

$$\omega^2 = gk\tanh(kh). \tag{3.58}$$

If this wave then propagates towards a beach of constant gradient, the depth decreases, but the frequency of the wave must stay the same. This can only continue to satisfy equation (3.58) if the wavelength, $L = (2\pi)/k$, decreases. Furthermore, the phase speed and group velocity will also decrease and as the wave gets closer to the shore, the phase speed will approach the group velocity. This causes the waves to become less dispersive and the variations in the group velocity also cause variations in local wave energy (Holthuijsen 2007). The net effect of shoaling is that, after an initial decrease, the amplitude of the waves will increase substantially.

3.2.2.2 Breaking Point

As the height of a wave increases in the surf zone due to shoaling, the steepness also increases and the wave eventually becomes unstable and breaks. There are many formulae (Svendsen 2006; Kinsman 2012) aimed at predicting the point at which this maximum

wave height and breaking point occurs. A rough estimate is that breaking occurs when the maximum wave height, H_{max}, is approximately 0.75 times the local water depth (Holthuijsen 2007), i.e.

$$\frac{H_{max}}{h} \approx 0.75. \tag{3.59}$$

However, this formula will not hold in all conditions as H_{max} will also be dependent on the beach steepness and the wind conditions. Other approximations depend on the wave steepness (Svendsen 2006) such as

$$\left(\frac{H}{L}\right)_{max} = 0.142 \tanh(kh), \tag{3.60}$$

or, alternatively, breaking could be defined as the point where the horizontal crest speed exceeds the phase speed, c_p (Kinsman 2012).

3.2.3 Breaker Types

Depth-induced breaking waves have different characteristics depending on factors such as the slope of a beach and the steepness of the wave. Breaking wave types are usually classified into four main categories: plunging, spilling, surging and collapsing breakers. The Iribarren number, ξ, (Iribarren and Nogales 1949; Battjes 1974) offers an approximate measure of the breaker type in the surf zone. The Iribarren number can be defined in two ways:

$$\xi_0 = \frac{\tan(\alpha)}{\sqrt{H_0/L_0}} \qquad \text{or} \qquad \xi_b = \frac{\tan(\alpha)}{\sqrt{H_b/L_0}}, \tag{3.61}$$

where α is the angle of the beach to the horizontal, H is the wave height, L is the wavelength and the subscripts 0 and b represent deep water and breaking point, respectively (Holthuijsen 2007). Table 3.2 gives the range of Iribarren numbers, based on observations, corresponding to each type of breaker.

3.2.3.1 Spilling Breakers

As can be seen in Table 3.2, spilling breakers occur when the Iribarren number is very low. Physically, this occurs when the wave steepness is large and the slope is gentle. Each

Breaker Type	ξ_0 Condition	ξ_b Condition
Spilling	$\xi_0 < 0.5$	$\xi_b < 0.4$
Plunging	$0.5 < \xi_0 < 3.3$	$0.4 < \xi_b < 2.0$
Collapsing or Spilling	$\xi_0 > 3.3$	$\xi_b > 2.0$

Table 3.2: Breaker type conditions based on the Iribarren number (Holthuijsen 2007).

wave gradually grows in height until the crest becomes unstable and cascades down the front of the wave as bubbles and foam.

3.2.3.2 Plunging Breakers

For moderate Iribarren numbers, generally related to waves of intermediate steepness breaking on steep beaches, plunging breakers occur. The plunging breaker is the iconic image associated with breaking waves. The front of the wave becomes vertical before curling over and plunging forwards as an intact mass of water.

3.2.3.3 Surging and Collapsing

For high Iribarren numbers, surging waves can occur. These breakers are associated with waves of low steepness breaking on very steep beaches. Surging breakers peak up as if they are going to plunge, but then the face of the wave surges up the beach face causing the crest to collapse and disappear. Collapsing breakers are an intermediate stage between the plunging and surging breakers. However, since breaking wave types are a continuum it is not always possible to assign a breaking wave to a particular category.

3.3 Sediment Transport

Sediment transport is the movement of solid particles due to the fluid flow. This has great importance in many fields such as coastal erosion or accretion, scour around structures and biological processes in ecosystems.

This section is aimed at providing the basic processes involved in the transport of sediment, with particular emphasis on the sediment which is in suspension since it is the focus of this study.

3.3.1 Basic Concepts

3.3.1.1 Modes of Transport

It is common to split sediment transport into three different mechanisms. These are the bed load, the suspended load and the wash load. The wash load consists of very fine particles, which can be transported by the water for very long periods of time without settling and hence are not always available in the bed at the sample site. Therefore, the wash load cannot be predicted by the composition of the bed material and, taking this into account, the total sediment load is usually considered to be just the bed load and suspended load components (Fredsøe and Deigaard 1992).

The bed load is defined as the part of the total load that is transported along the bed without being suspended by the fluid turbulence. The bed load usually consists of particles which roll, slide or jump along the bed. Therefore, the bed load is primarily determined by the effective bed shear stress acting on the surface of the grains (Fredsøe and Deigaard 1992). The suspended load is defined as the particles that are maintained in suspension in the flowing water for considerable periods of time without contact with the bed (van Rijn 1993).

3.3.1.2 Sediment Size

Sediment is often classified according to the size of the grains. As well as allowing beaches to be categorised in terms of sediment type, it also allows formulations which only hold for certain sediment sizes. Komar (1998) splits up the classes into grain sizes as shown in Table 3.3. Since this study focuses on the suspended load, the sediment that will be considered will generally be fine sand.

3.3.1.3 Bed Shear Stresses

The effects of waves and currents on sediment dynamics mainly take place through the friction they exert on the bed. For mathematical convenience, the bed shear stress, τ_w, can

Name	Diameter (mm)
Boulder	> 256
Cobbles	64 to 256
Pebbles	4 to 64
Granule	2 to 4
Very Coarse Sand	1 to 2
Coarse Sand	0.5 to 1
Medium Sand	0.25 to 0.5
Fine Sand	0.125 to 0.25
Very Fine Sand	0.0625 to 0.125
Silt	0.0039 to 0.0626

Table 3.3: Classification of grain sizes by their diameters (Komar 1998).

also be written in units of velocity as the friction velocity, u_*, through the relationship

$$\tau_w = \rho u_*^2 \tag{3.62}$$

where ρ is the density of water. Although it is termed the friction velocity, it does not correspond to a "real" velocity in the flow (Soulsby 1997).

3.3.1.4 Shields Parameter

A commonly used parameter in sediment transport formulations is the Shields parameter, θ, defined as

$$\theta = \frac{\tau_w}{g(\rho_s - \rho)d} = \frac{u_*^2}{g(s-1)d}. \tag{3.63}$$

This is a non-dimensional form of the bed shear stress, where ρ_s is the density of the sediment grains, d is the diameter of the sediment grains, and s is the ratio of sediment and fluid densities, $s = \rho_s/\rho$.

3.3.1.5 Nikuradse Roughness

The bed shear stress does not only depend on the speed of the flow but also on the roughness of the bed, which is usually either expressed in terms of the Nikuradse roughness, k_N, or the roughness height, z_0. The Nikuradse roughness can be related to the sediment grain size, whereas the roughness height can be derived from the velocity profile. One of the

most commonly used relationships between the Nikuradse roughness and the grain size is $k_N = 2.5d_{50}$ (Soulsby 1997), although many other relationships have been proposed depending upon other grain-size percentiles including $1.25d_{35}$, d_{65} and $2d_{90}$ (van Rijn 1993). Soulsby (1997) notes that although there is substantial disagreement between the choice of k_N, the discrepancies in bed shear stress will be much smaller since it depends on the logarithmic value of k_N.

3.3.2 Thresholds of Motion

3.3.2.1 Angle of Repose

The angle of repose, ϕ_i, (or the angle of internal friction) is a measure of when sediment grains begin to roll (Soulsby 1997). The angle of repose depends on many factors including size, shape and porosity of the bed. Laboratory experiments have shown that ϕ_i increases with decreasing roundness and decreases with increasing porosity. Natural sands typically have an angle of repose in the range 30° to 40° (van Rijn 1993), and Soulsby (1997) suggests $\phi_i = 32^\circ$ as a good general purpose value to be used in calculations to assess slope effects on the threshold of motion.

Another measure is the angle of final repose, ϕ_r, which is the angle of the final slope after equilibrium is reached, i.e. when avalanching has ceased. This value is always less that the angle of repose and a typical value for natural sand in water is 28°.

3.3.2.2 Critical Bed Shear Stress

The critical bed shear stress is a common measure of the threshold of motion: the conditions required to make a grain begin to move. Shields (1936) developed the method in terms of the ratio of the bed shear stress acting to move a grain on the bed, to the submerged weight of the grain counteracting this (Soulsby 1997). This ratio is the critical Shields parameter, θ_{cr}, defined as

$$\theta_{cr} = \frac{\tau_{cr}}{g(\rho_s - \rho)d}, \tag{3.64}$$

where τ_{cr} is the critical bed shear stress, for which there is a number of algebraic expressions available (Shields 1936; Miller et al. 1977; van Rijn 1993; Soulsby and Whitehouse

1997).

On a sloping bed, gravity provides a component of force on the grain which may alter the critical bed shear stress. Taking this into consideration, the critical bed shear stress, on a bed sloping at angle α to the horizontal, $\tau_{\alpha,cr}$, in a flow making an angle θ to the up-slope direction, can be related to the critical bed shear stress on a horizontal bed, τ_{cr}, by (Soulsby 1997)

$$\frac{\tau_{\alpha,cr}}{\tau_{cr}} = \frac{\cos(\theta)\sin(\alpha) + [\cos^2(\alpha)\tan^2(\phi_i) - \sin^2(\theta)\sin^2(\alpha)]^{1/2}}{\tan(\phi_i)}. \tag{3.65}$$

In equation (3.65), ϕ_i is the angle of repose of the sediment at which slope the sediment will avalanche, i.e. if $\beta > \phi_i$, then avalanching occurs. Equation (3.65) is the general case but the expression simplifies in the cases where the flow is either up the slope ($\omega = 0^\circ$), down the slope ($\omega = 180^\circ$) or laterally across the slope ($\omega = \pm 90^\circ$). The expressions are then

$$\frac{\tau_{\alpha cr}}{\tau_{cr}} = \frac{\sin(\phi_i + \alpha)}{\sin(\phi_i)} = \cos(\alpha) + \frac{\sin(\alpha)}{\tan(\phi_i)}, \tag{3.66}$$

$$\frac{\tau_{\alpha cr}}{\tau_{cr}} = \frac{\sin(\phi_i - \alpha)}{\sin(\phi_i)} = \cos(\alpha) - \frac{\sin(\alpha)}{\tan(\phi_i)}, \tag{3.67}$$

$$\frac{\tau_{\alpha cr}}{\tau_{cr}} = \cos(\alpha)\left(1 - \frac{\tan^2(\alpha)}{\tan^2(\phi_i)}\right)^{1/2}, \tag{3.68}$$

for up, down and across the slope, respectively (van Rijn 1993). When dealing with 2-D cross-shore flows, like those being considered in this work, either equation (3.66) or (3.67) will always be applicable.

3.3.2.3 Suspension

When the bed shear stress becomes comparable with the settling velocity, particles may go into suspension. Particles will only remain in suspension if the vertical velocity component of turbulent eddies is larger than the settling velocity, w_s, of the particle (Bagnold 1966). This gives us a criterion for suspension of

$$(\overline{|w'|^2})^{0.5} \geq w_s, \tag{3.69}$$

where w' is the vertical velocity component of the turbulence (van Rijn 1993). By studying boundary layer flows, it has been shown that the vertical turbulence velocity has a maximum value of the same order of magnitude as the friction velocity, u_*, for both hydraulically smooth and rough flows (van Rijn 1993). This implies that the critical friction velocity, u_{*cr}, for suspension is

$$u_{*cr} = w_s, \tag{3.70}$$

or, in terms of the critical Shields parameter,

$$\theta_{cr} = \frac{(u_{*cr})^2}{(s-1)gd} = \frac{(w_s)^2}{(s-1)gd}. \tag{3.71}$$

3.3.3 Settling Velocity

The settling velocity, w_s, is defined as the terminal velocity of the sediment grain when it is settling in still water under the influence of gravity. The settling velocity depends on many parameters including the ratio of the grain and the fluid densities, the grain size and the viscosity of the fluid (Fredsøe and Deigaard 1992).

3.3.3.1 Grain Reynolds number

In analogy to the turbulent Reynolds number, it is often useful to define a grain Reynolds number, Re_g, using the grain diameter and settling velocity as the characteristic length scale and velocity (Fredsøe and Deigaard 1992),

$$Re_g = \frac{w_s d}{\nu}. \tag{3.72}$$

This is sometimes found in sediment transport formulations, or used as a criterion, as will be seen in the following sections.

3.3.3.2 Settling Velocity in a Still Fluid

By considering the drag force on a single spherical particle and relating to the forces at equilibrium, it is possible to show that the settling velocity must take the form (van Rijn

1993)

$$w_s = \sqrt{\frac{4(s-1)gd}{3c_D}}. \tag{3.73}$$

For very fine spherical particles, the drag force follows Stokes law (Nielsen 1992) and hence the drag coefficient and settling velocity can be described by the simple expressions

$$c_D = \frac{24}{Re_g}, \tag{3.74}$$

$$w_s = \frac{(s-1)d^2 g}{18\nu}, \tag{3.75}$$

respectively. However, outside the Stokes law region, there is no simple expression for the drag coefficient with it decreasing rapidly at first before yielding $w_s \approx d^{0.5}$. Furthermore, the expressions for a sphere are not valid for natural sediment due to the differences in shape, leading to many alternative formulations (Rubey 1933; van Rijn 1984*b*; Soulsby 1997), which largely depend on the median grain diameter.

3.3.3.3 Effects of sediment concentration

At high concentrations the drag around adjacent particles becomes larger than observed for an isolated sediment grain. This leads to a reduction in the settling velocity known as hindered settling (Soulsby 1997). It is common to assume that the variation in w_s follows a simple power law between clear water, $C = 0$, and the concentration at the non-moving bed, $C = C_{max}$ (Nielsen 2009)

$$w_{s,hind}(C) = w_s(1-C)^n \quad \text{for} \quad 0 < C < C_{max}, \tag{3.76}$$

where w_s is the settling velocity in clear water, and n is a coefficient to be determined. There is not a commonly agreed value for n, with experimental studies conducted in settling columns generally implying a value between 3 and 4 for natural sand (Nielsen 2009). The value of n also depends on the grain size: Soulsby (1997) suggested $n = 4.7$ and 2.35 for fine and coarse grains, respectively, whereas Richardson and Zaki (1954) provided an

expression for n based on the grain Reynolds number, Re_g, (Fredsøe and Deigaard 1992)

$$n = \begin{cases} 4.35Re_g^{-0.03} & 0.2 < Re_g < 1 \\ 4.45Re_g^{-0.1} & 1 < Re_g < 500 \\ 2.39 & 500 < Re_g. \end{cases} \tag{3.77}$$

3.3.3.4 Sediment concentration at the bed

The sediment concentration at a non-moving bed, C_{max}, depends on a number of parameters including grain shape and packing. For spherical particles of uniform size the concentration falls in the range $0.52 < C_{max} < 0.74$, depending on the configuration of the bed (Nielsen 2009), whereas natural sand has a maximum attainable concentration of around 0.65 (Fredsøe and Deigaard 1992).

3.3.4 Modelling Suspended Sediment Distributions

The distribution of the suspended load is often modelled through a transport equation balancing settling, flow advection and turbulent diffusion. This is often referred to as advection-diffusion theory and is the basis of many suspended sediment predictions in numerical models. In full, the governing equation for the problem is

$$\frac{\partial C}{\partial t} + \nabla \cdot (\mathbf{u}C) + \nabla \cdot (\mathbf{w_s}C) = \nabla \cdot (\nu_s \nabla C), \tag{3.78}$$

where C is the suspended concentration, ν_s is the sediment diffusivity coefficient, $\mathbf{u}$ and $\mathbf{w_s}$ are the flow and settling velocities, respectively. However, depending on the flow, it is possible to perform numerous simplifications. For instance, in a steady state flow through a horizontal channel all horizontal derivatives, along with the vertical flow velocity, can be neglected, simply leaving the balance of vertical diffusion and settling contribution,

$$w_s C + \nu_s \frac{\partial C}{\partial z} = 0. \tag{3.79}$$

3.3.4.1 Rouse Profile

In flows with a constant horizontal current, the vertical distribution of sediment concentration takes a distinct profile, known as the Rouse profile, which can be derived starting from the governing equation (equation 3.79). In a steady channel flow the vertical shear stress varies linearly with depth, and the velocity follows a logarithmic profile (Fredsøe and Deigaard 1992). These relationships, along with assumption that the eddy viscosity is related to the sediment diffusivity imply that ν_s follows a parabolic profile

$$\nu_s = \kappa u_* z \left(1 - \frac{z}{h}\right), \tag{3.80}$$

where u_* is the friction velocity, z is the vertical distance above the bed, and h is the water depth. Combining equations (3.80) and (3.79), integrating with respect to z and using the boundary condition $C = C_a$ at $z = a$ provides an analytical solution for the vertical suspended sediment distribution

$$C(z) = C_a \left(\frac{h-z}{h-a} \cdot \frac{a}{z}\right)^b, \qquad b = \frac{w_s}{\kappa u_*}. \tag{3.81}$$

This is known as the Rouse profile, with the coefficient b often referred to as the Rouse parameter (Soulsby 1997).

3.3.4.2 Turbulent Schmidt Number

The turbulent Schmidt number, σ_c, is a dimensionless number defined as the ratio of the turbulent viscosity and sediment diffusivity associated with the turbulent suspension process (Flesch et al. 2002; Amoudry et al. 2005),

$$\sigma_c = \frac{\nu_t}{\nu_s}. \tag{3.82}$$

This description is often used in numerical models where ν_t is known (Hsu and Liu 2004; Ma et al. 2014). By assuming a value for σ_c, the sediment diffusivity can be estimated based on the eddy viscosity, for use as the input for the suspended sediment model.

3.3.5 Sediment exchange at the bed

An important consideration when modelling suspended sediment concentrations is the deposition and entrainment of sediment at the bed. This is a complex procedure due to the nature of the flow near the bed where strong shear stresses and the turbulent boundary layer are often present. Traditionally, a reference concentration formulation has been adopted, but pickup functions, which set an upward flux rather than the concentration itself, have become increasingly popular in more recent models (Nielsen 2009).

3.3.5.1 Reference Concentration

The concept of a reference concentration is to define the bottom boundary of the suspended sediment model at a set distance, $z = a$ above the bed, and consider the transport of all particles below this height as bed load (van Rijn 1984*b*). This removes the need to model the complex phenomena very close to the bed and instead sets the concentration C_a at the reference height $z = a$. A number of different expressions for C_a have been suggested (Einstein 1950; Engelund and Fredsøe 1976; Smith and McLean 1977; van Rijn 1984*b*; Garcia and Parker 1991; Zyserman and Fredsøe 1994), each based on a different value for a. Applying any of these formulations, the reference concentration approach is relatively simple to implement but it is mostly only applicable for steady and uniform flow conditions (Nielsen 2009).

3.3.5.2 Pickup functions

An alternative to the reference concentration method is the pickup function. This strategy aims to specify the upward flux at the bed by comparing the balance of deposition, D, and entrainment, E, which is modelled using a pickup function (Nielsen 2009). There are a number of existing formulations describing the entrainment of sediment (Nielsen 1979; van Rijn 1984*a*; Nielsen et al. 2002), and they are usually based on the Shields parameter, θ. In a steady uniform flow the entrainment and deposition must be the same, i.e. $E = D$. In unsteady conditions, E and D are usually different leading to bed level changes due to accretion or erosion. The main advantage of using a pickup model is that it is capable

of responding to the flow conditions making it applicable in unsteady conditions. Nielsen (1979) presented a pickup function which, in the case of waves propagating over ripples, was capable of predicting two peaks per wave period at the flow reversal (Nielsen 2009), indicating that it works well in oscillatory conditions.

Chapter 4

The Numerical Model

There are many existing methods for simulating fluid flows covering a wide range of complexity. However, to accurately capture the characteristics of breaking waves, a fully nonlinear solver must be used. The most accurate method available is to directly solve the Navier-Stokes equations, which are the governing equations for fluid flows. Two common models that solve these equations are Computational Fluid Dynamics (CFD) and Smoothed Particle Hydrodynamics (SPH). The fundamental difference between the two methods is that CFD finds a solution at finite locations on a domain, whereas SPH tracks particle movements.

In this study, CFD has been chosen as the basis for the numerical model. There are a number of reasons for this choice. The first is that there are a good selection of well established CFD codes, both commercial and open source, available. Secondly, since turbulence is a fundamental component of this work, the choice of turbulence modelling options that are available in CFD is considered to be extremely practical. Furthermore, CFD has been widely used for applications such as wave-structure interaction and breaking waves, and hence methods for wave generation are available.

This chapter describes the numerical model used in this study. Firstly, general CFD methodologies are presented, along with details specific to the Open source Field Operation And Manipulation (OpenFOAM®) CFD toolbox, which has been chosen as the basis of the model in this work. Details of wave generation and turbulence modelling, within OpenFOAM®, are then described, before the novel suspended sediment transport model developed in this work is presented in Section 4.5.

4.1 Computational Fluid Dynamics

CFD is a form of analysis, based on computer-based simulations, for the study of fluid flows (Versteeg and Malalasekera 1995), and is used in a variety of fields including aerodynamics of aircraft and vehicles, marine engineering, oceanography and weather prediction. CFD solves various forms of the momentum (Navier-Stokes) and mass conservation equations, an example being the incompressible Navier-Stokes equations given by equations (3.2)-(3.5). In order to obtain a computational solution, the governing equations must be discretised to allow the fluid properties to be integrated over small time intervals. Once discretised, the solution is then obtained through iterative processes.

CFD is a very powerful tool since it allows the user to have access to the flow parameters in the whole computational domain, unlike physical experiments which only give information about the flow at certain sampling locations or in small spatial windows. There are many further advantages of using CFD. Firstly, very few assumptions are made about the governing equations for the fluid flow and therefore results closely follow reality. Secondly, CFD simulations are much cheaper to run than physical experiments and it is possible to obtain results without using intrusive equipment, which may alter the properties of the flow. Finally, it is possible to simulate idealistic conditions, allowing isolation of particular flow properties, of varying complexity.

However, there are some limitations. The results are only as good as the physics behind the simulation, which are usually obtained from physical experiments. Furthermore, the simulation is driven by the boundary conditions so it is of vital importance to specify these correctly. Inevitable numerical errors also occur due to round-off and truncation errors originating from characteristics such as the mesh cell size and the finite memory of the computer. Possibly the biggest drawback is that it is very computationally expensive, and is not intended for large time or space scales. Stability of the problem is often governed by the Courant number, C_o, where

$$C_o = \frac{u\Delta t}{\Delta x} \leq C_{o,max}. \tag{4.1}$$

In order to get the problem to converge, a maximum Courant number is often specified by the user, which limits the size of the time step. It is usually impractical to simulate fully turbulent flows using the full Navier-Stokes equations since, in order to capture all of the turbulent scales the cell size must be less than the smallest eddies , i.e. $\Delta x < \eta_k$. However, if Δx is small then the time step, Δt, must also be small to avoid violating the condition (4.1), leading to extremely long simulation times. When all turbulent scales are resolved in this way, the simulation is usually referred to as a direct numerical simulation (DNS).

It is possible to save computational effort by using averaging methods on the governing equations, and then modelling the effects of turbulence through approximate measures based on the mean flow variables. Reynolds-averaged simulation (RAS) solve the Reynolds-Averaged Navier-Stokes (RANS) equations (see equations 3.9-3.12), which describe the time-averaged quantities of the flow variables in the simulation. Therefore, none of the turbulent eddies (i.e. fluctuations from the mean velocity) are resolved, and their effect must be modelled using a turbulence closure model to estimate the Reynolds stresses. Another method, which is a compromise between DNS and RAS, is the large eddy simulation (LES) where the equations are filtered spatially to resolve the largest eddies, and model the sub-grid smaller eddies. Finally, to counter problems with LES in the near-wall region a hybrid method, detached eddy simulation (DES), has been developed, which applies LES far away from the wall region and RAS near to it. The information on the scale sizes that are resolved and modelled as sub-grid are summarised in Table 4.1 for each of the different simulation types.

Simulation Type	Resolved	Modelled
DNS	All Scales	None
LES	Large Scales	Small Scales
RAS	None	All Scales

Table 4.1: The turbulent length scales which are resolved in each CFD simulation type.

Multiple CFD codes have been developed, both commercially, and as open source software. Examples of open source software include OpenFOAM® and Gerris, whereas alternative commercial options are ANSYS CFX, ANSYS FLUENT and STAR-CCM+. All of

these software packages have their advantages and disadvantages, but this project utilises open source options since it allows the freedom to adapt solvers as needed. Therefore, the focus was limited to either OpenFOAM® or Gerris, and, based on a preliminary study, the former was chosen for this work.

OpenFOAM® is an open source CFD toolbox, developed by OpenCFD Ltd. and consisting of a variety of solvers to simulate specific problems in many fields across engineering and science. Pre- and post-processing utilities are also provided including tools for meshing and data visualisation. The structure of the code is modular, written in C++ and makes use of object-orientation, with features collected into a series of shared libraries, allowing solvers to then be linked to these collections.

There are many features implemented in OpenFOAM®, which are particularly useful for this project including multiphase solvers using the volume of fluid (VOF) method, existing wave generation tools, (e.g. `waves2Foam`), parallel computing, and the ability to easily switch between RAS and LES turbulence models. Furthermore, OpenFOAM® has a large user base to draw upon when developing new code or encountering problems, and the code is reasonably well documented. Due to these existing features, OpenFOAM® has been chosen as the platform on which to base the CFD component of this work.

4.2 Implementation of General CFD Methods in OpenFOAM®

General CFD methodologies are described in detail in this section, with particular emphasis on their implementation in OpenFOAM® (v. 2.1.1). Firstly, the discretisation of the governing equations is discussed, before algorithms for solving these discretised equations are considered.

4.2.1 Discretisation

Several procedures for evaluating differential equations at discrete locations on a meshed geometry (discretisation) exist, including the Finite Difference, Finite Volume, and Finite Element methods. OpenFOAM® uses the Finite Volume method for discretisation, which requires splitting a domain into a series of control volumes.

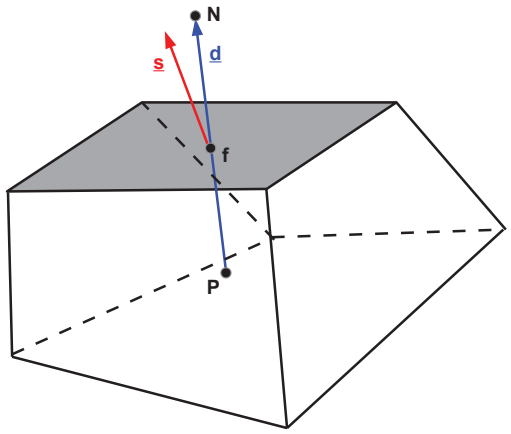

Figure 4.1: Illustration of a control volume along with the surface normal vector, $\mathbf{s}$, and the vector, $\mathbf{d}$, joining the centres of the present control volume ($\mathbf{P}$) and the neighbouring control volume ($\mathbf{N}$) . The point $\mathbf{f}$ is where vector $\mathbf{d}$ intersects the face joining the two control volumes.

4.2.1.1 Control Volumes

These control volumes completely fill the computational domain but do not overlap (Patankar 1980; Jasak 1996). The point $\mathbf{P}$, where all the computations are performed, is located at the centre of the control volume, determined by

$$\int_{V_P} (\mathbf{x} - \mathbf{x}_P)\, dV = 0, \tag{4.2}$$

where $\mathbf{x}_P$ and V_P are the position vector at the centre, and the volume of the control volume, respectively. Control volumes are bounded by a set of flat faces, where each face is shared with only one neighbouring control volume. The shape of a control volume is not important and is generally a polyhedron (Jasak 1996). Cell faces are either an internal face (between two control volumes), or a boundary face which coincides with the boundaries of the domain.

Each control volume is given a label (a number). The face area vector, $\mathbf{s}_f$, is constructed for each face such that it points outwards from the cell with the lower label, is normal to the face, and has magnitude equal to the area of the face (Jasak 1996). The cell with the lower

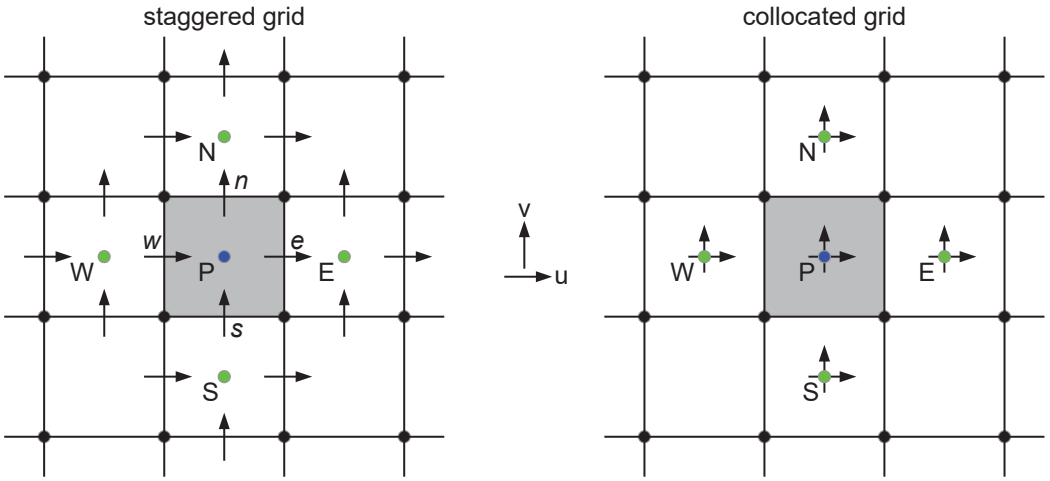

Figure 4.2: Illustration of the stored velocity points using the staggered (left) and collocated (right) grid techniques. In the former the velocity is stored at **n**, **e**, **s** and **w**, whereas in the latter it is stored at **N**, **E**, **S** and **W**.

label is known as the "owner" of the face and the other cell is known as the "neighbour". Boundary face area vectors point out of the computational domain, and the owner is the adjacent cell (Jasak 1996).

4.2.1.2 Collocated Grid

If the velocity is stored at the same point as the scalar fields (e.g. pressure, temperature), it is possible that highly non-uniform fields can act like uniform fields in the discretised momentum equations. Versteeg and Malalasekera (1995) illustrates this problem using a checker-board pressure field, where, although there are oscillations in pressure in every direction, all of the discretised pressure gradients are zero at the nodal points (for full details see Versteeg and Malalasekera (1995), pages $136 - 137$).

To avoid this problem, there are two approaches which are commonly adopted. The first is the "staggered grid" approach, where the velocity components (and other flux based quantities) are stored and evaluate at the cell faces, whereas the remaining scalar fields are stored and evaluated at a single point in the control volume. The second approach is the "collocated grid", where all of the fluid flow fields, including the velocity, are stored at a single node in the the control volume. To avoid the previously mentioned oscillations in pressure, inter-

polation linking the face velocity to the driving pressure difference (Rhie and Chow 1983) is required before integration can take place. The collocated grid arrangement is generally considered as more suitable for unstructured and multiple grids (Tu et al. 2008).

Figure 4.2 illustrates both of these approaches on a structured, 2-D grid. On the staggered grid (left), the velocity is stored at cell faces $\mathbf{n}$, $\mathbf{e}$, $\mathbf{s}$ and $\mathbf{w}$, whereas the scalar quantities are stored at point $\mathbf{P}$. On the other hand, the collocated grid (right) has all fields stored at point $\mathbf{P}$.

Similar to many commercial CFD codes, OpenFOAM® only provides the option to use a collocated grid (Jasak 1996). The Rhie-Chow correction in OpenFOAM® makes use of a separate velocity flux field, ϕ, defined as the dot product of the interpolated velocity and cell face normal (the magnitude of the cell face normal is the cell face area). This will be discussed further in Section 4.2.1.6.

4.2.1.3 Interpolation Schemes

As was discussed previously (Section 4.2.1.2), interpolation is necessary to achieve oscillation free fields on a collocated grid. Hence for all spatial derivatives both an integration and interpolation scheme (from cell centre to face centre) must be specified, whereas time schemes only require an integration scheme. This section describes some of the commonly used interpolation methods. To find the value of a general field, a, at an internal face (subscript f), all of the methods utilise the values of a in the present and neighbouring control volumes (subscripts P and N, respectively).

The first interpolation method is the upwind differencing scheme, which is first order accurate. The method calculates the direction of the flow and uses the value in the present control volume if it is positive and the neighbouring control volume if it is negative:

$$a_f = \begin{cases} a_P & \phi \geq 0 \\ a_N & \phi < 0. \end{cases} \tag{4.3}$$

This method guarantees boundedness, i.e. the solution cannot become unphysical, but at

the expense of accuracy due to numerical diffusion (Jasak 1996).

A more accurate scheme is the central differencing (or linear) scheme, which assumes a linear variation of a between the two control volumes

$$a_f = f_x a_P + (1 - f_x) a_N, \tag{4.4}$$

where f_x is the interpolation factor, and is defined as the ratio of the distance of f and P from N:

$$f_x = \frac{||f - N||}{||P - N||}. \tag{4.5}$$

If there is symmetric weighting, i.e. the face is at equal distances from P and N, then a special version of the central differencing scheme, the midpoint scheme, is derived since equation (4.4) reduces to

$$a_f = \frac{a_P + a_N}{2}. \tag{4.6}$$

These central differencing schemes are second order accurate and, hence, introduce less numerical diffusion than the upwind scheme, but at the expense of guaranteed boundedness, potentially leading to unphysical solutions or oscillations (Jasak 1996). To try and achieve a bounded solution without introducing as much numerical diffusion, a blend of the upwind and central differencing schemes, known as linear upwind, is sometimes used,

$$a_f = (1 - \gamma)(a_f)_{UD} + \gamma (a_f)_{CD}, \tag{4.7}$$

where γ is a blending function, and can be specified between 0 and 1. The blending factor γ determines the quantity of numerical diffusion that will be introduced, with a value of 0 and 1 giving the upwind and central differencing schemes, respectively. For more details on the interpolation schemes, the reader is referred to the thesis of Jasak (1996), Chapter 3.

The interpolation method should be of the same order or higher than the equation it is solving (Jasak 1996). Therefore, in this work the Navier-Stokes equations use central differencing interpolation, although the convection term includes a limiting scheme to help

avoid unphysical oscillations. On the other hand, the turbulent transport equations used in the turbulence models, and sediment module, generally use upwind interpolation for boundedness, unless otherwise stated.

4.2.1.4 Spatial Discretisation

Although OpenFOAM® does offer alternative options for certain spatial discretisation (e.g. gradient schemes can use a least squares calculation), the common method for integration relies heavily on the generalised form of Gauss' Theorem, which states the following identities:

$$\int_V \nabla a \, dV = \oint_{\partial V} d\mathbf{s} \, a \tag{4.8}$$

$$\int_V \nabla \mathbf{a} \, dV = \oint_{\partial V} d\mathbf{s} \, \mathbf{a}, \tag{4.9}$$

$$\int_V \nabla \cdot \mathbf{a} \, dV = \oint_{\partial V} d\mathbf{s} \cdot \mathbf{a}. \tag{4.10}$$

Here ∂V represents the closed surface bounding the volume V, $d\mathbf{s}$ is an infinitesimal surface element with associated outward pointing normal on ∂V, whereas a and $\mathbf{a}$ are a general scalar or vector, respectively. Since the control volume is known to be bounded completely by a number of faces, the surface integrals, $\oint$, can be represented as a summation over the integrals of each individual face, for example equation (4.10) becomes

$$\int_V \nabla \cdot \mathbf{a} \, dV = \oint_{\partial V} d\mathbf{s} \cdot \mathbf{a} = \sum_f \left(\int f d\mathbf{s} \cdot \mathbf{a} \right). \tag{4.11}$$

Assuming a linear variation (equation 4.4) can simplify equation (4.11) further (Jasak 1996), to give a second order accurate discretised form of Gauss' equation:

$$(\nabla \cdot \mathbf{a}) V_P = \sum_f \mathbf{s} \cdot \mathbf{a}_f. \tag{4.12}$$

Here V_P is the volume of the cell, the subscript f implies the value of the variable in the middle of the face, and $\mathbf{s}$ is the outward-pointing face area vector. In OpenFOAM® the face area vector $\mathbf{s}_f$ points outward from P if the face f is owned by P, and inwards if it is a neighbouring face. This needs to be taken into account when computing the summation of

the faces and is therefore split into sums over owned and neighbouring faces (Jasak 1996)

$$\sum_f \mathbf{s}\cdot\mathbf{a}_f = \sum_{owner} \mathbf{s}_f\cdot\mathbf{a}_f - \sum_{neighbour} \mathbf{s}_f\cdot\mathbf{a}_f. \tag{4.13}$$

As an example consider the convection term $\nabla\cdot(\rho\mathbf{u}a)$, for a general flow variable, a. Using Gauss' Theorem (equation 4.12) yields

$$\int_V \nabla\cdot(\rho\mathbf{u}a)\,dV = \sum_f \mathbf{s}\cdot(\rho\mathbf{u}a)_f = \sum_f \mathbf{s}\cdot(\rho\mathbf{u})_f a_f = \sum_f \phi a_f, \tag{4.14}$$

where ϕ is the velocity flux term discussed in Section 4.2.1.2, and represents the mass flux through the face

$$\phi = \mathbf{s}\cdot(\rho\mathbf{u})_f. \tag{4.15}$$

Since values on the face are essential for the calculation, interpolation from the control volume centre to the face is required, as has been previously discussed in Section 4.2.1.3.

A similar approach can be followed for a diffusion term, e.g. $\nabla\cdot(\Gamma_a\nabla a)$:

$$\int_{V_P} \nabla\cdot(\Gamma_a\nabla a)\,dV = \sum_f \mathbf{s}\cdot(\Gamma_a\nabla a)_f = \sum_f (\Gamma_a)_f\mathbf{s}\cdot(\nabla a)_f. \tag{4.16}$$

However, there is an additional difficulty in comparison to the convection term, since the calculation of this diffusion term requires knowledge of the surface normal gradient of a. On an orthogonal mesh the value is easily calculated using the difference between the values of a in N and P,

$$\mathbf{s}\cdot(\nabla a)_f = |\mathbf{s}|\frac{a_N - a_P}{||N-P||}. \tag{4.17}$$

Unfortunately, when solving on a non-orthogonal mesh, $\mathbf{s}$ does not necessarily point in the same direction as $\mathbf{d}$, the vector joining P and N (see Figure 4.3), and hence equation (4.17) does not provide the correct surface normal gradient. In this case, OpenFOAM® splits the calculation into two components: an orthogonal contribution using equation (4.17), and a non-orthogonal correction (see Jasak (1996) for details). Hence, in OpenFOAM®, for all Laplacian calculations the user must specify both an interpolation scheme (for the diffusion

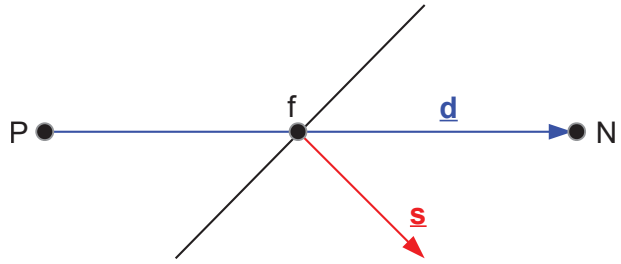

Figure 4.3: Illustration of the surface normal vector, **s**, and the vector **d**, which joins P and N.

coefficient, Γ_a), and a surface normal gradient scheme: corrected, uncorrected (just uses the orthogonal calculation), or a blend of the two methods. In this work, the surface normal gradient is corrected unless otherwise stated.

4.2.1.5 Temporal Discretisation

Any time derivatives can be approximated directly using finite differences, for example

$$\frac{\partial \rho a}{\partial t} \approx \frac{\rho^n a^n - \rho^o a^o}{\Delta t} \tag{4.18}$$

where

$$a^n = a(t+\Delta t), \qquad a^o = a(t). \tag{4.19}$$

The time at which the rest of the governing equations are evaluated is determined by the time scheme used. Implicit Euler evaluates the time dependent variables at the present time step ($t+\Delta t$), for example the face value of a is evaluated (using central differencing) with

$$a_f = f_x a_P^n + (1-f_x) a_N^n \tag{4.20}$$

An explicit version of the Euler method also exists, utilising the old time step (t) so that a^n is replaced with a^o in equation (4.20). Both of these methods are first order accurate but the Implicit version is unconditionally stable and guarantees boundedness whereas the explicit version becomes unstable if the time step is too large. OpenFOAM® only offers the option of the implicit version of this method.

Crank-Nicholson is an implicit second order accurate method which calculates the time

derivative in the same way as in the Euler methods (equation 4.18). However, when integrating the time dependent variables, temporal variation of the face values is considered. Hence both the old and new time steps are used in the calculation:

$$\int_t^{t+\Delta t} a(t)\,dt = \frac{1}{2}(a^o + a^n)\Delta t, \tag{4.21}$$

and the face values are calculated (using central differencing) with

$$a_f = \frac{1}{2}(f_x a_P^n + (1-f_x)a_N^n + f_x a_P^o + (1-f_x)a_N^o). \tag{4.22}$$

The Crank-Nicholson scheme is unconditionally stable but does not guarantee boundedness. Boundedness can be achieved by decreasing the accuracy of the discretisation but this yields the Implicit Euler method (equation 4.20).

A final method is the Backwards Differencing scheme, which is second order accurate but like the Implicit Euler, neglects the temporal variation in the face values. To do this, three time levels are used, $t+\Delta t$, t, and $t-\Delta t$ ($a^{oo} = a(t-\Delta t)$). Using Taylor series expansions the time derivative can be shown (Jasak 1996) to be approximated by

$$\frac{\partial a}{\partial t} = \frac{\frac{3}{2}a^n - 2a^o + \frac{1}{2}a^{oo}}{\Delta t}. \tag{4.23}$$

Once again, the boundedness of the solution cannot be guaranteed. All of the methods produce a system of algebraic equations that must be solved for a_P^n. For every control volume the following equation is assembled

$$\mathscr{A}_P a_P^n + \sum_N \mathscr{A}_N a_N^n = R_P, \tag{4.24}$$

which create a system of algebraic equations

$$\mathbf{A}\mathbf{a} = \mathbf{R}. \tag{4.25}$$

Here $\mathbf{A}$ is a sparse matrix with coefficients $\mathscr{A}_P$ on the diagonal and $\mathscr{A}_N$ off diagonal, $\mathbf{a}$ is the

vector of a's for all control volumes and $\mathbf{R}$ is the source term vector. The pattern of matrix $\mathbf{A}$ depends on the order in which the control volumes are labelled, with every off-diagonal coefficient above and below the diagonal corresponding to one of the faces in the mesh (Jasak 1996).

In this work, Implicit Euler is used for all simulations unless otherwise stated.

4.2.1.6 Discretised Governing Equations

Now that the framework for discretising both spatial and temporal derivatives has been introduced, the discretisation of the Navier-Stokes equations is discussed. Starting with the incompressible Navier-Stokes equations, which expressed in vector form are

$$\frac{\partial \mathbf{u}}{\partial t} + \nabla \cdot (\mathbf{u}\mathbf{u}) - \nabla \cdot (\nu \nabla \mathbf{u}) = -\nabla p, \tag{4.26}$$

$$\nabla \cdot \mathbf{u} = 0, \tag{4.27}$$

it is clear that there are two issues which require special attention before a solution can be found. The first is the nonlinear convection term, $\nabla \cdot (\mathbf{u}\mathbf{u})$, and the second is the pressure-velocity coupling. The nonlinear term can be discretised using Gauss' Theorem yielding

$$\nabla \cdot (\mathbf{u}\mathbf{u}) = \sum_f \mathbf{s} \cdot \mathbf{u}_f \mathbf{u}_f = \sum_f \phi \mathbf{u}_f = \mathscr{A}_P \mathbf{u}_P + \sum_N \mathscr{A}_{\mathscr{N}} \mathbf{u}_N, \tag{4.28}$$

where N represent the neighbouring control volumes, P is the centre of the control volume and $\mathscr{A}_P$, $\mathscr{A}_N$, and ϕ are all functions of $\mathbf{u}$. The fluxes, ϕ should all satisfy the discretised continuity equation

$$\nabla \cdot \mathbf{u} = \sum_f \mathbf{s} \cdot \mathbf{u}_f = 0, \tag{4.29}$$

which will need to be solved simultaneously with the momentum equation, creating a larger non-linear system. Hence, it is common to linearise the convection term, implying that an existing velocity flux field that satisfies the continuity equation exists and will be used to calculate $\mathscr{A}_p$ and $\mathscr{A}_N$ (Jasak 1996).

The method used by OpenFOAM® starts with a semi-discretised form of the momentum equations, obtained using the discretisation procedure described in Sections 4.2.1.4 and 4.2.1.5 on the integral form of the momentum equation,

$$\mathscr{A}_P \mathbf{u}_P = \mathscr{H}(\mathbf{u}) - \nabla p. \tag{4.30}$$

Equation (4.30) has been divided through by the volume, which enables face interpolation of the coefficients. Also note that the pressure gradient term has not yet been discretised, which is consistent with the Rhie-Chow procedure (Rhie and Chow 1983; Jasak 1996).

The term $\mathscr{H}(\mathbf{u})$ consists of two components: a transport, and a source part (Jasak 1996). The transport component includes the matrix coefficients multiplied by the velocities for all the neighbouring cells, whereas the source component includes the transient term and all other source terms excluding the pressure gradient,

$$\mathscr{H}(\mathbf{u}) = -\sum_N \mathscr{A}_N \mathbf{u}_N + \frac{\mathbf{u}^o}{\Delta t}. \tag{4.31}$$

The semi-discretised momentum equation (equation 4.30) can now be rearranged to get an expression for $\mathbf{u}$:

$$\mathbf{u}_P = \frac{\mathscr{H}(\mathbf{u})}{\mathscr{A}_P} - \frac{1}{\mathscr{A}_P}\nabla p. \tag{4.32}$$

Velocities on the cell face are then expressed as the face interpolation of equation (4.32) (Jasak 1996)

$$\mathbf{u}_f = \left(\frac{\mathscr{H}(\mathbf{u})}{\mathscr{A}_P}\right)_f - \left(\frac{1}{\mathscr{A}_P}\right)_f (\nabla p)_f, \tag{4.33}$$

which can be used to calculate the face fluxes

$$\phi = \mathbf{s} \cdot \mathbf{u}_f = \mathbf{s} \cdot \left[\left(\frac{\mathscr{H}(\mathbf{u})}{\mathscr{A}_P}\right)_f - \left(\frac{1}{\mathscr{A}_P}\right)_f (\nabla p)_f\right]. \tag{4.34}$$

As previously mentioned, the face fluxes must be conservative. To guarantee this, the discretised continuity equation (equation 4.29), and expression for $\mathbf{u}$ (equation 4.32) must

be solved simultaneously. Taking the divergence of equation (4.32), and substituting into the continuity equation yields an equation for pressure

$$\nabla \cdot \left(\frac{1}{\mathscr{A}_P} \nabla p \right) = \nabla \cdot \left(\frac{\mathscr{H}(\mathbf{u})}{\mathscr{A}_\mathscr{P}} \right). \tag{4.35}$$

As long as this pressure equation holds, the face fluxes are guaranteed to be conservative, as desired. Therefore, using the discretisation techniques for Laplacian, divergence and gradient operators, described in Section 4.2.1.4, to discretise equation (4.35) and the pressure gradient in equation (4.30) the final form of the discretised incompressible Navier-Stokes equations is obtained

$$\mathscr{A}_P \mathbf{u}_P = \mathscr{H}(\mathbf{u}) - \sum_f \mathbf{s}(p)_f \tag{4.36}$$

$$\sum_f \left[\left(\frac{1}{\mathscr{A}_\mathscr{P}} \right)_f (\nabla p)_f \right] = \sum_f \mathbf{s} \cdot \left(\frac{\mathscr{H}(\mathbf{u})}{\mathscr{A}_P} \right)_f \tag{4.37}$$

Kärrholm (2008) suggests that there are four important points regarding the OpenFOAM® discretisation of the Navier-Stokes equations:

1. ϕ does not include any effects from pressure when solving the continuity equation;
2. $\mathscr{A}_P$ does not include pressure effects when solving the continuity or final velocity corrector;
3. the Laplacian of pressure uses the gradient of pressure on the control volume's faces. The gradient is calculated using neighbouring control volumes rather than neighbouring faces;
4. the gradient of pressure is calculated from the pressure values on the control volume's faces.

Although the interpolation scheme described in Rhie and Chow (1983) is not explicitly applied, the correction used in OpenFOAM® gives an oscillation-free velocity, consistent with the Rhie-Chow methodology (Kärrholm 2008).

4.2.2 Pressure-Velocity Coupling

In order to solve the Navier-Stokes equations, an algorithm which solves for both pressure and velocity is required. This section describes the methodology of two of the commonly used algorithms: Semi-Implicit Method for Pressure-Linked Equations (SIMPLE), which is only applicable for steady state solutions, and Pressure Implicit with Splitting of Operators (PISO), which is intended for use in transient flows. In general, the mathematical details have been omitted from this section for simplicity. For a full mathematical example of steady 2-D laminar flow, the reader is referred to Versteeg and Malalasekera (1995), Chapter 6.

4.2.2.1 SIMPLE

In short, the SIMPLE algorithm, originally suggested by Patankar and Spalding (1972), is an iterative method that utilises an initial guess for pressure which is then corrected (Versteeg and Malalasekera 1995).

The procedure begins with the initiation of the pressure field with a guess, p^*. The discretised momentum equations are then solved using this guessed pressure field to obtain the velocity components (u^*,v^*,w^*). A correction term, p', is then defined as the difference between the correct pressure field, p, and the guessed pressure field p^*. The same definition is applied to the velocity yielding

$$p = p^* + p', \qquad (u,v,w) = (u^*,v^*,w^*) + (u',v',w') \tag{4.38}$$

If the correct pressure, p, is substituted into the momentum equations then, following an approximation, formulae for the velocity components can be obtained in terms of the pressure correction term, p'.

In order to determine the value of p' for the final governing equation, the continuity equation must be considered. The correct velocities are substituted into the continuity equation, and identifying coefficients yields an equation in p' only that can be solved. This gives us the value of p' at every point in the domain, which can be substituted into the previous formulae for pressure and velocity components to yield the final pressure p, and velocity

field, **u**=(u,v,w). Any other transport equations can now be solved using the values of **u** and p. If the solution has converged then $p^* = p$ and (u^*,v^*,w^*)=(u,v,w) and the algorithm stops. If convergence has not been achieved then the solution from this iteration is used as the initial guess for the next. Figure 4.4 shows a flowchart of the algorithm, summarising what has been written in the above description.

To avoid divergence of the pressure correction equation, under-relaxation has to be used during the iterative process using

$$p^{new} = p^* + \alpha_p p', \tag{4.39}$$

where α_p is the pressure under-relaxation factor. When $\alpha_p = 1$, no under-relaxation is applied which can lead to unstable computations, especially if p^* is far away from the final solution. Therefore, to achieve a more stable simulation α_p is chosen between 0 and 1. To help convergence of the solution, and generally improve computational speed, alternative methods based on SIMPLE have been developed. SIMPLE Revised (SIMPLER) developed by Patankar (1980) derives a discretised equation for pressure rather than the pressure correction term, allowing the pressure field to be obtained without use of a correction (Versteeg and Malalasekera 1995). SIMPLE-Consistent (SIMPLEC) developed by Van Doormaal and Raithby (1984), manipulates the momentum equations so that the velocity correction equations omit less significant terms than the ones omitted in SIMPLE (Versteeg and Malalasekera 1995).

4.2.2.2 PISO

The PISO algorithm, developed by Issa (1986), is a non-iterative computation for unsteady flows. The algorithm is similar to the SIMPLE algorithm, except that it introduces an additional correction step.

The procedure begins with the initialisation of the pressure field with a guess, p^*, which is then used to calculate (u^*,v^*,w^*). The velocity field (u^*,v^*,w^*) will not satisfy continuity unless the pressure field p^* is correct and hence a first correction step is introduced to

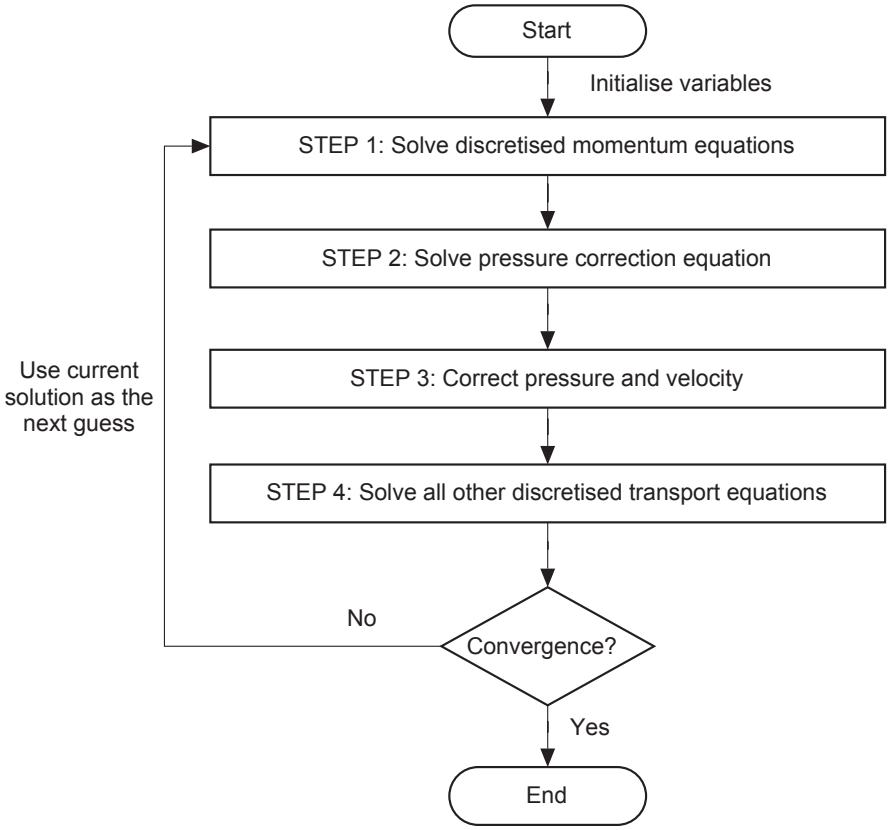

Figure 4.4: Flowchart of the SIMPLE algorithm.

comply with the discretised continuity equation. Since there will be a second correction step, different notation will be used to that in the SIMPLE algorithm:

$$p^{**} = p^{*} + p', \qquad (u^{**}, v^{**}, w^{**}) = (u^{*}, v^{*}, w^{*}) + (u', v', w'). \tag{4.40}$$

As in the SIMPLE algorithm, the formulae in equation (4.40) allow the corrected velocities, (u^{**},v^{**},w^{**}), to be defined in terms of the pressure correction term, p'. Through substitution of the corrected velocities into the continuity equation, an expression for p' can be found, and solved for the whole domain. This gives a solution for (u^{**},v^{**},w^{**}), as required.

Up to this point the PISO algorithm has been identical to the procedure in SIMPLE. However, instead of iterating this procedure until convergence is achieved, a second corrector step is

applied. Defining the twice-corrected pressure and velocity as

$$p^{***} = p^{**} + p'', \quad (u^{***}, v^{***}, w^{***}) = (u^{**}, v^{**}, w^{**}) + (u'', v'', w''), \tag{4.41}$$

and solving the momentum equations a second time yields expressions for the twice-corrected velocity field in terms of the second pressure correction term, p''. Substituting (u^{***},v^{***},w^{***}) into the continuity equation allows an equation for p'' to be formulated and solved for the whole domain. This yields the twice-corrected pressure field

$$p^{***} = p^{**} + p'' = p^{*} + p' + p'', \tag{4.42}$$

and velocity field as required. Any other scalar transport equations, such as turbulence and concentration, may then be solved using this solution for pressure and velocity. Since the procedure is non-iterative, the twice-corrected pressure and velocity fields are considered to be the correct solution, and the solver progresses to the next time step. This is repeated until $t = t_{max}$, where the simulation stops. Figure 4.5 summarises the main procedures of the algorithm in a flowchart.

By not performing the iterative process, the algorithm is considered less computationally expensive than the SIMPLE algorithm. However, in reality this method is limited to very small time steps, since Issa (1986) showed the temporal accuracy achieved by the algorithm for pressure and momentum to be of order 3 (Δt^3) and 4 (Δt^4), respectively (Versteeg and Malalasekera 1995).

4.2.2.3 PIMPLE

The above algorithms are for generic cases. Another algorithm that OpenFOAM® offers merges the PISO and SIMPLE algorithms and is named PIMPLE. PIMPLE has a number of parameters which allow the user to take advantage of the strengths of both PISO and SIMPLE. This is done through a selection of options including the number of corrector steps (`nCorrectors`), the number of iterations (`nOuterCorrectors`), as well as tolerance of convergence and under-relaxation. If `nOuterCorrectors` $= 1$, the solver performs one

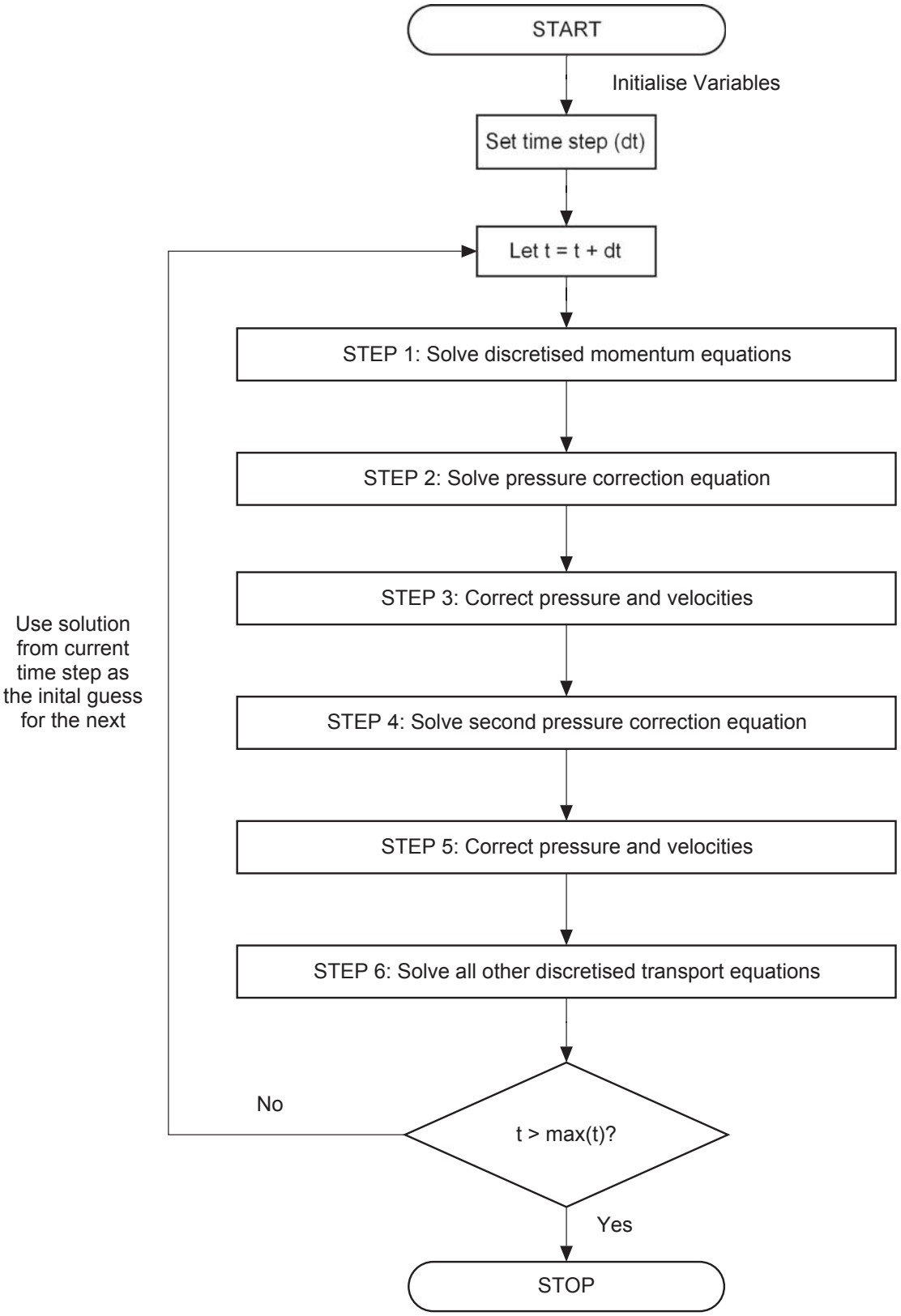

Figure 4.5: Flowchart of the PISO algorithm.

iteration, i.e. it operates in PISO mode. If `nOuterCorrectors` $= n > 1$, the solver operates in PIMPLE mode, where it performs n iterations, unless residual tolerance is reached first. This allows a much larger time step to be used than in PISO mode.

In this work, the solver is run in PISO mode, with three pressure correction steps (`nOuterCorrectors` $= 1$, `nCorrectors` $= 3$).

4.3 Wave Generation in OpenFOAM®

As previously mentioned, wave generation and absorption has already been implemented within the OpenFOAM® environment based upon a multiphase solver, "`interFoam`", which uses the VOF method (see Rusche (2002) for more details on the solver). The first wave generation method allows boundary conditions to be given as expressions to be evaluated. Although this method can only consider "wet" or "dry" cells, it works to a certain degree for less complicated wave theories such as linear and Stokes second order waves, but is less practical with more complicated conditions. A more sophisticated version of this method has been developed and validated by Jacobsen (2011) as part of a full hydro- and morphodynamic solver, with the hydrodynamic aspect later freely released as an additional toolbox for OpenFOAM® under the name `waves2Foam` (Jacobsen et al. 2012). The general concept is that the wave generating boundary conditions are implemented by setting surface elevation and velocity to analytical wave theory solutions at the inlet. Furthermore, it is capable of setting the boundary cells to a partially full value, allowing the free surface to be captured more accurately, and avoiding the stepped solution that is often obtained when using cells that can only be either "wet" or "dry". Another model, `IHFOAM`, which uses a similar wave generation method with the addition of a piston-type wave maker replication option, has also been developed by Higuera et al. (2013*a*), and validated for a series of coastal engineering processes in Higuera et al. (2013*b*).

With respect to wave absorption, both toolboxes offer different approaches: `waves2Foam` utilises relaxation zones, a region where waves are forced to a target solution, whereas active absorption, which corrects the boundary condition in response to reflected waves, is implemented within `IHFOAM`. Jacobsen et al. (2012) has shown that relaxation zones

perform well for cases satisfying the ratio

$$\lambda > L, \tag{4.43}$$

where λ is the length of the relaxation zone. This implies that the domain must be extended by at least one wavelength in order to include the relaxation zone which is an obvious disadvantage, due to the extra computational cost, compared to the active absorption.

Despite the drawback of an extended computational domain, the toolbox which will be used in the present work is `waves2Foam` for the following reasons:

1. it has been validated for breaking waves in the surf zone by Jacobsen et al. (2012);
2. the present domain does not require dissipation of waves at the outlet, hence the domain is only increased at the inlet;
3. it is freely available to download.

4.3.1 Relaxation Zones

The concept for relaxation zones is to reduce reflections within the computational domain, which could affect wave generation. This is achieved by including a region near the boundary where the simulated values (i.e. from RANS) and analytical solutions are blended according to a weighting, α_R, i.e.

$$f = \alpha_R f_{simulation} + (1 - \alpha_R) f_{analytical}. \tag{4.44}$$

The weighting in the relaxation zone can be changed but in this work is set to that of Jacobsen et al. (2012), namely

$$\alpha_R(\chi_R) = 1 - \frac{\exp(\chi_R^{3.5}) - 1}{\exp(1) - 1}, \qquad \text{for } \chi_R \quad \in [0,1]. \tag{4.45}$$

Here, $\chi_R = 0$ at the boundary, and $\chi_R = 1$ at the interface between the end of the relaxation zone and the computational domain . Using this, along with equations (4.44) and (4.45), it is

clear that at the boundary, the solution is exactly analytical and at the end of the relaxation zone is completely simulated.

4.4 Turbulence Modelling in OpenFOAM®

There are many turbulence models available within OpenFOAM®. Each turbulence model falls into two categories, either RAS or LES. However, LES realistically requires a 3-D domain since eddies are not 2-D, causing the computational time to increase considerably. This work focuses on the RAS based turbulence models: four popular two-equation turbulence closure models ($k-\omega$, $k-\omega$ SST, RNG $k-\varepsilon$, nonlinear (NL) $k-\varepsilon$), and a Reynolds stress model (RSM), which solves for all components of the Reynolds stress (Launder et al. 1975) are considered. All of the two-equation models use an eddy viscosity to calculate the Reynolds stress, obtained by solving equations for the turbulent kinetic energy (TKE), k, and either the turbulence dissipation rate, ε, ($k-\varepsilon$ models) or a characteristic frequency, ω, associated with the turbulence ($k-\omega$ models). This section describes the different models used and the advantages and disadvantages of each.

$k-\varepsilon$ models are a commonly used method for turbulence closure. Hence, the weaknesses of the standard $k-\varepsilon$ model are generally well known. One of these weaknesses is that the transport equation for ε becomes singular near the wall, so, in order to model the viscous sublayer accurately, it is necessary to introduce damping at the wall. Furthermore, fully developed, isotropic turbulence is assumed, so the model generally under-performs under transitional turbulence or adverse pressure gradients (Versteeg and Malalasekera 1995; Wilcox 2006). The renormalised group (RNG) $k-\varepsilon$ aims to address some of the weaknesses of the standard $k-\varepsilon$ model. Originally developed using an additional expansion parameter by Yakhot et al. (1992), the RNG $k-\varepsilon$ has been shown to perform better than the standard $k-\varepsilon$ model in transitional flows (Versteeg and Malalasekera 1995). However, the additional expansion parameter has been shown to cause the model to become overly sensitive to the magnitude of the strain rate. Furthermore, the model is also based upon the assumption of isotropy, which is not valid for all flow conditions.

Another model being evaluated is the $k-\omega$ model (Wilcox 2006). It offers improved near-

wall treatment, removing the necessity for wall damping. It has also been shown to obtain more accurate predictions than the standard $k-\varepsilon$ model in cases of adverse pressure gradients (Wilcox 2006). However, it can be overly sensitive to the inlet free stream boundary conditions, and still relies on the isotropic turbulence assumption. A variation on this model is the $k-\omega$ shear stress transport (SST) model, developed by Menter (1994) and is a blend of both the $k-\omega$ and $k-\varepsilon$ model. It aims to address the sensitivity to the free stream value of ω, whilst keeping the improved near-wall treatment. To achieve this, a blending function is utilised, which applies the $k-\omega$ model for near-wall treatment, and the $k-\varepsilon$ in the free stream. However, not all of the problems with $k-\omega$ and $k-\varepsilon$ models are fixed by this method, since it also assumes that turbulence is isotropic.

In this study, the validity of the isotropic assumption is considered in two ways. The first is to use the nonlinear $k-\varepsilon$ model developed by Shih et al. (1996), which accounts for anisotropic effects through introduction of a nonlinear Reynolds stress term into the standard $k-\varepsilon$ model. Shih et al. (1996) showed that the nonlinear $k-\varepsilon$ model performs better than the standard $k-\varepsilon$ model for flows under strong adverse pressure gradients, as well as for separated and swirling flows. The second model is a Reynolds Stress model (RSM) developed by Launder et al. (1975). This model resolves all directions of the Reynolds Stress directly, along with an ε equation, for closure, eliminating the need for an eddy viscosity and, hence, the assumptions on the isotropy of the turbulence. This model is expected to produce the most accurate results since it captures the physics more realistically, but at the cost of computational efficiency since seven equations are solved. However, it uses the same ε equation as the isotropic turbulence models, indicating that if this is not modelled correctly then it will perform no better than the other models considered in this study.

The rest of this section describes the mathematical formulae controlling the five turbulence models. The transport equations for each of the turbulence models under consideration are discussed with particular emphasis on how they are implemented in OpenFOAM® (v.

2.1.1). The general form of the equations is such that

$$\textit{rate of change} + \textit{transport by convection} = \textit{production} - \textit{dissipation} + \textit{transport by diffusion}.$$

Each model has two transport equations, one for TKE (other than the Reynolds stress model which solves for the Reynolds stress, τ) and another for either ε or ω. The values obtained from solving these equations are then used to compute the eddy viscosity. For the models which do not solve an equation for τ, the eddy viscosity is used to model the Reynolds stress through the relationship

$$\tau = \frac{2}{3}k\mathbf{I} - 2\nu_t\mathbf{S}, \tag{4.46}$$

where $\mathbf{S}$ is the mean rate of strain of the flow defined as

$$\mathbf{S} = \frac{1}{2}(\nabla\mathbf{u} + \nabla\mathbf{u}^T). \tag{4.47}$$

It is worth noting that all of the incompressible solvers implemented in OpenFOAM®, including those for multiphase flows, do not include density explicitly but instead model the kinematic eddy viscosity, ν_t rather than the dynamic form, μ_t. In this work, density has been introduced to the transport equations to account for changes in density around the free surface, and the effects of this change are discussed in detail in Section 5.2.2 and Brown et al. (2014).

4.4.1 The $k-\omega$ model

The $k-\omega$ model originally developed by Wilcox (1988), solves the following transport equations for k and ω,

$$\frac{\partial\rho k}{\partial t} + \nabla\cdot(\rho\mathbf{u}k) = P_k - \rho C_\mu\omega k + \nabla\cdot[\rho(\nu+\sigma_k\nu_t)\nabla k], \tag{4.48}$$

$$\frac{\partial\rho\omega}{\partial t} + \nabla\cdot(\rho\mathbf{u}\omega) = \frac{\gamma\omega}{k}P_k - \rho\beta\omega^2 + \nabla\cdot[\rho(\nu+\sigma_\omega\nu_t)\nabla\omega], \tag{4.49}$$

with $\sigma_k = \sigma_\omega = 0.5$, $C_\mu = 0.09$, $\beta = 0.072$ and $\gamma = 0.52$. The production term is defined as $P_k = \rho \nu_t |S|^2$, defining S, in terms of $\mathbf{S}$, as $S = \sqrt{2\mathbf{S}:\mathbf{S}}$, where $:$ is the double inner product. The values of k and ω are obtained by solving equations (4.48) and (4.49), and are then used to compute the eddy viscosity, $\nu_t = k/\omega$.

4.4.2 The $k-\omega$ SST model

Menter (1994) originally developed the $k-\omega$ SST model, which solves the equations

$$\frac{\partial \rho k}{\partial t} + \nabla \cdot (\rho \mathbf{u} k) = \min(P_k, \rho c_1 C_\mu k \omega) - \rho C_\mu \omega k + \nabla \cdot [\rho(\nu + \sigma_k \nu_t)\nabla k], \tag{4.50}$$

$$\frac{\partial \rho \omega}{\partial t} + \nabla \cdot (\rho \mathbf{u} \omega) = \frac{\gamma P_k}{\nu_t} - \rho \beta \omega^2 + \nabla \cdot [\rho(\nu + \sigma_\omega \nu_t)\nabla \omega] + 2\rho(1 - F_1)\frac{\sigma_{\omega 2}}{\omega}\nabla k \cdot \nabla \omega, \tag{4.51}$$

where P_k is the same as in the $k-\omega$ model. The coefficients σ_k, σ_ω, β and γ are a blend of an inner constant (subscript 1), and an outer constant (subscript 2), blended according to

$$\phi = F_1 \phi_1 + (1 - F_1)\phi_2. \tag{4.52}$$

The function $F_1 = \tanh(\Gamma_1^4)$ used in the blending function, depends upon the argument Γ_1 described by

$$\Gamma_1 = \min\left(\min\left(\left[\max\left\{\frac{k}{C_\mu \omega \Delta z_w}, \frac{500\nu}{\Delta z_w^2 \omega}\right\}\right], \frac{4\sigma_{\omega 2} k}{C_{D,k\omega}\Delta z_w^2}\right), 10\right), \tag{4.53}$$

where

$$C_{D,k\omega} = \max\left\{\frac{2\sigma_{\omega 2}}{\omega}\nabla k \cdot \nabla \omega, 10^{-10}\right\}, \tag{4.54}$$

and Δz_w is the distance from the field point to the nearest wall. The values for the inner and outer constants are given in Table 4.2. The eddy viscosity is then calculated through

$$\nu_t = \frac{a_1 k}{\max\{a_1 \omega, b_1 F_2 \sqrt{2} S\}}, \tag{4.55}$$

where

$$F_2 = \tanh(\Gamma_2^2), \qquad \Gamma_2 = \min\left(\max\left\{\frac{2\sqrt{k}}{\omega\Delta z_w}, \frac{500\nu}{\Delta z_w^2\omega}\right\}, 100\right). \tag{4.56}$$

σ_{k1}	σ_{k2}	$\sigma_{\omega1}$	$\sigma_{\omega2}$	β_1	β_2	γ_1	γ_2
0.85034	1.0	0.5	0.85616	0.075	0.0828	0.5532	0.4403

Table 4.2: Default values for the inner and outer constants in the $k-\omega$ SST model.

4.4.3 The RNG $k-\varepsilon$ model

The Renormalised group (RNG) $k-\varepsilon$ model solves two equations for k and ε defined as

$$\frac{\partial\rho k}{\partial t} + \nabla\cdot(\rho\mathbf{u}k) = P_k - \rho\varepsilon + \nabla\cdot[\rho(\nu+\sigma_k\nu_t)\nabla k], \tag{4.57}$$

$$\frac{\partial\rho\varepsilon}{\partial t} + \nabla\cdot(\rho\mathbf{u}\varepsilon) = \frac{C_{1\varepsilon}^* P_k\varepsilon}{k} - \frac{\rho C_{2\varepsilon}\varepsilon^2}{k} + \nabla\cdot[\rho(\nu+\sigma_\varepsilon\nu_t)\nabla\varepsilon]. \tag{4.58}$$

The coefficient $C_{1\varepsilon}^*$ differs between the standard $k-\varepsilon$ and RNG $k-\varepsilon$ models (Speziale and Thangam 1992). In the former it is just $C_{1\varepsilon}$ and in the latter is derived as

$$C_{1\varepsilon}^* = C_{1\varepsilon} - \frac{\eta(1-\eta/\eta_0)}{1+\beta\eta^3}. \tag{4.59}$$

In equation (4.59), η is the additional expansion parameter used in the derivation by Yakhot et al. (1992), defined as the time scale ratio of the turbulent to the mean strain rate, $\eta = Sk/\varepsilon$. The eddy viscosity is computed by

$$\nu_t = C_\mu\frac{k^2}{\varepsilon}. \tag{4.60}$$

All of the model coefficients, except β, which is obtained through experiments, are obtained through the derivation of the RNG $k-\varepsilon$ model and are set to $C_\mu = 0.0845$, $\sigma_k = \sigma_\varepsilon = 1.39$, $C_{1\varepsilon} = 1.42$, $C_{2\varepsilon} = 1.68$, $\eta_0 = 4.38$ and $\beta = 0.012$.

4.4.4 Nonlinear $k-\varepsilon$ model

Nonlinear (NL) $k-\varepsilon$ models are an alternative to Reynolds stress closure models. In this work, a model developed by Shih et al. (1996) is used, which relates the mean strain rate of the flow to the Reynolds stress tensor through the algebraic nonlinear Reynolds stress model. The model adjusts the Reynolds stress, $\boldsymbol{\tau}$, by adding a nonlinear stress term $\boldsymbol{\tau}_{NL}$, defined as

$$\boldsymbol{\tau}_{NL} = \frac{1}{2}(\boldsymbol{\chi} + \boldsymbol{\chi}^T), \tag{4.61}$$

$$\boldsymbol{\chi} = \frac{k^3}{(A_2 + \eta^3)\varepsilon^2}\left(C_{\tau 1}[\nabla\mathbf{u}\cdot\nabla\mathbf{u} + (\nabla\mathbf{u}\cdot\nabla\mathbf{u})^T] + C_{\tau 2}[\nabla\mathbf{u}\cdot(\nabla\mathbf{u})^T] + C_{\tau 3}[(\nabla\mathbf{u})^T\cdot\nabla\mathbf{u}]\right), \tag{4.62}$$

where $C_{\tau 1}$, $C_{\tau 2}$, $C_{\tau 3}$ and A_2 are constants. The parameter η is defined the same as in the RNG $k-\varepsilon$ model, with k and ε being calculated using equations (4.57) and (4.58), with different values for the coefficients ($C^*_{1\varepsilon} = 1.44$, $C_{2\varepsilon} = 1.92$, $\sigma_\varepsilon = 0.77$, $\sigma_k = 1$). The nonlinear stress term is also used in the production term, P_k, which is defined as

$$P_k = \rho(\nu_t \mathbf{S}\!:\!\nabla\mathbf{u} - \boldsymbol{\tau}_{NL}\!:\!\nabla\mathbf{u}). \tag{4.63}$$

The eddy viscosity is obtained through the same relationship as in the RNG $k-\varepsilon$ (equation 4.60) except that the value of C_μ depends upon the values of ξ and η,

$$C_\mu = \frac{2}{3(A_1 + \eta + \alpha_\xi \xi)}, \tag{4.64}$$

where α_ξ and A_1 are constants and $\xi = \Omega k/\varepsilon$ is an additional parameter, where Ω, defined in terms of the mean rate of rotation, $\boldsymbol{\Omega}$, is

$$\Omega = \sqrt{2\boldsymbol{\Omega}\!:\!\boldsymbol{\Omega}}, \qquad \boldsymbol{\Omega} = \frac{1}{2}\left(\nabla\mathbf{u} - (\nabla\mathbf{u})^T\right). \tag{4.65}$$

Using the eddy viscosity, the Reynolds Stress, $\boldsymbol{\tau}$, is calculated through the relationship

$$\boldsymbol{\tau} = \frac{2}{3}k\mathbf{I} - 2\nu_t\mathbf{S} + \boldsymbol{\tau}_{NL}. \tag{4.66}$$

4.4.5 Reynolds Stress Model

Reynolds stress models (RSM) solve equations for ε and all six components of the Reynolds Stress ($\boldsymbol{\tau}$). In this work, a RSM based on the work of Launder et al. (1975) is applied. All the components of $\boldsymbol{\tau}$ are solved in a single transport equation

$$\begin{aligned}\frac{\partial \rho \boldsymbol{\tau}}{\partial t} + \nabla \cdot (\rho \mathbf{u} \boldsymbol{\tau}) = \rho(1 - C_{2\tau})\mathbf{P} + \frac{\rho}{3} C_{2\tau} \mathrm{tr}(\mathbf{P})\mathbf{I} - \frac{2\rho}{3}(1 - C_{1\tau})\varepsilon \mathbf{I} \\ -\rho C_{1\tau} \frac{\varepsilon}{k} \boldsymbol{\tau} + \nabla \cdot [\rho(\nu + \nu_t)\nabla \boldsymbol{\tau}],\end{aligned} \tag{4.67}$$

where $C_{1\tau} = 1.8$, $C_{2\tau} = 0.6$, $\mathbf{I}$ is the identity matrix and $\mathrm{tr}(\mathbf{P})$ represents the trace of matrix $\mathbf{P}$, defined as

$$\mathbf{P} = -\left[\boldsymbol{\tau} \cdot \nabla \mathbf{u} + (\boldsymbol{\tau} \cdot \nabla \mathbf{u})^T \right]. \tag{4.68}$$

The equation for ε is the same as the nonlinear $k - \varepsilon$ (equation 4.57 with coefficient values of $C^*_{1\varepsilon} = 1.44$, $C_{2\varepsilon} = 1.92$, $\sigma_\varepsilon = 0.77$, $\sigma_k = 1$) except that the production term is defined as $P_k = 0.5|\mathrm{tr}(\mathbf{P})|$.

TKE is defined as $k = 0.5(u'^2_x + u'^2_y + u'^2_z)$, and can therefore be calculated in this model by taking half the trace of the Reynolds stress, i.e. $k = 0.5\mathrm{tr}(\boldsymbol{\tau})$. The eddy viscosity can then be calculated through the same relationship as in the RNG $k - \varepsilon$ model (equation 4.60).

4.4.6 Wall Functions

At a wall boundary, it is often easier to model the boundary layer rather than resolve the different sublayers, and this is commonly achieved through the use of wall functions. In order to use wall functions, OpenFOAM® requires that the type of wall function must be specified for k, ν_t, and either ε or ω depending on the model. This section describes some of the available options in OpenFOAM® v. 2.1.1.

4.4.6.1 The Laminar and Turbulent Cut-off

Before the different conditions for the turbulent variables are discussed, it is beneficial to consider how OpenFOAM® calculates the dimensional wall units, z^+, since it plays an important part in the OpenFOAM® wall functions. There are two choices of how to calculate

z^+. The first option determines the friction velocity from the near-wall TKE

$$z^+ = \frac{u_* \Delta z_w}{\nu_w}, \qquad u_* \approx k^{1/2} C_\mu^{1/4}. \tag{4.69}$$

Alternatively, the value can be determined iteratively using the difference between velocity near and at the wall

$$z^+ = \frac{\kappa |\mathbf{u}_{nw} - \mathbf{u}_w| \Delta z_w + \nu_w z^+}{\nu_w (1 + \log(E z^+))} \tag{4.70}$$

where k is the TKE, C_μ is a constant ($= 0.09$), Δz_w is the distance between the near-wall cell centre and the wall itself, and ν_w is the near-wall viscosity. It is also important to realise that most of the wall functions in OpenFOAM® are dependent on whether the cell centre closest to the wall is located in the logarithmic or viscous regions of a boundary layer. In this work, if the centre of the cell adjacent to the boundary is in the logarithmic region, the simulation will be referred to as a high Reynolds number (HRN) case, whereas a cell centre in the viscous sublayer will be considered to be low Reynolds number (LRN). This classification is required since the standard wall functions are designed to satisfy the log-law. Hence, the wall functions are inaccurate if the first cell centre lies outside this region, making it a necessary to integrate all the way to the wall in LRN simulations (Versteeg and Malalasekera 1995). OpenFOAM® considers a cell centre to be in the logarithmic region if the z^+ value is greater than the laminar to turbulent cut-off, z^+_{lam}, determined iteratively by satisfying the condition

$$z^+_{lam} = \begin{cases} \frac{\log(z^+_{lam} E)}{\kappa} & \text{if } 1 < z^+_{lam} E \\ 0 & \text{if } 1 \geq z^+_{lam} E. \end{cases} \tag{4.71}$$

where $\kappa \approx 0.41$ is the von Kármán constant, and E is an integration constant. For smooth walls, $E = 9.81$ and, therefore, the laminar to turbulent cut-off is approximately 11.53.

4.4.6.2 Boundary Condition for k

The wall function which determines the near-wall TKE is a simple zero gradient condition normal to a wall, i.e. for a horizontal wall

$$\frac{\partial k}{\partial z} = 0. \tag{4.72}$$

4.4.6.3 Boundary Condition for ε

The ε wall function is responsible for setting the near-wall production term, P_{kw}, and ε. The value of epsilon is set according to

$$\varepsilon_w = \frac{C_\mu^{3/4} k^{3/2}}{\kappa \Delta z_w}, \tag{4.73}$$

whereas the production term is defined as

$$P_{kw} = (\nu_{tw} + \nu_w) \frac{|\mathbf{u}_w| C_\mu^{1/4} \sqrt{k}}{\kappa \Delta z_w}, \tag{4.74}$$

where ν_{tw} and $\mathbf{u}_w$ are the near-wall eddy viscosity and velocity, respectively.

4.4.6.4 Boundary Condition for ω

The wall function for ω uses a blend of the solutions of the ω-equation in the viscous sublayer, ω_{vis}, and logarithmic sublayer, ω_{log} (Pilegaard 2012). The blending function used is

$$\omega_w = \sqrt{\omega_{vis} + \omega_{log}} \tag{4.75}$$

and the solutions to the ω-equations are given by (Wilcox 2006)

$$\omega_{vis} = \frac{6\nu_w}{\beta_1 \Delta z_w^2}, \qquad \omega_{log} = \frac{k^{1/2}}{C_\mu^{1/4} \kappa \Delta z_w}, \tag{4.76}$$

where β_1 and C_μ are constants, and ν_w is the near-wall viscosity value. The default values for the constants are $\beta_1 = 0.075$ and $C_\mu = 0.09$. The near-wall production term, P_{kw} is

also set in the ω wall function, using the same calculation as in the ε wall function, i.e. equation (4.74).

4.4.6.5 Boundary Condition for ν_t

The choice of the eddy viscosity wall function determines the method for calculating z^+, either equation (4.69) or equation (4.70), respectively. The value of the eddy viscosity at each cell centre adjacent to the wall, ν_{tw}, is dependent on z^+ and is set by OpenFOAM® according to

$$\nu_{tw} = \begin{cases} \nu_w \left(\frac{\kappa z^+}{\ln(E z^+)} - 1 \right) & \text{if } z^+ > z^+_{lam} \\ 0 & \text{if } z^+ \leq z^+_{lam}. \end{cases} \tag{4.77}$$

If the z^+ value is known to always reside in the laminar region, OpenFOAM® provides a further option, which automatically sets $\nu_{tw} = 0$, but still allows other parts of the code to access the function which calculates the z^+ value.

4.4.6.6 Wall Roughness

Surface roughness can also be taken into account through the choice of ν_t wall function, by modifying the value of E. The value of ν_t is used to compute the wall shear stress and hence the velocity near the wall (Pilegaard 2012). To be consistent with turbulent boundary theory the ν_t wall function determines the near-wall velocity by

$$\mathbf{u}^+ = \begin{cases} z^+ & \text{if } z^+ < z^+_{lam} \\ \frac{1}{\kappa} \ln \left(\frac{z^+ E}{\exp^{(\kappa \Delta B)}} \right) & \text{if } z^+ \geq z^+_{lam}. \end{cases} \tag{4.78}$$

The surface roughness is accounted for by the $\exp^{(\kappa \Delta B)}$ function, using a non-dimensionalised form of the user defined Nikuradse roughness, $k_N^+ = u_* k_N / \nu_w$, where $u_* = C_\mu^{1/4} k^{1/2}$, as well as a roughness constant C_s, which is set to 0.5 by default. The

function is determined by the k_N^+ value and is defined by

$$\exp^{(\kappa\Delta B)} = \begin{cases} 1 & \text{if } k_N^+ \leq 2.25 \\ \left(\frac{(k_N^+ - 2.25)}{87.75} + C_s k_N^+\right)^{\sin\{0.4258(\ln(k_N^+) - 0.811)\}} & \text{if } 2.25 < k_N^+ < 90 \\ 1 + C_s k_N^+ & \text{if } k_N^+ \geq 90. \end{cases} \tag{4.79}$$

This factor is then used to modify the integration factor, E, and the eddy viscosity is given by

$$\nu_{tw} = \begin{cases} \nu_w \left[\frac{z^+\kappa}{\ln\left(\frac{Ez^+}{\exp^{(\kappa\Delta B)}}\right)} - 1\right] & \text{if } \frac{Ez^+}{\exp^{(\kappa\Delta B)}} > 1.0001 \\ \nu_w \left[\frac{z^+\kappa}{\ln(1.0001)} - 1\right] & \text{if } \frac{Ez^+}{\exp^{(\kappa\Delta B)}} \leq 1.0001 \\ \frac{\nu_w}{2} \approx 5 \times 10^{-7} & \text{if } \nu_{tw} \leq \frac{\nu_w}{2}. \end{cases} \tag{4.80}$$

Since the eddy viscosity is only modified if $z^+ > z_{lam}^+$, it is important to make sure the first cell centre is in the logarithmic sublayer, which is satisfied by placing it at the same order of magnitude as the Nikuradse roughness, i.e. $\Delta z_w \approx k_N$ (Jacobsen 2011; Pilegaard 2012).

4.5 Suspended Sediment Transport Model

In this section the details of the suspended sediment model are presented. Although many authors have coupled sediment transport models with multiphase solvers in the OpenFOAM® environment using a variety of techniques (Bohórquez 2008; Liu 2008; Jacobsen 2011), none of the models have been publicly released, to the best of the present author's knowledge. Therefore, a sediment transport model, based upon the published details of these studies, has been implemented by the present author.

Following the approach of the authors discussed in Section 2.2.2, an advection-diffusion equation for suspended sediment concentration, C, is introduced

$$\frac{\partial C}{\partial t} + \nabla \cdot [(\mathbf{u} + \mathbf{w_s}(\mathbf{x}))C] = \nabla \cdot [\nu_s \nabla C], \tag{4.81}$$

where $\mathbf{w_s}$ is the settling velocity vector and ν_s is the sediment diffusivity coefficient.

This is generally set to the eddy viscosity, ν_t, determined by the turbulence model (Christensen et al. 2000; Liu 2008; Jacobsen 2011), which is equivalent to assuming a Schmidt number of 1. The dimensions of C are $\mathrm{m}^3\,\mathrm{m}^{-3}$ in the numerical model, but for consistency with experimental data, all of the suspended sediment concentrations will be presented in g/l in this work. To obtain C in g/l, the concentration in $\mathrm{m}^3\,\mathrm{m}^{-3}$ is simply multiplied by the density of the sediment.

The final variable that must be known to solve the equation is the settling velocity. The settling velocity vector is set up such that $\mathbf{w_s} = (0, 0, -w_s)$ where w_s is the magnitude of the settling velocity. There are many formulae for settling velocity (see Section 3.3.3), but in this work the formula (Fredsøe and Deigaard 1992),

$$w_s = \frac{(s-1)d^2 g}{18\nu_1} = \frac{(\frac{\rho_s}{\rho}-1)d^2 g}{18\nu_1}, \tag{4.82}$$

will be used. Note that the viscosity of the water, ν_1, is used rather than a weighted value based on both phases, as is common when using the VOF method. This has been used to avoid large changes in the settling velocity for small changes in the colour function, α_1, as was discussed by Jacobsen (2011). Also note that the effect of large concentrations, i.e. hindered settling, is not included in the present model.

The sediment concentration equation is solved after the turbulence model. Hence the procedure for each time step of the new solver is:

1. solve the VOF equation;
2. solve the velocity-pressure coupling to obtain the velocity and pressure;
3. solve the turbulence model to obtain the eddy viscosity;
4. solve the suspended sediment concentration equation.

Following Jacobsen (2011) a sub-time step is introduced to solve the suspended sediment concentration equation. Jacobsen (2011) noted that near the bottom of the wave flume the velocity is small, and that the settling velocity could therefore substantially increase the

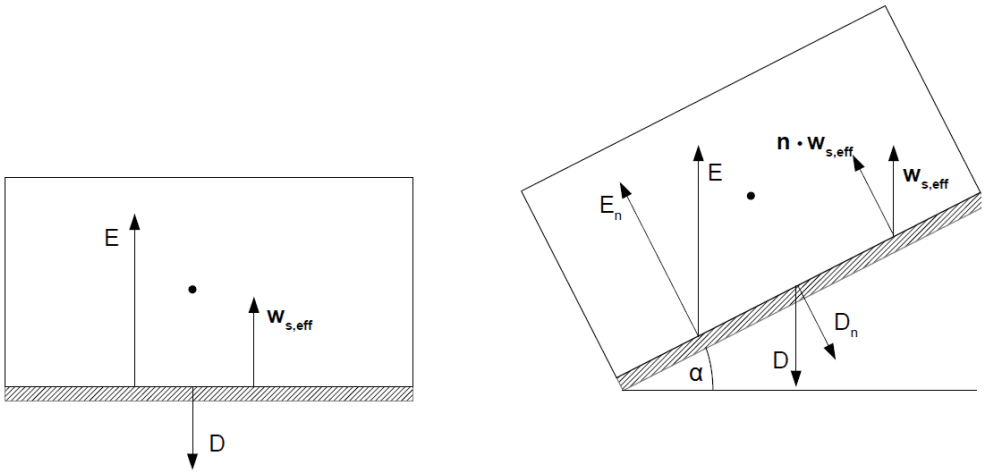

Figure 4.6: Example of the bottom boundary for $\alpha = 0$ (left) and an arbitrary slope (right). The effective settling velocity is calculated using E and D, but for the arbitrary slope this is combined with the normal vector.

magnitude of the total velocity. This could lead to the Courant number becoming too large. Instead of reducing the global time step to counteract this problem, a sub-time step is used where the sediment equation is solved N times for every global time step ($\Delta t_{sub} = \Delta t / N$). In this work, N is chosen as 10 unless otherwise stated.

4.5.1 Sediment Bed Boundary Condition

Now that an equation for suspended sediment concentration has been implemented, the spatial and temporal variation in the concentration can be tracked in the flow. However, a new type of boundary condition is required, representing the settling and pickup of sediment from the bed.

The approach used at the sand bed boundary in this work follows the implementation of Liu (2008). One of the reasons that this approach is being used is due to it being able to solve the fluid and sediment components of a problem on a single mesh (rather than a separate mesh for the sediment calculations). The general approach is to determine the net vertical flux at the boundary by comparing the entrainment, E, with the deposition, D:

$$\mathbf{q_s} \cdot \mathbf{n} = E - D. \tag{4.83}$$

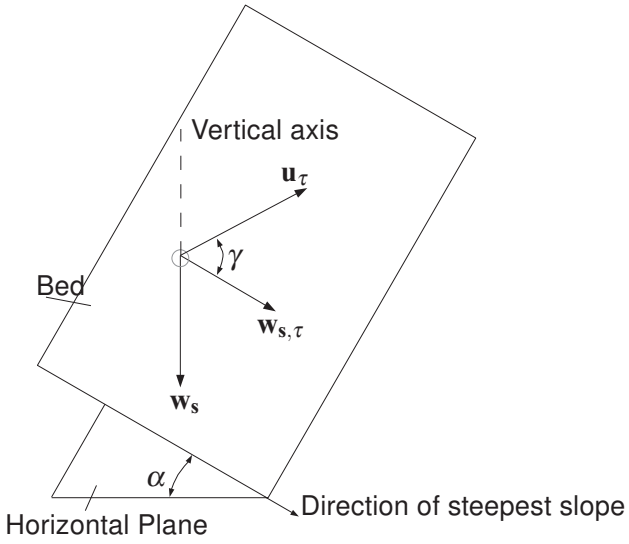

Figure 4.7: Diagram illustrating the angles and vectors used in the calculation of θ and θ_c.

There are two ways to manipulate the variables to achieve this flux. The first is to vary the concentration on the bottom face so that the equation holds. The second is to calculate an effective settling velocity and fix the concentration on the boundary. The latter method is chosen here since varying the concentration would cause it to become negative, which is unphysical and could cause major instabilities within the model.

The equation for suspended sediment flux at any point in the domain, including diffusive and convective fluxes is given as (Liu 2008)

$$\mathbf{q_s} = \left(\mathbf{u} + \mathbf{w_s}\right) C - (\nu_s)\nabla C. \tag{4.84}$$

At the bed, $\mathbf{u} = (0,0,0)$ and therefore the flux through the bottom face is

$$q_s = \mathbf{w_s} C - (\nu_s)\nabla C, \tag{4.85}$$

and substituting into equation (4.84) yields

$$\mathbf{w_s} C \cdot \mathbf{n} = (E - D + D_f), \tag{4.86}$$

where D_f is the diffusion term. Assuming a flat bed for simplicity, i.e. $\alpha = 0$, The effective settling velocity is set to

$$w_{s,eff} = \frac{E - D + D_f}{C}, \tag{4.87}$$

and the settling velocity becomes $\mathbf{w_s} = (0, 0, w_{s,eff})$. As previously, discussed, the value of the concentration on the bottom boundary, C_{bed}, has been set to a fixed value since an effective settling velocity has been introduced. The value it is set to does not change the results (although it cannot be zero) since it gets cancelled out, but has been chosen as $C_{bed} = 0.65$, the maximum attainable concentration, in this work.

If the bed is at an angle to the horizontal then the effective settling velocity is still calculated in the same way. However, the flux is computed by OpenFOAM® using the normal vector, and the effective settling velocity component normal to the face will be used

$$\mathbf{w_s} \cdot \mathbf{n} = w_{s,eff} \cos\alpha = \frac{E - D + D_f}{C_{bed}} \cos\alpha = \frac{E_n - D_n + D_{f,n}}{C_{bed}}, \tag{4.88}$$

where E_n, D_n and $D_{f,n}$ are the slope normal components of entrainment, deposition and diffusion, respectively. This process is illustrated in Figure 4.6, which shows how the effective velocity is calculated for a cell on a flat bed (left) and an arbitrary orientation (right).

In order to use equation (4.87), E and D must be determined. D can be found by simply multiplying the concentration in the cell adjacent to the bed, C_{nb}, by the settling velocity, i.e. $D = w_s C_{nb}$. In the present author's experience this approach only works when the time step is small since, otherwise, cells adjacent to the boundary begin to oscillate between full and empty. To avoid this a maximum time step is set such that $\Delta t < \Delta z_w / w_s$, or in words the sediment can not fall from further than the bottom cell in the time step.

Unlike the deposition, the entrainment must be calculated through an empirical formula, which generally apply at a reference height, often chosen as the bed level (Nielsen 1992). The empirical formula used in this work was developed by van Rijn (1984*a*), (implemented according to the description in Nielsen 1992) and has been used in many other numerical

models (Hsu and Liu 2004; Ma et al. 2014):

$$E = \begin{cases} 0.00033\left(\frac{\theta-\theta_c}{\theta_c}\right)\frac{(s-1)^{0.6}g^{0.6}d^{0.8}}{\nu^{0.2}} & \text{for} \quad \theta > \theta_c, \\ 0 & \text{otherwise.} \end{cases} \tag{4.89}$$

Therefore, the entrainment relies on determining the Shields parameter, θ, accurately, and is calculated using equation (3.63), where, following Jacobsen (2011), the magnitude of the friction velocity, u_*, is obtained through

$$\frac{\mathbf{u}_\tau}{u_*} = \frac{1}{\kappa}\log\left(\frac{15\Delta z_w}{k_N}\right). \tag{4.90}$$

Here, $\mathbf{u}_\tau$ is the velocity vector tangential to the wall and has been obtained using (Jacobsen 2011)

$$\mathbf{u}_\tau = \frac{1}{||\mathbf{n}||_2^2}(\mathbf{n}\times(\mathbf{u}\times\mathbf{n})) \tag{4.91}$$

The final variable to calculate is the critical Shields parameter, θ_c. Although in this work all of the flows are considered to be 2-D, the model has been created so that it can easily be adapted for 3-D flows. Hence the critical Shields parameter has been calculated using the general formula for 3-D flow, i.e. a rearranged version of equation (3.65)

$$\theta_c = \theta_{c0}\left(\cos\alpha\sqrt{1-\frac{\sin^2\gamma\tan^2\alpha}{\mu_s^2}} - \frac{\cos\gamma\sin\alpha}{\mu_s}\right), \tag{4.92}$$

where α is the angle between the slope and the horizontal. μ_s is the static friction, and is calculated using a user defined angle of repose. In this study, an angle of repose of 32° is used as suggested by Soulsby (1997), which corresponds to $\mu_s = 0.625$. The angle, γ, is defined as the angle between the tangential flow direction, $\mathbf{u}_\tau$, and the tangential component of the settling velocity, $\mathbf{w}_{\mathbf{s},\tau}$ (i.e. the direction of the steepest slope). $\mathbf{w}_{\mathbf{s},\tau}$ is calculated by applying equation (4.91) for $\mathbf{w_s}$ rather than $\mathbf{u}$. Hence, γ is obtained by

$$\gamma = \cos^{-1}(\mathbf{w}_{\mathbf{s},\tau}\cdot\mathbf{u}_\tau) \tag{4.93}$$

The effective settling velocity can now be computed and the concentration equation solved. A flow chart of the processes involved in the suspended sediment model is give in Figure 4.8.

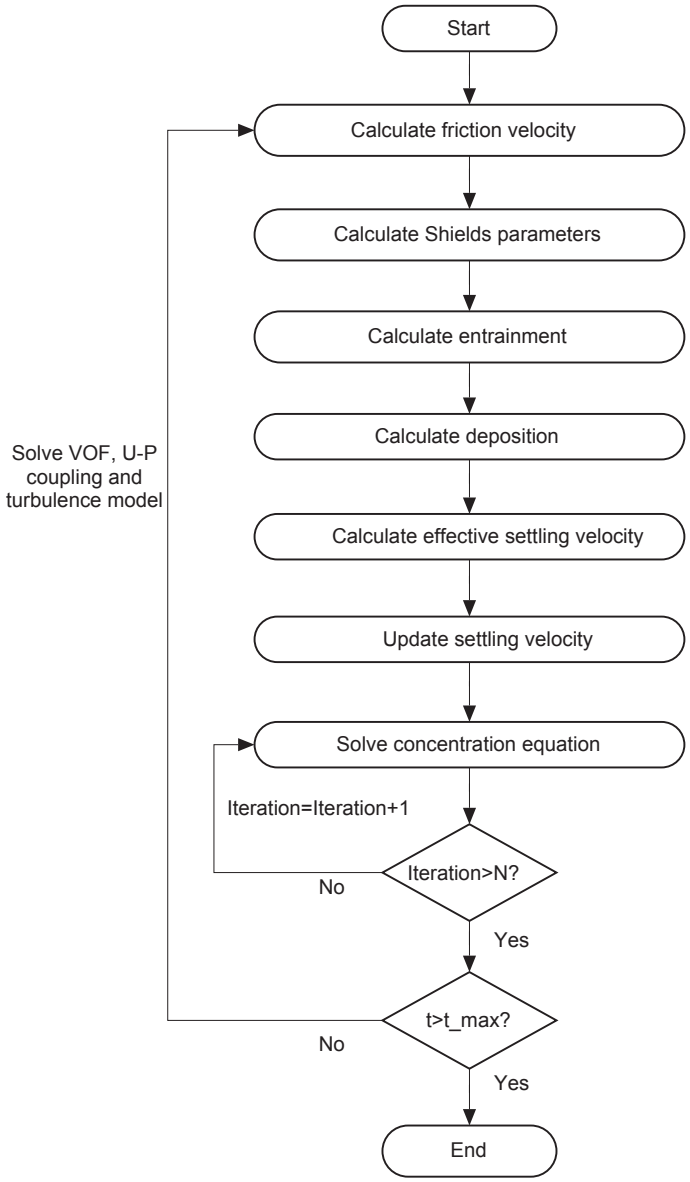

Figure 4.8: Flowchart of processes involved in the suspended sediment model.

Chapter 5

Validation I: Breaking Waves

The aim of this chapter is to discuss the development of a numerical wave tank capable of simulating breaking waves within the OpenFOAM® environment. The model must be able to generate waves, cause them to shoal and break, and ideally predict the velocity and turbulent kinetic energy (TKE) accurately. This chapter focuses on the considerations involved in creating the numerical wave tank such as mesh generation, boundary conditions and sensitivity. However, the main focus is to thoroughly evaluate five turbulence closure models for accuracy in predictions of surface elevation, horizontal velocity and TKE, relative to existing experimental data for both spilling and plunging breakers. The surface elevation, velocity and TKE data used for comparison has been gathered by Ting and Kirby (1994), through a thorough set of laboratory experiments for both spilling and plunging breakers on a beach of slope $1/35$. The results were obtained by producing cnoidal waves and phase-averaging (denoted by a tilde, i.e. $\widetilde{\eta}$) the waves over a period of twenty minutes.

This chapter is organised as follows. First, the numerical setup is discussed, before being assessed for sensitivity to various properties, including the comparison of the turbulence models against laboratory data. The model is then compared against other numerical studies.

5.1 Numerical Setup

The turbulence models discussed in Chapter 4 have been tested for 2-D spilling and plunging breakers propagating perpendicular to the shore. The free surface was tracked using a two-phase volume of fluid (VOF) technique, solved together with the incompressible Reynolds-Averaged Navier-Stokes (RANS) equations for the fluid flow field. The coordinate

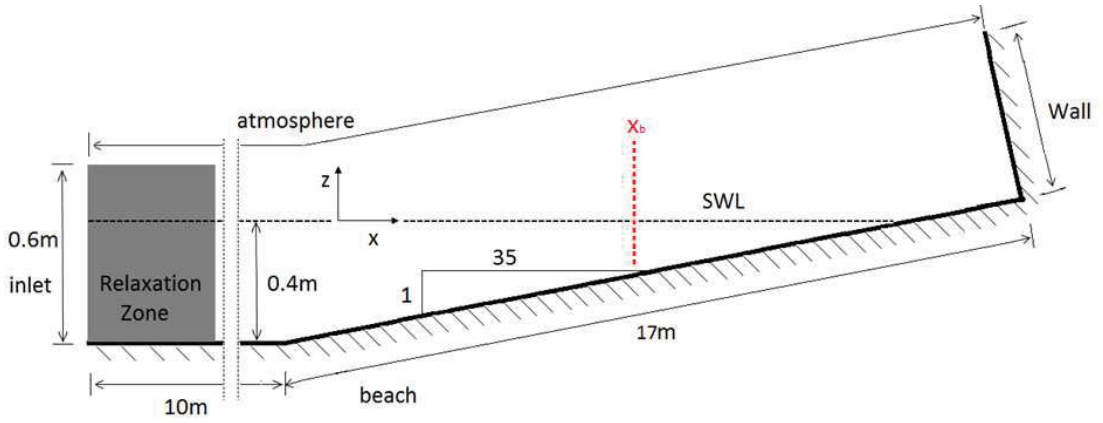

Figure 5.1: Diagram of the computational domain (not to scale) and the boundary names used.

system (x, y, z) was taken such that x corresponds to the cross-shore direction, with positive x in the direction of wave propagation. The waves were generated at the inlet boundary, and propagated towards a beach located at the right hand side of the domain (see Figure 5.1). The coordinates y and z were the long-shore and vertical directions, respectively. Waves were generated at the inlet, using the `waves2Foam` library, by setting a time-dependent boundary condition for the velocity and the free surface, both based on analytical solutions of the wave equations. A relaxation zone at the inlet permitted absorption of wave reflections at the boundary. In order to obtain numerical stability, maximum Courant numbers of 0.2 and 0.1 were chosen, for the spilling and plunging breaker cases, respectively. It was found that this condition was necessary for both explicit and implicit schemes. Second order time and spatial numerical schemes were used for the spilling breakers analysis. However, these numerical schemes could not be used in the plunging breaker due to instability. Therefore, first order numerical schemes were used in this case.

5.1.1 Computational Domain & Boundary Conditions

The computational domain was setup to be consistent with the laboratory experiments of Ting and Kirby (1994) and is illustrated in Figure 5.1. There was a sloping beach of gradient $1/35$, the water depth, h, was 0.4 m at the inlet, and the origin was located at the still water level (SWL), 0.7 m shoreward of the start of the slope, where $h = 0.38$ m (see Figure 5.1). Approximately $320,000$ cells were used to discretise the domain in the spilling

breakers case, whereas $360,000$ cells were used for the plunging breakers. The domain was designed to be only one cell thick in the y direction, and in the x and z directions, the cells have an aspect ratio (AR) of 1 where possible, i.e. $\Delta x = \Delta z$, for both cases. This was shown to improve the breaking point and height of the wave by Jacobsen et al. (2012), who suggested that this was due to larger VOF flux in cells of aspect ratio greater than one. The cell size in the internal domain was set to 0.01 m with additional refinement around the free surface in the x and z directions (see Section 5.1.3 for details). Adjacent to the beach boundary, six layers of thinner cells (in the z direction) have been used, with each layer away from the boundary being twice the size of the last. Following Jacobsen (2011), the cell closest to the bed is set to 0.1 mm. The mesh generation and resolution will be discussed further in Sections 5.1.2 and 5.1.3.

Regular waves were generated at the inlet boundary using Stream Function wave theory (Rienecker and Fenton 1981), since it was found that this followed the experimental profile more accurately than Cnoidal wave theory (see Section 5.2.1). The spilling breakers were created by incoming, regular waves of period $T = 2$ s and height $H = 0.125$ m, whereas the plunging breakers were generated using $T = 5$s, and $H = 0.127$ m. A relaxation zone was applied at the inlet boundary for both cases: for the spilling breakers the relaxation zone was approximately one wavelength, L, in length, whereas in the plunging case it was $L/2$. This has been shown to allow simulation, and therefore averaging, of a large number of waves (Jacobsen et al. 2012). The model was run for fifty wavelengths, with the final twenty waves averaged, and used for the results in this section. Data was sampled relative to the breaking point of the wave at the probe locations considered by Ting and Kirby (1994).

The beach and Wall boundaries were considered as solid walls, and therefore no-slip conditions have been applied, along with zero gradient conditions for pressure and VOF. The top boundary also used a Neumann boundary condition for the VOF, but the boundary condition for the velocity varied according to the near boundary flux, using a zero gradient condition for outflow, and the internal cell value of the normal component to the patch face

for the inflow. The top boundary condition for pressure was defined as the total pressure

$$p = p_0 + \frac{1}{2}|\mathbf{u}|^2, \tag{5.1}$$

where p_0 is the user defined reference value, and $\mathbf{u}$ is the velocity. In this study, p_0 was set to zero since the solver uses the difference between total pressure and hydrostatic pressure.

OpenFOAM® provides the option to run in "laminar" mode. This dummy turbulence model assumes that the TKE and the Reynolds stresses are zero, representing laminar flow conditions. To speed up convergence of the numerical model, an initial simulation of fifty wavelengths was run with the model in laminar mode, and the flow fields obtained from this simulation were then used as the initial condition for the turbulence model simulations. Furthermore, a further fifty wavelengths were simulated using laminar mode, starting from these same initial conditions, and these flow fields will be presented as a reference solution in this section. This case will be referred to as "laminar" flow conditions throughout this chapter.

For the turbulent fields, wall functions were applied at the beach boundary (see Section 4.4.6). Neumann boundary conditions were applied for each of the turbulent fields at the Wall boundary. At all of the other boundaries the turbulent boundary conditions must be chosen carefully since the transport equations become singular if $k = 0$, making it necessary to 'seed' a small quantity of TKE. Following Lin and Liu (1998*a*), the TKE at the inlet was calculated using

$$k = \frac{1}{2}(c_p I)^2, \tag{5.2}$$

where I and $c_p = L/T$ are the turbulence intensity and phase speed of the wave, respectively. The ε or ω value is then adjusted so that the eddy viscosity is a fraction, ζ, of the kinematic viscosity, i.e. $\nu_t = \zeta\nu$. Following Lin and Liu (1998*a*), I and ζ are chosen as 0.0025 and 0.1, respectively, in this study. The sensitivity of the model to these parameters is evaluated in Section 5.2.1. The atmosphere boundary condition used a flux based condi-

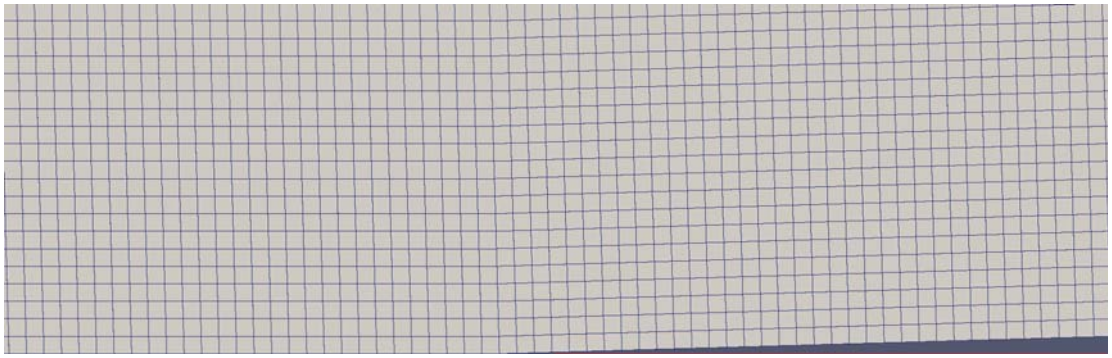

Figure 5.2: A magnified view of the near-wall discretisation for the mesh generated using the merging technique.

tion similar to that used for the velocity, specifying the turbulent values at the inlet for inflow, and applying a zero gradient condition for outflow. The initial conditions for the turbulent fields were set to the value specified at the inlet.

5.1.2 Mesh Generation

To create the computational domain, two rectangular domains were created, one of which had been rotated to the desired angle of the beach, before merging them together. The general procedure for generating the mesh is as follows:

1. create one rectangular mesh with the bottom left corner at $(0,0,0)$. The rectangle should have dimensions of length of the sloping beach $\times$ inlet height;
2. rotate the mesh to the required angle of the sloping beach;
3. create another rectangular mesh, with dimensions length of the constant depth region $\times$ inlet height, and the bottom right corner at $(0,0,0)$;
4. merge the two meshes together;
5. modify the internal patches to become internal faces;
6. translate the mesh so that the start of the slope is at the correct coordinates.

Creating the mesh in this way ensured that the cells remained close to orthogonal with an AR of 1, allowing greater control over the cell discretisation near the beach patch. However, it does cause the air region to progressively increase in size along the sloping beach and,

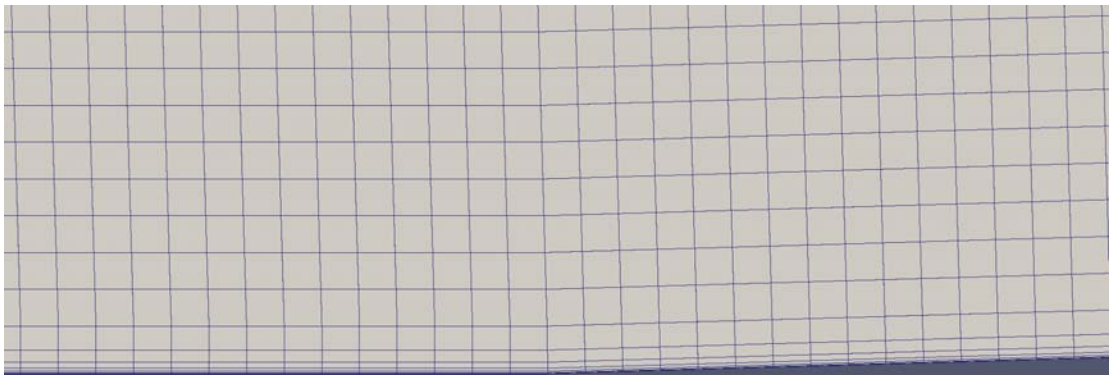

Figure 5.3: A magnified view of the near-wall discretisation for the mesh generated using the merging technique, shown in Figure 5.2, with additional near-wall layers included using `snappyHexMesh`.

although this does ensure that the water phase does not get too close to the atmosphere boundary, this additional air region does increase the total number of cells within the domain and, hence, the computational expense.

The method can be improved by using `snappyHexMesh`, another tool provided by OpenFOAM®, which is primarily designed for importing a geometry into a background mesh. However, `snappyHexMesh` also offers the option to introduce layers adjacent to a boundary, and it is possible to use this functionality without snapping to a geometry. Figure 5.3 shows a case where `snappyHexMesh` has been used to apply boundary layers to a mesh generated as described above, shown in Figure 5.2. In all of the meshes used in this work, layers have been applied in this way. This feature becomes particularly useful when setting the cell adjacent to the beach boundary to a size relative to the sediment grain as is done in Chapter 7.

5.1.3 Grid Refinement Study

Now that a mesh generation technique has been established, a grid refinement study can be conducted. This will be a balance between gaining a mesh independent solution while not making the computational expense unfeasible. To evaluate these two properties, each turbulence model has been used to simulate the first eight waves of the spilling breaker case from still water. Three meshes of different resolution, 0.01 m (Mesh 1), 0.005 m (Mesh 2) and 0.0025 m (Mesh 3) are evaluated, with an AR of approximately 1 used in all cases. Also

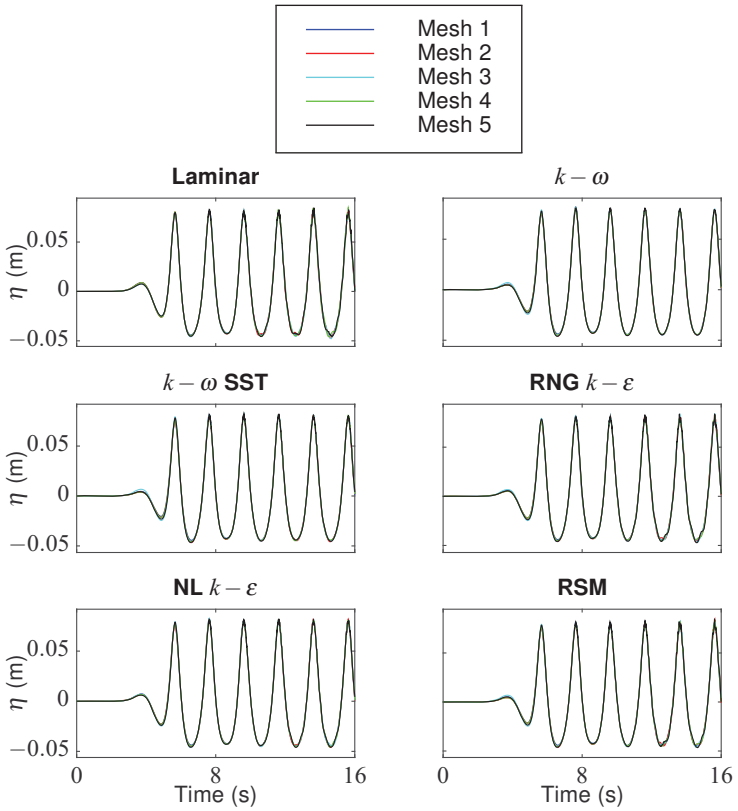

Figure 5.4: Grid refinement study: comparison of the free surface elevation time series, sampled at the toe of the beach. Results from each of the five grids are plotted, with the subplots representing the turbulence model indicated above that plot.

considered are two grids where just the free surface has been refined to 0.005 m (Mesh 4) and 0.0025 m (Mesh 5), with mesh resolution set to 0.01 m in the rest of the domain. The information about each of the meshes is summarised in Table 5.1. Since the value of z^+ varies with flow speed, it varies during the different phases of the wave. Hence, the maximum value has been specified in Table 5.1 and was found to be $z^+_{max} = 1$, indicating that the viscous sublayer is being resolved. Results are collected at the toe of the beach, and time series of surface elevation, velocity, and TKE are compared.

Figure 5.4 shows the surface elevation profiles obtained on the five different grids plotted on top of each other. Each of the subplots represent a different turbulence model, which is indicated at the top of each plot. Although there are very small variations in the profiles,

	Background Δx (m)	Free Surface Δx (m)	AR	Max z^+	# of cells
Mesh 1	0.01	0.01	1	1	178200
Mesh 2	0.005	0.005	1	1	883905
Mesh 3	0.0025	0.0025	1	1	2646000
Mesh 4	0.01	0.005	1	1	320532
Mesh 5	0.01	0.0025	1	1	680400

Table 5.1: Summary of the details of each of the grids used in the grid refinement study.

	Laminar	$k-\omega$	$k-\omega$ SST	RNG $k-\varepsilon$	NL $k-\varepsilon$	RSM
Mesh 1 and 2	0.817	0.612	0.763	0.728	0.587	0.776
Mesh 2 and 3	1.005	0.622	0.748	0.867	0.677	0.781
Mesh 2 and 4	1.220	0.196	0.422	0.771	0.565	0.623
Mesh 3 and 5	0.899	0.562	0.698	0.862	0.694	0.795

Table 5.2: Normalised root mean square difference in the free surface profiles obtained from the different meshes, presented as a percentage.

they are generally limited to the regions close to the trough and crest of the waves. Furthermore, the differences are much smaller than the wave height for all of the turbulence models considered. Table 5.2 gives the normalised root mean square differences between the meshes, presented as percentages. The four rows give information on two important properties: firstly, if the solution is mesh independent, and, secondly, whether refining just the free surface gave similar results to refining the whole mesh. The results imply that refining the whole mesh leads to less than 1% difference in the free surface results for all turbulence models, except when laminar flow conditions are assumed. It also appears that just refining the free surface does not change the wave profile substantially with all results (with the exception of the laminar case) changing by less than 1%.

A similar study has also been performed further into the surf zone where the waves have broken. Although there were some larger changes in surface elevation profiles, they were generally between 1% and 3%. Therefore, it is concluded that in terms of free surface elevation, the mesh is suitably refined in all cases.

Figures 5.5 and 5.6 show time series of horizontal and vertical velocity, respectively, obtained from the five grids considered in this section, and for each of the turbulence models. The results shown have been taken near mid-depth of the water column at the toe of the

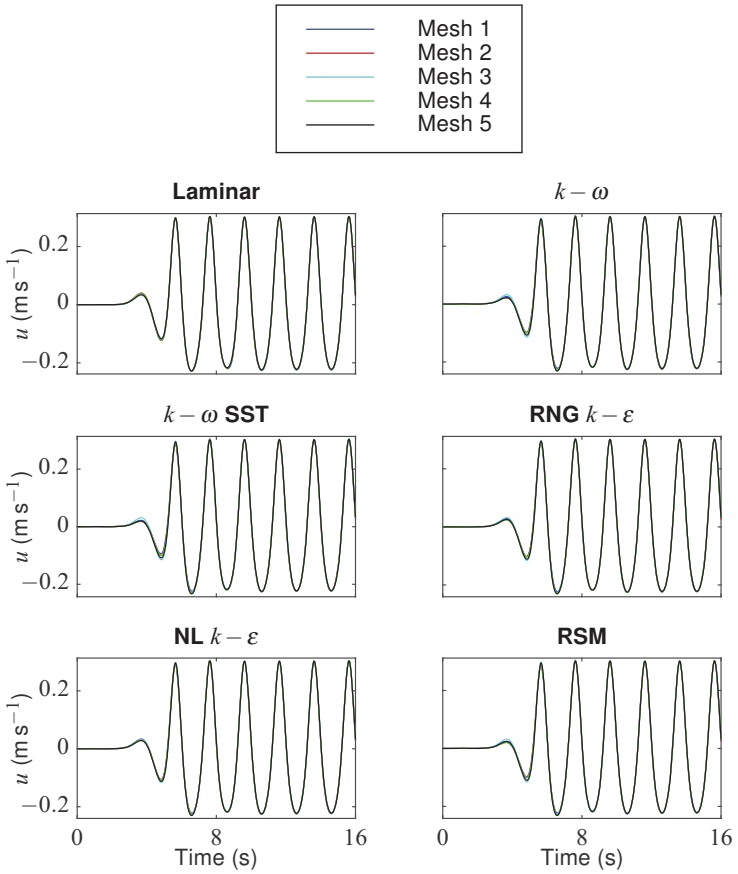

Figure 5.5: Grid refinement study: comparison of the horizontal velocity time series, sampled near mid-depth in the water column, at the toe of the beach. Results from each of the five grids are plotted, with the subplots representing the turbulence model indicated above that plot.

beach. Similar to the results presented for the surface elevation, there are only small variations in the time series for each of the different grids. These variations tend to occur during the first wave to pass the toe of the beach, with the time series becoming virtually identical for the subsequent waves.

Figure 5.7 presents the time series of TKE for each combination of mesh and turbulence model. The results are taken at the same sampling location as the velocity profiles (Figures 5.5 and 5.6). It is clear that the TKE is much more sensitive to the choice of mesh than either the surface elevation or velocity. The trend of the results implies that the mag-

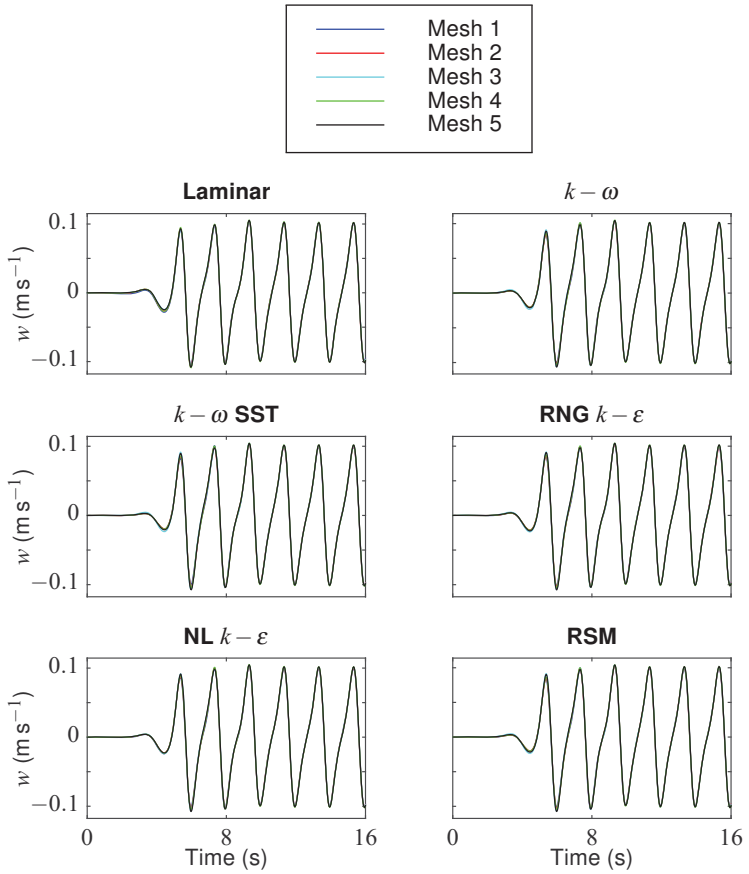

Figure 5.6: Grid refinement study: comparison of the vertical velocity time series, sampled near mid-depth in the water column, at the toe of the beach. Results from each of the five grids are plotted, with the subplots representing the turbulence model indicated above that plot.

nitude of the TKE decreases as the cell size decreases. Since turbulence is not expected to be present at this location in the wave flume, this implies that the finer grids obtain more accurate results. Despite this, there appears to be a much larger (absolute) jump in magnitude between Mesh 1 and 2 than there is between Mesh 2 and 3. Furthermore, the mesh with refinement around the free surface only, gives similar results to the mesh with refinement throughout the whole domain, indicating that only the free surface region needs to be refined.

Figure 5.8 shows the normalised root mean square difference between the meshes, for

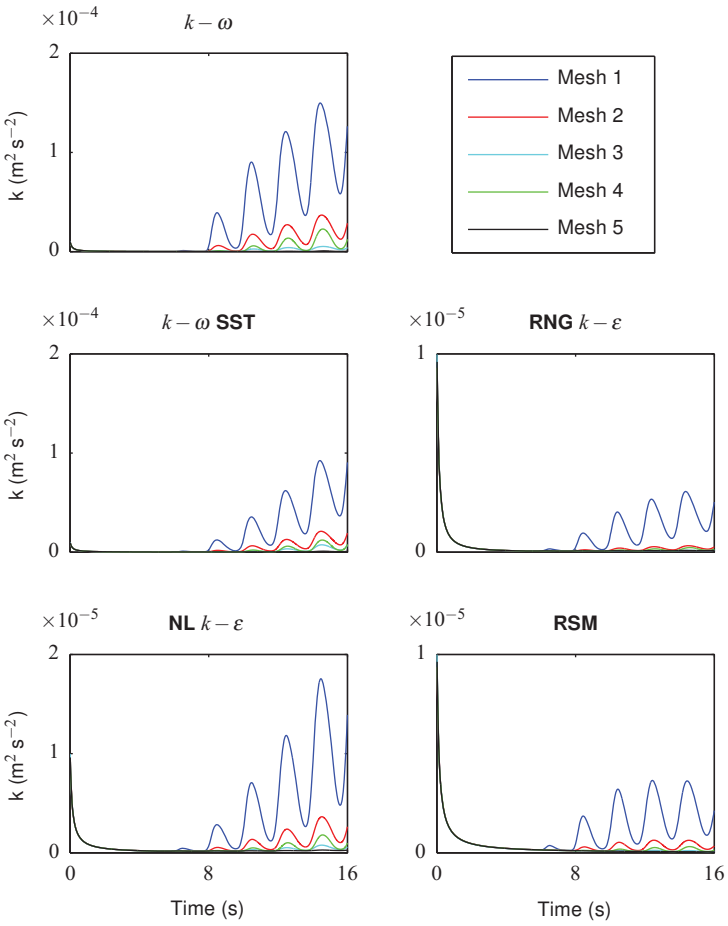

Figure 5.7: Grid refinement study: comparison of the TKE time series, sampled near mid-depth in the water column, at the toe of the beach. Results from each of the five grids are plotted, with the subplots representing the turbulence model indicated above that plot.

horizontal velocity ($\times$), vertical velocity ($+$), and TKE ($*$), presented as a percentage. The whole water column from the wave trough down has been calculated, with each row representing a different turbulence model. The formula used to calculate the difference (in terms of %) is

$$\text{Difference (\%)} = \frac{100}{\max(Q_i) - \min(Q_i)} \sqrt{\frac{1}{N}\sum_{i=1}^{N}(P_i - Q_i)^2}, \tag{5.3}$$

where P and Q are the results from the two grids considered. Before the formula is applied,

the time series have been truncated to remove the time taken for the first wave to arrive at the toe of the beach. The first two columns in Figure 5.8 represent the difference between the three levels of refinement (first refinement is between $\Delta x = 0.01$ m and 0.005 m. The second is between 0.005 m and 0.0025 m). In this case, P is considered the results from the refined mesh and Q from the coarser mesh in equation (5.3). The simulations run with turbulence models predict the horizontal velocity profile to within 1% on all of the meshes considered. When laminar flow conditions are assumed, the maximum deviation between Mesh 1 and 2 is 1.7%, but also changes by less than 1% when comparing the other four grids. The difference between refining the free surface and refining the whole mesh varies between 0.1% and 0.9% in all cases, implying that only the free surface needs to be refined. The vertical velocity follows a similar pattern, although there is slightly more variation with convergence achieved within 1.5%.

As was observed in Figure 5.7 the difference in TKE is much larger than for the velocity and varies between the turbulence models. Refining from Mesh 1 to 2 causes a large change in TKE over the whole water column, except near the bottom where all of the turbulence models seem to give similar values on each of the meshes. In particular, near the centre of the water column values can get as high as 50% difference between the two grids. This trend continues for the next refinement level. The mean change over the water depth is around 25% for all of the turbulence models on Mesh 1 and 2, whereas it varies between 16% ($k-\omega$ SST) and 27% ($k-\omega$) for Mesh 2 and 3. However, since Mesh 2 is used as the reference (Q) in the latter case, the absolute change is much smaller between the two grids, since Mesh 2 predicts lower magnitude than Mesh 1.

The comparisons between Mesh 2 and 4, as well as Mesh 3 and 5 gives information on the difference between the results from the mesh refined everywhere (Q in equation 5.3) and mesh refined around the free surface only (P in equation 5.3). Over the water column, the difference in results on the different grids changes unpredictably, ranging between values of 0.1% and 40%. In most cases these large values exist close to mid-depth in the water column, which could be caused by the change in cell size from the free surface resolu-

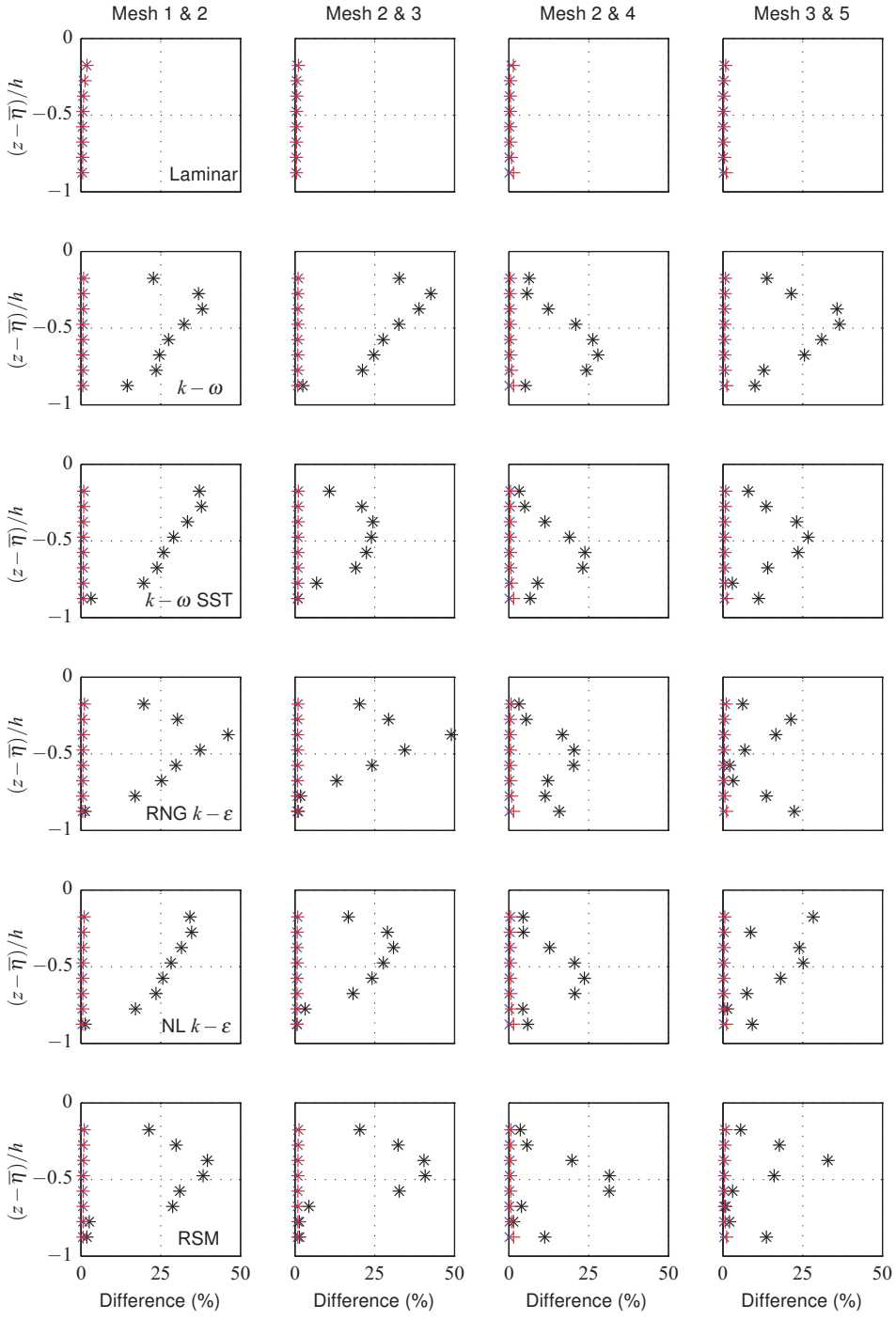

Figure 5.8: Comparison of the percentage difference between the grids with depth, calculated using equation (5.3). Horizontal ($\times$) and vertical ($+$) velocity are plotted along with the TKE ($*$). The left two columns represent refinement of the whole mesh, whereas the right two represent refining only the free surface (see Table 5.1). Each row presents the results for a different turbulence model.

tion to the background mesh. However, since the values near the bottom appear to have converged, it seems unlikely that the difference is down to the change in mesh resolution alone. Overall the mean differences between Mesh 2 and 4, as well as Mesh 3 and 5, over the whole water column are around 15% for each of the turbulence models. This is less sensitive than the change in resolution observed in the comparison between either Mesh 1 and 2 or Mesh 2 and 3. Hence, it is assumed that refining the free surface alone will still give reasonable results.

It is interesting that, while the velocity and free surface are captured to around 1% accuracy, the TKE has such a sensitivity to the chosen mesh. One hypothesis could be that since the scale of the TKE is much smaller (of order 10^{-5} to 10^{-4}) than either the velocity or free surface, any numerical error which is introduced by the model negatively affects the TKE substantially more than the other profiles. In the future it would be interesting to investigate this problem more thoroughly, but for the present study where a large number of waves need to be run, it is unfeasible to refine the mesh any further. Considering the execution time obtained from each of the meshes for the final two wave periods it appears that to increase the refinement level from $\Delta x = 0.01$ m to 0.005 m and then from 0.005 m to 0.0025 m would increase simulation time by 10 times and 20 times, respectively. That makes the simulation time 200 times longer to run than with the original mesh. This can be reduced by just refining the free surface, as this leads to only 4 times the simulation time of Mesh 1. For the second refinement, just refining the free surface leads to approximately 50 times the simulation time of Mesh 1. Hence it seems sensible to only refine the free surface region to save computational expense.

In summary, neither the free surface elevation nor the velocity at the toe of the beach are considerably affected by refining the mesh, either by refining the whole domain or just the free surface. TKE is more sensitive to the mesh resolution, although there is a much larger jump in magnitude during the first refinement than the second refinement level. Furthermore, just refining the free surface region changes the result by around 15% on average, which is less than observed between refinement levels. Combining this information with the

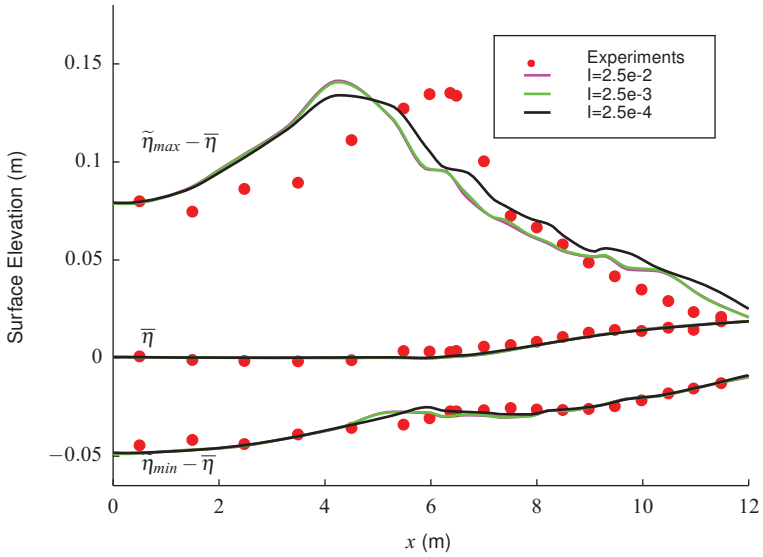

Figure 5.9: Sensitivity of the phase-averaged surface elevation profile to the value of I used at the inlet boundary. The x-axis is the horizontal distance from the origin and the maximum ($\widetilde{\eta}_{max}$), minimum ($\widetilde{\eta}_{min}$), and mean ($\overline{\eta}$) profiles are shown. In this plot ζ is kept constant while I is varied. The numerical results (lines) are compared with the experimental data (●) gathered by Ting and Kirby (1994).

time taken to simulate the final two waves, led to the selection of Mesh 4 as the best for the present study. For this mesh, the free surface has been refined by one level to give a discretisation of 0.005 m around the free surface and 0.01 m elsewhere. This mesh gives reasonable results and does not take too long to run, which is key since a large number of waves will be run in order to obtain the averaged results.

5.2 Model Sensitivity Analysis

This section is dedicated to the analysis of the model sensitivity to variations of a number of parameters, including the boundary conditions at the inlet, and the fluid density in the turbulence model transport equations. Firstly, the sensitivity to I and ζ, used to determine the turbulent inlet boundary conditions, (see Section 5.1.1) is assessed. Then the analytical wave theory used to generate the waves is evaluated. Finally, the effect of explicitly including density in the turbulence model transport equations is discussed.

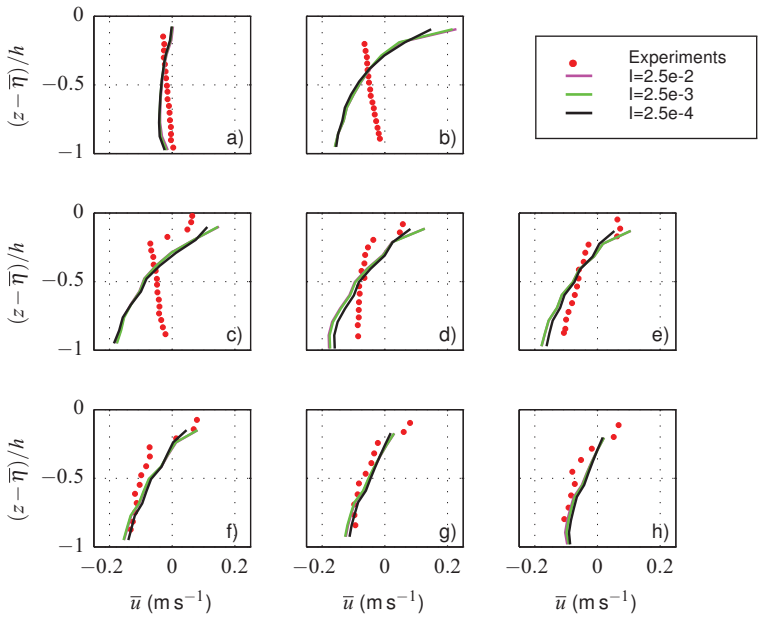

Figure 5.10: Sensitivity of the vertical $\overline{u}$ profile to the value of I used at the inlet boundary. In this plot ζ is kept constant while I is varied. Each plot represents a different location, $x =$ a) -1.265 m, b) 5.595 m, c) 6.665 m, d) 7.275 m, e) 7.885 m, f) 8.495 m, g) 9.11 m, and h) 9.725 m. The numerical results (lines) are compared with the experimental data (•) collected by Ting and Kirby (1994).

5.2.1 Inlet Sensitivity

The first parameter to be evaluated for sensitivity is the turbulence intensity, I. A series of simulations were run using the spilling breakers setup, where the value of ζ was fixed to 0.1 and I was varied. Figure 5.9 shows the sensitivity of the free surface to the value of I. The mean water line (MWL), $\overline{\eta}$, as well as the phase-averaged maximum ($\widetilde{\eta}_{max}$) and minimum profiles ($\widetilde{\eta}_{min}$) are plotted, relative to the MWL, as a function of horizontal distance from the toe of the beach. The numerical predictions (lines) are compared with the experimental data (•) presented by Ting and Kirby (1994). The predictions for $I = 2.5 \times 10^{-2}$ and $I = 2.5 \times 10^{-3}$ are very similar for each of the three profiles. However, the $I = 2.5 \times -4$ gives a very different maximum wave profile, with the breaking point shifting slightly closer to that observed by Ting and Kirby (1994). Smaller values of I were also run but became unstable and eventually crashed. Hence it is unclear whether this shift is physical or due to numerical instability. The mean and minimum profiles are much less sensitive to the value

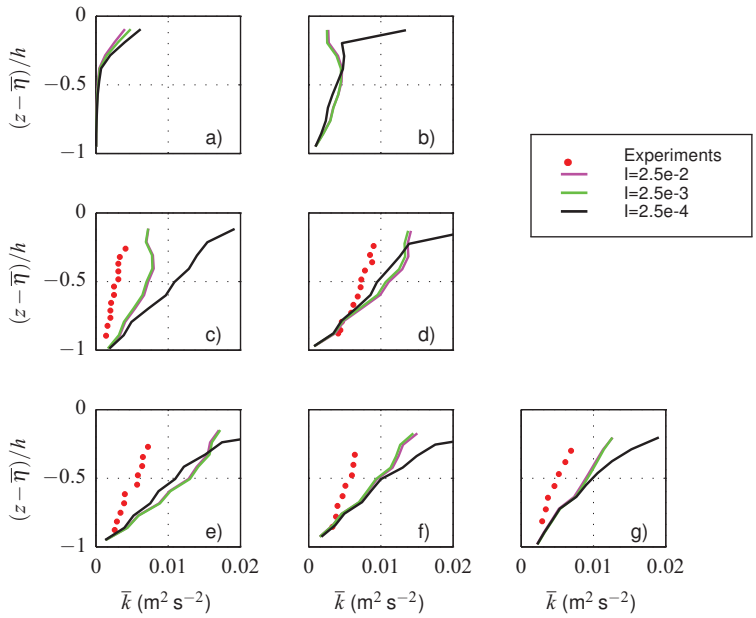

Figure 5.11: Sensitivity of the vertical $\overline{k}$ profile to the value of I used at the inlet boundary. In this plot ζ is kept constant while I is varied. Each plot represents a different location, $x =$ a) 5.595 m, b) 6.665 m, c) 7.275 m, d) 7.885 m, e) 8.495 m, f) 9.11 m, and g) 9.725 m. The numerical results (lines) are compared with the experimental data (•) gathered by Ting and Kirby (1994).

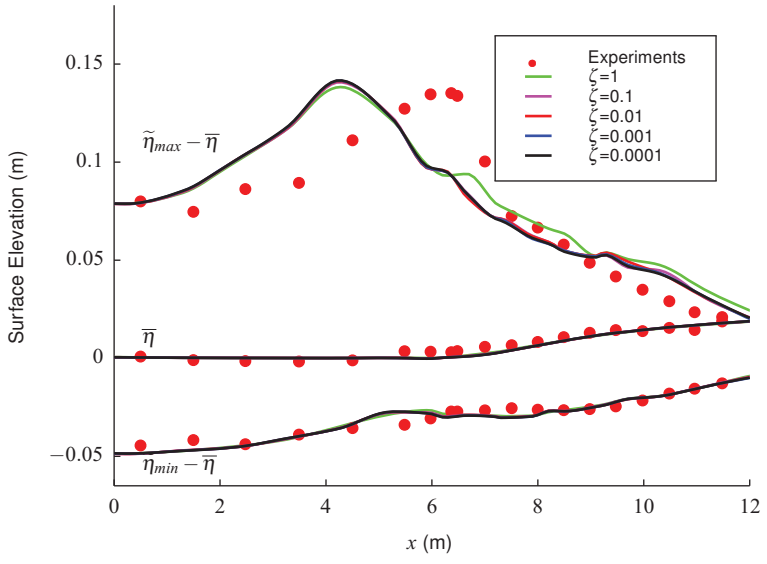

Figure 5.12: Sensitivity of the phase-averaged surface elevation profile to the value of ζ used at the inlet boundary. The x-axis is the horizontal distance from the origin and the maximum ($\widetilde{\eta}_{max}$), minimum ($\widetilde{\eta}_{min}$), and mean ($\overline{\eta}$) profiles are shown. In this plot ζ is kept constant while I is varied. The numerical results (lines) are compared with the experimental data (•) presented by Ting and Kirby (1994).

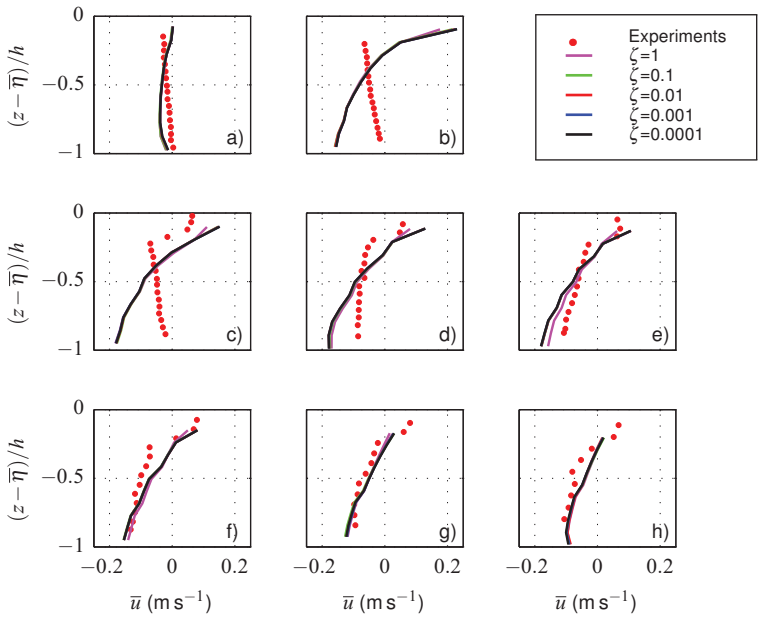

Figure 5.13: Sensitivity of the vertical $\overline{u}$ profile to the value of ζ used at the inlet boundary. In this plot I is kept constant while ζ is varied. Each plot represents a different location, $x =$ a) -1.265 m, b) 5.595 m, c) 6.665 m, d) 7.275 m, e) 7.885 m, f) $8.495m$, g) 9.11 m, and h) 9.725 m. The numerical results (lines) are compared with the experimental data (•) gathered by Ting and Kirby (1994).

of I.

Figure 5.10 shows the time-averaged horizontal velocity, $\overline{u}$, profiles against dimensionless depth, $(z-\overline{\eta})/h$. Once again, the experimental data (•) gathered by Ting and Kirby (1994) has been included for comparison. Each plot represents a different sampling location $x =$ a) -1.265 m, b) 5.595 m, c) 6.665 m, d) 7.275 m, e) 7.885 m, f) 8.495 m, g) 9.11 m, and h) 9.725 m. Similar to the observations about the free surface elevation, the profiles for $I = 2.5 \times 10^{-2}$ and 2.5×10^{-3} are similar at all locations sampled. The predictions with $I = 2.5 \times 10^{-4}$ tend to deviate near the top of the water column, although the undertow near the bed in plots d, e and f is captured better than in the other profiles.

Figure 5.11 presents the time-averaged TKE profiles at the same locations as in Figure 5.10, and are compared with the experimental data (•) collected by Ting and Kirby (1994). The trend continues with the $I = 2.5 \times 10^{-2}$ and $I = 2.5 \times 10^{-3}$ profiles being very similar, whereas the $I = 2.5 \times 10^{-4}$ profile varies substantially. The profiles tend to increasingly

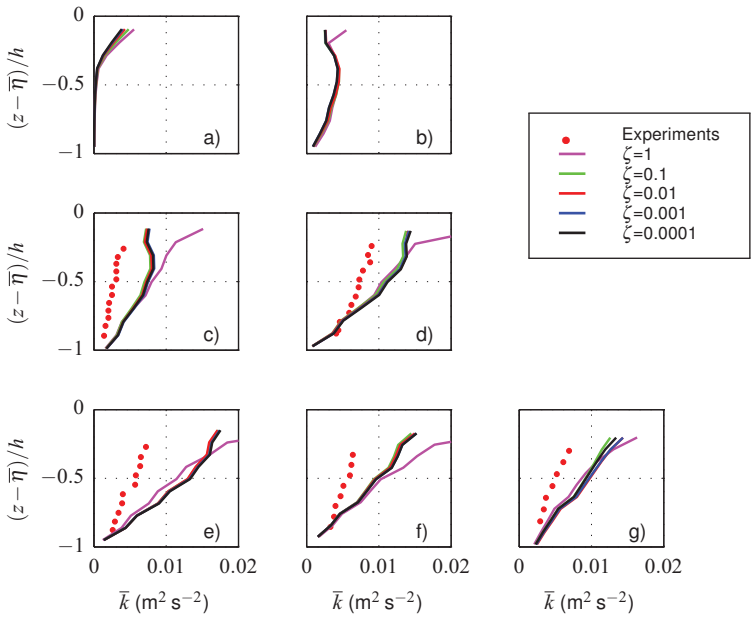

Figure 5.14: Sensitivity of the vertical $\overline{k}$ profile to the value of ζ used at the inlet boundary. In this plot I is kept constant while ζ is varied. Each plot represents a different location, $x =$ a) 5.595 m, b) 6.665 m, c) 7.275 m, d) 7.885 m, e) 8.495 m, f) 9.11 m, and g) 9.725 m. The numerical results (lines) are compared with the experimental data (•) collected by Ting and Kirby (1994).

deviate as the distance above the bed increases. The larger values of I generally appear to agree with the experimental TKE data better, but it is unclear which is the best value to choose, especially as decreasing I further causes the simulation to crash. Hence 0.0025, the value stated in Lin and Liu (1998*a*), will be used for all remaining simulations.

A similar method has been used to evaluate the sensitivity of the model to ζ by fixing the turbulence intensity and varying ζ. Figures 5.12, 5.13 and 5.14 show the equivalent free surface, horizontal velocity and TKE plots, respectively. The minimum and mean free surface profiles do not seem to be very sensitive to ζ. The maximum profiles are also very similar except in the case where $\zeta = 1$. In this case, the wave breaks at the same point but with slightly less height, and deviates substantially in the turbulent bore. The velocity profiles indicate that the model is not overly sensitive to ζ, although the undertow is captured better by $\zeta = 1$ in Figure 5.13e. In the TKE plots there is evidence that the model has a small sensitivity to the choice of ζ near the top of the water column. However, $\zeta = 1$

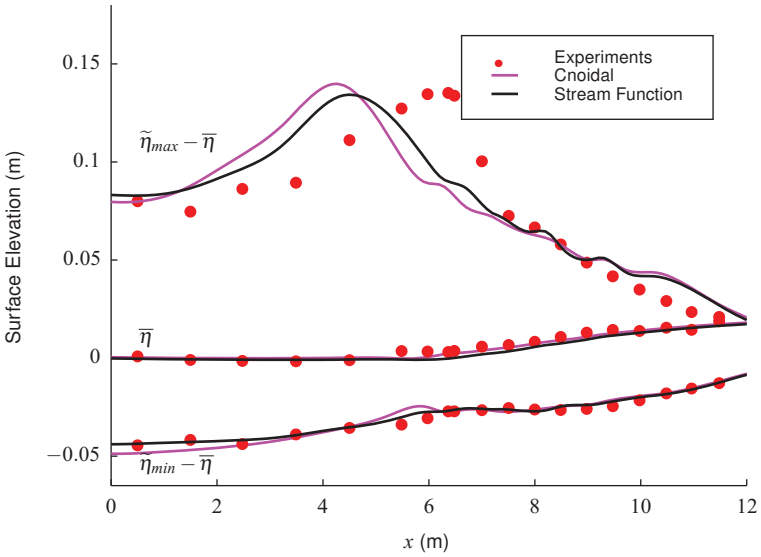

Figure 5.15: Sensitivity of the phase-averaged surface elevation profile to the wave theory used for generation at the inlet. The x-axis is the horizontal distance from the origin and the maximum ($\widetilde{\eta}_{max}$), minimum ($\widetilde{\eta}_{min}$), and mean ($\overline{\eta}$) profiles are shown. The numerical results (lines) are compared with the experimental data (•) presented by Ting and Kirby (1994).

is once again very different throughout. Again it is unclear what value to choose so $\zeta = 0.1$, the value suggested by Lin and Liu (1998*a*), is used for all subsequent simulations in this work.

The final parameter to be assessed is the theory used for wave generation. So far in this sensitivity analysis, Cnoidal first order wave theory has been used but in this section Stream Function wave theory, (Rienecker and Fenton 1981) will also be considered. The results imply that there are only small differences in the velocity and TKE profiles. However, as can be seen in Figure 5.15, which compares the predicted free surface profiles for both wave theories, the waves break slightly later, and at a height closer to the observations of Ting and Kirby (1994) when using the Stream Function wave theory. Furthermore, the minimum profile is much closer to the experimental data (•) near the beginning of the slope. This indicates that Stream Function wave theory leads to a more accurate incident wave at the toe of the beach and, hence, will be used as the wave generation method in the rest of this work.

5.2.2 Effects of Density

As previously mentioned (Section 4.4), the OpenFOAM® turbulence models for incompressible flows do not include density explicitly in the transport equations and instead represent it through the kinematic eddy viscosity, $\nu_t = \mu_t/\rho$. This is fine for single-phase flows. However, as will be seen in this section, this approach can lead to substantial over-estimations of TKE in multiphase flows. In the derivation of turbulence models, density appears in many of the derivatives, and, in order to be able to take ρ outside of the derivative, it must be assumed that it is constant, which is true for incompressible flows of a single phase. In a VOF scheme, the two phases are modelled as a fluid with a variable density. Hence, around the free surface the assumption of constant density will not hold since it will vary between the value for air and the value of water over time. As noted by Jacobsen (2011), this causes excessive diffusion of turbulence over the free surface interface, and since $\nu_{t,water} \ll \nu_{t,air}$, the wave will be damped. Therefore, following Jacobsen (2011), the turbulence models are made weakly compressible through explicit inclusion of density in the transport equations. In this section, the effects of this change on the $k-\omega$ model are presented, with the effects on other turbulence models published by Brown et al. (2014).

The transport equations used by the $k-\omega$ model in OpenFOAM® version 2.1.1 are:

$$\frac{\partial k}{\partial t} + \nabla \cdot (\mathbf{u}k) = P_k - C_\mu \omega k + \nabla \cdot [(\nu + \sigma_k \nu_t)\nabla k], \tag{5.4}$$

$$\frac{\partial \omega}{\partial t} + \nabla \cdot (\mathbf{u}\omega) = \frac{\gamma\omega}{k} P_k - \beta \omega^2 + \nabla \cdot [(\nu + \sigma_\omega \nu_t)\nabla \omega], \tag{5.5}$$

where all of the terms are discussed in Section 4.4. Note the absence of density, ρ, from both equations. The equations with density explicitly included are simply

$$\frac{\partial \rho k}{\partial t} + \nabla \cdot (\rho \mathbf{u}k) = P_k - \rho C_\mu \omega k + \nabla \cdot [(\mu + \sigma_k \mu_t)\nabla k], \tag{5.6}$$

$$\frac{\partial \rho \omega}{\partial t} + \nabla \cdot (\rho \mathbf{u}\omega) = \frac{\gamma\omega}{k} P_k - \rho\beta \omega^2 + \nabla \cdot [(\mu + \sigma_\omega \mu_t)\nabla \omega], \tag{5.7}$$

where $\mu_t = \rho \nu_t$, and the production term, P_k, also includes density. The same approach has

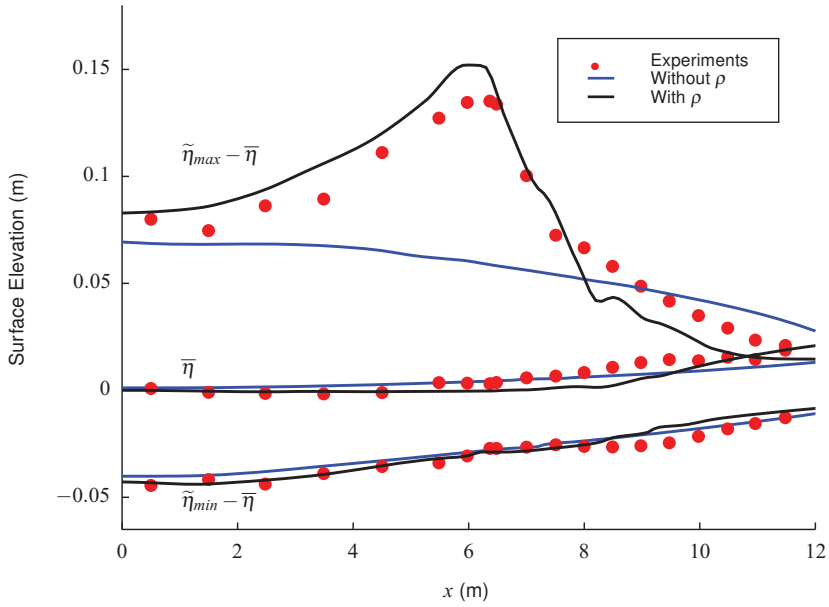

Figure 5.16: Effect of explicitly including density in the $k-\omega$ model on the phase-averaged maximum, minimum, and mean surface elevation profile. The numerical predictions (lines) are compared to the experimental data (•) published by Ting and Kirby (1994).

been applied to all of the turbulence models considered in this study yielding the equations discussed in Section 4.4. The original OpenFOAM® and modified $k-\omega$ models are now run for the spilling breakers case, and compared to the surface elevation and time-averaged TKE experimental data (•) gathered by Ting and Kirby (1994). Other than the inclusion of density, both of the simulations are set up identically.

Figure 5.16 shows a plot of the variation in the maximum, minimum, and mean phase-averaged surface elevation as a function of distance along the wave flume, x. The results imply that the inclusion of density does not affect the minimum and mean surface elevation profiles considerably, with both models performing reasonably well with respect to the experimental data. However, very obvious differences occur in the maximum surface elevation profile, with the inclusion of density substantially increasing the performance of the $k-\omega$ turbulence model. The maximum value now has more reasonable agreement with the experimental data, although, the maximum surface elevation seems to be slightly overestimated prior to breaking, with the breaking point also occurring slightly earlier in the wave

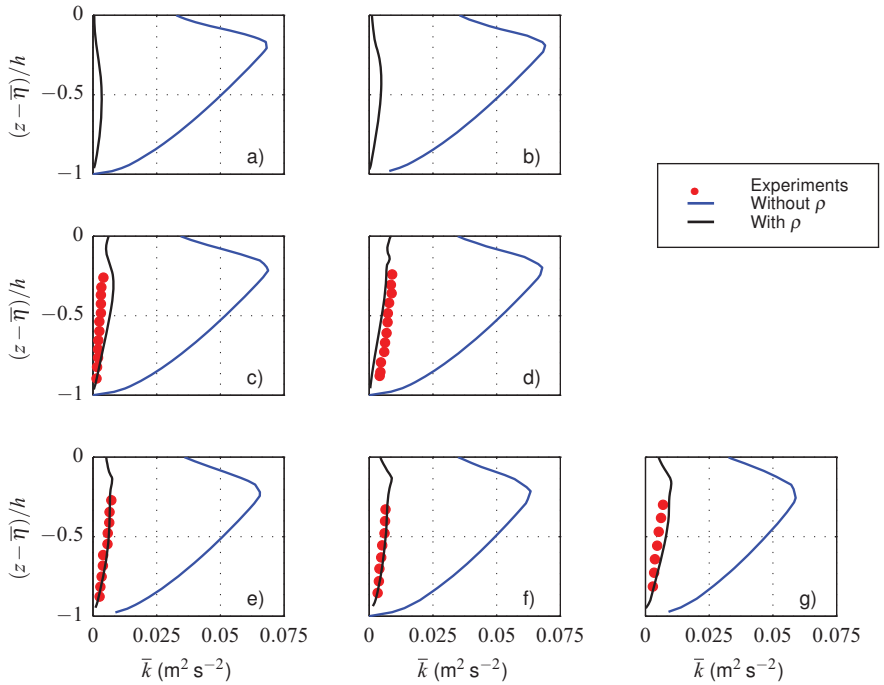

Figure 5.17: Effect of explicitly including density in the $k-\omega$ model on the time-averaged TKE profiles with depth. The numerical predictions (lines) are compared to the experimental data (●) published by Ting and Kirby (1994).

flume than expected.

Figure 5.17 shows the time-averaged TKE variation with dimensionless depth for the $k-\omega$ model. It is clear that the mean TKE is substantially over-estimated (up to ten times larger than the experimental data) by the turbulence model without density included. It is believed that this substantial over-prediction of mean TKE is responsible for the excessive damping observed in the free surface when using the OpenFOAM® turbulence models (i.e. without density) since it corresponds to larger contributions to the Reynolds stress, which is a negative contribution to the RANS equations, and hence relates to more energy being removed from the mean flow. By introducing density to the $k-\omega$ model, the levels of TKE fall back to a similar level as observed by Ting and Kirby (1994).

As presented by Brown et al. (2014), the $k-\omega$ model is an extreme case, which seems to be particularly sensitive to the inclusion of density. However, all of the turbulence models considered here over-estimate mean TKE in the spilling breaker without density explicitly

included. Furthermore, they all observe a reduction in mean TKE making them more consistent with laboratory data. Root mean square errors are also presented by Brown et al. (2014), confirming this increase in accuracy. Therefore, all of the turbulence models used from here onwards have been adapted to include density, unless otherwise stated.

5.3 Evaluation of Turbulence Models

The final decision before beginning to validate the suspended sediment concentration model is which turbulence closure model to use. Therefore a detailed evaluation of some of the options available within the OpenFOAM® environment, is conducted for application to spilling and plunging breakers.

5.3.1 Spilling Breakers

Tests are first performed for the spilling breakers case. Comparisons between the model predictions and observations by Ting and Kirby (1994), under the same wave conditions, for the maximum, mean, and minimum surface elevation (Figure 5.18), for the time-averaged velocity (Figure 5.21), and for mean TKE profiles (Figure 5.22), are presented.

Figure 5.18 shows the phase-averaged surface elevations $\widetilde{\eta}_{max} - \overline{\eta}$, $\overline{\eta}$ and $\widetilde{\eta}_{min} - \overline{\eta}$ for the spilling breakers case as a function of horizontal distance, x, along the numerical wave flume. Here $\widetilde{\eta}_{max}$ and $\widetilde{\eta}_{min}$ are the maximum and minimum phase-averaged surface elevation and $\overline{\eta}$ is the mean surface elevation. Furthermore, the shaded regions around the maximum and minimum profiles in the figure represent one standard deviation. Each subplot compares a different turbulence closure model to the experimental data (•) gathered by Ting and Kirby (1994): a) Laminar, b) $k-\omega$, c) $k-\omega$ SST, d) RNG $k-\varepsilon$, e) nonlinear $k-\varepsilon$, and f) Reynolds stress model (RSM). The overall root mean square error (RMSE) for each turbulence model, combining the results for maximum, minimum and mean profiles, is indicated on each plot (denoted by E). The overall RMSE clearly indicates that the RNG and nonlinear $k-\varepsilon$ models most accurately reproduce the phase-averaged surface elevation out the models considered in this study. If each of the three profiles are considered individually, visual observations and RMSE (for each profile rather than the combined value stated

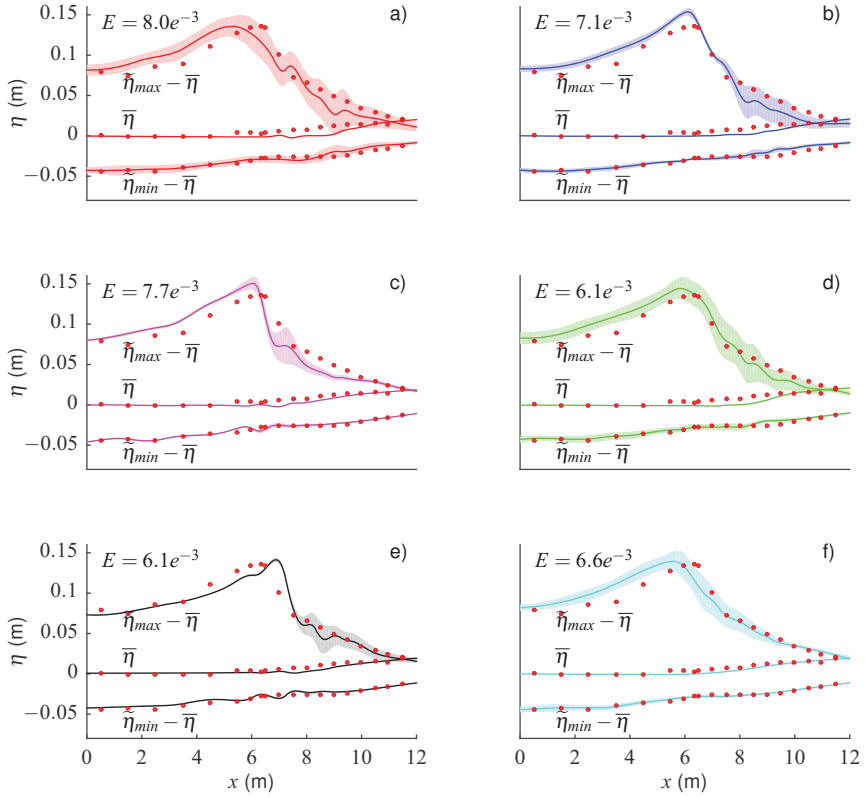

Figure 5.18: Comparison of surface elevation profiles $\overline{\eta}$, $\widetilde{\eta}_{max} - \overline{\eta}$, and $\widetilde{\eta}_{min} - \overline{\eta}$ for the spilling breakers. Each subplot represents a different model: a) Laminar, b) $k-\omega$, c) $k-\omega$ SST, d) RNG $k-\varepsilon$, e) NL $k-\varepsilon$, and f) RSM, with an overall RMSE value, E (representing the maximum, minimum and mean profiles combined), given with respect to the laboratory data (•) gathered by Ting and Kirby (1994). One standard deviation either side of the maximum and minimum surface elevations is indicated by the shaded area.

in Figure 5.18) imply that the RSM captures the minimum and mean profiles the best, although the other models do perform reasonably well with respect to the experimental data. All of the turbulence models capture the wave setup more accurately than when laminar flow conditions are assumed (subplot a), although in general, the wave setup is predicted to occur slightly further along the flume than was shown in the laboratory data. Furthermore, the shaded region shows a much larger variation in maximum and minimum profiles when laminar flow conditions are assumed, suggesting that the waves are more repeatable when a turbulence model is used.

When considering the maximum profiles, there are more obvious differences between the turbulence models. The RNG $k-\varepsilon$ model follows the experimental data the closest and has the lowest RMSE for the maximum profile. The $k-\omega$ and $k-\omega$ SST turbulence models all substantially over-estimate the maximum surface elevation prior to breaking but do predict the breaking point, x_b, at a similar location in the flume as indicated by the experimental data. The nonlinear $k-\varepsilon$ model also over-estimates the breaking height but is the only model to predict the breaking point later than shown in the laboratory. The remaining models all break at a similar wave height as the experimental data, but the breaking point occurs slightly earlier in the numerical wave flume than expected. Interestingly, the RSM, which solves for all of the components of the Reynolds Stress, and therefore was expected to be the most accurate model, predicts breaking to occur at the earliest point out of all of the turbulence models considered (but still later than when laminar flow conditions are assumed), 0.8 m earlier than observed in the experimental data. However, it does capture the breaking height well, and is the turbulence model which follows the experimental data most accurately in the turbulent bore.

Comparing the shaded profiles before breaking occurs, it is clear that the nonlinear $k-\varepsilon$ model and $k-\omega$ SST models have very small variation in both minimum and maximum surface elevation, indicating that every wave is almost identical in terms of wave height. On the other hand, the RSM and RNG $k-\varepsilon$ models have reasonable variation prior to breaking, implying that each wave has a slightly different shape. The RNG $k-\varepsilon$ model appears to follow the laminar case particularly closely in terms of profile shape, and inter-wave variation at the different regions of the wave flume. It is also interesting to note that the upper envelope of the maximum profile generally captures the profile well after breaking, whereas the mean value under-estimates the shape shown in the physical experiments. As is to be expected, all of the models exhibit much larger inter-wave variation after breaking has occurred. This represents that the wave shape is more repeatable before breaking, i.e. each wave has a similar surface elevation profile, whereas the waves are less predictable after breaking, which is expected due to the chaotic nature of broken waves.

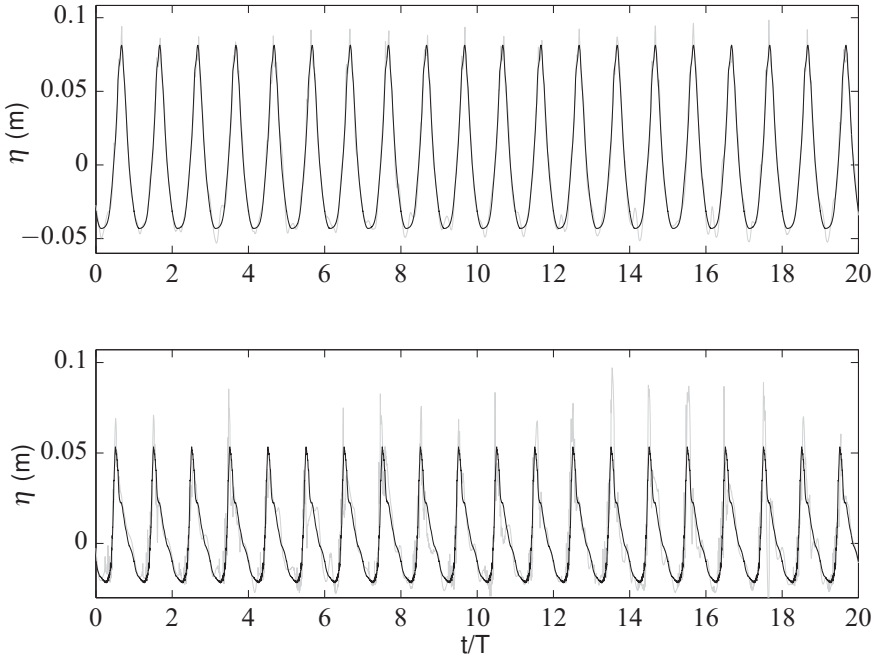

Figure 5.19: Phase-averaged surface elevation (black) overlaying the time series for the twenty waves used to create it (grey) for the spilling breakers case. Both the constant depth region at $x = -1.265$ m (top) and after breaking at $x = 8.495$ m (bottom) for the RNG $k-\varepsilon$ model are shown.

Figures 5.19 and 5.20 emphasise the previously mentioned repeatability of waves prior to breaking and the lack of predictability post-breaking. They present the phase-average surface elevation for spilling breakers overlaying the twenty waves used to create the phase-average, for the RNG $k-\varepsilon$ and nonlinear $k-\varepsilon$ models, respectively. The top plot represents the constant depth, pre-breaking profile ($x = -1.265$ m), and the bottom post-breaking, in the region with the largest variation ($x = 8.495$ m), as can be seen in Figure 5.18. Comparing the constant depth profiles, it is clear that every wave has an almost identical wave shape, as is to be expected, when the nonlinear $k-\varepsilon$ model is used. On the other hand, for the RNG $k-\varepsilon$ model, the twenty waves vary considerably in shape from the phase-average profile as was implied in Figure 5.18. This explains the large variation, relative to the nonlinear $k-\varepsilon$ model, in the pre-breaking profile obtained with the RNG $k-\varepsilon$. Furthermore, the post-breaking profiles provide an explanation for the much larger variation observed in Figure 5.18 further along the wave flume. Both turbulence models have large variations

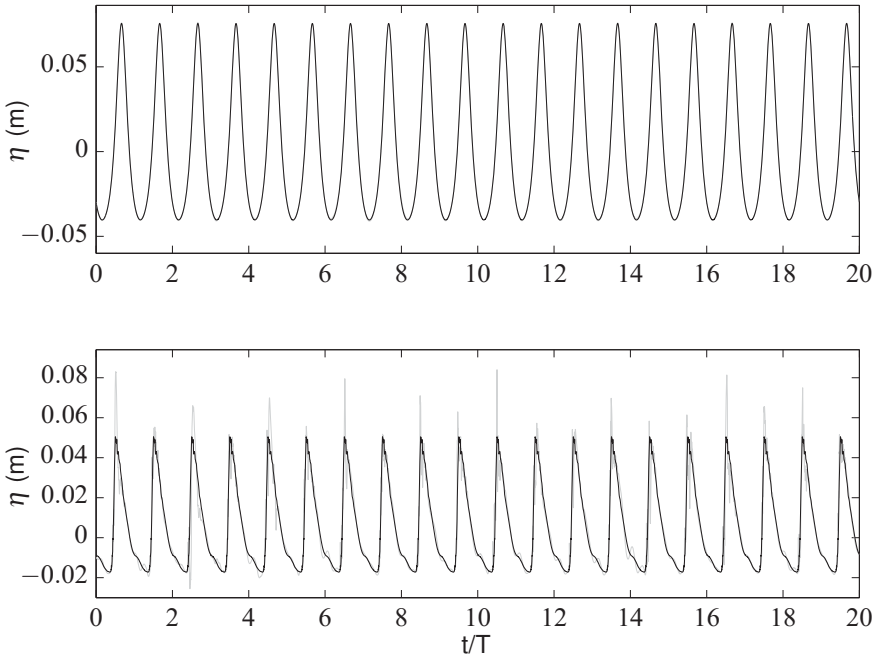

Figure 5.20: Phase-averaged surface elevation (black) overlaying the time series for the twenty waves used to create it (grey) for the spilling breakers case. Both the constant depth region at $x = -1.265$ m (top) and after breaking at $x = 8.495$ m (bottom) for the nonlinear $k-\varepsilon$ model are shown.

in shape, especially in terms of maximum height compared to the phase-averaged surface elevation.

Overall, the best models, only taking into account the RMSE, are the nonlinear $k-\varepsilon$ and RNG $k-\varepsilon$ models. However, the RSM could be considered the best model since it captures the wave setup, as well as the minimum profile most accurately with respect to the physical experiments. It also captures the maximum profile breaking height and the turbulent bore region well, but the pre-breaking profile is much less accurate than other models. The breaking points of each of the models have been summarised in Table 5.3, along with the water depths and wave height at breaking.

Figure 5.21 shows the time-averaged horizontal velocity, $\overline{u}$ (m s^{-1}), profiles with dimensionless depth, $(z-\overline{\eta})/h$, for the spilling breakers case. As before, the experimental data (●) presented by Ting and Kirby (1994) has been included for comparison. Each row of sub-

	Laminar	$k-\omega$	$k-\omega$ SST	RNG $k-\varepsilon$	NL $k-\varepsilon$	RSM	Ting (1994)
x_b	5.3	6.1	6.0	5.9	6.9	5.6	6.4
$h_{swl,b}$	0.2286	0.2057	0.2086	0.2114	0.1829	0.2200	0.196
$\overline{\eta_b}$	-0.0013	-0.0004	-0.0009	-0.0010	0.0028	-0.0009	0.0033
h_b	0.2273	0.2052	0.2077	0.2105	0.1856	0.2191	0.1993
H_b	0.1679	0.1833	0.1797	0.1744	0.1717	0.1703	0.1621

Table 5.3: Summary of the spilling breaker predictions at the breaking point for each turbulence model. x_b is the breaking point, $h_{swl,b}$, h_b are the depth from the SWL ($z=0$) and MWL ($z=\overline{\eta_b}$), respectively, and H_b is the wave height at breaking.

plots shows a different sampling location relative to the breaking point, location a is prior to the breaking point (5.945 m in Ting and Kirby 1994), and locations b-g are post-breaking (6.665, 7.275, 7.885, 8.495, 9.11, and 9.725 m in Ting and Kirby 1994). Each column of subplots represents a different turbulence closure model, with the laminar case also shown for reference. As a measure of accuracy with respect to the experimental data, the RMSE value (denoted by E) is indicated for each profile at the top of that individual plot. The laboratory data suggests that the mean velocity is negative throughout the majority of the water column with a relatively small region of positive mean velocity near the free surface. All of the turbulence models capture this change between positive and negative mean velocity, with good agreement in comparison to the experimental data.

Another trend in the laboratory data presented by Ting and Kirby (1994) is that the gradient of the mean horizontal velocity profile changes sign after breaking has occurred. Around the breaking point (locations a and b), the gradient is negative: the mean velocity is very small near the bottom of the water column, and grows in magnitude closer to the free surface. Further along the wave flume (locations d, e, f and g), a large undertow is present, leading to a positive velocity gradient.

Qualitatively, there is only one turbulence model, the RNG $k-\varepsilon$, which captures the negative gradient profile accurately. However, the model does not have the lowest RMSE due to the poor prediction seen in the profile near the top of the water column. Instead the nonlinear $k-\varepsilon$ has the lowest RMSE, despite not predicting the velocity profile near the bottom of the water column correctly. It is interesting to note that when laminar flow conditions

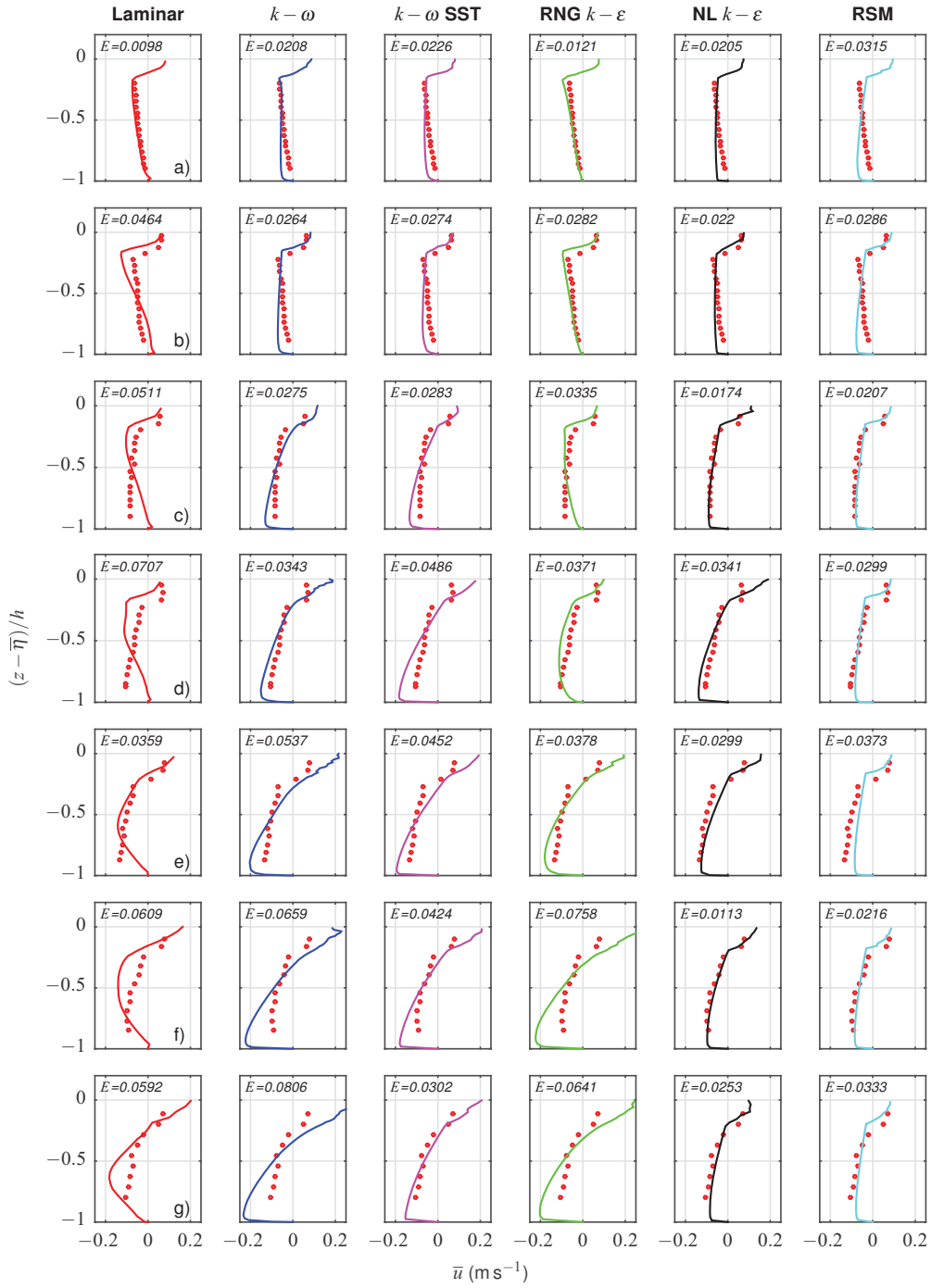

Figure 5.21: Comparison of time-averaged horizontal velocity profiles with depth for the spilling breakers against the experimental data (●) reported by Ting and Kirby (1994). The RMSE for each profile with respect to the experiments is indicated at the top of each plot (denoted by E). Each column represents a different turbulence model whereas the rows represent different sampling locations relative to the breaking point $x-x_b =$ a) -0.455, b) 0.265, c) 0.875, d) 1.485, e) 2.095, f) 2.71, and g) 3.325 m.

are assumed, the negative gradient is also captured at location a but once breaking occurs there is substantial variation from the experimental data (location b). The remaining models predict similar magnitudes of velocity over the whole water column and therefore perform well closer to the free surface and reduce in accuracy near the bottom.

Location c appears to be the transition between the two profile shapes, i.e. where the gradient of the profile changes sign and the mean velocity is almost constant with depth. The various turbulence models give very different predictions for this profile, with the RSM and nonlinear $k-\varepsilon$ model capturing the shape very well: the profile is similar to that predicted at locations a and b where the mean velocity is almost constant over the water depth. The RNG $k-\varepsilon$ model still predicts the profile shape required at locations a and b, whereas the remaining turbulence models exhibit a shape closer to the positive velocity gradient found at locations d-g in the experiments. This could suggest that the profile gradient changes sign too late for the RNG $k-\varepsilon$ model, and too early for the $k-\omega$ and $k-\omega$ SST models.

At location d, all of the turbulence models follow a similar shape to the experimental data although the $k-\omega$ and $k-\omega$ SST models both over-predict the magnitude of the undertow. The RMSE values show that the nonlinear $k-\varepsilon$ and RSM models perform the best, with the laminar case performing very poorly. This pattern generally continues throughout the remaining sampling locations (e-g) except that like the $k-\omega$ models, the RNG $k-\varepsilon$ model also over-estimates the mean velocity profile near the bottom substantially.

Although the RNG $k-\varepsilon$ model performs best near the breaking point, the nonlinear $k-\varepsilon$ gives the best results overall, implying that it could be important to assume anisotropic turbulence, which is further backed up by the RSM being the second best model for mean horizontal velocity profiles.

Figure 5.22 shows the time-averaged TKE, $\overline{k}$ ($\mathrm{m}^2\,\mathrm{s}^{-2}$), profiles with dimensionless depth for the spilling breakers case. Once again, the points (●) represent the experimental data collected by Ting and Kirby (1994), and the lines indicate the numerical predictions using each of the turbulence models. Each subplot represents a different sampling location relative to the breaking point. Locations a and b are near the breaking point (5.945 and

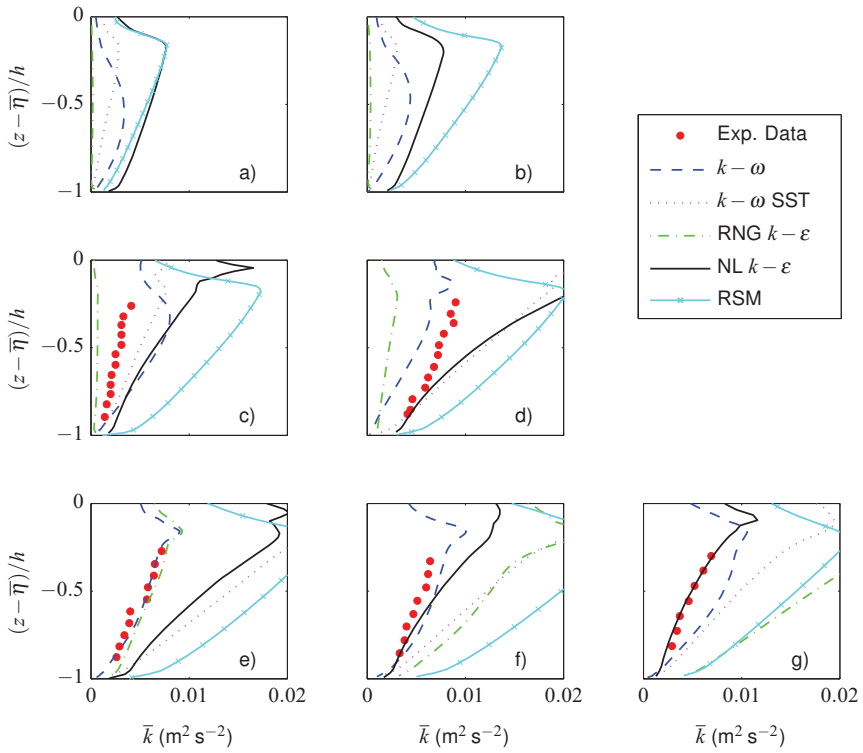

Figure 5.22: Comparison of time-averaged TKE profiles with depth for the spilling breakers at sampling locations relative to the breaking point $x - x_b =$ a) -0.455, b) 0.265, c) 0.875, d) 1.485, e) 2.095, f) 2.71, and g) 3.325 m. Each line represents a different turbulence closure model and the predictions are compared to the experimental data (●) gathered by Ting and Kirby (1994).

6.665 m in Ting and Kirby 1994), whereas the remaining sampling points are placed after breaking has occurred and correspond to locations 7.275, 7.885, 8.495, 9.11, and 9.725 m in Ting and Kirby (1994). However, Ting and Kirby (1994) only provided TKE results for the post-breaking locations, presumably because turbulence levels were low prior to breaking. As can be seen in plots a and b, the RNG $k-\varepsilon$ model predicts very little TKE across the whole water column, whereas every other model predicts levels similar to after breaking has occurred. Since this occurs at the location where the RNG $k-\varepsilon$ was the only model capable of capturing the mean horizontal velocity profile, this could imply that there is a correlation between predictions of very small levels of mean TKE prior to breaking, and the negative gradient in the velocity profile exhibited by the unbroken wave. Furthermore, the experimental profile at location a was captured when laminar conditions were assumed,

$x - x_b$ (m)	$k-\omega$	$k-\omega$ SST	RNG $k-\varepsilon$	NL $k-\varepsilon$	RSM
0.875	0.0035	0.0021	0.0021	0.0036	0.0096
1.485	0.0025	0.0045	0.0048	0.0047	0.0076
2.095	0.0005	0.0080	0.0009	0.0061	0.0117
2.71	0.0013	0.0060	0.0064	0.0018	0.0129
3.325	0.0026	0.0046	0.0119	0.0003	0.0099

Table 5.4: RMSE associated with the time-averaged TKE predictions for spilling breakers, with respect to the experimental data gathered by Ting and Kirby (1994). All of the different turbulence model predictions at the five locations where data is available are presented and correspond to plots c-g in Figure 5.22.

which backs up the hypothesis that a turbulence model must be able to predict low levels of TKE prior to breaking.

For the five remaining sampling locations, where experimental data is available, the RMSE has been calculated for each turbulence model and is recorded in Table 5.4. Together with Figure 5.22, it is clear that all of the models generally over-estimate the levels of mean TKE. However, the $k-\omega$ model performs well and is the most accurate of the models overall. The $k-\omega$ SST model obtains good accuracy at the sampling locations closer to the breaking point (subplots c and d) but progressively over-estimates the magnitude further along the flume. The RNG $k-\varepsilon$ model follows a similar pattern, it begins by under-estimating the mean TKE in subplots c and d, before over-estimating it in subplots f and g. Finally, the nonlinear $k-\varepsilon$ model gives similar results to the $k-\omega$ model, except at locations d and e where it substantially over-predicts the magnitude of the mean TKE. Interestingly, the RSM, which was expected to be the most accurate model, substantially over-estimates the mean TKE everywhere that has been sampled, leading to much larger RMSE values than the other models, despite giving reasonable results for both surface elevation and undertow.

In summary, for the spilling breakers, the different models which have been evaluated vary in performance over the three criteria considered. The RSM performed well on both surface elevation and mean horizontal velocity, but substantially over-estimates levels of time-averaged TKE. On the other hand, the $k-\omega$ model performs well for mean TKE and surface elevation but over-estimates the magnitude of the undertow. Overall, the most consistent model is the nonlinear $k-\varepsilon$, which performs reasonably well for all three criterion.

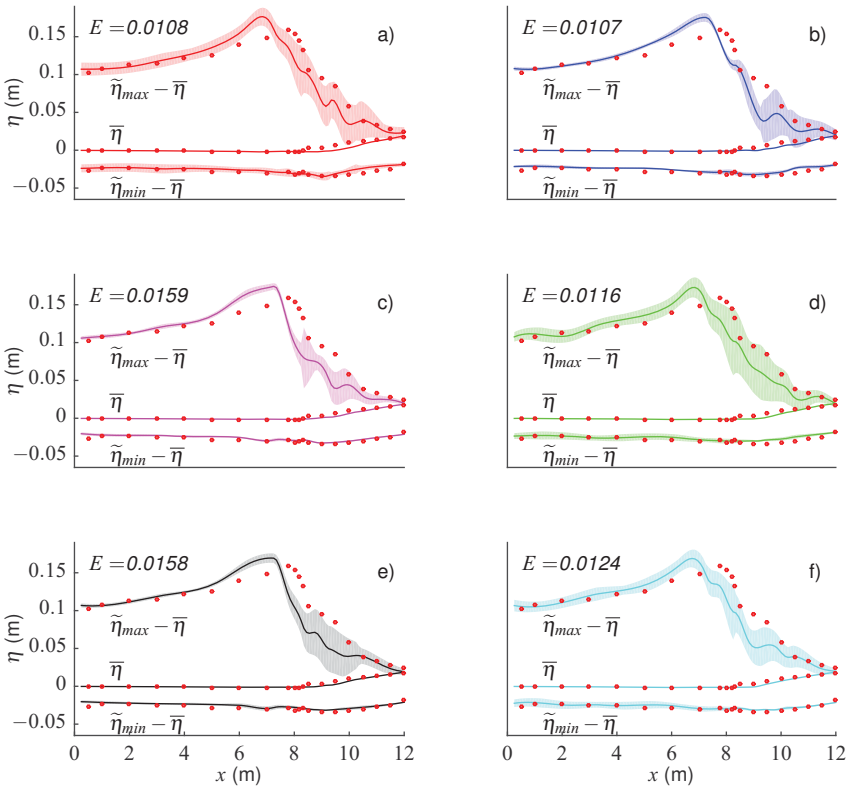

Figure 5.23: Comparison of surface elevation profiles $\overline{\eta}$, $\widetilde{\eta}_{max} - \overline{\eta}$ and $\widetilde{\eta}_{min} - \overline{\eta}$ for the plunging breakers. Each subplot represents a different model: a) Laminar, b) $k-\omega$, c) $k-\omega$ SST, d) RNG $k-\varepsilon$, e) NL $k-\varepsilon$, f) RSM, with an overall RMSE value, E (representing the maximum, minimum and mean profiles combined), given with respect to the laboratory data (•) collected by Ting and Kirby (1994). One standard deviation either side of the maximum and minimum surface elevations is indicated by the shaded area.

5.3.2 Plunging Breakers

Tests are now performed for the plunging breakers case. Comparisons between the model predictions and observations presented by Ting and Kirby (1994), under the same wave conditions, for the maximum, mean, and minimum surface elevation (Figure 5.23), for the time-averaged velocity (Figure 5.24), and for mean TKE profiles (Figure 5.25), are presented.

Figure 5.23 presents the same surface elevation profiles presented in Figure 5.18, except for the plunging breaker results. Again, each subplot compares a different turbulence clo-

sure model, a) Laminar, b) $k-\omega$, c) $k-\omega$ SST, d) RNG $k-\varepsilon$, e) nonlinear $k-\varepsilon$, and f) RSM, to the experimental data (•) gathered by Ting and Kirby (1994) with the overall RMSE (for minimum, mean and maximum profiles combined) indicated by E in each plot. The results for the minimum and mean surface elevation profiles follow a similar pattern to the spilling breakers case. There is not much to choose between the different turbulence models since they all predict the minimum surface elevation accurately, although, there is substantially more variation in the laminar and RNG $k-\varepsilon$ model cases, indicating that the waves are less repeatable, which was also observed in the spilling breakers. The $\overline{\eta}$ profile implies that the wave setup occurs at a similar rate as shown in the experimental data and is therefore slightly more accurate than was seen in the spilling breakers. It seems that once again, the wave setup is more accurately captured when a turbulence model is used since it occurs further down the wave flume than shown in the laboratory data when laminar flow conditions are assumed.

When the maximum surface elevation profile is considered it is clear that there is much less variation between the different models than was seen in the spilling breakers (see Figure 5.18). This is reflected in the RMSE values, which are all very similar. All of the models shown, including the laminar case, predict the waves to break a little earlier in the wave flume than was shown in the experimental data, as well as over-estimating the breaking height (see Table 5.5). Once again, the RNG $k-\varepsilon$ model seems to follow the profile shape and variation of the laminar case, especially prior to breaking. Although there is not much to choose between the models in terms of profile shape, there are large differences in the variation of the maximum and minimum profiles, which follows the observations made in the spilling breakers case. All of the models have smaller variation before breaking, with a much larger variation in wave shape occurring further along the tank (between 8 and $10\,$m). As previously discussed (see Figures 5.19 and 5.20 for the time series relating to the spilling breakers) this pattern implies that the waves are much more repeatable before breaking than after, as is to be expected. Out of all of the models, the RNG $k-\varepsilon$ model appears to have a slightly larger standard deviation prior to breaking, suggesting a variation in wave shape even when the wave has not broken. The nonlinear $k-\varepsilon$, $k-\omega$ and $k-\omega$ SST

	Laminar	$k-\omega$	$k-\omega$ SST	RNG $k-\varepsilon$	NL $k-\varepsilon$	RSM	Ting (1994)
x_b	6.85	7.25	7.25	6.85	7.15	6.75	7.795
$h_{swl,b}$	0.1843	0.1729	0.1729	0.1843	0.1757	0.1871	0.1573
$\overline{\eta_b}$	-0.0018	-0.0013	-0.0013	-0.0016	-0.0011	-0.0015	-0.0022
h_b	0.1825	0.1715	0.1716	0.1827	0.1746	0.1856	0.1550
H_b	0.2040	0.2042	0.2031	0.2007	0.1976	0.1973	0.1887

Table 5.5: Summary of the plunging breaker predictions at the breaking point for each turbulence model. x_b is the breaking point, $h_{swl,b}$, h_b are the depth from the SWL ($z=0$) and MWL ($z=\overline{\eta_b}$), respectively, and H_b is the wave height at breaking.

models have very small variation as the wave starts propagating up the slope, suggesting the waves are almost identical, as would generally be expected. Interestingly, the upper envelope follows the turbulent bore region from the experiments for many of the turbulence models, especially the RNG $k-\varepsilon$.

In summary, there does not appear to be a model which captures the free surface of plunging breakers substantially better than the others, although the variation before breaking indicates that the waves are much more repeatable in the $k-\omega$, $k-\omega$ SST and nonlinear $k-\varepsilon$ models.

Figure 5.24 shows the same time-averaged horizontal velocity, $\overline{u}$, presented in Figure 5.21, except for the results of the plunging breakers. Each row of subplots indicates a different sampling location relative to the breaking point: location a is prior to the breaking point (7.295 m in Ting and Kirby 1994), location b is at the breaking point (7.795 m in Ting and Kirby 1994) and locations c-g are post-breaking (8.345, 8.795, 9.295, 9.795, and 10.395 m in Ting and Kirby 1994). Similar to the spilling breaker experimental results, the mean horizontal velocity is negative over the majority of water column at all sampling locations, with a relatively small region of positive mean velocity near the free surface. Again, all of the turbulence models capture this characteristic, with particularly good results at locations a-c.

The laboratory data implies that the gradient of the horizontal velocity profile with depth is negative at locations a-c, similar to the profile seen in the spilling breakers case. This negative gradient is not captured particularly well by any of the turbulence models at location

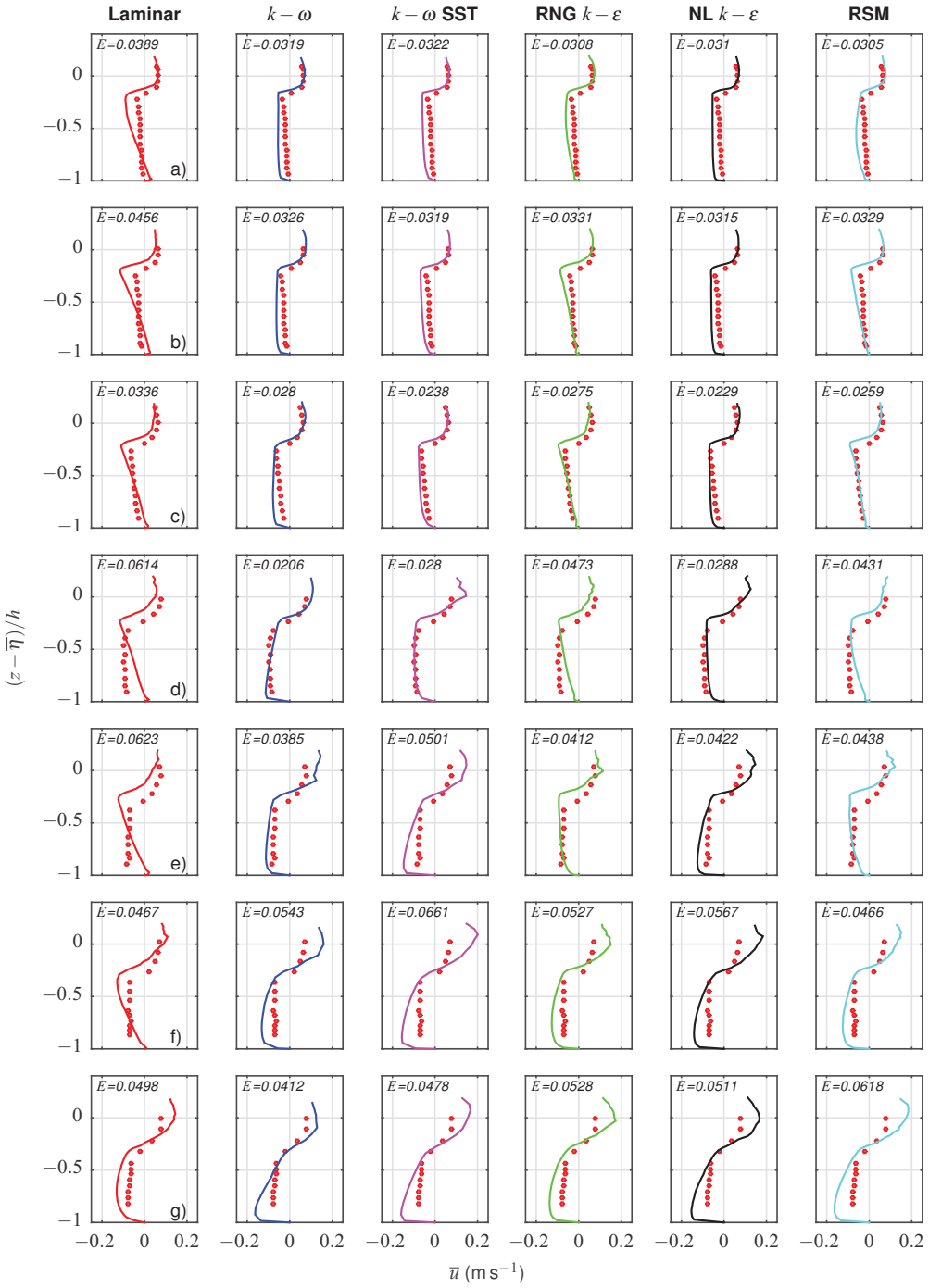

Figure 5.24: Comparison of time-averaged horizontal velocity profiles with depth for the plunging breakers against the experimental data (•) gathered by Ting and Kirby (1994). The RMSE for each profile with respect to the experiments is indicated at the top of each plot (denoted by E). Each column represents a different turbulence model whereas the rows represent different sampling locations relative to the breaking point $x - x_b =$ a) -0.5, b) 0.0, c) 0.55, d) 1.0, e) 1.5, f) 2.0, and g) 2.6 m.

a, since all of the models over-estimate the magnitude of the velocity. All of the turbulence models have a very similar RMSE value, but the laminar case performs slightly worse. However, at sampling locations b-c, the RSM and RNG $k-\varepsilon$ predict a negative gradient shape, but the nonlinear $k-\varepsilon$ and $k-\omega$ SST models possess the smallest RMSE. This is mainly due to the increased accuracy where the mean velocity changes sign near the free surface.

Contrary to the spilling breaker case, where the gradient changed sign further along the wave flume, the experimental data shows the magnitude of the mean velocity to become close to constant with depth (except near the free surface) in the plunging breaker case. This is captured well at location d by the $k-\omega$, $k-\omega$ SST and nonlinear $k-\varepsilon$ models. However, at locations e-f, all of these models predict a profile shape similar to that seen in the spilling breakers, i.e. the undertow is largest near the bottom of the water column and decreases with height. The RSM and RNG $k-\varepsilon$ predict a similar profile shape at location d as they did for a-c and then develop much the same as the other models for the final three locations.

Overall, using the RMSE, the most accurate model for mean horizontal velocity under plunging breakers is the $k-\omega$ model, followed closely by the nonlinear $k-\varepsilon$ model. The least accurate results occur when laminar flow conditions are assumed. However, the present numerical model, in general, appears to predict the velocity profiles under spilling breakers to a greater accuracy than under plunging breakers.

Figure 5.25 shows the same time-averaged TKE, $\overline{k}$, presented in Figure 5.22, except for the plunging breaker data. The subplots a-g represent the same seven locations presented in Figure 5.24. Furthermore, Table 5.6 gives the RMSE values for each of the five turbulence models, at the locations where experimental data is available. The laboratory data implies that the mean TKE has a much smaller change in depth in comparison to the spilling breakers (Figure 5.22), and is almost constant with depth at some of the sampling locations. None of the models capture this shape since they generally predict a considerable decrease in the TKE with depth.

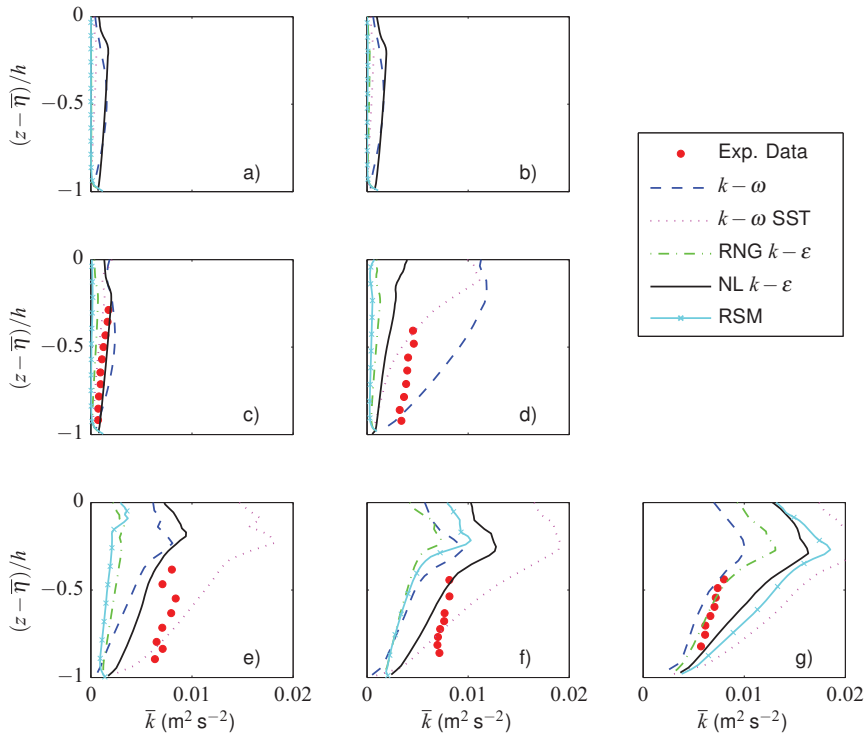

Figure 5.25: Comparison of time-averaged TKE profiles with depth for the plunging breakers at sampling locations relative to the breaking point $x-x_b =$ a) -0.5, b) 0.0, c) 0.55, d) 1.0, e) 1.5, f) 2.0, and g) 2.6 m. Each line represents a different turbulence closure model and the predictions are compared to the experimental data (●) gathered by Ting and Kirby (1994).

The RNG $k-\varepsilon$ model and RSM predict very low levels of TKE at sampling locations a, b, c and d, which corresponds to the negative gradient of mean horizontal velocity with depth, observed in Figure 5.24. The other models have larger levels of TKE at these locations and do not capture the velocity profile. This further backs up the hypothesis from the spilling breakers that a model must predict low levels of turbulence in order to capture this profile shape.

Interestingly, the magnitudes of the mean TKE profiles are generally lower than observed in the spilling breakers case, and increase along the wave flume at a similar rate to that shown in the experiments. The $k-\omega$ SST model performs well at location c but grows progressively larger along the flume as was seen in the spilling breakers. The nonlinear $k-\varepsilon$ also follows this pattern but generally under-estimates the levels of TKE. However, it

$x-x_b$ (m)	$k-\omega$	$k-\omega$ SST	RNG $k-\varepsilon$	NL $k-\varepsilon$	RSM
0.55	0.0008	0.0005	0.0008	0.0003	0.0011
1.00	0.0034	0.0018	0.0032	0.0024	0.0036
1.50	0.0044	0.0026	0.0054	0.0028	0.0060
2.00	0.0041	0.0025	0.0044	0.0018	0.0043
2.60	0.0012	0.0064	0.0005	0.0030	0.0044

Table 5.6: RMSE associated with the time-averaged TKE predictions for plunging breakers, with respect to the experimental data gathered by Ting and Kirby (1994). All of the different turbulence model predictions at the five locations where data is available are presented, and correspond to plots c-g in Figure 5.25.

is the most consistent of the models at the sampling locations used. The remaining models generally under-predict the TKE which is reversed from the pattern seen in spilling breakers.

Overall, the nonlinear $k-\varepsilon$ model predicts the time-averaged TKE for the plunging breaker case the most accurately, followed by the $k-\omega$ model. On the other hand, the RSM gives the least accurate results, which was also observed for the spilling breakers. However, the lack of accuracy is due to an under-estimate for the plunging breaker whereas, in the spilling breaker case, there was a substantial over-estimate.

5.3.3 Discussion

Choosing a numerical model is usually a balance of accuracy and numerical efficiency. In this section, both of these aspects are evaluated relative to assuming that laminar flow conditions apply in the surf zone. Table 5.7 gives the execution times along with the number of iterations relative to the laminar case. The results were obtained by running one wave period for each turbulence model using seven cores of a 3.4 GHz CPU (Intel(R) Core(TM) i7-2600) on the same computer, which had 12 GB of RAM, without any other applications running. The results imply that for both the plunging and spilling breakers the execution time is reduced, compared to the laminar case, by using a turbulence model. This may seem counter intuitive since each iteration should take slightly longer to compute. However, as can be seen in the table, the use of a turbulence model can substantially reduce the number of iterations, which can be less than half as many in some cases. For the spilling breakers, the number of iterations seems to be lower in the more complex models such as the nonlinear $k-\varepsilon$ and RSM. On the other hand, in the plunging breakers there is

		Laminar	$k-\omega$	$k-\omega$ SST	RNG $k-\varepsilon$	NL $k-\varepsilon$	RSM
Spilling	CPU Time	19580 s	0.978	0.802	0.828	0.673	0.641
	Iterations	11751	0.835	0.733	0.732	0.568	0.483
	Time/Iter.	1.666 s	1.171	1.095	1.132	1.184	1.328
Plunging	CPU Time	50621 s	0.941	0.707	0.865	0.748	0.861
	Iterations	25237	0.794	0.646	0.743	0.633	0.667
	time/iter	1.992 s	1.184	1.094	1.165	1.181	1.291

Table 5.7: Execution time, number of iterations and time per iteration for one wave period relative to the laminar case. The results were obtained using seven cores of a 3.4 GHz CPU (Intel(R) Core(TM) i7-2600) on a computer with 12 GB of RAM.

less variation in the number of iterations. However, the time per iteration for both types of breaker are consistent and generally follow the pattern expected. The RSM, which resolves all six components of the Reynolds Stress, takes longer to compute than the models which use the isotropic assumption. Overall, based on the two breaker types considered in this work, it appears that the nonlinear $k-\varepsilon$ model is the most economical for these test cases, since it generally requires less iterations and the time per iteration is similar to the isotropic turbulence models.

To evaluate which of the turbulence closure models is the most accurate for surf zone dynamics, a skill score (SS) is applied. The SS determines whether a model is an improvement on a reference model by using the mean square error (MSE), defined as

$$\text{MSE} = \frac{1}{N}\sum_{i=1}^{N}(x_i - y_i)^2, \tag{5.8}$$

where y_i is the experimental data and x_i is the results from the model. Following Murphy (1988), the skill score is then defined as

$$SS = 1 - \frac{\text{MSE}_{\text{model}}}{\text{MSE}_{\text{ref}}}. \tag{5.9}$$

Hence if the model has perfect prediction it will have $SS = 1$. If the SS is positive, the model is an improvement on the reference, $SS = 0$ gives results identical to the reference and a negative SS is a decrease in accuracy from the reference. Initial tests were run

		$k-\omega$	$k-\omega$ SST	RNG $k-\varepsilon$	NL $k-\varepsilon$	RSM
Spilling	η	0.2232	0.0684	0.4207	0.4147	0.3156
	$\overline{u}$	0.2110	0.4919	0.2897	0.7693	0.6569
	$\overline{k}$	0.7812	-0.0620	-0.2778	0.3669	-3.0165
Plunging	η	0.0127	-1.1789	-0.1630	-1.1572	-0.3372
	$\overline{u}$	0.4434	0.2770	0.2919	0.3713	0.2902
	$\overline{k}$	0.7143	0.6662	0.6587	0.8521	0.4936
Overall		0.3229	0.3609	0.2850	0.5474	0.4541

Table 5.8: Turbulence model skill score for surface elevation (η), time-averaged horizontal velocity ($\overline{u}$), and time-averaged TKE ($\overline{k}$). The skill score is calculated using the mean square error and the laminar case is used as a reference.

with the standard $k-\varepsilon$ turbulence model with the intention of using it as the baseline, but unfortunately the solutions given by this model were very poor due to excessive dissipation. Therefore, in this section, the reference solution is chosen as that given under laminar flow conditions. Clearly, the assumption of laminar flow under a breaking wave is physically dubious, but the focus of this section is on the performance of the turbulence models and the choice of reference solution will have no effect on the ranking order.

Table 5.8 gives the SS for surface elevation (η), time-averaged horizontal velocity ($\overline{u}$), and mean TKE ($\overline{k}$). Each turbulence model is shown for both plunging and spilling breakers, and is given an overall SS. Comparing the skill scores for spilling breakers, it is clear that the use of any of the turbulence models considered in this study improves the accuracy of predictions of surface elevation and time-averaged horizontal velocity compared to the laminar case, which is to be expected. However, it is interesting to note that the predictions of mean TKE in some cases are large enough that it is more accurate to assume there is not any turbulence generated, rather than use a turbulence model. In particular the RSM, expected to perform the best, gives very poor performance for the mean TKE, despite having reasonable predictions for free surface and velocity. The nonlinear $k-\varepsilon$ and $k-\omega$ models have positive skill score for all three criteria, implying that they are better approximations than the laminar case in all areas considered. The RNG and nonlinear $k-\varepsilon$ models exhibit the best performance for free surface and undertow, respectively, whereas the $k-\omega$ predicts mean TKE most accurately.

The skill scores for the plunging breakers tell a slightly different story. The $k-\omega$ is the only model to perform better than the laminar case in all three criteria, although it is only a slight improvement with regards to η. All of the other models have a negative skill score for free surface, which is particularly large in the case of the $k-\omega$ SST and nonlinear $k-\varepsilon$ models, implying that they predict substantially worse results than those obtained through the assumption of laminar flow conditions. However, the use of a turbulence model improves all results for velocity and mean TKE with the $k-\omega$ and nonlinear $k-\varepsilon$ being the best models in these areas, respectively.

Overall, all of the turbulence models are an improvement over assuming laminar flow conditions in the surf zone, both in terms of accuracy and numerical efficiency. The RSM, which was initially expected to perform the best, had the second best skill score, influenced largely by the poor prediction of TKE under spilling breakers. Despite the $k-\omega$ performing better than the reference values in all three areas for both types of breaker, the nonlinear $k-\varepsilon$ model comes out as the model with the highest skill score. It was also one of the more efficient models and hence it is logical to consider it to be the best turbulence closure model for application to surf zone dynamics out of the ones considered in this study. However, all the models still exhibit differences from the experimental data, in particular the under-estimate of TKE for plunging breakers and over-estimate for spilling breakers.

These differences raise the question of the benefit of using a complex model over a computationally cheaper option such as a depth-integrated model. Although it is possible to simulate breaking waves using a depth-integrated model through the use of dissipation terms, the breaking process cannot be fully reproduced since the model is unable to resolve the overturning of the free surface (Roeber and Cheung 2012). A RANS solver, coupled with the VOF method, is able to resolve this highly-nonlinear process. As will be seen later in this section, capturing this process leads to predictions of turbulence generation which agree qualitatively with laboratory observations. Further advantages of the Computational Fluid Dynamics (CFD) approach is that data can be obtained anywhere in the computational domain, and that the model can easily be adapted for more complex phenomena such as the

interaction with structures.

To understand the variation in the predictions of the turbulence models considered in this study, instantaneous spatial maps are compared qualitatively to experimental investigations. Ting and Kirby (1994) found that TKE is transported seaward under the spilling breakers and the dissipation rate is slow, whereas under the plunging breaker TKE is transported landward and is dissipated within one wave cycle. Additionally, the TKE varies with depth in the spilling case, which is not evident under the plunging breakers. Furthermore, Ting and Kirby (1995) found that under the crest of plunging breakers the turbulence intensity is largest and rapidly decreases after the wave passes so that the turbulence dies out between breakers. For plunging breakers the rate of vertical mixing is large since turbulence is spread down by the large eddies, causing any turbulence generated by the broken wave to saturate the entire depth in the inner surf zone. Ting and Kirby (1996) show that the mixing length of the spilling case is much smaller, suggesting that it lies somewhere in the region of $10-20\%$ of the water depth. Particle image velocimetry (PIV) data, presented by Huang et al. (2009), generally agrees with the observations of Ting and Kirby (1996), but indicates that the TKE spreads to around half the water depth. Furthermore, the surface generated turbulence in spilling breakers is spread slowly down, mainly through diffusion, whereas in the plunging case both advective and diffusive transport are important since the large eddies generated in the surface roller are advected behind the wave front.

Many of these observed characteristics are also evident in the present numerical model. In a RANS simulation, small scale features are not resolved but fluctuations from the mean flow are instead represented by an additional dissipation term in the governing equations. This term is generally referred to as the Reynolds stress (see equation 4.46) and is related to the TKE, eddy viscosity and rate of strain of the flow. Therefore, for the present work, the Reynolds stress is a good indication of the presence of turbulence in the flow. Furthermore, it was found that the distributions of TKE and Reynolds stress (magnitude) followed very similar patterns for all of the turbulence models considered. Therefore, this allows qualitative comparison of the predicted (numerical) Reynolds stress with either TKE or Reynolds

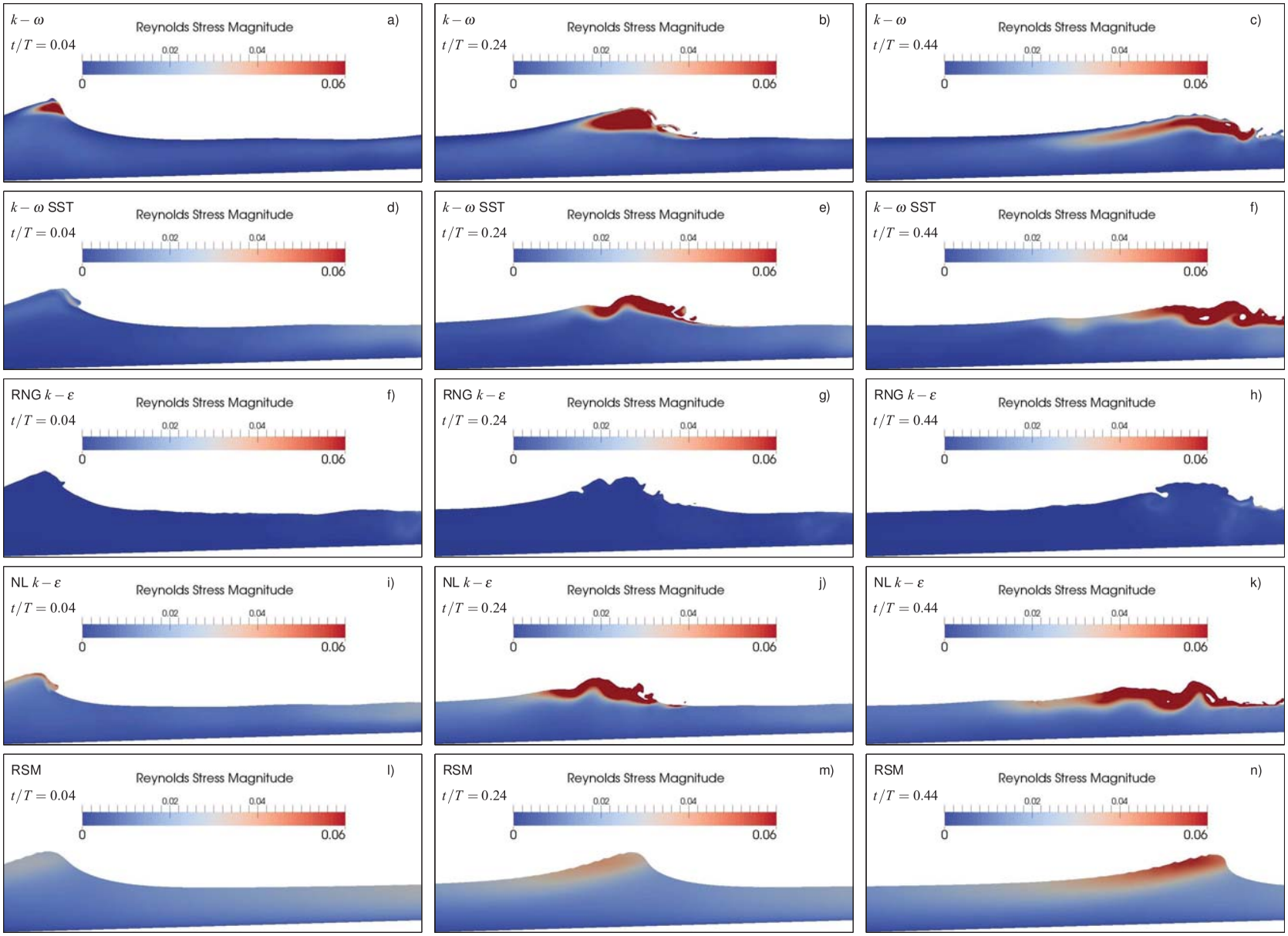

Figure 5.26: Example snapshots of the Reynolds stress (magnitude) distribution under spilling breakers with each row representing a different turbulence model. From left to right the columns show different phases of the wave: $t/T = 0.04$, 0.24 and 0.44, respectively.

stress from experiments.

Figure 5.26 shows colour plots of the predicted Reynolds stress magnitude for spilling breakers using the different turbulence models (rows) at three different phases of the breaking process (columns). The phase $t/T = 0$ is considered to be the phase where breaking occurs. It is clear that both the magnitude and distribution of the Reynolds stress varies between the different turbulence models. The RNG $k-\varepsilon$ model predicts smaller Reynolds stress magnitude than the other four models at all of the three times presented. However, there is a region near the right hand side of each plot where there is a relatively larger Reynolds stress, indicating that the turbulence from the previous wave has not dissipated yet. The other four models generate turbulence in the crest during the breaking process and, as the wave passes, the turbulence spreads slowly seaward and downwards, which is consistent with the observations of Ting and Kirby (1996) and the PIV experiments conducted by Huang et al. (2009). At the first breaking phase shown, the $k-\omega$ model predicts a large region of high Reynolds stress spanning the majority of the front of the wave crest. The $k-\omega$ SST and nonlinear $k-\varepsilon$ models predict the Reynolds stress to be generated in the spilling region of the wave. The predictions from the $k-\omega$ and $k-\omega$ SST models in the other two phases of the wave ($t/T = 0.24$ and 0.44) indicate that the turbulence spreads to around 20% of the water depth, which is consistent with Ting and Kirby (1996) but conflicts with Huang et al. (2009). Conversely, the RSM and nonlinear $k-\varepsilon$ predictions of Reynolds stress indicate that there is always a reasonable level throughout the water column. Furthermore, the distribution of the Reynolds stress predicted by the RSM, i.e. large turbulence throughout the wave, seems to lead to the wave not visibly breaking.

Figure 5.28 presents τ_{xz}, i.e. the horizontal-vertical component of Reynolds stress, under spilling breakers at $t/T = 0.44$. Each plot represents a different turbulence model: a) $k-\omega$, b) $k-\omega$ SST, c) RNG $k-\varepsilon$, d) nonlinear $k-\varepsilon$, and e) RSM. The $k-\omega$, $k-\omega$ SST and nonlinear $k-\varepsilon$ models predict similar distributions of τ_{xz}, and generally agree with experimental studies of weak hydraulic jumps, which are believed to be a simplified method to study the flow under spilling breakers in the inner surf zone (Misra et al. 2008). Like the

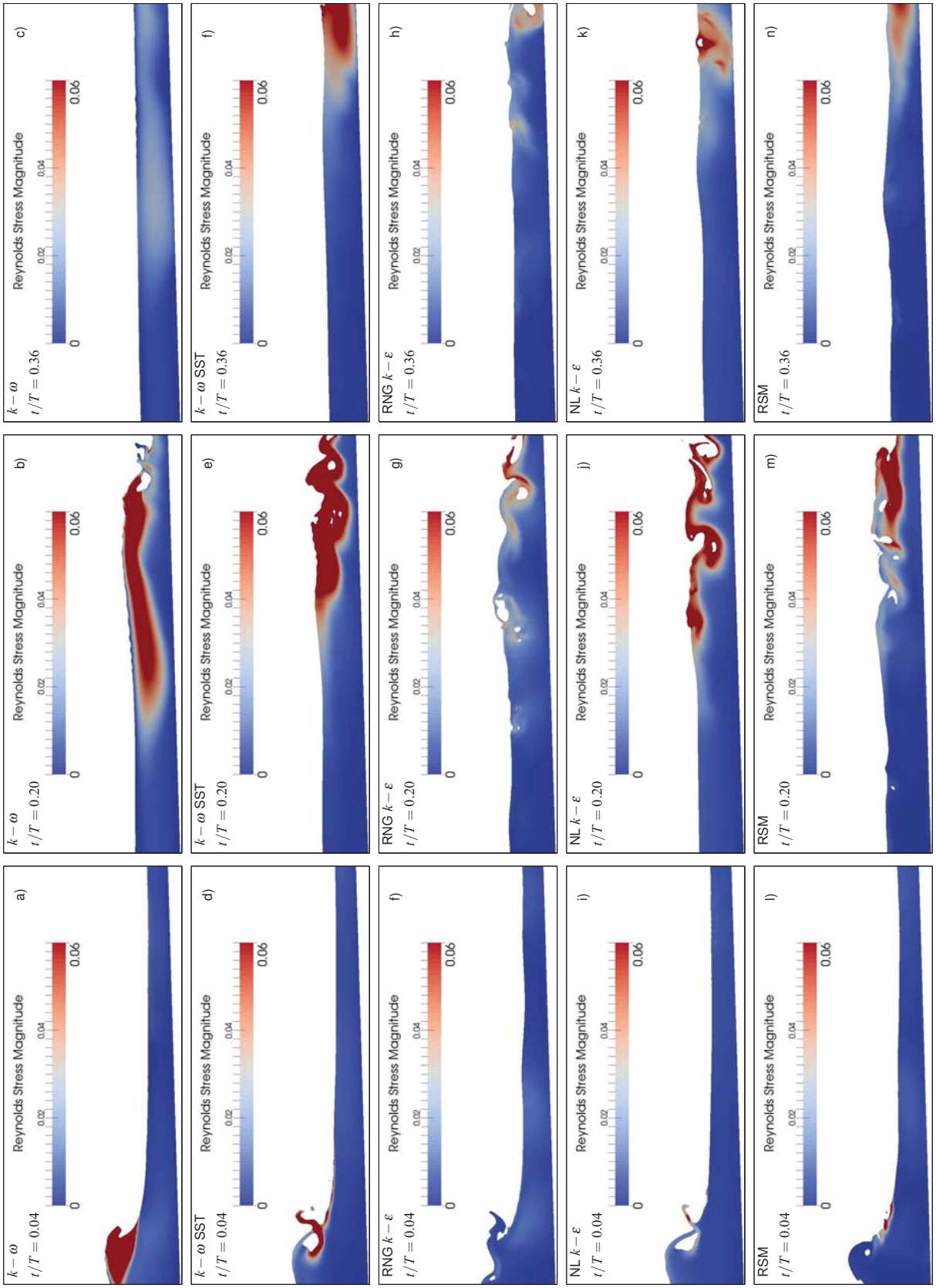

Figure 5.27: Example snapshots of the Reynolds stress (magnitude) distribution under plunging breakers with each row representing a different turbulence model. From left to right the columns show different phases of the wave: $t/T = 0.04$, 0.20 and 0.36, respectively.

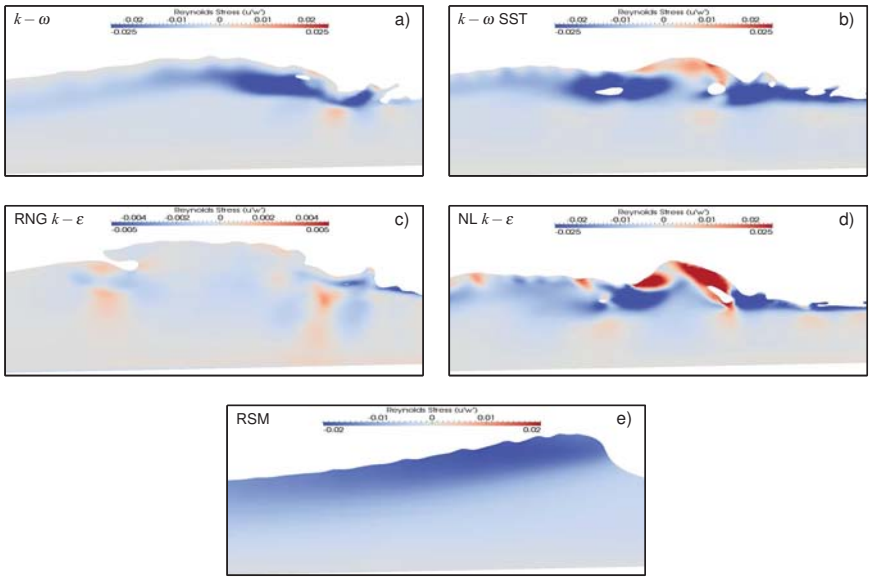

Figure 5.28: Snapshots of τ_{xz} under spilling breakers at $t/T = 0.44$. Each plot is a different turbulence model: a) $k-\omega$, b) $k-\omega$ SST, c) RNG $k-\varepsilon$, d) nonlinear $k-\varepsilon$, and e) RSM.

experimental data for hydraulic jumps, there are two clear regions in the spilling breaker: the reverse flow region, and the breaker shear layer region. In the reverse flow region τ_{xz} is much smaller than in the breaker shear layer, which is consistent with Misra et al. (2008). In the breaker shear layer, τ_{xz} is predominantly negative, with the largest magnitude occurring just below the free surface near the toe of the breaker, which agrees with experimental data (see Figures 18d and 19 of Misra et al. 2008). Further similarities can be observed at the free surface where a layer of positive τ_{xz} is present. At the toe, the breaker shear layer is relatively thin but behind the front the region of Reynolds stress spreads out to incorporate more of the water depth, and decreases in magnitude. The width of the breaker shear layer was observed to be around 20% of the water depth by Misra et al. (2008), which is consistent with the predictions presented in Figure 5.28. Overall, the numerical model appears to have good qualitative agreement with experimental data for a similar situation, and hence provides further evidence that weak hydraulic jumps are a valid representation of spilling breakers.

Figure 5.27 presents similar spatial maps of the Reynolds stress magnitude as described

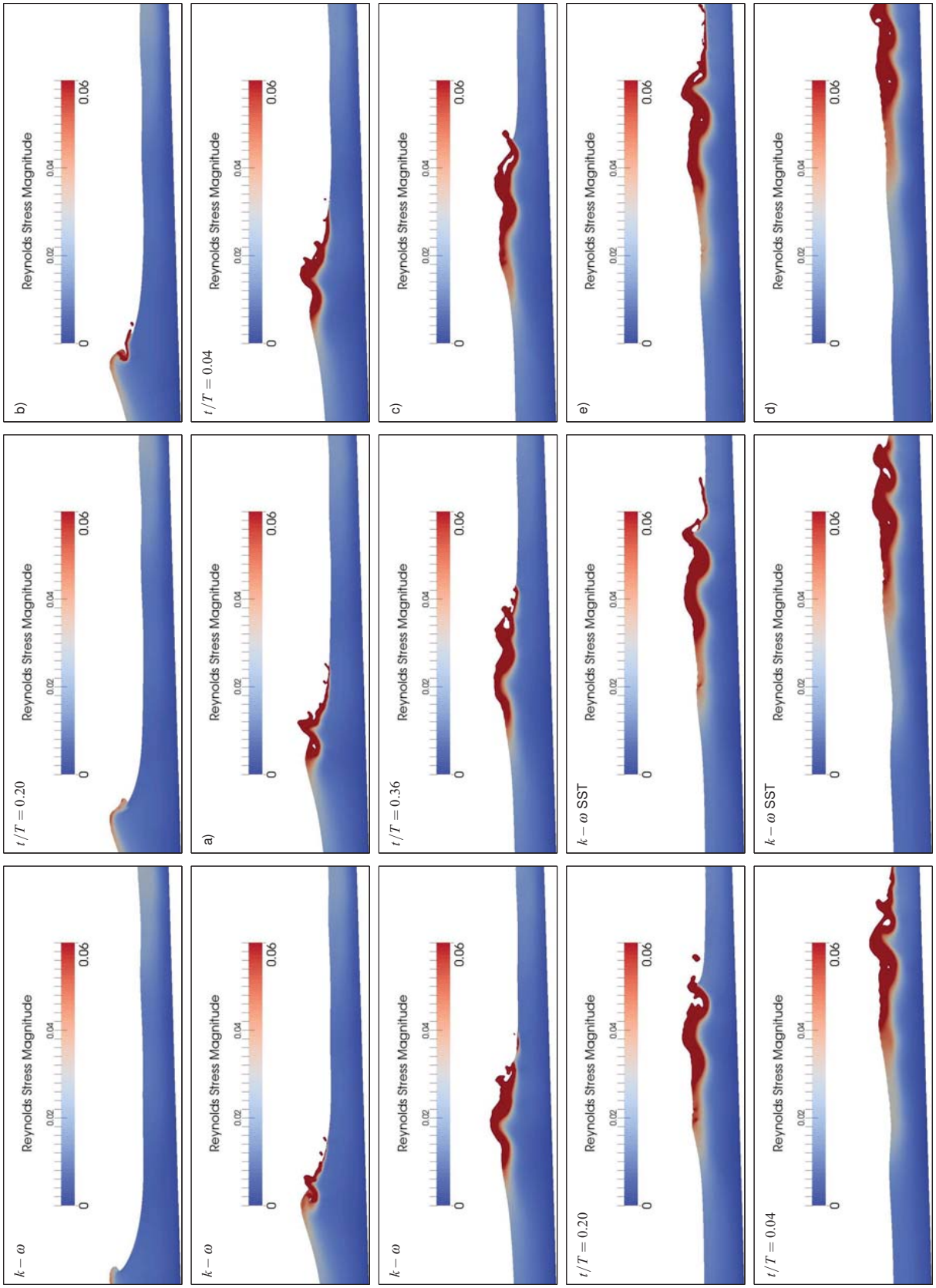

Figure 5.29: Snapshots of the nonlinear $k-\varepsilon$'s predictions of the Reynolds stress (magnitude) distribution under the different phases ($t/T = 0$ to $t/T = 0.56$) of a spilling breaker.

in Figure 5.26 for the plunging breakers case. At the breaking point the predictions from the nonlinear $k-\varepsilon$, $k-\omega$ SST and RSM models indicate that turbulence is generated from the impact of the overturning wave hitting the water and causing splash up. Conversely, the $k-\omega$ model predicts Reynolds stress to be generated throughout the crest of the wave as was observed in the spilling breaker. Another similarity to the spilling case is that the RNG $k-\varepsilon$ model predicts the smallest Reynolds stress out of the turbulence models. However, the model predicts substantially larger regions of Reynolds stress, particularly in the areas where air has become trapped, and the turbulence spreads throughout the whole depth of the water column as can be seen at the right hand side of the phase $t/T = 0.36$ (plot h). At phase $t/T = 0.2$, it is clear that any entrapped air leads to large Reynolds stress predictions by all of the models. The turbulence generally remains with the wave front and can be seen to be advected with the flow. At the $t/T = 0.36$ phase, all of the models considered in this study predict the turbulence to spread over the whole water depth, which also agrees well with the description given by Ting and Kirby (1995). The PIV experiments of Kimmoun and Branger (2007), showed that the Reynolds stress saturates the water depth in the turbulent bore whilst little turbulence occurred below the trough level at the breaking point. This is consistent with all of the models considered in this study. Interestingly, the $k-\omega$ model has a region of Reynolds stress which breaks off from the wave front and remains in the water column (centre of plot c). The detached region resembles observations from PIV experiments of unsteady deep-water breaking waves (Melville et al. 2002; Drazen and Melville 2009). The experimental results implied that the turbulence is generated at the top of the water column and diffuses downwards after the wave has passed. Although only the magnitude is shown in Figure 5.27, the horizontal-vertical component τ_{xz}, is negative and is therefore consistent with downward transport of positive horizontal momentum, and hence PIV experiments (Melville et al. 2002; Drazen and Melville 2009). This region of turbulence occurs where there is a change between the positive velocity of the passing wave and the undertow preceding the next wave, and rapidly dissipates before the next wave occurs, similar to the observations of Ting and Kirby (1995).

Figures 5.29 and 5.30 show additional spatial maps of Reynolds stress magnitude at fur-

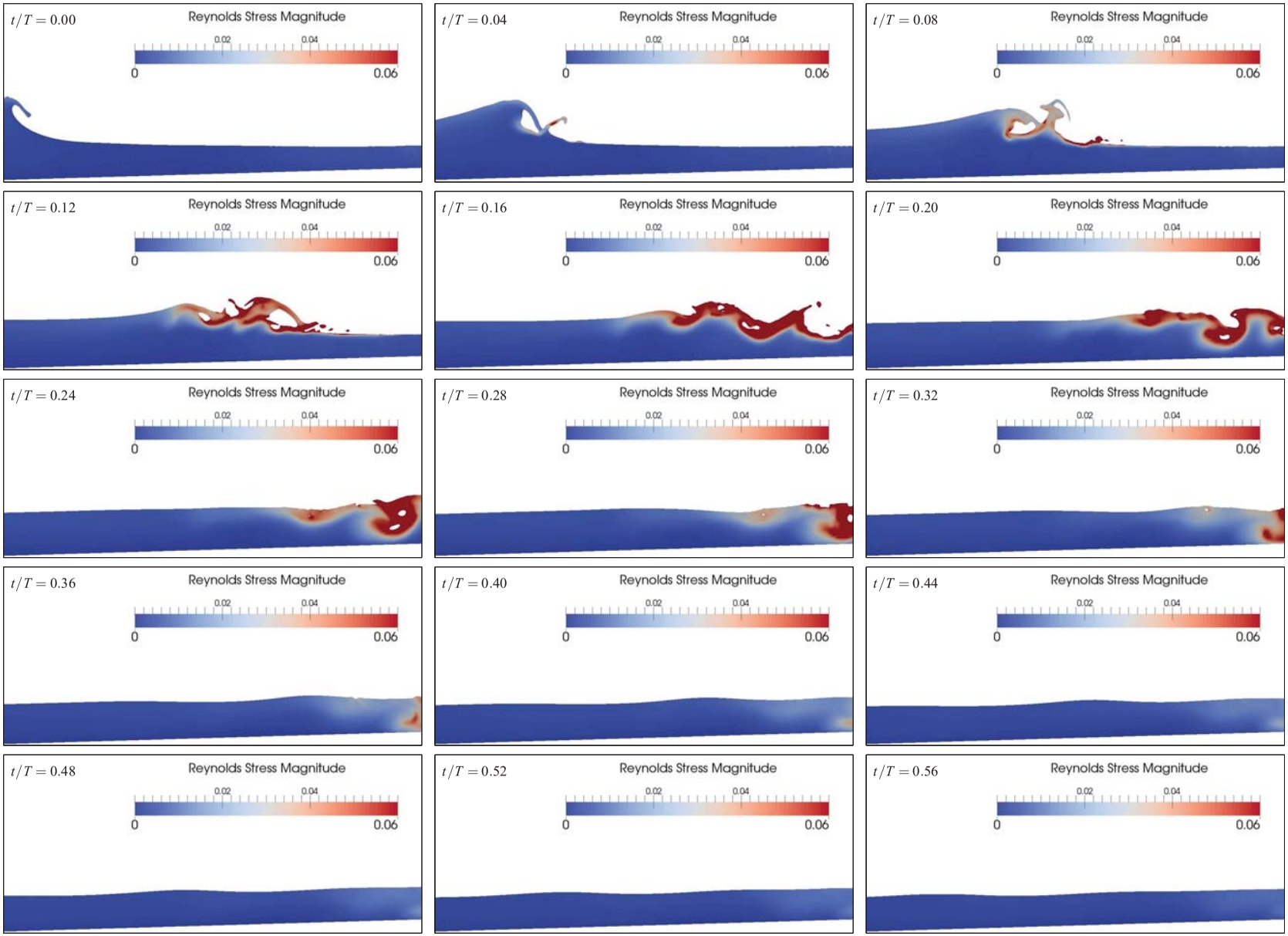

Figure 5.30: Snapshots of the nonlinear $k-\varepsilon$'s predictions of the Reynolds stress (magnitude) distribution under the different phases ($t/T = 0$ to $t/T = 0.56$) of a plunging breaker.

ther phases of the breaking process for spilling and plunging breakers, respectively. The nonlinear $k-\varepsilon$ model is used for this analysis since it has been shown to have the best overall skill score. At the breaking phase ($t/T = 0.00$), there is a large difference between the two breaking types. The spilling breaker has Reynolds stress already existing in the water column, whereas the plunging breaker has very little. This implies that the turbulence from the previous wave has dissipated in the plunging breaker, whereas it has not in the spilling breaker as was observed by Ting and Kirby (1994). Furthermore, there is a small amount of Reynolds stress existing in the water column under the spilling breaker prior to breaking, while it is not apparent in the plunging case. This could be due to turbulence being transported seaward as was noted by Ting and Kirby (1994).

Phases $t/T = 0.16$ to 0.32 show another characteristic observed by Ting and Kirby (1995, 1996). In the plunging breaker, as the surface roller develops, turbulence spreads rapidly downwards spanning the whole depth around phase $t/T = 0.24$. The turbulence rapidly dissipates after the surface roller has passed, explaining the small magnitude of Reynolds stress observed by the time the next wave arrives. On the other hand, there is a fairly large level of turbulence existing in the water column as the spilling breaker arrives. As the surface roller progresses along the wave flume, the turbulence generated in the spilling breaker slowly spreads seawards and downwards from the roller. This leads to larger concentrations near the surface, which decrease with depth. The majority of the turbulence is shown to be located within the top half of the water column as has been observed in experiments (Ting and Kirby 1995; Huang et al. 2009).

In the latter phases presented in Figures 5.29 and 5.30 ($t/T = 0.48$ to 0.56), it is clear that the turbulence rapidly dissipates once the surface roller has passed in the plunging breaker, whereas it spreads out behind the spilling breaker. This leads to turbulence from the previous wave interacting with the next wave. This could be due to the shorter period of the wave. Hence, in the future, it would be interesting to repeat the analysis on the two breaker types if the beach slope has been adjusted and wave period kept constant. In summary, the present numerical model generally predicts similar turbulent characteristics to those seen

in laboratory experiments. The spatial maps also imply that a number of turbulence models used in this study agree qualitatively with experimental studies but require further research in order to gain better quantitative agreement.

5.4 Comparison With Numerical Investigations

As a final validation, the nonlinear $k-\varepsilon$ (since it produced the highest skill score) is compared to the results of three previous numerical studies: Bradford (2000) used the software FLOW-3D along with a RNG $k-\varepsilon$ turbulence model, Jacobsen (2011) and Jacobsen et al. (2012), who also used OpenFOAM® along with `waves2Foam`, and a modified $k-\omega$ model and Xie (2013) who used a two-phase code with a $k-\varepsilon$ model. Along with including density, Jacobsen et al. (2012) modified the $k-\omega$ model, following Mayer and Madsen (2000), by changing the production term, P_k, in equation (4.48) to depend on the mean vorticity rather than the mean rate of strain of the flow. This was done in order to prevent any generation of TKE prior to breaking.

5.4.1 Spilling

Figure 5.31 shows the surface elevation profiles $\widetilde{\eta}_{max}-\overline{\eta}$, $\overline{\eta}$ and $\widetilde{\eta}_{min}-\overline{\eta}$ as a function of horizontal distance, x, along the numerical wave flume. The predictions (lines) from each of the numerical models are compared with the experimental data (•) presented by Ting and Kirby (1994). There is very little to choose between the numerical models in terms of minimum and mean surface elevation. The maximum surface elevation at the breaking point is predicted best by the present model, since the models of Xie (2013) and Bradford (2000) under-estimate this value, whereas Jacobsen et al. (2012) is over-predicted. However, the models of Jacobsen et al. (2012) and Xie (2013) capture the breaking point slightly better than the present model.

Figure 5.32 shows a comparison of the time-averaged horizontal velocity profiles, $\overline{u}$, with dimensionless depth. Once again, the points (•) represent the experimental data presented by Ting and Kirby (1994), and the lines are the results from each of the numerical models considered. Each subplot shows a different sampling location relative to the breaking

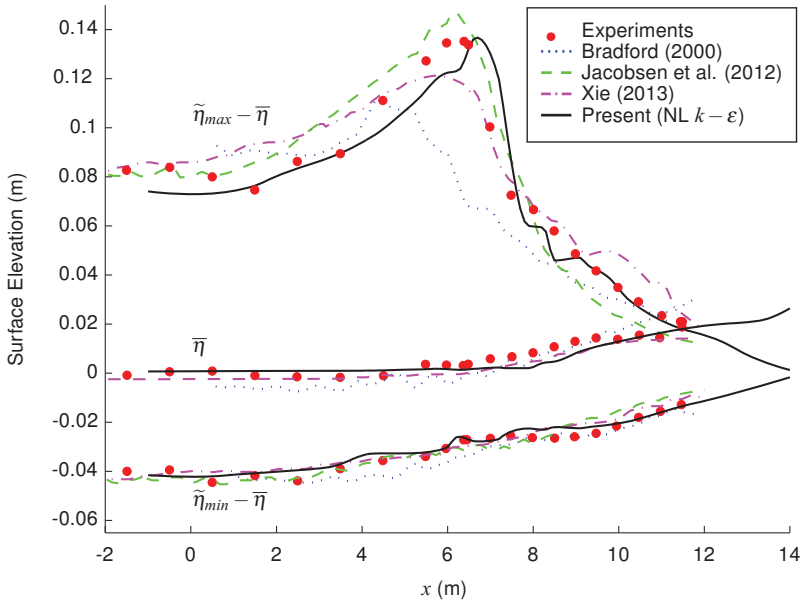

Figure 5.31: Comparison of the maximum, minimum, and mean phase-averaged surface elevation against x coordinate for the spilling breaker case. Predictions from the present model (nonlinear $k-\varepsilon$), as well as previous numerical models, are compared with the experimental data (•) reported by Ting and Kirby (1994).

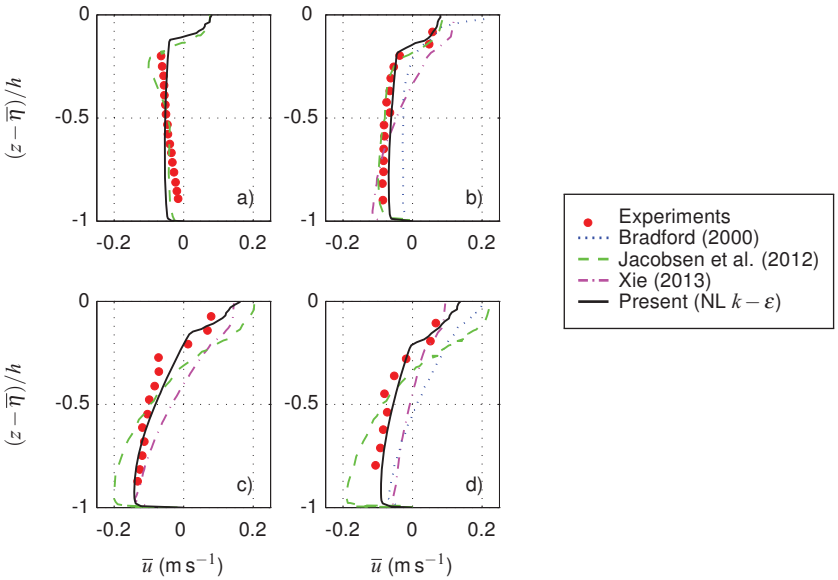

Figure 5.32: Comparison of time-averaged horizontal velocity profiles with depth at sampling locations $x-x_b =$ a) -0.455, b) 0.875, c) 2.095, and d) 3.325 m for the spilling breaker case. Predictions from the present model (nonlinear $k-\varepsilon$), as well as previous numerical models, are compared with the experimental data (•) collected by Ting and Kirby (1994).

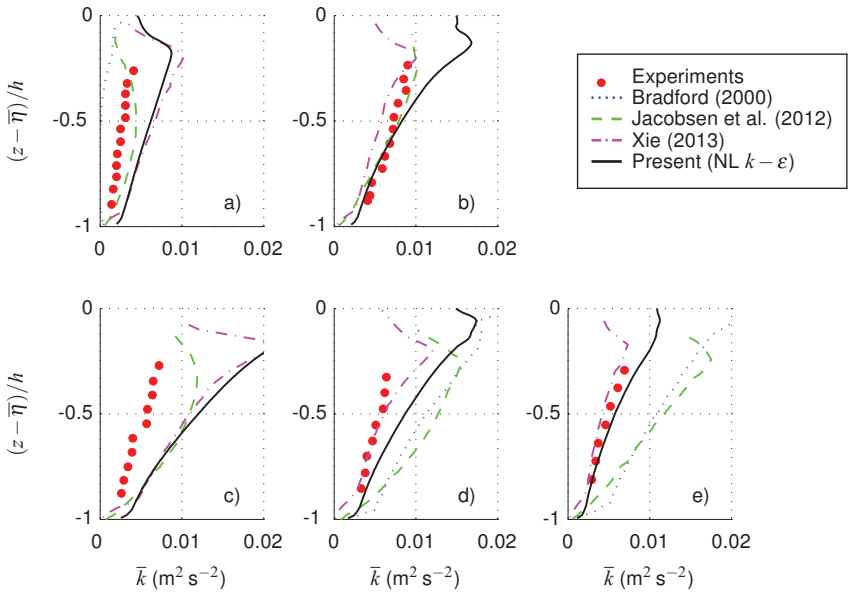

Figure 5.33: Comparison of time-averaged TKE profiles with depth at sampling locations $x - x_b =$ a) 0.875, b) 1.485, c) 2.095, d) 2.71, and e) 3.325 m for the spilling breaker case. Predictions from the present model (nonlinear $k-\varepsilon$), as well as previous numerical models, are compared with the experimental data (●) published by Ting and Kirby (1994).

point, one corresponding to pre-breaking (5.945 m in Ting and Kirby 1994), and three post-breaking (7.275, 8.495, and 9.725 m in Ting and Kirby 1994). The model of Jacobsen et al. (2012) captures the profile prior to breaking (subplot a) much more accurately than the nonlinear $k-\varepsilon$ model from the present study, especially in the lower half of the water column.

However, similar to the RNG $k-\varepsilon$ considered earlier in this study, as the sampling location is moved down the flume, the undertow becomes over-predicted by the model of Jacobsen et al. (2012), whereas the nonlinear $k-\varepsilon$ model from the present work performs better in this region. The models of Xie (2013) and Bradford (2000) do not capture any of the profiles as well as the present model.

Figure 5.33 presents the time-averaged TKE, $\overline{k}$, profiles with dimensionless depth. As before, the points (●) represent the experimental data gathered by Ting and Kirby (1994), and the lines indicate the predictions by each of the numerical models. Each subplot represents a different sampling location relative to the breaking point. All five locations are placed after breaking has occurred, and correspond to locations 7.275, 7.885, 8.495, 9.11, and

9.725 m in Ting and Kirby (1994). The results imply that the model of Xie (2013) performs best, especially in subplots d and e. The present model follows a similar pattern to Xie (2013): at locations a and c there are large discrepancies between the experimental data and present numerical model, but good predictions occur at locations b and e. Bradford (2000) under-predicts the profile at location a and over-estimates at locations d and e. This is consistent with the RNG $k-\varepsilon$ model considered in the present study. Jacobsen (2011) captures the mean TKE levels well at the earlier sampling locations, but the predictions become progressively larger further away from the breaking point.

Table 5.9 gives the normalised root mean square error (NRMSE) for the different numerical models and all of the plots shown in this section, with the best model shown in bold for each case. Along with an overall mean NRMSE, the mean error for surface elevation, time-averaged velocity and time-averaged TKE profiles are shown in Table 5.9. The largest errors in every model, except the one from Bradford (2000), occur in the mean TKE predictions and the lowest in the surface elevation predictions. Furthermore, it is clear that the nonlinear $k-\varepsilon$ in the present study performs better than the previous author's models in terms of surface elevation and mean velocity profiles, but does not perform as well as Xie (2013) for mean TKE predictions. The $k-\omega$ model considered earlier in the study (Table 5.8) shows a similar pattern to the $k-\omega$ model used in Jacobsen et al. (2012), except that the error in the mean TKE seems to be smaller in the present study.

Overall, it seems that the nonlinear $k-\varepsilon$ in the present study is similar if not more accurate than the previous numerical models when simulating spilling breakers. The strengths of the model are predictions of surface elevation and time-averaged velocity, but it is weaker than the $k-\varepsilon$ model used by Xie (2013), as well as the $k-\omega$ in the present study (see Table 5.8) in terms of mean TKE. This weakness is mainly due to the large differences between the model and experiments at sampling locations a and c. However, it is believed that out of the models considered in this study, the nonlinear $k-\varepsilon$ is the best compromise for the application of spilling breakers.

		Bradford (2000)	Jacobsen et al (2012)	Xie (2013)	Present (NL $k-\varepsilon$)
η	Max	1.5619	0.0883	0.088	**0.0868**
	Min	2.3137	0.1194	0.092	**0.0715**
	MWL	1.2663	-	0.1503	**0.1459**
	Mean	1.7140	0.1039	0.1101	**0.1014**
$\overline{u}$	plot a	-	**0.3797**	-	0.3869
	plot b	0.3291	**0.0802**	0.3207	0.1240
	plot c	-	0.3123	0.3034	**0.1199**
	plot d	0.341	0.3883	0.3217	**0.1149**
	Mean	0.3351	0.2901	0.3153	**0.1864**
$\overline{k}$	plot a	0.9038	**0.4894**	1.3691	1.2175
	plot b	-	**0.1847**	0.3039	0.3780
	plot c	-	**0.9936**	1.2198	1.3368
	plot d	1.8299	2.0313	**0.3611**	0.9572
	plot e	1.069	1.6369	**0.1865**	0.2450
	Mean	1.2676	1.0672	**0.6881**	0.8269
Mean		1.2018	0.6095	**0.4288**	0.4320

Table 5.9: NRMSE, with respect to the spilling breaker experimental data presented by Ting and Kirby (1994), for surface elevation as well as time-averaged velocity and TKE profiles with depth for both the present and previous numerical models. The model with the lowest NRMSE is indicated by bold text in each case. Also shown are the mean NRMSE for surface elevation, time-averaged velocity, TKE and overall, including all the plots considered in this study.

5.4.2 Plunging

The nonlinear $k-\varepsilon$ model is now compared to the previous numerical studies of plunging breakers by Bradford (2000) and Xie (2013). Figure 5.34 shows the equivalent free surface comparison for plunging breakers as presented for the spilling breakers (Figure 5.31). The predictions of the minimum free surface profile obtained from the numerical model in the present study and Xie (2013) both agree well with the experimental data, although the former performs better around the breaking point. The minimum profile presented by Bradford (2000) does not follow the experimental data as well, especially before breaking since the troughs are predicted to be much shallower. All three numerical models predict the mean profile well with respect to the laboratory data, although Bradford (2000) results exhibit variation in MWL either side of the breaking point.

As observed in the spilling breakers case, the numerical studies all predict very different profiles for the maximum profile. This is consistent with the results presented in Section 5.3.2,

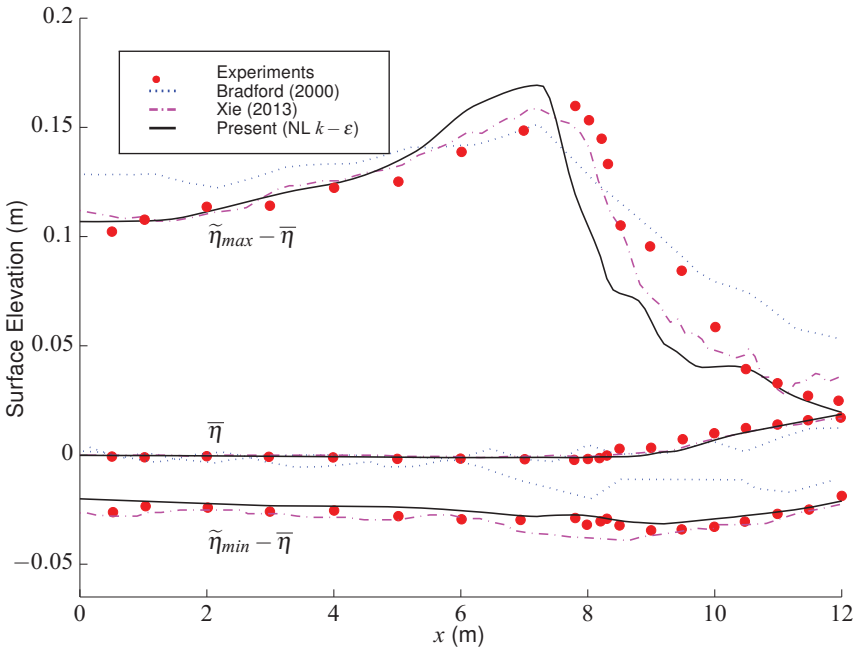

Figure 5.34: Comparison of the maximum, minimum and mean phase-averaged surface elevation against x coordinate for the plunging breaker case. Predictions from the present model (nonlinear $k-\varepsilon$), as well as previous numerical models, are compared with the experimental data (•) gathered by Ting and Kirby (1994).

which implied that using different turbulence models within the same code and setup had a much larger effect on maximum free surface profile than the minimum and mean. All three numerical predictions give the maximum value of the profile to occur at a very similar locations in the wave flume, around 1 m before the value observed in the experiments. However, the nonlinear $k-\varepsilon$ used in the present model over-predicts the breaking wave height, whereas the other two studies under-predict with respect to the laboratory data. After breaking has occurred, the present model predicts a much faster drop in amplitude than observed in either the numerical studies or experiments. The results of Xie (2013) are more consistent with the experimental data, and imply that the wave crest remains near the maximum height for around 1 m before starting to lose amplitude. Table 5.10 presents the NRMSE for each of the profiles and models discussed in this section. The free surface values indicate that the minimum profile is captured best by the present model but Xie (2013) performs slightly better for the maximum and MWL profiles. Both of these models perform

		Bradford (2000)	Xie (2013)	Present (NL $k-\varepsilon$)
η	Max	0.1513	**0.0906**	0.2013
	Min	1.2120	0.2852	**0.1808**
	MWL	0.2142	**0.0817**	0.0909
	Mean	0.1459	**0.0675**	0.0813
$\overline{u}$	plot a	0.2547	0.3170	**0.1763**
	plot b	-	0.1944	**0.1670**
	plot c	**0.3264**	0.3579	0.3876
	plot d	0.6535	**0.1451**	0.3350
	Mean	0.4115	**0.2536**	0.2664
$\overline{k}$	plot a	0.4347	0.7825	**0.3233**
	plot b	-	**0.8982**	1.6953
	plot c	-	1.3881	**1.3826**
	plot d	**1.3964**	4.4236	1.4865
	plot e	1.9169	2.5914	**1.3079**
	Mean	1.2493	2.0168	**1.2391**
Mean		0.7289	0.9630	**0.6445**

Table 5.10: NRMSE, with respect to the plunging breaker experimental data presented by Ting and Kirby (1994), for surface elevation as well as time-averaged velocity and mean TKE profiles with depth for both the present and previous numerical models. The model with the lowest NRMSE is indicated by bold text in each case. Also shown are the mean NRMSE for surface elevation, time-averaged velocity, TKE and overall, including all the plots considered in this study.

better overall than the numerical model used by Bradford (2000).

Figure 5.35 shows an equivalent plot of the comparison of time-averaged horizontal velocity under plunging breakers, as presented for the spilling breakers (Figure 5.32). The four locations shown in the plots are $x-x_b$ = a) 0.55 m, b) 1 m, c) 2 m, and d) 2.55 m. At locations a and c, the numerical predictions of Bradford (2000) agree well with the laboratory data near the bottom of the water column, whereas the other two models predict a larger undertow. However, further up the water column Bradford (2000) under-estimates the velocity and the other two models have much better performance. Xie (2013) captures the profile well throughout the water column at locations b and d. The present model performs better at locations a and b since at the other locations, a much larger undertow than observed in the experiments is predicted. The NRMSE values presented in Table 5.10 indicate that the present model performs best at locations a and b, with Bradford (2000) and Xie (2013) performing better at locations c and d, respectively. Overall, the present model has similar

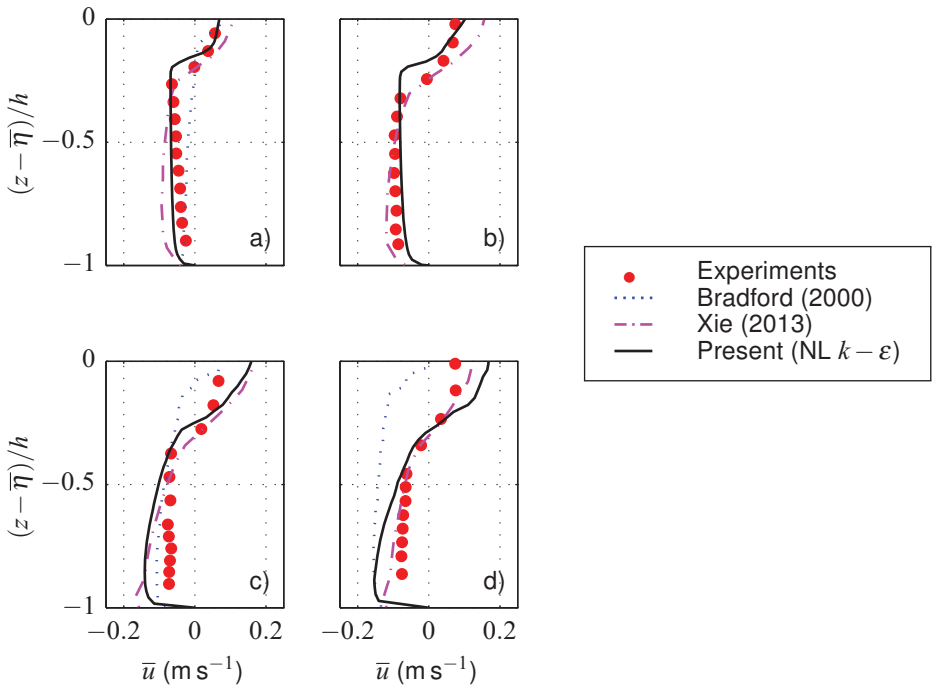

Figure 5.35: Comparison of time-averaged horizontal velocity profiles with depth at sampling locations $x-x_b =$ a) 0.55 m, b) 1 m, c) 2 m, and d) 2.55 m for the plunging breaker case. Predictions from the present model (nonlinear $k-\varepsilon$), as well as previous numerical models, are compared with the experimental data (•) presented by Ting and Kirby (1994).

NRMSE for mean velocity profiles as Xie (2013), which is much smaller than the one from Bradford (2000).

Figure 5.36 presents an equivalent comparison of numerical predictions of mean TKE under plunging breakers, as presented for the spilling breakers (Figure 5.33). The five locations shown in the plots are $x-x_b$ = a) 0.55 m, b) 1 m, c) 1.5 m, d) 2 m, and e) 2.55 m. Each of the numerical models possess the same general trend over the locations shown. The mean TKE predictions grow in magnitude as the locations progress away from the breaking point. At location a, all of the models do a reasonable job of predicting the mean TKE profile with depth. At location b the present model under-estimates the mean TKE magnitude, whereas the model of Xie (2013) gets much closer to the experimental data. Both profiles show the mean TKE increasing with height above the bottom boundary, which is inconsistent with the experimental data, which implies that the mean TKE is of a similar magnitude throughout

the water column. This observation is valid for all of the models at locations b through to e, indicating that none of the models are capable of capturing the experimental profile shape. Location c predictions follow the observations noted about location b, although near the top of the water column the predictions of Xie (2013) begin to over-estimate the mean TKE.

At locations d and e the present model switches from under-predicting the mean TKE, to over-predicting it. Bradford (2000) gives reasonably good predictions at location d but over-predicts at location e. The predictions presented by Xie (2013) substantially over-estimate the mean TKE at both locations. This is evident in the NRMSE data (Table 5.10), where the values jump up to more than 4, representing that the predictions are more than 400% out. Overall, the NRMSE implies that the nonlinear $k-\varepsilon$ model gives the best predictions of mean TKE over the five locations.

In summary, the nonlinear $k-\varepsilon$ model more accurately simulates flow variables under plunging breakers than the other models considered in this section. This is mainly due to more accurate predictions of mean TKE profiles, particularly in the sampling locations furthest from the breaking point. However, the NRMSE is slightly higher than Xie (2013) for predictions of free surface and mean horizontal velocity profiles. This is converse to the observations in the spilling breakers case, indicating that the choice of turbulence model is very sensitive to the case it is applied to.

5.5 Summary

In this section, a new library of turbulence closure models for multiphase flows has been evaluated for application to surf zone dynamics using the open source CFD software, OpenFOAM®, along with the additional toolbox, `waves2Foam`. The results from the models were averaged over twenty wave periods and compared to previous experimental data. The models were evaluated both in terms of accuracy (for surface elevation, velocity, and TKE) and numerical efficiency using laminar flow conditions as a reference. It was found that using a turbulence model could substantially decrease the computational time since although each iteration took longer to compute, the simulation required less iterations.

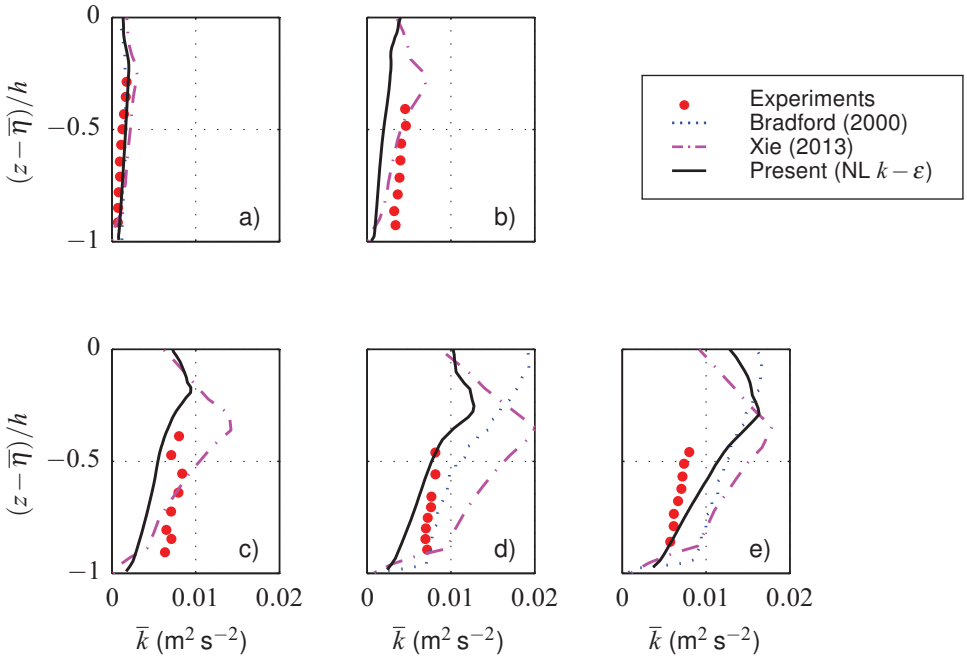

Figure 5.36: Comparison of time-averaged TKE profiles with depth at sampling locations $x - x_b =$ a) 0.55 m, b) 1 m, c) 1.5 m, d) 2 m, and e) 2.55 m for the plunging breaker case. Predictions from the present model (nonlinear $k-\varepsilon$), as well as previous numerical models, are compared with the experimental data (•) collected by Ting and Kirby (1994).

To assess accuracy, a skill score based on the mean squared error was used in order to evaluate which of the turbulence models is the best. Interestingly, it was found that assuming laminar flow conditions led to more accurate predictions of TKE levels under spilling breakers than some of the turbulence models, which can substantially over-predict these quantities. However, using a turbulence model generally improved the free surface and undertow profiles in the spilling breaker case. There appears to be a correlation between models that predict very little TKE prior to breaking, and models which capture the negative gradient of velocity prior to breaking, observed in the experiments. The RNG $k-\varepsilon$ model is the only model to capture this profile shape in both plunging and spilling breakers. However, the nonlinear $k-\varepsilon$ model captures the velocity profiles more accurately over the whole surf zone. For plunging breakers, using a turbulence model improves the mean TKE and horizontal velocity profiles, but generally decreases the accuracy of the free surface predictions. Despite the RSM being expected to produce the best results, it gave very poor

predictions of mean TKE in spilling breakers leading to a smaller skill score compared to the nonlinear $k-\varepsilon$ model. The $k-\omega$ model was shown to be the only model to improve on the laminar case in all criteria. However, in this study the overall best model for surf zone dynamics, both in terms of accuracy and numerical efficiency, was found to be the nonlinear $k-\varepsilon$. Based on the skill score alone the ranking of the turbulence models would be:

1. Nonlinear $k-\varepsilon$
2. RSM
3. $k-\omega$ SST
4. $k-\omega$
5. RNG $k-\varepsilon$

Spatial maps of the Reynolds stress magnitude distribution were then used to compare the turbulence models predictions for both breaker types. The spilling breaker was shown to have good qualitative agreement with experimental data on weak hydraulic jumps. The nonlinear $k-\varepsilon$ model was then shown to exhibit many of the features noted in the experimental data relating to the transport of turbulence under different breaker types. The turbulence spread over the whole water depth before rapidly dissipating prior to the arrival of the next plunging breaker. On the other hand, the spilling breakers turbulence spread seaward and only slowly diffused downwards. Slow dissipation in this case led to turbulence generated by a wave still existing in the water column when the following wave arrives.

Chapter 6

Validation II: Near-Bed Hydrodynamics

Chapter 5 focused on validation of the numerical model against time-averaged experimental data (Ting and Kirby 1994). In this chapter, the accuracy of the model predictions of near-bed hydrodynamics are tested against Otsuka and Watanabe (2012). Here, only the near-bed velocity and TKE will be considered with the sediment transport formulations being left for Chapter 7.

6.1 Experimental Comparison

6.1.1 The Data Set

In this chapter the model validations are performed in the near-bed region, against data gathered in a small-scale wave flume using an optical concentration sensor and an ultrasonic velocity profiler (Otsuka and Watanabe 2012). In terms of the present work, there are many advantages of using this data set over other studies. The temporal and spatial scales of the experiments are short and small, respectively, with time scales of the order of seconds rather than hours or even days as is often seen in large flume experiments. Hence the use of Computational Fluid Dynamics (CFD), which is computationally expensive, is feasible. Also, Otsuka and Watanabe (2012) used a beach of constant gradient and smoothed it after each run, which, along with the short time scales, minimised changes in the bed morphology. This suits the present model since it focuses on the suspended sediment concentrations and does not simulate changes in bed elevation. Furthermore, results are provided for both spilling and plunging breakers allowing validation of both wave types considered in Chapter 5.

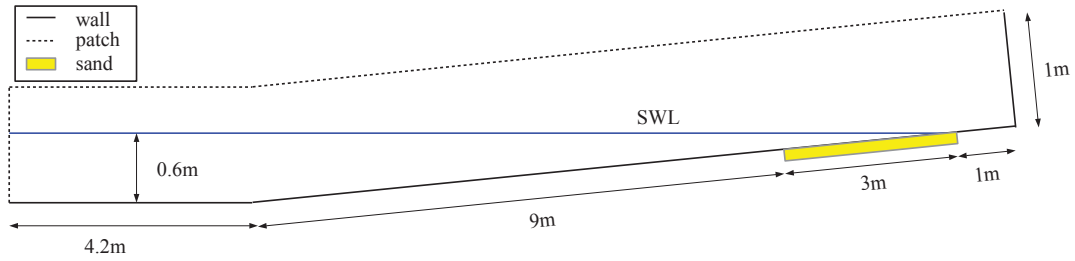

Figure 6.1: Diagram of numerical domain for comparison with Otsuka and Watanabe (2012). The slope is split into 3 regions, two smooth wall regions either side of a sediment bed, which is considered to be rough. The z direction has been scaled by a factor of 2.

H (m)	0.07	0.075	0.08	0.085	0.09	0.095	0.1
x_b (m)	9.3	9.0	9.0	8.8	8.6	8.5	8.6
H_b (m)	0.118	0.126	0.132	0.139	0.144	0.147	0.154

Table 6.1: Results of the simulations to determine the correct inlet height for the plunging breakers case. H represents the inlet wave height, whereas x_b and H_b are the point and height where breaking occurs.

6.1.2 Numerical Setup

The model is largely setup with the same geometry, mesh and boundary conditions as described in Section 5.1. However, there are a few important differences. Firstly, the slope has a gradient of $1/20$ rather than $1/35$. Secondly, the water depth is 0.6 m as opposed to 0.4 m. The overall height of the computational domain was increased to 1 m to allow for the larger water depth and gradient of the slope. Following Otsuka and Watanabe (2012), the slope is split into three regions: $x = 0 - 9$ m is considered a smooth wall, $x = 9 - 12$ m is a sediment bed with roughness $k_N = 2.5d$, and $12 - 13$ m is also modelled as a smooth wall. A diagram of the numerical domain is illustrated in Figure 6.1.

Although the nonlinear $k - \varepsilon$ model was shown to have the best overall skill score in Chapter 5, the focus of this project is on the effect of turbulent diffusion on suspended sediment dynamics, and hence the model with the highest skill score for turbulent kinetic energy (TKE) in the surf zone is considered to be the most suitable. Therefore, the $k - \omega$ model has been applied in this section, and for the rest of this study, which exhibits the additional advantage of improved near-wall behaviour (see Section 4.4), and is expected to model the

near-bed processes more accurately.

As in Chapter 5, waves are generated using a time dependent boundary condition at the inlet boundary, along with a relaxation zone for absorption of internal reflections. Stream Function wave theory (Rienecker and Fenton 1981) is applied, with periods of $T = 1.4$ s and $T = 2.0$ s for the spilling and plunging cases, respectively. Although Otsuka and Watanabe (2012) gave the wave height at the breaking point (H_b) in each case, the heights of the waves (H) in the region of constant depth have not been published. Hence, to obtain an input value for H, a series of simulations have been run to determine an initial wave height which produces a similar breaking height and point as observed by Otsuka and Watanabe (2012) for the plunging breaker. In their work, Otsuka and Watanabe (2012) state the water depth at the breaking point as $h_b = 0.141$ m and, assuming this is in relation to the still water level (SWL), this corresponds to $x_b = 9.18$ m, where $x = 0$ is the toe of the beach. The spilling breakers will be assumed to have been generated using the same wave amplitude as chosen for the plunging breakers case, with the change in wave period determining the breaker type.

In order to reproduce the laboratory conditions of Otsuka and Watanabe (2012), a plunging breaker needs to break as close as possible to the point $x = 9.18$ m and at a height of $H_b = 0.137$ m. To achieve this with the numerical model, the inlet wave height was varied from 0.07 m to 0.1 m, and simulations were run for 30 s, from initial still water conditions. Time series of surface elevation were recorded at horizontal intervals of 0.1 m, as in Otsuka and Watanabe (2012), with the final eight waves of the series selected for phase-averaging. The maximum and minimum values of the phase-averaged profile are used to calculate the wave height at the different locations in the wave flume. The breaking point, x_b, is considered to be the point in the wave flume at which the maximum wave height is obtained. Table 6.1 presents the breaking point and height for each inlet wave height considered. The wave height $H = 0.08$ m gives the best results, and hence will be used for all the simulations in this work that are compared with the data set presented by Otsuka and Watanabe (2012).

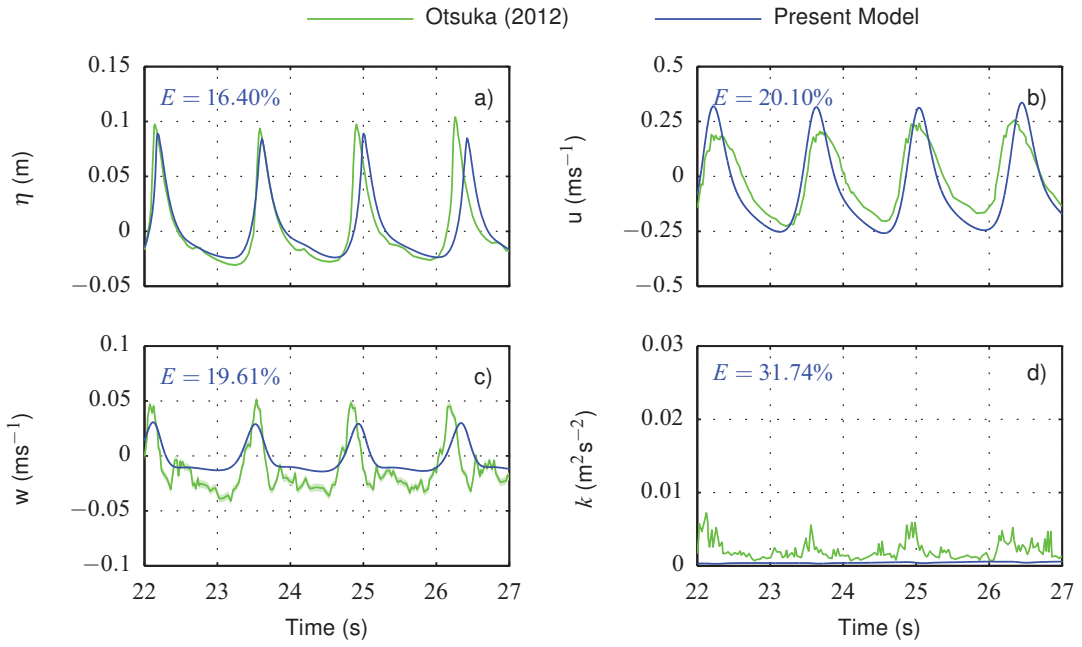

Figure 6.2: Comparison of the numerical predictions of spilling breakers at $x = 9.24$ m with the laboratory data gathered by Otsuka and Watanabe (2012). 5 s segments of time series for different variables, sampled 1 cm above the bed are presented: a) surface elevation, b) horizontal velocity, c) vertical velocity, and d) TKE. The NRMSE (E) of each predicted variable, relative to the experimental data, is indicated in each plot.

6.1.3 Spilling Breakers Case

Figure 6.2 presents a comparison of the hydrodynamics predicted by the present CFD model and the laboratory data collected by Otsuka and Watanabe (2012), sampled 1 cm above the bed at the breaking point (9.24 m). The laboratory data has been obtained from multiple runs, and are the ensemble-averaged profiles. Each plot is a section of the time series (22 to 27 s) of different quantities: a) surface elevation, b) horizontal velocity, c) vertical velocity, and d) TKE. The time series have been aligned so that the first peak in surface elevation predicted by the numerical model is in phase with the laboratory results. The normalised root mean square error (NRMSE) (E), relative to the experimental data, is also presented for each flow variable at the top of each plot.

The surface elevation plot shows that the model follows the experimental data well for the first two wave periods. This good agreement implies that the assumption of $H = 0.08$ m is

reasonable for the spilling breakers. After the initial agreement, the numerical and experimental results appear to be slightly out of phase with each other for the next two periods. This seems to be due to a change in period of the experimental data since the model remains at $T = 1.4$ s, as specified. It is suggested that this could be due to slight discrepancies in the experimental wave period, i.e. $T_{exp} = 1.4 \pm 0.05$ s.

The horizontal velocity time series (Figure 6.2b) indicates that the peak velocity in both flow directions is over-estimated by the model, but the shape of the profile is reasonably consistent with the experimental data. On the other hand, the peak values in the vertical velocity component (Figure 6.2c) are under-predicted, both in the positive and negative phases of the flow. Despite this difference in magnitude, which lead to a NRMSE of around 20% for both velocity components, the general shape of the profile seems to be acceptable. It is also worth noting that both components of velocity exhibit the shift in periodicity observed in the surface elevation plot, which will be a substantial contribution to the calculated error.

The largest differences occur in the TKE time series (Figure 6.2d). The model predicts very small levels of TKE, which seems reasonable near the bed at the breaking point. However, the laboratory data implies that there is a larger level of TKE at the breaking point. The method used by Otsuka and Watanabe (2012) for calculating TKE is the common method of isolating the fluctuating components of velocity, which could include any noise associated with the data collection process. If substantial levels of noise were observed then the TKE will be over-predicted, and could possibly explain differences between the numerical model and experimental data. Furthermore, there appears to be little variation in the TKE time series, which could imply that wave-induced turbulence is not a major driver of suspended sediment transport at this sampling location. Therefore, it is assumed that this disagreement may be caused by noise in the experimental data and will not affect the model's ability to predict turbulence and sediment dynamics.

Figure 6.3 shows similar plots of surface elevation, velocity and TKE, sampled 1 cm above the bed at a location 60 cm after the breaking point, horizontally (9.84 m from the toe of the beach). The time series have been shifted by the same factor as in Figure 6.2. As was

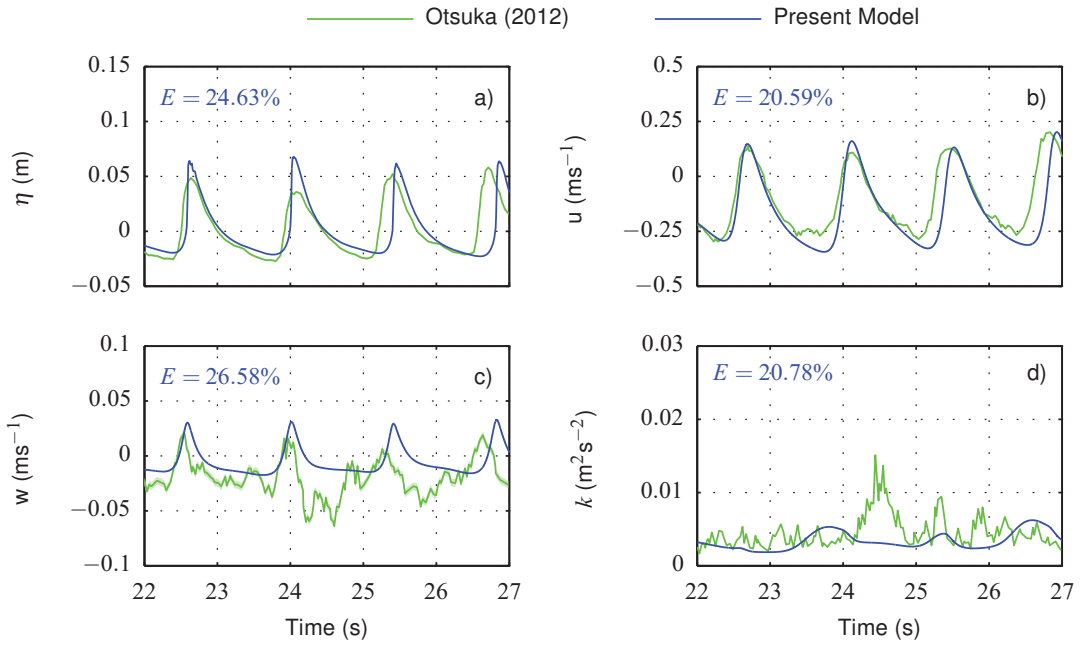

Figure 6.3: Comparison of the numerical predictions of spilling breakers at $x = 9.84$ m with the laboratory data gathered by Otsuka and Watanabe (2012). 5 s segments of time series for different variables, sampled 1 cm above the bed are presented: a) surface elevation, b) horizontal velocity, c) vertical velocity, and d) TKE. The NRMSE (E) of each predicted variable, relative to the experimental data, is indicated in each plot.

observed at the previous sampling location, the model predictions are in phase with the experimental data for the first two waves shown, but are slightly out of phase for the next two. The model predicts very similar surface elevation profiles (Figure 6.3a) for each of the four waves presented, but the experimental waves vary slightly, especially in terms of wave height.

The model's prediction of the horizontal velocity (Figure 6.3b) is reasonable, but the vertical velocity (Figure 6.3c) exhibits large deviations from the experimental data. In particular, the numerical results are closer to periodic than observed in the experimental data. The laboratory's vertical velocity component during the first wave period shown in the plot is similar to the numerical prediction, but after this wave the vertical velocity is less repeatable, and a large downward velocity can be observed around $t = 24.5$ s. This large downward burst is not present in the numerical predictions at any time during the 30 s time series. Furthermore, the peaks in vertical velocity occur slightly later in the model than indicated by

the laboratory data. These deviations are reflected in the calculated error, since the vertical component is found to be 6% larger than the horizontal component.

The laboratory TKE time series (Figure 6.3d) contains a large spike near the 24.5 s mark. This occurs at a similar time as the large downward burst that was previously discussed. It is hypothesised that this could be an artefact from the TKE calculation method discussed in the analysis of Figure 6.2. If a run that varied largely from the other runs was used to calculate the ensemble-average, then all of the other runs seem further from the ensemble-average than they should. This would lead to larger fluctuations and, hence, a spike in TKE. The model does not exhibit this spike in TKE at any point in the 30 s run. Another interesting difference is that, the spike in TKE occurs at a time when the model predicts a trough. The rest of the experimental time series shown does not contain periodic peaks and troughs but instead remains at an almost constant magnitude. On the other hand, the model does exhibit periodic behaviour with the peaks occurring just before the crests of the waves. The magnitude of the predicted TKE can be seen to be more comparable with the experimental data than observed at the breaking point, and this is supported by the NRMSE which is more than 10% reduced at the present location.

Figure 6.4 shows similar plots of surface elevation, velocity and TKE, sampled 1 cm above the bed at a location 1.40 m after the breaking point, horizontally ($x = 10.64$ m). The time series have been shifted by the same factor as in Figure 6.2. Similar to the previous two sampling locations, the surface elevation (Figure 6.4a) is well predicted by the model, especially for the first two waves presented.

The horizontal velocity component (Figure 6.4b) predictions generally compare favourably with the experimental data, although the backflow is over-predicted. This was also noted in Section 5.3, where the undertow was shown to be over-estimated when using most of the turbulence closure models, including the $k-\omega$ model being used here. Overall, the NRMSE for the horizontal velocity component is larger by more than 6% at this location than observed at either of the previous two sampling points. On the other hand, the vertical velocity component is predicted around 4% better at this sampling location (Figure 6.4c)

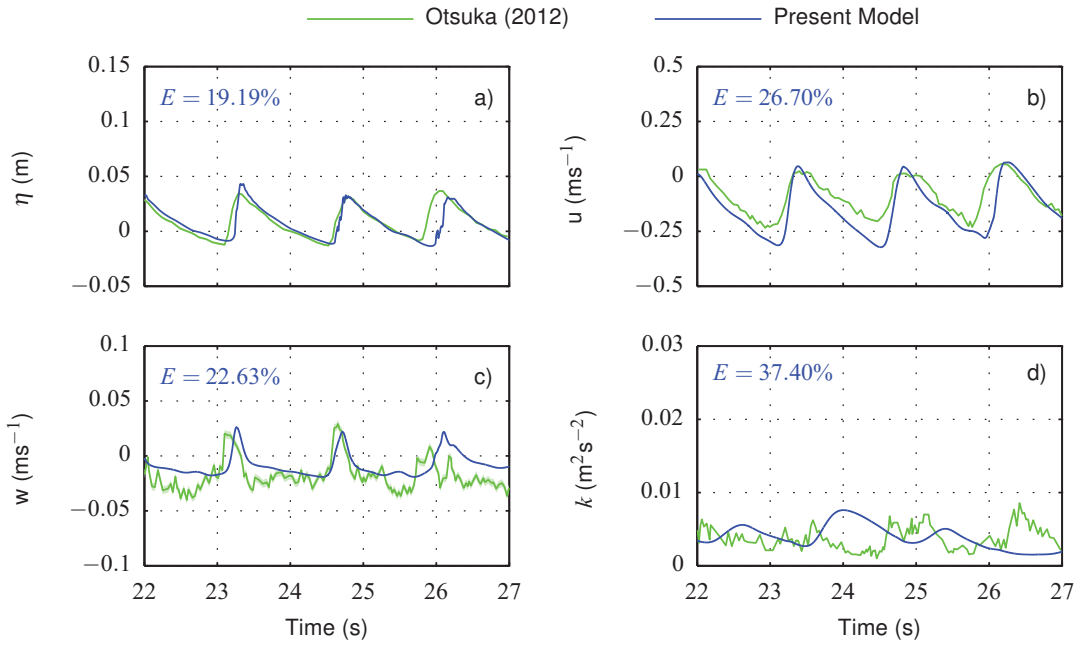

Figure 6.4: Comparison of the numerical predictions of spilling breakers at $x = 10.64$ m with the laboratory data gathered by Otsuka and Watanabe (2012). 5 s segments of time series for different variables, sampled 1 cm above the bed are presented: a) surface elevation, b) horizontal velocity, c) vertical velocity, and d) TKE. The NRMSE (E) of each predicted variable, relative to the experimental data, is indicated in each plot.

than at the previous one (Figure 6.3c), since the periodicity in the experimental data seems to be reproduced by the numerical model.

The peaks in vertical velocity still do not quite occur at the same time as in the laboratory, and the downward velocity is generally smaller. However, the scale of the vertical velocity is quite small and therefore these slight differences in shape are not expected to cause large changes in the sediment predictions.

The TKE at $x = 10.64$ m (Figure 6.4d) varies less than at the previous sampling location (Figure 6.3d) and the predicted magnitude of the TKE agrees reasonably well with the physical data. Therefore, it is believed that the model captures the TKE under spilling breakers to an acceptable standard.

Otsuka and Watanabe (2012) only presented the 5 s shown in Figures 6.2-6.4. However, it is interesting to consider the whole 30 s time series given by the present numerical model

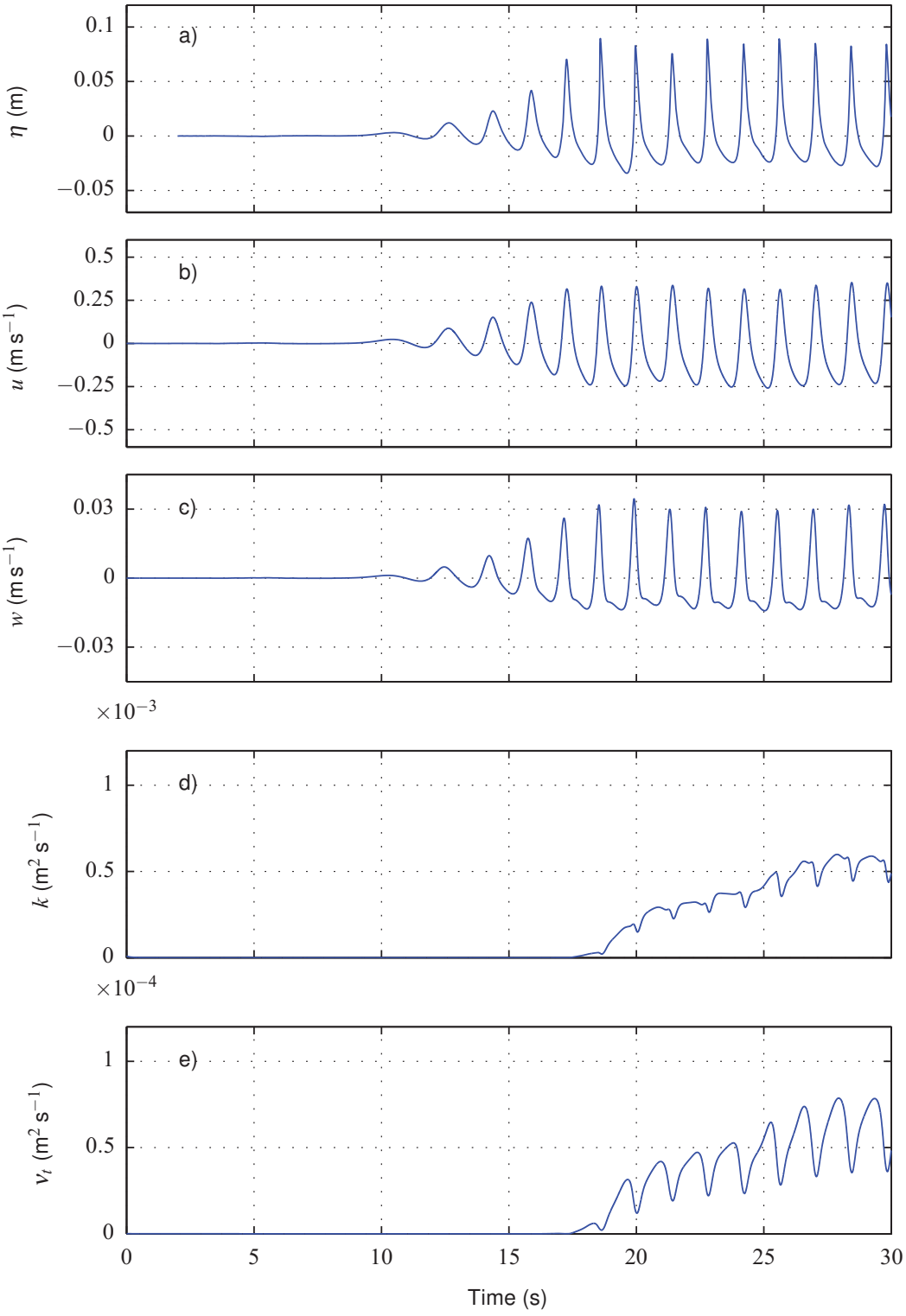

Figure 6.5: Numerical predictions of flow variables sampled at $x = 9.24$ m, 1 cm above the bed under spilling breakers. The presented variables are: a) surface elevation, b) horizontal velocity, c) vertical velocity, d) TKE, and e) eddy viscosity.

to determine whether it has converged to a periodic solution. Figures 6.5-6.7 give the time series for flow variables at the three sampling locations considered previously (x_b, $x_b + 0.6$ m and $x_b + 1.4$ m, respectively). The presented variables are a) surface elevation (η), b) horizontal velocity component (u), c) vertical velocity component (w), d) TKE (k), and e) eddy viscosity (ν_t).

Starting with the sampling location x_b (Figure 6.5), it is clear that all of the variables become close to periodic at around 20 s, when approximately 9 waves have passed. This implies that the 5 s sample of the time series used for comparison with the data of Otsuka and Watanabe (2012) was reasonable since it occurs after the model becomes quasi-steady. The surface elevation and velocity components become almost periodic quickly after around 3 or 4 waves have passed. The horizontal velocity is in phase with the surface elevation, i.e. peaks and troughs occur at the same time, whereas the vertical velocity component is slightly out of phase, with the maximum vertical velocity occurring slightly before the crest of the wave arrives.

The turbulent quantities appear to take longer to settle down to a repeatable state. Where the surface elevation and velocity components are reasonably similar after the third wave, the turbulence takes time to ramp up, with both TKE and eddy viscosity reaching a more consistent magnitude after around 20 s (9 waves). There is still some small variation in both the TKE and the eddy viscosity between wave periods but the model generally seems to have settled down to a quasi-steady state.

At sampling location $x_b + 0.8$ m (Figure 6.6), the surface elevation and horizontal velocity component settle down to a quasi-steady state after 20 s. However, in contrast with the observations at the breaking point, there are small variations in the vertical velocity throughout the 30 s run, mostly in the downward phases of the wave period. However, these variations are very small, particularly towards the end of the time series, so the effect on the sediment predictions are also likely to be small.

The turbulence quantities take longer to enter a quasi-steady state at this location than at the breaking point. The model takes about four waves to ramp up but does not converge

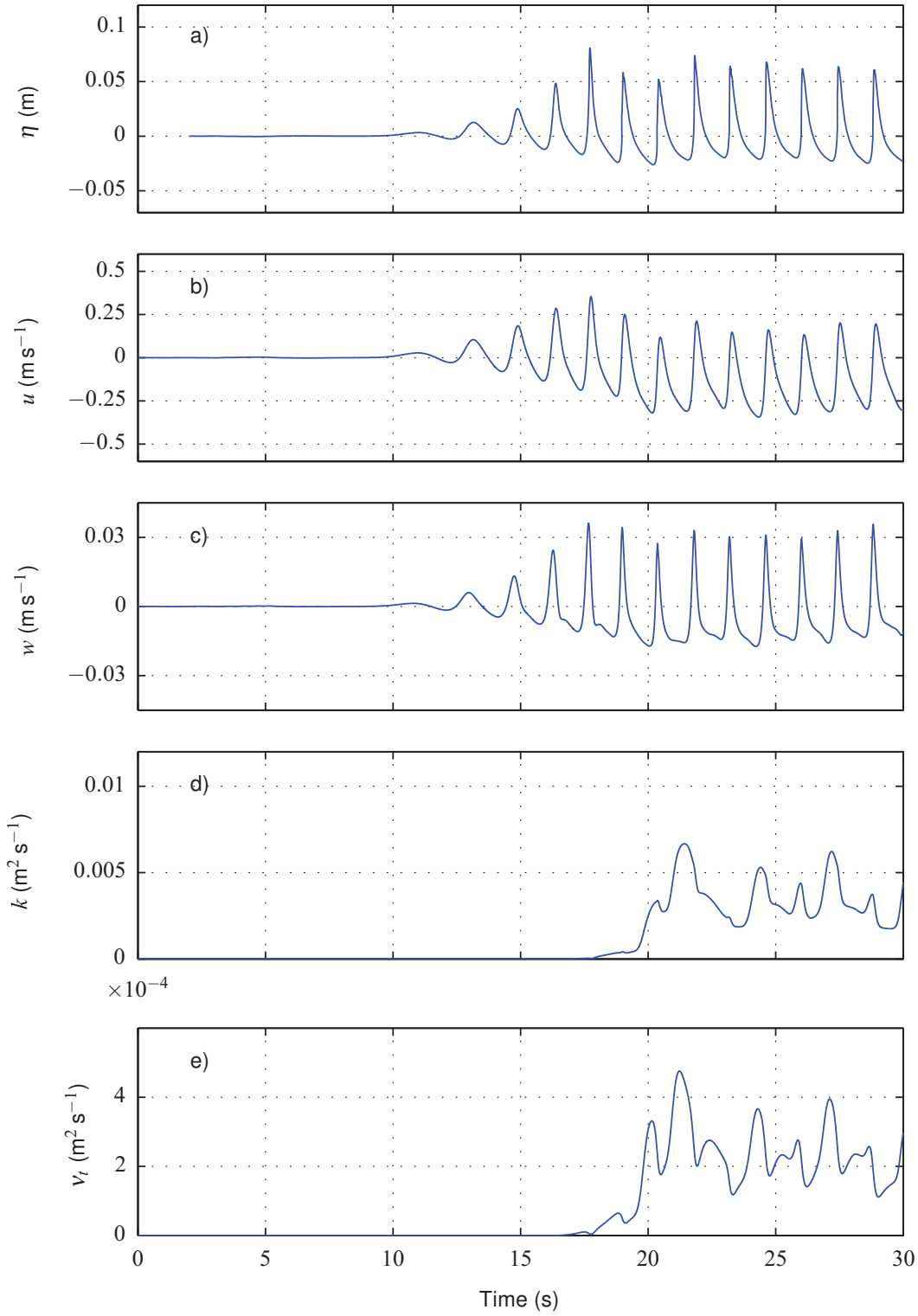

Figure 6.6: Numerical predictions of flow variables sampled at $x = 9.84$ m, 1 cm above the bed under spilling breakers. The presented variables are: a) surface elevation, b) horizontal velocity, c) vertical velocity, d) TKE, and e) eddy viscosity.

until around 25 s. After this time there is evidence of a possible periodic behaviour, with a frequency half that of the waves. It may be necessary to run the model for longer than 30 s in order for the turbulence to converge and hence to get a more accurate time-averaged sediment concentration.

The final sampling location, $x_b + 1.4$ m (Figure 6.7) exhibits much more variation than the previous two sampling locations. The surface elevation indicates that the waves after 20 s are almost quasi-steady. However, closer inspection shows inter-wave variations, which is to be expected due to the nature of broken waves. The horizontal velocity is also quasi-steady after 20 s, but the vertical velocity varies throughout the full simulation. The TKE and eddy viscosity predictions overshoot before dropping to a lower magnitude after around 20 s. Once again there are slight variations between wave periods which might indicate that the simulation times need to be extended to reach the quasi-steady state.

In summary, the sampling locations x_b and $x_b + 0.8$ m appear to have reached a quasi-steady state by the end of the 30 s, but there are still small variations at the final sampling location, $x_b + 1.4$ m. However, the model agrees reasonably well with the spilling breaker data of Otsuka and Watanabe (2012) and, hence, is considered to predict the hydrodynamics accurately enough to warrant extending the model so that sediment dynamics are included.

6.1.4 Plunging Breakers Case

The analysis performed for the spilling breakers in the previous section will now be repeated for the plunging breakers. Figure 6.8 compares the model and laboratory results, presented by Otsuka and Watanabe (2012), 1 cm above the bed at the breaking point, x_b ($x = 9.18$ m). Each plot is a 5 s segment (16 to 21 s) of the 30 s run and represents a different hydrodynamic variable: a) free surface elevation, b) horizontal velocity component, c) vertical velocity component and d) TKE. Similar to the spilling data, the experimental time series have been obtained from multiple runs and are the ensemble-averaged profiles. The time series have been aligned so that the first crest in the surface elevation plots are at the same phase in both the model and experimental results. The shift required to obtain this align-

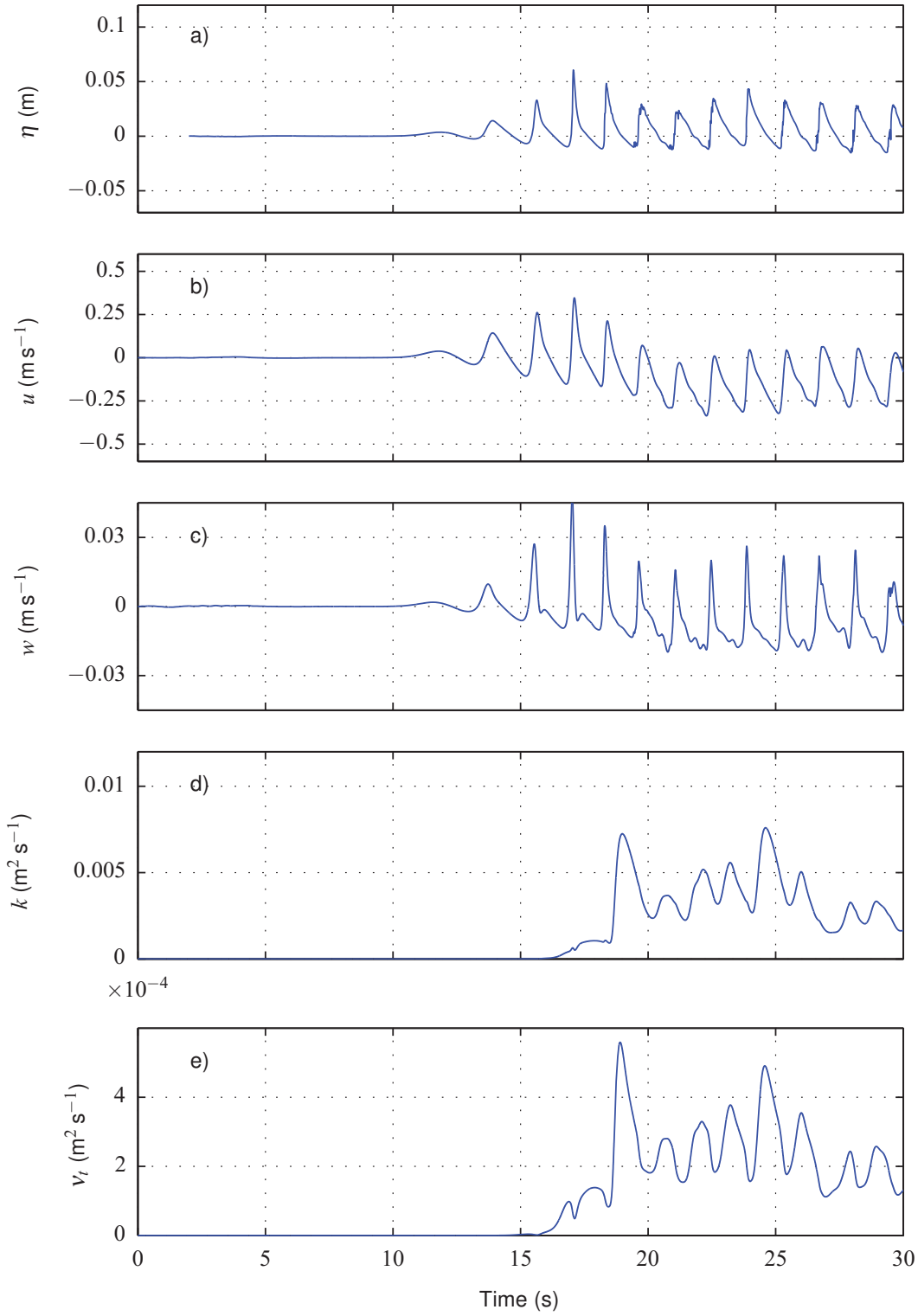

Figure 6.7: Numerical predictions of flow variables sampled at $x = 10.64$ m, 1 cm above the bed under spilling breakers. The presented variables are: a) surface elevation, b) horizontal velocity, c) vertical velocity, d) TKE, and e) eddy viscosity.

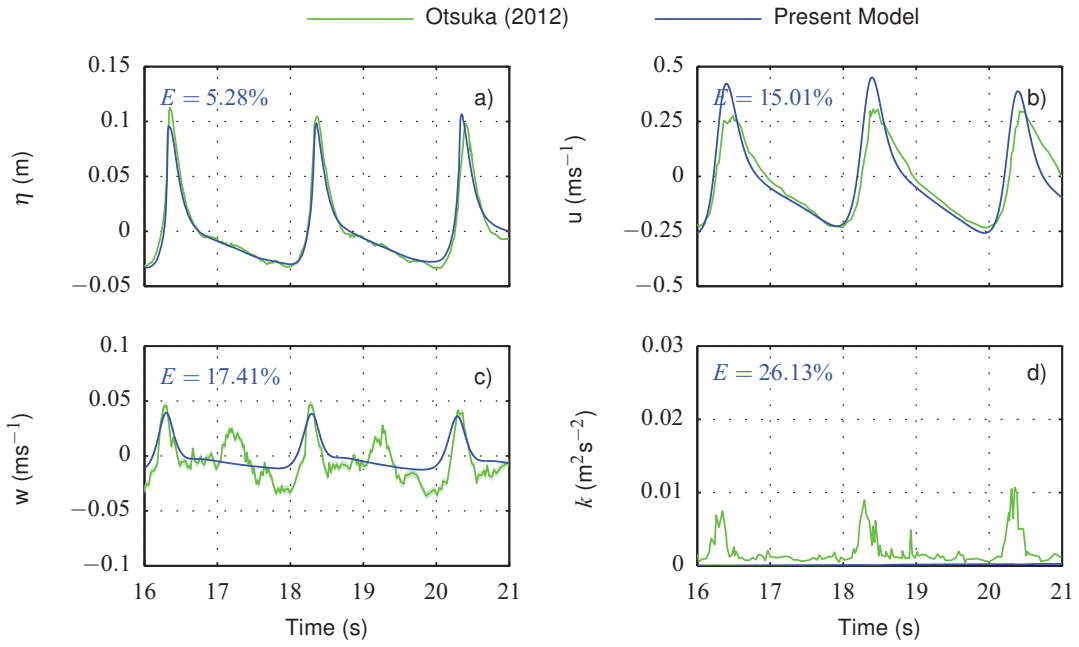

Figure 6.8: Comparison of the numerical predictions of plunging breakers at $x = 9.18$ m with the laboratory data gathered by Otsuka and Watanabe (2012). 5 s segments of time series for different variables, sampled 1 cm above the bed are presented: a) surface elevation, b) horizontal velocity, c) vertical velocity, and d) TKE. The NRMSE (E) of each predicted variable, relative to the experimental data, is indicated in each plot.

ment has been used to adjust all of the time series, including those at different sampling locations. The NRMSE (E), relative to the experimental data, is also indicated for each flow variable at the top of each plot.

Figure 6.8a shows that the model predicts the surface elevation well. The model captures the change in wave height between the three waves shown, and all of the waves stay close to being in phase with the experimental data. This leads to a much smaller error of 5%, than the 16% calculated for the spilling breakers case. The horizontal velocity time series (Figure 6.8b) indicates reasonable agreement, although the positive section of the period is over-estimated for all three waves shown, leading to a NRMSE of 15%.

On the other hand, the vertical velocity time series (Figure 6.8c) exhibits some differences between the numerical model and laboratory measurements. Both time series appear to be periodic, but the laboratory data contains two peaks in upward velocity per period. Following

the second peak, which occurs after the crest of the wave has passed, a relatively large downward velocity is observed in the laboratory measurements. In contrast, the numerical results only contain one peak per period, which occurs just before the crest arrives. This peak is close to being aligned with one of the peaks in the experimental data, and is of a similar magnitude. Neither the second upward velocity, nor the relatively large downward velocity are observed at any point in the numerical predictions. It is possible that these differences could be caused by an experimental artefact, such as intrusive measurements or lack of uniformity in the bed (see Figure 6.1). Since the model is predicting the velocity to be in a completely different direction at this time, it is thought that it could considerably affect the sediment dynamics and hence is an important problem to address. First, the numerical predictions were thoroughly investigated to see if this effect could be a numerical artefact. Hence a number of 3-D simulations were run, where large eddy simulation (LES) was also tried to see if the effect could be linked to the $k-\omega$ model not resolving any of the eddy structure in the flow. Further considerations included evaluating the flow variables higher up in the water column (3 cm above the bed) and running the simulation for longer to see if the shape developed over time. Although some simulations exhibited a very small "bump" in the profile, none predicted a peak of a similar magnitude to that observed in the experiments. Having ruled out a 3-D or mesh effect in the numerical model, a new series of laboratory experiments were conducted, which will be discussed further in Section 6.2.

The TKE (Figure 6.8d) is under-predicted by the model. The experimental time series shows periodic spikes of TKE near the crest of the waves. If the model results are considered independently (see Figure 6.11), it is evident that this periodic behaviour is captured by the model, but at a much lower magnitude. Therefore, this is not considered a problem since, although the suspended sediment concentrations are likely to be under-predicted, the processes behind them should be qualitatively correct.

Figure 6.9 shows the flow characteristics 1 cm above the bed at sampling location $x = x_b + 0.8$ m ($x = 9.98$ m). The time series have been shifted by the same factor as in Figure 6.8. Once again, the surface elevation is predicted reasonably well. The horizontal velocity

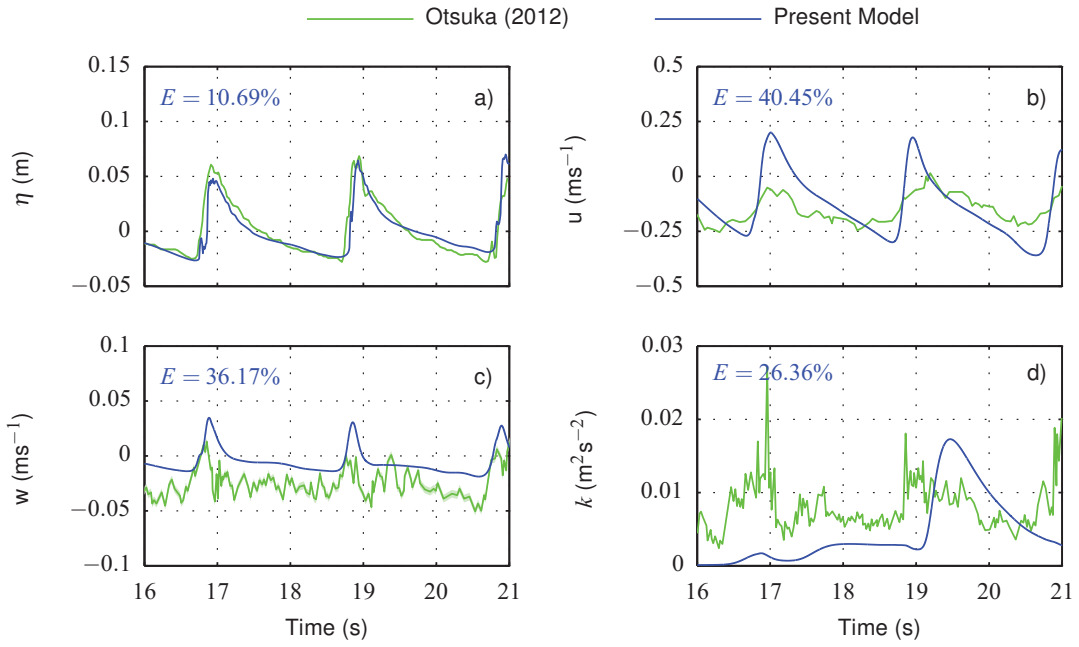

Figure 6.9: Comparison of the numerical predictions of plunging breakers at $x = 9.98$ m with the laboratory data gathered by Otsuka and Watanabe (2012). 5 s segments of time series for different variables, sampled 1 cm above the bed are presented: a) surface elevation, b) horizontal velocity, c) vertical velocity, and d) TKE. The NRMSE (E) of each predicted variable, relative to the experimental data, is indicated in each plot.

(Figure 6.9b) is over-predicted, both in the forward and the backward phases which, along with some phase differences, leads to a large NRMSE of 40%. The experimental vertical velocity series (Figure 6.9c) exhibits little variability whereas the numerical model has a more distinct shape, predicting a periodic maximum to occur before the crest arrives, as has been noted at other sampling locations, for this case and the spilling breakers case too.

The TKE series (Figure 6.9d) is more interesting since both the model predictions and the experiments exhibit a single spike in TKE at very different times. The experimental data has a spike at around 17 s whereas the model predicts one at around 20 s. There is also an indication of the experiments having another spike at the end of the record (21 s) but this cannot be confirmed since a longer time series was not presented by Otsuka and Watanabe (2012). It turns out that the large spike in the model corresponds with it reaching its quasi-steady state, and it just happens to have occurred during this section of the record. This can be seen in Figure 6.12, and will be discussed in more detail later in this section.

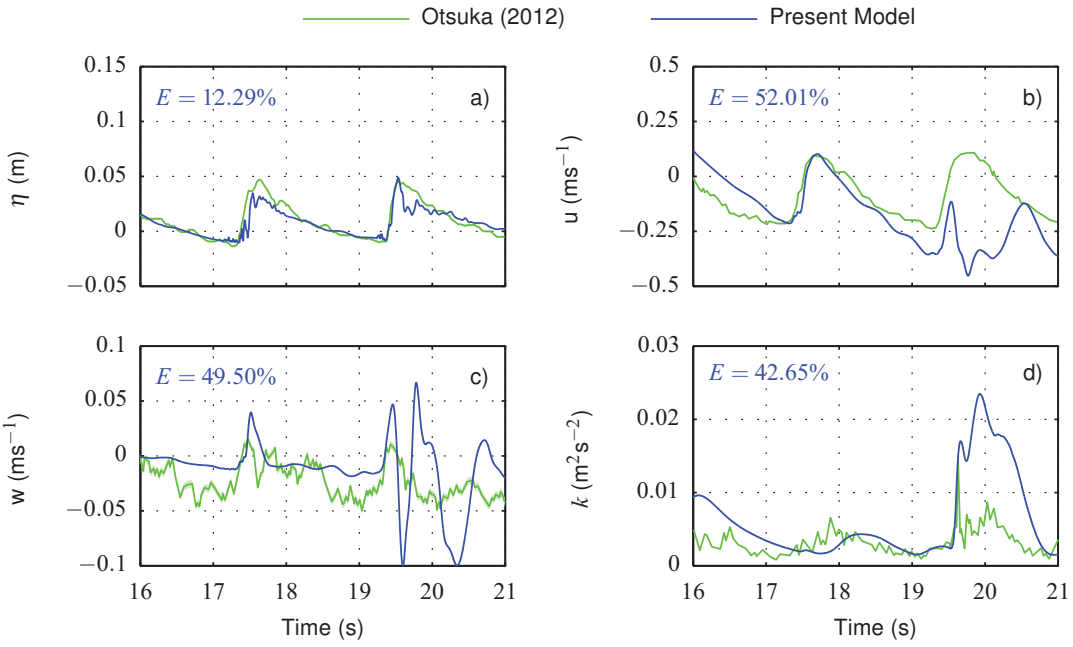

Figure 6.10: Comparison of the numerical predictions of plunging breakers at $x = 10.78$ m with the laboratory data gathered by Otsuka and Watanabe (2012). 5 s segments of time series for different variables, sampled 1 cm above the bed are presented: a) surface elevation, b) horizontal velocity, c) vertical velocity, and d) TKE. The NRMSE (E) of each predicted variable, relative to the experimental data, is indicated in each plot.

Figure 6.10 shows the flow features 1 cm above the bed at sampling location $x = x_b + 1.6$ m (10.78 m), with the time series shifted, as before. The surface elevation is slightly underpredicted by the model. It is worth noting that this sampling location is located in a region where there is a lot of entrapped air. Since the air is treated as an incompressible fluid in this model, it is likely that there will be errors in the dynamics of the entrapped air phase. This could also explain differences in other hydrodynamic parameters, such as the horizontal velocity (Figure 6.10b), which exhibits a larger backflow than shown in the experiments. In fact, the horizontal velocity is negative for the majority of the section of the time series shown. This could lead to larger offshore directed sediment concentration fluxes. Further differences can be observed in the TKE (Figure 6.10d), with the model predicting similar TKE levels as in the experiments with the exception of a large peak around $t = 20$ s. This peak occurs at a time when both the vertical and horizontal components exhibit complex behaviour. As can be seen in the full time series (Figure 6.13d), this behaviour appears to

be an isolated event and could be due to the development of the undertow, since it occurs in the first wave where u is negative at all phases.

Similar to the spilling breaker data, Otsuka and Watanabe (2012) only presented the 5 s shown in Figures 6.8-6.10. However, it is worth considering the full 30 s time series, given in Figures 6.11-6.13, at 1 cm above the bed, predicted by the model for different variables at the three sampling locations considered previously (x_b, x_b+0.8 m and x_b+1.6 m, respectively). The presented flow variables are a) surface elevation (η), b) horizontal velocity component (u), c) vertical velocity component (w), d) TKE (k), and e) eddy viscosity (ν_t).

The first sampling location (Figure 6.11) shows that all of the five quantities have become periodic after around 20 s. Similar to the corresponding plot for the spilling breakers (Figure 6.5), the surface elevation and velocity become close to being periodic much quicker than the TKE and hence the eddy viscosity. This implies that the turbulence model takes longer to ramp up than the rest of the model. The results at this location seem reasonable and there is no obvious sign of problems with the model predictions.

The second sampling location, $x_b + 0.8$ m (Figure 6.12) indicates slightly more variation between wave periods. The surface elevation and velocity components become quasi-steady after around 20 s, although slight changes in the vertical velocity do occur in the backflow. On the other hand, the TKE and eddy viscosity do not exhibit periodic behaviour until after 20 s. The final two wave periods are then similar, which could suggest that the model has reached a quasi-steady state, but the simulation would need to be run for longer to be certain.

The final sampling location, $x_b + 1.6$ m (Figure 6.13) differs from all other sampling locations for either spilling or plunging data. Although the peaks and troughs caused by the passing waves can be observed in the surface elevation and horizontal velocity component, in both cases every wave period is different. The TKE spike that was previously discussed, can be seen as an isolated event and seems to be strongly correlated with complex behaviour in both the horizontal and vertical velocity. Since this behaviour occurs in the first wave in which the horizontal velocity is negative at all phases, it could be an artefact of the

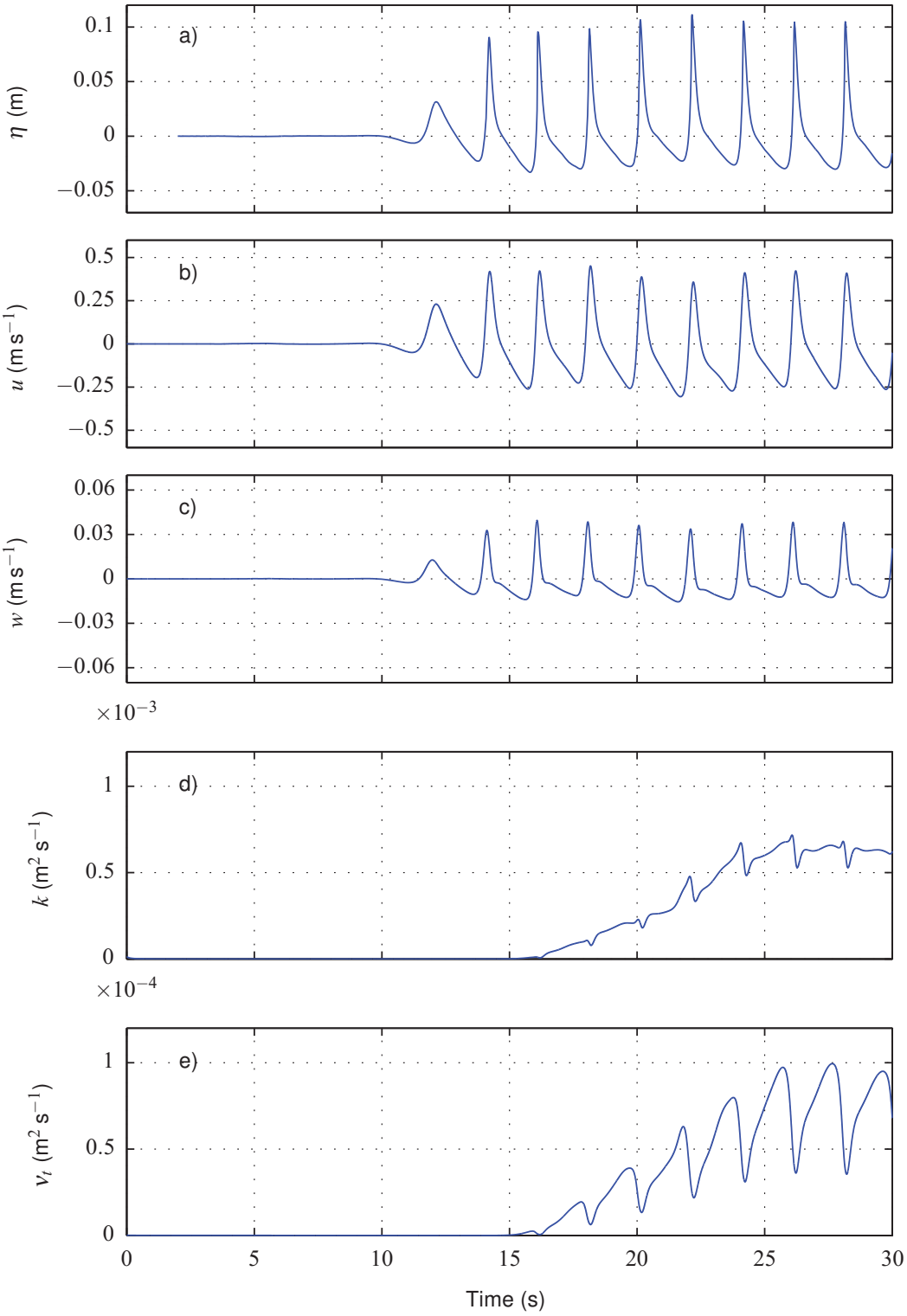

Figure 6.11: Numerical predictions of flow variables sampled at $x = 9.18$ m, 1 cm above the bed under plunging breakers. The presented variables are: a) surface elevation, b) horizontal velocity, c) vertical velocity, d) TKE, and e) eddy viscosity.

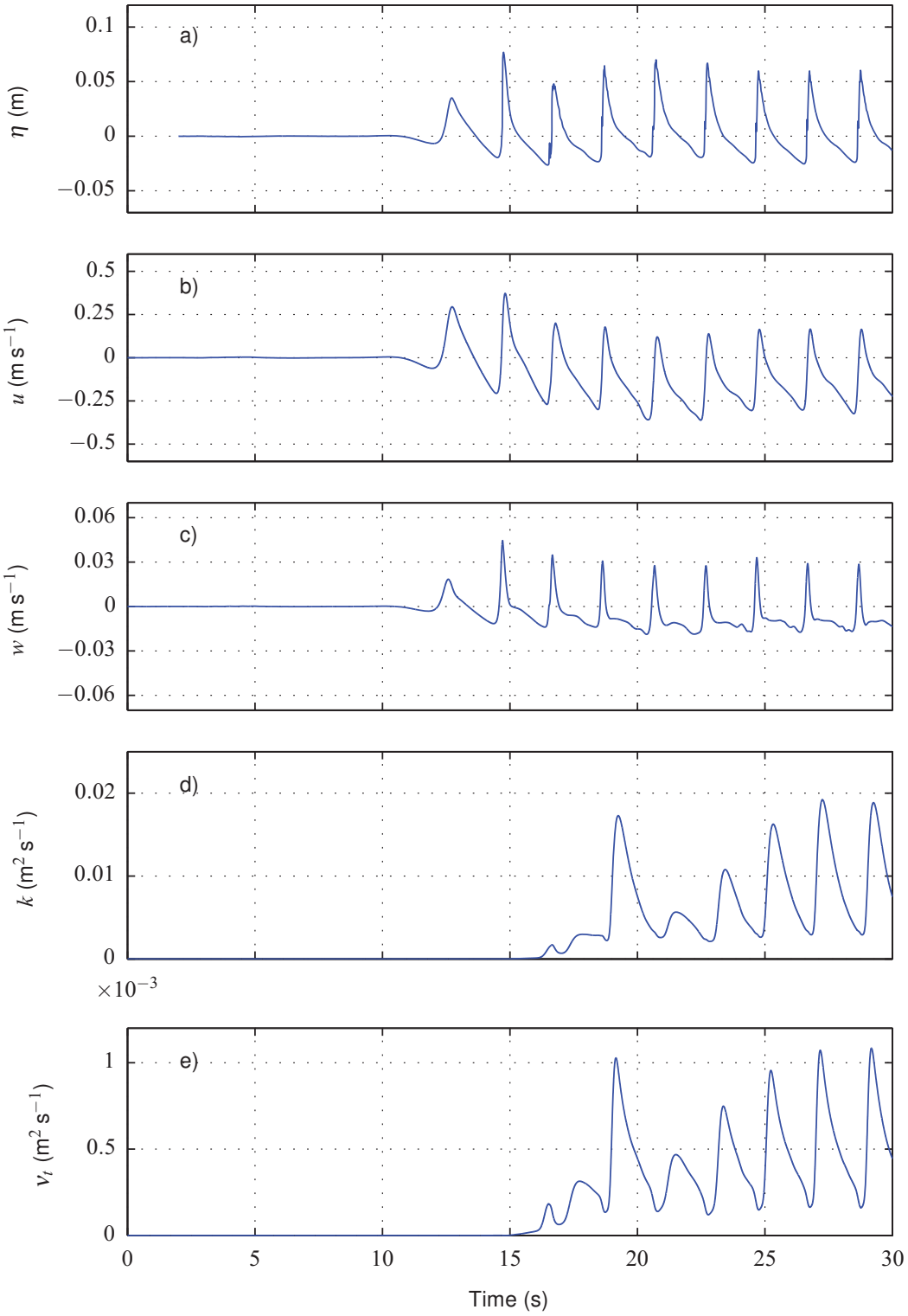

Figure 6.12: Numerical predictions of flow variables sampled at $x = 9.98$ m, 1 cm above the bed under plunging breakers. The presented variables are: a) surface elevation, b) horizontal velocity, c) vertical velocity, d) TKE, and e) eddy viscosity.

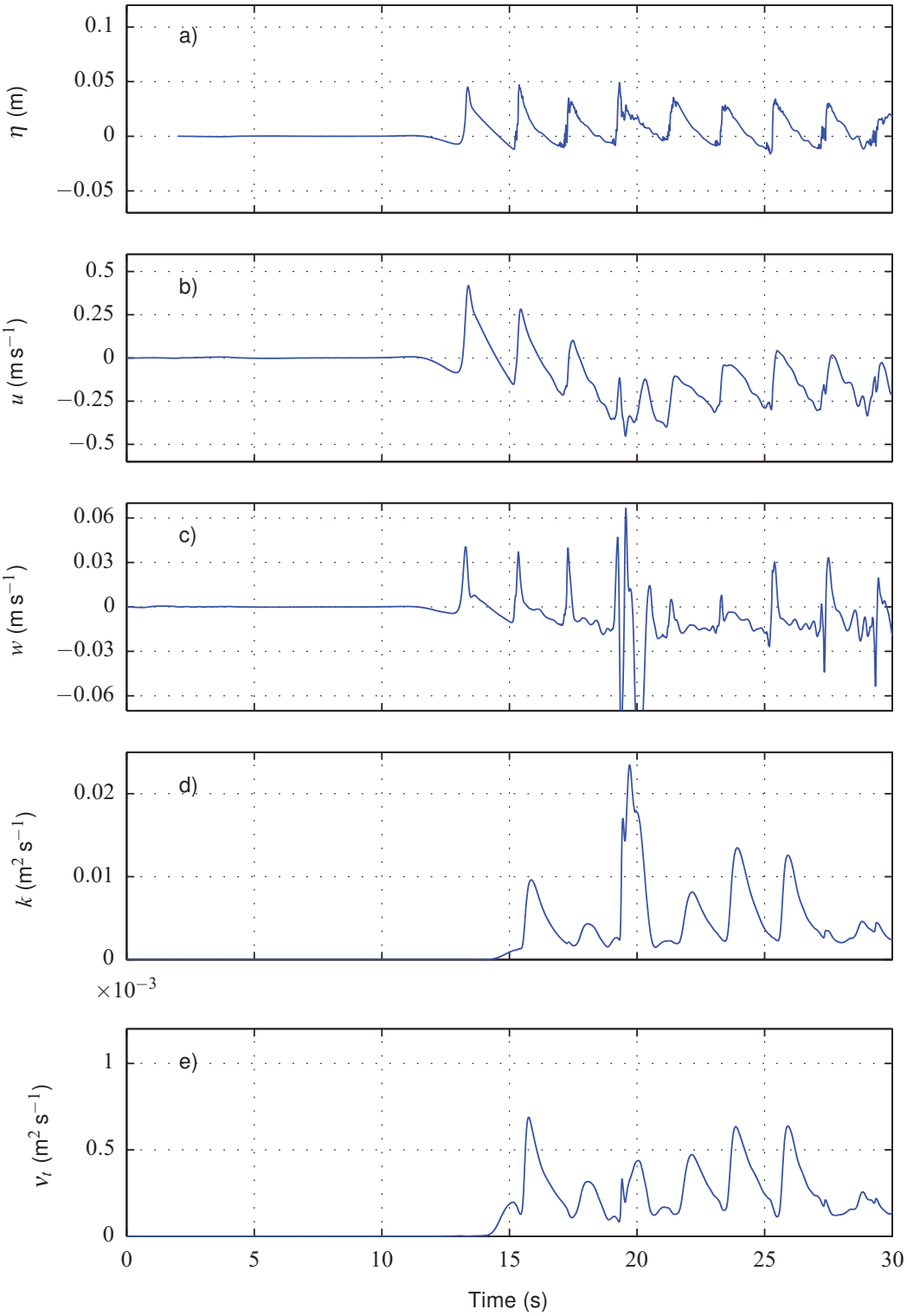

Figure 6.13: Numerical predictions of flow variables sampled at $x = 10.78$ m, 1 cm above the bed under plunging breakers. The presented variables are: a) surface elevation, b) horizontal velocity, c) vertical velocity, d) TKE, and e) eddy viscosity.

development of the undertow. Alternatively, it is possible that at this time, entrapped air comes closer to the sampling location, with larger values of TKE then occurring in these regions. This could potentially cause problems within the suspended sediment model, and if it is caused by the air being modelled as incompressible then the model would have to be adapted to include compressible effects. However, this is outside of the scope of the present study and will therefore be considered as possible future work.

Overall the model compares reasonably well with the plunging breaker experiments presented by Otsuka and Watanabe (2012). A few of the differences between the model and the experiments might be caused by modelling the air as incompressible. However, the most concerning problem is the second peak at the breaking point, since CFD generally performs well in laminar flow. Therefore, this is investigated further before validating the sediment model.

6.2 Wave Flume Experiments

As discussed in Section 6.1, the time series of near-bed velocity presented by Otsuka and Watanabe (2012) exhibits two peaks per period in the vertical component at the breaking point (see Figure 6.8). Since the numerical model is unable to reproduce this result, experiments have been conducted in the Coastal, Ocean and Sediment Transport (COAST) sediment flume at Plymouth University. These experiments aim to reproduce the vertical profile observed by Otsuka and Watanabe (2012), as well as providing spatial and temporal hydrodynamic data under breaking waves for further comparison with the model. The methodology uses a high speed camera and particle tracking velocimetry (PTV) through the image processing application, Streams (Nokes 2014).

6.2.1 Particle Tracking Velocimetry

PTV and particle image velocimetry (PIV) are methods for calculating velocity fields in an illuminated particle seeded flow. These techniques are generally used to calculate a velocity field in a 2-D plane, although it is possible to obtain a 3-D field (Nokes 2014). A light source is used to illuminate the particles in the chosen plane, and video footage is obtained

from a camera pointing perpendicular to the light sheet. PIV determines a velocity field by cross-correlating sub-windows of consecutive frames and considering the peaks in the field. Since the velocity field can be captured directly from the image sequence, this method is relatively computationally efficient and is generally considered the more popular of the two methods (Nokes 2014). However flows with high spatial variability may not be well resolved. Furthermore, this method only gives good results if the fluid has a high particle seeding.

On the other hand, PTV identifies particles in the flow and matches these between consecutive frames. By considering the distance travelled over the time between frames, a velocity field can be constructed. Since individual particles are being tracked, the seeding density is less important than in the PIV method, although the computation is easier with a lower density. However, it is a more complex methodology than PIV since the flow information cannot be directly obtained from the frames of the video. Instead four main stages are required to obtain the velocity field: image capture (and pre-processing), particle identification (PID), particle tracking, and velocity field generation. Since large spatial variation is to be expected under breaking waves, the PTV method was applied in the present work.

6.2.2 Image Capture

The experiments were carried out in the COAST sediment flume at Plymouth University and will be referred to as the "in-house" experiments in this section. The sediment flume is 35 m long, 0.6 m wide and has a maximum SWL of 0.8 m. A flat beach of gradient $1/20$, was constructed in the flume using 12 mm polypropylene sheets and a stainless steel box section for the frame, with the toe of the beach located 15.71 m horizontally from the wave maker. The sides of the flume are glass, allowing full flow visualisation. Any gaps between the beach and the sides of the flume were filled with silicon. Due to other work being conducted in the wave flume, the water depth was set to 0.5 m (as opposed to the 0.6 m used by Otsuka and Watanabe 2012). Figure 6.14 shows a diagram of the experimental setup from plan and side view.

The light box was constructed using LEDs and was suspended over the area of interest, parallel to the side walls and near to the centre of the flume. Seeding (Plascoat) was added

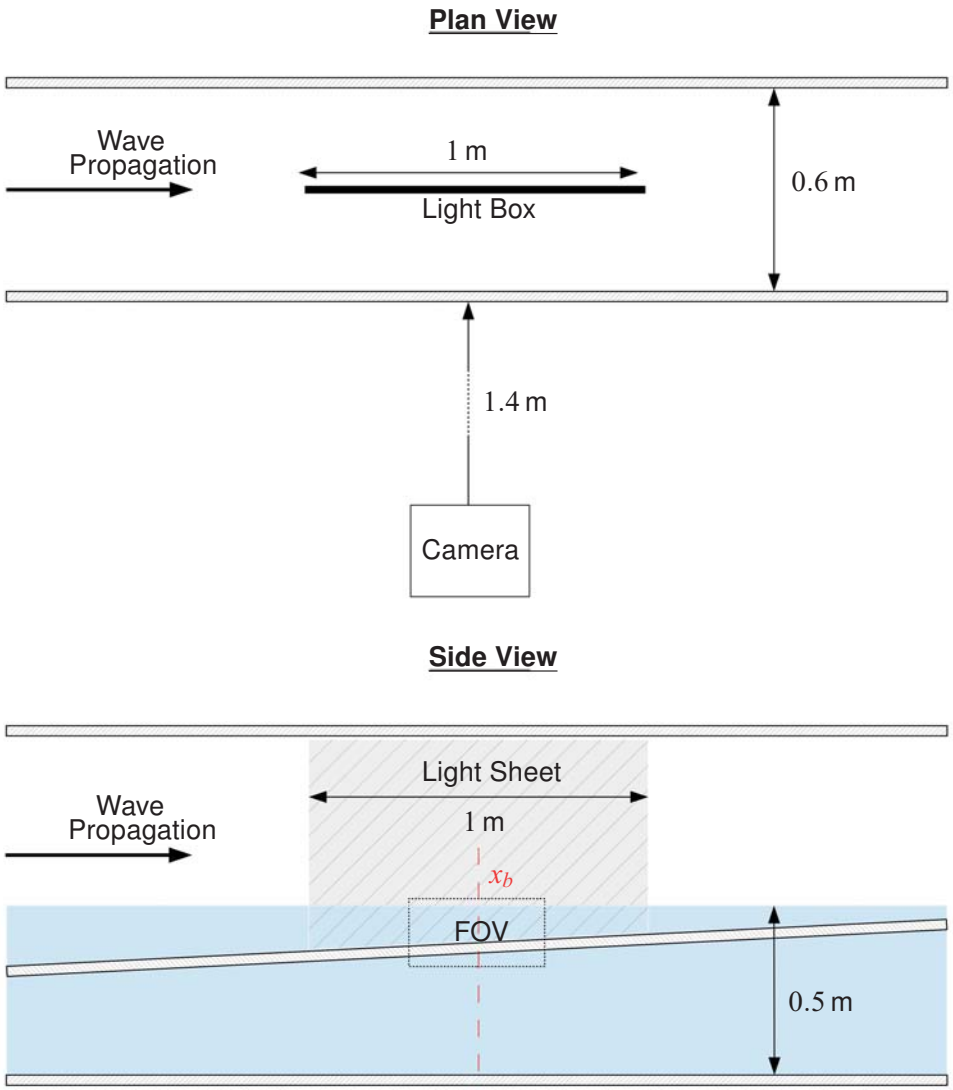

Figure 6.14: Laboratory setup for the in-house PTV experiments conducted in the COAST sediment flume.

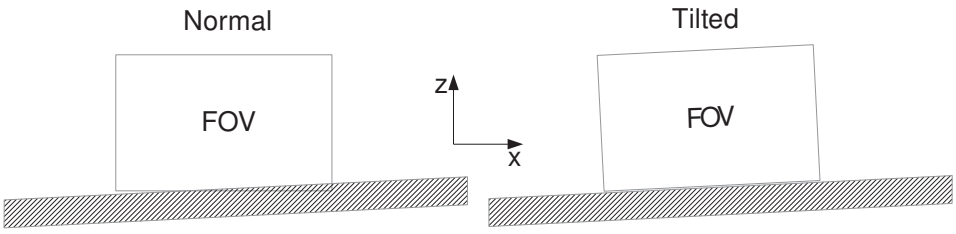

Figure 6.15: Alignment of the camera's field of view relative to the beach for the experiments conducted in the COAST sediment flume. Two orientations of the camera were used: normal (left) and tilted (right)

and mixed during filling of the flume in order to have particles reflecting the light emitted from the light box. If the seeding was left for too long (of the order of hours) it would rise to the surface and clump together since Plascoat is very slightly positively buoyant. To avoid this, the water surface was mixed and a run of plunging breakers was used to re-suspend the seeding if there was a long break between experimental runs.

A high speed camera (Photron SA4 fastcam) was placed on a tripod 1.4 m from the side of the wave flume. The camera is positioned so that it was pointing through the clear side walls and hence could be focused on the light sheet created by the light box. Two orientations of the camera were tried in these experiments, and are illustrated in Figure 6.15 relative to the beach. In the first (left of Figure 6.15), the camera was level so that it pointed in the $x-z$ plane, i.e. the horizontal and vertical directions correspond to u and w components, respectively. The second orientation (right of Figure 6.15) had the camera tilted so that the horizontal and vertical directions correspond to the components of velocity parallel and perpendicular to the slope, respectively. The velocity obtained from the PTV analysis was then transformed using a change of coordinates to get u and w. It was expected that the detail near the bottom would be obtained more easily with the parallel-perpendicular orientation than the $x-z$ orientation, since the images could be cropped rather than filtered. This removes the possibility of parts of the beach being incorrectly identified as particles. In both orientations, the camera was focused on the particles in the plane of light emitted from the light box through the following procedure. Firstly, a ruler was attached to the light box, at the correct horizontal measurement location and spanning the whole water depth. The camera was then focused so that the numbers on the ruler were as clear as possible. This procedure also ensured that the image was centred near the point of interest (i.e. 10 mm above the bed at the breaking water depth), minimising any potential error due to distortion. Furthermore, to produce a clearer image, as much ambient light as possible was removed by switching off lights in the laboratory and using blackout curtains. Furthermore, a black screen was placed behind the flume so that the particles showed as light objects on a dark surface.

Following Otsuka and Watanabe (2012), thirty seconds of regular waves with wave periods of $T = 1.4$ s (spilling) and $T = 2.0$ s (plunging) were generated for each run, and the amplitude is set to 0.04 m. The camera was set to record at 125 frames per second (FPS), with a shutter speed of $1/$FPS. Five runs were conducted for each of the plunging and spilling cases, and in each orientation. Between runs, the water was left to settle for at least 10 minutes before the next run was conducted. It was assumed that the change in SWL will not change the breaking water depth. Therefore, the sampling location was chosen as the breaking depth stated by Otsuka and Watanabe (2012) and 1 cm above the beach.

6.2.3 Streams

Streams is an image processing application, developed by the Department of Civil and Natural Resources Engineering at the University of Canterbury (Nokes 2014). After obtaining video footage of a particle seeded fluid flow, Streams can be utilised to calculate the velocities of that flow using PTV. Streams provides many options at each of the stages in the PTV process, and this section discusses the methodology applied in the present study.

6.2.3.1 Image Pre-Processing

The raw images were first trimmed to focus on the region around the point of interest: the water depth stated by Otsuka and Watanabe (2012) at the breaking point. A 114 mm $\times$ 25 mm rectangle was selected around the point of interest, where the bottom of the rectangle was the beach in the tilted orientation. In the normal orientation the bottom of the rectangle intercepted the slope at the x coordinate of interest. The point of interest was located at coordinate $(50,10)$ in both cases. Figure 6.16 shows the trimmed image (a) and intensity matrix (b) for an example frame, from a plunging breaker run. The particles should show up as bright regions on a dark background in the intensity matrix. Instead, there are large regions of similar intensity, making it hard to identify where the particles are located. This could be caused by non-uniform lighting, making the background intensity vary across the image. Hence the background has been removed using a filter on the trimmed image, with the intention of leaving only the true particles. This filter splits the window into sub-windows with a specified number of pixels (chosen as 20 in both x and z directions). The average

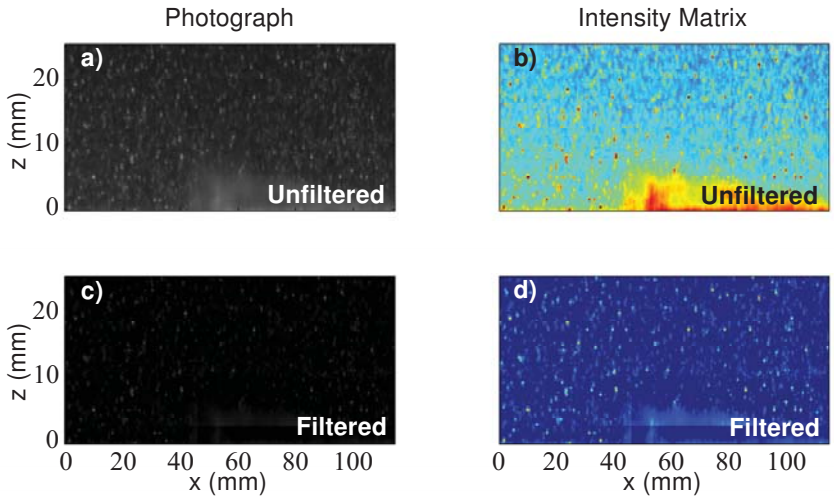

Figure 6.16: Example frame indicating the effect of using the background filter on the image sequence (left) and intensity matrix (right). The top and bottom rows correspond to the raw and filtered data respectively.

intensity is then calculated in each sub-window, which is considered to be the background intensity. The background intensity field is then subtracted from the original image to give a filtered image. Also shown in Figure 6.16 is the filtered image (c) and corresponding intensity matrix (d). Comparing the intensity matrix for the filtered and unfiltered data shows that the particles are much clearer for the filtered data. This is important since it will increase the accuracy at the particle identification (PID) stage.

6.2.3.2 Particle Identification

The PID stage is critical, for particle tracking to be computed accurately. The PID algorithm identifies particles using a peak threshold. If the identification algorithm is too strict then not enough particles will be identified to create a velocity field. If the algorithm is too lenient then particles which do not exist might be identified, or large particles may be split up into multiple small particles. This can lead to the particles appearing and disappearing between frames as well as creating additional computational expense.

The present experiments had a few additional difficulties. The first was that the light box emits a periodic flickering. The second was that there was a large range of velocities throughout the record (from still water to the large velocities observed under the breaker). Thirdly, the entrapped air in the breaking process causes light to be reflected, leaving a

darker region under the breaker. Therefore, the algorithm has been optimised to capture the breaking process more accurately. To deal with the dark regions and high velocity observed at the breaking point, a more lenient algorithm has been applied, at the expense of additional noise in the record, particularly at the beginning of the record where there was still water. Furthermore, as can be seen in the image (see unfiltered image in Figure 6.16), there was a small region near the bottom that was obstructed by silicon used in the construction of the beach. To avoid particles being identified in this region (and then subsequently being used in particle tracking), this region has been omitted from the PID process.

The algorithm used in this work was the double threshold method. A peak intensity threshold was used to signify the presence of a particle in the flow. This value must be specified as a number between 0 (low intensity) and 255 (high intensity), and was set to 8 in the present study. The PID searches the pixels around a potential particle for the maximum value and then multiplies this value by the edge threshold factor (defined by the user as 0.4, equivalent to 40% of the peak intensity threshold), which determines whether the surrounding pixels are part of the particle or not. This is important to identify the size of each particle, and avoid large particles being split up into smaller ones. It is also possible to specify a minimum and maximum size of a particle. In this work a minimum size has not been set, but a maximum of 5 mm was used. Using this double threshold algorithm, the PID calculates the position of each particle to better than half pixel accuracy (Nokes 2014). Figure 6.17 shows the PID algorithm used on an example frame from under the plunging breaker. The subplots correspond to a) the filtered image, b) the intensity matrix, and c) the intensity matrix with particles ($+$) identified by the algorithm. In general, the algorithm has identified the particles well: there are very few obvious particles which have been missed and not many particles which have been incorrectly identified. This will help to make the accurate particle matches as discussed in the next section.

6.2.3.3 Particle Tracking

The next stage of the calculation is to match particles between consecutive frames. This is the core of a PTV system and accuracy is critical since these matches will be used to

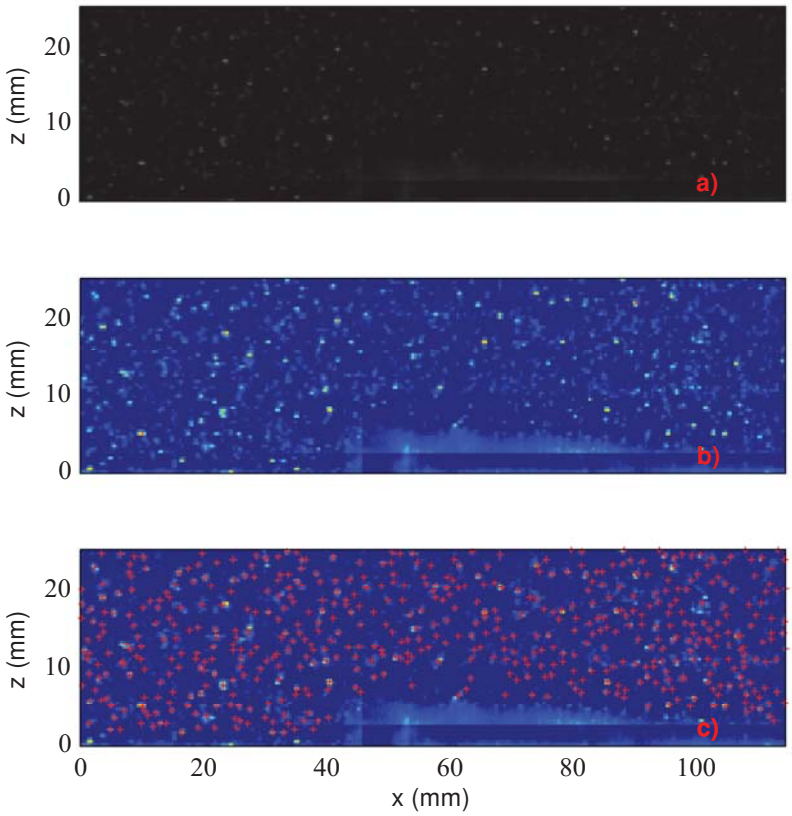

Figure 6.17: Example of PID for a single frame. The plots show a) the filtered image, b) the intensity matrix, and c) the intensity matrix with the particles identified (+).

calculate the Lagrangian velocity and, hence, the Eulerian velocity field.

The basic principal of the matching process is to calculate matching costs to determine which of the particles in the second frame represents one in the first. This is done through an auction algorithm, where the particles in the first frame are considered to be the bidders and the second frame contains the particles on which they are bidding. The aim of the algorithm is to match the particles so that the overall cost is minimised. A particle in the first frame bids on the particles within a user specified window size in the second frame. The choice of window size is important since the computational expense can become very large if the whole frame is considered. This bidding process gives the particle a list of possible matches with an associated cost. This process is repeated for each of the particles in the first frame. The overall cost can then be minimised by selecting the matches that give the

lowest cost. Note that this could mean that individual matches are not the lowest possible cost since multiple bidders could identify the same particle as their lowest match.

There are many methods for calculating the cost of a match, and Streams offers a number of these options (Nokes 2014). The algorithms are split into two categories. State-based costings, which determine the cost based upon the state of the particle in a frame, including information about the size, location and intensity. On the other hand, matching-based costings utilise existing matches to determine costings. All of these algorithms calculate a non-dimensional cost, which lies between 0 (highly desirable) and 1 (least desirable) where possible. A maximum matching cost (MMC) can be specified by the user so that any match above this value will be discarded. Similar to the search window size, the MMC helps to reduce the number of possible matches and, hence, improves the computational efficiency. The choice of MMC is very important since if it is set too low then good matches can be discarded and if it is set too high then poor matches can be included (Nokes 2014).

In this work a state-based costing, the pseudo-correlation algorithm, was initially used with a high MMC (0.9) so that a large number of matches are included. This was found to be necessary since frames with high velocity often lost light, and hence particles, due to reflection from entrained air. A matching-based costing, known as local velocity, was then applied with a lower MMC (0.5) to ensure only high quality matches are retained which agree with the surrounding flow.

The pseudo-correlation costing attempts to imitate a correlation costing, a method based upon the cross-correlation of the intensity field, in a more computationally efficient manner (Nokes 2014). The pseudo-correlation considers the particle where the surrounding particles are of a similar shape between frames (adjacent). If the particle centres are coincident then the correlation between these particles is 1. If they do not overlap at all then the correlation is 0. Therefore, the pseudo-correlation attempts to mimic this behaviour using the costing:

$$C_{12} = \frac{1}{n}\sum_{i=1}^{n}\frac{\min\{d_i, r_i + r_j\}}{r_i + r_i'}. \tag{6.1}$$

In equation (6.1), r_i is the radius of particle i in frame 1 and r_i' is the radius of the particle

adjacent to particle i in frame 2. d_i is the distance between the centre of particle i in frame 1 and its adjacent particle in frame 2. If particle i does not have an adjacent particle in frame 2 then d_i is set to infinity. If all adjacent particle pairs have coincident centres then the cost will be 0. If none actually touch one another then the cost will be 1. The radius of the particles can be amplified by the user, which tends to decrease the cost (Nokes 2014) and has been set to 3 times larger in this work.

The local velocity costing is a match-based costing, which uses the estimates of particle velocities in the neighbourhood of particle p_1 to predict the likely location in the next frame. The user specifies a rectangle around p_1, and all particles in this rectangle with a velocity estimate available, due to a match in the previous or next frame, are used to calculate a representative velocity for p_1 (Nokes 2014). In this work, the representative velocity was simply the weighted average, where the weighting reduces towards the edges of the search window, which was set as a $10\,\text{mm}\times 10\,\text{mm}$ square. Furthermore, six iterations are applied, alternating between forward and backward directions, to increase accuracy. The costing was calculated using

$$C_{12} = \frac{|\mathbf{r}_{pred} - \mathbf{r}_{p_2}|}{|\mathbf{r}_{pred} - \mathbf{r}_{p_1}|}, \tag{6.2}$$

where $\mathbf{r}_{pred}$ is the predicted location of p_1 in frame 2 using the weighted average, whereas $\mathbf{r}_{p_1}$ and $\mathbf{r}_{p_2}$ are the location of p_1 and p_2 in frames 1 and 2, respectively. It is clear that if the location of p_2 is close to the prediction then the cost is small, as required.

Once this procedure is complete, every frame will have a set of matches, which provides the Lagrangian velocity. The final stage is to interpolate the Lagrangian velocities onto a Eulerian grid.

6.2.3.4 Velocity Field Interpolation

The aim of these experiments was to gain hydrodynamic information at a single point in the flow. In order to do this, the Lagrangian particle velocities must be interpolated onto a regular grid. Depending on the availability of matches, Streams uses a forward differencing (if only available in next frame), backwards differencing (only available in previous frame)

or central differencing (available in both frames).

The user must specify a grid. Although it would seem desirable to use a very fine grid to resolve small-scale flows, if the density of the particles is too low then the detail will not be captured (Nokes 2014). The interpolation scheme used is based on Thiessen Triangulation (Cline and Renka 1984; Nokes 2014), and the velocity is estimated at a grid point, by obtaining a containing triangle, and interpolating linearly from the velocities of the particles at the triangle's corners (Nokes 2014). If a grid point is located outside the triangulation, the velocity is left undefined or extrapolation will be required. Therefore, data can be lost near the boundaries of the frame where particles may not be available. In this work, a grid with a resolution of 1 mm in both x and z directions is used, with extrapolation turned off.

6.2.4 Plunging Breaker Results

Figure 6.18 and Figure 6.19 show the time series for the horizontal and vertical velocity components, respectively. The results are obtained from the experiments conducted with a tilted field of view (FOV), with all of the five runs (black) presented, and the ensemble-average of the same five experiments overlaid (red). The results have not been smoothed in any way but have been converted into the x-z coordinate system using

$$u = \cos(\alpha)u_r - \sin(\alpha)w_r, \tag{6.3}$$

$$w = \sin(\alpha)u_r + \cos(\alpha)w_r, \tag{6.4}$$

where u_r and w_r are the vertical and horizontal components of velocity in the rotated system.

The horizontal velocity is very repeatable, with few large deviations away from the ensemble-averaged series in any of the five runs. Although there is some noise around the maximum backflow in Figure 6.18, the results are generally considered to be good. The vertical velocity time series is noisier, although it is worth noting that the scale is much smaller than in the horizontal component. Therefore, any noise in the horizontal direction will generally be less obvious than in the vertical direction. There are also some large spikes in the vertical velocity: for example at around 22 s in Run 5. This could either be due to a badly matched

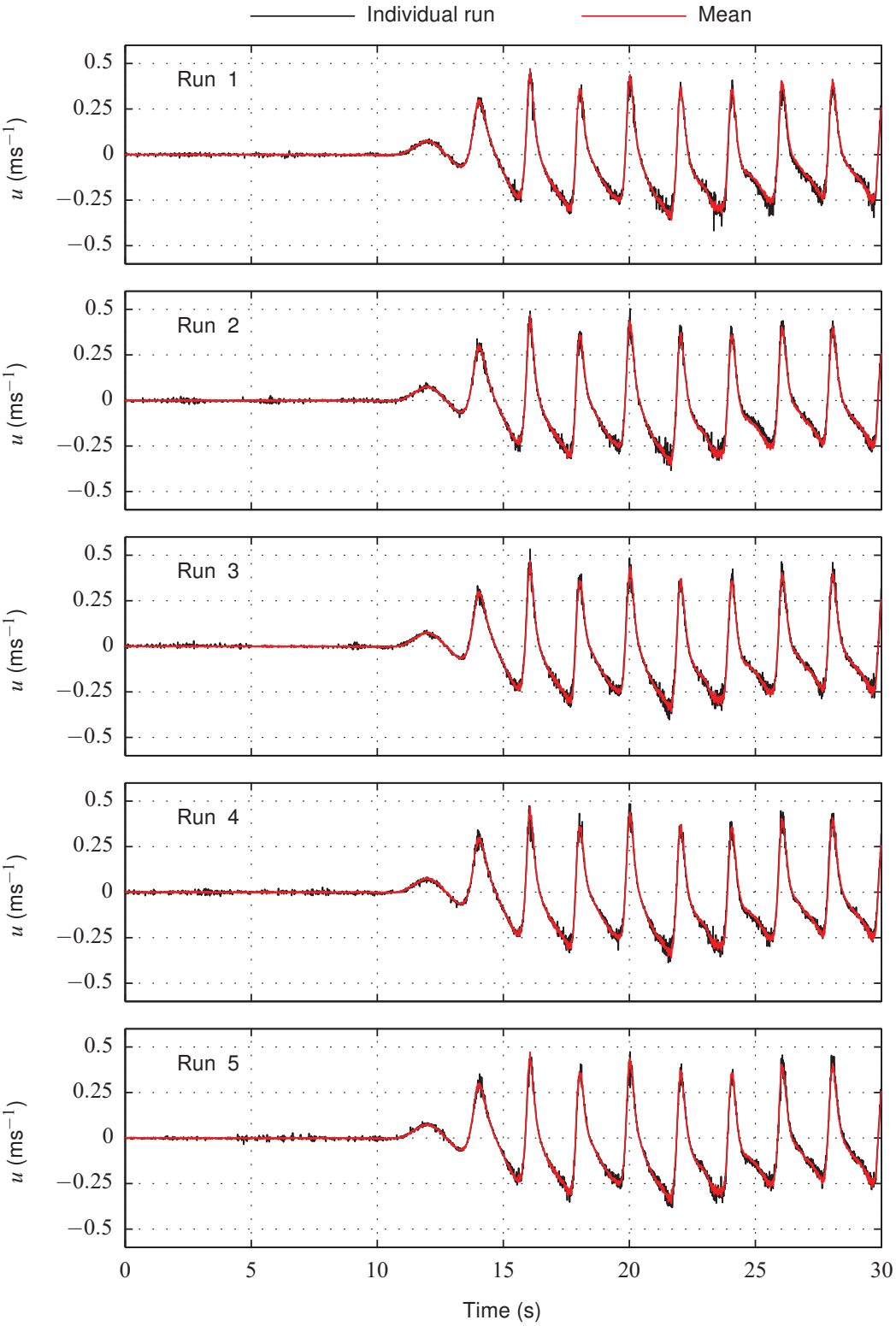

Figure 6.18: Time series of the horizontal velocity, sampled 1 cm above the bed at the point of breaking in the plunging case. All five runs (black) of the plunging breaker case with the tilted orientation are presented, along with the ensemble-average of the runs (red).

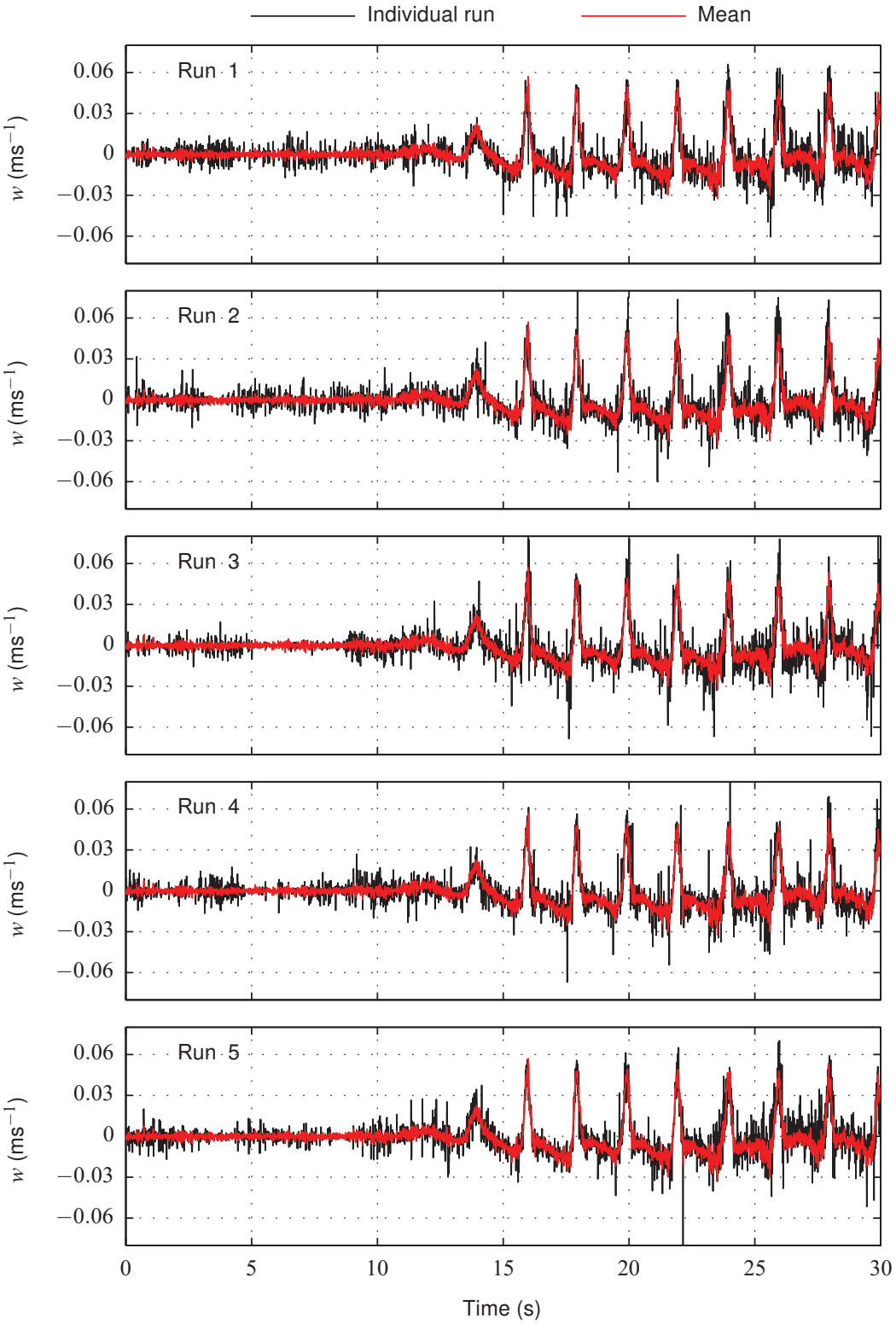

Figure 6.19: Time series of the vertical velocity, sampled 1 cm above the bed at the point of breaking in the plunging case. All five runs (black) of the plunging breaker case with the tilted orientation are presented, along with the ensemble-average of the runs (red).

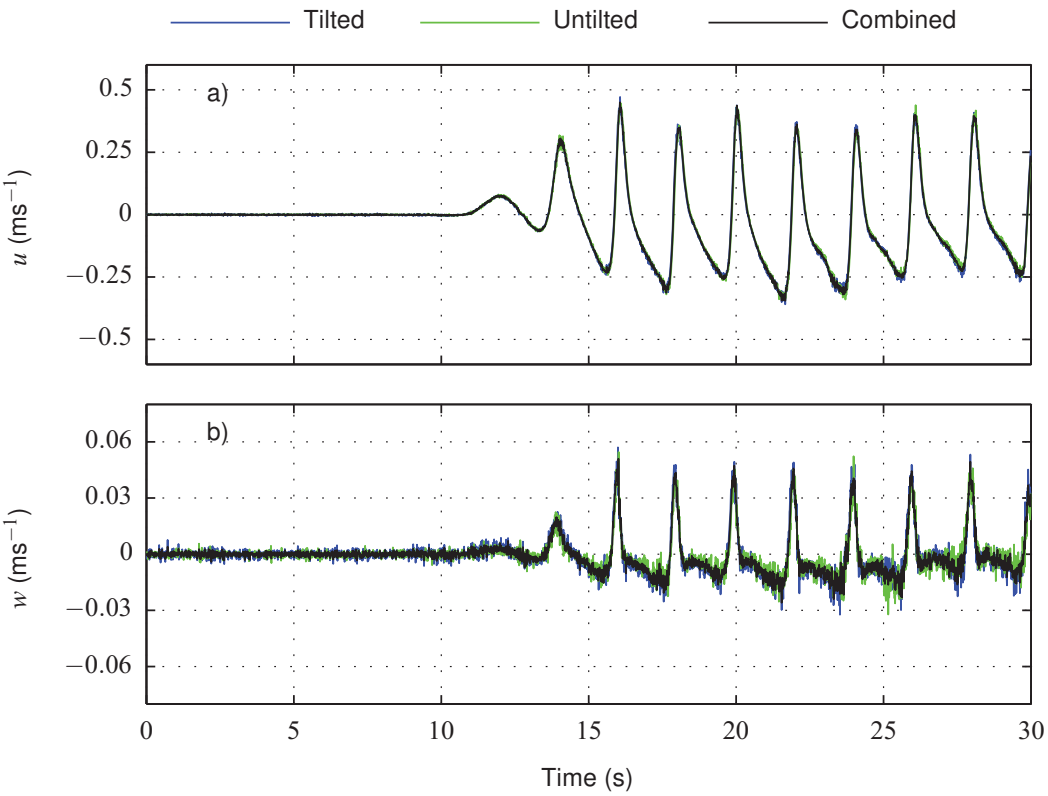

Figure 6.20: Ensemble-averaged time series from the normal (green) and tilted (blue) orientations of a) horizontal, and b) vertical velocity, sampled 1 cm above the bed at the breaking point in the plunging case. Also shown is the ensemble-average of a combination of the results from both orientations (black).

particle, a lack of particles around the point of interest at this time or turbulence. Despite these bad matches, the ensemble-averaged time series generally agrees well with all of the five runs, and a lot of the noise has been removed through the averaging process.

Figure 6.20 shows the ensemble-averaged profiles of a) horizontal velocity, and b) vertical velocity obtained from the tilted experiments and untilted experiments. As can be seen in the figure, both orientations of the camera yield similar results, and neither exhibit the same profile shape observed by Otsuka and Watanabe (2012). Taking this into consideration, and to give more confidence in the in-house results, both sets of results have been combined to give an ensemble-average over ten runs. This combined ensemble-average profile will now be compared to the CFD results.

A simulation using the same numerical setup described in Section 6.1 was run. The only dif-

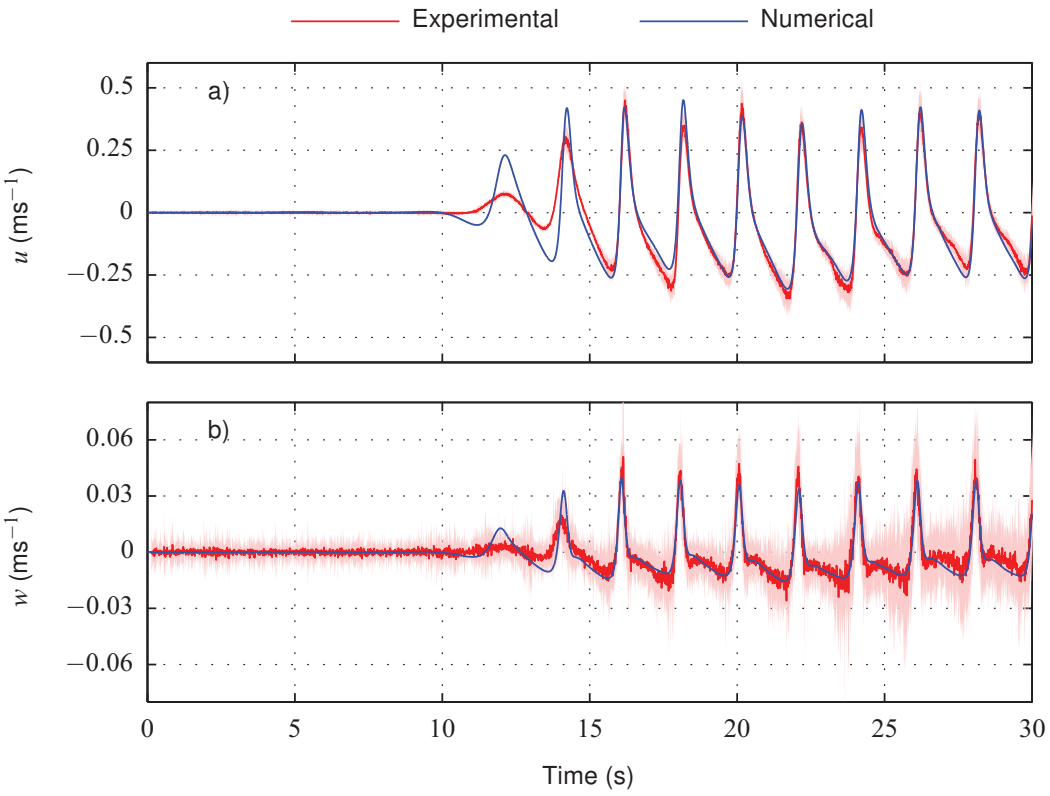

Figure 6.21: Comparison of the numerical predictions (blue) and in-house experimental data (red) for a) horizontal, and b) vertical velocity components, sampled 1 cm above the bed at the breaking point of the plunging breakers. The experimental time series are the ensemble-average obtained from both normal and tilted orientations, with the shaded region indicating the 95% confidence interval.

ferences being that a water depth of 0.5 m has been used instead of 0.6 m and the numerical wave flume is setup to match the full length of the flume at COAST laboratory. Figure 6.21 shows a comparison between the numerical and physical results. The full 30 second time series at the point 1 cm above the bed at the breaking depth stated in Otsuka and Watanabe (2012) is illustrated with the top and bottom plots representing horizontal and vertical velocity, respectively. Also shown is the 95% confidence interval (CI), which is indicated by the shaded region in the plots and was obtained using 1.96σ, where σ is the standard deviation of the 10 runs. The numerical results have been shifted slightly so that the waves are in phase. This shift could have been caused by slight delays between the camera and wave maker or alternatively due to the different ramp up algorithms. The differences in the ramp up period can clearly be seen in the first wave, occurring at around 12 seconds.

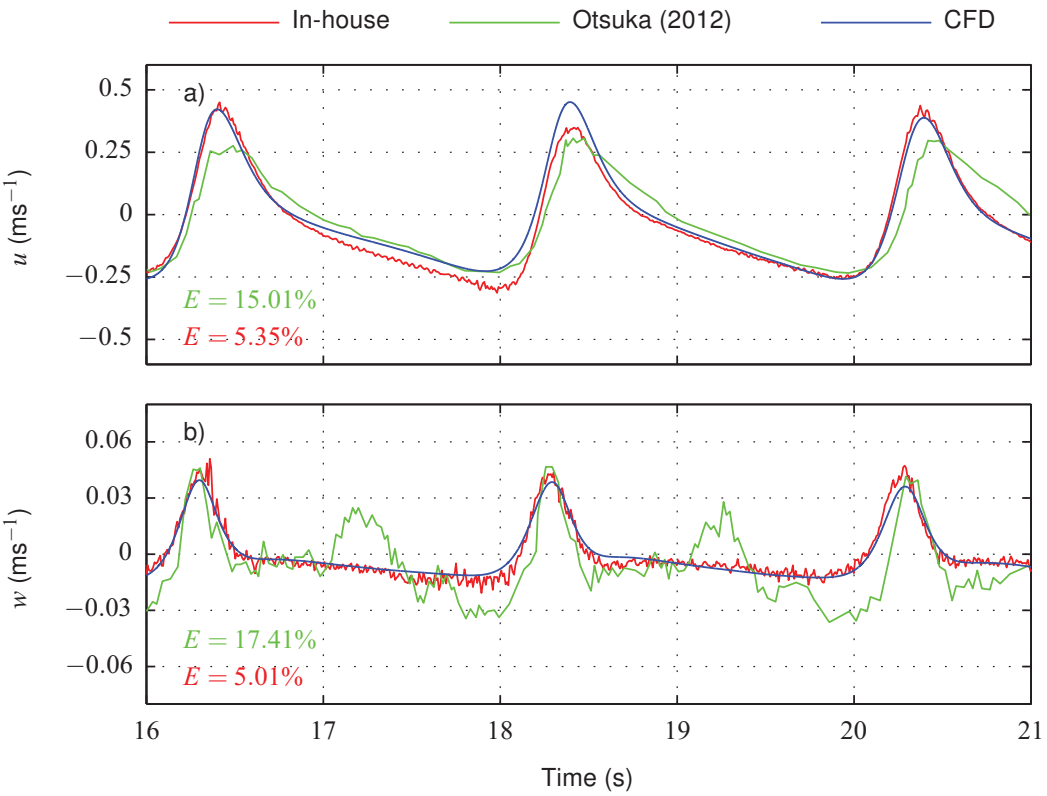

Figure 6.22: Comparison of the numerical predictions (blue) with the in-house (red), and Otsuka and Watanabe (2012) (green), experimental time series for a) horizontal, and b) vertical velocity components sampled 1 cm above the bed at the breaking point of the plunging breakers. The NRMSE (E) of the numerical predictions relative to each experimental time series is indicated in the corresponding colour.

The vertical velocity series does not show any evidence of the second peak, observed in the data of Otsuka and Watanabe (2012), at any point in the 30 second experiment. Instead, the velocity time series measured in the in-house experiments are predicted well by the CFD model. Other than the previously mentioned ramp up period, the model prediction lies within the 95% CIs of the experimental data. In the downward velocity phases of the wave period, the agreement is particularly good. However, the model consistently under-predicts the maximum upward velocity. The predictions of the horizontal velocity are also agreeable but there are times where the model falls outside of the 95% CI.

Figure 6.22 shows the 5 s sample presented by Otsuka and Watanabe (2012) (green) of a) the horizontal and b) the vertical velocity component. The corresponding in-house ex-

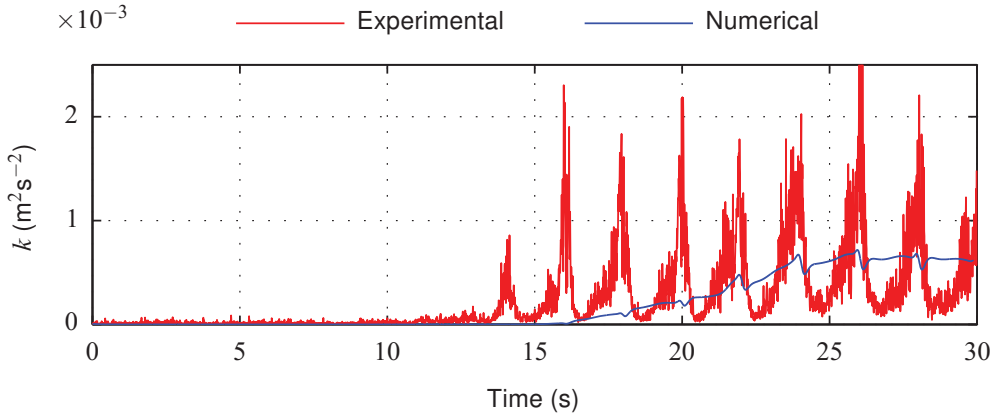

Figure 6.23: Comparison of the numerical predictions (blue) of near-bed TKE, sampled 1 cm above the bed at the breaking point, with the in-house experimental series (red) for the plunging breaker case. The experimental time series was obtained by isolating the fluctuating components of velocity and using equation (6.5).

perimental and CFD results are also shown, but have been shifted so that the first peak in the plot are aligned. The NRMSE (E) of the numerical predictions, with respect to the experimental studies, is presented in the corresponding colour to the data. As noted previously when analysing Figure 6.21, neither the CFD nor the in-house experiments exhibit the second peak that is evident in the vertical velocity data of Otsuka and Watanabe (2012). Furthermore, the minimum observed by Otsuka and Watanabe (2012) before the maximum upward velocity (i.e. around 18 and 20 seconds), is not predicted by the model or apparent in the in-house experiments. The horizontal velocity predictions agree reasonably well with both experimental data sets. Out of the three wave periods shown, the first and third predictions agree well with the in-house experiments. However, the backflow observed in the first period in the in-house experiments is much larger than observed in Otsuka and Watanabe (2012) or the present model, which agree well. Overall, the numerical predictions agree better with the in-house experiments, with a NRMSE of 5% for both velocity components, as opposed to the 15% and 17% calculated relative to the horizontal and vertical velocity presented by Otsuka and Watanabe (2012), respectively.

However, some differences are evident in the TKE comparison. Figure 6.23 compares the TKE data obtained from the in-house experiments and the numerical predictions for the plunging breaker case. The experimental TKE was obtained in the standard way: the

ensemble-averaged velocity components were used to calculate the fluctuations, u' and w' for each run. The TKE is then calculated using

$$k = \frac{2}{3}(u' + w')^2. \tag{6.5}$$

This gives a TKE time series for each run, and is then used to create an ensemble-averaged TKE, which is the value plotted in Figure 6.23. The experimental series exhibits a periodic spike in TKE which is not captured by the numerical model. The magnitude of the TKE is similar and the model does have a periodic rise and fall but the range of TKE in a period is much smaller than in the experiments. There could be many reasons for this. The TKE from the experiments was obtained using individual time series which still included noise from the PTV method, which could lead to a much larger TKE magnitude. Furthermore, the numerical model may not be capable of capturing the rapid change in TKE caused by the breaking wave. This could have a large effect on the numerical model's ability to predict suspended sediment concentrations and, hence, future work will need to be conducted to improve turbulence predictions.

Overall, the experiments have provided confidence in the model's ability to predict near-bed horizontal and vertical velocity under plunging breakers. In particular they have allowed differences between the model and the data gathered by Otsuka and Watanabe (2012) to be investigated. Since the model agrees better with the in-house experiments, it is assumed that the results presented by Otsuka and Watanabe (2012) are affected by the way the velocity is being measured or by differences in the experimental setup. The cause of the second peak in Figure 6.8 could be due to the use of intrusive measurement devices or the non-uniformity in the join between sediment and fixed bed (see Figure 6.1), which is located near the breaking point according to the experimental sketches presented in Otsuka and Watanabe (2012).

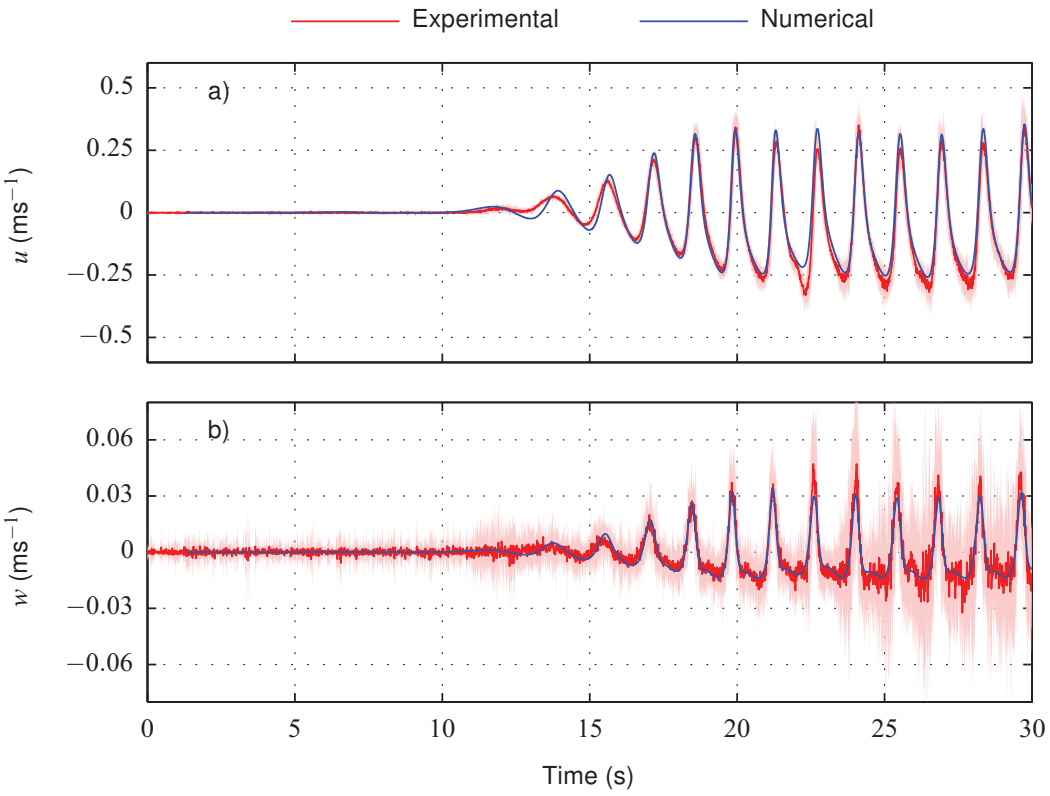

Figure 6.24: Comparison of the numerical predictions (blue) and in-house experimental data (red) for a) horizontal, and b) vertical velocity components, sampled 1 cm above the bed at the breaking point of the spilling breakers. The experimental time series are the ensemble-average obtained from both normal and tilted orientations, with the shaded region indicating the 95% CI.

6.2.5 Spilling Breaker Results

For completeness, the results of the spilling breakers case in the in-house experiments will be briefly discussed here. The results were obtained in the same way as in the plunging breakers analysis: i.e. five runs from the tilted camera and the five runs from the flat camera orientation were combined to create an ensemble-averaged result.

Figure 6.24 shows the spilling breaker equivalent of Figure 6.21. The ensemble-averaged horizontal (a), and vertical (b) time series obtained from the experiments and the numerical model are presented along with the 95% CI (shaded region). Many similarities to the plunging breakers case can be seen. Firstly, the model generally falls within the 95% CI, although the CI is much larger, especially near the end of the time series, indicating that

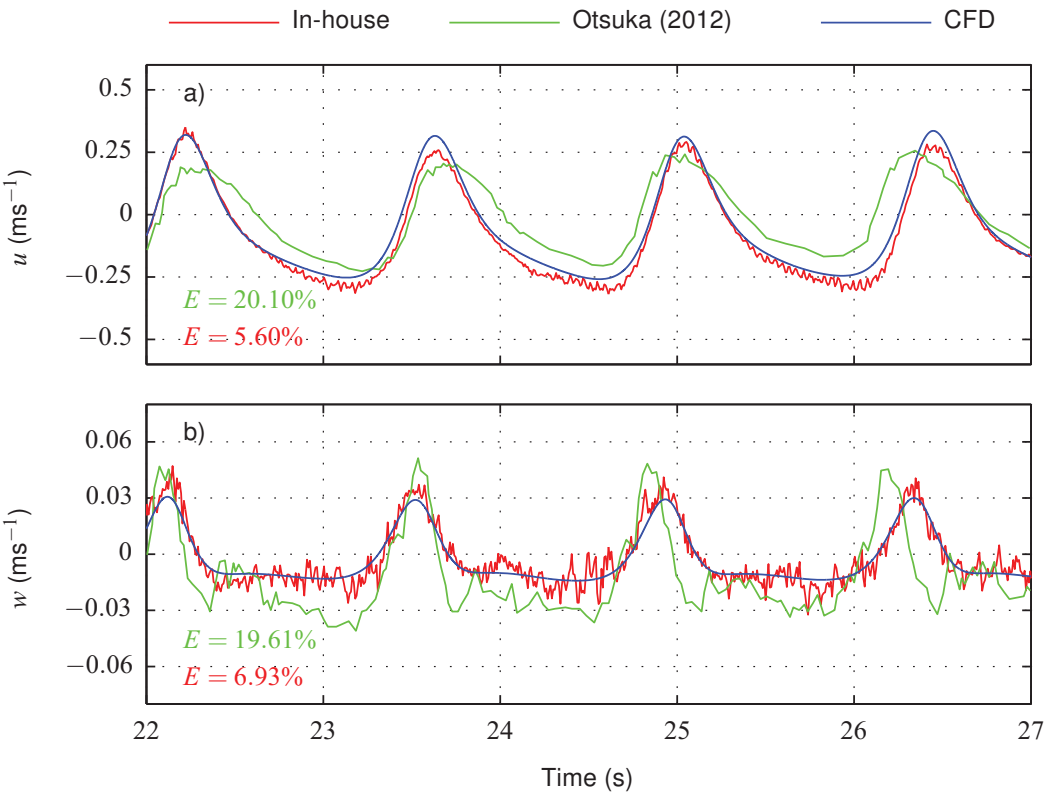

Figure 6.25: Comparison of the numerical predictions (blue) with the in-house (red), and Otsuka and Watanabe (2012) (green), experimental time series for a) horizontal, and b) vertical velocity components sampled 1 cm above the bed at the breaking point of the spilling breakers. The NRMSE (E) of the numerical predictions relative to each of the experimental results is indicated in the corresponding colour.

there is more variability between the different runs. Secondly, the vertical velocity is predicted better in the downward region than the upward, since the maximum upward velocity is generally under-predicted. Finally, the horizontal velocity follows the experiments well other than under-estimating the backflow in some wave periods. Overall the model seems to be doing a good job of capturing the near-bed velocity.

Figure 6.25 shows the 5 s sample (22 to 27 s) of a) horizontal and b) vertical velocity presented by Otsuka and Watanabe (2012) (green). Also shown are the CFD and in-house experimental results, which have been shifted to align all of the time series at the first peak in the vertical velocity plot. Similar to the plunging breakers, the vertical velocity predicted by the numerical model follows the in-house data set more closely than the data

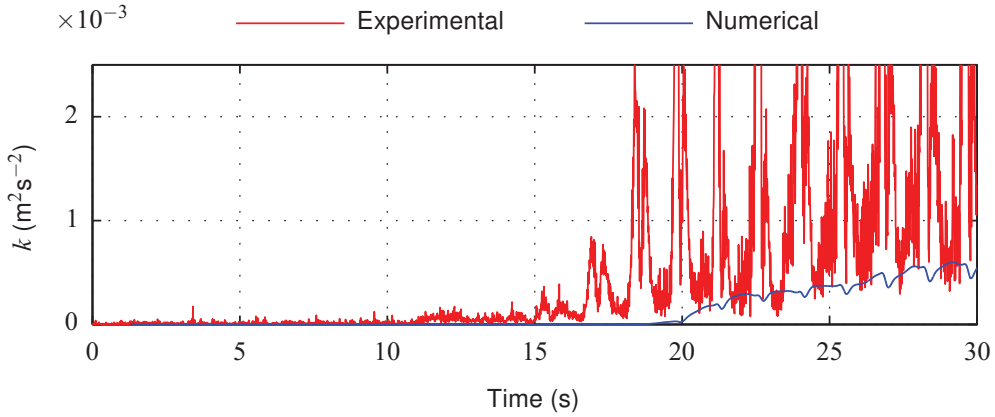

Figure 6.26: Comparison of the numerical predictions (blue) of near-bed TKE, sampled 1 cm above the bed at the breaking point, with the in-house experimental time series (red) for the spilling breaker case. The experimental time series was obtained by isolating the fluctuating components of velocity and using equation (6.5).

provided by Otsuka and Watanabe (2012). Furthermore, the discrepancies in wave period, noted in Section 6.1, in the Otsuka and Watanabe (2012) data are not observed in either the in-house experiments nor the numerical model. This can be seen in the last two waves presented in the plot, in both the horizontal and vertical velocity, where the peaks of the numerical model and in-house experimental data are still aligned, but the Otsuka and Watanabe (2012) data is not in phase. The horizontal velocity is also larger, in both positive and negative phases, in the numerical model and in-house experiments than observed by Otsuka and Watanabe (2012). Similar to the plunging breaker case, the numerical predictions agree better with the in-house experimental data than the data presented by Otsuka and Watanabe (2012), with errors of around 5% rather than 20%, for both velocity components. Therefore, the in-house experiments have helped to resolve some of the discrepancies noted in Section 6.1.

Figure 6.26 shows the TKE from the in-house spilling breaker experiments and the numerical model calculated using equation (6.5). The TKE time series obtained in the in-house experiments has a lot less structure than the one observed in the plunging breakers. This is probably due to the larger variation in vertical velocity runs as was noted when considering the CI earlier in this section. Taking this into consideration more runs would probably be required in order to get a more accurate description of the TKE. Furthermore, since the result

includes noise from the experimental methodology, the TKE is most likely much smaller than presented, which could explain the substantial under-prediction by the numerical model. As noted in the plunging case, not capturing the peaks in near-bed TKE could lead to substantial errors in predictions of suspended sediment concentrations. Since the peaks are under-predicted it is likely to lead to considerably smaller suspended sediment concentrations than observed in physical experiments due to a reduction in both entrainment and suspension time. Hence, further work should be conducted focusing on better understanding the discrepancies between the numerical model and experimental data. However, this is considered to be future work, and the present capabilities of the numerical model to predict suspended sediment concentrations will now tested.

6.3 Summary

The aim of this chapter was to validate the CFD model's ability to predict near-bed hydrodynamics. The data set which was used to validate this was gathered by Otsuka and Watanabe (2012). This data set also includes suspended sediment concentrations and will be used in Chapter 7 to validate the sediment model, that was developed by the present author as part of this work. Otsuka and Watanabe (2012) included instantaneous results for surface elevation, velocity and TKE, which were all compared to the numerical model, using the $k-\omega$ turbulence model since it was shown to be the best for TKE predictions in Chapter 5.

Although the predictions of the model were generally good, a few concerning features needed further investigation, such as a second spike of vertical velocity in each period at the breaking point observed in the experimental data set presented by Otsuka and Watanabe (2012). Experiments in the COAST wave flume at Plymouth University were conducted using a light box, high speed camera and the PTV software, Streams (Nokes 2014). The numerical model agrees better with the in-house experiments and many of the discrepancies with the Otsuka and Watanabe (2012) data set have been resolved. However, the TKE predictions did not follow the results of the in-house experiments so well, which could be due to the experimental methodology used to calculate these values. Future work clearly needs

to be conducted to further understand the discrepancies between the numerical model and experimental observations of near-bed TKE.

Given the success of the model validations in this chapter, the numerical model was then extended to include suspended sediment dynamics (SSD). The SSD formulations implemented in the model (see Section 4.5) will be discussed in Chapter 7.

Chapter 7

Validation III: Suspended Sediment

In this chapter the suspended sediment model, described in Section 4.5, is validated with the `waves2Foam` code. A series of validation tests are presented of increasing complexity. The first test considers suspended sediment transport under steady, purely diffusive flow conditions, which allows the code to be verified against an analytical solution. The second test examines steady state advection-diffusion conditions, and compares to experimental data obtained in tilting flumes (Sumer et al. 1996; Cellino 1998). This test case is used to analyse the sensitivity of the numerical model to various parameters, with particular emphasis placed on the near-bed mesh resolution. The numerical predictions of near-bed concentrations under regular waves are then evaluated, and comparison made with experimental data obtained by Dohmen-Janssen and Hanes (2002), along with other numerical studies (Hsu and Liu 2004; Ma et al. 2014). The final tests are used to assess the performance of the model under breaking waves. The numerical model is validated against laboratory data (Sato et al. 1990; Otsuka and Watanabe 2012), of similar scale and setup as the data used to validate the hydrodynamics in Chapter 5 (Ting and Kirby 1994). Further comparison with other numerical models is also performed (Hsu and Liu 2004; Ma et al. 2014).

This chapter is organised so that the purely diffusive and steady state flow conditions are presented in Sections 7.1 and 7.2, respectively. Regular waves are then analysed in Section 7.3, before breaking waves are considered in Section 7.4. Finally the conclusions are drawn in Section 7.5.

7.1 Case 1: Purely Diffusive Flows

The tests in this section are based on steady, purely diffusive flow conditions, and use a constant diffusivity profile, either uniform, or parabolic, with depth. They have been presented to verify that the numerical model performs as expected when only the diffusion term is included, i.e. the flow advection term is neglected from equation (4.81).

The OpenFOAM® solver "`scalarTransportFoam`" has been adapted to include the effects of the settling velocity. The original `scalarTransportFoam` solves an advection-diffusion equation for a passive scalar in a steady velocity field and a constant diffusivity defined by the user. For the purpose of the present tests, the flow advection term is neglected and the advection occurs through settling of the sediment particles. Therefore, the advection term is based on the settling velocity field, $\mathbf{w_s}$, rather than a flow field **u**, and the equation that is being solved is

$$\frac{dC}{dt} + \nabla \cdot (\mathbf{w_s} C) = \nabla \cdot (\nu_s \nabla C). \tag{7.1}$$

A domain of length (x) 2 m, height (z) 0.1 m and width (y) 0.01 m has been created with a discretisation of $\Delta x = \Delta y = 0.01$ m and $\Delta z = 0.0001$ m. The side walls and top are modelled as walls whereas the bottom boundary is considered to be a sediment bed. The sediment settling velocity is set to $0.02\,\mathrm{m\,s^{-1}}$, which corresponds to sediment with a mean diameter of $d = 0.15$ mm (fine sediment).

The boundary condition for the concentration on the bottom boundary is fixed to the maximum attainable concentration $0.65\,\mathrm{m^3\,m^{-3}}$ suggested by Fredsøe and Deigaard (1992) (see Section 3.3.3.4). In these tests, the entrainment and deposition boundary condition is not used, but instead sediment only enters the domain through the diffusion term in equation (7.1). Therefore, sediment will only enter the domain if the diffusion term is larger than the advective term (the settling velocity term) at the bottom boundary. At the top wall, the settling velocity is set to (0,0,0) and a zero gradient condition is used for the concentration. This ensures that sediment does not enter from the top boundary.

The solver iterates until an acceptable tolerance is reached, which for these purely diffusive flow tests is set to 1×10^{-6} based on the information presented in the OpenFOAM® user manual (Greenshields 2015).

7.1.1 Constant Sediment Diffusivity

Assuming that the sediment diffusivity is constant and depth independent, an analytical solution of equation (7.1) can be obtained, which for the present tests, takes an exponential form

$$C = 0.65 \exp\left(-\frac{w_s}{\nu_s} z\right), \tag{7.2}$$

where ν_s is the specified value for the sediment diffusivity coefficient. Simulations were run with ν_s ranging from $1 \times 10^{-5}\,\mathrm{m^2\,s^{-1}}$ up to $1 \times 10^{-2}\,\mathrm{m^2\,s^{-1}}$ to determine whether the model accurately predicts the analytical solution in each case.

Figure 7.1 compares the concentration profiles given by the numerical model with the analytical solution. The individual plots represent different sediment diffusivities: $\nu_s =$ a) $1 \times 10^{-5}\,\mathrm{m^2\,s^{-1}}$, b) $1 \times 10^{-4}\,\mathrm{m^2\,s^{-1}}$, c) $1 \times 10^{-3}\,\mathrm{m^2\,s^{-1}}$ and d) $1 \times 10^{-2}\,\mathrm{m^2\,s^{-1}}$, with the normalised root mean square error (NRMSE) (E) indicated for each case in the corresponding plot. Note that in Figure 7.1a and Figure 7.1b, the concentration has been plotted on a logarithmic scale. For the largest three cases (Figure 7.1b-7.1d) the model almost perfectly predicts the analytical solution, with NRMSE of less than 0.7% in each case. However for the smallest case (Figure 7.1a) the first sampling point above the bed agrees well, but above this location the concentrations become very small (below 1×10^{-10} g/l) and discrepancies between the numerical and analytical results occur, leading to a large error of 160%. This is assumed to be due to numerical artefacts such as rounding errors, which will be more substantial for small concentrations (of the order 10^{-10} in this case). Furthermore, these errors are considered to be acceptable for such small magnitudes of concentration.

7.1.2 Parabolic Sediment Diffusivity

The numerical model has been shown to work for a constant sediment diffusivity that is uniform with depth. In this section, a constant sediment diffusivity profile, that is parabolic with

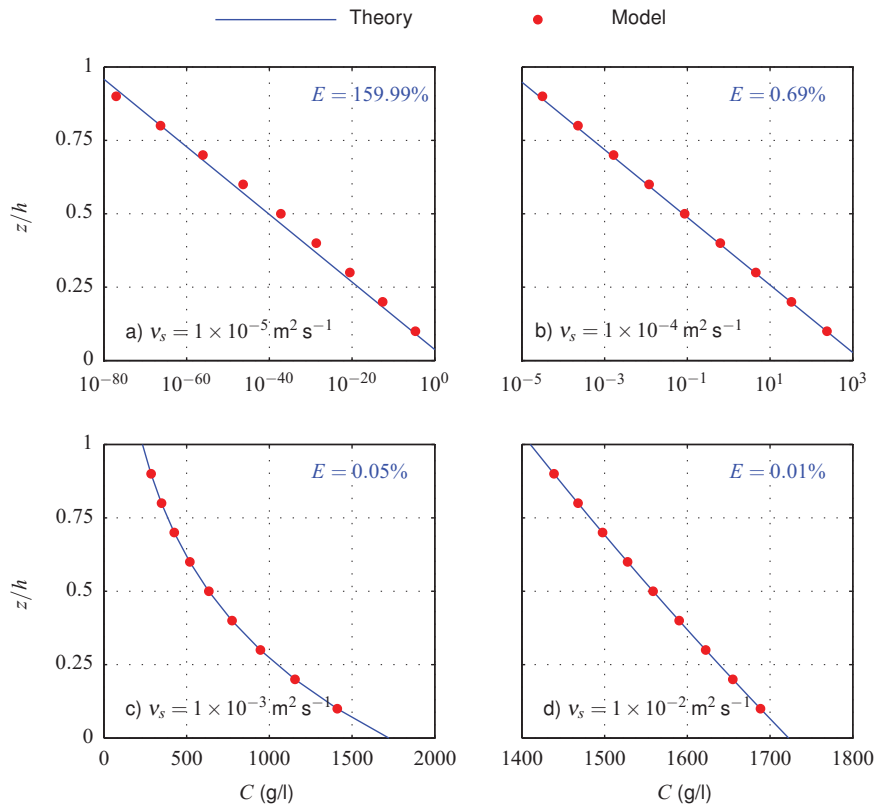

Figure 7.1: Plots comparing the analytical and model concentration profiles in a purely diffusive flow condition. A range of constant sediment diffusivities are shown: $v_s =$ a) $1 \times 10^{-5}\,\mathrm{m^2\,s^{-1}}$, b) $1 \times 10^{-4}\,\mathrm{m^2\,s^{-1}}$, c) $1 \times 10^{-3}\,\mathrm{m^2\,s^{-1}}$ and d) $1 \times 10^{-2}\,\mathrm{m^2\,s^{-1}}$. The NRMSE ($E$) for each case is indicated in the corresponding plot.

depth, is used with the aim of obtaining the Rouse profile (see Section 3.3.4.1). Therefore the sediment diffusivity is set such that

$$\nu_s = \kappa u_* z \left(1 - \frac{z}{h}\right), \tag{7.3}$$

with the value of u_* set arbitrarily at $0.05\,\mathrm{m\,s^{-1}}$. Since the parabolic profile becomes zero at the wall, an artificial value was used on the sediment boundary to ensure that sediment entered the domain. This was arbitrarily set to $1 \times 10^{-5}\,\mathrm{m^2\,s^{-1}}$. Figure 7.2a shows the sediment diffusivity profile described by equation (7.3) for this case.

Introduction of this parabolic sediment diffusivity allows an analytical solution to be obtained

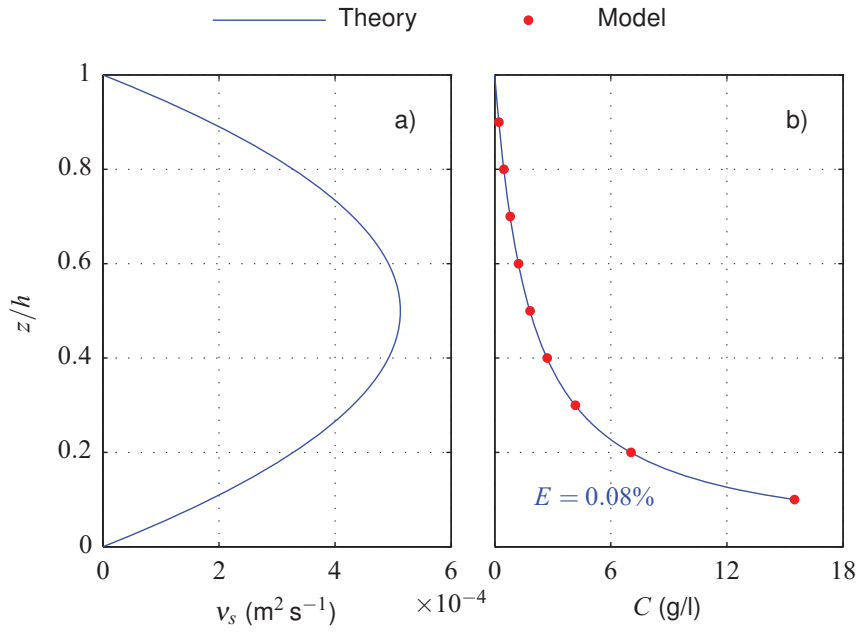

Figure 7.2: Verification of the suspended sediment model in a purely diffusive flow with a parabolic sediment diffusivity profile with depth (a). Comparison of the analytical (line) and numerically predicted (•) concentration profiles (b) is presented along with the NRMSE.

(see Section 3.3.4.1), which takes the form

$$C = C_a \left(\frac{h-z}{h-z_a} \cdot \frac{a}{z} \right)^{\frac{w_s}{\kappa u_*}}, \tag{7.4}$$

where C_a is the concentration at the reference height, z_a, set to 1 cm above the bed for this test. Figure 7.2b presents the concentration profile predicted by the numerical model and the analytical solution given by equation (7.4). As expected, the profile predicted by the numerical model has almost perfect agreement with the Rouse profile, with an error of 0.08%. Hence the diffusion term is considered to be working as expected for a given sediment diffusivity profile. Furthermore, obtaining the analytical solutions, which are based on the settling velocity, verifies that this effect has been correctly introduced into the numerical model.

7.2 Case 2: Steady State Advection-Diffusion

In this section, the suspended sediment concentration model is tested under steady state advection-diffusion flow conditions, to check that realistic results are obtained, both in terms of magnitude and vertical distribution. This also allows verification of the entrainment-deposition flux boundary condition, that has been developed as part of this work, and is described in Section 4.5.1. To determine whether the model predicts this profile correctly, comparison is made with existing experimental data for horizontal channel flows, obtained in tilting flumes. As well as conducting their own experiments, Cellino (1998) summarised channel flow data from a number of other sources including Sumer et al. (1996). Both the data presented by Cellino (1998) and the data gathered by Sumer et al. (1996), summarised by Cellino (1998), will be used for validation in this work.

Sumer et al. (1996) conducted 158 runs in a 10 m tilting flume with varying fluid flow speeds, water depths, and sediment sizes. However, vertical concentration distributions have only been presented for nine of these runs by Sumer et al. (1996). This data, digitised by Cellino (1998), is used for comparison in this section. A summary of the experimental properties used for simulations in this section is presented in Table 7.1.

7.2.1 Numerical Setup

The simulation domain is a horizontal channel of length 10 m containing water between two plates. The inlet boundary condition is set to the mean velocity specified by Sumer et al. (1996), and the concentration is set to a fixed value of zero, corresponding to clear water. The initial condition for the concentration in the internal domain is also considered to be clear water. The outlet boundary condition uses a zero gradient condition for all variables. The settling velocity is set to zero at the top boundary so that sediment cannot be introduced from this boundary. Although setting the concentration to zero at this boundary would have a similar effect, it was found that doing so caused changes in the vertical suspended sediment distribution and hence the theoretical profiles discussed in Section 7.1 could not be obtained. The top and the bottom boundaries are assumed to be walls and have no-slip boundary conditions applied to them. Setting the velocity to a uniform value at the inlet

Name	Study	Type	d	s	w_s	h	u
		-	mm	-	ms^{-1}	m	ms^{-1}
Run 112	Sumer et al. (1996)	acrylic	0.6	1.13	0.02	0.1115	0.402
Run 120	Sumer et al. (1996)	acrylic	0.6	1.13	0.02	0.1135	0.537
Run 126	Sumer et al. (1996)	acrylic	0.6	1.13	0.02	0.118	0.636
Run 133	Sumer et al. (1996)	acrylic	0.6	1.13	0.02	0.1243	0.721
Run 137	Sumer et al. (1996)	acrylic	0.6	1.13	0.02	0.1322	0.773
Run 142	Sumer et al. (1996)	sand	0.13	2.65	0.012	0.1032	0.833
Run 150	Sumer et al. (1996)	sand	0.13	2.65	0.012	0.1009	1.024
Run 155	Sumer et al. (1996)	sand	0.13	2.65	0.012	0.1046	1.138
Q50S01	Cellino (1998)	sand	0.135	2.65	0.012	0.12	0.792
Q57S0175	Cellino (1998)	sand	0.135	2.65	0.012	0.12	0.855
Q60S02	Cellino (1998)	sand	0.135	2.65	0.012	0.12	0.905
Q70S025	Cellino (1998)	sand	0.135	2.65	0.012	0.12	0.917
Q50S01_II	Cellino (1998)	sand	0.23	2.65	0.021	0.12	0.801
Q57S0175_II	Cellino (1998)	sand	0.23	2.65	0.021	0.12	0.836
Q60S02_II	Cellino (1998)	sand	0.23	2.65	0.021	0.12	0.850
Q70S025_II	Cellino (1998)	sand	0.23	2.65	0.021	0.12	0.868

Table 7.1: Details of test cases used to validate the model in steady state advection-diffusion flow conditions. The name and experimental study are given along with sediment type, diameter (d), ratio between sediment and fluid densities (s), sediment settling velocity (w_s), channel depth (h), and mean flow velocity (u).

has the consequence that the boundary layer is not initially present, and only develops as the flow progresses along the channel. The absence of a boundary layer would lead to an over-prediction of the friction velocity at this part of the channel, since the near-wall velocity would be much greater. To limit the consequences of this problem, the bottom boundary has been split into two regions (see Figure 7.3). A 4 m inlet region is considered to be a wall and hence does not release sediment. The remaining segment of the boundary represents a sediment bed, which uses the new boundary condition to evaluate the balance of entrainment and deposition. All results presented in this section are sampled at $x = 7$ m, the centre of the sediment bed, unless otherwise stated.

The domain is modelled as horizontal, rather than tilted, with the critical Shields parameter adjusted as if the slope existed (see Section 4.5.1). It is assumed that by making this adjustment and setting the correct mean velocity, modelling a horizontal domain will not substantially affect the results since the angles to the horizontal are minimal (less than $0.5°$).

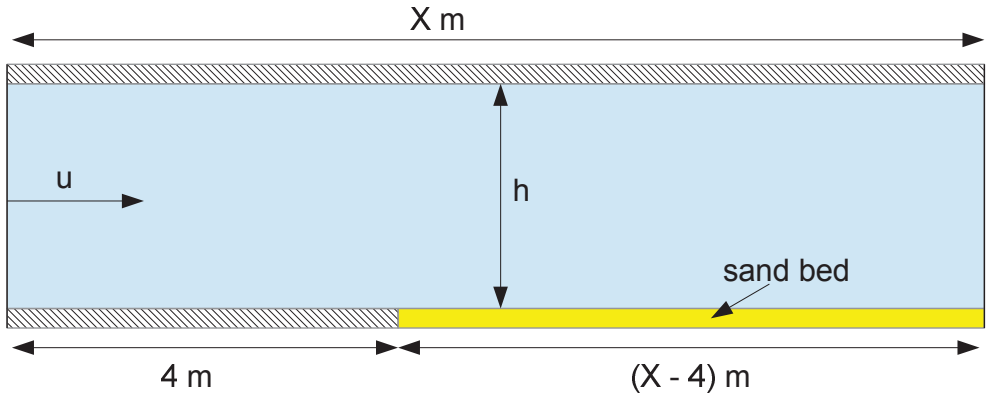

Figure 7.3: Domain setup for the channel flow numerical simulations. The yellow region represents the sediment bed which uses the entrainment-deposition balance approach, developed as part of this work, as the boundary condition. X is $10\,\text{m}$ for comparison with Sumer et al. (1996) or $16\,\text{m}$ for Cellino (1998), with h and u varying according to the case (see Table 7.1).

Since a free surface is not present, it is unnecessary to use a volume of fluid (VOF) solver. Furthermore, as the inlet is set to a constant velocity, the simulation should converge to a steady state. Therefore, in this section, `simpleFoam`, a steady state solver for incompressible, turbulent flows, is used to obtain the fluid properties. The values for the eddy viscosity and velocity are then used as the input to a modified version of `scalarTransportFoam`, which solves the governing equation (equation 4.81) for the suspended sediment model (with the flow advection term included), along with the entrainment-deposition flux boundary condition, described in Chapter 4, to obtain predicted suspended sediment concentrations. For the simulations in this section, the settling velocity has been fixed to the value stated by Sumer et al. (1996) or Cellino (1998).

For consistency, the $k-\omega$ model is applied in this section as it was shown to be the best model for predicting turbulence under breaking waves (Chapter 5), and hence is used when considering breaking waves in Section 7.4. The inlet turbulent quantities are calculated in the same way as for the breaking waves (equation 5.2), except that the mean velocity, rather than the phase velocity has been used. Sensitivity analysis of the inlet conditions showed that the choice of turbulent boundary values does not considerably influence the results in these flow conditions. Therefore, the turbulence intensity is set to $I = 1\%$ and, based on

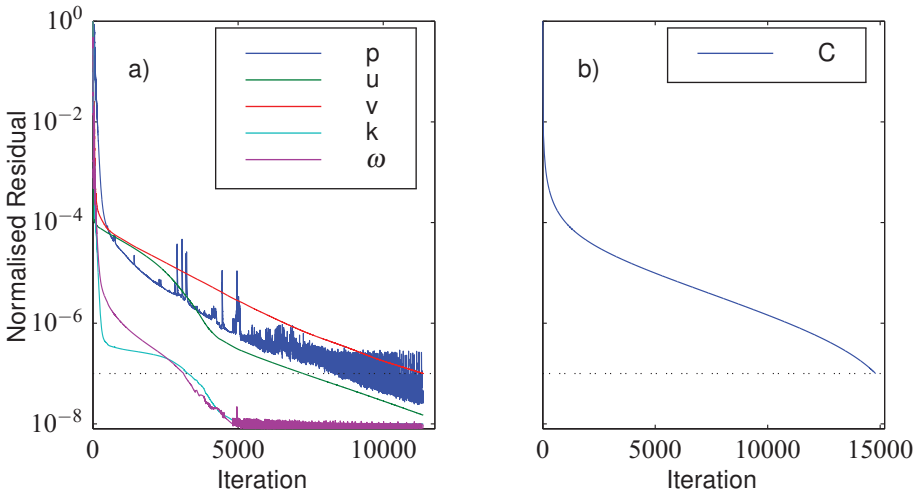

Figure 7.4: Example of the convergence of the steady state advection-diffusion simulations (Q50S01 from Cellino (1998)). The plots represent normalised residuals against number of iterations for a) the fluid variables, and b) simulation for sediment concentration, using converged values from plot a as the flow parameters. The dashed line is the user specified tolerance, which indicates when convergence has been achieved.

the results of the initial sensitivity analysis, the eddy viscosity to fluid viscosity ratio is set to $\zeta = 1000$. At the top and bottom boundaries, wall functions are used, whereas at the sand bed, rough wall functions have been applied, setting the roughness constant to $k_N = 2.5d$, and C_s to 0.5. The size of the cell adjacent to the bottom boundary has been fixed so that the cell centre is at a reference height of k_N, i.e. the cell height is set to $2k_N$.

The `simpleFoam` solver utilises the steady state Semi-Implicit Method for Pressure-Linked Equations (SIMPLE) algorithm (see Section 4.2.2), for the velocity-pressure coupling. Therefore the solver iterates until the residuals are small enough for the model to consider that a steady state has been achieved. The convergence and relaxation criterion are shown in Table 7.2 for all of the variables in the model. Note that `simpleFoam` uses the total pressure, p, rather than the non-hydrostatic component, $p_{rgh} = p - \rho g h$, used by the `interFoam` solver. The `simpleFoam` solver is initially run without the suspended sediment model to determine the converged flow properties. This converged solution is then used as the flow conditions to drive the modified `scalarTransportFoam` simulations, which predict the suspended sediment concentrations. An example of the solver convergence (Q50S01 from

	p	u	w	k	ω	C
Residuals	1×10^{-7}	1×10^{-7}	1×10^{-7}	1×10^{-7}	1×10^{-7}	1×10^{-7}
α_p	0.3	0.7	0.7	0.95	0.95	1

Table 7.2: Residual convergence criterion and under-relaxation, α_p values for all of the variables solved in the steady state simulations.

	Mesh 1	Mesh 2	Mesh 3	Mesh 4	Mesh 5	Mesh 6
Δx (mm)	20	10	10	10	10	10
Δz (mm)	4	4	2	1	0.5	0.25
AR	5	2.5	5	10	20	40

Table 7.3: Details of the horizontal, vertical, and aspect ratio (AR) of the grids used in the grid refinement study, based on the flow conditions of run 155 presented by Sumer et al. (1996).

Cellino 1998) is shown in Figure 7.4. Variation in the maximum residuals, normalised by the characteristic convection-diffusion transport for a control volume (Jasak 1996), are presented as a function of iteration number for a) the `simpleFoam` simulation used to obtain the converged fluid variables, and b) is the `scalarTransportFoam` simulation for the sediment concentrations, which uses the fluid variables from the previous simulation as the initial condition. Note that the simulation terminates when all of the residuals for the different variables are below the user specified tolerance (Table 7.2), which is indicated by the dashed line in Figure 7.4.

7.2.1.1 Mesh Convergence

To determine the required grid resolution for the internal domain, a mesh refinement study is conducted. To do this the simulation with the most extreme flow properties (Run 155: $u = 1.138\,\mathrm{m\,s^{-1}}$, $h = 0.1046\,\mathrm{m}$) is used, fixing the cell size next to the sediment boundary to $2k_N$, as was previously discussed. The resolution next to the top boundary is also fixed and is set to $0.1\,\mathrm{mm}$, with an expansion ratio of 2 for the subsequent cells. Six grids were evaluated for five different Δz and two Δx. The Δz values range from 0.25 to $4\,\mathrm{mm}$. Since the VOF is not used in this solver, it is assumed that the aspect ratio (AR) does not need to remain close to one, and hence the range for Δx is $1-2\,\mathrm{cm}$. The grids used in this study are summarised in Table 7.3.

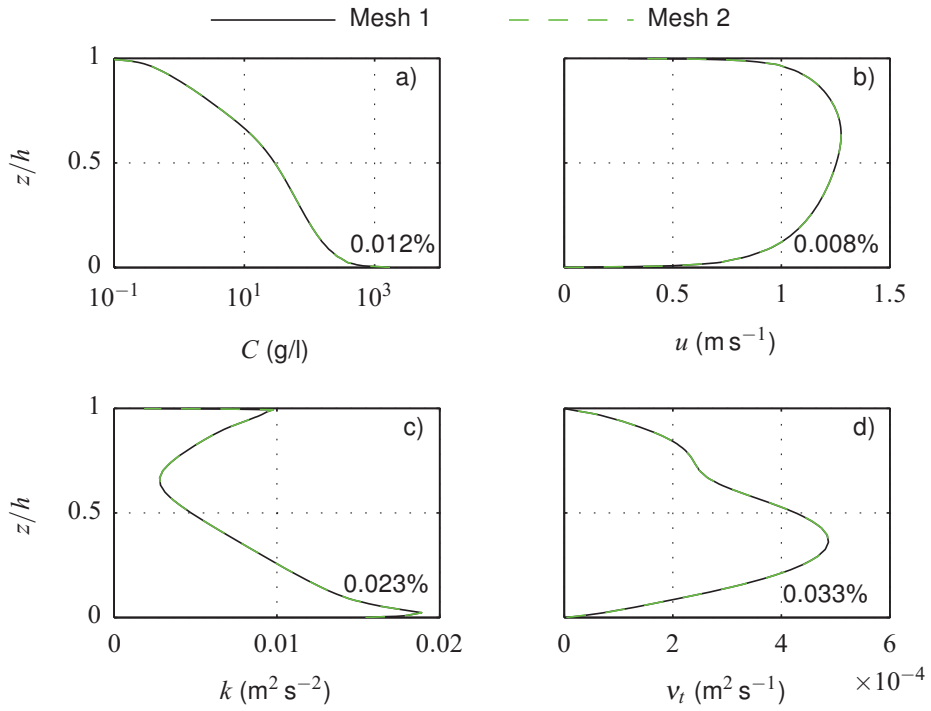

Figure 7.5: Comparison of a) sediment concentration, b) horizontal velocity, c) TKE, and d) eddy viscosity in steady state flow conditions (Run 155, Sumer et al. 1996) against normalised depth for Mesh 1 and 2. The relative difference between the two solutions is also presented on each plot.

Figure 7.5 compares the steady state solution of Mesh 1 and Mesh 2 for a) suspended sediment concentration, b) horizontal velocity, c) turbulent kinetic energy (TKE), and d) eddy viscosity, against normalised height above the bed. Visually, it is clear that the solution from both meshes are very similar. At the bottom right of each plot is the difference (in %) between the solutions on the two grids, computed using equation (5.3). These values are very small, confirming the visual observation that the solutions from both grids lie very close to one another. This indicates that the simulation is not overly sensitive to the value of Δx, most likely due to small variability in the horizontal flow conditions and hence is set to 10 mm for the rest of this section.

The vertical gradients of the profiles are much larger, and hence it is expected that the simulation is more sensitive to the vertical discretisation. Figure 7.6 shows the steady state results for five consecutively refined grids. Each subplot is a different variable: a) sus-

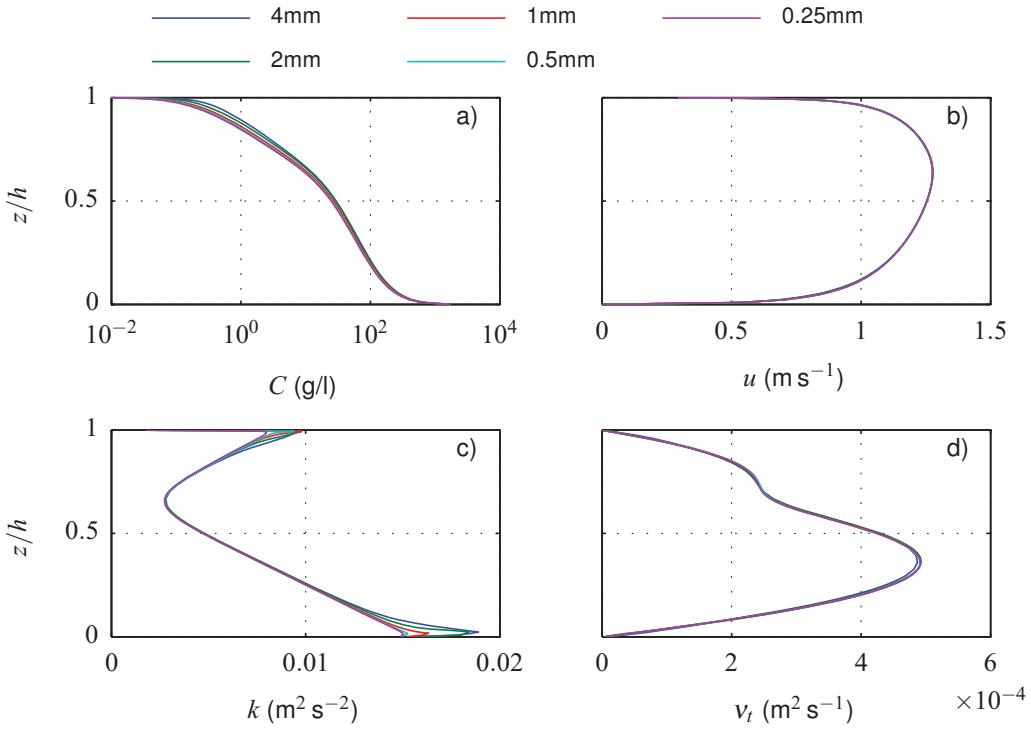

Figure 7.6: Comparison of a) sediment concentration, b) horizontal velocity, c) TKE, and d) eddy viscosity against normalised depth, in steady state flow conditions (Run 155, Sumer et al. 1996), for a range of different Δz.

pended sediment concentration, b) horizontal velocity, c) TKE, and d) eddy viscosity. Once again, visual observations imply that a converged solution has been found for the horizontal velocity since all of the simulations give very similar results. However, the other variables show some variability between simulations, particularly near the walls for the TKE.

Figure 7.7 presents a bar chart of the percentage difference (calculated using equation 5.3) between subsequent grid refinement levels, for each of the variables in the model. Choosing a 1% difference as the desired convergence criterion, it is clear that four of the variables (C, u, ν_t and ω) can be considered to be converged for all of the grids. However, the TKE and vertical velocity exhibit much larger differences: up to 2.5% for the first two refinement levels. The reason for the higher difference appears to be due to the near-wall TKE values as can be seen in Figure 7.6. The vertical velocity is also small, and hence any error will be more obvious in this parameter. After $\Delta z = 1$ mm the difference in both of these variables is much closer to the 1% level, indicating that there is a smaller jump in results after this

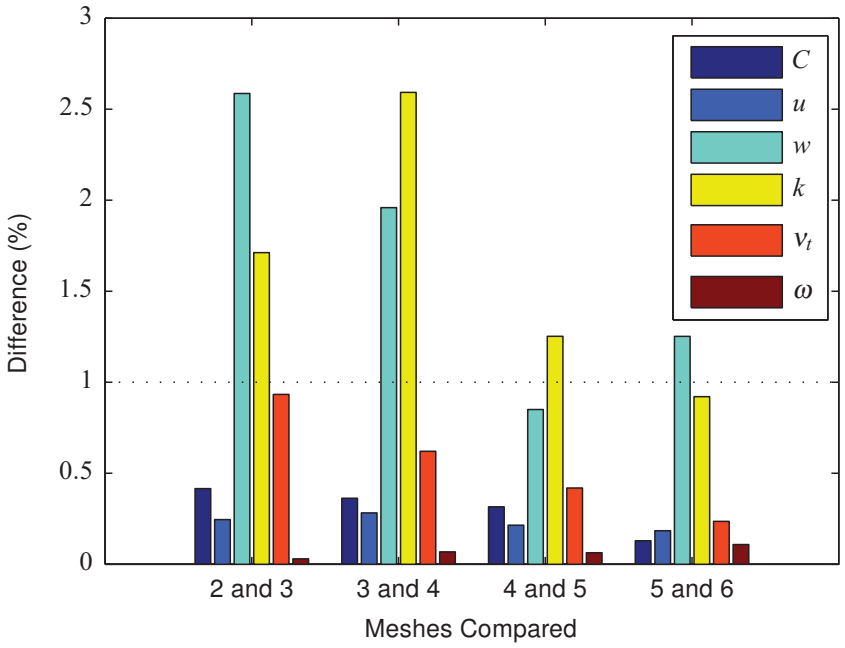

Figure 7.7: Bar chart presenting the relative difference (%) in solution for a number of variables with different vertical mesh refinement levels. The x-axis indicates the mesh numbers being compared (see Table 7.3 for details).

refinement level.

The concentration model relies on the velocity and eddy viscosity variables, so it is important that these values have converged. Since u and ν_t are considered to be converged in all of the simulations, for computational efficiency the mesh is chosen as the smallest refinement level to exhibit a difference of around 1% in w. Hence Mesh 4 ($\Delta z = 1\,\text{mm}$) will be used for the rest of this section.

7.2.2 Model Sensitivity to Near-Bed Cell Size

For a steady state flow, the entrainment-deposition method used at the sediment boundary in this work causes the concentration in the cell adjacent to the bed, C_{nb}, to converge to the value which balances the entrainment and settling velocity, i.e.

$$C_{nb} = \frac{E}{w_s}. \tag{7.5}$$

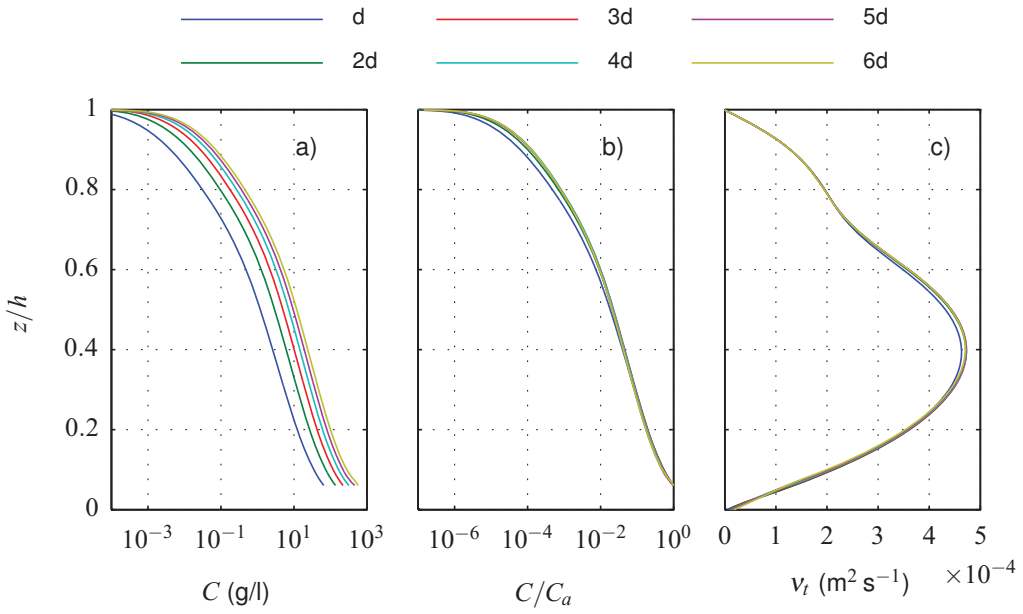

Figure 7.8: Sensitivity of the numerical model to the centre of the cells adjacent to the bed, z_a/d. Each plot is a different variable: a) sediment concentration, b) normalised suspended sediment concentration, and c) eddy viscosity.

Therefore the cell centre of the near-bed cell can be considered the reference height, z_a and C_{nb} as a reference value. As previously mentioned, the size of the cell adjacent to the sediment bed has been fixed to $2k_N$, corresponding to a reference height of $z_a = k_N$. This section investigates the sensitivity of the numerical model to the choice of z_a. The domain and flow parameters represent Run 137 of Sumer et al. (1996), summarised in Table 7.1, and the cell size near the sediment bed, Δz_w has been varied for each test. The internal mesh discretisation is fixed to the value obtained in the previous section.

Figure 7.8 shows the effect of the variation in Δz_w on a) the concentration profile (g/l), b) the concentration profile normalised by the concentration at $z_{ref} = 8\,\text{mm}$, and c) the eddy viscosity profile ($\text{m}^2\,\text{s}^{-1}$). Each line in the plot represents a different reference height ($z_a = \Delta z_w/2$). The concentration profiles (Figure 7.8a-b) indicate that the choice of Δz_w affects the magnitude but does not have such a great effect on the shape of the distribution. The only simulation which has an obvious difference in shape from the others is the one with the smallest cell size, $z_a = d$. As can be seen in the eddy viscosity plot (Figure 7.8c), this cell size is also the only one to have a noticeably different eddy viscosity profile (around

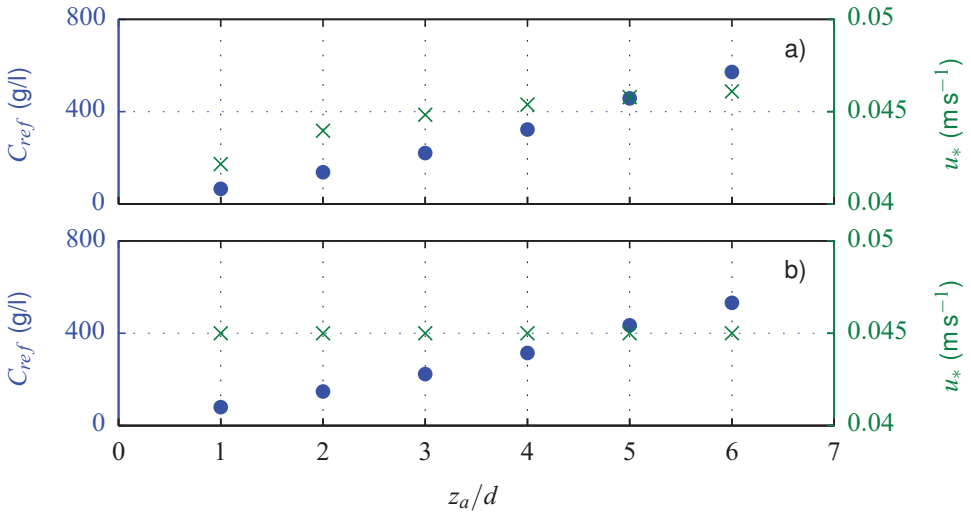

Figure 7.9: Sensitivity of the reference concentration, C_{ref}, to the distance of the cell centre adjacent to the bed, from the bottom boundary, z_a. Plot a) shows the sensitivity in cases where the cell size is varied and the friction velocity, u_* is set according to the flow in the this cell (see Chapter 4). Plot b) presents the sensitivity of C_{ref} to variation in cell size for a fixed value of u_*.

2% difference). This change in eddy viscosity could be due to the cell not falling within the logarithmic region of the boundary layer, which occurs at around $\Delta z_w = k_N$ (Jacobsen 2011; Pilegaard 2012). Since this is the only cell size to be below this threshold, and is also the only simulation with a substantially different eddy viscosity, it is assumed that this is the cause of the change. This would imply that the sediment diffusion is the dominant factor in determining the shape of the distribution in this case, probably due to the low values of vertical velocity.

As the value of Δz_w increases, the magnitude of the distribution also increases, while keeping a similar profile shape. Figure 7.9a presents the value of the concentration (•) at the first data point ($z_{ref} = 8$ mm) in Sumer et al. (1996), and the friction velocity, u_* (×) against the different reference heights z_a, normalised by the grain diameter. As Δz_w (and consequently z_a) becomes larger, the value of C_{ref} also appears to increasing, as does the friction velocity. Since both the friction velocity and cell size are increasing, it is difficult to determine which is causing the increase in reference value. To isolate the effect of cell size, the friction velocity was fixed to $0.045\,\mathrm{m\,s^{-1}}$ and the simulations run again. Figure 7.9b shows the same results as Figure 7.9a except with a constant friction velocity. Although the reference value plot

does change slightly from when u_* was being modelled, the reference concentration still exhibits similar values as the previous simulations. This implies that the numerical model is much more sensitive to the choice of cell size, Δz_w, than it is to the calculation of the friction velocity. Although a cell with a larger volume will take longer to fill up, for a fixed u_* the value in the near-bed cell at the steady state will always be the same. Since the eddy viscosity increases further from the bed, it is thought that setting the concentration higher in the water column will lead to larger transport by turbulent diffusion.

When considering the sediment diffusivity profiles, the shape of the concentration's vertical distribution will be more important than the magnitude, since the calculation relies largely on the vertical concentration gradient. Hence it is believed that the sensitivity to Δz_w will not substantially compromise the rest of this work. Therefore, in all of the simulations to follow, Δz_w was set to $5d$ so that the reference height is at k_N. This satisfies the need to be large enough to fall in the logarithmic region and is also consistent with the work of van Rijn (1984*b*), who developed the pickup model used in the present study.

7.2.3 Results

The numerical model has been run for eight of the test cases presented by Sumer et al. (1996), which are summarised in Table 7.1. Two sediment types are considered with different settling velocities ($0.012\,\mathrm{m\,s^{-1}}$ and $0.02\,\mathrm{m\,s^{-1}}$). The smaller settling velocity cases were conducted using fine natural sands, whereas acrylic particles were used for the large settling velocity cases. The acrylic particles are much larger and less dense than the natural sand and, hence, provide an interesting comparison of sediment types.

Figure 7.10 presents the comparison of the numerical predictions of concentrations against normalised depth with the observed experimental data for the eight test cases from Sumer et al. (1996). Each plot represents a different test case and the NRMSE (E) is also presented and was calculated using

$$E(\%) = \frac{100}{C_{obs,max} - C_{obs,min}} \sqrt{\frac{1}{N} \sum_{i=1}^{N} (C_{pred,i} - C_{obs,i})^2}, \tag{7.6}$$

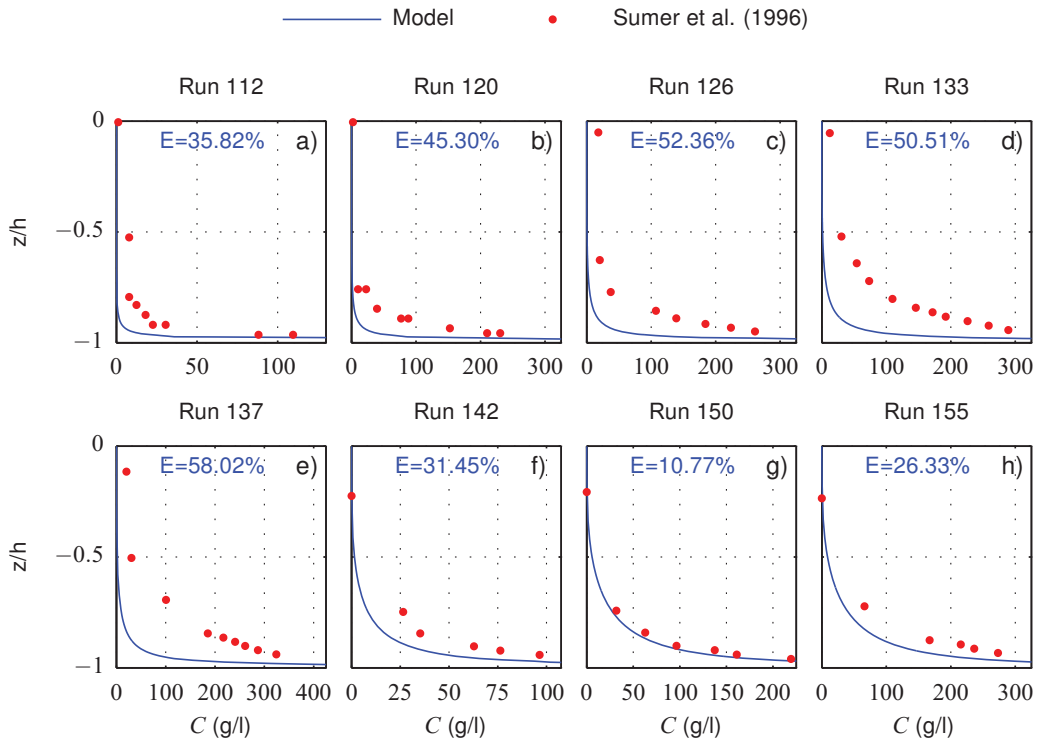

Figure 7.10: Comparison of the numerical predictions (lines) of concentration with the experimental data (•) gathered by Sumer et al. (1996). Each plot is a different test case, indicated above the plot (see Table 7.1 for details). The NRMSE (%) is presented at the top of every plot.

where C_{pred} and C_{obs} are the values predicted by the model and observed in the experiments, respectively. Plots a-e represent the larger settling velocity cases and are ordered according to flow velocity. It is clear that the model under-estimates the concentrations throughout the water depth, particularly in the higher velocity cases (c-e). The shape of the vertical distribution is also different: near the bottom the concentration decreases far quicker than observed in the experiments. Once again, this deviation from the experiments appears to become larger as the flow speed increases. The NRMSE supports these observations with a general trend of the error increasing with flow speed, from 36% at $u = 0.402\,\mathrm{m\,s^{-1}}$ to 58% at $u = 0.733\,\mathrm{m\,s^{-1}}$.

The natural sand results (f-h) are more promising. The numerical model predicts the concentration profile shape and magnitude accurately for Run 150, with a NRMSE of approximately 10%. In the other two cases the general shape of the distribution is captured well by

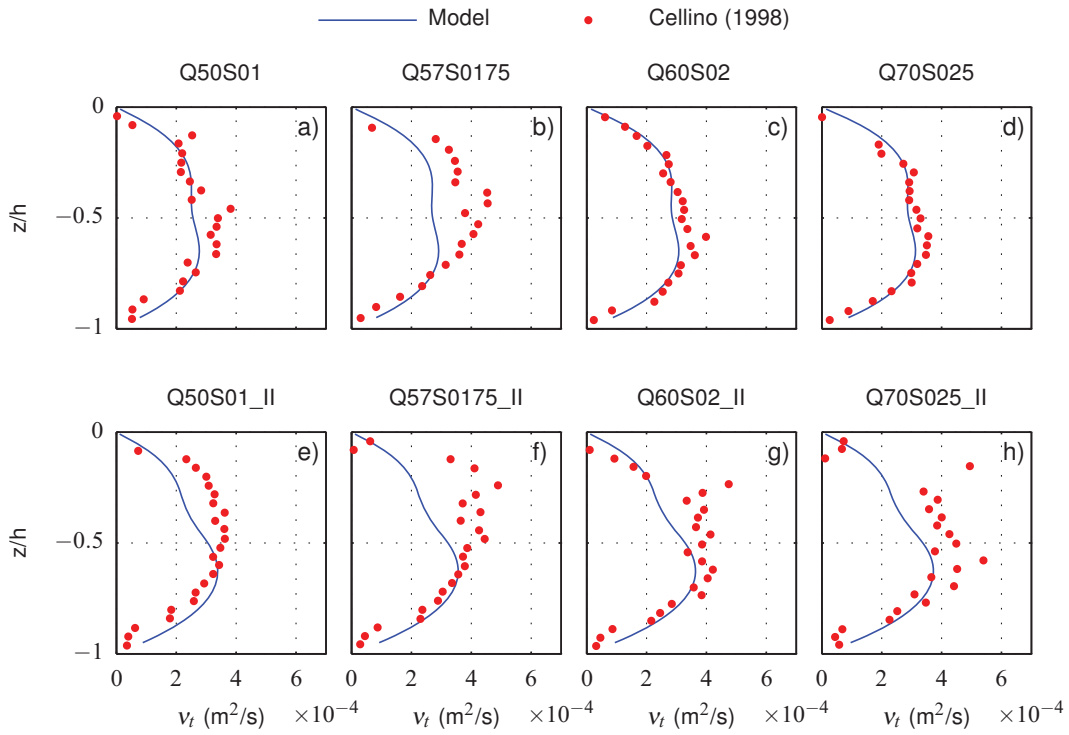

Figure 7.11: Comparison of the numerical predictions (lines) of eddy viscosity with the experimental data (•) presented by Cellino (1998). Each plot is a different test case, indicated above the plot (see Table 7.1 for details).

the numerical model. The concentrations are under-predicted, but to a lesser degree than observed with the larger particles. This is also indicated in the NRMSE, which are smaller in all three cases than for any of the larger settling velocity cases.

Bearing in mind that Cellino (1998) encountered difficulties when digitising the data due to the size of the plots, comparison with Sumer et al. (1996) implies that the numerical model performs well when using fine natural sands, but less well for the larger acrylic particles. To determine whether this is true, another set of eight test cases were run for comparison with the data gathered by Cellino (1998), and are summarised in Table 7.1. These tests were conducted under similar flow conditions and water depths as by Sumer et al. (1996) and hence are set up in a similar way to the Sumer et al. (1996) cases described in Section 7.2.1, but the channel is 16 m long and the water depth is 0.12 m. The inlet wall length is kept the same length and the results are still sampled at 7 m. One of the major advantages of using this data set is that the two settling velocities considered (0.012 m s^{-1}

and $0.021\,\mathrm{m\,s^{-1}}$) are of similar magnitude to those used by Sumer et al. (1996), but natural sand was used in both cases. By running these cases, the effect of using larger, less dense particles can be evaluated.

Figure 7.11 shows a comparison of the predicted eddy viscosity against normalised depth with the experimental data for each of the eight test cases from Cellino (1998). The test case label is shown at the top of each subplot. The numerical predictions of ν_t largely agree with the experimental data in the bottom half of the water column. This should lead to a similar vertical distribution shape in this region, as that observed in the experimental data. However, very close to the bed the eddy viscosity is slightly over-estimated in all cases, which could lead to excessive diffusion of the sediment. Above the middle of the water column the agreement varies between test cases: plots a,c, and d have very good agreement, whereas b, e and f show less agreement. In a few of the cases where the agreement is not as good, the experimental data is scattered, which could indicate less confidence in the results in this region. The concentration gradients in the top half of the water column are generally very small and hence it is assumed that the numerical model should not be overly sensitive to any discrepancy in eddy viscosity in this region.

Figure 7.12 shows the concentration profiles against normalised depth for the eight test cases from Cellino (1998). These test cases represent increasing flow velocity from left to right, and the rows present two different settling velocity cases, $w_s = 0.012\,\mathrm{m\,s^{-1}}$ (top) and $0.021\,\mathrm{m\,s^{-1}}$ (bottom). Once again, the numerical predictions (lines) are compared with the experimental data (●) collected by Cellino (1998). The NRMSE of the model predictions, relative to the experimental data is presented on each plot, and has been calculated using equation (7.6). The smaller settling velocity cases (Figure 7.12a-d) indicate that the shape of the distribution is reasonable, although the near-bed gradient is slightly smaller than observed in the experimental data. This could be due to excessive diffusion, caused by the over-estimation of the near-bed eddy viscosity, as previously observed in Figure 7.11.

Interestingly, the numerical model generally over-predicts the sediment concentration with respect to Cellino (1998), whereas it was shown to be under-predicted, in very similar flow

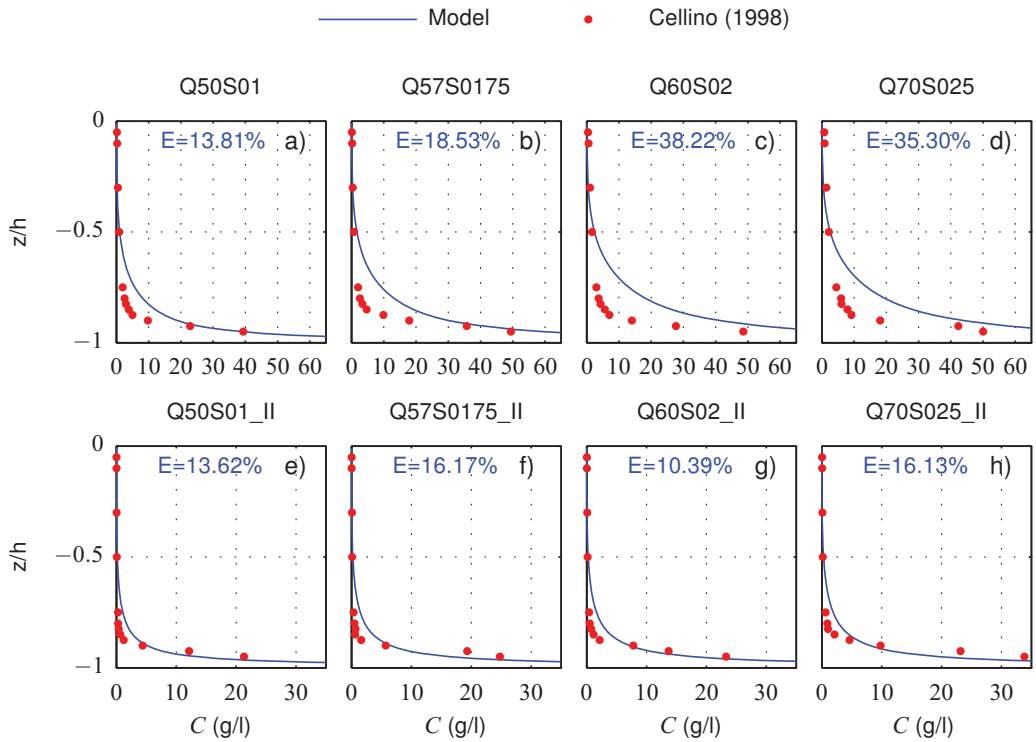

Figure 7.12: Comparison of the numerical predictions (lines) of concentration with the experimental data (•) presented by Cellino (1998). Each plot is a different test case, indicated above the plot (see Table 7.1 for details). The NRMSE of the model results (%) are presented at the top of every plot.

conditions, compared to Sumer et al. (1996). Therefore, for natural sand with a settling velocity of $0.012\,\mathrm{m\,s^{-1}}$ the model seems to predict values between the two experimental studies, which is considered to be acceptable. The NRMSE indicate that the model performs better for cases with flow velocity $u = 0.792\,\mathrm{m\,s^{-1}}$ (Figure 7.12a) and $0.855\,\mathrm{m\,s^{-1}}$ (Figure 7.12b) than for $0.905\,\mathrm{m\,s^{-1}}$ (Figure 7.12c) or $0.917\,\mathrm{m\,s^{-1}}$ (Figure 7.12d). This could indicate that the model performs better for lower flow speeds. However, there is a substantial jump in NRMSE between the flow speeds $u = 0.855\,\mathrm{m\,s^{-1}}$ and $u = 0.905\,\mathrm{m\,s^{-1}}$, which seems to be inconsistent with other observations, especially as the case with the fastest flow speed has a slightly smaller error. Therefore it seems plausible that at least some of the disagreement could be due to errors associated with the experiments.

Contrary to the numerical predictions presented for the larger settling velocity cases of Sumer et al. (1996), the model with $w_s = 0.021\,\mathrm{m\,s^{-1}}$ performs well in comparison to Cellino

(1998), for all flow velocities presented (Figure 7.12e-h). Both the magnitude and the shape of the distribution are captured accurately. This is supported by the NRMSE where the error values are in the region $10-16\%$ as opposed to the $35-58\%$ observed when comparing to Sumer et al. (1996). There could be a number of reasons for the large error associated with the acrylic particle cases. Considering the large differences in presented concentration despite having the same settling velocity, it seems likely that there are additional processes which are not being considered in the present model. One possibility is that a one-directional coupling approach is not valid for sediments of larger grain diameter, and that drag on the fluid should be considered as an additional source/sink in the turbulence transport equations. The absence of hindered settling could also be a process which would need to be accounted for. Baldock et al. (2004) presented a thorough evaluation of conditions in which hindered settling can be neglected, using experimental data for a variety of sediment types. Their findings indicate that for concentrations of less than 10% of the maximum attainable, the settling velocity reduces by less than 10% from the clear water value. However, above this concentration, the settling velocity is substantially reduced, indicating that hindered settling should be considered. The largest concentrations in the acrylic particle experiments conducted by Sumer et al. (1996) are approximately 40% of the maximum attainable value, which according to Baldock et al. (2004) would reduce the settling velocity by around 70% from the clear water value. On the other hand, the largest concentrations in the natural sand cases presented by Cellino (1998) are around 3% of the maximum attainable concentration, and hence hindered settling can largely be neglected.

Another possible explanation for the discrepancies in the acrylic particle cases could be the choice of Schmidt number. The shape of the vertical distribution of concentration is mainly controlled by the diffusion term, and can be seen to match better for the natural sand cases than with the experimental results for the acrylic particles, which exhibit sharper near-bed gradients in the predicted profiles than observed in the physical data. Hence, it could be that the assumption of $\sigma_c = 1$ is more valid when considering natural sand than acrylic particles. If σ_c was set to a value less than unity, more diffusion would occur leading to a smaller concentration gradient with depth. In this way it is possible that the vertical

concentration profile shape may be obtained, if not the magnitude. Furthermore, there is existing experimental evidence of a dependency of the Schmidt number on grain diameter (Cellino 1998), and dependencies on other factors have also been considered in previous numerical models (Amoudry et al. 2005; Absi 2010). Determining the exact cause of the poor performance of the model when using large acrylic particles is considered to be outside of the scope of this work, but could be an interesting research direction to consider in the future.

Overall, the model performs well for natural sand and hence is considered to be suitably validated for fine sediments in steady flows. Therefore, any subsequent test cases will be limited to fine natural sand with diameter no larger than 0.25 mm (classified by Komar (1998) as fine sand. See Table 3.3.).

7.3 Case 3: Regular Waves

Before running the breaking wave simulations, the model will be validated for oscillatory flows. In this section, sediment concentrations under regular, non-breaking waves are compared to the experimental data of Dohmen-Janssen and Hanes (2002) as well as other numerical models (Hsu and Liu 2004; Ma et al. 2014).

7.3.1 Numerical Setup

The numerical domain is set up such that the test region is similar to the experiments of Dohmen-Janssen and Hanes (2002), which were conducted in a large wave flume in Hannover, Germany, and is shown in Figure 7.13. The dimensions of the numerical wave flume are $200\,\text{m}\times 7\,\text{m}$, with a water depth of $4.25\,\text{m}$. The origin is located on the still water level (SWL) at the inlet. A horizontal sand bed, of depth $0.75\,\text{m}$, is located between $x = 65\,\text{m}$ and $x = 110\,\text{m}$ and is comprised of sediment of size, $d = 0.24\,\text{mm}$ and density $\rho_s = 2650\,\text{kg m}^{-3}$. The test region is assumed to join to the bottom of the wave flume by a slope of constant gradient (chosen as $1/33$) since no details were provided by Dohmen-Janssen and Hanes (2002).

The wave period and height at the inlet are set to $6.5\,\text{s}$ and $1.6\,\text{m}$, respectively (test "mh" of

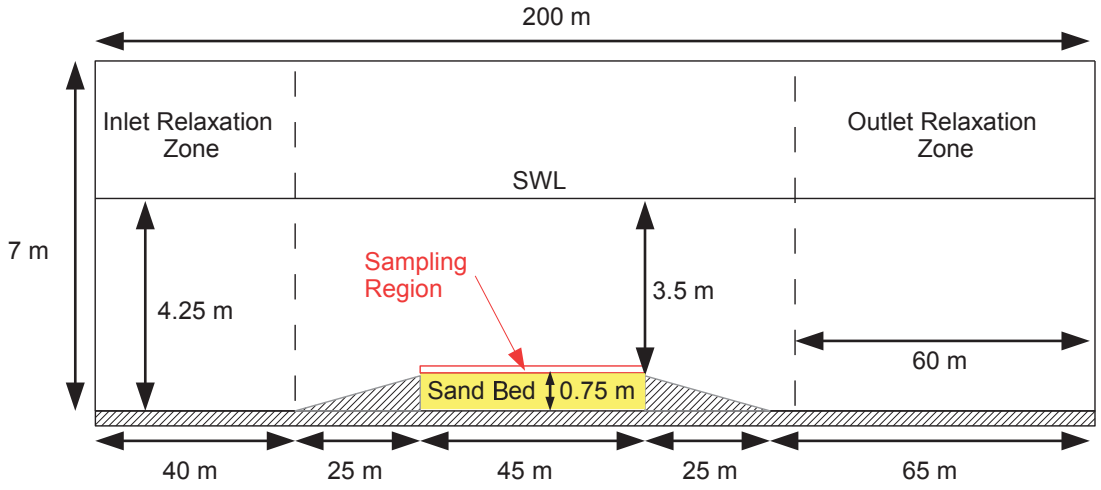

Figure 7.13: Diagram of the numerical domain for the regular, non-breaking waves, used for validation of the sediment module. The vertical scale has been exaggerated by a factor of 10.

Dohmen-Janssen and Hanes 2002) and are generated using Stream Function wave theory (Fenton 1988). The simulation is run for $200\,\text{s}$ (approximately 30 wave periods), with the last ten periods used for averaging. The sampling location has been chosen to be near the centre of the test region ($x = 85\,\text{m}$). A relaxation zone of $40\,\text{m}$ (approximately one wavelength) is used at the inlet to absorb any reflections within the numerical domain. At the outlet a relaxation zone of length $60\,\text{m}$ was applied for wave absorption, with the value at the outlet boundary set to zero velocity and water depth equal to that at still water. According to Jacobsen et al. (2012) a relaxation zone of this length should lead to reflections of less than 1% for the waves of this height and period.

The discretisation was chosen as $0.04\,\text{m}$ for the background mesh, with an aspect ratio of 1. This gives 40 mesh cells over the wave height, which allows the wave to be resolved to a tolerance of 1%, according to Ransley (2015). Further refinement was provided around the test region so that the discretisation is $0.005\,\text{m}$ in the near-bed region ($0.2\,\text{m}$ above the bed). This allows more accurate sampling in this region and is more in line with the grid refinement study previously conducted for the channel flow tests. The cell size adjacent to the bed is set to $5d$ to be consistent with the steady state simulations with each subsequent cell increasing in size by 50%.

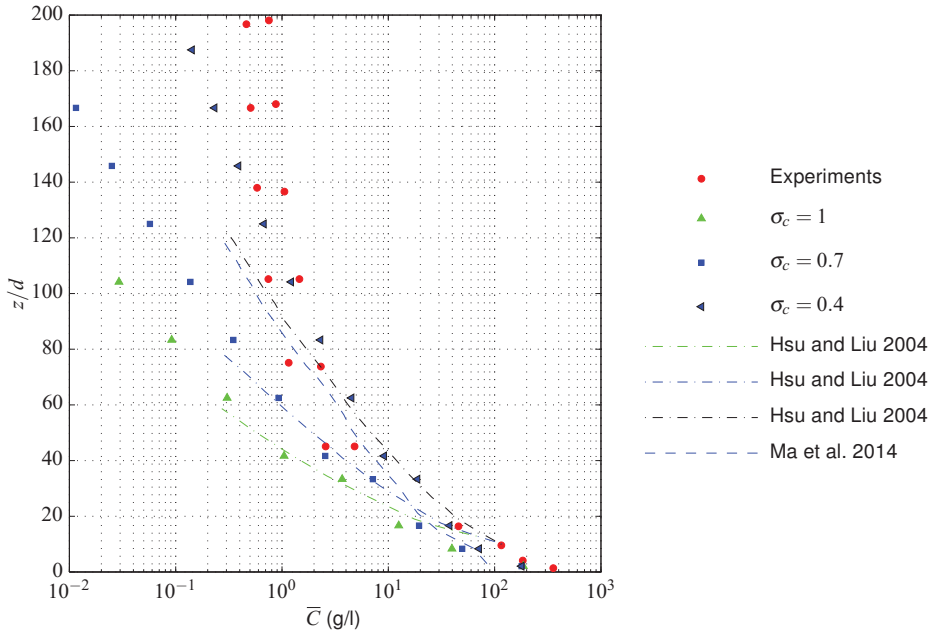

Figure 7.14: Time-averaged concentration (g/l) as a function of the number of grain diameters above the bed (z/d). The results of the present numerical model are given with $\sigma_c = 1$ (▲), 0.7 (■), and 0.4 (◀). Experimental data gathered by Dohmen-Janssen and Hanes (2002) is shown (●) along with previous numerical studies (lines) (Hsu and Liu 2004; Ma et al. 2014).

The bottom boundary, including the sloping regions, is considered to be a wall with a no-slip boundary condition, along with a zero gradient condition for the sediment concentration. The sand bed also has a no-slip boundary condition applied for the fluid and the sediment concentration has the effective settling velocity formulation applied (see Section 4.5.1). The $k-\omega$ turbulence model is used for consistency with the other validation tests, and the inlet conditions are set as $I = 0.25\%$ and $\zeta = 0.1$, as discussed in Sections 5.1.1 and 5.2.1. Wall functions have been used on the bottom boundary, with a rough wall function applied to the sand bed (with $k_N = 2.5d$).

7.3.2 Results

The experimental study of Dohmen-Janssen and Hanes (2002) has been used as a benchmark by other numerical models. Two of these are considered for comparison. The first one is a model developed by Hsu and Liu (2004), coupled with the wave hydrodynamic model Cornell Breaking Wave and Structure, COBRAS (Lin and Liu 1998*a*,*b*). The second numer-

ical model has been developed by Ma et al. (2014) and coupled with NHWAVE (Ma et al. 2012), which is a non-hydrostatic wave resolving model.

Figure 7.14 gives the time-averaged concentrations (g/l), as a function of the number of grain diameters above the bed. Predictions for a number of Schmidt numbers in comparison to the experimental data of Dohmen-Janssen and Hanes (2002) are presented. Near the bottom of the water column, the numerical model under-predicts the mean concentration for all of the Schmidt numbers considered. Further up the water column, the mean concentration profiles for the three different Schmidt numbers vary considerably, with a trend of increasing concentration with decreasing Schmidt number. Compared to the experimental data, the numerical model always under-estimates the time-averaged concentration when assuming $\sigma_c = 1$ and 0.7, although the latter case does predict reasonably agreeable values around $z/d = 40$. Conversely, the $\sigma_c = 0.4$ case over-predicts the mean concentration below $z/d = 100$ and agrees well with the experiments between $z/d = 100$ to 140. Above this height the concentration is under-predicted by the numerical model. This case highlights an interesting discrepancy with the experimental data: the concentration gradient is very small in the experiments whereas the numerical model reduces quite quickly with height above the bed. This was also noted by Dohmen-Janssen and Hanes (2002), describing it as "somewhat perplexing" and suggesting that it could be due to the presence of finer sediments or a build up of background level turbulence. Taking this into consideration, Hsu and Liu (2004) suggested that concentrations lower than approximately 1 g/l ($z/d \approx 80$) may not be reliable. This highlights one of the difficulties in validating a numerical model against experimental data for suspended sediment concentrations: there is usually a distribution of sediment grain sizes, rather than the one considered in the model, which can substantially affect the experimental measurements. Therefore, it would be interesting, and potentially very useful, to develop a numerical model which is capable of modelling a distribution of sediment grain sizes simultaneously.

Figure 7.14 also presents the results from previous numerical studies (Hsu and Liu 2004; Ma et al. 2014). In general, the mean concentrations predicted by Hsu and Liu (2004) are

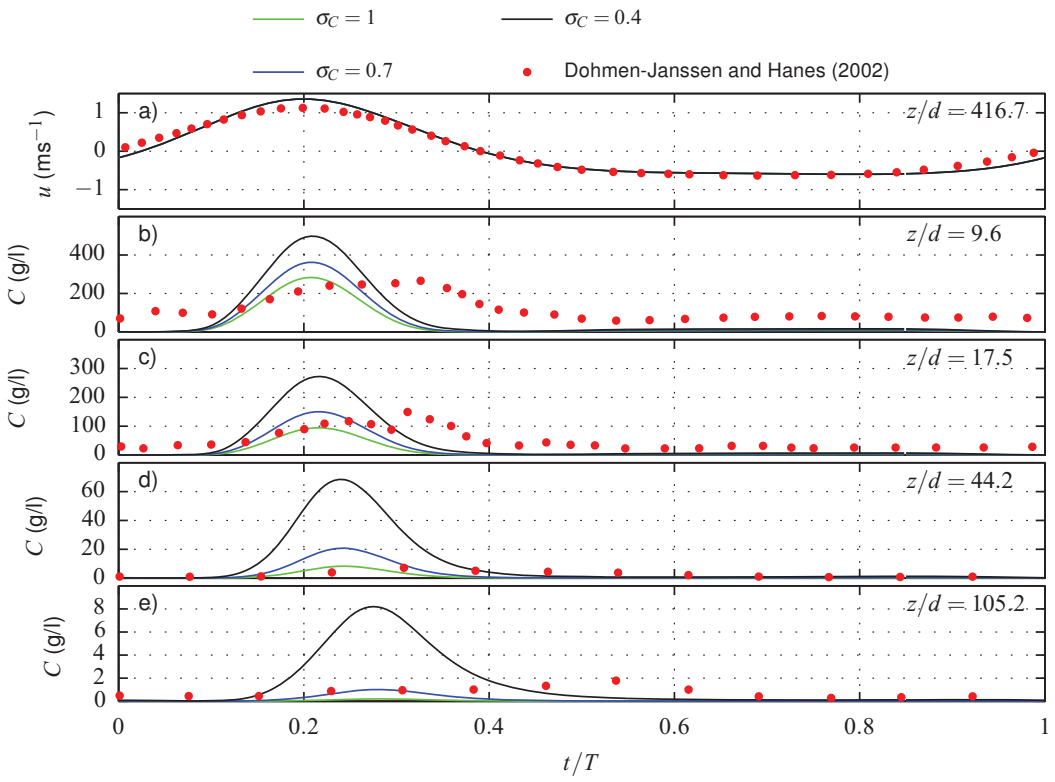

Figure 7.15: Comparison of the phase-averaged horizontal velocity, ($\widetilde{u}$) 0.1 m above the bed (a) as well as the phase-averaged sediment concentrations ($\widetilde{C}$) at $z/d =$ 9.6 (b), 17.5 (c), 44.2 (d) and 105.4 (e). Profiles for three different Schmidt numbers are shown: $\sigma_c = 1$ (green), $\sigma_c = 0.7$ (blue), and $\sigma_c = 0.4$ (black), and are compared to the data (●) gathered by Dohmen-Janssen and Hanes (2002).

similar to the present model for all three Schmidt numbers. However, at the sampling location near the bed the present numerical model does predict smaller concentrations, particularly for the $\sigma_c = 1$ and $\sigma_c = 0.7$ cases at $z/d \approx 17$. Ma et al. (2014) only presented results for $\sigma_c = 0.7$ and generally predicts larger concentrations than either of the other two models, particularly above $z/d = 40$. However, near-bed predictions are reasonably similar to the values predicted by the present numerical model.

To gain further insight into the inconsistencies of the numerical models, phase-averaged profiles are considered at various heights above the bed. Figure 7.15 presents a) the phase-averaged horizontal velocity, ($\widetilde{u}$) 0.1 m above the bed, and the phase-averaged suspended sediment concentrations ($\widetilde{C}$) at b) $z/d = 9.6$, c) 17.5, d) 44.2 and e) 105.4. The results for three different Schmidt numbers are shown, $\sigma_c = 1$ (green), $\sigma_c = 0.7$

(blue), and $\sigma_c = 0.4$ (black), and are compared to the experimental data (●) gathered by Dohmen-Janssen and Hanes (2002). The velocity prediction by the numerical model agrees well with the experimental data, although the maximum velocity is slightly over-estimated. This discrepancy in maximum value could be due to a slightly different sampling location since it was described as being "about 0.1 m above the bed" by Dohmen-Janssen and Hanes (2002).

The suspended sediment concentration plots clearly show the trend in σ_c observed in the mean profiles: as the value of σ_c decreases, the concentration increases. This trend becomes more evident as the distance above the bed increases, with the peak value for $\sigma_c = 0.4$ approximately an order of magnitude larger than the profile for $\sigma_c = 1$ at $z/d = 105.2$. On the other hand, the peak values close to the bed ($z/d = 9.6$) differ by less than a factor of 2. This is the effect expected since the decrease in σ_c leads to an increase in sediment diffusion, hence causing higher sediment concentrations further up the water column.

Comparing the profiles with the experimental data indicates that the model predicts peak concentrations of a similar order of magnitude, especially for $\sigma_c = 0.7$. However, the shape of the profile is considerably different. At $z/d = 9.6$ and $z/d = 17.5$ the experimental data indicates that there is always a reasonably large concentration present. As the wave passes the sediment concentration increases to a peak value, which is maintained for around 20% of the wave period before settling back to a relatively constant value for the rest of the wave period. The numerical model, on the other hand, predicts a sharp increase in the concentration, similar to the experiments, but then reduces to a much smaller value than observed by Dohmen-Janssen and Hanes (2002). This seems to be the main reason for the under-prediction observed in the mean profiles (Figure 7.14). There could a number of reasons for this effect: the settling velocity could be over-predicted by the numerical model, or the eddy viscosity under-predicted. Another possible explanation is that the experiments contain a range of sediment grain sizes, rather than the single (median) grain size used in the numerical model. This could lead to finer sediments being suspended for longer, which

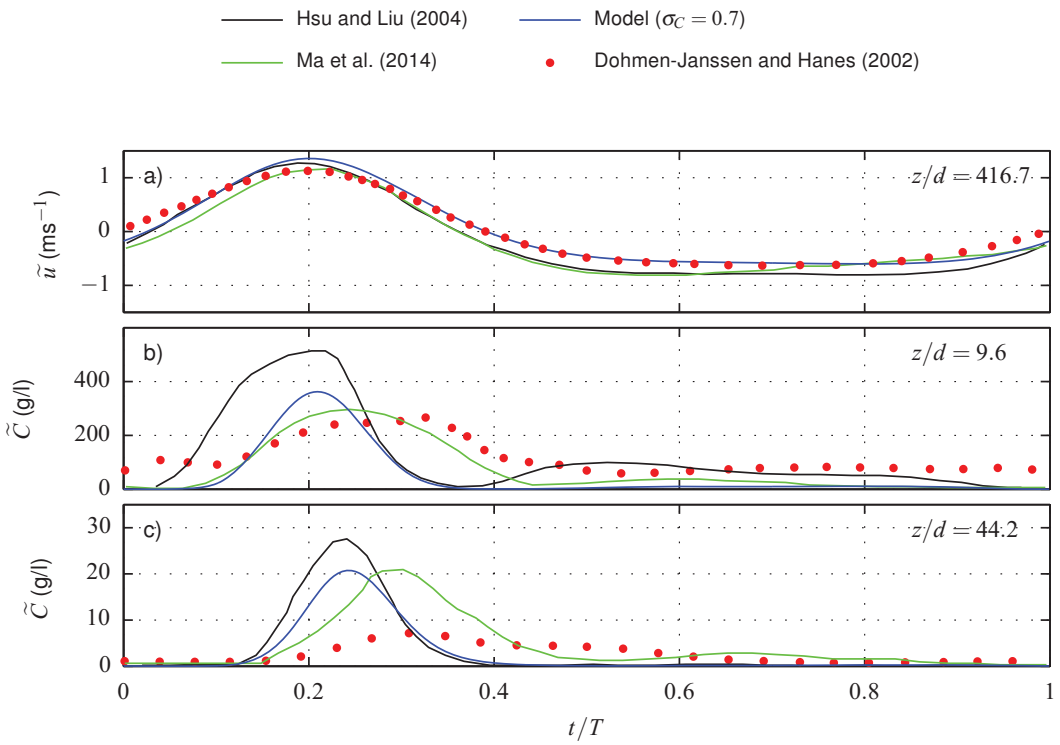

Figure 7.16: Comparison of the phase-averaged horizontal velocity and concentration profiles with other numerical studies (Hsu and Liu 2004; Ma et al. 2014). The velocity profile (a) is evaluated 0.1 m above the bed, whereas the concentrations are taken at $z/d = 9.6$ (b), and $z/d = 44.2$ (c). Experimental data presented by Dohmen-Janssen and Hanes (2002) is also shown (●).

would potentially explain the under-prediction seen in the numerical model.

Another interesting comparison, that could not be obtained from the time-averaged concentration profile, is the phase at which the peak concentration occurs. The experiments indicate that the peak concentration occurs later (relative to the wave passing), further above the bed, which is particularly evident at $z/d = 105.2$. This makes sense since sediment can not instantaneously change location and the numerical model follows this general trend. However, the change in phase is much smaller than seen in the experiments, indicating that the speed of suspension of the sediment is over-predicted, either by vertical advection or turbulent diffusion. Further work would be required to establish the exact reason for this discrepancy and is considered to be outside of the scope of this work since the process of calculating the sediment diffusivity uses time-averaging.

Figure 7.16 gives a comparison of the present numerical model with the results of Hsu and Liu (2004) and Ma et al. (2014), all using $\sigma_c = 0.7$, along with the experimental data of Dohmen-Janssen and Hanes (2002). The phase-averaged horizontal velocity at 0.1 m above the bed (a) is presented along with the phase-averaged suspended sediment concentration profiles at $z/d = 9.6$ (b), and $z/d = 44.2$ (c). The velocity profiles are similar for all of the numerical models. The present numerical model does have the largest peak velocity but, in general, it agrees better with the experimental profile for the rest of wave cycle, particularly in the phases with negative velocity.

Despite having similar velocity predictions, the concentration profiles vary considerably between numerical models at both locations shown. The present numerical model and the model of Ma et al. (2014) predict similar values for the peak concentration, whereas the model developed by Hsu and Liu (2004) predicts substantially larger concentrations at both locations. At $z/d = 9.6$, Hsu and Liu (2004) predict a longer period of increased sediment concentration than the present numerical model, beginning earlier in the wave cycle before reducing at a similar point. Ma et al. (2014) also observe a longer period of high concentration but, contrary to Hsu and Liu (2004), it begins at a similar phase in the wave cycle as the present numerical model and reduces later. The length of suspension appears to be the main difference between the models and explains why the present numerical model predicted lower mean concentrations (Figure 7.14) than the other two models at this height above the bed. At sampling location $z/d = 44.2$ a similar trend can be observed in Ma et al. (2014). However, the numerical predictions of Hsu and Liu (2004) now follow a profile comparable to the present numerical model, with slightly increased peak values. This reveals the reason that the numerical model of Hsu and Liu (2004) gave similar values for mean concentration as the present study (Figure 7.14), whereas predictions by Ma et al. (2014) follow the experimental data more closely. There could be a number of reasons behind the increased suspension time but one of the most likely is that both previous numerical studies used a modified turbulence model to account for the presence of sediment, which has not been included in the present work. This could also help to explain the greater concentrations in the negative velocity phases of the wave exhibited by both of the previous

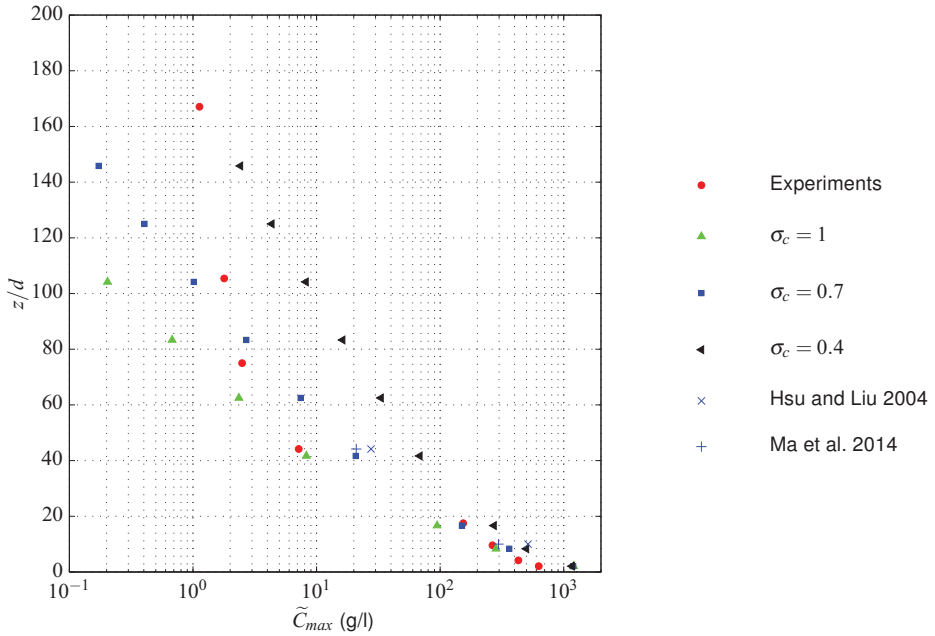

Figure 7.17: Peak sediment concentrations as a function of number of grain diameters above the bed (z/d). The results of the present numerical model are given with $\sigma_c = 1$ (▲), 0.7 (■) and 0.4 (◀). Experimental data gathered by Dohmen-Janssen and Hanes (2002) is shown (●) along with the previous numerical studies of Hsu and Liu 2004 ($\times$) and Ma et al. 2014 ($+$).

numerical models. However, this could also be partially due to the velocity over-estimation in the previous numerical models, at these phases.

Figure 7.17 presents the peak value of the phase-averaged concentration as a function of dimensionless height above the bed. Different Schmidt numbers are presented along with experimental (Dohmen-Janssen and Hanes 2002) and previous numerical predictions (Hsu and Liu 2004; Ma et al. 2014). In general the present numerical model gives predictions of peak concentration which are in reasonable agreement with the experimental data for $\sigma_c = 1$ and $\sigma_c = 0.7$. When assuming $\sigma_c = 0.4$, the peak value is substantially over-predicted by the numerical model, which could indicate that the Schmidt number is too small. The numerical model of Ma et al. (2014) has a very similar peak concentration as the present numerical model, whereas Hsu and Liu (2004) predict slightly larger values for the same Schmidt number. This further reinforces the need for the numerical model to keep the sediment in suspension for a longer period of time, which could indicate the need to modify the turbulence model to include the effects of sediment. However, in general the numerical

model seems to perform to a similar standard as other numerical models and hence is considered to be sufficiently validated for oscillatory flows bearing in mind the main purpose of this work: evaluating the implicit estimation of the sediment diffusivity based on time-averaged quantities, compared to a phase-resolved calculation. Therefore, concentrations in the surf zone will be considered in the next section.

7.4 Case 4: Breaking Waves

This section evaluates the numerical predictions of suspended sediment concentrations under spilling ($T = 1.4$ s) and plunging ($T = 2$ s) breakers through comparison with the experimental data of Otsuka and Watanabe (2012). The computational domain used in this validation work is the same as that described in Chapter 6, and is illustrated in Figure 6.1. The domain is setup to be consistent with the experiments of Otsuka and Watanabe (2012) and consists of two regions: a region of 0.6 m constant depth and a sloping beach with gradient $1/20$. The slope is further split into three regions as shown in Figure 7.18: a 3 m long sand bed is applied, starting from near the breaking point (9 m along the slope) with smooth walls, making up the slope either side of this region. The bottom of the constant depth region is also assumed to be smooth, and the origin is located at SWL at the toe of the beach, with x representing the cross-shore direction orientated such that positive x is in the direction of wave propagation, y and z are the long-shore and vertical coordinates, respectively. The domain is one cell thick in the y direction, the AR is kept to approximately one, and refinement is applied around the free surface. The cells near the bottom of the wave flume are reduced in size so that the cell centre closest to the wall is at the roughness height, i.e. $\Delta z_w = 2k_N$. To improve the spatial sampling of the variables, additional refinement was applied so that the whole of the water phase has the same discretisation as the free surface, i.e. $\Delta z = 5$ mm. This allows accurate sampling every 5 mm rather than every 1 cm. Simulations were run for 200 s with the last 15 waves used for averaging, i.e. $179-200$ s for the spilling breakers and $170-200$ s in the plunging case.

The hydrodynamic boundary conditions for the region of constant depth, top, end wall and the smooth sections of the sloping beach are the same as for the experiments presented

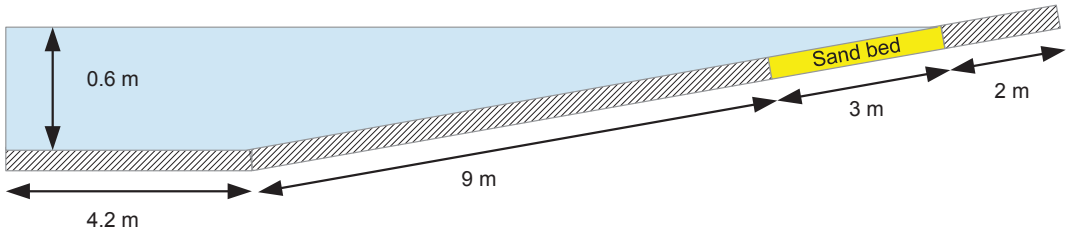

Figure 7.18: Diagram of the domain setup for the breaking wave simulations used for comparison with Otsuka and Watanabe (2012). The sand bed is 3 m long, starting at $x = 9$ m. Either side of the bed are smooth walls.

in Chapter 6 (see Section 6.1 for full details). However, the sand bed is considered rough and hence a rough wall function is applied, with $k_N = 2.5d$ (See Section 4.4.6.6 for details), along with a no-slip boundary condition.

The boundary conditions for the concentration at the sand bed are as follows. Zero gradient conditions are applied on the end wall, at the bottom boundary in the region of constant depth, and the smooth parts of the slope. At the top boundary, the concentration is set to a fixed value of zero. At the inlet, a condition dependent on the flux direction is used. If the flux is out of the domain a zero gradient condition is applied, allowing sediment to pass out of the domain. However, if the flux is into the domain then the concentration is zero, corresponding to clear water. Finally, the sand bed uses the boundary condition described in Section 4.5.1, which evaluates the difference between entrainment and deposition.

7.4.1 Near-Bed Results

Figure 7.19 shows the near-bed suspended sediment concentration (g/l), 1 cm above the bed, at three locations relative to the breaking point: a) $x = x_b$, b) $x = x_b + 0.6$ m, and c) $x = x_b + 1.4$ m under the spilling breakers. At the breaking point (Figure 7.19a) the concentrations vary substantially between wave periods for the first 30 s, then settle down to a reasonably steady state until around $t = 80$ s. After this time, a clear reduction in the concentration can be observed, which is particularly noticeable in the peak concentration. The model settles down again at around 170 s becoming quasi-steady. At $x_b + 0.6$ m (Figure 7.19b) a similar pattern can be observed. Interestingly, further into the surf zone (Figure 7.19c)

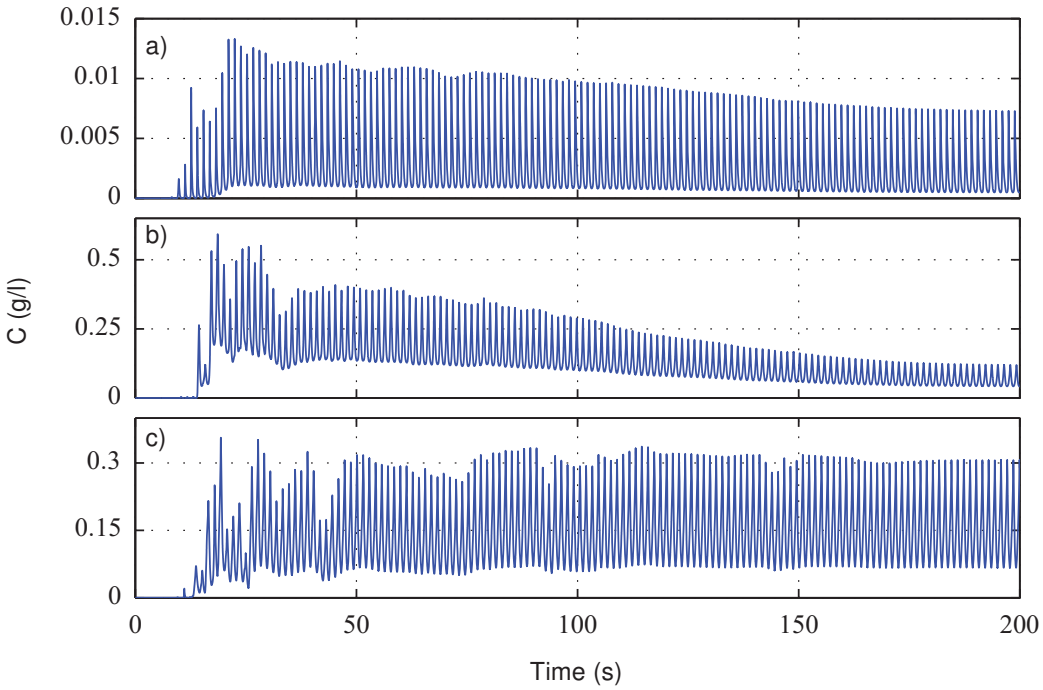

Figure 7.19: Time series of the numerical predictions of suspended sediment concentration (g/l), sampled 1 cm above the bed under spilling breakers at $x - x_b =$ a) 0 m, b) 0.6 m and c) 1.4 m.

this pattern cannot be observed. Instead the model gives an unpredictable concentration time series up until 120 s, where, other than a slight change around 150 s, it settles down to a quasi-steady solution. Comparing the end of the time series, the concentration magnitude follows a reasonably intuitive pattern: it starts relatively small at the breaking point (≈ 0.007 g/l) and increases by two orders of magnitude as the turbulence develops and the water depth gets shallower.

Figure 7.20 compares the predicted eddy viscosity time series at the three locations in Figure 7.19, and offers an explanation for the reduction in sediment concentration. A reduction in eddy viscosity is clearly seen around the same time as observed in the concentration series at x_b and $x_b + 0.6$ m. It is not immediately obvious what causes this reduction since the time series initially appears to be steady from 50 s to 80 s, indicating that the turbulence model has converged. It could possibly be due to internal reflections within the numerical domain, which take time to occur. Alternatively, processes from further into the surf zone could begin to spread further seaward. Taking all of this into consideration, the final

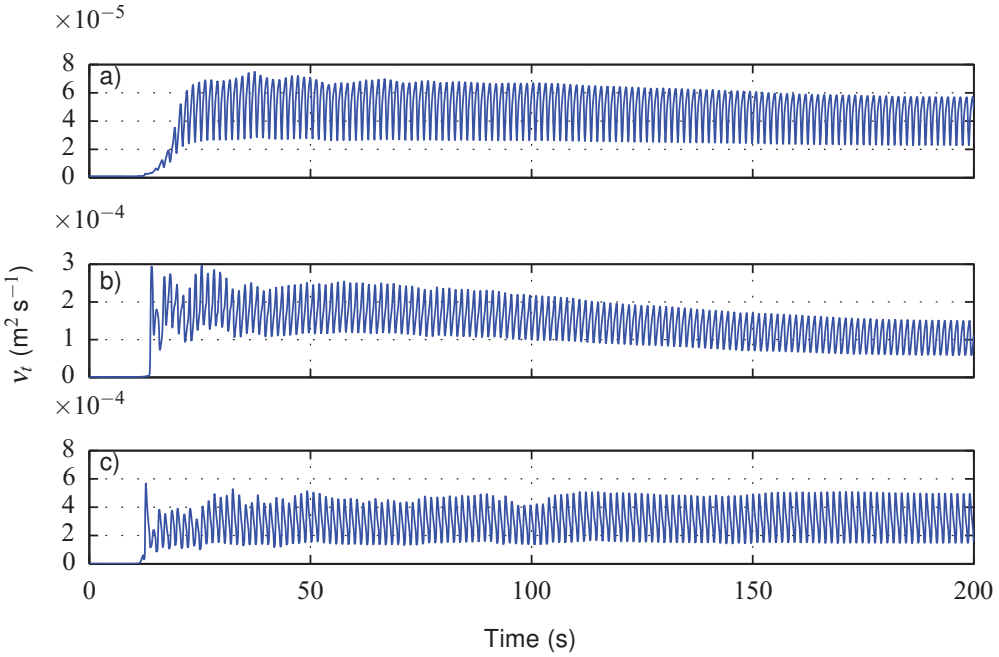

Figure 7.20: Time series of the numerical predictions of eddy viscosity, sampled 1 cm above the bed under spilling breakers at $x - x_b =$ a) 0 m, b) 0.6 m and c) 1.4 m.

15 waves are used for time-averaging since all of the three locations appear to be quasi-steady. Comparing the mean concentration of these 15 waves to the mean concentration of the final wave indicates that the relative error is 1%, 1.75% and 0.1% for x_b, $x_b + 0.6$ m, and $x_b + 1.4$ m, respectively. This is considered to be small enough to consider the simulation converged.

Figure 7.21 shows the predicted suspended sediment concentration time series under plunging breakers, 1 cm above the bed at sampling locations a) $x = x_b$ m, b) $x = x_b + 0.8$ m and c) $x = x_b + 1.6$ m. At the latter two locations the concentration magnitude is larger than under spilling breakers, which is to be expected due to the high impact nature of a plunging breaker, and is also observed in the experiments conducted by Otsuka and Watanabe (2012). At the breaking point (Figure 7.21a) the numerical model settles down to a quasi-steady state after around 50 s, which is much quicker than seen under spilling breakers. At $x_b + 0.8$ m (Figure 7.21b) the concentration can clearly be seen to be responding to the waves, but the peak and minimum concentration tend to a change substantially between

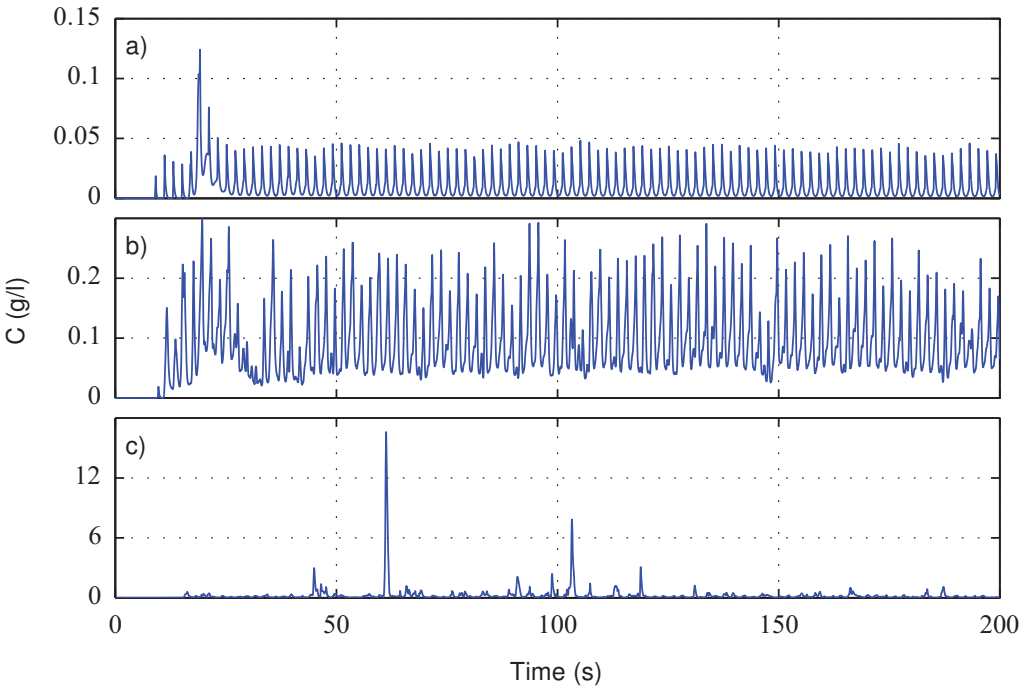

Figure 7.21: Time series of the numerical predictions of suspended sediment concentration (g/l), sampled 1 cm above the bed under plunging breakers at $x - x_b =$ a) 0 m, b) 0.8 m and c) 1.6 m.

wave periods, which is most likely due to differences between individual waves.

Interestingly, at sampling location $x_b + 1.6$ m (Figure 7.21c), one can observe sporadic sediment bursts, with a particularly large burst occurring around $t = 60$ s. The peak value of this burst is around 18 g/l, two orders of magnitude larger than the concentrations found at either of the other two sampling locations, as well as at any location under spilling breakers. Therefore, it is considered important to analyse the cause of this large spike in concentration, and hence, other variables are evaluated around the 60 s peak. Figure 7.22 presents time series of a) free surface elevation, b) horizontal and c) vertical velocity, d) TKE, e) friction velocity, and f) suspended sediment concentration between $t = 50$ s and $t = 70$ s, and have been sampled at $x_b + 1.6$ m. It is clear that each wave is different and hence the velocity and TKE vary substantially under each wave. This supports the hypothesis that the variability at sampling location $x_b + 0.8$ m (Figure 7.21b) could be caused by non-identical waves. These differences in wave profile are most likely caused by the entrainment of the air phase, which has been observed in this study to vary considerably depending on many

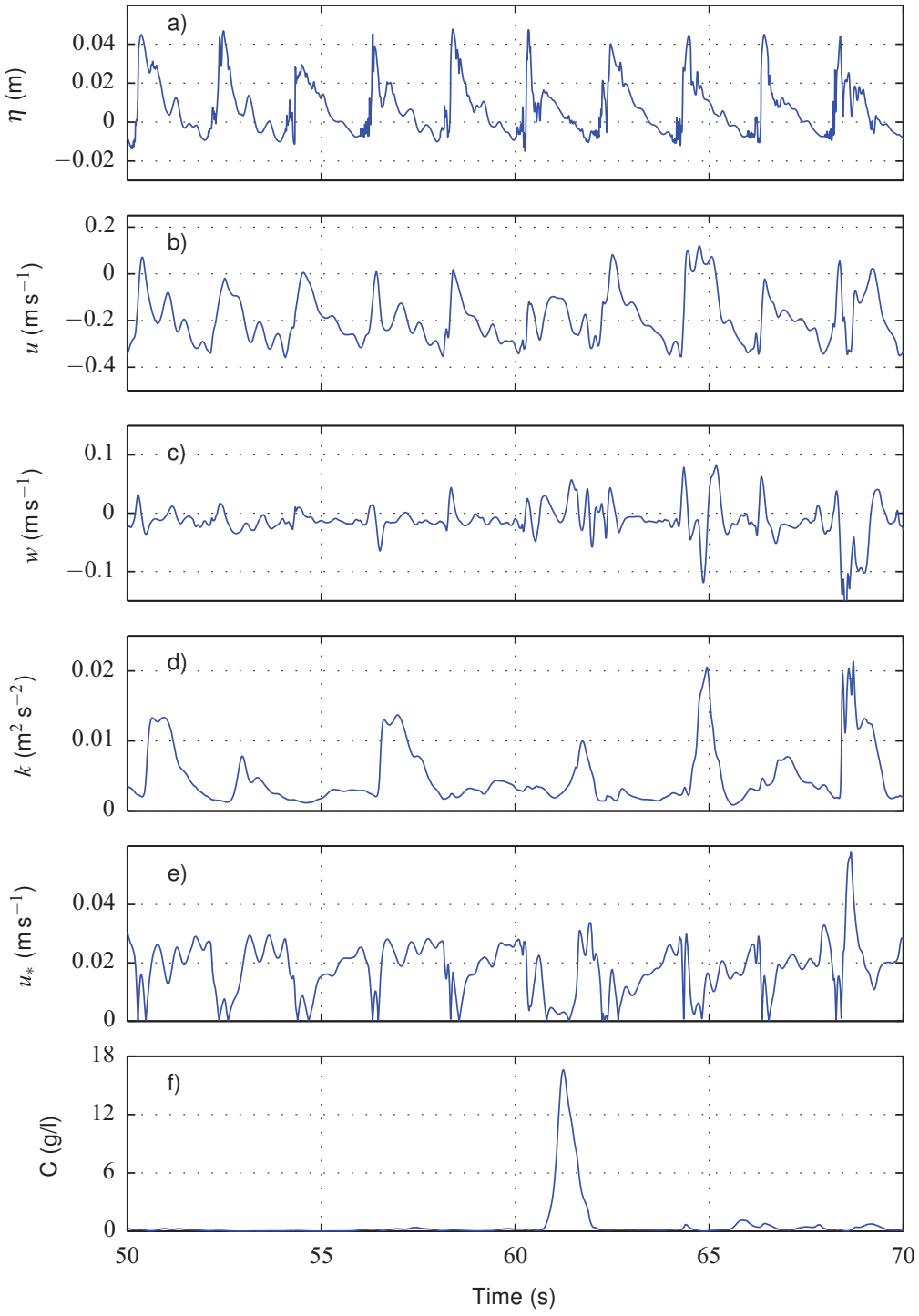

Figure 7.22: Time series of the hydrodynamics and sediment concentration around the time of the sediment concentration burst at $x = x_b + 1.6$ m under the plunging breaker. The plots are a) free surface elevation, b) horizontal velocity, c) vertical velocity, d) TKE, e) friction velocity, and f) sediment concentration.

factors including time step. However, there is not a clear link between any of the variables shown and the observed concentration spike. There are spikes in many of the other variables but none seem to occur around the time of the sediment burst. Therefore, it seems that the cause of this burst of concentration is not at this location but must occur due to conditions elsewhere.

Figure 7.23 presents full spatial colour plots of concentration (g/l) in the region surrounding the sampling location ($x = 10.78$ m to $x = 11$ m), which is marked as $+$ on the plot (see bottom left). Each plot represents a different time ranging from $t = 60.6$ s (a) to $t = 61.65$ s (h) with increments of 0.15 s. The velocity in the flow is presented using arrows, with the size representing the strength of the flow. Figure 7.23a shows entrained air, which occurred in the interaction between the wave front and the reverse flow. This interaction leads to a series of vortices, initially around the entrained air, as can be observed at the left and right of Figure 7.23a. The latter is close enough to the sea bed to cause an increase in the horizontal velocity near the bed, leading to increased bed shear stress, and hence greater sediment entrainment. After the entrained air has disappeared (see Figure 7.23b), the vortices still remain in the water column, and are advected by the reverse flow and positive velocity near the free surface. The vortex on the right in Figures 7.23a-e, gradually suspends the sediment to higher regions in the water column between $t = 60.60$ s and $t = 61.05$ s. This process has been occurring further shoreward than the sampling location being considered. However, the reverse flow begins to advect the vortex seaward, eventually crossing the location presented in Figure 7.21c (see time $t = 61.20$ s). As the velocity near the free surface reduces, the vortex weakens and eventually dissipates, leading to the suspended sediment diffusing and settling and therefore smaller concentrations ($t = 61.35$ s to $t = 61.65$ s). How the air is entrained may play a vital role in the prediction of these bursts of concentration, which would possibly account for their sporadic nature and the location at which they occur.

Figure 7.23 provides an explanation for the numerical prediction of a large concentration burst, but the physical validity of the process still needs to be assessed. Sumer et al. (2013) conducted experimental tests with plunging breakers in order to analyse a similar

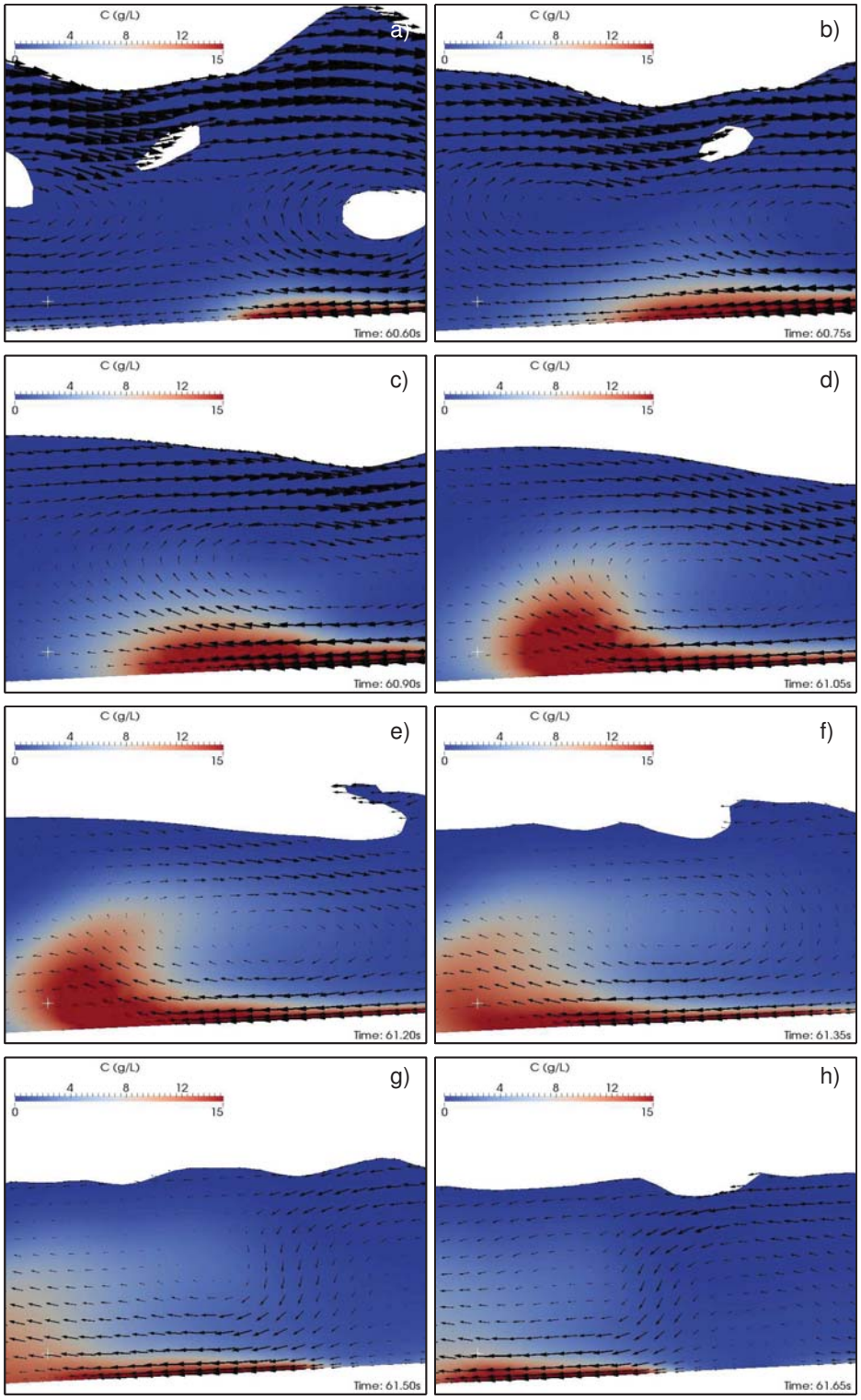

Figure 7.23: Colour spatial plots of the suspended sediment concentration (g/l) in the region of the concentration spike at $t =$ a) 60.60 s, b) 60.75 s c) 60.90 s, d) 61.05 s, e) 61.20 s, f) 61.35 s, g) 61.50 s, and h) 61.65 s. The arrows represent the fluid velocity and the sampling location is indicated by $+$.

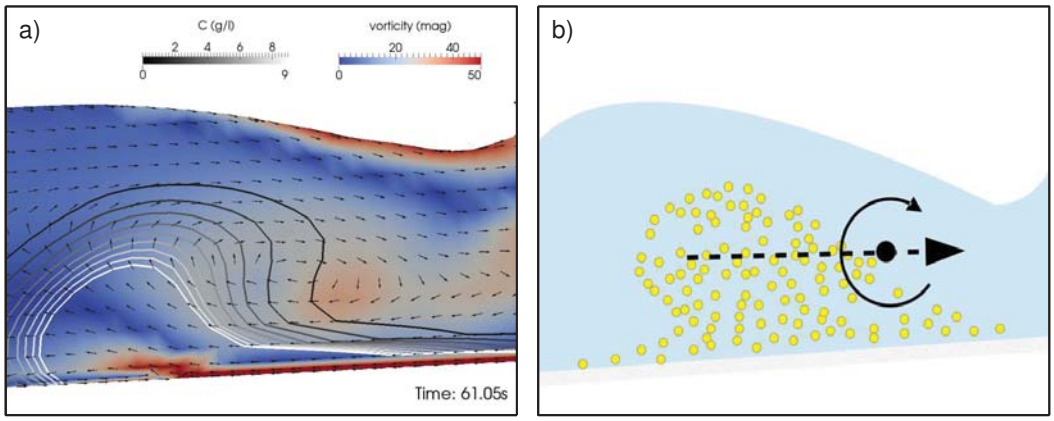

Figure 7.24: Spatial comparison of the predicted concentration plume with an experimental study (Sumer et al. 2013). Plot a) shows the generated vortex in the numerical model coloured by vorticity (magnitude), with contours of concentration (contours spaced by 1 g/l). Plot b) presents a diagram based on the work of Sumer et al. (2013), showing the sediment plume and vortex observed in their study.

phenomena. Using particle image velocimetry (PIV), they found that a series of vortices occur shoreward of the breaking point of plunging breakers, and that these vortices led to increased bed shear stress, similar to the numerical model developed here. Furthermore, they found that the vortices created large vertical pressure gradients, leading to sediment plumes shoreward of the breaking point. Again this description seems to agree qualitatively with the numerical model. Figure 7.24 compares a snapshot ($t = 61.05$ s) of the vortex from the numerical model (a), with a diagram (b) of the vortex and sediment plume from the work of Sumer et al. (2013). The numerical plot is coloured by vorticity magnitude and the contours are of suspended sediment concentration and are in intervals of 1 g/l. There are clear similarities between the present model and the experiments of Sumer et al. (2013), including the direction of rotation of the vortex and the sediment plume occurring on the back edge of the vortex. Sumer et al. (2013) observed vortices, at three different locations in the surf zone. Although there is not any evidence of the first two vortices in the present numerical model, the one that forms in the inner surf zone where the turbulent bore interacts with the backwash from the previous wave does occur sporadically. Hence it seems likely that the process is qualitatively correct, but further work would be needed to assess the typical concentration magnitudes of the sediment plumes. Further work would also be required

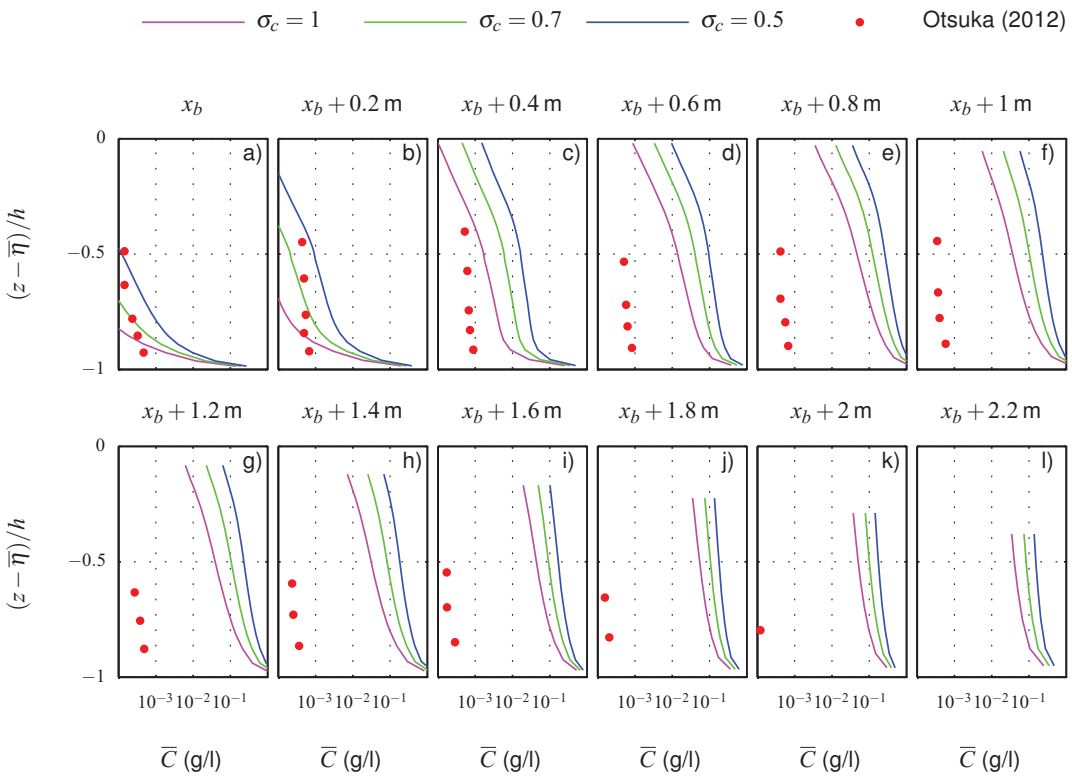

Figure 7.25: Comparison of the numerical predictions of time-averaged suspended sediment concentration under spilling breakers to experimental data (●) gathered by Otsuka and Watanabe (2012) at a number of sampling locations relative to x_b. Each line represents results using a different Schmidt number: $\sigma_c = 1$ (magenta), 0.7 (green), and 0.5 (blue).

to investigate the air entrainment process, as well as evaluating why the flow patterns are different.

7.4.2 Mean Vertical Concentration Profile

In this section, the numerical model is evaluated for its effectiveness in predicting the time-averaged vertical concentration profile under breaking waves. These profiles are particularly important to the present study since they will be heavily utilised as part of the evaluation of the implicit methodology for estimation of sediment diffusivity (see Chapter 8). Time series of the concentration have been collected every 5 mm over the water column, at a number of horizontal locations relative to the breaking point. The time series are averaged over the final 15 wave periods as discussed in Section 7.4.1. The first set of laboratory experiments used for comparison were conducted by Otsuka and Watanabe (2012), which

were presented in units of parts per million (ppm).

Figure 7.25 presents the time-averaged concentration, $\overline{C}$ (g/l) plotted against normalised depth for three different Schmidt numbers. The x-scale ($\overline{C}$) is presented in a logarithmic format, and the horizontal sampling locations shown range from the breaking point, x_b (a), to $x_b + 2.2$ m (l), at intervals of 0.2 m. It is clear that the numerical model substantially overestimates the concentration for all Schmidt numbers and at all locations other than x_b and $x_b + 0.2$ m. The experimental data was presented in units of ppm, and have been converted to g/l. However, ppm is of the order of mg/l, whereas the numerical model predicts concentrations of the order of g/l (≈ 1000 ppm), and, hence, there is a discrepancy of around three orders of magnitude between the numerical model and the experimental data. The plunging breaker results were also generally found to be around three orders of magnitude higher than the experiments. After validating the capability of the model for predicting hydrodynamics under breaking waves (Chapters 5 and 6) and for concentrations in steady and oscillating flows (Chapter 7), it is very surprising that the numerical model performs so poorly for breaking waves, with grain diameters similar to those previously validated. Therefore, comparison with another set of laboratory experiments is considered for clarity.

7.4.2.1 Comparison with Sato et al. (1990)

The second set of breaking wave laboratory experiments that are used for comparison with the numerical model were conducted by Sato et al. (1990). There are a number of reasons for selecting this data set. The first is that the slope of the beach is the same as in Otsuka and Watanabe (2012), and the scale of the experiments in the spilling breakers case is similar too. The second is that the experiments by Sato et al. (1990) have been used as validation cases for numerical models developed by Hsu and Liu (2004) and Ma et al. (2014), which have already been shown to have many similarities with the present numerical model (see Section 7.3).

The simulation set up is the same as in Section 7.4 with the following amendments. The water depth is set to 0.395 m and the wave period and height are 1.35 s and 0.099 m, respectively. This produces a spilling breaker with an Iribarren number of $\xi_0 = 0.24$. 200 s

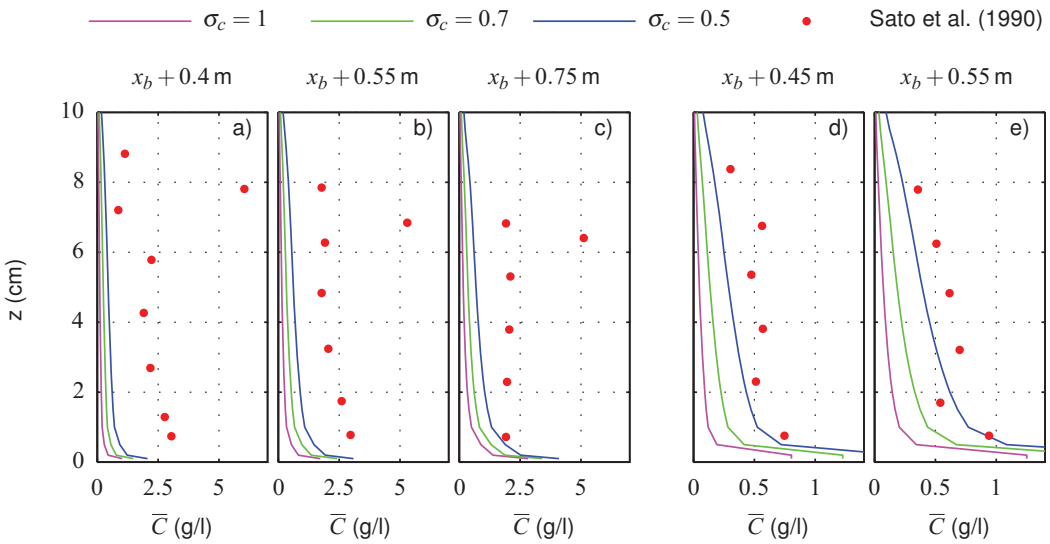

Figure 7.26: Comparison of the predicted time-averaged suspended sediment concentration profile, as a function of height above the bed (cm), with experimental data (•) gathered by Sato et al. (1990) at a number of sampling locations relative to x_b. Plots a,b and c use a grain diameter of $d = 0.15$ mm, whereas for d and e it is $d = 0.18$ mm. Results for $\sigma_c = 1$ (magenta), $\sigma_c = 0.7$ (green), and $\sigma_c = 0.5$ (blue) are presented.

are simulated with the final 15 waves used for averaging. The sand bed is located between $x = 4.5$ m and $x = 6.5$ m, and the grain diameter is set to either 0.15 mm or 0.18 mm. The maximum wave height was found to be at $x = 5$ m and this is taken as the wave's breaking point, with all sampling points relative to this location. The total length of the domain is 18 m and is made up of a 9 m sloping beach and a 9 m constant depth region. The inlet boundary is 0.8 m in height. A relaxation zone of length 2.5 m (approximately one wavelength) is used at the inlet boundary.

Figure 7.26 compares numerical predictions for the time-averaged suspended sediment concentration, $\overline{C}$ (g/l), as a function of height above the bed (cm). The experimental data of Sato et al. (1990) is shown for comparison and two grain diameters have been considered. Each plot is at a different sampling location relative to the breaking point with results assuming three different values of Schmidt number presented. In the $d = 0.15$ mm cases (Figure 7.26a-c), the numerical model under-estimates the mean concentration throughout the water column, at all locations sampled. In the $d = 0.18$ mm case, the numerical

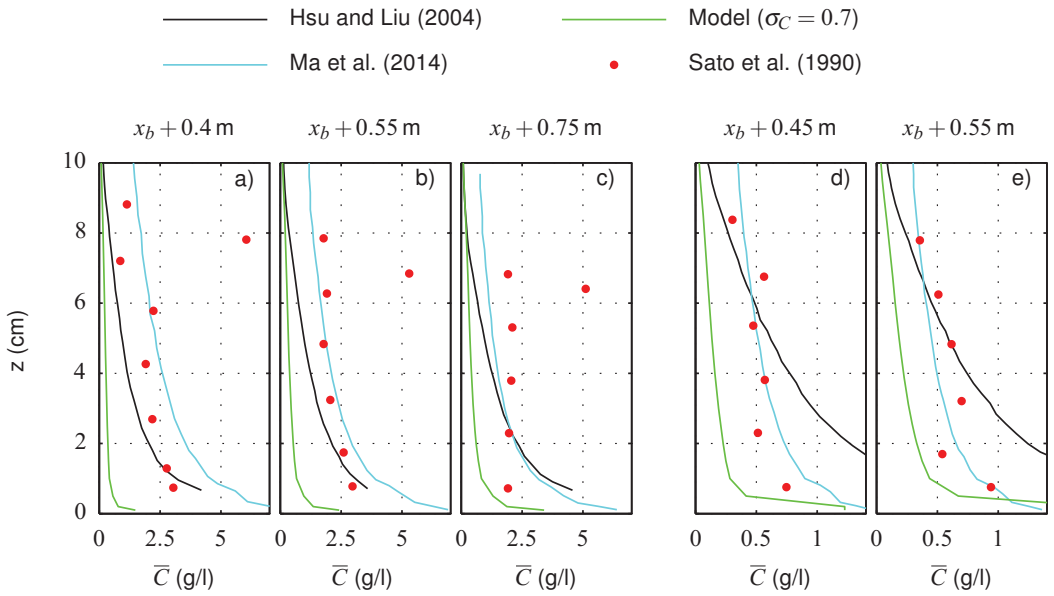

Figure 7.27: Comparison of the numerical time-averaged suspended sediment concentration profile (with $\sigma_c = 0.7$), as a function of height above the bed (cm), with experimental data (•) gathered by Sato et al. (1990), and other numerical models (Hsu and Liu 2004; Ma et al. 2014). Plots a,b and c use a grain diameter of $d = 0.15$ mm, whereas for d and e it is $d = 0.18$ mm.

model also under-predicts the time-averaged concentrations when $\sigma_c = 1$ and $\sigma_c = 0.7$, but for $\sigma_c = 0.5$ the predictions agree well with the experimental data. This case captures the near-bed time-averaged concentrations and follows the experimental profile reasonably well throughout the rest of the water column.

In general, the numerical results are of a similar order of magnitude as the experimental data, and hence are a lot more promising than the initial comparison with Otsuka and Watanabe (2012) (see Figure 7.25). Furthermore, the trend in the numerical predictions compared to Sato et al. (1990) follow the observations made for the regular waves more closely. The numerical model under-estimates the concentration magnitude, which could possibly be due to a short suspension period, similar to the regular waves. This trend is much easier to explain than the severe over-prediction seen in the comparison with data from Otsuka and Watanabe (2012). Hence further analysis of the Otsuka and Watanabe (2012) case will be performed in Section 7.4.2.2.

The present numerical model is now compared with other numerical studies. Figure 7.27

shows the same five plots as Figure 7.26, except for the lines, which represent predictions from different numerical studies, all with $\sigma_c = 0.7$. The other numerical models seem to give slightly better predictions for the $d = 0.15$ mm case. The model of Ma et al. (2014) predicts larger near-bed mean concentrations than observed in the experiments but performs better further up the water column, particularly at sampling location $x_b + 0.55$ m (Figure 7.27b). The model of Hsu and Liu (2004) also over-estimates the near-bed mean concentrations, but exhibits a much larger concentration gradient leading to substantial under-predictions further above the bed. This leads to the numerical predictions crossing the experimental profile at approximately 2 cm above the bed, and hence it performs well in this region. These predictions seem consistent with the regular waves, where it was shown that near the bed, the model of Hsu and Liu (2004) substantially over-predicted the peak concentration, before changing to be more in line with the present numerical model. Furthermore, Ma et al. (2014) had a much longer suspension period which could explain the larger mean value observed here.

In the $d = 0.18$ mm case, the numerical model of Ma et al. (2014) performs slightly better than the present model, following a similar profile shape, but with a magnitude more comparable with the experimental data. On the other hand, the model presented by Hsu and Liu (2004) substantially over-estimates the near-bed mean concentrations. This could be due to the model's additional contributions to the Shields parameter, in the form of a near-bed TKE and a user specified numerical coefficient representing the sediment suspension efficiency, which was obtained through fitting to experimental data. Hsu and Liu (2004) included this parameter to account for sediment pickup due to breaker-induced turbulence, which they claim is not fully accounted for by bottom friction. Before this parameterisation was considered, the numerical predictions were an order of magnitude smaller for the $d = 0.15$ mm case and the fitted efficiency for that case was then applied to the $d = 0.18$ mm case. It is possible that the efficiency depends on grain size, which could explain the lack of agreement for the larger grain size. However, neither the present study nor that of Ma et al. (2014) included this parameter and still obtained reasonable results for both grain diameters, raising the question of the value of such a parameterisation.

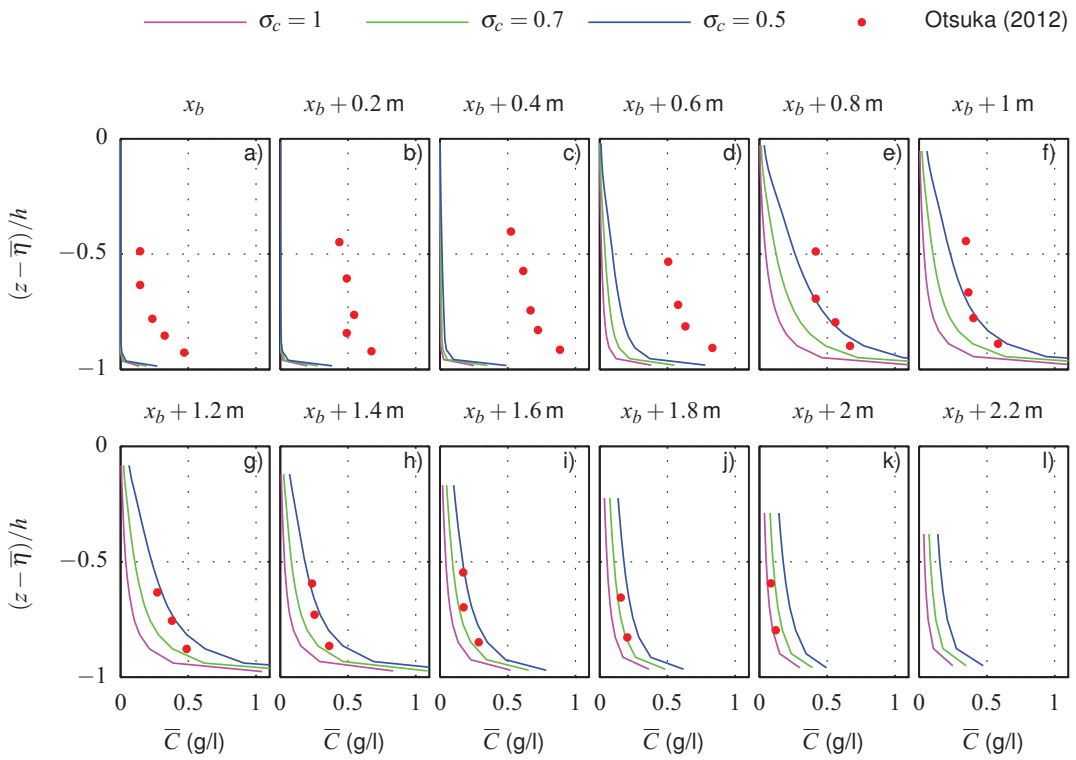

Figure 7.28: Comparison of the numerical predictions of time-averaged suspended sediment concentration under spilling breakers with correctly scaled experimental data (•) gathered by Otsuka and Watanabe (2012) at a number of sampling locations relative to x_b. Results with three values of σ_c are presented.

Overall, the present numerical model gives mean concentration predictions comparable to both experimental data (Sato et al. 1990) and other numerical studies (Hsu and Liu 2004; Ma et al. 2014). As discussed in the regular waves analysis (Section 7.3), it is possible that improvements could be made by applying additional processes such as hindered settling or effects of sediment concentration on turbulence generation. However, additional parameterisations are considered to be outside of the scope of this study and hence the present focus returns to the large discrepancy with the work of Otsuka and Watanabe (2012).

7.4.2.2 Re-evaluating the comparison with Otsuka and Watanabe (2012).

As discussed in Section 7.4.2.1, there seems to be considerable disagreement between the experimental results of Sato et al. (1990) and Otsuka and Watanabe (2012). The former give time-averaged suspended sediment concentrations three orders of magnitude larger than the latter study. This seems surprising since both studies sampled in comparable lo-

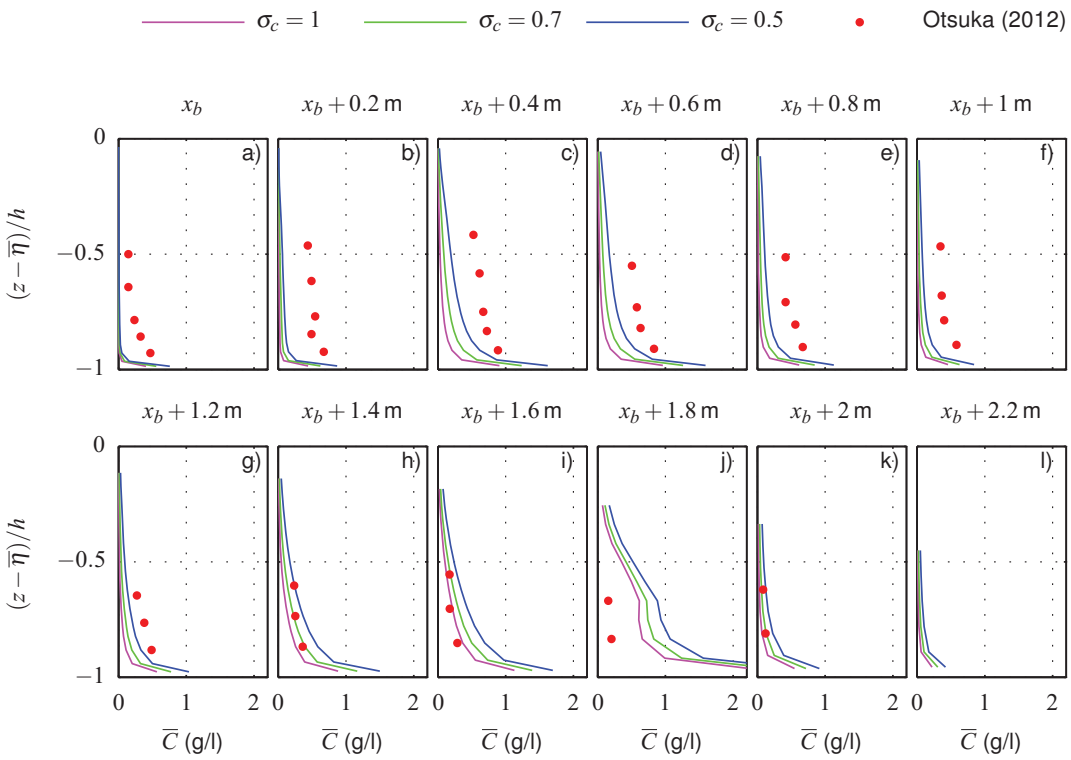

Figure 7.29: Comparison of the numerical predictions of time-averaged suspended sediment concentration under plunging breakers with correctly scaled experimental data (•) gathered by Otsuka and Watanabe (2012) at a number of sampling locations relative to x_b. Results with three values of σ_c are presented.

cations relative to the breaking point and the setup is very similar for both experiments: the grain size is smaller in the case of Sato et al. (1990) 0.15 mm or 0.18 mm compared to 0.2 mm used by Otsuka and Watanabe (2012). However, the results from Sato et al. (1990) do not vary enough between grain sizes to explain three orders of magnitude. Furthermore, the wave is smaller in the experiments of Sato et al. (1990) which will lead to smaller bed shear stresses and hence smaller concentrations. Overall, it seems that there is a lack of consistency between the experiments and working on the basis that three orders of magnitude is the difference between ppm and g/l, it was hypothesised that one of the studies is labelled with the wrong units. Since the numerical model gives comparable results with Sato et al. (1990), as do other numerical models, the comparison with Otsuka and Watanabe (2012) is going to be re-evaluated, assuming that the results are actually in g/l but are incorrectly labelled as ppm in the paper.

Figure 7.28 presents the same results for the spilling breaker as in Figure 7.25 with the experimental data assumed to be in g/l, rather than ppm. It is clear that the numerical predictions agree with the experimental data much better than before for all of the three Schmidt numbers considered. In particular, from $x_b + 0.8$ m onwards the results for $\sigma_c = 0.5$ generally show good predictions both in terms of magnitude and vertical profile shape. The results for $\sigma_c = 1$ under-predict the mean suspended sediment concentration at all locations. The $\sigma_c = 0.7$ result lies somewhere in between the two and hence performs best from around $x_b + 1.6$ m, where the mean concentrations are over-predicted using $\sigma_c = 0.5$. However, from x_b to $x_b + 0.6$ m the numerical model predictions are poor and are at least one order of magnitude smaller than the measured values. In this region the wave is still reasonably well formed and very little turbulence has been generated, particularly near the bottom. Hence it is consistent with the regular waves case (Section 7.3), where it was observed that mean concentration reduced with height above the bed much more rapidly in the numerical model than in the laboratory experiments. Once again, this could be due to processes that are not captured by the numerical model, small concentrations being difficult to measure, or the presence of finer sediments.

Figure 7.29 shows the equivalent plots as Figure 7.28 but for the plunging breaker. The results follow a similar pattern as the spilling breaker case. The numerical model under-predicts the mean concentrations close to the breaking point but performs much better further shoreward. The results agree better at locations $x_b + 0.4$ m and $x_b + 0.6$ m than observed in the spilling breaker, but the mean concentrations are under-estimated by all values of σ_c up until $x_b + 1.4$ m. At locations $x_b + 1.6$ m and $x_b + 1.8$ m the effect of the sporadic concentration plumes discussed in Section 7.4.1 can be observed, where there is a clear over-prediction in mean concentration. Overall, it seems that the agreement between the numerical model and the data gathered by Otsuka and Watanabe (2012) is much more comparable if the data is indeed in g/l rather than ppm. It also agrees with the trends previously noted such as the under-estimate of concentrations discussed in the regular waves section (Section 7.3), and likewise explains the discrepancy in magnitude with Sato et al. (1990). It was later confirmed by the authors (personal communication, Jan. 26, 2017),

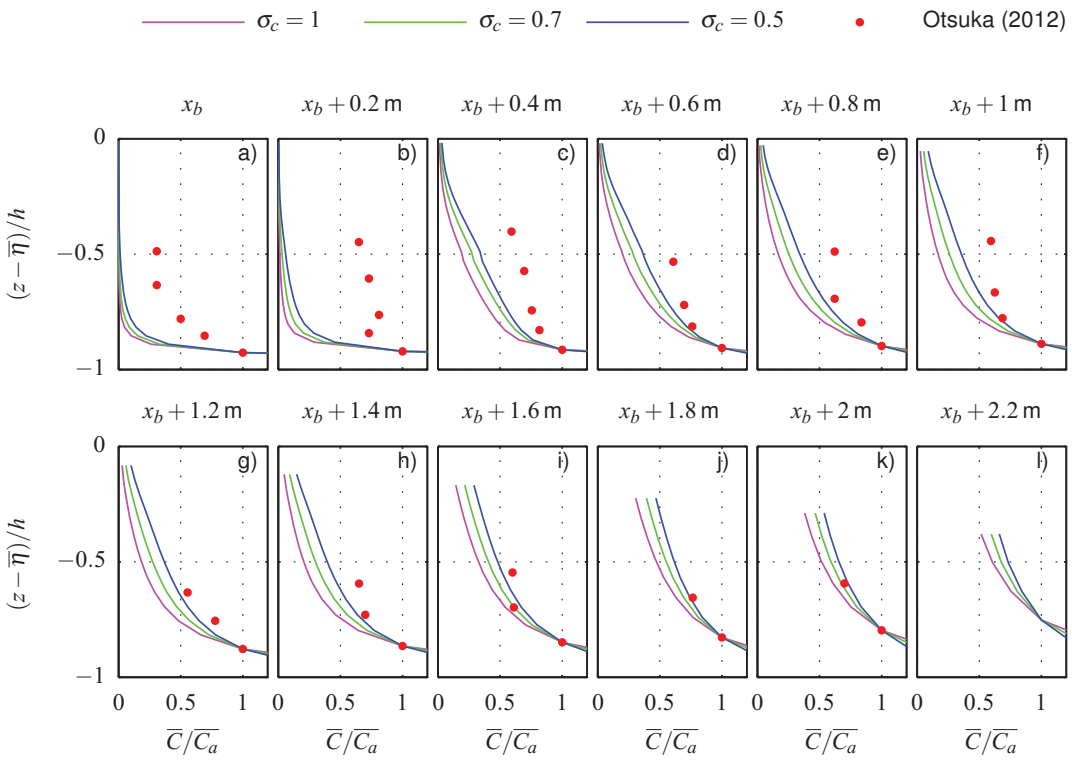

Figure 7.30: Comparison of the normalised predicted mean sediment concentration profiles under spilling breakers with experimental data (•) gathered by Otsuka and Watanabe (2012) at a number of sampling locations relative to x_b. Results with three values of σ_c are presented.

that all of the suspended sediment concentration plots presented by Otsuka and Watanabe (2012) were missing a 10^3 scale, and hence comparing the numerical predictions with the experimental data in g/l is correct.

The implicit estimation of the sediment diffusivity is mostly independent of the magnitude of the mean suspended sediment concentration, but instead depends considerably on the the shape of the time-averaged distribution. Hence, Figures 7.30 and 7.31 present the time-averaged concentration profiles, normalised by the mean concentration 1 cm above the bed, for the spilling and plunging breakers, respectively. The presented locations are the same as shown in Figure 7.25. The trend seen in the regular waves is further emphasised at locations x_b and $x_b + 0.2$ m of the spilling breaker. The concentration rapidly decreases away from the sediment bed, which is not seen in experimental data. This is not so apparent in the plunging breaker case, which instead is more consistent with the sampling locations further

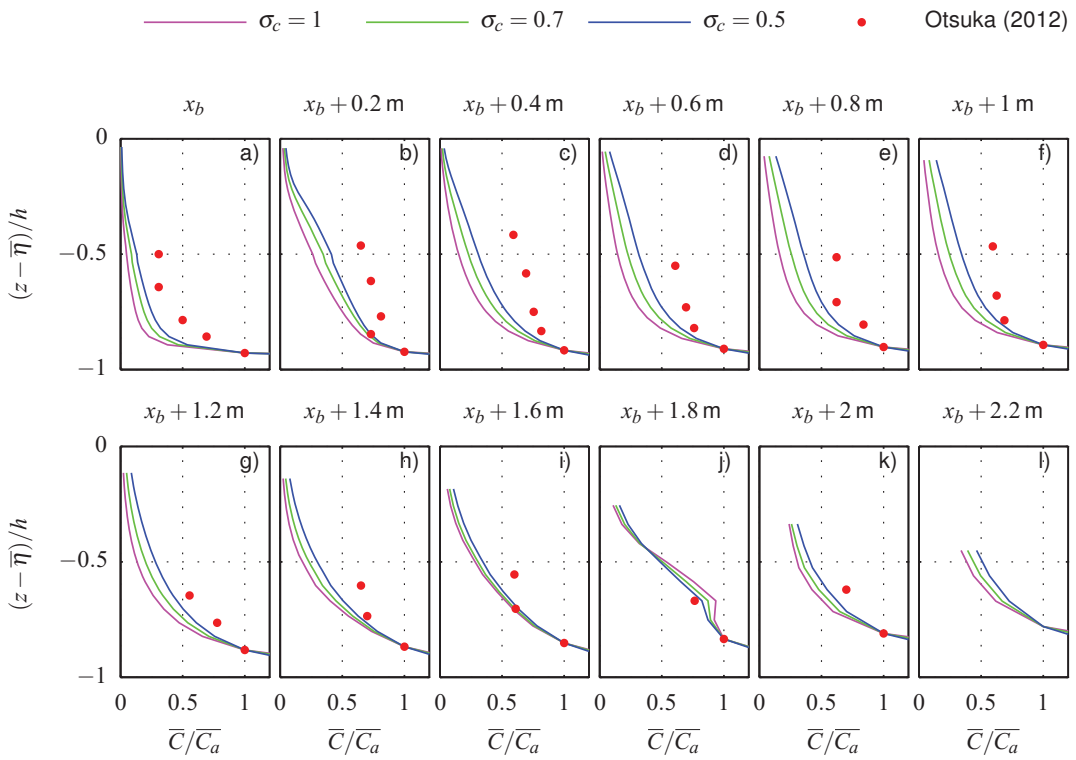

Figure 7.31: Comparison of the normalised predicted mean sediment concentration profiles under plunging breakers with experimental data (•) gathered by Otsuka and Watanabe (2012) at a number of sampling locations relative to x_b. Results with three values of σ_c are presented.

into the surf zone. After this location the numerical model predicts vertical concentration profiles more in line with the experimental data further shoreward of the breaking point, particularly near the bottom. Overall, the results using $\sigma_c = 0.5$ follow the experimental data best, most notably from $x_b + 1.4$ m onwards. This implies that sediment diffusion is around twice as efficient as turbulent diffusion, which is in agreement with a number of other studies (Hsu and Liu 2004; Amoudry et al. 2005; Malarkey et al. 2015).

7.5 Summary

In this chapter the suspended sediment concentration model has been validated using a series of test cases of varying complexity. These validation cases considered both experimental and numerical studies. The numerical model has been shown to give exact analytical solutions when a parabolic eddy viscosity has been imposed, verifying that the

correct equations are being solved. Furthermore, when considering a steady state flow, it was found that the numerical model gave good concentration predictions for fine natural sand with diameters between 0.13 mm and 0.23 mm. However, when considering large acrylic particles, the numerical model gave large under-predictions, most likely attributed to processes not included in the present numerical model such as hindered settling.

Under regular waves, the numerical model was shown to perform to a similar standard as the previous numerical study of Hsu and Liu (2004), although it did under-predict the mean concentration profile compared to the experimental data gathered by Dohmen-Janssen and Hanes (2002), particularly for sampling locations far above the bed. However, the peak concentration generally agreed well with the experimental data, indicating that the sediment does not stay in suspension for as long as observed experimentally. This was confirmed by comparing the wave-averaged suspended sediment concentration profiles at a number of locations. The numerical model of Ma et al. (2014) predicted a similar peak concentration value as the present model but the sediment remained in suspension for a time that was more in agreement with the experimental data and hence gave a larger mean concentration. This indicates that the numerical model can be improved in the future, possibly through inclusion of other processes or modification of turbulence closure models.

Finally, under breaking waves the numerical model was shown to perform well when compared to the experimental data presented by Sato et al. (1990), particularly for the larger grain size considered. Furthermore, comparison with other numerical models generally shows similar trends as observed for regular waves. Ma et al. (2014) predicted larger concentrations, possibly due to the suspension period previously noted. However, when compared to the experimental data of Otsuka and Watanabe (2012) it was found that the numerical model predicted concentrations a number of orders of magnitude too large. Comparing the concentrations from both experiments, which were of similar scale, it was observed that the concentrations differed by around three orders of magnitude. After contacting the authors (personal communication, Jan. 26, 2017), it was confirmed that all of the concentration plots in the paper published by Otsuka and Watanabe (2012) were labelled incorrectly,

and were in fact in g/l. Making this correction led to good agreement with the numerical model. Another interesting observation is the occasional generation of vortices under plunging breakers, which lead to sediment plumes, qualitatively comparable to the work of Sumer et al. (2013). This would be an interesting research direction to pursue in the future.

Overall, the numerical model gives reasonable predictions under a number of different flow conditions. However, it is clear that improvements could be made in order to more accurately capture some of the experimental profiles, but this is being treated as future work. Therefore, the numerical model is considered to be validated to a point that the calculation of the sediment diffusivity can be evaluated.

Chapter 8

Evaluation of an Implicit Method for Estimating Sediment Diffusivity

The sediment diffusivity, ν_s, as defined in equation (4.81), is a fundamental component of suspended sediment numerical models (Hsu and Liu 2004; Jacobsen et al. 2012; Ma et al. 2014). This parameter has substantial influence on suspended sediment dynamics but there is great uncertainty regarding its value since it can only be measured implicitly, through other variables such as the vertical concentration profile and the eddy viscosity. Until ν_s is accurately quantified in physical experiments, it could introduce substantial error into numerical models.

One way of determining the sediment diffusivity is to use the turbulent Schmidt number,

$$\sigma_c = \frac{\nu_t}{\nu_s}, \tag{8.1}$$

which relates the sediment diffusivity, ν_s, to the eddy viscosity, ν_t. In theory this is a very useful relationship for both experimental and numerical studies since the eddy viscosity is often calculated, or already known. Hence, using equation 8.1, the sediment diffusivity can also be assumed to be known, up to a constant of proportionality, $\beta = 1/\sigma_c$ (see Section 2.3). However, there is considerable uncertainty regarding the value of this constant of proportionality. In numerical models, it is commonly assumed that $\beta = 1$, implying that sediment diffusion has the same efficiency as turbulent diffusion. However, a wide range of values, with evidence for both more (Cellino 1998; Ogston and Sternberg 2002) and less (van Rijn 1984*b*) efficiency, have been obtained from various studies. Accurate predictions

of both ν_s and eddy viscosity, ν_t, are vital to determine the relationship between the two, and the inconsistencies amongst studies indicate that both variables are difficult to estimate accurately.

This chapter focuses on a common experimental methodology for estimation of the sediment diffusivity, with emphasis on the quantification of the error in such an implicit approach. The method utilises the vertical concentration profile, which is convenient in field or laboratory experiments since this variable is often measured. As will be discussed in detail later in the chapter, the basis of the methodology is the vertical balance of diffusion and settling, neglecting flow advection and all horizontal gradients. These are perfectly reasonable assumptions in steady horizontal flow conditions. However, it is common practice to extend the approach to unsteady wave-driven environments, through time-averaging of suspended sediment concentrations, which introduces substantial uncertainty since the assumption that the phase-resolved components are negligible has largely been untested. This will be explored in this chapter, along with the effect of neglecting flow advection, and horizontal gradients.

The methodology is applied to the four cases discussed in Chapter 7. These test cases range from conditions in which the methodology is expected to work well, to those where there is considerable uncertainty. In all of the cases the analysis begins at equation (4.81), and based on the assumption of small horizontal gradients, all of the horizontal terms are neglected to obtain the vertical balance

$$\frac{\partial C}{\partial t}+\frac{\partial (wC)}{\partial z}-w_s\frac{\partial C}{\partial z}=\frac{\partial}{\partial z}\left(\nu_s\frac{\partial C}{\partial z}\right). \tag{8.2}$$

Following common conventions, equation (8.2) can be simplified to derive a formulation for the sediment diffusivity, based on known quantities. As will be seen later in the chapter, for unsteady flow conditions, this expression will take the form

$$\overline{\nu_s}=\frac{-w_s\overline{C}}{\partial\overline{C}/\partial z}. \tag{8.3}$$

In the present numerical model, the sediment diffusivity is directly determined using the eddy viscosity, and a user specified value for σ_c. The time-average of this directly determined value can be compared against the estimated value, obtained through application of equation (8.3), using the time-averaged vertical concentration profiles predicted by the numerical model. This is the key advantage of using the present numerical model to investigate the problem: in the field and laboratory the sediment diffusivity is unknown and hence it is unclear when the formula is valid. A summary of the approach adopted in this study for an unsteady flow is as follows:

1. Specify the value of $\beta = 1/\sigma_c$.
2. Start the simulation at time $t = 0$.
3. Calculate the eddy viscosity, ν_t, using a turbulence closure model.
4. Calculate the sediment diffusivity, $\nu_s = \beta \nu_t$.
5. Use ν_s in the governing equation (equation 4.81) of the suspended sediment concentration model.
6. Progress to the next time step, $t_{i+1} = t_i + \Delta t$.
7. Repeat steps $3-6$ until simulation end time is reached.
8. Calculate the time-average of the sediment diffusivity, $\overline{\nu_{s,num}}$, over 15 wave periods. This directly determined value will be referred to as the "numerically applied" time-averaged sediment diffusivity in this section.
9. Calculate an estimated value for the time-averaged sediment diffusivity, $\overline{\nu_{s,est}}$, through application of equation (8.3) using the vertical time-averaged concentration profiles predicted by the numerical model. This will be referred to as the "estimated" time-averaged sediment diffusivity in this chapter.
10. Compare and quantify the difference between the estimated and numerically applied sediment diffusivities, and explore possible explanations for the differences.

A similar approach is applied for the steady state flow condition cases (Section 8.1 and

8.2) except that time-averaging is not required, and hence the numerically applied sediment diffusivity, $\nu_{s,num}$, is compared with the estimated value, $\nu_{s,est}$, calculated based on the steady state concentration field. Hence the overbar's can be dropped from equation (8.3) for these steady cases. The approach used to quantify the difference between the estimated and numerical applied (time-averaged) sediment diffusivities in each of the different flow conditions, is described at the beginning of each of the relevant sections.

The chapter is constructed such that purely diffusive flows are considered first, followed by steady state advection-diffusion conditions. Analysis of regular waves follows, with breaking waves considered last.

8.1 Case 1: Purely Diffusive Flows

The methodology is first applied to purely diffusive flow conditions with a parabolic sediment diffusivity profile, as described in Section 7.1.2. In this case, the solution is steady and the advection term is based on the settling of the particles alone with no contribution arising from the fluid flow. Hence, equation (8.2) simplifies to

$$-w_s\frac{\partial C}{\partial z}=\frac{\partial}{\partial z}\left(\nu_s\frac{\partial C}{\partial z}\right). \tag{8.4}$$

Integrating with respect to z, and rearranging gives a formulation for the estimated sediment diffusivity,

$$\nu_{s,est}=\frac{-w_sC}{\partial C/\partial z}. \tag{8.5}$$

This approximation is very appealing when dealing with physical data, and field measurements in particular, since only the vertical suspended sediment concentration profile as a function of depth needs to be known. In the present case, the sediment diffusivity has been specified as a parabolic profile (equation 7.3), which allows an analytical solution for the vertical suspended sediment concentration profile to be obtained, known as the Rouse profile (see Section 7.1.2). The Rouse profile can be differentiated with respect to z to obtain

an analytical solution of the vertical concentration gradient,

$$\frac{\partial C}{\partial z} = \frac{w_s C}{\kappa u_*}\left(\frac{-h}{z(h-z)}\right). \tag{8.6}$$

Substituting this into equation (8.5), along with the Rouse profile for C (equation 7.4), gives

$$\nu_{s,est} = \frac{-w_s C}{\frac{w_s C}{\kappa u_*}\left(\frac{-h}{z(h-z)}\right)} = \kappa u_* z\left(1-\frac{z}{h}\right), \tag{8.7}$$

which is exactly the numerically applied parabolic sediment diffusivity profile specified in equation (7.3). This case shows that in trivial problems, where terms such as the flow advection and time derivative can be disregarded, the formula can perfectly reproduce the sediment diffusivity in the flow. Therefore, the rationale of attempting to use a sediment diffusivity formula based on the vertical concentration gradient in more complex problems seems sensible. However, in general, more complex fluid flows do not have analytical solutions, and hence application of equation (8.5) is unlikely to give perfect agreement, contrary to the purely diffusive flow considered here.

8.2 Case 2: Steady State Advection-Diffusion

The methodology is applied here to the steady state advection-diffusion simulations presented in Section 7.2. The simulations that were run for comparison with Cellino (1998) will be used for the analysis. Once again, the case is considered to be steady, so the time derivative in equation (8.2) can be neglected, giving

$$\frac{\partial wC}{\partial z} - w_s\frac{\partial C}{\partial z} = \frac{\partial}{\partial z}\left(\nu_s\frac{\partial C}{\partial z}\right). \tag{8.8}$$

Integrating with respect to z and rearranging provides a formulation for the sediment diffusivity

$$\nu_{s,est} = \frac{wC - w_s C}{dC/dz} = \frac{(w-w_s)C}{\partial C}\partial z, \tag{8.9}$$

which depends only on the vertical concentration profile and the vertical velocity. However, the vertical flow should be relatively small in the case considered here: horizontal flow in a channel. Thus the vertical velocity is neglected in the present case and the simplified formulation (equation 8.5) used in the pure-diffusion case (Section 8.1) will be applied here.

Unlike the pure diffusion case discussed in Section 8.1, there is not an analytical solution for the vertical concentration profile and, hence, not for the vertical concentration gradient. One option would be to fit the data with an exponential or power law profile. However, this would lead to either a constant or linear sediment diffusivity, which, considering Figure 7.11, is clearly not the case for this problem. This was reflected in the fit to the model predictions, which were generally very poor in both cases. A Rouse profile gave a slightly more accurate fit to the data, but again it is clear from Figure 7.11 that the profile for the sediment diffusivity is not perfectly parabolic. Spline interpolation was found to give poor predictions in the sharp concentration gradient near the sand bed. Therefore, the vertical concentration gradient has been obtained from the numerical model output, which is directly calculated using central differencing between cell centres.

Figure 8.1 presents the estimated sediment diffusivity as a function of normalised depth, z/h, obtained using equation (8.5) at sampling location $x = 7\,\mathrm{m}$ (magenta line), and is compared with the numerically applied values (•) for the eight cases from Cellino (1998), as discussed in Section 7.2. The top row represents tests conducted using sediment with settling velocity, $w_s = 0.012\,\mathrm{m\,s^{-1}}$, whereas the bottom row are cases with $w_s = 0.021\,\mathrm{m\,s^{-1}}$. The flow velocity increases from left to right (see Table 7.1 for full details of all eight cases). The NRMSE (E) for each of the estimated profiles, calculated using equation (7.6) but for ν_s rather than C, is indicated (in magenta) at the top of each plot. There is a clear difference between the two settling velocities: for all cases conducted using $w_s = 0.021\,\mathrm{m\,s^{-1}}$ the agreement between the estimated and numerically applied sediment diffusivity is very good (less than 5% difference), but the $w_s = 0.012\,\mathrm{m\,s^{-1}}$ predictions show substantial discrepancies ($20 - 25\%$ error).

The dependency on the settling velocity was initially somewhat perplexing since the velocity

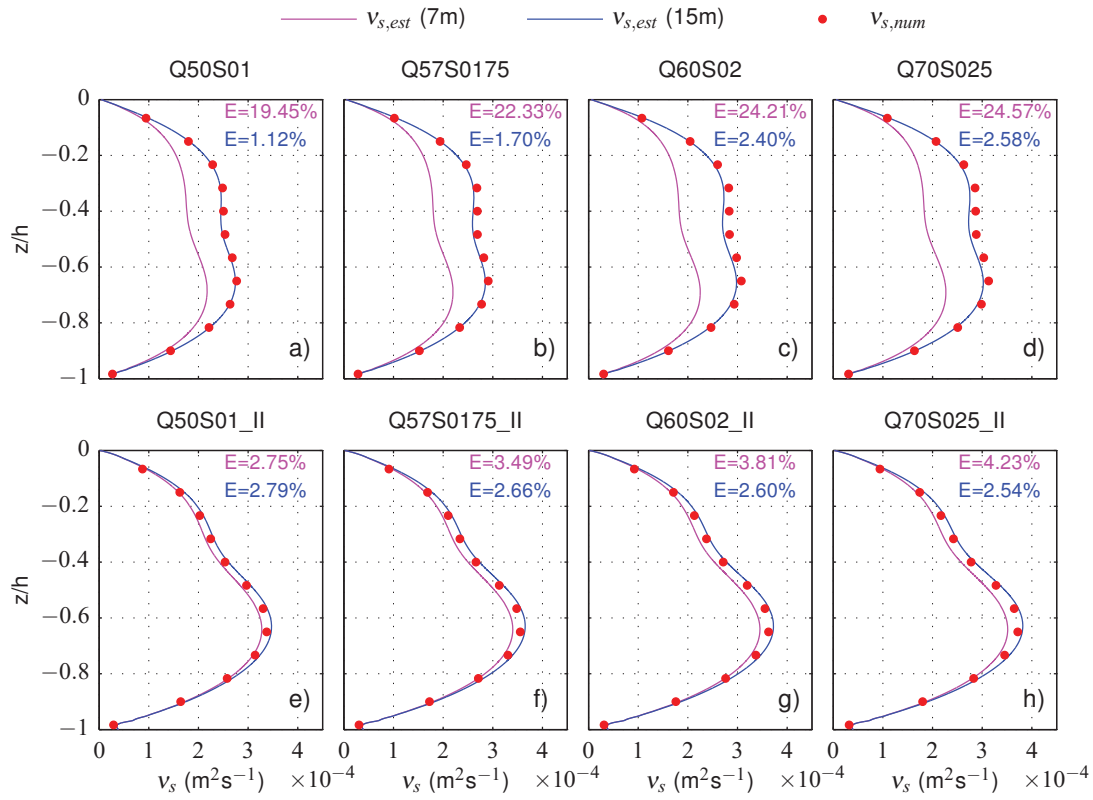

Figure 8.1: Evaluation of the sediment diffusivity for the eight cases from Cellino (1998), described in Section 7.2. Values estimated (equation 8.5) using the predicted vertical concentration profiles sampled at $x = 7$ (magenta) and 15 m (blue) are compared to the numerically applied values (•). The normalised root mean square error (NRMSE) for each profile is indicated at the top of each plot (in the corresponding colour). The top and bottom rows represent simulations conducted with $w_s = 0.012$ and 0.021 m s^{-1}, respectively, and the flow speed is increasing from left to right.

and turbulence was expected to be near-identical throughout the channel. Hence, further work has been conducted to determine an explanation for this sensitivity. Equation (8.9) was applied, including the vertical velocity term, but this was found to make negligible difference. Therefore, horizontal variation in the flow variables was examined at the centre line of the channel, for the cases with the largest error for each settling velocity, Q70S025 and Q70S025_II. The results showed that there was not a substantial horizontal gradient in the velocity and sediment diffusivity profiles at the centre line at 7 m. However, the concentration profile does have a horizontal dependency. Figure 8.2 shows the horizontal gradient in suspended sediment concentration, at the centre line of the channel, as a function of x, where $x = 0$ is the inlet boundary.

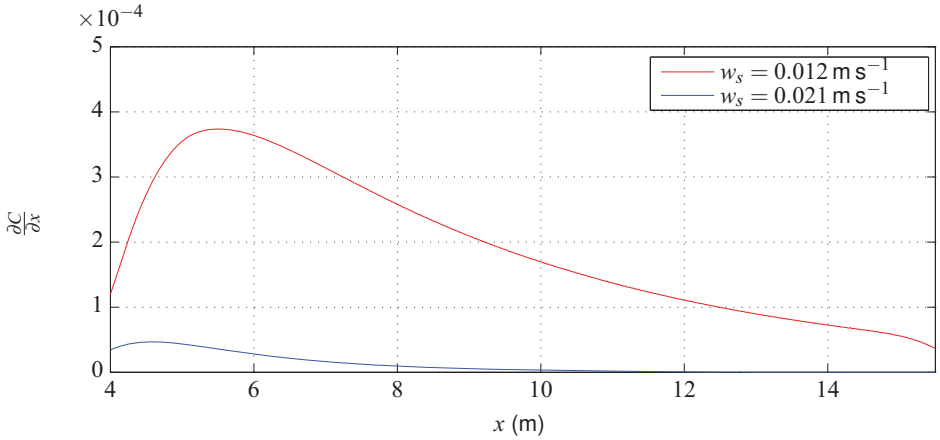

Figure 8.2: Variation of the horizontal concentration gradient at the centre line of the channel ($z = 0.06$ m) as a function of x in the steady state advection-diffusion test cases. Two settling velocity cases have been presented $w_s = 0.012\,\mathrm{m\,s^{-1}}$ (red) and $w_s = 0.021\,\mathrm{m\,s^{-1}}$ (blue).

The results clearly show that the lower settling velocity case has a much larger horizontal gradient of concentration for all values of x, with a particularly large value observed at the 7 m sampling location. This horizontal dependence for the sediment concentration may be caused by the boundary layer not fully developing before the start of the sediment bed (see Figure 7.3). This would lead to increased friction velocity near the start of the sediment bed, which in turn would cause higher entrainment rates, with the sediment then advected further along the tank. The effect of this would be more substantial for smaller settling velocities due to a combination of increased entrainment (see equation 3.63), and sediment being advected further before settling due to the relative differences in settling and flow velocities. This potential explanation for the horizontal dependency of concentration, as observed in Figure 8.2, could be capable of causing the horizontal flow advection and diffusion terms to be too large to be neglected. Therefore, the magnitudes of the horizontal flow advection term, $\frac{\partial(uC)}{\partial x}$, and the settling term, $-w_s\frac{\partial C}{\partial z}$, have been compared (see Fig 8.3), as functions of normalised depth. Both settling velocity cases have been presented, with a sampling location of $x = 7$ m. Near the bottom ($z/h < -0.9$), the ratio is large indicating that the settling term is at least an order of magnitude larger than the horizontal flow advection term, and hence the assumption that the latter is negligible is valid. However, further above the bed the ratio becomes much smaller, ranging between 1 and 3 for the $w_s = 0.012\,\mathrm{m\,s^{-1}}$ case, indicating that the terms are comparable in magnitude and hence the horizontal flow advec-

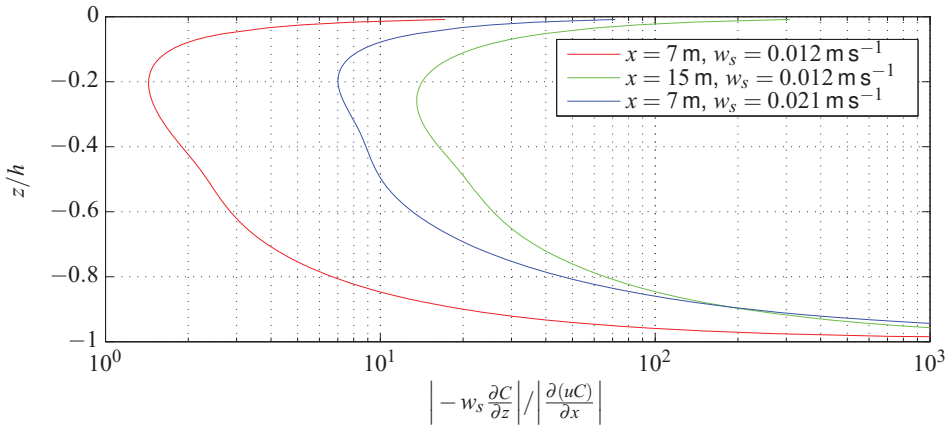

Figure 8.3: Vertical variation in the ratio of the settling and horizontal flow advection term magnitudes under steady state advection-diffusion. Results are taken from tests Q70S025 (sampled at $x = 7$ m (red) and $x = 15$ m (green)) and Q70S025_II (sampled at $x = 7$ m (blue)), representing two different settling velocities.

tion term cannot be neglected. On the other hand, for the case with a larger settling velocity, the ratio remains closer to 10, i.e. the settling term is approximately an order of magnitude larger and hence neglecting the horizontal flow advection term is more acceptable. This can be seen in the results presented in Figure 8.1. The formula (equation 8.5) gives very good agreement near the bed for both settling velocities but, further up the water column, the lower settling velocity case performs poorly, and the larger w_s case still gives reasonable results. It is worth noting that the horizontal diffusion term was also considered but this was found to be several orders of magnitude smaller and hence can be safely neglected.

The results just presented imply that if a large horizontal concentration gradient is present then the formula (equation 8.5) breaks down. It may be possible to achieve a more uniform flow and concentration field through redesigning the simulations, possibly by increasing the length of the inlet wall (see Figure 7.3), or running them with stricter tolerances. However, instead of running the cases again, the spatial distribution of the estimated and numerically applied ν_s are examined for both settling velocity cases.

Figures 8.4 and 8.5 present the spatial distribution of a) $\nu_{s,est}$, b) $\nu_{s,num}$, c) the relative error, and d) the ratio of the settling to flow advection contributions under steady state conditions, between $x = 6$ m and 16 m, for the $w_s = 0.012\,\mathrm{m\,s^{-1}}$ and $w_s = 0.021\,\mathrm{m\,s^{-1}}$ cases (Q70S025

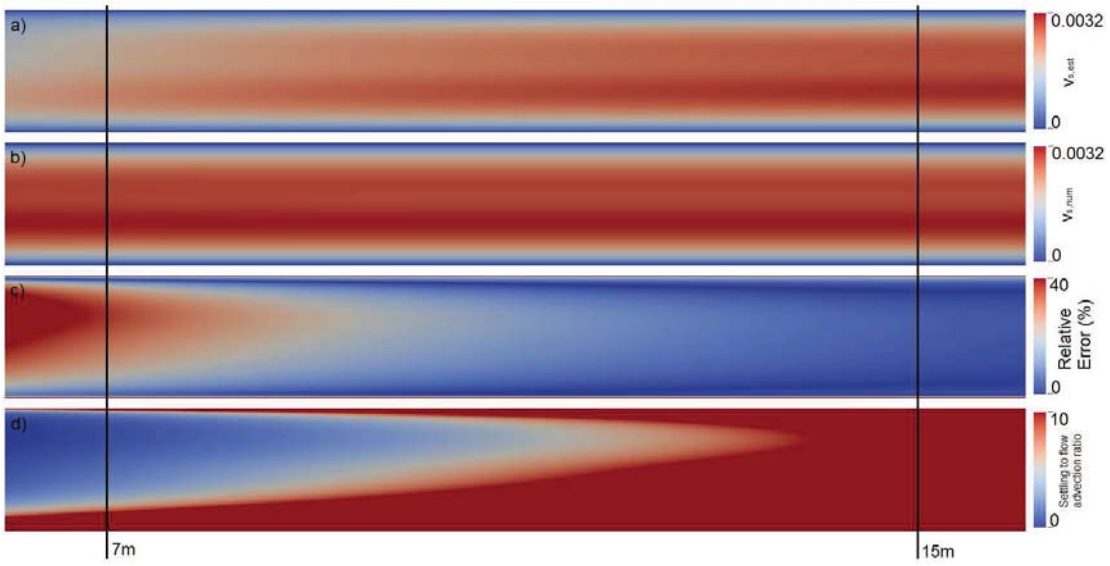

Figure 8.4: Spatial plots of a) $v_{s,est}$ (eqn 8.5), b) $v_{s,num}$, c) the relative error (eqn 8.10), and d) the advection ratio (eqn 8.11), between $x = 6$ m and 16 m, for the $w_s = 0.012\,\mathrm{m\,s^{-1}}$ steady state case (Q70S025). The vertical lines indicate sampling locations at 7 m (left) and 15 m (right).

and Q70S025_II), respectively. In both cases, the numerically applied sediment diffusivity ($v_{s,num}$) does not vary considerably with x, which is to be expected due to the uniform flow conditions. However, in the $w_s = 0.012\,\mathrm{m\,s^{-1}}$ case, the estimated values ($v_{s,est}$) have a substantial dependence on x, with much smaller magnitudes than observed in $v_{s,num}$ at $x = 7$ m, which was evident in Figure 8.1. Progressing along the channel, $v_{s,est}$ begins to resemble the $v_{s,num}$ profile more closely and, towards the end of the domain ($x > 14$ m), the agreement appears to be reasonable. This is backed up by the relative errors (Figure 8.4c), which were calculated using

$$\text{Relative Error} = 100 \times \frac{|v_{s,est} - v_{s,num}|}{v_{s,num}}. \tag{8.10}$$

Near the top and bottom boundaries, there is a thin layer of poor agreement that runs the length of the channel, most likely arising from the small magnitudes of $v_{s,num}$ at these locations. Large errors occur just above the centre line of the channel which reduce in magnitude as x increases. At the sampling location, $x = 7$ m, the maximum error is approximately 30% in this region.

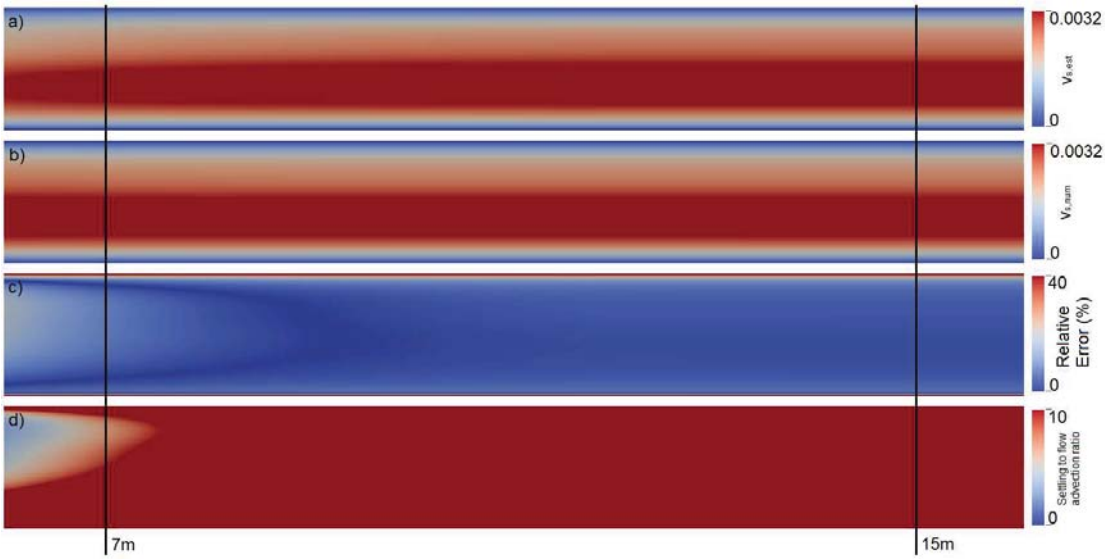

Figure 8.5: Spatial plots of a) $v_{s,est}$ (eqn 8.5), b) $v_{s,num}$, c) the relative error (eqn 8.10), and d) the advection ratio (eqn 8.11), between $x = 6\,\text{m}$ and $16\,\text{m}$, for the $w_s = 0.021\,\text{m}\,\text{s}^{-1}$ steady state case (Q70S025_II). The vertical lines indicate sampling locations at $7\,\text{m}$ (left) and $15\,\text{m}$ (right).

On the other hand, considering the relative errors in the larger settling velocity case (Figure 8.5c), it is clear that they are much smaller, although a small region of $10-20\%$ error does exist between 6 and $8\,\text{m}$. This can also be seen in the $v_{s,est}$ plot (Figure 8.5a), where the most obvious differences from the $v_{s,num}$ profile (Figure 8.5b) occur near the left hand side of the channel. Building on the previous discussion regarding the effect of neglecting flow advection on the accuracy of the estimations (see Figure 8.3), the ratio of the settling to horizontal flow advection terms,

$$\text{Advection Ratio} = \left| -w_s \frac{\partial C}{\partial z} \right| \Big/ \left| \frac{\partial (uC)}{\partial x} \right|, \tag{8.11}$$

have also presented in Figure 8.4d and Figure 8.5d for the $w_s = 0.012\,\text{m}\,\text{s}^{-1}$ and $w_s = 0.021\,\text{m}\,\text{s}^{-1}$ cases, respectively. In these plots, red indicates that the contribution from the settling of the particles is at least an order of magnitude larger than the horizontal flow advection, and hence the latter can be neglected. Conversely, blue regions indicate that the flow advection cannot be safely neglected when using this implicit approach to estimate v_s. There is a clear correlation between the blue regions in the advection ratio plot and

the relative error in both cases. Furthermore, the blue region is much larger in the smaller settling velocity case, and at 7 m the horizontal flow advection can largely not be neglected throughout the water column, as was indicated in Figure 8.3. For the larger settling velocity case, the effect of neglecting flow advection is less clear since there is a region at mid-depth where the advection ratio is around 7, which is not quite an order of magnitude.

Taking all of this into consideration, the implicit approach for estimating ν_s is reapplied using the concentration profiles obtained at 15 m, since the flow advection is negligible in both cases at this sampling location. The advection ratio (equation 8.11) at 15 m has also been plotted in Figure 8.3, and confirms that, at this location, the advection due to settling is always at least an order of magnitude larger than the horizontal flow advection. Therefore, equation (8.5) has been applied to the concentration profile obtained at 15 m in all eight cases and has been plotted in Figure 8.1 (in blue). The agreement is good in all eight cases with small errors in the range of $1-3\%$. As discussed previously, the advection ratio indicated that settling was just below an order of magnitude larger in case Q70S025_II at sampling location $x = 7$ m. By sampling in a location where this was greater than an order of magnitude the NRMSE has dropped slightly from 4.23% to 2.54%, indicating that the flow advection was still having a small effect on the estimation in this case.

Overall, the errors are considered to be acceptable and indicate that the formula works as expected in steady state flows. However, the analysis conducted into the sensitivity of the horizontal flow advection raises questions about the applicability of using a similar formulation in non-uniform flows, and could potentially cause problems in the more complex test cases.

8.3 Case 3: Regular Waves

The regular wave case, discussed in Section 7.3, is considered here. Since waves are time dependent, this case is not steady state and, unlike the cases discussed in Sections 8.1 and 8.2, the time derivative term cannot be neglected. However, many researchers attempt to extend the implicit methodology to obtain a time-averaged sediment diffusivity, in these wave-driven conditions, through time-averaging the concentration profiles. This ap-

proach neglects the fluctuations in sediment diffusivity, and the effect of this has largely been untested. This will be addressed in this section, along with determining the contribution from wave orbital motion and flow advection.

Following the common approach of taking the time-average of equation (8.2) gives,

$$\overline{\frac{\partial C}{\partial t}} + \overline{\frac{\partial wC}{\partial z}} - \overline{w_s \frac{\partial C}{\partial z}} = \overline{\frac{\partial}{\partial z}\left(\nu_s \frac{\partial C}{\partial z}\right)}. \tag{8.12}$$

If the time period that is used for averaging is large enough, then the time derivative term can be assumed to be near zero, $\overline{\frac{\partial C}{\partial t}} \approx 0$, and hence can be neglected. Using the time-averaging rules defined for Reynolds decomposition (equation 3.7), equation (8.12) reduces to

$$\frac{\partial \overline{wC}}{\partial z} - w_s \frac{\partial \overline{C}}{\partial z} = \frac{\partial}{\partial z}\left(\overline{\nu_s \frac{\partial C}{\partial z}}\right), \tag{8.13}$$

which can be integrated with respect to z, to give,

$$\overline{wC} - w_s \overline{C} = \overline{\nu_s \frac{\partial C}{\partial z}}. \tag{8.14}$$

In order to obtain a formulation for ν_s the term on the right hand side must be split up, which would be trivial if ν_s has a constant value. However, ν_s varies with the passing waves and hence a similar approach to Reynolds-averaging is adopted. The variables are considered as a combination of a mean value and a fluctuating component generated by the waves,

$$C = \overline{C} + C', \qquad \nu_s = \overline{\nu_s} + \nu_s'. \tag{8.15}$$

Using this in equation 8.14 along with the Reynolds-averaging laws (equation 3.7) yields,

$$\overline{wC} - w_s \overline{C} = \overline{\nu_s} \frac{\partial \overline{C}}{\partial z} + \overline{\nu_s' \frac{\partial C'}{\partial z}}, \tag{8.16}$$

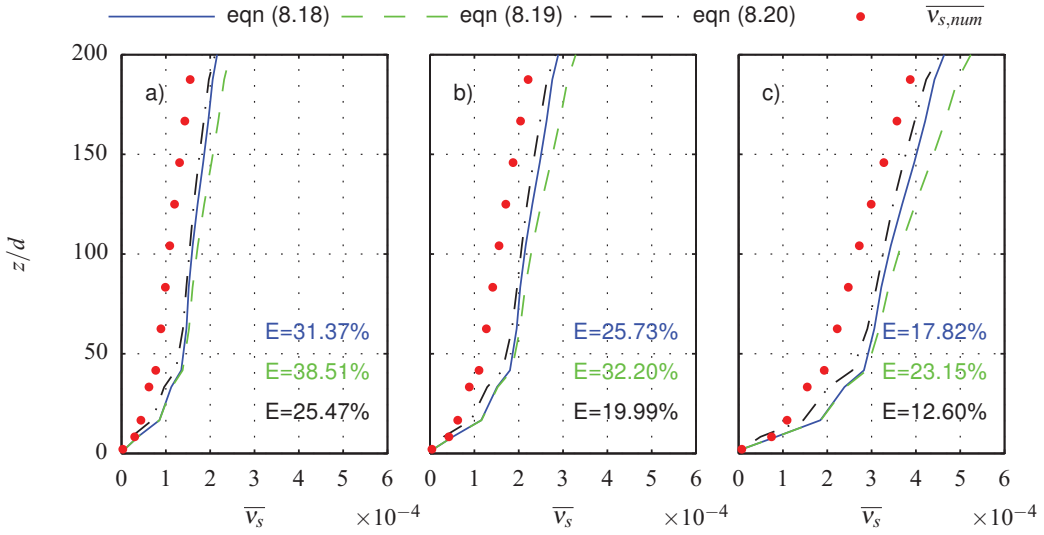

Figure 8.6: Comparison of the estimated (lines) and numerically applied (•) time-averaged sediment diffusivity profiles under regular wave conditions. The estimated profiles have been obtained using equations 8.18 (blue), 8.19 (green) and 8.20 (black). Each plot presents results for a different Schmidt number: a) $\sigma_c = 1$, b) $\sigma_c = 0.7$, and c) $\sigma_c = 0.4$.

which can be rearranged to give a formulation for the time-averaged sediment diffusivity,

$$\overline{v_{s,est}} = \frac{\overline{wC} - w_s\overline{C} - \overline{v_s'\frac{\partial C'}{\partial z}}}{\partial\overline{C}/\partial z}. \tag{8.17}$$

Since it is difficult to measure, and requires prior knowledge of v_s, the term $-\overline{v_s'\frac{\partial C'}{\partial z}}$ is dropped, for now. The formulation can be further simplified by neglecting the vertical component of the wave orbital motion, which, using linear wave theory, has been estimated to contribute less than 20% high in the water column, and very little near the bed (Ogston and Sternberg 2002). This leaves the formulation

$$\overline{v_{s,est}} = \frac{-w_s\overline{C}}{\partial\overline{C}/\partial z}, \tag{8.18}$$

which is similar to the one used in steady state flows (equation 8.5), except that the variables are now time-averaged.

Figure 8.6 compares the vertical, time-averaged sediment diffusivity profile, estimated (blue) using equation (8.18) and compared with the numerically applied values (•). The vertical

scale is presented as the number of grain diameters above the bed, z/d. The time-averaging is conducted over 10 wave periods, starting at 70 s. This period of time was chosen since the mean values of $\partial C/\partial t$ were found to be small. Three different Schmidt numbers have been considered: a) $\sigma_c = 1$, b) $\sigma_c = 0.7$, and c) $\sigma_c = 0.4$. The NRMSE (E) in each case is indicated at the bottom right of the plot (in blue). The results imply that the time-averaged sediment diffusivity is over-estimated when using equation (8.18) but follows a similar profile shape as the numerically applied values: i.e. the time-averaged sediment diffusivity increases with height above the bed. Comparing the NRMSE for each Schmidt number, it is clear that the error decreases as the Schmidt number decreases, starting at 31% for $\sigma_c = 1$ and reducing to 18% for $\sigma_c = 0.4$. This is assumed to be due to a combination of increased sediment diffusion, causing the other terms to become relatively smaller, and a larger range of mean sediment diffusivity for normalising the error.

In an attempt to improve the estimations, a similar analysis was conducted with the vertical flow advection term included, and hence ν_s is calculated using

$$\overline{\nu_{s,est}} = \frac{\overline{wC} - w_s\overline{C}}{\partial\overline{C}/\partial z}, \tag{8.19}$$

with the profile and error both shown in green in Figure 8.6. The inclusion of this contribution increases the estimations of ν_s, indicating that $\overline{wC}$ is negative, leading to a larger NRMSE ($5-7\%$) for all of the Schmidt numbers presented.

Exclusion of the term $\overline{\nu_s'\frac{\partial C'}{\partial z}}$ has also been considered. Figure 8.7 presents the percentage error in $\overline{\nu_s\frac{\partial C}{\partial z}}$, assuming that $\overline{\nu_s'\frac{\partial C'}{\partial z}}$ is negligible, as a function of number of grain diameters above the bed. The three Schmidt number cases are shown, with little variation between them evident, indicating that the percentage error is not overly sensitive to this value. The results clearly show that, near the bottom of the water column, large errors (up to 33%) occur, whereas further away from the bed, the error drops to between 5 and 10%. Comparison of the magnitude of ν_s' at each location in the water column was conducted, and indicated that the values are similar throughout. This would lead to relatively larger errors at locations where $\overline{\nu_s}$ is smallest, i.e. near the bed. Furthermore, the fluctuations in the concentration

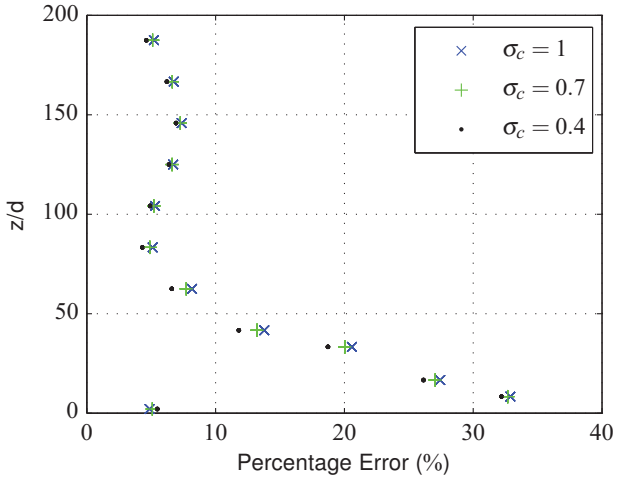

Figure 8.7: Percentage error (%) in $\overline{v_s \frac{\partial C}{\partial z}}$, as a function of the number of grain diameters above the bed, when assuming that $\overline{v_s' \frac{\partial C'}{\partial z}}$ is negligible under regular wave conditions. The results for three Schmidt numbers have been presented: $\sigma_c = 1$ ($\times$), $\sigma_c = 0.7$ ($+$), and $\sigma_c = 0.4$ ($\bullet$).

gradient are much larger near the bed, causing a relatively large error in $\overline{v_s \frac{\partial C}{\partial z}}$, and hence the calculation of $\overline{v_s}$. Figure 8.6 also presents the estimated $\overline{v_s}$ profile (black), calculated using

$$\overline{v_{s,est}} = \frac{-w_s \overline{C} - \overline{v_s' \frac{\partial C'}{\partial z}}}{\partial \overline{C}/\partial z}, \tag{8.20}$$

which includes the fluctuating term but neglects the wave orbital motion term, along with the NRMSE. Inclusion of this term reduces the magnitude of $\overline{v_{s,est}}$, indicating that $\overline{v_s' \frac{\partial C'}{\partial z}}$ is negative. This shift in the profile reduces the error by $5-6\%$ from the value obtained using the standard formula equation (8.18), implying that neglecting this term does introduce additional uncertainties in the values of $\overline{v_{s,est}}$. However, in physical experiments and field measurements, v_s' is difficult, if not impossible, to measure accurately. Furthermore, in order to calculate v_s', prior knowledge of v_s would be required, removing the need to calculate $\overline{v_s}$ using other parameters. Therefore, this term must be considered as an unavoidable error.

Clearly a $10-30\%$ error in estimation of the value of $\overline{v_{s,est}}$ is not ideal. Determining the exact source of this error has been fruitless but there are a number of factors which could be contributing. Figure 8.8 shows the time-average of the flow advection and diffusion terms from the governing equation (equation 4.81), all normalised by advection due to settling, as

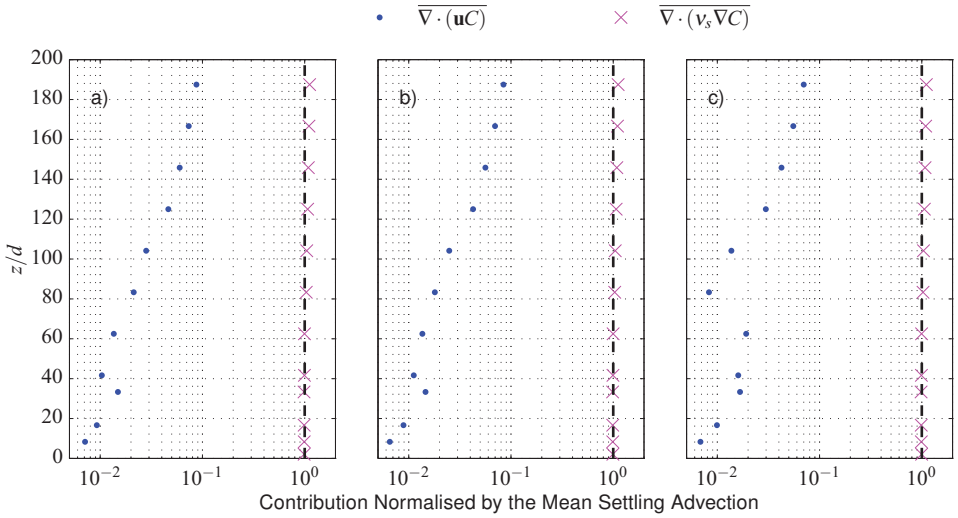

Figure 8.8: Contribution of the time-averaged diffusion (×) and flow advection (•) terms from the governing suspended sediment equation (equation 4.81), normalised by the settling advection, as a function of grain diameters above the bed z/d. The presented case is regular wave conditions and three Schmidt number are considered: a) $\sigma_c = 1$, b) $\sigma_c = 0.7$, and c) $\sigma_c = 0.4$.

a function of grain diameters above the bed. Three Schmidt numbers are presented, a) $\sigma_c = 1$, b) $\sigma_c = 0.7$, and c) $\sigma_c = 0.4$. The results imply that the contribution of each term is not overly sensitive to σ_c. This implies that the advection due to both the fluid flow and settling increases as the diffusion term increases. It is clear that in this case the settling and diffusion terms are at least an order of magnitude larger than the flow advection term. This is unsurprising since the orbital velocity will be small near the bed. However, it highlights that the advective term, also ignored in the calculation, has a finite value and so may be considerable in some situations. It could be that considering each of the small finite terms, such as the flow advection terms, horizontal diffusion term, and fluctuating components, leads to a reasonably large cumulative error. Furthermore, numerical inaccuracies arising from solving the equations and interpolation of cell values to the sampling locations could also have an influence, particularly in regions with low concentration.

Overall, the implicit methodology, which is based solely on the time-averaged vertical concentration profile, can estimate the sediment diffusivity to within a $10-30\%$ accuracy under regular wave flow conditions. The source of the error still needs to be identified but it is

likely that it is due to a combination of other factors such as fluctuations in the sediment diffusivity, flow advection and horizontal gradients. It is possible that the magnitude of the error is case specific: for example, in waves of greater height, the fluctuations may be larger, leading to increased error through the time-averaging process. Further work is clearly required to determine the error in a range of wave conditions. Until this has been quantified, and the source identified, any researcher that uses this implicit approach should be aware of the potential introduction of error from the methodology.

8.4 Case 4: Breaking Waves

The formulae for estimation of the time-averaged sediment diffusivity, derived in Section 8.3, are applied here to the breaking wave cases analysed in Section 7.4. The case representing the Sato et al. (1990) experiments are analysed first, before considering both the plunging and spilling breakers presented by Otsuka and Watanabe (2012).

8.4.1 Sato et al. (1990)

Figure 8.9 presents a comparison of the vertical variation in the estimated (lines) and numerically applied values (•) of time-averaged sediment diffusivity, in the breaking wave conditions described by Sato et al. (1990). The lines represent estimations obtained through various formulations: the blue line is the formulation based purely on the vertical time-averaged concentration profile (equation 8.18), whereas the green and black lines include the vertical orbital motion (equation 8.19) and fluctuations in the sediment diffusivity (equation 8.20), respectively. The NRMSE for each of the estimated profiles is indicated at the bottom right of each plot in the corresponding colour. The rows represent results using different Schmidt number: $\sigma_c = 0.5$ (top), $\sigma_c = 0.7$ (middle), and $\sigma_c = 1$ (bottom). The columns present results from different sampling locations, relative to the breaking point, x_b, indicated at the top of each column: from left to right $x - x_b =$ a) 0.4 m, b) 0.55 m, c) 0.75 m, d) 0.45 m, and e) 0.55 m. The first 3 columns are results obtained with $d = 0.15$ mm and the remaining 2 columns use $d = 0.18$ mm.

The results imply that at sampling location $x_b + 0.4$ m, all of the formulations give poor

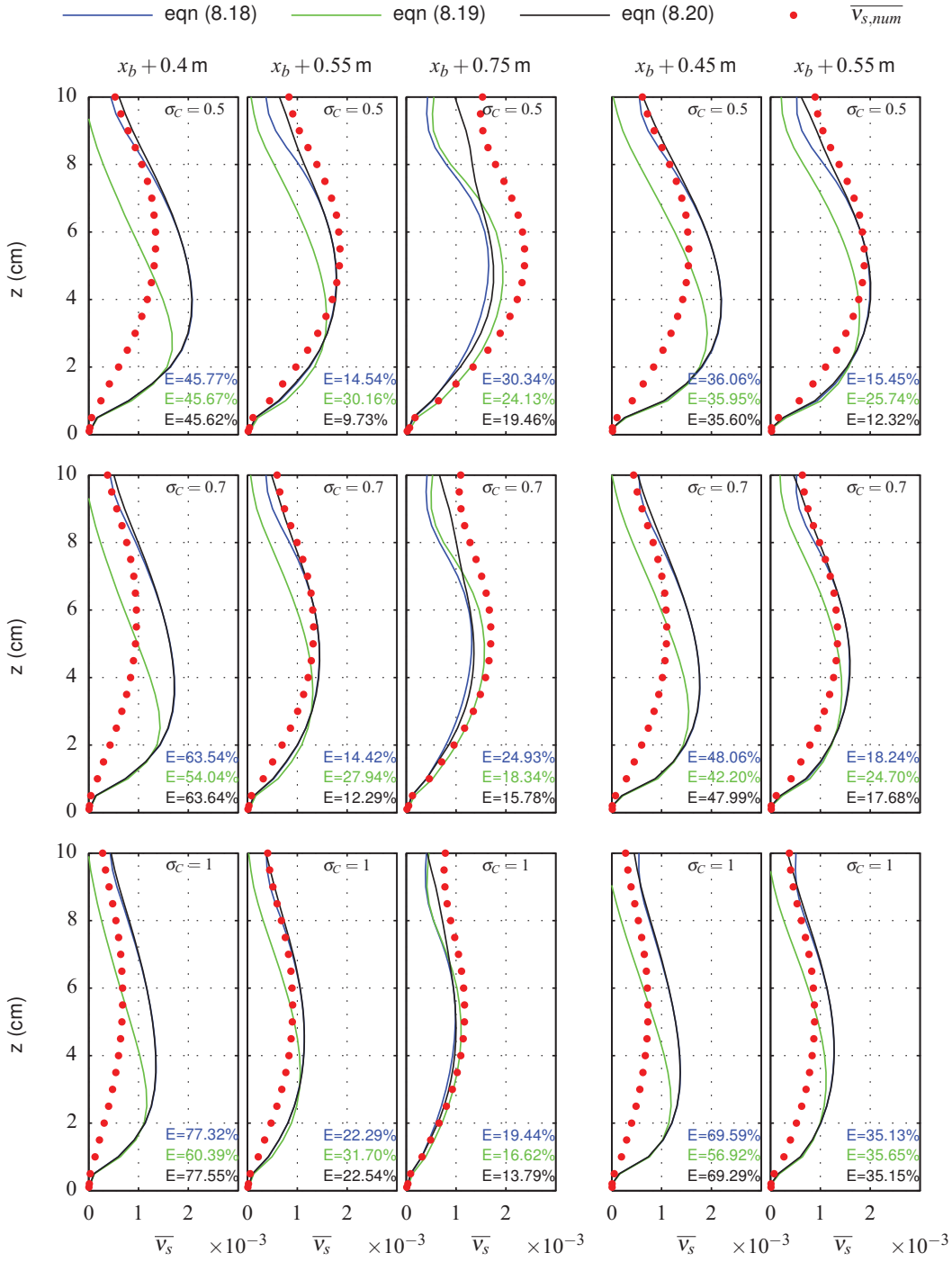

Figure 8.9: Comparison of time-averaged sediment diffusivity, estimated using equations 8.18 (blue), 8.19 (green) and 8.20, with the numerically applied values (●) for the Sato et al. (1990) breaking waves. Each column represents a different sampling location. The first three consider $d = 0.15$ mm and the remaining two $d = 0.18$ mm. Each row presents a different Schmidt number, $\sigma_c = 0.5$ (top), $\sigma_c = 0.7$ (middle) and $\sigma_c = 1$ (bottom). NRMSE for each profile is presented on the plot, with the text colour indicating the equation used.

predictions, particularly in the region 1 to 7 cm above the bed. This is reflected in the NRMSE, which ranges between 46% and 85% for the different Schmidt numbers, with the smallest Schmidt number performing best at this location. Despite clear differences in NRMSE for each σ_c, there is not a consistent trend across the sampling locations. At $x_b + 0.75$ m the predictions are more accurate for the larger value of σ_c. From $x_b + 0.5$ m onwards, all three estimated profiles have greater accuracy, with NRMSE in a similar range to that seen in the regular wave cases ($10 - 30\%$).

Comparison of the estimations at $x_b + 0.55$ m indicates that similar profiles and associated errors are obtained for the different grain diameters, particularly for the small Schmidt numbers. This implies that the time-averaged sediment diffusivity has very little dependence on the magnitude of the mean concentration profile. This is to be expected since the concentration appears in both the numerator and denominator of equation (8.18).

In general, the estimations made using equations (8.18) and (8.20) give very similar profiles with errors varying by less than 2% at many of the locations sampled. The exception appears to be $x_b + 0.75$ m, where there is a large deviation between the two profiles at the top of the water column, leading to a 10% increase in accuracy achieved by including this term. As discussed earlier, the fluctuating component of v_s is not available in experimental studies. Bearing in mind the relatively small error associated with this parameter, it seems justifiable to neglect this term and hence it will not be considered any further in this study.

Conversely, the inclusion of the vertical wave orbital motion changes the profiles substantially, particularly near the top of the water column. Near the bed (less than 2 cm) the estimated profile is very similar to that obtained without the vertical flow advection term included. However, above this height the $\overline{v_{s,est}}$ values reduce rapidly at sampling locations $x_b + 0.4$ m and $x_b + 0.55$ m, indicating that $\overline{wC}$ is large and positive, leading to a much larger error than obtained using equation (8.18). However, a smaller change can be seen at $x_b + 0.75$ m, which follows a similar pattern to that observed for the regular wave case. The shape of the profile remains in agreement with that obtained from equation (8.18) but the magnitude increases slightly, which is consistent with negative values of $\overline{wC}$, causing in-

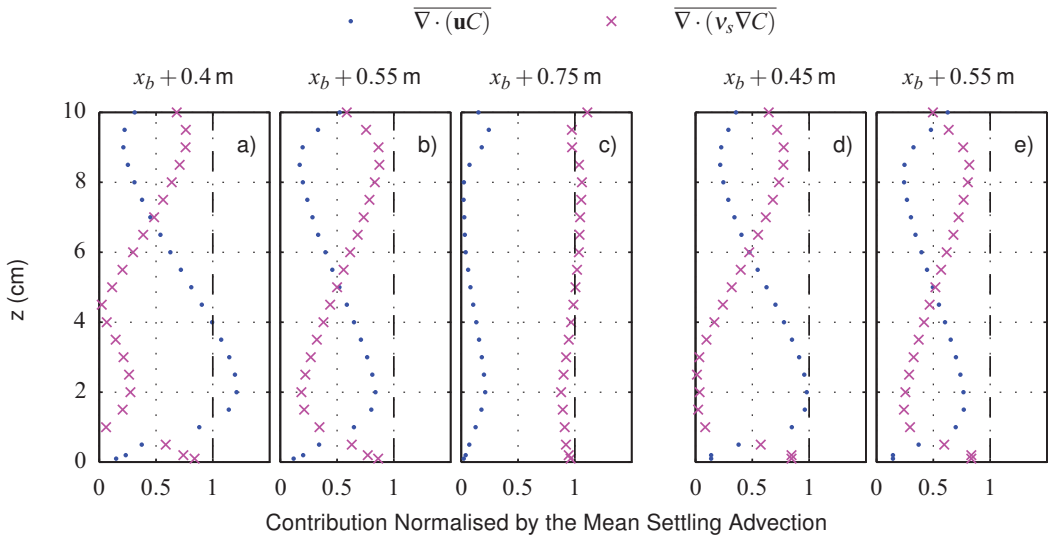

Figure 8.10: Magnitude of the time-averaged flow advection (•) and diffusion (×) terms from the governing (equation 4.81), relative to the advection due to settling, $\overline{\nabla \cdot (\mathbf{w}_s C)}$, as a function of distance above the bed. The presented case is the spilling breakers ($\sigma_c = 1$) used for comparison with Sato et al. (1990) and each plot represents a different sampling location, indicated at the top. Plots a-c consider $d = 0.15$ mm, whereas d-e are $d = 0.18$ mm. The dashed line represents the value equal to the settling contribution.

creased accuracy at this location. It is clear that the inclusion of this term can considerably affect the prediction of $\overline{\nu_s}$, implying that it cannot be neglected. Therefore, the contribution of the flow advection term is considered in more detail.

Figure 8.10 shows the mean magnitude of the flow advection (•) and diffusion (×) terms from the governing equation (equation 4.81) normalised by the magnitude of the settling advection, as a function of depth, for the Sato et al. (1990) breaker case. The results presented assume $\sigma_c = 1$ and the columns represent the same sampling locations as in Figure 8.9. A dashed line has been included at 1 to indicate the magnitude of the settling term. The results imply that the contribution from each term changes substantially between the different sampling locations, as well as between different depths. The profiles between $x_b + 0.4$ m and $x_b + 0.55$ m consist of three regions. Near the bed (less than 1 cm) the diffusion term is substantially larger than the flow advection term. Moving up the water column there is a region where the flow advection term is dominant, and the contribution from the diffusion term is very small. Near the top of the water column, the diffusion term becomes

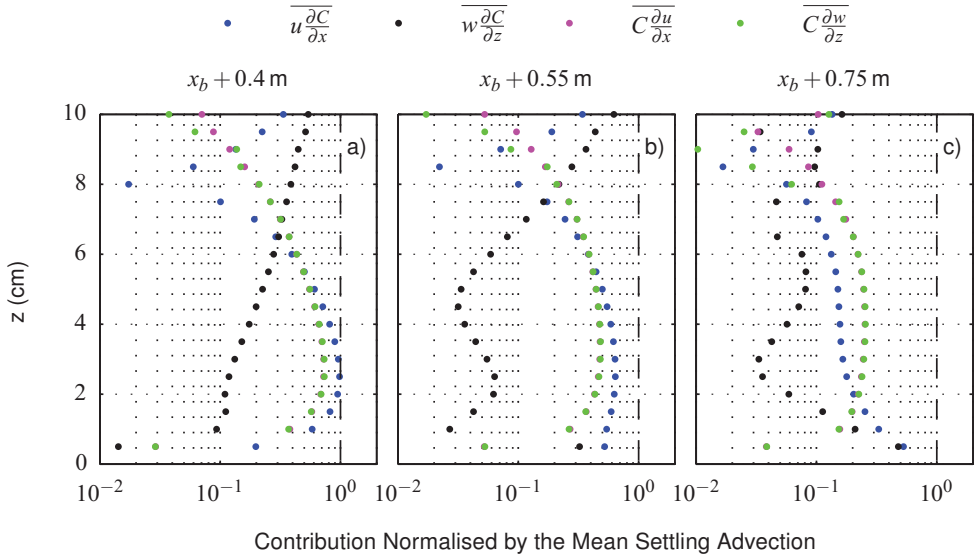

Figure 8.11: Magnitude of each of the contributions to the flow advection term (equation 8.21) relative to the settling term under spilling breakers (Sato et al. 1990). The results are obtained from simulations with $d = 0.15$ mm and $\sigma_c = 1$, and are sampled at $x - x_b =$ a) 0.4 m , b) 0.55 m, and c) 0.75 m. The dashed line indicates the value equal to the settling contribution.

more dominant again. The size of these regions depends on the sampling location and it seems likely that the high diffusion region near the bottom corresponds to the wave boundary layer, and the upper region is the boundary layer thickness correlating with the depth which turbulence penetrates under spilling breakers.

Furthermore, there appears to be a correlation between the dominance of the terms and the accuracy of equation (8.18). Comparing Figures 8.9 and 8.10, it seems that the formulation works well when diffusion is large and flow advection small. The largest error occurs at $x_b + 0.4$ m, and at a similar depth as the largest flow advection ($2 - 3$ cm above the bed). On the other hand, the predictions are much better very near the bed (less than 1 cm) and in the top region of the water column. This region is larger at $x_b + 0.55$ m and the NRMSE is much smaller than at the other locations. Furthermore, at $x_b + 0.75$ m the agreement is good throughout the water column, and the diffusion term is similar to the settling contribution, both of which are at least an order of magnitude larger than the flow advection.

The accuracy of the implicit estimation in different regions of the surf zone will be discussed in more detail later in this section, when the Otsuka and Watanabe (2012) cases are con-

sidered. First, the flow advection term is analysed to further understand the cause of the large flow advection at certain locations. Using the vector calculus identity,

$$\nabla \cdot (\zeta \mathbf{f}) = \mathbf{f} \cdot \nabla \zeta + \zeta (\nabla \cdot \mathbf{f}),$$

where ζ and $\mathbf{f}$ are scalar and vector quantities, respectively, the flow advection term can be expressed as

$$\nabla \cdot (\mathbf{u}C) = u\frac{\partial C}{\partial x} + w\frac{\partial C}{\partial z} + C\frac{\partial u}{\partial x} + C\frac{\partial w}{\partial z}. \tag{8.21}$$

In this form it is clear that both the gradient in concentration and velocity components must be small in order for the individual terms to be neglected. Therefore, the contribution of each term relative to the magnitude of the settling contribution, $|\overline{w_s \frac{\partial C}{\partial z}}|$, is analysed as a function of depth.

Figure 8.11 presents the magnitude of the time-average of each of the four terms in equation (8.21), normalised by the settling contribution. Since the profiles in Figure 8.10 were shown to have little dependence on grain diameter, only the $d = 0.15$ mm cases have been presented (with $\sigma_c = 1$), relating to Figure 8.10a-c. A dashed line has also been included to identify where contributions from the fluid flow advection exceed that arising from the settling of the particles. In general the settling term is larger than any of the components of the flow advection term. However, in the region of substantial flow advection ($1 - 5$ cm above the bed at $x_b + 0.4$ m), observed in Figure 8.10, three of the components are of a similar order of magnitude as the settling term. Clearly, if all three contribute in the same direction then the flow advection term becomes considerably larger than the settling term as is observed in Figure 8.10. Near the bed, the vertical flow advection term included in Figure 8.9 is an order of magnitude smaller than the settling contribution, which explains the lack of change in the $\overline{v_s}$ profile observed in this region (see Figure 8.9).

At $x_b + 0.55$ m, each of the flow advection contributions become less substantial, around half the magnitude of the settling advection. However, the combination of the terms could still potentially be substantial. The vertical flow advection term is large near the top of

the water column, explaining the large deviations between equations (8.18) and (8.19), observed in Figure 8.9. At the final sampling location, all of the flow advection components are approximately an order of magnitude less than the settling term and hence even the sum is small as reflected in Figure 8.10. Therefore, the flow advection term can be neglected at this location, whilst still obtaining reasonable accuracy using equation (8.18).

In summary, by applying the formulation for estimation of time-averaged sediment diffusivity to the simulations setup used to evaluate Sato et al. (1990), a number of interesting results have been found. Firstly, the methodology appears to be more applicable further into the surf zone than near the breaking point. Just after breaking, large errors can be observed in the middle of the water column, which correlate with regions of high flow advection and low diffusion. The large contribution from the flow advection term was found to be attributed to horizontal, rather than vertical, flow advection. This is likely to be due to a jet-like structure with a strong horizontal component at locations close to the breaking point. This indicates that only considering the vertical processes could be the cause of the large observed error in this region. This jet like structure appears to quickly dissipate as the bore moves towards the shore. The horizontal dependency is discussed further in the analysis of the spilling and plunging breakers from Otsuka and Watanabe (2012), which follows.

8.4.2 Otsuka and Watanabe (2012)

Figure 8.12 presents a comparison of the estimated time-averaged sediment diffusivity, obtained using equation (8.18), with the numerically applied (•) time-averaged profiles under the spilling breakers described by Otsuka and Watanabe (2012). The results have been plotted as a function of normalised depth, $(z-\overline{\eta})/h$, and were obtained using $\sigma_c = 1$. A number of locations, relative to the breaking point, are presented and correspond to the same locations as the time-averaged concentration profiles reported in Figure 7.28. The NRMSE (E) for each profile is indicated at the bottom of each plot.

As was observed for the Sato et al. (1990) case, the profiles and associated errors change considerably between sampling locations. However, more sampling locations have been considered in this case and, hence, a clear trend can be observed in the data. From

$x_b + 0.8$ m onwards the results agree very well, ranging between 1% and 18% difference from the numerically applied values. This implies that the formulation works well close to the shallow areas of the surf zone where the turbulent bore has developed. Between x_b and $x_b + 0.6$ m the estimations are poor, (other than at a small region near the bed), leading to errors of up to 225%. At x_b, the majority of the error is attributed to the estimations in the upper half of the water column. The numerically applied values tend towards zero, whereas the estimated profile stays at an almost constant value. This is consistent with experimental data for unbroken waves (Ogston and Sternberg 2002). As the wave propagates further along the wave flume there is a region, in the lower half of the water column, in which the $\overline{v_{s,est}}$ profile is found to increase much more rapidly than $\overline{v_{s,num}}$, with the largest error observed at sampling location $x_b + 0.4$ m. Progressing further along the wave flume the numerically applied values increase, eventually leading to the region of good agreement.

The errors before $x_b + 0.6$ m are concerning and hence require further investigation into the contributions of various terms, similar to that described in Section 8.4.1. For the spilling breakers, Figure 8.13 presents the magnitude of the mean numerical flow advection ($\bullet$) and diffusion ($\times$) terms, relative to the settling contribution, as a function of normalised depth. Each of the plots represents a different sampling location, corresponding to the same as presented in Figure 8.12, and hence are labelled the same. The dashed black line represents the contribution from the settling term. The results further reinforce that there is correlation between error and regions of high flow advection and/or small diffusion. At x_b, the diffusion is of a similar order of magnitude as the settling term near the bottom, and the estimated and numerically applied values are similar. Further up the water column the diffusion term becomes smaller and tends towards a similar magnitude as the flow advection term. As the flow advection and profiles get closer together, the numerically applied and estimated sediment diffusivities seem to diverge. Additional proof of this can be observed at $x_b + 0.4$ m, where, in the lower half of the water column, there is a region of very poor estimations of $\overline{v_s}$. This region seems to directly correlate with very small diffusion and high flow advection. Similar trends exist at $x_b + 0.2$ m and $x_b + 0.6$ m where the highest errors occur at the points where the flow advection is most substantial relative to the diffusion term.

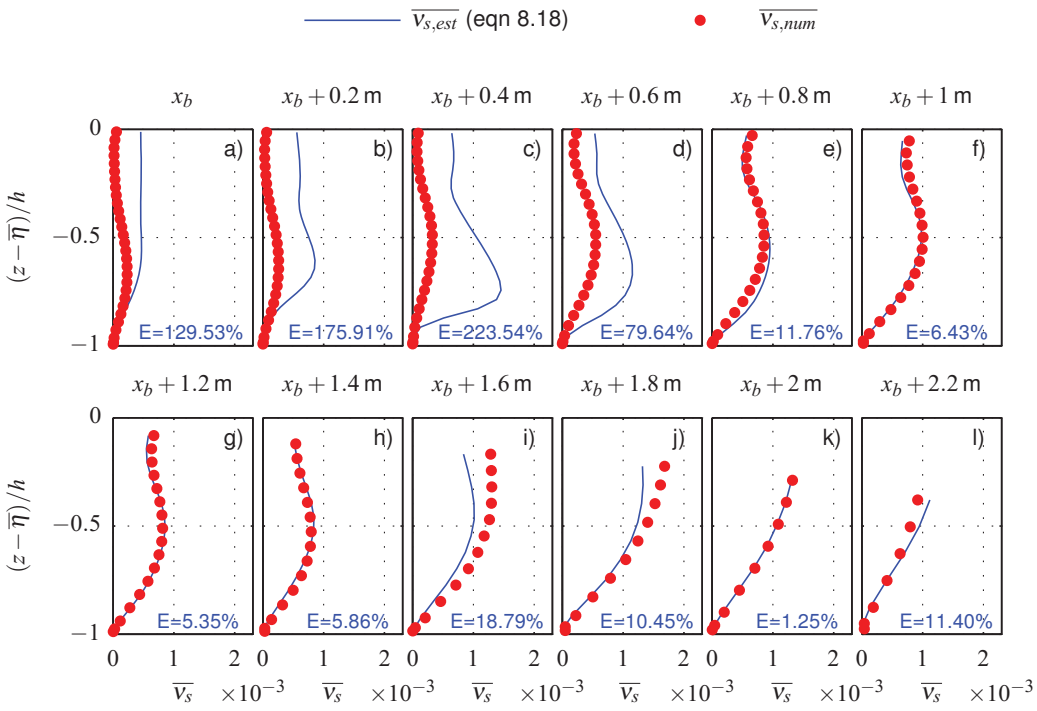

Figure 8.12: Comparison of estimated $\overline{v_s}$, obtained using eqn. (8.18), with the numerically applied values (•) under spilling breakers with $\sigma_c = 1$. NRMSE (E) is indicated at the bottom of each plot, which represent different sampling locations relative to x_b.

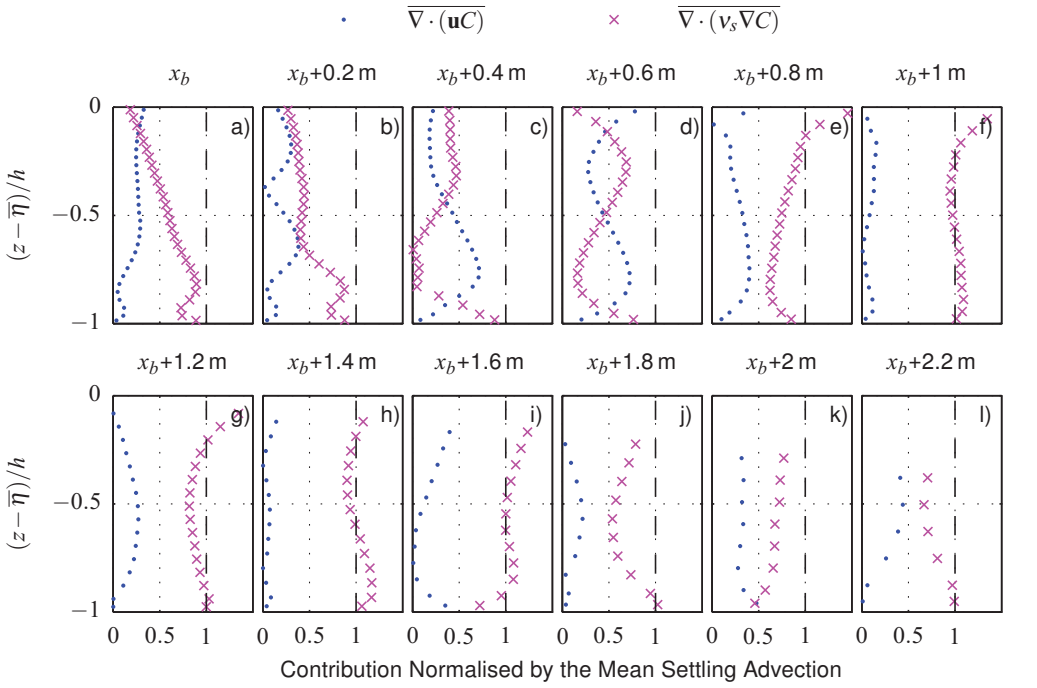

Figure 8.13: Comparison of the mean advection and diffusion magnitude, relative to the settling contribution, under spilling breakers ($\sigma_c = 1$). Each plot relates to a different sampling locations consistent with the locations in Figure 8.12.

From $x_b + 0.8$ m onwards the diffusion term is always larger than the flow advection term, with very few regions where the contributions are similar. This agrees well with observations discussed in the Sato et al. (1990) case (see Section 8.4.1).

In summary, the formulation (equation 8.18) works well for spilling breakers, particularly in the turbulent bore region. However, care must be taken when applying this formula since there are clearly regions where it is not applicable. These regions seem to occur at mid-depth of the water column, before the turbulent bore has formed, where flow advection is considerably larger than diffusion.

Figure 8.14 presents an equivalent plot of Figure 8.12 for the plunging breaker case. Once again the Schmidt number has been set to $\sigma_c = 1$ and the sampling locations are relative to the breaking point. Similar patterns can be observed for the plunging breaker as were noted for the spilling breaker case. Just after breaking, the error in the estimated profile is large but reduces further along the numerical wave flume. However, the plunging breaker has much larger error from $x_b + 1.2$ m onwards, particularly for location $x_b + 1.8$ m. The explanation for the very large error (over 600%), at this location, is the occurrence of a sediment plume (see Section 7.4.1) at around 180 s, which also caused a very different concentration profile to the other sampling locations presented in Figure 7.29. It is likely that this sediment plume is at the origin of the errors in $\overline{v_{s,est}}$ at sampling location $x_b + 1.6$ m, due to the high concentration gradients in this region.

Figure 8.15 shows the contributions of the flow advection ($\bullet$) and diffusion ($\times$) terms, relative to the settling term, under plunging breakers. The format of the plot is the same as described for Figure 8.13. Similar to the spilling breaker case, the poorest agreement appears to occur where the flow advection term is considerably larger than the diffusion term. Furthermore, the best agreement occurs when the diffusion term provides a contribution of a similar order of magnitude as the settling term, and is much larger than the flow advection. Further into the surf zone the plots show considerable regions of large flow advection, which were not observed in the spilling breaker. Again this is likely to be due to the sediment plume. High concentrations and gradients will cause this term to become larger, as can be easily seen

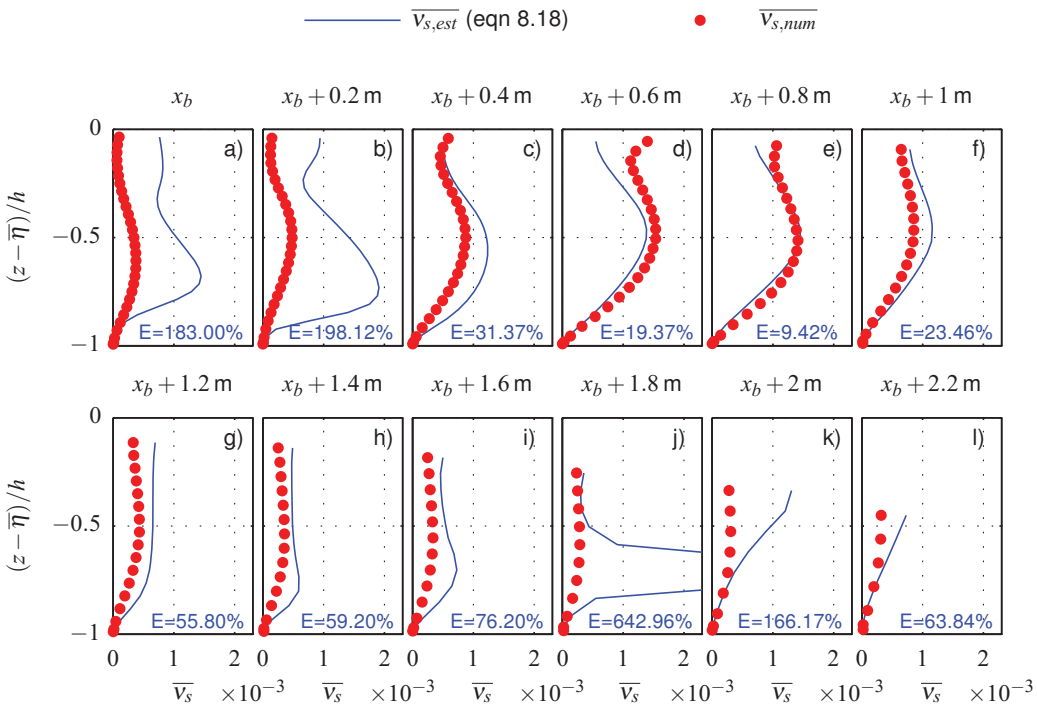

Figure 8.14: Comparison of estimated $\overline{v_s}$, obtained using eqn. (8.18), with the numerically applied value (•) under plunging breakers with $\sigma_c = 1$. NRMSE (E) is indicated at the bottom of each plot, which represent different sampling locations relative to x_b.

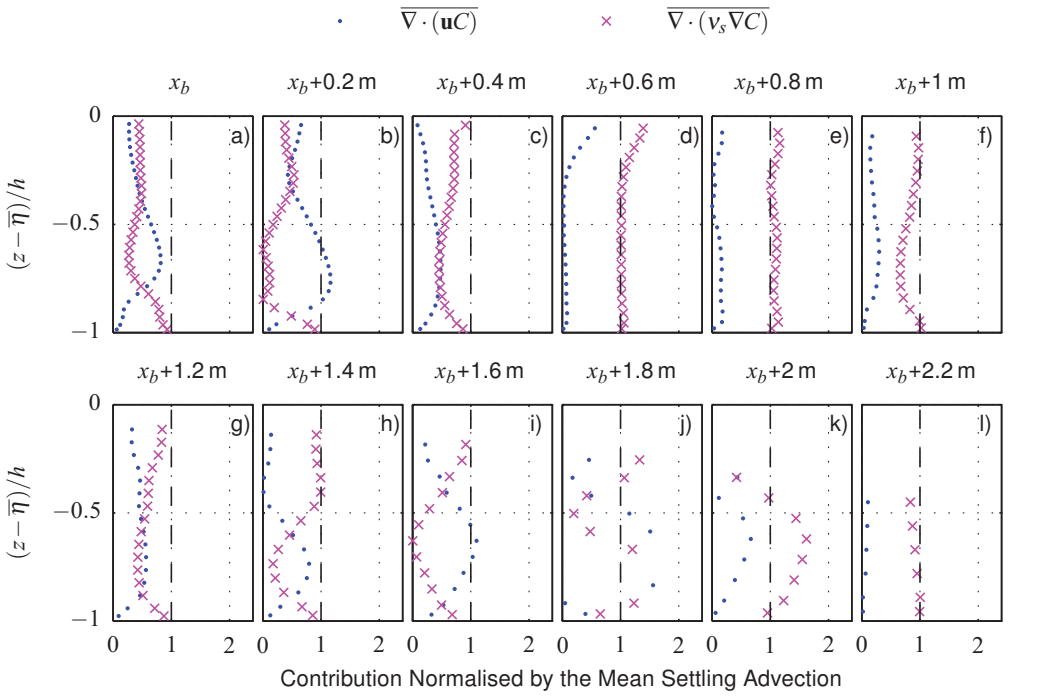

Figure 8.15: Comparison of the mean flow advection and diffusion magnitude, relative to the settling contribution, under plunging breakers ($\sigma_c = 1$). Each plot relates to a different sampling location, consistent with the locations in Figure 8.12.

by considering equation (8.21).

To remove the influence of the sediment plume, a different segment of the time series, consisting of 15 wave periods, have been averaged, starting at 140 s. Due to the sporadic nature of these sediment plumes, this segment of the time series did not contain an event, and hence the effect of the plume can be analysed. Figure 8.16 presents the estimated (lines) and numerically applied (●) time-averaged sediment diffusivity profiles (top row) for the plunging breaker, similar to Figure 8.14, except for sampling locations $x_b + 1.2$ m to $x_b + 2.2$ m only. Averaging these 15 wave periods has considerably reduced the error, which now lies in the range of $20 - 70\%$. However, these errors are still much larger than observed in the spilling breakers case, where the errors were found to be between 1 and 20%. Therefore, the vertical flow advection term (equation 8.19) has also been included for comparison and is plotted, along with the NRMSE, in green in Figure 8.16. At all but one of the locations, the inclusion of this term reduces the error by up to 20% with most of the change occurring towards the top of the water column. This implies that the plunging breaker is more sensitive to the flow advection term than the spilling breaker (see Section 8.4.1), which may be expected due to the high energy nature of plunging breakers.

Also shown in Figure 8.16 is the relative magnitude of the flow advection and diffusion terms (bottom row) at the same locations as $\overline{v_s}$. At a number of locations (g,h and i) the flow advection provides a similar contribution as the diffusion. This is reflected in the $\overline{v_s}$ profiles, which exhibit regions of poor agreement and hence high NRMSE. However, location $x_b + 1.8$ m provides evidence that this is not the exclusive cause of the error. At this location, the diffusion is much larger relative to the flow advection term throughout the water column, and yet it has the largest error in the $\overline{v_s}$ profile. This is reflected in the $\overline{v_s}$ profile, which does not change considerably when the vertical flow advection term is included, indicating that it is can be neglected. Further confirmation can be observed near the free surface at location $x_b + 1.2$ m, where there is a reasonable error despite having a large diffusion and small flow advection term. All of the locations have substantial error in this near surface region and it is hypothesised that the entrapped air, and relatively chaotic dynamics (see Figures 5.29

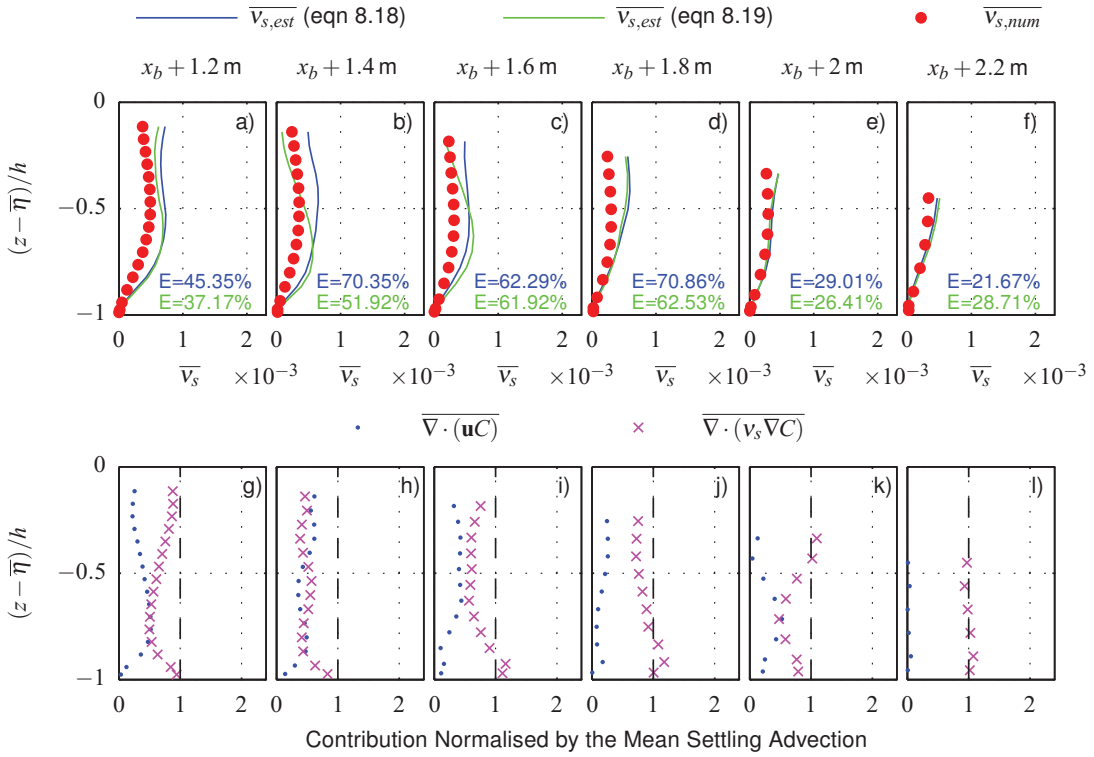

Figure 8.16: Comparison of the numerically applied (•) and estimated time-averaged sediment diffusivity profiles (top row) as a function of depth under plunging breakers. The bottom row shows the mean contribution of the diffusion (×) and flow advection (•) terms relative to the settling term. Locations $x_b + 1.2$ m to $x_b + 2.2$ m are presented with the 15 waves between 140 and 170 s used for time-averaging to avoid a sediment plume event.

and 5.30), may be negatively affecting the calculation. Another possible explanation for the larger error could be that the magnitude of $\overline{v_s}$ is much smaller in these locations than observed in the spilling breakers case, where the agreement was much better. Therefore, it is thought that any errors arising from interpolation due to sampling, as well as from neglecting terms, may have had a larger effect in the plunging breaker case.

In summary, before the turbulent bore forms, the observed errors are large under plunging breakers, similar to those found for the spilling breakers case. This seems to be largely due to the flow advection term being considerably larger than the diffusion term at mid-depth of the water column. Further into the surf zone the turbulent bore forms and the methodology captures the profile within 70% accuracy in the plunging breaker case, which is much poorer than observed in the spilling breaker case. This is likely to be due to the chaotic

nature of plunging breakers, but also could be due to lower magnitudes of time-averaged sediment diffusivity. However, the analysis disregards sediment plumes, which have been shown to cause substantial error (up to 600%) if present, due to large flow advection caused by the increased concentration gradients in the region surrounding the plume. In general, the implicit approach will give very poor estimations for the sediment diffusivity in any flow that contains large concentration gradients, since the method is based on the assumption that the flow advection is negligible. In order to draw any firm conclusions about using the methodology for plunging breakers, the sediment plumes would need to be investigated further. The existence of sediment plumes is physical (Sumer et al. 2013) but it is unclear whether they occur sporadically or are generated with every wave. In the numerical model, the sediment plumes are sporadic, which causes them to affect mean concentrations substantially. Furthermore, the magnitude of the concentration in these plumes needs to be assessed. If the numerical model is capturing them well then clearly using the methodology under plunging breakers is dangerous, and would require careful consideration.

8.5 Summary

In this chapter, a common implicit experimental methodology for the estimation of the sediment diffusivity is assessed under a number of flow conditions. By comparing the numerical and estimated values, the validity of the methodology is evaluated. The steady state, purely diffusive case highlights the thinking behind the formulation since it has an analytical solution. In this case it was shown that the sediment diffusivity could be obtained exactly. Furthermore, in steady state advection-diffusion flow conditions, the implicit approach could estimate the ν_s profile to within 3% accuracy, providing that the sampling location was not in a region of high horizontal flow advection relative to the rate of settling of sediment particles.

The implicit methodology was expected to work well under these steady conditions since the assumptions made in the derivation of the formulation seem perfectly reasonable. However, this work focused on wave-driven environments, where many researchers extend the application of the implicit methodology through the process of time-averaging, which has largely been untested. In this study it was found that extending this approach to unsteady

flows can work to within a reasonable accuracy under certain conditions. These seem to be flows where diffusion and settling advection dominate flow advection. For example, in the turbulent bore formed by spilling breakers the methodology gave good results ($1-20\%$ NRMSE). Furthermore, near the bed under regular waves, profiles could be obtained to within 30% accuracy, which could be improved by considering the fluctuations of v_s in the derivation of the formulation.

However, when flow advection is not negligible, or diffusion is small, substantial errors can be introduced through this methodology. Near the breaking location of the waves, large errors were observed, owing largely to a region around mid-depth of the water column, where flow advection is much larger than the diffusion. This problem is not limited to the time-averaged unsteady conditions: in the steady state channel flow conditions the error was also shown to be considerably larger (errors of up to 25% were observed) when sampling in a region of high horizontal concentration gradients.

An extreme example of this are sediment plumes, which were shown to be predicted sporadically under the plunging breaker conditions. These sediment plumes led to very large concentration gradients and hence flow advection. The resulting errors were huge: errors of up to 600% were observed in this study.

The magnitude of the error seems to be very case specific and hence future research effort should be conducted into the conditions in which the methodology is applicable: can it be applied in any water depth, wave height or wave period? Further work to determine a formulation which works in all regions of the surf zone also needs to be conducted. However, this will likely lead to formulae that depend on second derivatives and on variables which are much harder to measure. In fact, in an attempt to reproduce $\overline{v_s}$ exactly, the full formulation obtained from expanding the governing equation (4.81) has been evaluated as part of this study. However, it has not been possible to reproduce the profile exactly. This could be due to a number of factors but one particular difficulty has been observed in the calculation of second derivatives in OpenFOAM®, which uses finite volume to calculate the terms, and the Laplacian is calculated as a whole term rather than components. Therefore, to get the

second derivatives, which form the Laplacian calculation, the gradient is applied twice to the concentration, allowing a time series to be obtained for each component separately. Unfortunately, recombining these components did not give the same result as the output of the diffusion term from OpenFOAM®. This may be due to other numerical factors such as non-orthogonal correction terms and interpolation used by OpenFOAM®, making it not possible to obtain the second derivatives in this way.

Overall, the methodology (equation 8.18) performs reasonably well under certain flow conditions, especially when taking into account that a complicated process, depending on a number of parameters, has been simplified to a formulation depending only on the mean vertical concentration profile. However, attention must be drawn to the poor agreement around the breaking point. Further work must be performed to better understand the problem with applying the formula in these regions, or in any region of low diffusion. Until this has been determined, any researcher that uses this implicit methodology to estimate sediment diffusivity should be aware of substantial errors arising as an artefact of such an approach, particularly in flows with potential to exhibit large horizontal concentration gradients.

Chapter 9

Conclusions

The overall aim of this study has been to improve our understanding of the role played by turbulent motion in suspended sediment dynamics, through analysis of the sediment diffusivity. In the following the main novel contributions of this work are summarised and, consist of:

- The evaluation of five different two-equation turbulence closure models under spilling and plunging breakers, on beaches of constant gradient (Brown et al. 2014, 2016).
- The collection and analysis of experimental data for the 2-D breaking wave process. Both spilling and plunging breakers have been considered, with the data obtained in the COAST laboratory 35 m-long wave flume using a light box and high speed camera.
- The development of a novel numerical model for analysis of suspended sediment dynamics, which solves an advection-diffusion equation and provides a boundary condition that evaluates the entrainment and deposition balance.
- Analysis of a common experimental approach, which implicitly estimates the sediment diffusivity, through comparison with values directly determined in the numerical model.

This chapter summarises the work carried out in each of these contributions, draws conclusions and suggests some possible future research directions that could be undertaken following the findings of this study.

9.1 Turbulence Modelling in the Surf Zone

In Chapter 5 a new library containing modified turbulence closure models, with density included explicitly in the equations (Jacobsen 2011; Brown et al. 2014), has been thoroughly

evaluated for application to wave breaking processes in the surf zone (Brown et al. 2016). Both spilling and plunging breakers were considered, and the results for time-averaged surface elevation, horizontal velocity and turbulent kinetic energy (TKE) are compared to existing laboratory data under the same conditions (Ting and Kirby 1994). A skill score based on the mean square error has been used to evaluate the predictions of each turbulence closure model, giving a quantitative description of model performance.

The results implied that all three of the tested variables were very sensitive to the choice of turbulence model. Based on the overall skill score alone the ranking of the turbulence models would be:

1. Nonlinear $k-\varepsilon$.
2. RSM.
3. $k-\omega$ SST.
4. $k-\omega$.
5. RNG $k-\varepsilon$.

However, the skill scores also indicated that each criterion was best achieved by a different turbulence model. In spilling breakers the RNG and nonlinear $k-\varepsilon$ models gave the best predictions for surface elevation and horizontal velocity, respectively, whereas the TKE predictions were best when using the $k-\omega$ model. For the plunging breaker case the most accurate predictions of surface elevation and velocity were achieved using the $k-\omega$ model, with the nonlinear $k-\varepsilon$ model performing best for TKE.

Further analysis has been conducted using instantaneous spatial plots at varying phases of the breaker. These plots allowed qualitative comparison of the Reynolds stress with existing particle image velocimetry (PIV) data sets. When using the $k-\omega$, $k-\omega$ SST and nonlinear $k-\varepsilon$ models, the spilling breaker plots qualitatively agree with experimental studies of weak hydraulic jumps, which are believed to be a simplified method for studying the flow under spilling breakers in the inner surf zone (Misra et al. 2008). The agreement with this data set both validates the numerical model and provides further evidence that weak hydraulic

jumps are a good representation of spilling breakers.

Since it achieved the highest skill score, the nonlinear $k-\varepsilon$ model was analysed in more detail, and was shown to exhibit many of the features noted in the experimental data relating to the transport of turbulence under different breaker types. The turbulence spread over the whole water depth before rapidly dissipating prior to the arrival of the next plunging breaker. On the other hand, the spilling breaker's turbulence spread seaward and only slowly diffused downwards. Slow dissipation in this case led to turbulence generated by a wave still existing in the water column when the following wave arrives.

Despite achieving the highest overall skill score, the nonlinear $k-\varepsilon$ model was not used for the analysis of suspended sediment dynamics that followed, since the TKE predictions were considered to be the most important criterion, and those were reproduced best with the $k-\omega$ model. Hence the $k-\omega$ model was used for all sediment concentration simulations, which had the added advantage of improved behaviour near the wall. Moreover, this was considered to be vital for the correct representation of the balance of entrainment and deposition at the bed.

9.2 Near-Bed Particle Tracking Velocimetry Experiments

Chapter 6 presented data from the experiments conducted in the sediment flume at Plymouth University's Coastal, Ocean and Sediment Transport (COAST) laboratory (from now on referred to as the in-house experiments). The rationale for performing these in-house experiments was the poor agreement in the vertical velocity profiles between the predictions of the model developed here, and experimental data presented by Otsuka and Watanabe (2012). In particular, under plunging breakers the existing experimental data exhibited two peaks in vertical velocity per wave period, which could not be replicated in the numerical model. Hence, a series of in-house experiments was conducted using similar hydrodynamic conditions as those in Otsuka and Watanabe (2012). Measurements were taken around the breaking location using a light box and a high speed camera, recording at 125 frames per second (FPS), providing a large number of images of the breaking process. Particle tracking velocimetry (PTV) was performed on the images, using the software Streams (Nokes

2014), to examine the velocity at a point location, and compared to Otsuka and Watanabe (2012), who used an ultrasonic velocity profiler.

The numerical results had much better agreement with the in-house experimental results than with those of Otsuka and Watanabe (2012). The double peak was not observed in the in-house experiments, which could potentially be explained by the intrusive nature of some of the instrumentation used by Otsuka and Watanabe (2012). Furthermore, the numerical predictions of peak horizontal velocity matched up more closely with the in-house results than with Otsuka and Watanabe (2012). An attempt to compare the in-house numerical and experimental results for TKE was also made. However, the agreement was poor under both breaker types. The experimental results for the plunging breakers clearly showed a much larger and periodic spike in TKE than observed in the numerical model, which had a periodic component but exhibited much less variation. Surprisingly, the in-house experimental data for the spilling breaker case was very noisy compared to the plunging breaker case, indicating that further post-processing, such as filtering, may be necessary in order to obtain meaningful results. Comparison of TKE with Otsuka and Watanabe (2012) further into the surf zone implied that the numerical model performs better in this region than near the breaking point.

9.3 Suspended Sediment Concentration Model

A novel numerical model was developed to investigate suspended sediment dynamics within the OpenFOAM® environment. The model uses an advection-diffusion approach with a new, in-house developed module to implement a new sediment transport condition at the sand bed based on an entrainment and deposition balance. In Chapter 7, the new module was thoroughly validated in a number of different flow conditions, with increasing complexity. First a pure diffusion case showed that the Rouse profile, an exact analytical solution, can be achieved, verifying that the correct equations are being solved. Then, the model was validated under steady state conditions, through consideration of the problem of a flow through a channel. Sensitivity analysis of the near-bed cells was conducted for this case, leading to a chosen cell size of $5d$ next to the sediment bed. Next, regular waves

introduced unsteady, oscillating conditions before the final test, corresponding to highly turbulent conditions associated with breaking wave processes.

In general, in steady flow conditions the numerical predictions were good for fine natural sand, with grain diameters of $0.125 - 0.25$ mm and density $2650\,\mathrm{kg\,m^{-3}}$. However, when comparing to experimental data from Sumer et al. (1996) the concentrations were slightly under-estimated, whereas comparison to similar laboratory experiments from Cellino (1998) yielded a slight over-estimate. Since the numerical model lies somewhere between the two physical data sets, it is assumed that the new sediment transport module is performing to a reasonable standard for fine sands. However, the module did not perform as well for other types of sediment. For example, simulations were run with larger acrylic particles with a similar settling velocity, and the concentrations were substantially under-estimated. The cause of this is likely to be processes not included in the present numerical model, such as hindered settling, or alternatively the assumption of a Schmidt number of unity is less valid for these acrylic particles.

Under regular waves the time-averaged concentrations were generally under-estimated when assuming a Schmidt number, $\sigma_c = \nu_t / \nu_s$, of one. Like previous numerical models, the effect of varying the Schmidt number was investigated, with $\sigma_c = 0.4$ achieving similar time-averaged concentration levels as the experiments. This indicates that sediment diffusion is around twice as effective as turbulent diffusion. However, considering the phase-averaged profiles it becomes clear that the numerical model predicts similar peak concentrations, but the sediment remains in suspension for a much shorter period of time than observed in the experiments. Other numerical models exhibit similar properties (Hsu and Liu 2004) but the one developed by Ma et al. (2014) captures the suspension time more accurately than the present model. Further work will be required to implement some potential improvements into the new sediment transport module. These improvements may include: using a more complex settling velocity calculation, introducing hindered settling, or modifying the turbulence model to include concentration effects and hence achieve an improved estimation of ν_t. However, despite the module's current limitations, the numerical model performs rea-

sonably well overall, and the sediment dynamics clearly respond to the oscillations caused by the non-breaking waves.

Similar trends can be observed under breaking waves, with the time-averaged concentrations being under-predicted, with $\sigma_c = 0.5$ generally giving the most accurate results. However, under plunging breakers sporadic spikes in concentration were observed in the time series at 1.5 m after the breaking point. After further investigation, it was found that entrapped air in this region was generating vortices, which in turn were suspending large concentrations of sediment, that were then transported by the backflow. These events have many qualitative characteristics in common with the sediment plumes observed by Sumer et al. (2013) under plunging breakers. In the future it would be interesting to investigate sediment plumes in more detail and determine whether the numerical predictions agree not only qualitatively with experimental observations, but also quantitatively.

Overall, the numerical model gives reasonable results for all cases evaluated in this study. Further work is clearly needed to improve the model through the introduction of additional physics but it is considered to be a good platform to build upon in the future.

9.4 Analysis of the Sediment Diffusivity

The validated numerical model was used to explore the application of a common experimental formulation for estimation of sediment diffusivity, ν_s, in the surf zone. In physical experiments, sediment diffusivity cannot be calculated directly, and hence an implicit methodology, based on the vertical concentration profiles, is often used to estimate ν_s. In this work, the methodology was applied using the concentration profiles predicted by the numerical model, to obtain an estimated sediment diffusivity, which was then compared to the numerically applied sediment diffusivity, determined directly from the numerical model. The assumptions that the implicit methodology relies on are perfectly reasonable in steady flows with small horizontal gradients, and this was backed up through comparison of the numerically applied and the estimates profiles, which differed by between 1% and 3% in the steady state advection-diffusion tests.

However, many researchers attempt to extend the use of this implicit methodology to wave-driven flows, using time-averaged concentration profiles. This introduces significant uncertainty to the approach since fluctuations in the sediment diffusivity are neglected, with little existing evidence that this assumption is valid. Furthermore, in the surf zone the flow is much more complex, potentially leading to large horizontal concentration gradients, which it was hypothesised could substantially reduce the accuracy of the methodology.

In this work, the accuracy of the approach was assessed and quantified under regular waves, as well as spilling and plunging breakers. It was found that extending the approach to unsteady flows can work to within a reasonable accuracy under certain conditions. These conditions seem to be flows where diffusion and settling advection dominate flow advection. In the turbulent bore formed by spilling breakers the methodology gave good results ($1-20\%$ error), and near-bed time-averaged sediment diffusivity profiles could be captured to within a 30% accuracy under regular wave conditions. The estimations could be improved in some flow conditions by considering the fluctuations of v_s in the derivation of the formulation. Furthermore, inclusion of the vertical flow advection could improve the results in some regions of the surf zone under plunging breakers, whereas under regular waves it caused the accuracy of the estimations to decrease. This highlights that many of the factors that are neglected in the derivation of the methodology are in fact finite, and hence a combination of these effects could be leading to a cumulative error, depending on the flow conditions.

Furthermore, when flow advection is not negligible, or diffusion is small, substantial errors were found to be introduced through this methodology. Near the breaking location of the waves, large errors were observed, attributed largely to a region around mid-depth of the water column, where flow advection is much larger than the diffusion. Sediment plumes, which were shown to be predicted sporadically under the plunging breaker conditions, are an extreme example of this effect. These sediment plumes led to very large concentration gradients and, hence, flow advection, potentially in both the horizontal and vertical component. The resulting errors were found to be very large in this study, with errors of up to 600% observed in the inner surf zone under plunging breakers. Discrepancies due to horizontal

gradients were also observed in the steady state channel flow conditions, where the error was shown to be considerably larger (errors of up to 25% were observed) when sampling in a region with horizontal concentration gradients.

Bearing in mind the simplicity of this implicit methodology, it generally seems to estimate sediment diffusivity to a reasonable accuracy. However, this study suggests that there are certain conditions, potentially occurring in the surf zone, in which the predictions are very poor. Hence, until the discrepancies presented in this work are further investigated, any researcher that uses this implicit approach to estimate sediment diffusivity should be aware of the possible introduction of error from the methodology, particularly in flows with potential to exhibit large concentration gradients.

9.5 Future Research Directions

There are a number of possible research directions which could be pursued following the conclusion of this study. For example, the turbulence model evaluation could be expanded to consider large eddy simulation (LES) models to determine whether the results, in particular the TKE profiles, improve enough to justify the increase in computational effort. It would also be interesting to repeat the analysis on the two breaker types in cases where the beach slope has been adjusted and wave period kept constant. This would provide further insight into the cause of the slow turbulence dissipation in the spilling breaker: is it linked to a shorter wave period or due to a physical difference between the two breaker types?

A third possibility, and possibly more interesting for its novelty regarding the detailed visualizations and analysis of the processes that it could lead to, would be an in-depth analysis of the video footage obtained in the COAST laboratory focusing on the breaking wave process using PTV or PIV. The breaking process predicted by the numerical model could also be analysed in more detail, with comparison to this footage.

Finally, the suspended sediment concentration model is currently quite simplistic and hence could be improved through accounting for additional physics such as hindered settling, or inclusion of turbulence generation/damping caused by the presence of sediment. Also,

including compressibility effects in the numerical model may improve the air entrainment model simulations, hence leading to more accurate TKE and velocity predictions. This may allow sediment plumes to be considered in more detail since the behaviour of the entrapped air phase and the generation and evolution of the sediment plumes seem strongly correlated. However, further physical experiments would most likely be required to understand whether the concentration levels predicted by the numerical model in these plumes are comparable to those seen in the laboratory. Further extensions of the numerical model could include a bed load component and a morphological routine. This would allow the numerical model to be used to evaluate environmental impacts from renewable energy devices, such as sediment accumulation around tidal barrages, and scour around the foundations of either modular tidal devices or wind turbines.

Additional understanding of the sediment diffusivity calculations is clearly required, particularly around the breaking point. The cause of the discrepancies must be addressed. The balance of advection and diffusion has clear correlation with the accuracy of the technique, but does not explain the observed error at every location. Further effort also needs to be conducted into obtaining the exact sediment diffusivity time series from the numerical output of other quantities and hence determine which terms in the equation can be safely neglected. Until this has been conducted, researchers should be cautious when using using this implicit approach to estimate sediment diffusivity.

List of References

Aagaard, T. and Hughes, M. G. (2006), 'Sediment suspension and turbulence in the swash zone of dissipative beaches.', *Mar. Geol.* **228**, 117–135.

Aagaard, T., Hughes, M. G., Sørensen, R. M. and Andersen, S. (2005), 'Hydrodynamics and sediment fluxes across an onshore migrating intertidal bar.', *J. Coast. Res.* **22**, 247–259.

Aagaard, T. and Jensen, S. G. (2013), 'Sediment concentration and vertical mixing under breaking waves.', *Mar. Geol.* **336**, 146–159.

Absi, R. (2010), 'Concentration profiles for fine and coarse sediments suspended by waves over ripples: An analytical study with the 1-dv gradient diffusion model.', *Adv. Water Resour.* **33**, 411–418.

Airy, G. B. (1845), 'Tides and waves.', *In Encyclopaedia metropolitana* **5**, 241–396.

Amoudry, L., Hsu, T.-J. and Liu, P. L.-F. (2005), 'Schmidt number and near-bed boundary condition effects on a two-phase dilute sediment transport model.', *J. Geophys. Res. Oceans* **110**, 12.

Bagnold, R. A. (1966), 'An approach to the sediment transport problem from general physics.', U.S. Geol. Surv. Prof. Paper 422-I.

Bakhtyar, R., Barry, D. A., Yeganeh-Bakhtiary, A., Li, L., Parlange, J.-Y. and Sander, G. C. (2010), 'Numerical simulation of two-phase flow for sediment transport in the inner-surf and swash zones.', *Adv. Water Resour.* **33**, 277–290.

Bakhtyar, R., Yeganeh-Bakhtiary, A., Barry, D. A. and Ghaheri, A. (2009), 'Two-phase hydrodynamic and sediment transport modeling of wave-generated sheet flow.', *Adv. Water Resour.* **32**, 1267–1283.

Baldock, T. E., Tomkins, M. R., Nielsen, P. and Hughes, M. G. (2004), 'Settling velocity of sediments at high concentrations.', *Coast. Eng.* **51**, 91–100.

Battjes, J. A. (1974), Surf similarity, *in* 'Proceedings of the 14^{th} International Conference on Coastal Engineering', pp. 466–480.

Baykal, C., Sumer, B. M., Fuhrman, D. R., Jacobsen, N. G. and Fredsøe, J. (2015), 'Numerical investigation of flow and scour around a vertical circular cylinder.', *Phi. Trans. R. Soc. A* **373**, 21.

Bohórquez, P. (2008), Study and Numerical Simulation of Sediment Transport in Free-Surface Flow, PhD thesis, Department of Mechanical Engineering and Fluid Mechanics, University of Málaga.

Bradford, S. F. (2000), 'Numerical simulation of surf zone dynamics', *J. Waterw. Port. C-ASCE* **126**.

Brennan, D. (2001), The Numerical Simulation of Two-Phase Flows in Settling Tanks., PhD thesis, Department of Mechanical Engineering, Imperial College of Science, Technology and Medicine, London.

Brown, S. A., Greaves, D. M., Magar, V. and Conley, D. C. (2016), 'Evaluation of turbulence closure models under spilling and plunging breakers in the surf zone.', *Coastal Eng.* **114**, 177–193.

Brown, S. A., Magar, V., Greaves, D. M. and Conley, D. C. (2014), An evaluation of RANS turbulence closure models for spilling breakers ., *in* 'Proceedings of the 34^{th} International Conference on Coastal Engineering', Vol. 1, p. 15.

Buscombe, D. and Conley, D. C. (2012), Schmidt number of sand suspensions under oscilalting grid turbulence., *in* 'Proceedings of the 33^{rd} International Conference on Coastal Engineering', Vol. 1, p. 11.

Cáceres, I. and Alsina, J. M. (2012), 'A detailed, event-by-event analysis of suspended sediment concentration in the swash zone.', *Cont. Shelf Res.* **41**, 61–76.

Calantoni, J., Puleo, J. A. and Holland, K. T. (2006), 'Simulation of sediment motions using a discrete particle model in the inner surf and swash-zones.', *Cont. Shelf Res.* **26**, 610–621.

Cellino, M. (1998), Experimental study of suspension flow in open channels., PhD thesis, Swiss Federal Institute of Technology in Lausanne.

CFDEM (2014), 'CFDEM - Open Source CFD, DEM and CFD.'. http://www.cfdem.com.

Christensen, E. D. (2006), 'Large eddy simulation of spilling and plunging breakers', *Coastal Eng.* **53**, 463–485.

Christensen, E. D., Jensen, J. H. and Mayer, S. (2000), Sediment transport under breaking waves., *in* 'Proceedings of the 27^{th} International Conference on Coastal Engineering', Vol. III, pp. 2467–2480.

Cline, A. K. and Renka, R. L. (1984), 'A storage-efficient method for construction of a Thiessen triangulation', *Rocky Mt. J. Math.* **14**, 119–139.

Coleman, N. L. (1970), 'Flume studies of the sediment transfer coefficient.', *Water Resour. Res.* **6**, 801–809.

Coleman, N. L. (1986), 'Effects of suspended sediment on the open-channel velocity distribution.', *Water Resour. Res.* **22**, 1377–1384.

Conley, D. C., Falchetti, S., Lohmann, I. P. and Brocchini, M. (2008), 'The effects of flow stratification by non-cohesive sediment on transport in high-energy wave-driven flows.', *J. Fluid Mech.* **610**, 43–67.

Dahl, C. P. (1995), Numerical modelling of flow and settling in secondary settling tanks., Series Paper 8, Aalborg: Hydraulics and Coastal Engineering Laboratory, Department of Civil Engineering, Aalborg University.

Davies, A. G. and Thorne, P. D. (2005), 'Modeling and measurement of sediment transport by waves in the vortex ripple regime.', *J. Geophys. Res.* **110**, 25.

Dean, R. G. (1965), 'Stream function representation of nonlinear ocean waves.', *J. Geophys. Res.* **70**, 4561–4572.

Dohmen-Janssen, C. M. and Hanes, D. M. (2002), 'Sheet flow dynamics under monochromatic nonbreaking waves.', *J. Geophys. Res.* **107**, 21.

Drazen, D. A. and Melville, W. K. (2009), 'Turbulence and mixing in unsteady breaking surface waves.', *J. Fluid Mech.* **628**, 85–119.

Einstein, H. A. (1950), Bed-load function for sediment transportation in open channel flows., Technical Bulletin 1027, United States Department of Agriculture.

Einstein, H. A. and Chien, N. (1955), Effects of heavy sediment concentration near the bed on velocity and sediment distribution., Report 8, Univ. of Calif., Berkley, and Missouri River Div., U.S. Army Corps of Eng.

Engelund, F. and Fredsøe, J. (1976), 'A sediment transport model for straight alluvial channels.', *Nord. Hydrol.* **7**, 293–306.

Fenton, J. D. (1988), 'The numerical solution of steady water wave problems.', *Comput. Geosci.* **14**, 357–368.

Flesch, T. K., Prueger, J. H. and Hatfield, J. L. (2002), 'Turbulent schmidt number from a tracer experiment.', *Agr. Forest. Meteorol.* **111**, 299–307.

Fredsøe, J. and Deigaard, R. (1992), *Mechanics of Coastal Sediment Transport*, Vol. 3 of *Advanced Series on Ocean Engineering*, World Scientific Publishing.

Fuhrman, D. R., Baykal, C., Sumer, B. M., Jacobsen, N. G. and Fredsøe, J. (2014), 'Numerical simulation of wave-induced scour and backfilling processes beneath submarine pipelines.', *Coast. Eng.* **94**, 10–22.

Garcia, M. and Parker, G. (1991), 'Entrainment of bed sediment into suspension.', *J. Hydraul. Eng.* **117**, 414–435.

Govender, K., Mocke, G. P. and Alport, M. J. (2002), 'Video-imaged surf zone wave and roller structures and flow fields.', *J. Geophys. Res.* **107**(C7), 9–1 – 9–21.

Graf, W. H. and Cellino, M. (2002), 'Suspension flows in open channels; experimental study', *J. Hydraul. Res.* **40**, 435–447.

Grant, W. D. and Madsen, O. S. (1979), 'Combined wave and current interaction with a rough bottom.', *J. Geophys. Res.* **84**, 12.

Greenshields, C. (2015), *OpenFOAM, The Open Source CFD Toolbox - User Guide*, CFD Direct Ltd.

Gruber, K. (2012), Sediment transport in open channel flows - experimental investigation and numerical simulation of local scour development downstream of a weir., Master's thesis, Department of Particulate Flow Modelling, Johannes Kepler University Linz.

Higuera, P., Lara, J. L. and Losada, I. J. (2013*a*), 'Realistic wave generation and active absorption for Navier-Stokes models application to OpenFOAM®.', *Coastal Eng.* **71**, 102–118.

Higuera, P., Lara, J. L. and Losada, I. J. (2013*b*), 'Simulating coastal engineering processes with OpenFOAM®.', *Coastal Eng.* **71**, 119–134.

Holthuijsen, L. H. (2007), *Waves in Oceanic and Coastal Waters*, Cambridge University Press.

Horikawa, K., Watanabe, A. and Katori, S. (1982), Sediment transport under sheet flow condition., *in* 'Proceedings of the 18^{th} International Conference on Coastal Engineering', Vol. 1, pp. 1335–1352.

Hsu, T.-J., Jenkins, J. T. and Liu, P. L.-F. (2003), 'On two-phase sediment transport: Dilute flow', *J. Geophys. Res.* **108**, 14.

Hsu, T.-J. and Liu, P. L.-F. (2004), 'Toward modeling turbulent suspension of sand in the nearshore', *J. Geophys. Res.* **109**.

Huang, Z.-C., Hwung, H.-H. and Chang, K.-A. (2009), 'Turbulence and energy dissipations of surf-zone spilling breakers.', *Coastal Eng.* **56**, 733–746.

Hurther, D. and Thorne, P. D. (2011), 'Suspension and near-bed load sediment transport processes above a migrating, sand-rippled bed under shoaling waves.', *J. Geophys. Res.* **116**, 17.

IPCC (2013), *Climate Change 2013: The Physical Science Basis. Contribution of Working Group I to the Fifth Assessment Report of the Intergovernmental Panel on Climate Change.*, Cambridge University Press, Cambridge, United Kingdom and New York, NY, USA.

Iribarren, C. R. and Nogales, C. (1949), Protection de ports, *in* 'XVIIth Int. Nav. Congress,', Vol. II, pp. 31–80.

Issa, R. I. (1986), 'Solution of the implicitly discretised fluid flow equations by operator-splitting.', *J. Comput. Phys.* **62**, 40–65.

Jacobsen, N. G. (2011), A Full Hydro- and Morphodynamic Description of Breaker Bar Development., PhD thesis, Technical University of Denmark, Department of Mechanical Engineering. DCAMM Special Report, no. S136.

Jacobsen, N. G., Fredsoe, J. and Jensen, J. H. (2014), 'Formation and development of a breaker bar under regular waves. part 1: Model description and hydrodynamics.', *Coast. Eng.* **88**, 182–193.

Jacobsen, N. G., Fuhrman, D. R. and Fredsøe, J. (2012), 'A wave generation toolbox for the open-source CFD library: OpenFoam®.', *Int. J. Numer. Meth. Fluids.* **70**, 1073–1088.

Jasak, H. (1996), Error analysis and estimation for the finite volume method with applications to fluid flows., PhD thesis, Department of Mechanical Engineering, Imperial College of Science, Technology and Medicine.

Kärrholm, F. P. (2008), Numerical Modelling of Diesel Spray Injection and Turbulence Inter-

action, Appendix A, PhD thesis, Department of Applied Mechanics, Chalmers University of Technology.

Kimmoun, O. and Branger, H. (2007), 'A particle image velocimetry investigation on laboratory surf-zone breaking waves over a sloping beach.', *J. Fluid Mech.* **588**, 353–397.

Kinsman, B. (2012), *Wind Waves: Their Generation and Propagation on the Ocean Surface.*, new edition. edn, Dover Publications.

Kobayashi, N. and Johnson, B. D. (2001), 'Sand suspension, storage, advection, and settling in surf and swash zones.', *J. Geophys. Res.* **106**, 9363–9376.

Kobayashi, N. and Lawrence, A. R. (2004), 'Cross-shore sediment transport under breaking solitary waves.', *J. Geophys. Res.* **109**.

Komar, P. D. (1998), *Beach processes and sedimentation.*, second edn, Prentice-Hall, Inc.

Korteweg, D. J. and de Vries, G. (1895), 'On the change of form of long waves advancing in a rectangular canal, and on a new type of long stationary waves.', *Phil. Mag.* **39**(5), 422–443.

Kothe, D. B., Mjolsness, R. C. and Torrey, M. D. (1991), Ripple: a computer program for incompressible flows with free surfaces., Technical Report LA-UR-91-2818, Los Alamos National Lab, Los Alamos, New Mexico.

Launder, B. E., Reece, G. J. and Rodi, W. (1975), 'Progress in the development of a reynolds-stress turbulence closure', *J. Fluid Mech.* **68**(3), 537–566.

Launder, B. E. and Sharma, B. I. (1974), 'Application of the energy-dissipation model of turbulence to the calculation of flow near a spinning disc.', *Lett. Heat Mass Transfer* **1**, 131–137.

Lee, G.-H., Friedrichs, C. T. and Vincent, C. E. (2002), 'Examination of diffusion versus advection dominated sediment suspension on the inner shelf under storm and swell conditions, duck, north carolina.', *J. Geophys. Res.* **107**, 29.

Lin, P. and Liu, P. L. F. (1998*a*), 'A numerical study of breaking waves in the surf zone.', *J. Fluid Mech.* **359**, 239–264.

Lin, P. and Liu, P. L. F. (1998*b*), 'Turbulence transport, vorticity dynamics and solute mixing under plunging waves in surf zone.', *J. Geophys. Res.* **103**(C8), 15677–15694.

Liu, P. L.-F. and P., L. (1997), A numerical model for breaking waves: The volume of fluid method., Technical Report CACR-97-02, University of Delaware Center for Applied Coastal Research.

Liu, X. (2008), Numerical Models for Scour and Liquefaction Around Object Under Currents and Waves., PhD thesis, University of Illinois at Urbana-Champaign.

Lyn, D. A. (1988), 'A similarity approach to turbulent sediment-laden flows in open channels.', *J. Fluid Mech.* **193**, 1–26.

Ma, G., Chou, Y. and Shi, F. (2014), 'A wave-resolving model for nearshore suspended sediment transport.', *Ocean Modell.* **77**, 33–49.

Ma, G., Shi, F. and Kirby, J. T. (2012), 'Shock-capturing non-hydrostatic model for fully dispersive surface wave processes', *Ocean Modell.* **43-44**, 22–35.

Magar, V. and Davies, A. G. (2005), *Suspended sediment dynamics over rippled beds in oscillatory flows based on a 2DHV discrete-vortex/particle-tracking model.*, Aqua Publications., The Netherlands., pp. AG1–AG9.

Malarkey, J. and Davies, A. G. (2002), 'Discrete vortex modelling of oscillatory flow over ripples.', *App. Ocean Res.* **24**, 127–145.

Malarkey, J., Magar, V. and Davies, A. G. (2015), 'Mixing efficiency of sediment and momentum above rippled beds under oscillatory flows.', *Cont. Shelf Res.* **108**, 76–88.

Mayer, S. and Madsen, P. A. (2000), 'Simulation of breaking waves in the surf zone using a navier-stokes solver', *Proceeding to Coastal Engineering Conference* **I**, 928–941.

Melville, W. K., Veron, F. and White, C. J. (2002), 'The velocity field under breaking waves: coherent structures and turbulence.', *J. Fluid Mech.* **454**, 203–233.

Menter, F. R. (1994), 'Two-equation eddy-viscosity turbulence models for engineering applications.', *AIAA Journal* **32**(8), 1598–1605.

Miller, M. C., McCave, I. N. and Komar, P. D. (1977), 'Threshold of sediment motion under unidirectional currents.', *Sedimentology* **24**, 507–527.

Misra, S. K., Kirby, J. T., Brocchini, M., Veron, F., Thomas, M. and Kambhamettu, C. (2008), 'The mean turbulent flow structure of a weak hydraulic jump.', *Phys. Fluids* **20**.

Murphy, A. H. (1988), 'Skill scores based on the mean square error and their relationships to the correlation coefficient.', *Monthly Weather Review* **116**, 2417–2424.

Nadaoka, K., Hino, M. and Koyano, Y. (1989), 'Structure of the turbulent flow field under breaking waves in the surf zone.', *J. Fluid Mech.* **204**, 359–387.

Nielsen, P. (1979), Some basic concepts of wave sediment transport., PhD thesis, Technical University of Denmark.

Nielsen, P. (1992), *Coastal Bottom Boundary Layers and Sediment Transport*, Vol. 4 of *Advanced Series on Ocean Engineering*, World Scientific Publishing.

Nielsen, P. (2009), *Coastal and Estuarine Processes.*, Vol. 29 of *Advanced Series on Ocean Engineering*, World Scientific Publishing.

Nielsen, P., van der Wal, K. and Gillan, L. (2002), 'Vertical fluxes of sediment in oscillatory sheet flow.', *Coast. Eng.* **45**, 61–68.

Nikuradse, J. (1933), 'Strömungsgesetze in rauhren rohren', *vDI Forschungshefte* **361**. [(English translation: Laws of flow in rough pipes). Tech. Rep. NACA Technical Memorandum 1292. National Advisory Commision for Aeronautics, Washington, DC, USA (1950)].

Nokes, R. (2014), *Streams: System Theory and Design*, University of Canterbury.

O'Donoghue, T., Doucette, J. S., van der Werf, J. J. and Ribberink, J. S. (2006), 'The dimensions of sand ripples in full-scale oscillatory flows.', *Coast. Eng.* **53**, 997–1012.

Ogston, A. S. and Sternberg, R. W. (2002), 'Effect of wave breaking on sediment eddy diffusivity, suspended-sediment and longshore sediment flux profiles in the surf zone', *Cont. Shelf Res.* **22**, 633–655.

Okayasu, A., Uno, Y., Kobayashi, T. and Shimaya, M. (2004), 'Laboratory measurement of suspended sediment concentration in surf zone with CT concentration meter.', *Coast. Eng.* **46**, 203–218.

Otsuka, J. and Watanabe, Y. (2012), Wave flume-based evaluation of suspended sand transport in breaking waves., *in* 'Proceedings of the 33^{rd} International Conference on Coastal Engineering', Vol. 1, p. sediment.56.

Otsuka, J. and Watanabe, Y. (2014), Laboratory measurement of sediment transport under a breaking wave turbulent flow field., *in* 'Proceedings of the 34^{th} International Conference on Coastal Engineering', Vol. 1, p. sediment.2.

Patankar, S. V. and Spalding, D. B. (1972), 'A calculation procedure for heat, mass and momentum transfer in three-dimensional parabolic flows.', *Int. J. Heat Mass Tran.* **15**, 1787–1806.

Patankar, V. M. (1980), *Numerical Heat Transfer and Fluid Flow.*, Hemisphere Publishing Corporation, Taylor & Francis Group.

Pilegaard, K. (2012), CFD of backfilling of scour holes around marine structures. pipelines., Master's thesis, Technical University of Denmark, Department of Mechanical Engineering.

Puleo, J. A., Holland, K. T., Plant, N. G., Slinn, D. N. and Hanes, D. M. (2003), 'Fluid acceleration effects on suspended sediment transport in the swash zone.', *J. Geophys. Res.* **108**(C11).

Ransley, E. J. (2015), Survivability of wave energy converter and mooring coupled system using CFD, PhD thesis, School of Marine Science and Engineering, Plymouth University.

Rhie, C. M. and Chow, W. L. (1983), 'Numerical study of the turbulent flow past an airfoil with trailing edge separation.', *AIAA J.* **21**, 1525–1532.

Ribberink, J. S. and Al-Salem, A. A. (1995), 'Sheet flow and suspension of sand in oscillatory boundary layers.', *Coast. Eng.* **25**, 205–225.

Ribberink, J. S., van der A, D. A., van der Zanden, J., O'Donoghue, T., Hurther, D., Cáceres, I. and Thorne, P. D. (2014*a*), Measurements of sand transport and its underlying processes under large-scale breaking waves (SANDT-PRO), *in* 'Proceedings of the 34^{th} International Conference on Coastal Engineering', Vol. 1, p. 14.

Ribberink, J. S., van der A, D. A., van der Zanden, J., O'Donoghue, T., Hurther, D., Cáceres, I. and Thorne, P. D. (2014*b*), SANDT-PRO: Sediment transport measurements under irregular and breaking waves., *in* 'Proceedings of the HYDRALAB IV Joing User Meeting', p. 8.

Richardson, J. F. and Zaki, W. N. (1954), 'Sedimentation and fluidisation, part 1.', *Trans. Instn. Chem. Engrs.* **32**, 35 – 53.

Rienecker, M. M. and Fenton, J. D. (1981), 'A Fourier approximation method for steady water waves.', *J. Fluid Mech.* **104**, 119–137.

Roeber, V. and Cheung, K. F. (2012), 'Boussinesq-type model for energetic breaking waves in fringing reef environments.', *Coastal Eng.* **70**, 1–20.

Roelvink, D., Reniers, A., van Dongeren, A., van Thiel de Vries, J., McCall, R. and Lescinski, J. (2009), 'Modelling storm impacts on beaches, dunes and barrier islands.', *Coastal Eng.* **56**, 1133–1152.

Rubey, W. W. (1933), 'Settling velocities of gravel, sand and silt particles.', *Am. J. Sci.* **225**, 325–338.

Rusche, H. (2002), Computational fluid dynamics of dispersed two-phase flows at high phase fractions., PhD thesis, Imperial College of Science, Technology and Medicine.

Sato, S., Homma, K. and Shibayama, T. (1990), 'Laboratory study on sand suspension due to breaking waves.', *Coastal Eng. Jpn.* **33**, 219–231.

Sheng, J. and Hay, A. E. (1995), 'Sediment eddy diffusivities in the nearshore zone, from multifrequency acoustic backscatter.', *Cont. Shelf Res.* **15**, 129–147.

Shields, A. (1936), 'Anwendung der ähnlichkeits-mechanik und turbulenzforschung auf die geschiebebewegung.', *Preussische Versuchsanstalt für Wasserbau und Schiffbau* **26**. [(English translation: Application of similarity principles and turbulence research to bed-load movement). Ott, W. P. and van Uchelen, J. C. (translators) Hydrodynamics Laboratory, California Institute of Technology, Pasadena, California, Report no. 167].

Shih, T. H., Zhu, J. and Lumley, J. L. (1996), 'Calculation of wall-bounded complex flows and free shear flows.', *Int. J. Numer. Meth. Fl.* **23**, 1133–1144.

Shimizu, T. and Ikeno, M. (1996), Experimental study on sediment transport in surf and swash zones using large wave flume, *in* 'Proceedings to Coastal Engineering Conference.', Vol. III, pp. 3076–3089.

Smith, J. D. and McLean, S. R. (1977), 'Spatially averaged flow over a wavy surface', *J. Geophys. Res.* **82**.

Sorensen, R. M. (2006), *Basic Coastal Engineering*, 3 edn, Springer.

Soulsby, R. (1997), *Dynamics of marine sands.*, Thomas Telford Publications.

Soulsby, R. L. and Whitehouse, R. J. S. (1997), Threshold of sediment motion in coastal environments., *in* 'Pacific Coasts and Ports '97: Proceedings of the 13th Australasian Coastal and Ocean Engineering Conference and the 6th Australasian Port and Harbour Conference', Vol. 1, pp. 145–150.

Speziale, C. G. and Thangam, S. (1992), 'Analysis of an RNG based turbulence model for separated flows.', *Int. J. Eng. Sci.* **30**(10), 1379–1388.

Stokes, G. G. (1847), 'On the theory of oscillatory waves', *Transactions of the Cambridge Philosophical Society* **8**, 441–455.

Sumer, B. M., Guner, H. A. A., Hansen, N. M., Fuhrman, D. R. and Fredsøe, J. (2013), 'Laboratory observations of flow and sediment transport induced by plunging regular waves.', *J. Geophys. Res. Oceans* **118**, 6161–6182.

Sumer, B. M., Kozakiewicz, A., Fredsøe, J. and Deigaard, R. (1996), 'Velocity and concentration profiles in sheet-flow layer of movable bed.', *J. Hydr. Eng.* **122**, 549–558.

Suzuki, T., Okayasu, A. and Shibayama, T. (2007), 'A numerical study of intermittent sediment concentration under breaking waves in the surf zone.', *Coast. Eng.* **54**, 433–444.

Svendsen, I. A. (2006), *Introduction to nearshore hydrodynamics*, World Scientic Publishing Co. Pte. Ltd.

Tennekes, H. and Lumley, J. L. (1972), *A First Course in Turbulence*, MIT Press.

Thorne, P. D., Davies, A. G. and Bell, P. S. (2009), 'Observations and analysis of sediment diffusivity profiles over sand rippled beds under waves.', *J. Geophys. Res.* **114**, 16.

Thorne, P. D., Williams, J. J. and Davies, A. G. (2002), 'Suspended sediments under waves measured in a large-scale flume facility', *J. Geophys. Res.* **107**, 3178–3193.

Ting, F. C. K. and Kirby, J. T. (1994), 'Observation of undertow and turbulence in a laboratory surf zone.', *Coastal Eng.* **24**, 51–80.

Ting, F. C. K. and Kirby, J. T. (1995), 'Dynamics of surf-zone turbulence in a strong plunging breaker.', *Coastal Eng.* **24**, 177–204.

Ting, F. C. K. and Kirby, J. T. (1996), 'Dynamics of surf-zone turbulence in a spilling breaker.', *Coastal Eng.* **27**, 131–160.

Tu, J., Yeoh, G. and Liu, C. (2008), *Computational Fluid Dynamics: A Practical Approach.*, 1 edn, Butterworth-Heinemann.

Ueberl, J. (1995), Verbesserung der Absetzwirkung von Nachklarbecken., PhD thesis, Swiss Federal Institute of Technology ETH, Zurich Switzerland. (In German.).

van der A, D. A., O'Donoghue, T. and Ribberink, J. S. (2010), 'Measurements of sheet flow transport in acceleration-skewed oscillatory flow and comparison with practical formulations.', *Coastal Eng.* **57**, 331–342.

van der Werf, J. J., Doucette, J. S., O'Donoghue, T. and Ribberink, J. S. (2007), 'Detailed measurements of velocities and suspended sand concentrations over full-scale ripples in regular oscillatory flow.', *J. Geophys. Res.* **112**, 18.

van der Werf, J. J., Magar, V., Malarkey, J., Guizien, K. and O'Donoghue, T. (2008), '2dv modelling of sediment transport processes over full-scale ripples in regular asymmetric oscillatory flow.', *Cont. Shelf Res.* **28**, 1040–1056.

van der Werf, J. J., Ribberink, J. S., O'Donoghue, T. and Doucette, J. S. (2006), 'Modelling and measurement of sand transport processes over full-scale ripples in oscillatory flow.', *Coast. Eng.* **53**, 657–673.

Van Doormaal, J. P. and Raithby, G. D. (1984), 'Enhancements of the SIMPLE method for predicting incompressible fluid flows.', *Numer Heat Transfer* **7**, 143–163.

van Rijn, L. C. (1984*a*), 'Sediment pickup functions', *J. Hydraul. Eng.* **110**, 1494–1502.

van Rijn, L. C. (1984*b*), 'Sediment transport, part II: Suspended load transport', *J. Hydraul. Eng.* **110**, 1613–1641.

van Rijn, L. C. (1993), *Principles of Sediment Transport in Rivers Estuaries and Coastal Seas.*, Aqua Publications.

van Rijn, L. C. (2007), 'Unified view of sediment transport by currents and waves. II: Suspended transport.', *J. Hydraul. Eng.* **133**(6), 668 – 689.

Vanoni, V. A. (1946), 'Transportation of suspended sediment by water.', *Trans. ASAE* **3**, 67–133.

Versteeg, H. K. and Malalasekera, W. (1995), *An Introduction to Computational Fluid Dynamics: The Finite Volume Method*, Pearson Education Ltd.

Wang, X. and Qian, N. (1989), 'Turbulence characteristics of sediment-laden flow.', *J. Hydraul. Eng.* **115**, 781–800.

Wilcox, D. C. (1988), 'Reassessment of the scale-determining equation for advance turbulence models.', *AIAA Journal* **26**(11), 1299–1310.

Wilcox, D. C. (2006), *Turbulence Modeling for CFD*, 3rd edn, DCW Industries, inc.

Xie, Z. (2013), 'Two-phase flow modelling of spilling and plunging breaking waves', *Applied Mathematical Modelling* **37**, 3698–3713.

Yakhot, V., Thangam, S., Gatski, T. B., Orszag, S. A. and Speziale, C. G. (1992), 'Development of turbulence models for shear flows by a double expansion technique.', *Phys. Fluids A* **4**(7), 1510 – 1520.

Zyserman, J. and Fredsøe, J. (1994), 'Data analysis of bed concentration of suspended sediment.', *J. Hydraul. Eng.* **120**, 1021–1042.

Bound Copies of Published Papers

Evaluation of turbulence closure models under spilling and plunging breakers in the surf zone.

S.A. Brown, D.M. Greaves, V. Magar, D.C. Conley

Electronic version of an article published in Coastal Engineering, 114, p. 177-193, doi:http://dx.doi.org/10.1016/j.coastaleng.2016.04.002 © Copyright World Scientific Publishing Company
https://www.journals.elsevier.com/coastal-engineering/

Evaluation of turbulence closure models under spilling and plunging breakers in the surf zone.

S. A. Brown[a,*], D. M. Greaves[a], V. Magar[b], D. C. Conley[a]

[a] *School of Marine Science and Engineering, Plymouth University, Plymouth, United Kingdom*
[b] *Department of Physical Oceanography, CICESE, Ensenada, Mexico*

Abstract

Turbulence closure models are evaluated for application to spilling and plunging breakers in the surf zone using open source computational fluid dynamics software. A new library of turbulence models for application to multiphase flows has been developed and is assessed for numerical efficiency and accuracy by comparing against existing laboratory data for surface elevation, velocity and turbulent kinetic energy profiles. Out of the models considered, it was found that, overall, the best model is the nonlinear $k - \epsilon$ model. The model is also shown to exhibit different turbulent characteristics between the different breaker types, consistent with experimental data.

Keywords:
spilling breakers, plunging breakers, turbulence models, computational fluid dynamics, OpenFOAM, surf zone

1. Introduction

In environments where a large quantity of fine sand is found, suspended sediment concentrations, and therefore transport, can become very significant. These suspended loads can have a great impact on physical and biological processes, for instance, coastal erosion and light penetration through the water column. Therefore, it is essential to be able to predict suspended sediment concentrations and sediment transport rates with good accuracy. As a consequence, substantial research effort has been put into understanding the processes behind suspended sediment dynamics in both the surf and swash zones (Puleo et al., 2003; van Rijn, 2007).

A significant consideration when predicting suspended sediment concentrations in the surf and swash zones, is the effect of breaking waves and the associated turbulence (Falchetti et al., 2010). In the surf zone, breaking waves

*Corresponding author
Email address: scott.brown@plymouth.ac.uk (S. A. Brown)

generate turbulence to levels capable of suspending and transporting large quantities of sediment. Such breaker-induced turbulence is influenced mainly by the Iribarren number, ξ_0, (Battjes, 1974; Iribarren and Nogales, 1949), linking the breaker's steepness and the beach slope. The value of the Iribarren number indicates the type of breaker, defined as spilling ($\xi_0 < 0.5$), plunging ($0.5 < \xi_0 < 3.3$) or collapsing ($3.3 < \xi_0$). A number of experimental investigations have been conducted on the dynamics of turbulence generated on a sloping beach by both spilling (Ting and Kirby, 1994, 1996; Govender et al., 2002; Huang et al., 2009) and plunging breakers (Ting and Kirby, 1994, 1995; Kimmoun and Branger, 2007). Many numerical models have also been developed to consider this problem. A number of these models have made use of a two equation turbulence model to represent turbulence generation and dissipation in the surf zone, with varying results, although they generally overestimate the levels of turbulent kinetic energy (TKE) generated by the breakers. A variety of two equation turbulence closure models has been applied in these numerical models; the $k-\epsilon$ (Bradford, 2000; Xie, 2013; Ma et al., 2014), $k-\omega$ (Christensen et al., 2000; Jacobsen et al., 2012), RNG $k-\epsilon$ (Bradford, 2000) and a nonlinear $k-\epsilon$ model (Lin and Liu, 1998a,b). However, to the authors best knowledge a thorough comparison of two equation turbulence models for spilling and plunging breakers in the surf zone has not been performed using the same code, although Bradford (2000) did compare the standard and RNG $k-\epsilon$ models.

In this work, five turbulence closure models are thoroughly evaluated for accuracy in predictions of surface elevation, horizontal velocity and TKE, in relation to experimental data for both spilling and plunging breakers. The open source computational fluid dynamics (CFD) code, "OpenFOAM" (OpenFOAM, 2014) based on the Reynolds Averaged Navier-Stokes (RANS) equations is utilised along with waves2Foam, a wave generation toolbox developed by Jacobsen et al. (2012). Following Jacobsen (2011), a new library of turbulence models has been created within the OpenFOAM environment, which account for density variations around the free surface (Brown et al., 2014). The surface elevation, velocity and TKE data used for comparison has been gathered by Ting and Kirby (1994), through a thorough set of laboratory experiments into both spilling and plunging breakers on a beach of gradient 1/35. The results were obtained by producing cnoidal waves and phase-averaging (denoted by a tilde, i.e. $\widetilde{\eta}$) the waves over a period of twenty minutes. The fluid velocities were obtained using a fibre-optic laser-Doppler anemometer and the TKE values were then calculated by the formula

$$k = \frac{2}{3}(\widetilde{u'^2} + \widetilde{w'^2}), \tag{1}$$

where u' and w' are the fluctuations from the mean velocity. Since only one component of the velocity could be measured at a time, the horizontal and vertical velocity time series, and subsequently the TKE, was obtained from separate twenty minute runs.

The paper is organised as follows. First, an overview of the turbulence models is given. Then, the numerical setup is presented, followed by a comparison

of the turbulence models against laboratory data. Finally, the conclusions are drawn.

2. Turbulence Models

This work focuses on four popular two equation turbulence closure models ($k-\omega$, $k-\omega$ SST, RNG $k-\epsilon$, nonlinear (NL) $k-\epsilon$) and a Reynolds stress model (RSM), which solves for all components of the Reynolds Stress (Launder et al., 1975). All of the two equation models use an eddy viscosity to calculate the Reynolds stress, obtained by solving equations for the turbulent kinetic energy (TKE), k, and either the turbulence dissipation rate, ϵ, ($k-\epsilon$ models) or a characteristic frequency, ω, associated with the turbulence ($k-\omega$ models). This section describes the different models used and the advantages and disadvantages of each.

$k-\epsilon$ models are a commonly used method for turbulence closure. Hence, the weaknesses of the standard $k-\epsilon$ model are generally well known. One of these weaknesses is that the transport equation for ϵ becomes singular near the wall, so, in order to model the viscous sublayer accurately, it is necessary to introduce damping at the wall. Furthermore, fully developed, isotropic turbulence is assumed, so the model generally under-performs under transitional turbulence or adverse pressure gradients (Versteeg and Malalasekera, 1995; Wilcox, 2006). The renormalised group (RNG) $k-\epsilon$ aims to address some of the weaknesses of the standard $k-\epsilon$ model. Originally developed using an additional expansion parameter by Yakhot et al. (1992), the RNG $k-\epsilon$ has been shown to perform better than the standard $k-\epsilon$ model in transitional flows (Versteeg and Malalasekera, 1995). However, the additional expansion parameter causes the model to become overly sensitive to the magnitude of the strain rate. Furthermore, the model is also based upon the assumption of isotropy, which is not valid for all flows.

Another model being evaluated is the $k-\omega$ model (Wilcox, 2006). It offers improved near wall treatment, removing the necessity for wall damping. It has also been shown to give more accurate predictions, than the standard $k-\epsilon$ model, in cases of adverse pressure gradients (Wilcox, 2006). However, it can be overly sensitive to the inlet free stream boundary conditions and still relies on the isotropic turbulence assumption. A variation on this model is the $k-\omega$ shear stress transport (SST) model, developed by Menter (1994) and is a blend of both the $k-\omega$ and $k-\epsilon$ model. It aims to address the sensitivity to the free stream value of ω, whilst keeping the improved near wall treatment. To achieve this, a blending function is utilised, which applies the $k-\omega$ model for near wall treatment and the $k-\epsilon$ in the free stream. However, not all of the problems with $k-\omega$ and $k-\epsilon$ models are fixed by this method, since it also assumes that turbulence is isotropic.

In this study, the validity of the isotropic assumption is considered in two ways. The first is to use the nonlinear $k-\epsilon$ model developed by Shih et al. (1996), which accounts for anisotropic effects by introducing a nonlinear Reynolds stress term into the standard $k-\epsilon$ model. Shih et al. (1996) showed that the nonlinear

$k-\epsilon$ model performs better than the standard $k-\epsilon$ model for flows under strong adverse pressure gradients, as well as for separated and swirling flows. The second model is a Reynolds stress model (RSM) developed by Launder et al. (1975). This model resolves all directions of the Reynolds stress directly, along with an equation for ϵ for closure, eliminating the need for an eddy viscosity and hence the assumptions on the isotropy of the turbulence. This model is expected to produce the most accurate results since it captures the physics more realistically, but at the cost of computational efficiency since seven equations are solved. However, it uses the same ϵ equation as the isotropic turbulence models, indicating that if this is not modelled correctly then it will perform no better than the other models considered in this study.

3. Numerical Model

The turbulence models discussed in Section 2 are tested for 2D spilling and plunging breakers propagating perpendicular to the shore. The free surface is tracked using a two-phase volume of fluid (VOF) technique, solved together with the incompressible RANS equations for the fluid flow field. The coordinate system (x, y, z) is taken such that x corresponds to the cross-shore direction, with positive x in the direction of wave propagation. The waves are generated on the left at the Inlet boundary and propagate towards a beach located on the right of the domain (see Figure 1). y and z are the long-shore and vertical coordinates, respectively. Waves are generated at the Inlet by setting a time-dependent boundary condition for the velocity and the free surface, both based on analytical solutions of the wave equations. A relaxation zone at the Inlet permits absorption of wave reflections at the boundary. A Courant number of 0.2 for the spilling and 0.1 for the plunging breaker cases was found to be necessary for numerical stability. The mesh has been designed using a mesh convergence study to ensure that a mesh independent solution is obtained with minimum computational expense. Two approaches were considered; both refining the whole computational domain and refining the region around the free surface only. Time series' of velocity, surface elevation and TKE were then compared to determine when a mesh independent solution had been achieved. To further minimise numerical diffusion, higher order numerical schemes (e.g. linear rather than upwind) were used where numerical stability allowed.

3.1. Computational Domain & Boundary Conditions

The computational domain is setup to be consistent with the laboratory experiments of Ting and Kirby (1994) and is illustrated in Figure 1. There is a sloping beach of gradient 1/35, the water depth, h, is 0.4 m and the origin is located at the still water line, 0.7 m shoreward of the start of the slope, where $h = 0.38$ m (see Figure 1). Approximately 320000 cells are used to discretise the domain in the spilling breakers case, whereas 360000 cells are used for the plunging breakers. The domain is only one cell thick in the y direction, and in the x and z directions, the cells have an aspect ratio of 1 where possible,

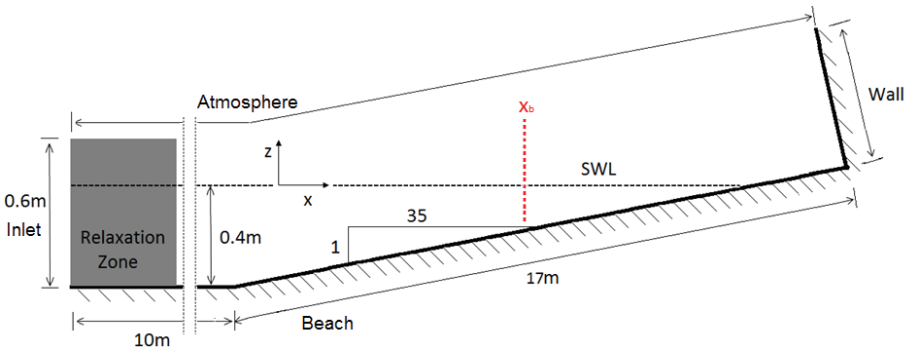

Figure 1: Diagram of the computational domain (not to scale) and the boundary names used.

i.e. $\Delta x = \Delta z$, for both cases. This was shown to improve the breaking point and height of the wave by Jacobsen et al. (2012), who suggested that this was due to larger VOF flux in cells of aspect ratio greater than one. The cell size in the internal domain is set to 0.01 m and, based on a balance of accuracy and CPU time, determined through the previously mentioned mesh refinement study, further refinement has been applied in the x and z directions around the free surface. Therefore, the discretisation is 0.005 m in this region. At the Beach boundary six layers of thinner cells (in the z direction) have been used, with each layer away from the boundary being twice the size of the last.

Regular waves are generated by stream function wave theory (Rienecker and Fenton, 1981) at the Inlet boundary. The spilling breakers are created by incoming, regular waves of period $T = 2\,\mathrm{s}$ and height $H = 0.125\,\mathrm{m}$, whereas the plunging breakers are generated using $T = 5\,\mathrm{s}$ and height $H = 0.127\,\mathrm{m}$. A relaxation zone is applied at the Inlet boundary for both cases; for the spilling breakers the relaxation zone is approximately one wavelength L long, whereas in the plunging case it is $L/2$. This has been shown to allow simulation, and therefore averaging, over a large number of waves (Jacobsen et al., 2012). The model is run for fifty wavelengths, with the final twenty waves averaged and used for the results in this study. Data is collected relative to the breaking point of the wave at the probe locations considered by Ting and Kirby (1994).

The Beach and Wall boundaries are considered as solid walls and therefore no-slip conditions have been applied along with zero gradient conditions for pressure and VOF. The top boundary also uses a Neumann boundary condition for the VOF but the boundary condition for the velocity varies according to the near boundary flux; using a zero gradient condition for outflow and the internal cell value of the normal component to the patch face for the inflow. The top boundary condition for pressure is defined as the total pressure

$$p = p_0 + \frac{1}{2}|\mathbf{u}|^2 \tag{2}$$

where p_0 is the user defined reference value, and $\mathbf{u}$ is the velocity. For this case p_0 is set to zero since the solver uses the difference between total pressure and

hydrostatic pressure. The initial conditions are set to the solution obtained after running the model without a turbulence model turned on for fifty wavelengths.

Wall functions are applied at the Beach boundary. The wall functions switch between low Reynolds number (LRN) and high Reynolds number (HRN) flows, depending on whether the near wall cell centre lies in the log or laminar sublayer. This is evaluated through the dimensionless wall distance

$$z^+ = \frac{\Delta z_w u_*}{\nu} = \frac{\Delta z_w \sqrt[4]{C_\mu}\sqrt{k}}{\nu}, \tag{3}$$

where Δz_w is the distance from the near wall cell centre to the wall. Comparing z^+ to the threshold value at the edge of the laminar sublayer, z^+_{lam}, gives an indication as to the region in which the near wall centre lies. The value of z^+_{lam} is obtained by solving

$$z^+_{lam} = \frac{\log(z^+_{lam}E)}{\kappa} \tag{4}$$

where E is an integration constant associated with the surface roughness and κ is the von Kármán constant. If $z^+ > z^+_{lam}$, the cell centre is assumed to be in the log layer and a HRN wall function is used. Conversely, if $z_+ \leq z^+_{lam}$ then the cell centre is assumed to be below the log layer and therefore a LRN wall function is used. Neumann boundary conditions are applied for each of the turbulent variables at the Wall boundary. At all the other boundaries the turbulent boundary conditions must be chosen carefully since, although TKE should not exist at the walls, Lin and Liu (1998a) note that the transport equations become singular if $k = 0$, making it necessary to 'seed' a small quantity of TKE. Following Lin and Liu (1998a), the TKE at the Inlet is calculated as

$$k = \frac{1}{2}(c_p I)^2 \tag{5}$$

where I and $c_p = L/T$ are the turbulence intensity and phase speed of the wave, respectively. The ϵ or ω value is then adjusted so that the eddy viscosity is a fraction, λ, of the kinematic viscosity, i.e. $\nu_t = \lambda\nu$. Following Lin and Liu (1998a), I and λ are chosen as 0.0025 and 0.1, respectively, in this study. The initial conditions are set to the value specified at the Inlet.

3.2. Implementation of Turbulence Models

In this section, the transport equations for each of the turbulence models under consideration are discussed with particular emphasis on how they are implemented in OpenFOAM (v. 2.1.1). The general form of the equations is such that

$$\begin{aligned} \textit{rate of change} + \textit{transport by convection} = \textit{production} - \textit{dissipation} \\ + \textit{transport by diffusion.} \end{aligned}$$

Each model has two transport equations, one for TKE (other than the Reynolds stress model which solves for the Reynolds stress, $\boldsymbol{\tau}$) and another for either ϵ or

ω. The values obtained from solving these equations are then used to compute the eddy viscosity. For the models which do not solve an equation for $\boldsymbol{\tau}$, the eddy viscosity is used to model the Reynolds stress through the relationship

$$\boldsymbol{\tau} = \frac{2}{3}k\mathbf{I} - 2\nu_t\mathbf{S}, \tag{6}$$

where $\mathbf{S}$ is the mean rate of strain of the flow defined as

$$\mathbf{S} = \frac{1}{2}(\nabla\mathbf{u} + \nabla\mathbf{u}^T). \tag{7}$$

It is worth noting that all of the incompressible solvers implemented in OpenFOAM, including those for multiphase flows, do not include density explicitly but instead model the kinematic eddy viscosity, ν_t rather than the dynamic form, μ_t. However, Brown et al. (2014) have shown that for simulations of breaking waves using the VOF method, more accurate results are obtained by including the density explicitly in the turbulence transport equations and therefore in this work a new library of turbulence models, within the OpenFOAM environment, has been developed to reflect this.

3.2.1. The $k-\omega$ model

The $k-\omega$ model originally developed by Wilcox (1988), solves the following transport equations for k and ω,

$$\frac{\partial\rho k}{\partial t} + \nabla\cdot(\rho\mathbf{u}k) = P_k - \rho C_\mu\omega k + \nabla\cdot[\rho(\nu+\sigma_k\nu_t)\nabla k], \tag{8}$$

$$\frac{\partial\rho\omega}{\partial t} + \nabla\cdot(\rho\mathbf{u}\omega) = \frac{\gamma\omega}{k}P_k - \rho\beta\omega^2 + \nabla\cdot[\rho(\nu+\sigma_\omega\nu_t)\nabla\omega], \tag{9}$$

with $\sigma_k = \sigma_\omega = 0.5$, $C_\mu = 0.09$, $\beta = 0.072$ and $\gamma = 0.52$. The production term is defined as $P_k = \rho\nu_t|S|^2$, defining S, in terms of $\mathbf{S}$, as $S = \sqrt{2\mathbf{S}:\mathbf{S}}$, where $:$ is the double inner product. The values of k and ω are obtained by solving equations (8) and (9), and are then used to compute the eddy viscosity, $\nu_t = k/\omega$.

3.2.2. The $k-\omega$ SST model

Menter (1994) originally developed the $k-\omega$ SST model, which solves the equations

$$\frac{\partial\rho k}{\partial t} + \nabla\cdot(\rho\mathbf{u}k) = \min\left(P_k, \rho c_1 C_\mu k\omega\right) - \rho C_\mu\omega k + \nabla\cdot[\rho(\nu+\sigma_k\nu_t)\nabla k], \tag{10}$$

$$\frac{\partial\rho\omega}{\partial t} + \nabla\cdot(\rho\mathbf{u}\omega) = \frac{\gamma P_k}{\nu_t} - \rho\beta\omega^2 + \nabla\cdot[\rho(\nu+\sigma_\omega\nu_t)\nabla\omega] + 2\rho(1-F_1)\frac{\sigma_{\omega 2}}{\omega}\nabla k\cdot\nabla\omega, \tag{11}$$

where P_k is the same as in the $k-\omega$ model. The coefficients σ_k, σ_ω, β and γ are a blend of an inner constant (subscript 1) and an outer constant (subscript 2), blended according to

$$\phi = F_1\phi_1 + (1-F_1)\phi_2. \tag{12}$$

The function $F_1 = \tanh(\Gamma_1^4)$ used in the blending function, depends upon the argument Γ_1 described by

$$\Gamma_1 = \min\left(\min\left(\left[\max\left\{\frac{k}{C_\mu\omega\Delta z_w}, \frac{500\nu}{\Delta z_w^2\omega}\right\}\right], \frac{4\sigma_{\omega 2}k}{CD_{k\omega}\Delta z_w^2}\right), 10\right), \tag{13}$$

where

$$CD_{k\omega} = \max\left\{\frac{2\sigma_{\omega 2}}{\omega}\nabla k\cdot\nabla\omega, 10^{-10}\right\}, \tag{14}$$

and Δz_w is the distance from the field point to the nearest wall. The values for the inner and outer constants are given in Table 1. The eddy viscosity is then calculated by

$$\nu_t = \frac{a_1 k}{\max\{a_1\omega, b_1 F_2\sqrt{2}S\}}, \tag{15}$$

where

$$F_2 = \tanh(\Gamma_2^2), \qquad \Gamma_2 = \min\left(\max\left\{\frac{2\sqrt{k}}{\omega\Delta z_w}, \frac{500\nu}{\Delta z_w^2\omega}\right\}, 100\right). \tag{16}$$

σ_{k1}	σ_{k2}	$\sigma_{\omega 1}$	$\sigma_{\omega 2}$	β_1	β_2	γ_1	γ_2
0.85034	1.0	0.5	0.85616	0.075	0.0828	0.5532	0.4403

Table 1: Default values for the inner and outer constants in the $k-\omega$ SST model.

3.2.3. The RNG $k-\epsilon$ model

The Renormalised group (RNG) $k-\epsilon$ model solves two equations for k and ϵ defined as

$$\frac{\partial\rho k}{\partial t} + \nabla\cdot(\rho\mathbf{u}k) = P_k - \rho\epsilon + \nabla\cdot[\rho(\nu+\sigma_k\nu_t)\nabla k], \tag{17}$$

$$\frac{\partial\rho\epsilon}{\partial t} + \nabla\cdot(\rho\mathbf{u}\epsilon) = \frac{C_{1\epsilon}^* P_k\epsilon}{k} - \frac{\rho C_{2\epsilon}\epsilon^2}{k} + \nabla\cdot[\rho(\nu+\sigma_\epsilon\nu_t)\nabla\epsilon]. \tag{18}$$

The coefficient $C_{1\epsilon}^*$ differs between the standard $k-\epsilon$ and RNG $k-\epsilon$ models (Speziale and Thangam, 1992). In the former it is just $C_{1\epsilon}$ and in the latter is derived as

$$C_{1\epsilon}^* = C_{1\epsilon} - \frac{\eta(1-\eta/\eta_0)}{1+\beta\eta^3}. \tag{19}$$

In equation (19), η is the additional expansion parameter used in the derivation by Yakhot et al. (1992), defined as the time scale ratio of the turbulent to the mean strain rate, $\eta = Sk/\epsilon$. The eddy viscosity is computed by

$$\nu_t = C_\mu\frac{k^2}{\epsilon}. \tag{20}$$

All of the model coefficients, except β which is obtained through experiments, are obtained through the derivation of the RNG $k-\epsilon$ model and are set to $C_\mu = 0.0845$, $\sigma_k = \sigma_\epsilon = 1.39$, $C_{1\epsilon} = 1.42$, $C_{2\epsilon} = 1.68$, $\eta_0 = 4.38$ and $\beta = 0.012$.

3.2.4. Nonlinear $k-\epsilon$ model

Nonlinear (NL) $k-\epsilon$ models are an alternative to Reynolds stress closure models. In this work, a model developed by Shih et al. (1996) is used, which relates the mean strain rate of the flow to the Reynolds stress tensor through the algebraic nonlinear Reynolds stress model. The model adjusts the Reynolds stress, $\boldsymbol{\tau}$, by adding a nonlinear stress term $\boldsymbol{\tau_{NL}}$, defined as

$$\boldsymbol{\tau_{NL}} = \frac{1}{2}(\boldsymbol{\chi} + \boldsymbol{\chi}^T), \tag{21}$$

$$\boldsymbol{\chi} = \frac{k^3}{(A_2+\eta^3)\epsilon^2}\left(C_{\tau 1}[\nabla\mathbf{u}\cdot\nabla\mathbf{u}+(\nabla\mathbf{u}\cdot\nabla\mathbf{u})^T]+C_{\tau 2}[\nabla\mathbf{u}\cdot(\nabla\mathbf{u})^T]+C_{\tau 3}[(\nabla\mathbf{u})^T\cdot\nabla\mathbf{u}]\right), \tag{22}$$

where $C_{\tau 1}$, $C_{\tau 2}$, $C_{\tau 3}$ and A_2 are constants. The parameter η is defined the same as in the RNG $k-\epsilon$ model, with k and ϵ being calculated using equations (17) and (18), with different values for the coefficients ($C^*_{1\epsilon} = 1.44$, $C_{2\epsilon} = 1.92$, $\sigma_\epsilon = 0.77$, $\sigma_k = 1$). The nonlinear stress term is also used in the production term, P_k, which is defined as

$$P_k = \rho(\nu_t \mathbf{S}{:}\nabla\mathbf{u} - \boldsymbol{\tau_{NL}}{:}\nabla\mathbf{u}). \tag{23}$$

The eddy viscosity is obtained through the same relationship as in the RNG $k-\epsilon$ (equation 20) except that the value of C_μ depends upon the values of ξ and η,

$$C_\mu = \frac{2}{3(A_1+\eta+\alpha_\xi\xi)}, \tag{24}$$

where α_ξ and A_1 are constants and $\xi = \Omega k/\epsilon$ is an additional parameter, where Ω, defined in terms of the mean rate of rotation, $\boldsymbol{\Omega}$, is

$$\Omega = \sqrt{2\boldsymbol{\Omega}{:}\boldsymbol{\Omega}}, \qquad \boldsymbol{\Omega} = \frac{1}{2}\left(\nabla\mathbf{u} - (\nabla\mathbf{u})^T\right), \tag{25}$$

Using the eddy viscosity, the Reynolds Stress, $\boldsymbol{\tau}$, is calculated through the relationship

$$\boldsymbol{\tau} = \frac{2}{3}k\mathbf{I} - \nu_t(\nabla\mathbf{u} + \nabla\mathbf{u}^T) + \boldsymbol{\tau_{NL}}. \tag{26}$$

3.2.5. Reynolds Stress Model

Reynolds stress models (RSM) solve equations for ϵ and all six components of the Reynolds Stress ($\boldsymbol{\tau}$). In this work, a RSM based on the work of Launder

et al. (1975) is applied. All the components of $\boldsymbol{\tau}$ are solved in a single transport equation

$$\frac{\partial \rho \boldsymbol{\tau}}{\partial t} + \nabla \cdot (\rho \mathbf{u} \boldsymbol{\tau}) = \rho(1 - C_{2\tau})\mathbf{P} + \frac{\rho}{3} C_{2\tau} \mathrm{tr}(\mathbf{P})\mathbf{I} - \frac{2\rho}{3}(1 - C_{1\tau})\epsilon \mathbf{I} - \rho C_{1\tau} \frac{\epsilon}{k} \boldsymbol{\tau} + \nabla \cdot [\rho(\nu + \nu_t)\nabla \boldsymbol{\tau}], \tag{27}$$

where $C_{1\tau} = 1.8$, $C_{2\tau} = 0.6$, $\mathbf{I}$ is the identity matrix and $\mathrm{tr}(\mathbf{P})$ represents the trace of matrix $\mathbf{P}$, defined as

$$\mathbf{P} = -\left[\boldsymbol{\tau} \cdot \nabla \mathbf{u} + (\boldsymbol{\tau} \cdot \nabla \mathbf{u})^T \right]. \tag{28}$$

The equation for ϵ is same as the nonlinear $k - \epsilon$ (equation 17) with coefficient values of $C^*_{1\epsilon} = 1.44$, $C_{2\epsilon} = 1.92$, $\sigma_\epsilon = 0.77$, $\sigma_k = 1$) except that the production term is defined as $P_k = 0.5|\mathrm{tr}(\mathbf{P})|$.

TKE is defined as $k = 0.5(u'^2_x + u'^2_y + u'^2_z)$, and can therefore be calculated in this model by taking half the trace of the Reynolds stress, i.e. $k = 0.5tr(\boldsymbol{\tau})$. The eddy viscosity can then be calculated through the same relationship as in the RNG $k - \epsilon$ model (equation 20).

4. Evaluation of Turbulence Models

4.1. Spilling Breakers

Tests are first performed for the spilling breakers case. Comparisons between the model predictions and observations by Ting and Kirby (1994), under the same wave conditions, for the maximum, mean and minimum surface elevation (Figure 2), for the time averaged velocity (Figure 5), and for mean turbulent kinetic energy profiles (Figure 6), are presented.

Figure 2 shows the phase averaged surface elevations $\eta_{max} - \overline{\eta}$, $\overline{\eta}$ and $\eta_{min} - \overline{\eta}$ for the spilling breakers case as a function of horizontal distance, x, along the numerical wave flume. Here η_{max} and η_{min} are the maximum and minimum phase averaged surface elevation and $\overline{\eta}$ is the mean surface elevation. Furthermore, the shaded regions around the maximum and minimum profiles in the figure represent one standard deviation. Each subplot compares a different turbulence closure model to the experimental data (dots) gathered by Ting and Kirby (1994), a) No turbulence model, b) $k - \omega$, c) $k - \omega$ SST, d) RNG $k - \epsilon$, e) nonlinear $k - \epsilon$ and f) RSM. The overall root mean square error (RMSE) for each turbulence model, combining the results for maximum, minimum and mean profiles, is indicated on each plot (denoted by E). The overall RMSE clearly indicates that the RNG and nonlinear $k - \epsilon$ models most accurately reproduce the phase averaged surface elevation out the models considered in this study. If each of the three profiles are considered individually, visual observations and RMSE (for each profile rather than the combined value stated in Figure 2) imply that the RSM captures the minimum and mean profiles the

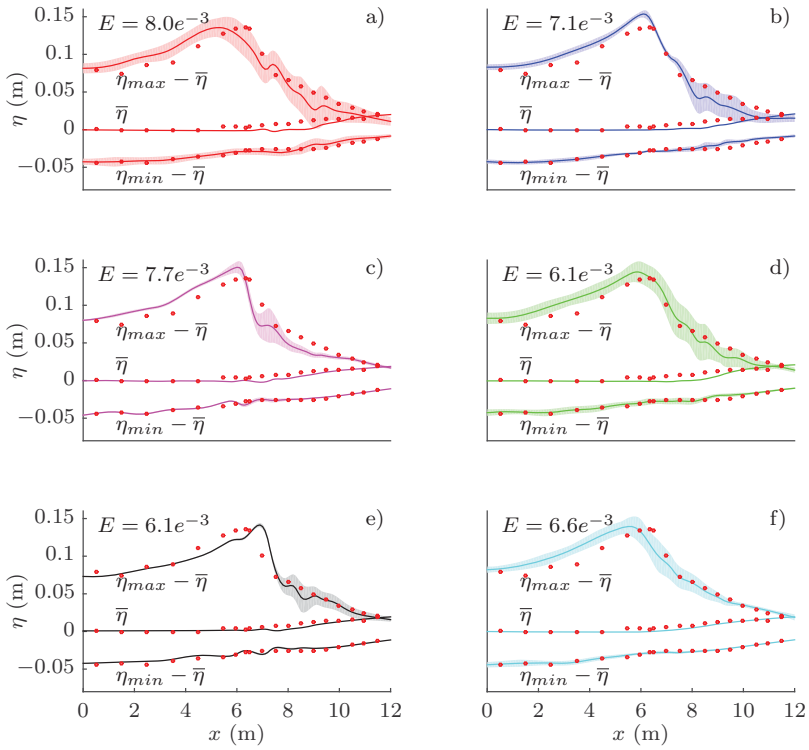

Figure 2: Comparison of surface elevation profiles $\overline{\eta}$, $\eta_{max} - \overline{\eta}$ and $\eta_{min} - \overline{\eta}$ for the spilling breakers. Each subplot represents a different model: a) No Turbulence Model, b) $k - \omega$, c) $k - \omega$ SST, d) RNG $k - \epsilon$, e) NL $k - \epsilon$, f) RSM, with an overall RMSE value, E (representing the maximum, minimum and mean profiles combined), given with respect to the laboratory data gathered by Ting and Kirby (1994), indicated by the dots. One standard deviation either side of the maximum and minimum surface elevations is indicated by the shaded area.

best, although the other models do perform reasonably well with respect to the experimental data. All of the turbulence models capture the wave setup more accurately than when there is no turbulence model used (subplot a), although in general, the wave setup is predicted to occur slightly further along the flume than was shown in the laboratory data. Furthermore, the shaded region shows a much larger variation in maximum and minimum profiles when no turbulence is assumed, suggesting that the waves are more repeatable when a turbulence model is used.

When considering the maximum profiles, there are more obvious differences between the turbulence models. The RNG $k - \epsilon$ model follows the experimental data the closest and has the lowest RMSE for the maximum profile. The $k - \omega$ and $k - \omega$ SST turbulence models all significantly over-estimate the maximum

surface elevation prior to breaking but do predict the breaking point, x_b, at a similar location in the flume as shown in the experiments. The nonlinear $k-\epsilon$ model also over-estimates the breaking height but is the only model to predict the breaking point later than shown in the laboratory. The remaining models all break at a similar height to the experimental data but the breaking point is slightly earlier in the numerical wave flume than expected. Interestingly, the RSM, which solves for all the components of the Reynolds Stress and therefore was expected to be the most accurate model, breaks the earliest of all the turbulence models (but still later than when there is no turbulence model used), 0.8 m earlier than the experimental data. However, it does capture the breaking height well and is the turbulence model which follows the experimental data most accurately in the turbulent bore.

Comparing the shaded profiles before breaking, it is clear that the nonlinear $k-\epsilon$ model and $k-\omega$ SST models have very small variation in both minimum and maximum surface elevation, indicating that every wave is almost identical in terms of wave height. On the other hand, the RSM and RNG $k-\epsilon$ model have reasonable variation prior to breaking, implying that each wave is a slightly different shape. The RNG $k-\epsilon$ model appears to follow the no turbulence model case particularly closely in terms of shape and variation in wave shape at the different regions of the wave flume. It is also interesting to note that the upper envelope of the maximum profile generally captures the profile well after breaking, whereas the mean value under-estimates the shape shown in the physical experiments. As is to be expected, all of the models have a much larger variation after breaking has occurred. This represents that the wave shape is more repeatable, i.e. each wave has a similar shape, before breaking and the waves are less predictable after breaking, which is expected due to the chaotic nature of broken waves.

Figures 3 and 4 emphasise the previously mentioned repeatability of waves prior to breaking and the lack of predictability post-breaking. They show the phase average surface elevation for spilling breakers overlaying the twenty waves used to create the phase average, for the RNG $k-\epsilon$ and nonlinear $k-\epsilon$ models, respectively. The top plot represents the constant depth profile ($x = -1.265$ m) and the bottom post-breaking, in the region with the largest variation ($x = 8.495$ m), as can be seen in Figure 2. Comparing the constant depth profiles, it is clear that every wave has an almost identical wave shape, as is to be expected, when the nonlinear $k-\epsilon$ model is used. On the other hand, for the RNG $k-\epsilon$ model, the twenty waves vary significantly in shape from the phase average profile as was implied in Figure 2. This explains the large variation, relative to the nonlinear $k-\epsilon$ model, in the pre-breaking profile obtained with the RNG $k-\epsilon$. Furthermore, the post-breaking profiles show why there is much larger variation in Figure 2 further down the wave flume. Both turbulence models have large variations in shape, especially in terms of maximum height compared to the phase averaged surface elevation.

Overall, the best models, only taking into account the RMSE, are the nonlinear $k-\epsilon$ and RNG $k-\epsilon$ models. However, the RSM could be considered the best model since it captures the wave setup, as well as the minimum pro-

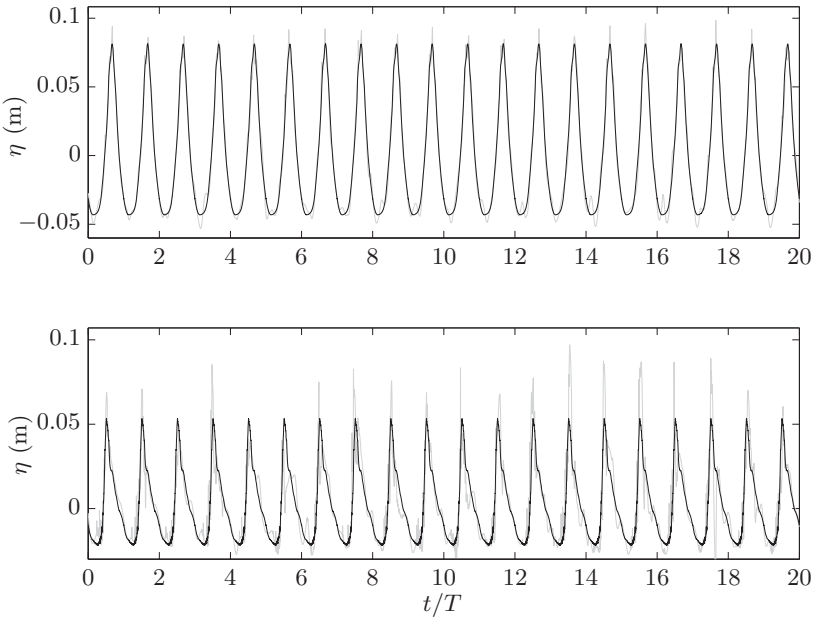

Figure 3: Phase averaged surface elevation (black) overlaying the time series for the twenty waves used to create it (grey) for the spilling breakers case. Both the constant depth region at $x = -1.265\,\mathrm{m}$ (top) and after breaking at $x = 8.495\,\mathrm{m}$ (bottom) for the RNG $k - \epsilon$ model are shown.

file most accurately with respect to the physical experiments. It also captures the maximum profile breaking height and the turbulent bore region well, but the pre-breaking profile is much less accurate than other models. The breaking points of each of the models have been summarised in Table 2, along with the water depths and wave height at breaking.

Figure 5 shows the mean horizontal velocity, $\overline{u}$ ($\mathrm{m\,s^{-1}}$), profiles with dimensionless depth, $(z - \overline{\eta})/h$, for the spilling breakers case. As before the dots represent the experimental data presented by Ting and Kirby (1994). Each row of subplots shows a different sampling location relative to the breaking point, location a is prior to the breaking point (5.945 m in Ting and Kirby (1994)), and locations b-g are post-breaking (6.665, 7.275, 7.885, 8.495, 9.11 and 9.725 m in Ting and Kirby (1994)). Each column of subplots represents a different turbulence closure model, with the no turbulence model case also shown for reference. As a measure of accuracy with respect to the experimental data, the RMSE value (denoted by E) is indicated for each profile at the top of that individual plot. The laboratory data suggests that the mean velocity is negative throughout the majority of the water column with a relatively small region of positive velocity near the free surface. All of the turbulence models capture this change between positive and negative mean velocity, with good agreement in comparison to the

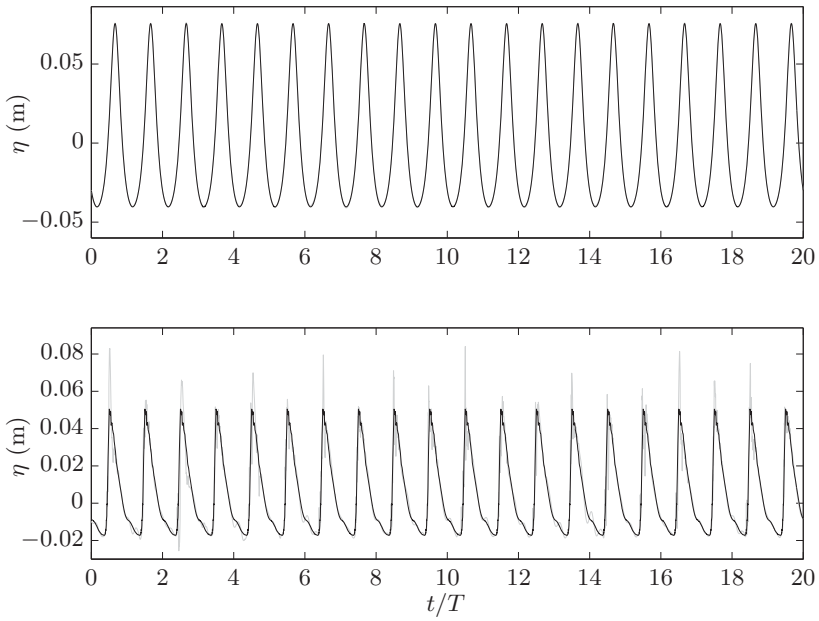

Figure 4: Phase averaged surface elevation (black) overlaying the time series for the twenty waves used to create it (grey) for the spilling breakers case. Both the constant depth region at $x = -1.265\,\mathrm{m}$ (top) and after breaking at $x = 8.495\,\mathrm{m}$ (bottom) for the nonlinear $k - \epsilon$ model are shown.

experimental data.

Another trend in the laboratory data presented by Ting and Kirby (1994) is that the gradient of mean horizontal velocity profile changes sign after breaking has occurred. Around the breaking point (locations a and b), the gradient is negative; the mean velocity is very small near the bottom of the water column, and grows in magnitude closer to the free surface. Further along the wave flume (locations d,e,f and g), a large undertow is present, leading to a positive velocity gradient.

Qualitatively, there is only one turbulence model, the RNG $k - \epsilon$, which captures the negative gradient profile accurately. However, the model does not have the lowest RMSE due to the poor prediction seen in the profile near the top of the water column. Instead the nonlinear $k - \epsilon$ has the lowest RMSE despite not predicting the velocity profile near the bottom of the water column correctly. It is interesting to note that when no turbulence is assumed, the negative gradient is also captured at location a but once breaking occurs there is a significant variation from the experimental data (location b). The remaining models predict similar magnitudes of velocity over the whole water column and therefore perform well closer to the free surface and reduce in accuracy near the bottom.

	No TM	$k-\omega$	$k-\omega$ SST	RNG $k-\epsilon$	NL $k-\epsilon$	RSM	Ting (1994)
x_b	5.3	6.1	6.0	5.9	6.9	5.6	6.4
d_b	0.2286	0.2057	0.2086	0.2114	0.1829	0.2200	0.196
ξ_b	-0.0013	-0.0004	-0.0009	-0.0010	0.0028	-0.0009	0.0033
h_b	0.2273	0.2052	0.2077	0.2105	0.1856	0.2191	0.1993
H_b	0.1679	0.1833	0.1797	0.1744	0.1717	0.1703	0.1621

Table 2: Summary of the spilling breakers information at the breaking point for each turbulence model. x_b is the breaking point, d_b, h_b are the depth from the SWL ($z = 0\,\mathrm{m}$) and MWL ($z = \xi_b\,\mathrm{m}$), respectively, and H_b is the wave height at breaking.

Location c appears to be the transition between the two profile shapes, i.e. where the gradient of the profile changes sign and the mean velocity is almost constant with depth. The turbulence models give very different predictions for this profile, with the RSM and nonlinear $k-\epsilon$ model capturing the shape very well; they appear to keep a similar profile to that predicted at locations a and b where the velocity is almost constant over the depth. The RNG $k-\epsilon$ model still predicts the profile shape required at locations a and b, whereas the remaining turbulence models exhibit a shape closer to the positive velocity gradient found at locations d-g in the experiments. This could suggest that the profile gradient changes sign too late for the RNG $k-\epsilon$ model and too early for the $k-\omega$ and $k-\omega$ SST models.

At location d, all of the turbulence models follow a similar shape to the experimental data although the $k-\omega$ and $k-\omega$ SST models both over-predict the magnitude of the undertow. The RMSE values show that the nonlinear $k-\epsilon$ and RSM models perform the best, with the no turbulence model case performing very poorly. This pattern generally continues throughout the remaining sampling locations (e-g) except that like the $k-\omega$ models, the RNG $k-\epsilon$ model also over-estimates the velocity profile near the bottom significantly.

Although the RNG $k-\epsilon$ model performs best near the breaking point, the nonlinear $k-\epsilon$ gives the best results overall, implying that it could be important to assume anisotropic turbulence, which is further backed up by the RSM being the second best model for mean horizontal velocity profiles.

Figure 6 shows the time averaged TKE, $\overline{k}$ ($\mathrm{m^2\,s^{-2}}$), profiles with dimensionless depth for the spilling breakers case. Once again, the dots represent the experimental data collected by Ting and Kirby (1994) and the lines indicate the predictions by each of the turbulence models. Each subplot represents a different sampling location relative to the breaking point. Locations a and b are near the breaking point (5.945 and 6.665 m in Ting and Kirby (1994)), whereas the remaining sampling points are placed after breaking has occurred and correspond to locations 7.275, 7.885, 8.495, 9.11 and 9.725 m in Ting and Kirby (1994). However, Ting and Kirby (1994) only provided TKE results for the post-breaking locations, presumably because there was no turbulence prior to breaking. As can be seen in plots a and b, the RNG $k-\epsilon$ model predicts very little TKE across the whole water column, whereas every other model predicts

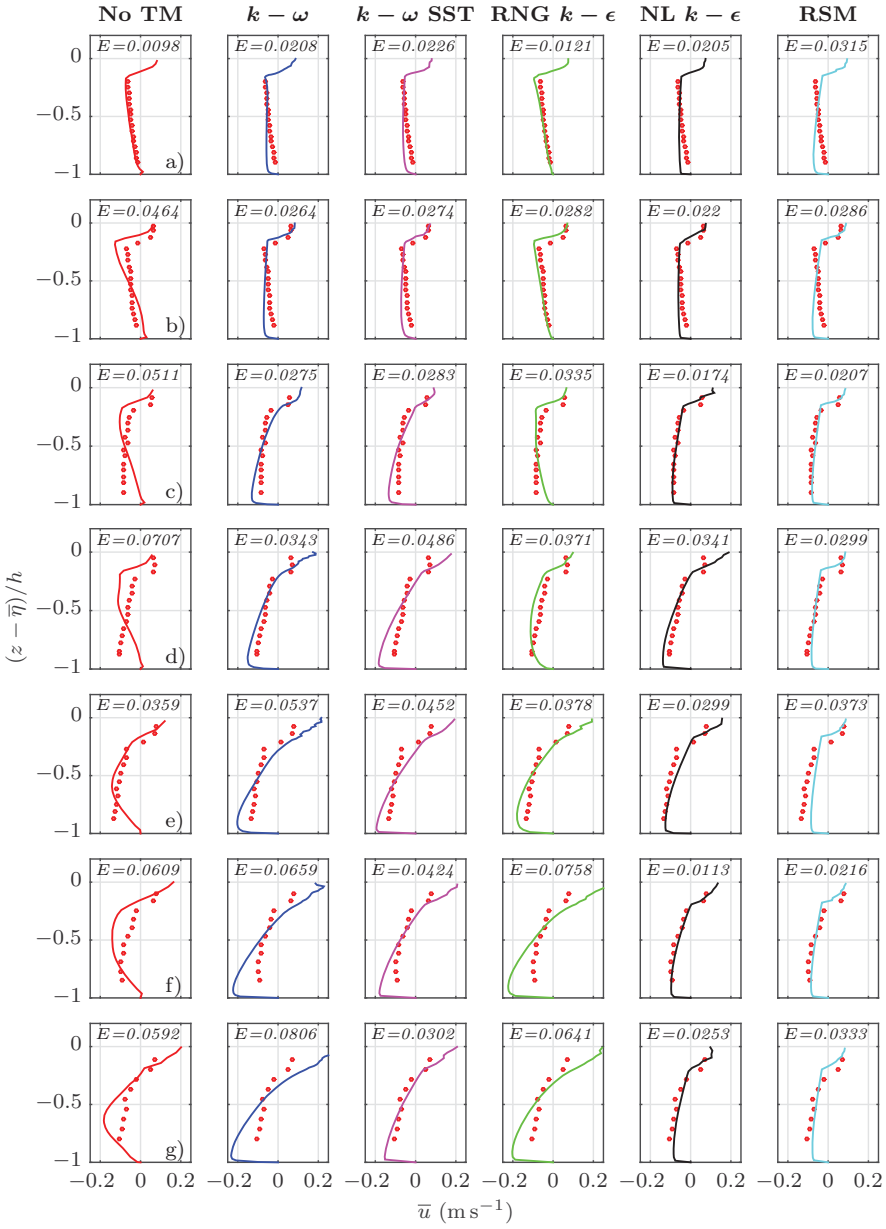

Figure 5: Comparison of time averaged velocity profiles with depth for the spilling breakers against the experimental data (dots) reported by Ting and Kirby (1994). The RMSE for each profile with respect to the experiments is indicated at the top of each plot (denoted by E). Each column represents a different turbulence model whereas the rows represent different sampling locations relative to the breaking point $x - x_b$ = a) -0.455, b) 0.265, c) 0.875, d) 1.485, e) 2.095, f) 2.71 and g) 3.325 m.

$x - x_b$ (m)	$k - \omega$	$k - \omega$ SST	RNG $k - \epsilon$	NL $k - \epsilon$	RSM
0.875	0.0035	0.0021	0.0021	0.0036	0.0096
1.485	0.0025	0.0045	0.0048	0.0047	0.0076
2.095	0.0005	0.0080	0.0009	0.0061	0.0117
2.71	0.0013	0.0060	0.0064	0.0018	0.0129
3.325	0.0026	0.0046	0.0119	0.0003	0.0099

Table 3: Root mean squared error associated with the TKE predictions for spilling breakers, with respect to the experimental data gathered by Ting and Kirby (1994). All of the different turbulence model predictions at the five locations where data is available are presented and correspond to plots c-g in Figure 6.

levels similar to after breaking has occurred. Since this occurs at the locations where the RNG $k - \epsilon$ model was the only one to capture the velocity profile, this could imply that there is a correlation between models which predict very small levels of TKE prior to breaking, and the negative gradient in the velocity profile exhibited by the unbroken wave. Furthermore, the experimental profile at location a was captured when no turbulence was assumed, which backs up the hypothesis that a turbulence model must be able to predict low levels of TKE prior to breaking.

For the five remaining sampling locations, where experimental data is available, the RMSE has been calculated for each turbulence model and is recorded in Table 3. Together with Figure 6, it is clear that all of the models generally over-estimate the levels of TKE. However, the $k - \omega$ model performs well and is the most accurate of the models overall. The $k - \omega$ SST model obtains good accuracy at the sampling locations closer to the breaking point (subplots c and d) but progressively over-estimates the magnitude further down the flume. The RNG $k - \epsilon$ model follows a similar pattern, it begins by under-estimating the TKE in subplots c and d and then over-estimates in subplots f and g. Finally, the nonlinear $k - \epsilon$ model gives similar results to the $k - \omega$ model, except at locations d and e where it significantly over-predicts the magnitude of the TKE. Interestingly, the RSM, which was expected to be the most accurate significantly over-estimates the TKE everywhere that has been sampled, leading to much larger RMSE values than the other models, despite giving reasonable results for both surface elevation and undertow.

In summary, for the spilling breakers, the different models which have been evaluated vary in performance over the three criteria considered. The RSM performed well on both surface elevation and velocity but significantly over-estimates levels of TKE. On the other hand, the $k - \omega$ model performs well for TKE and surface elevation but over-estimates the magnitude of the undertow. Overall, the most consistent model is the nonlinear $k - \epsilon$, which performs reasonably well for all three criteria.

4.2. Plunging Breakers

Tests are now performed for the plunging breakers case. Comparisons between the model predictions and observations by Ting and Kirby (1994), under

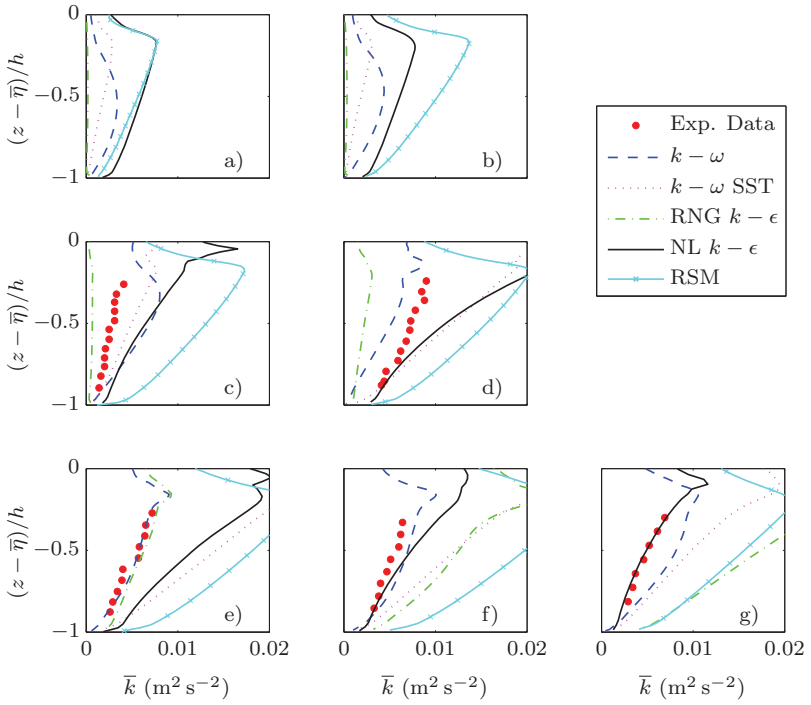

Figure 6: Comparison of time averaged TKE profiles with depth for the spilling breakers at sampling locations relative to the breaking point $x - x_b$ = a) -0.455, b) 0.265, c) 0.875, d) 1.485, e) 2.095, f) 2.71 and g) 3.325 m. Each line represents a different turbulence closure model and the dots represent the experimental data gathered by Ting and Kirby (1994).

the same wave conditions, for the maximum, mean and minimum surface elevation (Figure 7), for the time averaged velocity (Figure 8), and for mean turbulent kinetic energy profiles (Figure 9), are presented.

Figure 7 shows the same surface elevation profiles presented in Figure 2, except for the plunging breaker results. Again, each subplot compares a different turbulence closure model, a) No turbulence model, b) $k-\omega$, c) $k-\omega$ SST, d) RNG $k-\epsilon$, e) nonlinear $k-\epsilon$ and f) RSM, to the experimental data (dots) gathered by Ting and Kirby (1994) with the overall RMSE (for minimum, mean and maximum profiles combined) indicated by E in each plot. The results for the minimum and mean surface elevation profiles follow a similar pattern to the spilling breakers case. There is not much to choose between the different turbulence models since they all predict the minimum surface elevation accurately, although, there is significantly more variation in the no turbulence model and RNG $k-\epsilon$ model cases, suggesting that the waves are less repeatable, which was also observed in the spilling breakers. The $\overline{\eta}$ profile implies that the wave setup occurs at a similar rate as shown in the experimental data and is therefore

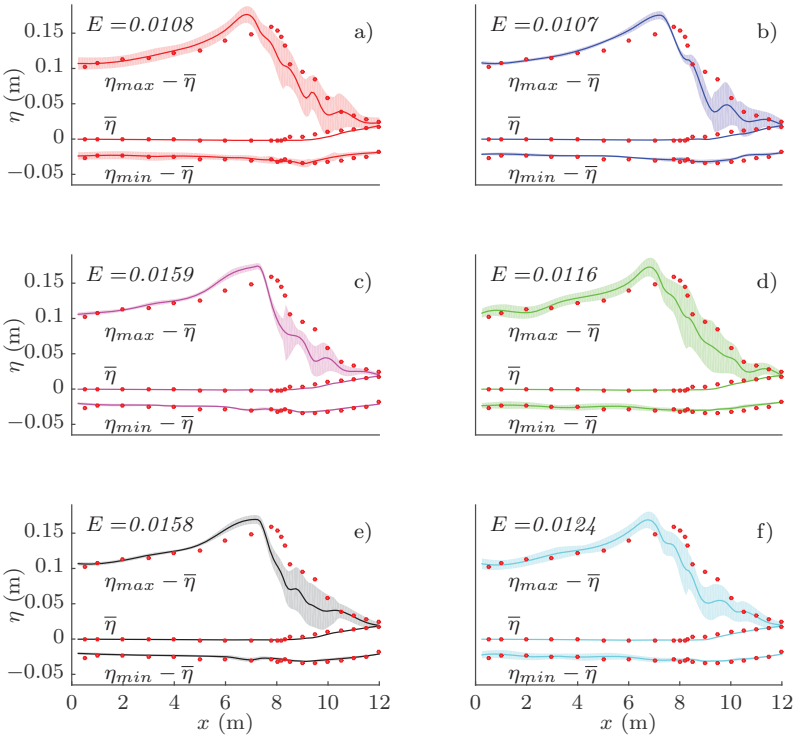

Figure 7: Comparison of surface elevation profiles $\overline{\eta}$, $\eta_{max} - \overline{\eta}$ and $\eta_{min} - \overline{\eta}$ for the plunging breakers. Each subplot represents a different model: a) No Turbulence Model, b) $k - \omega$, c) $k - \omega$ SST, d) RNG $k - \epsilon$, e) NL $k - \epsilon$, f) RSM, with an overall RMSE value, E (representing the maximum, minimum and mean profiles combined), given with respect to the laboratory data collected by Ting and Kirby (1994), indicated by the dots. One standard deviation either side of the maximum and minimum surface elevations is indicated by the shaded area.

slightly more accurate than was seen in the spilling breakers. It seems that once again, the wave setup is more accurately captured when a turbulence model is used since it occurs further down the wave flume than shown in the laboratory data when a dummy turbulence model is used.

When the maximum surface elevation profile is considered it is clear that there is much less variation between the different models than was seen in the spilling breakers (see Figure 2). This is reflected in the RMSE values, which are all very similar. All of the models shown, including the zero turbulence case, predict the waves to break a little earlier in the wave flume than was shown in the experimental data, as well as over-estimating the breaking height. Once again the RNG $k - \epsilon$ model seems to follow the profile shape and variation when no turbulence model is used, especially prior to breaking. Although there

	No TM	$k-\omega$	$k-\omega$ SST	RNG $k-\epsilon$	NL $k-\epsilon$	RSM	Ting (1994)
x_b	6.85	7.25	7.25	6.85	7.15	6.75	7.795
d_b	0.1843	0.1729	0.1729	0.1843	0.1757	0.1871	0.1573
ξ_b	-0.0018	-0.0013	-0.0013	-0.0016	-0.0011	-0.0015	-0.0022
h_b	0.1825	0.1715	0.1716	0.1827	0.1746	0.1856	0.1550
H_b	0.2040	0.2042	0.2031	0.2007	0.1976	0.1973	0.1887

Table 4: Summary of the plunging breakers information at the breaking point for each turbulence model. x_b is the breaking point, d_b, h_b are the depth from the SWL ($z = 0\,\mathrm{m}$) and MWL ($z = \xi_b\,\mathrm{m}$), respectively, and H_b is the wave height at breaking.

is not much to choose between the models in terms of profile shape, there are large differences in the variation of the maximum and minimum profiles, which follows the observations made in the spilling breakers. All of the models have smaller variation before breaking, with a much larger variation in wave shape occurring further down the tank (between 8 and 10 m). As previously discussed (see Figures 3 and 4 for the time series for spilling breakers) this pattern implies that the waves are much more repeatable before breaking than after, as is to be expected. Out of all the models, the RNG $k-\epsilon$ model appears to have a slightly larger standard deviation prior to breaking, suggesting a variation in wave shape even when the wave has not broken. The nonlinear $k-\epsilon$, $k-\omega$ and $k-\omega$ SST models have very small variation as the wave starts going up the slope, suggesting the waves are almost identical as would generally be expected. Interestingly, the upper envelope follows the turbulent bore region from the experiments for many of the turbulence models, especially the RNG $k-\epsilon$.

In summary there does not appear to be a model which captures the free surface of plunging breakers significantly better than the others, although the variation before breaking suggests that the waves are much more repeatable in the $k-\omega$, $k-\omega$ SST and nonlinear $k-\epsilon$ models.

Figure 8 shows the same mean horizontal velocity, $\overline{u}$, presented in Figure 5, except for the results of the plunging breakers. Each row of subplots indicates a different sampling location relative to the breaking point; location a is prior to the breaking point (7.295 m in Ting and Kirby (1994)), location b is at the breaking point (7.795 m in Ting and Kirby (1994))and locations c-g are post-breaking (8.345, 8.795, 9.295, 9.795 and 10.395 m in Ting and Kirby (1994)). Similar to the spilling breaker experimental results, the mean horizontal velocity is negative over the majority of water column at all sampling locations, with a relatively small region of positive mean velocity near the free surface. Again, all of the turbulence models capture this characteristic, with particularly good results at locations a-c.

The laboratory data implies that the gradient of the horizontal velocity profile with depth is negative at locations a-c, similar to the profile seen in the spilling breakers case. This negative gradient is not captured particularly well by any of the turbulence models at location a, since all of the models over-estimate the magnitude of the velocity. All of the turbulence models have a very similar

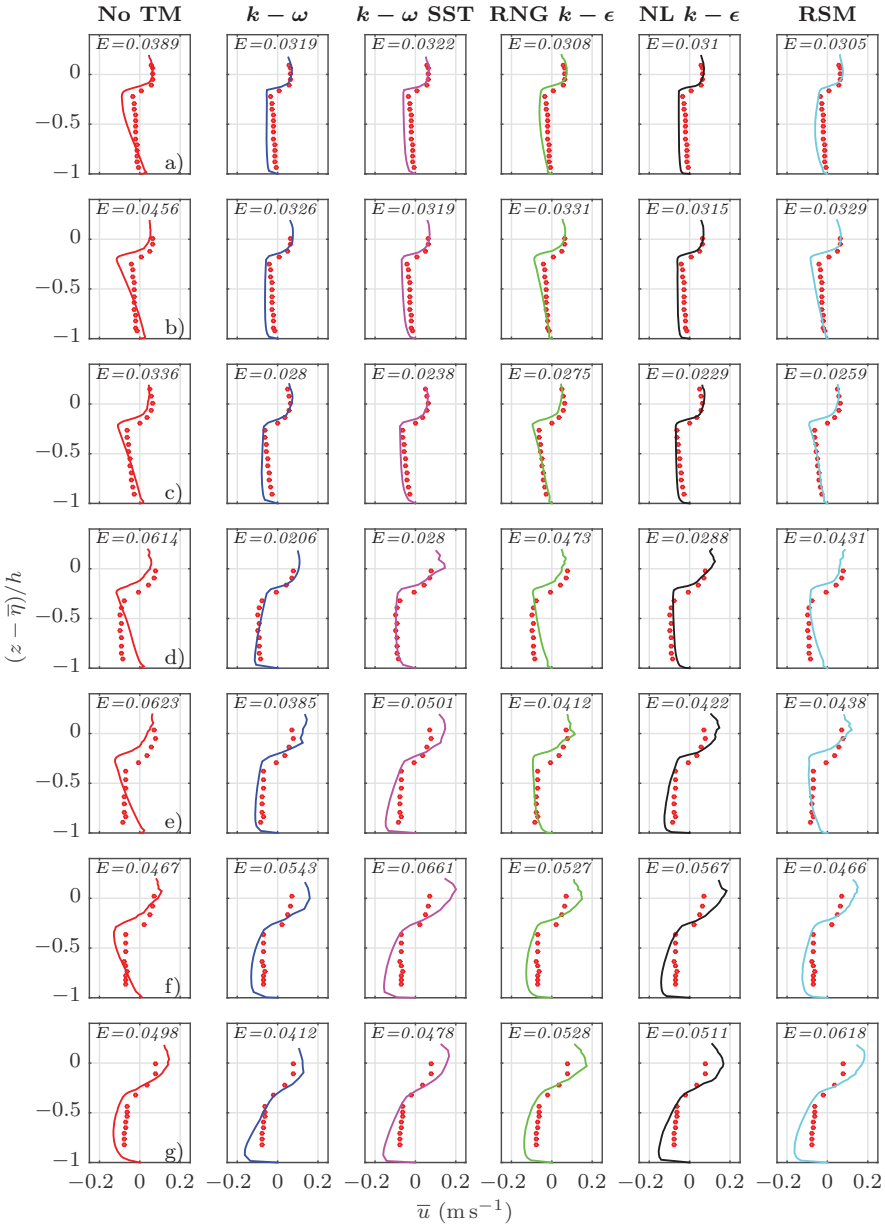

Figure 8: Comparison of time averaged velocity profiles with depth for the plunging breakers against the experimental data (dots) gathered by Ting and Kirby (1994). The RMSE for each profile with respect to the experiments is indicated at the top of each plot (denoted by E). Each column represents a different turbulence model whereas the rows represent different sampling locations relative to the breaking point $x - x_b$ = a) -0.5, b) 0.0, c) 0.55, d) 1.0, e) 1.5, f) 2.0 and g) 2.6 m.

RMSE value, but the no turbulence case performs slightly worse. However, at sampling locations b-c, the RSM and RNG $k-\epsilon$ predict a negative gradient shape, but the nonlinear $k-\epsilon$ and $k-\omega$ SST models possess the smallest RMSE. This is mainly due to the increased accuracy where the velocity changes sign near the free surface.

Contrary to the spilling breaker case, where the gradient changed sign further along the wave flume, the experimental data shows the magnitude of the mean velocity to become close to constant with depth (except near the free surface) in the plunging breaker. This is captured well at location d by the $k-\omega$, $k-\omega$ SST and nonlinear $k-\epsilon$ models. However, at locations e-f, all of these models predict a profile shape similar to that seen in the spilling breakers, i.e. the undertow is largest near the bottom of the water column and decreases with height. The RSM and RNG $k-\epsilon$ predict a similar profile shape at location d as they did for a-c and then develop much the same as the other models for the final three locations.

Overall, using the RMSE, the most accurate model for mean horizontal velocity under plunging breakers is the $k-\omega$ model, followed closely by the nonlinear $k-\epsilon$ model. The least accurate results occur when no turbulence is assumed. However, the current numerical model, in general, appears to predict the velocity profiles under spilling breakers to a greater accuracy than under plunging breakers.

Figure 9 shows the same time averaged TKE, $\overline{k}$, presented in Figure 6, except for the plunging breaker data. The subplots a-g represent the same seven locations presented in Figure 8. Furthermore, Table 5 gives the RMSE values for each of the five turbulence models, at the locations where experimental data is available. The laboratory data implies that the mean TKE has a much smaller change in depth in comparison to the spilling breakers (Figure 6), and is almost constant with depth at some of the sampling locations. None of the models capture this shape since they generally predict a significant decrease in the TKE with depth.

The RNG $k-\epsilon$ model and RSM predict very low levels of TKE at sampling locations a, b, c and d, which corresponds to the negative gradient of mean horizontal velocity with depth, observed in Figure 8. The other models have larger levels of TKE at these locations and do not capture the velocity profile. This further backs up the hypothesis from the spilling breakers that a model must predict low levels of turbulence in order to capture this profile shape.

Interestingly, the magnitude of the TKE is generally lower than observed in the spilling breakers case, and appears to increase along the wave flume at a similar rate to that shown in the experiments. The $k-\omega$ SST model performs well at location c but grows progressively larger down the flume as was seen in the spilling breakers. The nonlinear $k-\epsilon$ also follows this pattern but generally under-estimates the levels of TKE. However, it is the most consistent of the models at the sampling locations used. The remaining models generally under-predict the TKE which is reversed from the pattern seen in spilling breakers.

Overall, the nonlinear $k-\epsilon$ model predicts the TKE for plunging breakers the most accurately, followed by the $k-\omega$ model. On the other hand the

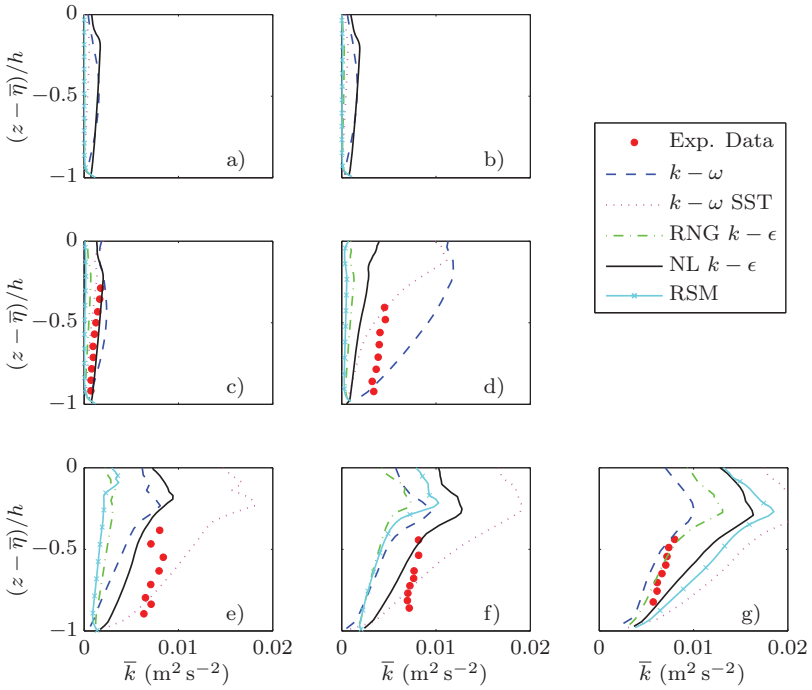

Figure 9: Comparison of time averaged TKE profiles with depth for the plunging breakers at sampling locations relative to the breaking point $x - x_b$ = a) -0.5, b) 0.0, c) 0.55, d) 1.0, e) 1.5, f) 2.0 and g) 2.6 m. Each line represents a different turbulence closure model and the dots represent the experimental data gathered by Ting and Kirby (1994).

RSM gives the least accurate results, which was also observed for the spilling breakers. However, the lack of accuracy is due to an under-estimate for the plunging breaker whereas in the spilling breaker there was a significant over-estimate.

4.3. Discussion

Choosing a numerical model is usually a balance of accuracy and numerical efficiency. In this section, both of these aspects are evaluated relative to assuming that there is no turbulence in the surf zone. Table 6 gives the execution times along with the number of iterations relative to when no turbulence is assumed. The results were obtained by running one wave period for each turbulence model on the same computer without any other applications running. The results imply that for both the plunging and spilling breakers the execution time is reduced, compared to assuming no turbulence, by using a turbulence model. This may seem counter intuitive since each iteration should take slightly longer to compute. However, as can be seen in the table, the use

$x - x_b$ (m)	$k-\omega$	$k-\omega$ SST	RNG $k-\epsilon$	NL $k-\epsilon$	RSM
0.55	0.0008	0.0005	0.0008	0.0003	0.0011
1.00	0.0034	0.0018	0.0032	0.0024	0.0036
1.50	0.0044	0.0026	0.0054	0.0028	0.0060
2.00	0.0041	0.0025	0.0044	0.0018	0.0043
2.60	0.0012	0.0064	0.0005	0.0030	0.0044

Table 5: Root mean squared error associated with the TKE predictions for plunging breakers, with respect to the experimental data gathered by Ting and Kirby (1994). All of the different turbulence model predictions at the five locations where data is available are presented and correspond to plots c-g in Figure 9.

		$k-\omega$	$k-\omega$ SST	RNG $k-\epsilon$	NL $k-\epsilon$	RSM
Spilling	CPU Time	0.978	0.802	0.828	0.673	0.641
	Iterations	0.835	0.733	0.732	0.568	0.483
	Time/Iter.	1.171	1.095	1.132	1.184	1.328
Plunging	CPU Time	0.941	0.707	0.865	0.748	0.861
	Iterations	0.794	0.646	0.743	0.633	0.667
	Time/Iter.	1.184	1.094	1.165	1.181	1.291

Table 6: Execution time, number of iterations and time per iteration for one wave period relative to the no turbulence model case.

of a turbulence model can significantly reduce the number of iterations, which can be over half as many in some cases. For the spilling breakers, the number of iterations seems to be lower in the more complex models such as the nonlinear $k-\epsilon$ and RSM. On the other hand, in the plunging breakers there is less variation in the number of iterations. However, the time per iteration for both types of breaker are consistent and generally follow the pattern expected; the RSM, which resolves all six components of the Reynolds Stress, takes longer to compute than the models which use the isotropic assumption. Overall, based on the two breaker types considered in this work, it appears that the nonlinear $k-\epsilon$ model is the most economical since it generally requires less iterations and the time per iteration is similar to the isotropic turbulence models.

To evaluate which of the turbulence closure models is the most accurate for surf zone dynamics, a skill score (SS) is applied. The SS determines whether a model is an improvement on a reference model by using the mean square error (MSE), defined as

$$\mathrm{MSE} = \frac{1}{N}\sum_{i=1}^{N}(x_i - y_i)^2, \tag{29}$$

where y_i is the experimental data and x_i is the results from the model. Following Murphy (1988), the skill score is then defined as

$$SS = 1 - \frac{\mathrm{MSE}_{\mathrm{model}}}{\mathrm{MSE}_{\mathrm{ref}}}. \tag{30}$$

		$k-\omega$	$k-\omega$ SST	RNG $k-\epsilon$	NL $k-\epsilon$	RSM
Spilling	η	0.2232	0.0684	0.4207	0.4147	0.3156
	$\overline{u}$	0.2110	0.4919	0.2897	0.7693	0.6569
	$\overline{k}$	0.7812	-0.0620	-0.2778	0.3669	-3.0165
Plunging	η	0.0127	-1.1789	-0.1630	-1.1572	-0.3372
	$\overline{u}$	0.4434	0.2770	0.2919	0.3713	0.2902
	$\overline{k}$	0.7143	0.6662	0.6587	0.8521	0.4936
Overall		0.3229	0.3609	0.2850	0.5474	0.4541

Table 7: Turbulence model skill score for surface elevation (η), time averaged velocity ($\overline{u}$) and TKE ($\overline{k}$). The skill score is calculated using the mean square error and the no turbulence model case is used as a reference.

Hence if the model has perfect prediction it will have $SS = 1$. If the SS is positive, the model is an improvement on the reference, $SS = 0$ gives results identical to the reference and a negative SS is a decrease in accuracy from the reference. In this work the reference is chosen as the case where no turbulence is assumed. Essentially the question that is being asked is whether it is beneficial to use a turbulence model, or whether assuming no turbulence actually yields more accurate results.

Table 7 gives the SS for surface elevation (η), time averaged velocity ($\overline{u}$) and TKE ($\overline{k}$). Each turbulence model is shown for both plunging and spilling breakers and is given an overall SS. Comparing the skill scores for spilling breakers it is clear that the use of any of the turbulence models considered in this study improves the accuracy of predictions of surface elevation and time averaged horizontal velocity. However, it is interesting to note that the predictions of TKE in some cases are high enough that it is more accurate to assume there is no turbulence rather than use a turbulence model. In particular the RSM, expected to perform the best, gives very poor performance for TKE despite having reasonable predictions for free surface and velocity. The nonlinear $k-\epsilon$ and $k-\omega$ models have positive skill score for all three criterion, implying that they are better than a dummy turbulence model in all areas. The RNG and nonlinear $k-\epsilon$ models give the best performance for free surface and undertow, respectively, whereas the $k-\omega$ predicts TKE most accurately.

The skill scores for the plunging breakers tell a slightly different story. The $k-\omega$ model is the only one to perform better than the dummy turbulence model in all three criteria, although it is only a slight improvement with regards to η. All of the other models have a negative skill score for free surface and is large in the case of the $k-\omega$ SST and nonlinear $k-\epsilon$ models implying they give significantly worse results compared to assuming there is no turbulence. However, the use of a turbulence model improves all results for velocity and TKE with the $k-\omega$ and nonlinear $k-\epsilon$ being the best models in these areas, respectively.

Overall, all of the turbulence models are an improvement over assuming zero turbulence in the surf zone both in terms of accuracy and numerical efficiency.

The RSM, which was initially expected to perform the best, had the second best skill score, influenced largely by the poor prediction of TKE under spilling breakers. Despite the $k-\omega$ performing better than the reference values in all three areas for both types of breaker, the nonlinear $k-\epsilon$ model comes out as the model with the highest skill score. It was also one of the more efficient models and hence it is logical to consider it to be the best turbulence closure model for application to surf zone dynamics out of the ones considered in this study. However, all the models still exhibit differences from the experimental data, in particular the under-estimate of TKE for plunging breakers and over-estimate for spilling breakers.

These differences raise the question of the benefit of using a complex model over a computationally cheaper option such as a depth-integrated model. Although it is possible to simulate breaking waves using a depth-integrated model through the use of dissipation terms, the breaking process cannot be fully reproduced since the model is unable to resolve the overturning of the free surface (Roeber and Cheung, 2012). A RANS solver, coupled with the VOF method, is able to resolve this highly-nonlinear process. As will be seen later in this Section, capturing this process leads to predictions of turbulence generation which agree qualitatively with laboratory observations. Further advantages of the CFD approach is that data can be gathered anywhere in the domain and the model can easily be adapted for more complex phenomena such as the interaction with structures.

To understand the variation in the predictions of the turbulence models considered in this study, instantaneous spatial maps are compared qualitatively to experimental investigations. Ting and Kirby (1994) found that TKE is transported seaward under the spilling breakers and the dissipation rate is slow, whereas under the plunging breaker TKE is transported landward and is dissipated within one wave cycle. Additionally, the TKE varies with depth in the spilling case, which is not evident under the plunging waves. Furthermore, Ting and Kirby (1995) found that under the crest of plunging breakers the turbulence intensity is largest and rapidly decreases after the wave passes so that the turbulence dies out between breakers. For plunging waves the rate of vertical mixing is large since turbulence is spread down by the large eddies, causing any turbulence created by the broken wave to saturate the entire depth in the inner surf zone. Ting and Kirby (1996) show that the mixing length of the spilling case is much smaller, suggesting that it lies somewhere in the region of 10-20% of the water depth. Particle Image Velocimetry data (PIV) presented by Huang et al. (2009) generally agrees with the observations of Ting and Kirby (1996) but indicates that TKE spreads to around half the water depth. Furthermore, the surface generated turbulence in spilling waves is spread slowly down, mainly through diffusion, whereas in the plunging case both advective and diffusive transport are important since the large eddies generated in the surface roller are advected behind the wave front.

Many of these observed characteristics are also evident in the present numerical model. In a RANS simulation, small scale features are not resolved but fluctuations from the mean flow are instead represented by an additional dissi-

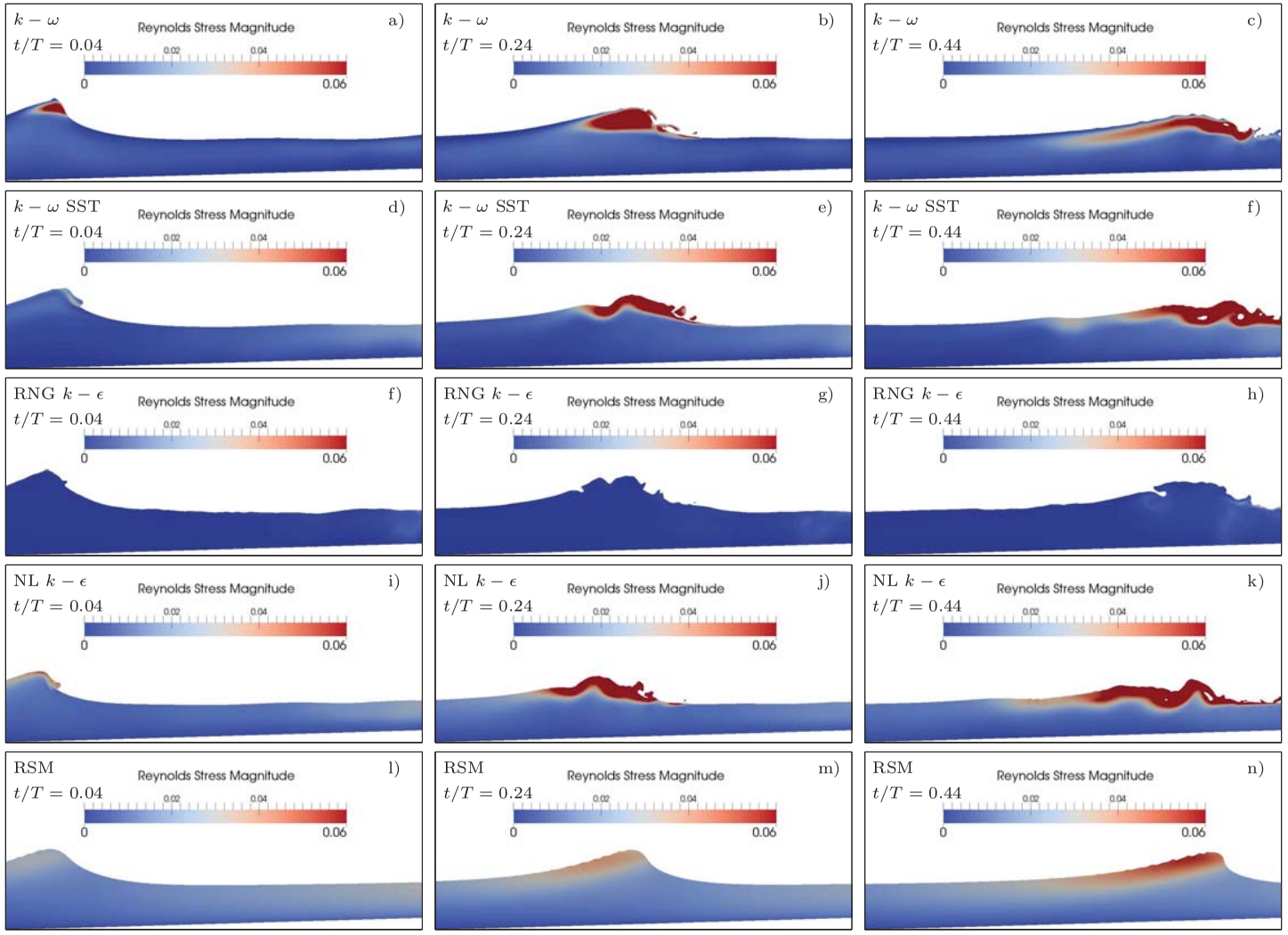

Figure 10: Example snapshots of the Reynolds stress (magnitude) distribution under spilling breakers with each row representing a different turbulence model. From left to right the columns show different phases of the wave: $t/T = 0.04$, 0.24 and 0.44, respectively.

pation term in the governing equations. This term is generally referred to as the Reynolds stress (see equation 6) and is related to the TKE, eddy viscosity and rate of strain of the flow. Therefore, for the current work, the Reynolds stress is a good indication of the presence of turbulence in the flow. Furthermore, it was found that the distributions of TKE and Reynolds stress (magnitude) followed very similar patterns for all of the turbulence models considered. Therefore, this allows qualitative comparison of the predicted (numerical) Reynolds stress with either TKE or Reynolds stress from experiments.

Figure 10 shows colour plots of the predicted Reynolds stress magnitude for spilling breakers using the different turbulence models (rows) at three different phases of the breaking process (columns). The phase $t/T = 0$ is considered to be the phase where breaking occurs. It is clear that both the magnitude and distribution of the Reynolds stress varies between the different turbulence models. The RNG $k-\epsilon$ model predicts smaller Reynolds stress magnitude than the other four models at all of the three times presented. However, there is a region near the right hand side of each plot where there is a relatively larger Reynolds stress, indicating that the turbulence from the previous wave has not dissipated. The other four models generate turbulence in the crest during the breaking process and as the wave passes the turbulence spreads slowly seaward and downwards, which is consistent with the observations of Ting and Kirby (1996) and the PIV experiments conducted by Huang et al. (2009). At the first breaking phase shown, the $k-\omega$ model predicts a large region of high Reynolds stress spanning the majority of the front of the wave crest. The $k-\omega$ SST and nonlinear $k-\epsilon$ models predict the Reynolds stress to be generated in the spilling region of the wave. The predictions from the $k-\omega$ and $k-\omega$ SST models in the other two phases of the wave ($t/T = 0.24$ and 0.44) indicate that the turbulence spreads to around 20% of the water depth, which is consistent with Ting and Kirby (1996) but conflicts with Huang et al. (2009). Conversely, the RSM and nonlinear $k-\epsilon$ predictions of Reynolds stress indicate that there is always a reasonable level throughout the water column. Furthermore, the distribution of the Reynolds stress predicted by the RSM, i.e. large turbulence throughout the wave, seems to lead to the wave not visibly breaking.

Figure 11 presents τ_{xz}, i.e. the horizontal-vertical component of Reynolds stress, under spilling breakers at $t/T = 0.44$. Each plot represents a different turbulence model; a) $k-\omega$, b) $k-\omega$ SST, c) RNG $k-\epsilon$, d) nonlinear $k-\epsilon$ and e) RSM. The $k-\omega$, $k-\omega$ SST and nonlinear $k-\epsilon$ predict similar distributions of τ_{xz}, and generally agree with experimental studies of weak hydraulic jumps, which are believed to be a simplified method to study the flow under spilling breakers in the inner surf zone (Misra et al., 2008). Like the experimental data for hydraulic jumps, there are two clear regions in the spilling breaker; the reverse flow region and the breaker shear layer region. In the reverse flow region τ_{xz} is much smaller than in the breaker shear layer, which is consistent with Misra et al. (2008). In the breaker shear layer, τ_{xz} is predominantly negative, with the largest magnitude occurring just below the free surface near the toe of the breaker, which agrees with experimental data (see Figures 18d and 19 of Misra et al. (2008)). Further similarities can be observed at the free surface

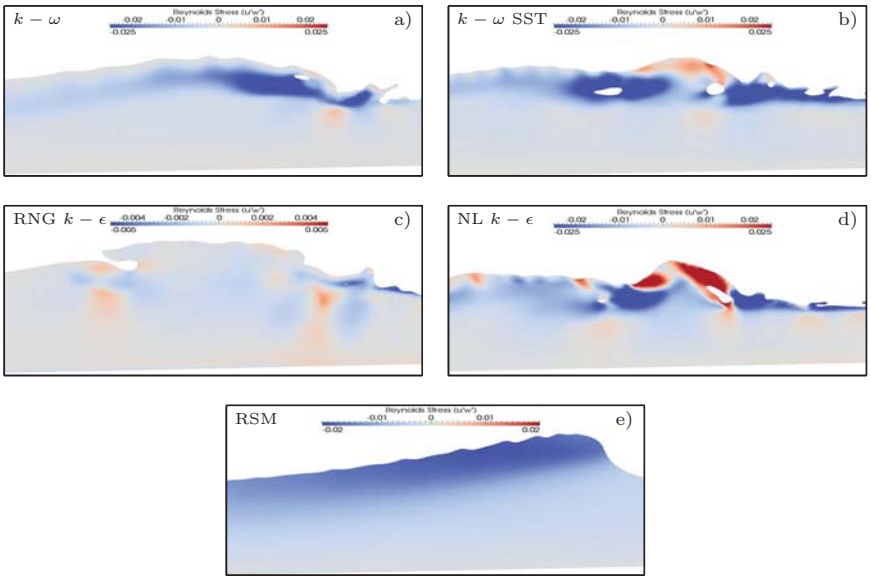

Figure 11: Snapshots of τ_{xz} under spilling breakers at $t/T = 0.44$. Each plot is a different turbulence model; a) $k-\omega$, b) $k-\omega$ SST, c) RNG $k-\epsilon$, d) nonlinear $k-\epsilon$ and e) RSM.

where a layer of positive τ_{xz} is present. At the toe, the breaker shear layer is relatively thin but behind the front the region of Reynolds stress spreads out to incorporate more of the water depth and decreases in magnitude. The width of the breaker shear layer was observed to be around 20% of the water depth by Misra et al. (2008), which is consistent with the predictions presented in Figure 11. Overall, the numerical model appears to have good qualitative agreement with experimental data for a similar flow, which both validates the current model and provides evidence that weak hydraulic jumps are a valid representation of spilling breakers.

Figure 12 presents similar spatial maps of the Reynolds stress magnitude as described in Figure 10 for the plunging breakers case. At the breaking point the predictions from the nonlinear $k-\epsilon$, $k-\omega$ SST and RSM model indicate that turbulence is generated from the impact of the overturning wave hitting the water and causing splash up. Conversely, the $k-\omega$ model predicts Reynolds stress to be generated throughout the crest of the wave as was observed in the spilling breaker. Another similarity to the spilling case is that the RNG $k-\epsilon$ model predicts the smallest Reynolds stress out of the turbulence models. However, the model predicts significantly larger regions of Reynolds stress, particularly in the areas where air has become trapped, and the turbulence spreads the whole depth of the water column as can be seen at the right hand side of the phase $t/T = 0.36$ (plot h). At phase $t/T = 0.2$ it is clear that any entrapped air leads to large Reynolds stress predictions by all of the models. The turbulence gener-

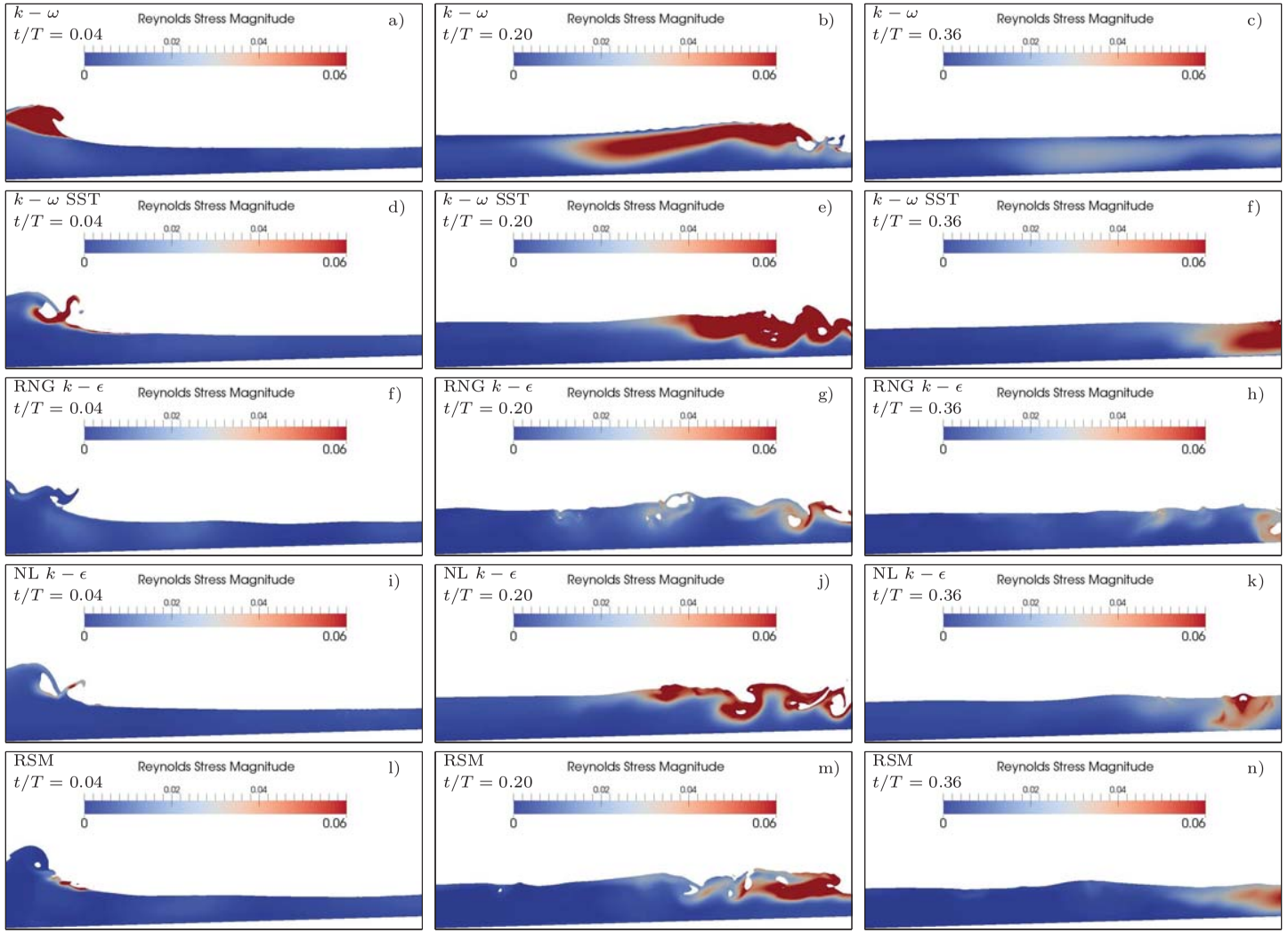

Figure 12: Example snapshots of the Reynolds stress (magnitude) distribution under plunging breakers with each row representing a different turbulence model. From left to right the columns show different phases of the wave: $t/T = 0.04$, 0.20 and 0.36, respectively.

ally remains with the wave front and can be seen to be advected with the flow. At the $t/T = 0.36$ phase, all of the models considered in this study predict the turbulence to spread over the whole water depth, which also agrees well with the description given by Ting and Kirby (1995). The PIV experiments of Kimmoun and Branger (2007), showed that the Reynolds stress saturates the water depth in the turbulent bore whilst little turbulence occurred below the trough level at the breaking point. This is consistent with all of the models considered in this study. Interestingly, the $k - \omega$ model has a region of Reynolds stress which breaks off from the wave front and remains in the water column (centre of plot c). The detached region resembles observations from PIV experiments of unsteady deep-water breaking waves (Melville et al., 2002; Drazen and Melville, 2009). The experimental results implied that the turbulence starts at the top of the water column and diffuses downwards after the wave has passed. Although only the magnitude is shown in Figure 12, the horizontal-vertical component τ_{xz}, is negative and is therefore consistent with downward transport of positive horizontal momentum and hence PIV experiments (Melville et al., 2002; Drazen and Melville, 2009). This region of turbulence occurs where there is a change between the positive velocity of the passing wave and the undertow preceding the next wave, and rapidly dissipates before the next wave occurs, similar to the observations of Ting and Kirby (1995).

Figures 13 and 14 show additional spatial maps of Reynolds stress magnitude at further phases of the breaking process for spilling and plunging breakers, respectively. The nonlinear $k-\epsilon$ model is used for this analysis since it has been shown to have the best overall skill score. At the breaking phase ($t/T = 0.00$), there is a large difference between the two breaking types. The spilling breaker has Reynolds stress already existing in the water column, whereas the plunging breaker has very little. This implies that the turbulence from the previous wave has dissipated in the plunging breaker, whereas it has not in the spilling breaker as was observed by Ting and Kirby (1994). Furthermore, there is a small amount of Reynolds stress existing in the water column under the spilling breaker prior to breaking, while it is not apparent in the plunging case. This could be due to turbulence being transported seaward as was noted in Ting and Kirby (1994).

Phases $t/T = 0.16$ to 0.32 show another characteristic observed by Ting and Kirby (1995, 1996). In the plunging breaker, as the surface roller develops, turbulence spreads rapidly downwards spanning the whole depth around phase $t/T = 0.24$. The turbulence rapidly dissipates after the surface roller has passed, explaining the small magnitude of Reynolds stress observed by the time the next wave arrives. On the other hand, there is a fairly large level of turbulence existing in the water column as the spilling breaker arrives. As the surface roller progresses down the wave flume, the turbulence generated in the spilling breaker slowly spreads seawards and downwards from the roller. This leads to larger concentrations near the surface, which decrease with depth. The majority of the turbulence is shown to be located in the near surface region as was observed in the experiments of Ting and Kirby (1995).

In the latter phases presented in Figures 13 and 14 ($t/T = 0.48$ to 0.56), it is clear that the turbulence rapidly dissipates once the surface roller has passed in

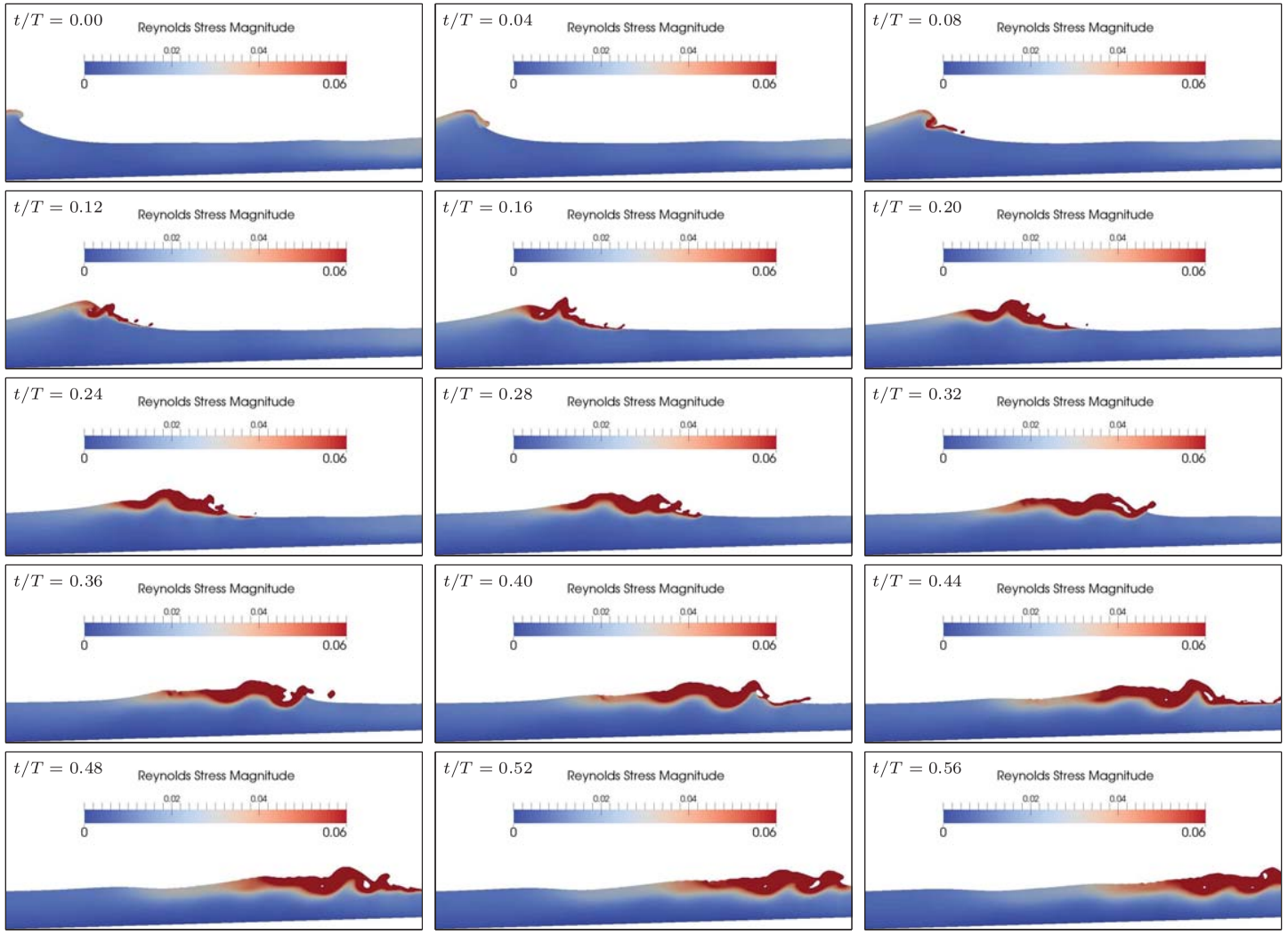

Figure 13: Snapshots of the nonlinear $k-\epsilon$'s predictions of the Reynolds stress (magnitude) distribution under the different phases ($t/T = 0$ to $t/T = 0.56$) of a spilling breaker.

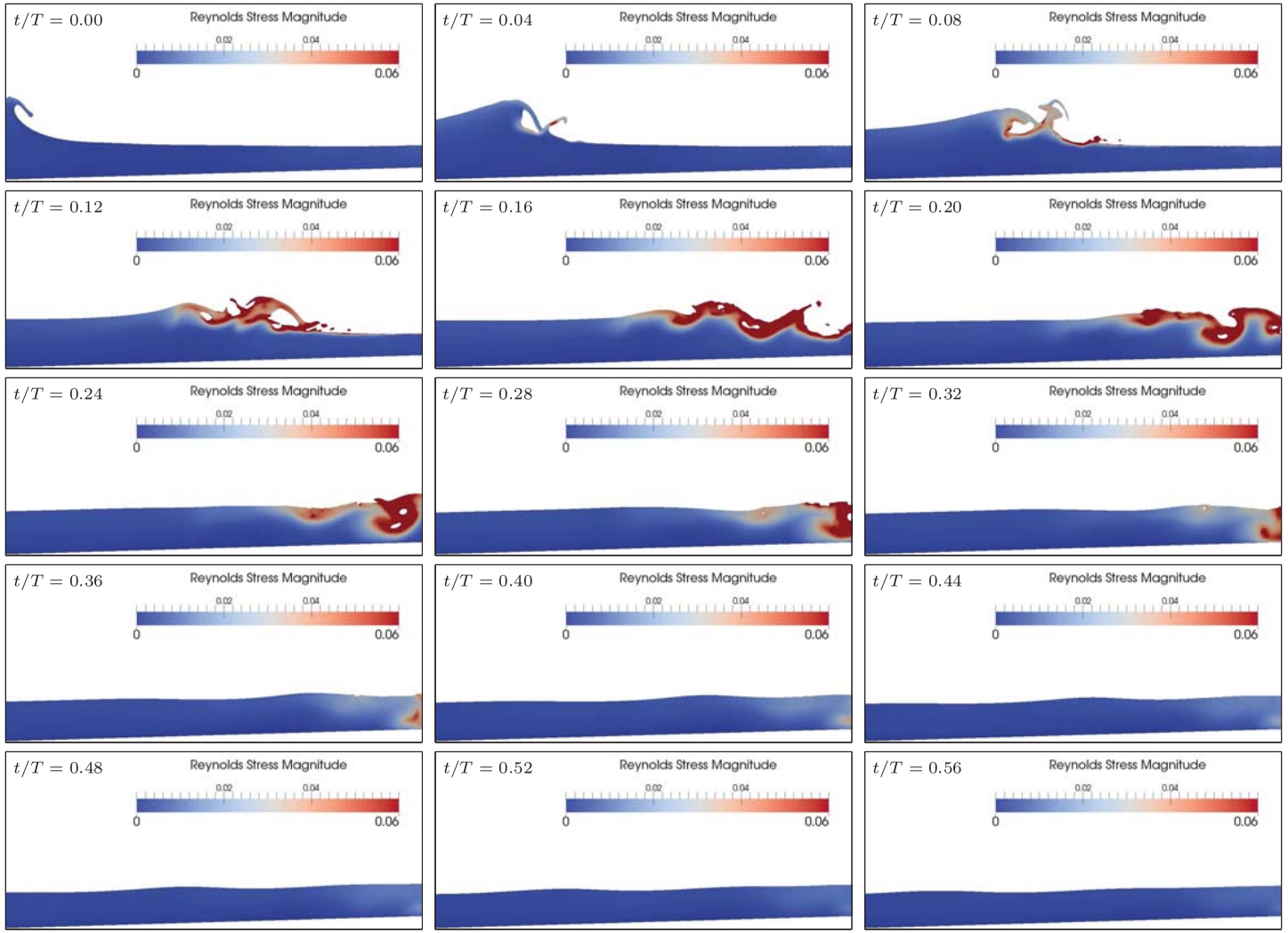

Figure 14: Snapshots of the nonlinear $k-\epsilon$'s predictions of the Reynolds stress (magnitude) distribution under the different phases ($t/T = 0$ to $t/T = 0.56$) of a plunging breaker.

the plunging breaker, whereas it spreads out behind the spilling breaker. This leads to turbulence from the previous wave interacting with the next wave. This could be due to the shorter period of the wave. Hence, in the future, it would be interesting to repeat the analysis on the two breaker types if the beach slope has been adjusted and wave period kept constant. In summary, the present numerical model generally predicts similar turbulent characteristics to those seen in laboratory experiments. The spatial maps also imply that a number of turbulence models used in this study agree qualitatively with experimental studies but require further research in order to gain better quantitative agreement.

5. Conclusion

In this work, a new library of turbulence closure models for multiphase flows has been evaluated for application to surf zone dynamics using the open source CFD software, OpenFOAM, along with the additional toolbox, waves2Foam. The models were averaged over twenty wave periods and compared to previous experimental data. The models were evaluated both in terms of accuracy (for surface elevation, velocity and TKE) and numerical efficiency using zero turbulence as a reference. It was found that using a turbulence model could significantly decrease the computational time since although each iteration took longer to compute, the simulation required less iterations.

To assess accuracy, a skill score based on the mean squared error was used in order to evaluate which of the turbulence models is the best. Interestingly, it was found that assuming no turbulence lead to more accurate predictions of TKE levels under spilling breakers than some of the turbulence models since they over-predicted these quantities significantly. However, using a turbulence model generally improved the free surface and undertow profiles in the spilling breakers. There appears to be a correlation between models which predict very little TKE prior to breaking and models which capture a negative gradient of velocity prior to breaking, as observed in the experiments. The RNG $k-\epsilon$ model is the only model to capture this profile shape in both plunging and spilling breakers. However, the nonlinear $k-\epsilon$ model captures the velocity profiles more accurately over the whole surf zone. For plunging breakers, using a turbulence model improves the TKE and velocity profiles but generally decreases the accuracy of the free surface predictions. Despite the RSM being expected to produce the best results, it gave very poor predictions of TKE in spilling breakers leading to a smaller skill score compared to the nonlinear $k-\epsilon$ model. The $k-\omega$ model was shown to be the only model to improve on the zero turbulence case in all criteria. However, in this study the overall best model for surf zone dynamics, both in terms of accuracy and numerical efficiency, was found to be the nonlinear $k-\epsilon$. Based on the skill score alone the ranking of the turbulence models would be:

1. Nonlinear $k-\epsilon$
2. RSM
3. $k-\omega$ SST

4. $k - \omega$
5. RNG $k - \epsilon$

Spatial maps of the Reynolds stress magnitude distribution were then used to compare the turbulence models predictions for both breaker types. The spilling breaker was shown to have good qualitative agreement with experimental data on weak hydraulic jumps. The nonlinear $k - \epsilon$ model was then shown to exhibit many of the features noted in the experimental data relating to the transport of turbulence under different breaker types. The turbulence spread over the whole water depth before rapidly dissipating prior to the arrival of the next plunging breaker. On the other hand, the spilling breakers turbulence spread seaward and only slowly diffused downwards. Slow dissipation in this case led to turbulence generated by a wave still existing in the water column when the following wave arrives.

In the future, it would be interesting to repeat the analysis on the two breaker types in cases where the beach slope has been adjusted and wave period kept constant. This would allow more thorough analysis as to the cause of the slow dissipation rate in the spilling breaker. Another interesting test would be to compare the results presented here to large eddy simulations, to see whether the results, in particular the TKE profiles, improve enough to justify the increase in computational effort.

Acknowledgements

The authors would like to thank the School of Marine Science and Engineering at Plymouth University for their financial support throughout this research. This work was conducted using the HPC facility at Plymouth University and the authors gratefully acknowledge Peter Mills for his continual support with this resource.

References

Battjes, J. A., 1974. Surf similarity. In: Proceedings of the 14^{th} International Conference on Coastal Engineering. pp. 466–480.

Bradford, S. F., 2000. Numerical simulation of surf zone dynamics. J. Waterw. Port. C-ASCE 126.

Brown, S. A., Magar, V., Greaves, D. M., Conley, D. C., 2014. An evaluation of rans turbulence closure models for spilling breakers. In: Proceedings of the 34^{th} International Conference on Coastal Engineering. Vol. 1. p. 5.

Christensen, E. D., Jensen, J. H., Mayer, S., 2000. Sediment transport under breaking waves. In: Proceedings of the 27^{th} International Conference on Coastal Engineering. Vol. III. pp. 2467–2480.

Drazen, D. A., Melville, W. K., 2009. Turbulence and mixing in unsteady breaking surface waves. J. Fluid Mech. 628, 85–119.

Falchetti, S., Conley, D. C., Brocchini, M., Elgar, S., 2010. Nearshore bar migration and sediment-induced buoyancy effects. Continental Shelf Research 30, 226–238.

Govender, K., Mocke, G. P., Alport, M. J., 2002. Video-imaged surf zone wave and roller structures and flow fields. J. Geophys. Res. 107 (C7), 9–1 – 9–21.

Huang, Z.-C., Hsiao, S.-C., Hwung, H.-H., Chang, K.-A., 2009. Turbulence and energy dissipations of surf-zone spilling breakers. Coastal Eng. 56, 733–746.

Iribarren, C. R., Nogales, C., 1949. Protection de ports. In: XVIIth Int. Nav. Congress,. Vol. II. pp. 31–80.

Jacobsen, N. G., 2011. A full hydro- and morphodynamic description of breaker bar development. Ph.D. thesis, Technical University of Denmark, Department of Mechanical Engineering, dCAMM Special Report, no. S136.

Jacobsen, N. G., Fuhrman, D. R., Fredsøe, J., 2012. A wave generation toolbox for the open-source CFD library: OpenFoam®. Int. J. Numer. Meth. Fluids. 70, 1073–1088.

Kimmoun, O., Branger, H., 2007. A particle image velocimetry investigation on laboratory surf-zone breaking waves over a sloping beach. J. Fluid Mech. 588, 353–397.

Launder, B. E., Reece, G. J., Rodi, W., 1975. Progress in the development of a reynolds-stress turbulence closure. J. Fluid Mech. 68 (3), 537–566.

Lin, P., Liu, P. L. F., 1998a. A numerical study of breaking waves in the surf zone. J. Fluid Mech. 359, 239–264.

Lin, P., Liu, P. L. F., 1998b. Turbulence transport, vorticity dynamics and solute mixing under plunging waves in surf zone. J. Geophys. Res. 103 (C8), 15677–15694.

Ma, G., Chou, Y., Shi, F., 2014. A wave-resolving model for nearshore suspended sediment transport. Ocean Modell. 77, 33–49.

Melville, W. K., Veron, F., White, C. J., 2002. The velocity field under breaking waves: coherent structures and turbulence. J. Fluid Mech. 454, 203–233.

Menter, F. R., 1994. Two-equation eddy-viscosity turbulence models for engineering applications. AIAA Journal 32 (8), 1598–1605.

Misra, S. K., Kirby, J. T., Brocchini, M., Veron, F., Thomas, M., Kambhamettu, C., 2008. The mean turbulent flow structure of a weak hydraulic jump. Phys. Fluids 20 (035106), 21pp.

Murphy, A. H., 1988. Skill scores based on the mean square error and their relationships to the correlation coefficient. Monthly Weather Review 116, 2417–2424.

OpenFOAM, 2014. The open source CFD toolbox. http://www.openfoam.com/.

Puleo, J. A., Holland, K. T., Plant, N. G., Slinn, D. N., Hanes, D. M., 2003. Fluid acceleration effects on suspended sediment transport in the swash zone. J. Geophys. Res. 108 (C11).

Rienecker, M. M., Fenton, J. D., 1981. A Fourier approximation method for steady water waves. J. Fluid Mech. 104, 119–137.

Roeber, V., Cheung, K. F., 2012. Boussinesq-type model for energetic breaking waves in fringing reef environments. Coastal Eng. 70, 1–20.

Shih, T. H., Zhu, J., Lumley, J. L., 1996. Calculation of wall-bounded complex flows and free shear flows. Int. J. Numer. Meth. Fl. 23, 1133–1144.

Speziale, C. G., Thangam, S., 1992. Analysis of an RNG based turbulence model for separated flows. Int. J. Eng. Sci. 30 (10), 1379–1388.

Ting, F. C. K., Kirby, J. T., 1994. Observation of undertow and turbulence in a laboratory surf zone. Coastal Eng. 24, 51–80.

Ting, F. C. K., Kirby, J. T., 1995. Dynamics of surf-zone turbulence in a strong plunging breaker. Coastal Eng. 24, 177–204.

Ting, F. C. K., Kirby, J. T., 1996. Dynamics of surf-zone turbulence in a spilling breaker. Coastal Eng. 27, 131–160.

van Rijn, L. C., 2007. Unified view of sediment transport by currents and waves. II: Suspended transport. J. Hydraul. Eng. 133 (6), 668 – 689.

Versteeg, H. K., Malalasekera, W., 1995. An Introduction to Computational Fluid Dynamics: The Finite Volume Method. Pearson Education Ltd.

Wilcox, D. C., 1988. Reassessment of the scale-determining equation for advance turbulence models. AIAA Journal 26 (11), 1299–1310.

Wilcox, D. C., 2006. Turbulence Modeling for CFD, 3rd Edition. DCW Industries, inc.

Xie, Z., 2013. Two-phase flow modelling of spilling and plunging breaking waves. Applied Mathematical Modelling 37, 3698–3713.

Yakhot, V., Thangam, S., Gatski, T. B., Orszag, S. A., Speziale, C. G., 1992. Development of turbulence models for shear flows by a double expansion technique. Phys. Fluids A 4 (7), 1510 – 1520.